PULSATILE FONTAN HEMODYNAMICS AND PATIENT-SPECIFIC SURGICAL PLANNING: A NUMERICAL INVESTIGATION

A Thesis
Presented to
The Academic Faculty

by

Diane de Julien de Zélicourt

In Partial Fulfillment
of the Requirements for the Degree
Doctor of Philosophy in the
School of Biomedical Engineering

Georgia Institute of Technology
May 2010

PULSATILE FONTAN HEMODYNAMICS AND PATIENT-SPECIFIC SURGICAL PLANNING: A NUMERICAL INVESTIGATION

Approved by:

Dr. Ajit P. Yoganathan, PhD, Advisor
Department of Biomedical Engineering
Georgia Institute of Technology, GA

Dr. Fotis Sotiropoulos, PhD, co-Advisor
Department of Civil Engineering
University of Minnesota, MN

Dr. Don P. Giddens, PhD
Department of Biomedical Engineering
Georgia Institute of Technology, GA

Dr. W. Robert Taylor, MD, PhD
Department of Biomedical Engineering
Georgia Institute of Technology, GA

Dr. Pedro J. Del Nido, MD
Department of Cardiothoracic Surgery
Children's Hospital Boston, MA

Dr. Kirk R. Kanter, MD
Division of Cardiothoracic Surgery
Emory University, GA

Dr Mark A. Fogel, MD
Division of Cardiology
Children's Hospital of Philadelphia, PA

Date Approved:

ACKNOWLEDGMENTS

A Ph.D. is not accomplished in one day, nor is it accompomplished by a single person alone. Now that the end draws closer, now that can let my mind wander freely, I want to take these few pages to thank all the people that stood by my side during these past eight years, through my Master's and Ph.D. degree. All the people who, here and away, inspired me, gave me support, and each one in his way helped me shape this research and my professional aspirations. One can safely say that as I finished high school hesitating between an engineering or a medical career, a Ph.D. or academic route never stood in the horizon of my aspirations. I guess that even as I enrolled in the Ph.D. program in 2005 the doubt subsisted. But, if I enrolled for the wrong reasons, I found a parsel of myself on the way and I would like to very sincerely thank the combined efforts of my advisor and co-advisor, Dr Yoganathan and Dr Sotiropoulos, who offered me all the tools and means needed to frame this thesis, nourish my scientific curiosity, and try to take one step towards the clinical needs. I truly believe that the decision to embark into this adventure was one of the best one I ever did. Research, teaching, mentoring, thinking a project through, overcoming roadblocks, are mind games and human interactions I truly enjoy and have learnt thanks to the two of you.

I would also like to thank Dr Fogel, Dr Kanter, Dr Giddens, Dr del Nido and Dr Taylor, for their support throughout my thesis research, for their critical inputs, and finally for seating on my thesis committee. Dr Don Giddens has followed my research

efforts since 2002, throughout my experimental Master's thesis and its numerical prolongation. Dr Fogel and Dr Kanter have both very closely followed the development of the patient-specific surgical planning framework, with a constantly renewed energy and interest. I have been very lucky to have worked with such an esteemed committee. Each one of them has helped me better identify not only my thesis research goals but frame more long-term perspectives and switch from an industry-oriented career towards a patient-oriented academic path.

This thesis is also addressed to all the surgeons and physicians who worked with us on the Fontan grant and whom I admire for their dedication to their patients and their availability and patience when it comes to answering our questions. Dr Fogel, Dr Whitehead, Dr Kanter, Dr del Nido, Dr. Sharma, Dr Marino, Dr Forbess, Dr Parks, to mention a few, were all a great help in bringing together engineering and medicine in this project.

I would like to express gratitude to Dr Yoganathan's assistants; the army of shadows without whom research would not be possible: Michelle Mayberry, Colly Mitchel, Lakeisha Wheaton, Cosetta Williams. They have done a great job of making making my life a lot easier. Special thanks also go to the departmental help, notably to Gail Spatt and Chris Ruffin; Gail for all the help she provided on the different NIH Grant submission and for always keeping a smile throughout the submission hoops; and Chris for constantly running after me to make sure I had filled in the appropriate paperwork. I would also like to sincerely thank the IT management team, Steven Marzec and Jesus

Mata-Acosta, without whom this thesis simply would not be, as I would never have had the computer capabilities to conduct the two to three hundred simulations reported herein.

My deepest thanks go to the multiple generations of students and post-docs whom I saw joining, leaving or staying (yes Jorge, but even the best ones have to leave) the cardiovascular fluid mechanics laboratory. Hélène, Jenni, Jorge, Hiroumi, Dave, Dennis, Yun, Suchitra, Kartik S., Bartik B., Ashley, Zhoaming, Chang Wang, Steffan, Kerem, Prasad, Leo, Chris, Maria, Erin, J.P., David, Brandon, Murali. Thank you to all of you, for you helped in all aspects of my research, and more importantly in all the life that goes around it. Endless meetings, heated debates, outings, tennis tournament, gossips and tension relievers. Special thanks go to Erin, because social events are indeed what keeps everythink together. To Chris, Kartik S. and Kerem for the long Grant writing nights and the great feeling of recess after submission. To Philsub Jung, who worked with me throughout his undergraduate years. To Hélène, Chris, and Franklin for reviewing my thesis with record turn-around times, and to the whole Fontan subgroup for suffering through my defense rehearsals without a sigh. And to all of you, who over the years became more than just co-workers, but also very close friends.

Five years is a chunk of life, and if it wasn't for my friends from engineering school and for the friends I met here, these years would have been a long and arid crossing. To Leon, Timo, Vivek, Sieur Oezbeck, Aensley, the homepark mice, and all my roommates, who made home a place to go back to. To the Atlanta Frenchies (or almost!), Marto, Gilou, Chlutz, Nathalie, Igor, Fred, Brett, Kheldar, Hélène, Dr Bridier, Aurelija,

Murali (India is almost France, isn't it?) and to all my friends from Polytechnique, Fred, Olive, d'Ju, Phiphi, Cédric, Tof, Yann, Matthieu and Marina, who provide me with infinite comfort, a hint of craziness and the will to reach far beyond. I would have liked to be able to list the the small details that make these friendships so dear and unique, but would not know where to start. I count on you to fill in the blanks, and see that beyond a simple list there is a gratitude that I cannot fully express.

Finally, I would like to thank all my family, who though spread out around the world, has always been present, providing unconditional support through good and hard times. I dedicate this thesis to my parents, Anne and Marc, brother and sister, Olivier and Claire, my two grand-mothers, Comtesse Gérard de Brosses and Vicomtesse Gaston de Zélicourt, the tiny newcomer, Margaux; and to one person who deserves this thesis maybe more than I do, Franklin Genin, my closest companion and husband. Dear mister Genin, thank you for your attention, your patience, for the last minutes cross-Atlantic flights, for putting up with my crankiness on days when things were not going all that well, for bringing a little "peacefulness" when the world stresses out, and having motivated me to enter this race. I have always been a long distance runner, but that one was quite a challenge I have to say!

In a word like in a thousand, to all of you who were there:

THANK YOU!!!

TABLE OF CONTENTS

LIST OF TABLES

LIST OF FIGURES

LIST OF ANIMATIONS

LIST OF ABBREVIATIONS

AC	artificial compressibility
AMR	adaptive mesh refinement
AP	atrio-pulmonary connection
BDG	bidirectional Glenn
CAD	computer-aided design
CFD	computational fluid dynamics
CHB	Children's Hospital Boston
CHD	congenital heart defect
CHOA	Children's Healthcare of Atlanta
CHOP	Children's Hospital of Philadelphia
CT	X-ray computed tomography
FGMRES	Flexible Generalized Minimal Residual Method
FSPP	fractional step pressure projection
GFD	global flow distribution
GMRES	Generalized Minimal Residual Method
HepV	hepatic veins
HF	hemi-Fontan
HFD	hepatic flow distribution
HLHS	hypoplastic left heart syndrome
IB	immersed-boundary method
IV	innominate vein

IVC	inferior vena cava
LA	left atrium
LPA	left pulmonary artery
LSVC	left superior vena cava
LV	left ventricle
MPA	main pulmonary artery
MRI	magnetic resonance imaging
PA	pulmonary artery
PAVM	pulmonary artero-venous malformation
PC MRI	phase contrast magnetic resonance imaging
PLE	protein losing enteropathy
PVR	pulmonary vascular resistance
RA	right atrium
RPA	right pulmonary artery
RV	right ventricle
SIIB	sharp-interface immersed boundary method
SV	single ventricle
SVC	superior vena cava
SVHD	single ventricle heart defect
TCPC	total cavopulmonary connection
True-FISP	true fast imaging with steady-steate precession (MRI sequence)
WU	Wood units

LIST OF SYMBOLS

$\vec{\mathbf{x}}$	position vector
t	physical time
τ	pseudo time (for artificial compressibility method only)
A_i	area of the cross-section i
D_i	equivalent diameter of cross-section i, defined as $D_i = 2\sqrt{A_i/\pi}$
$Q_i(t)$ and $\overline{Q_i}$	instantaneous and time-averaged flow rate through cross-section i
$\overline{U_i}$	mean velocity through cross-section i
$\vec{\boldsymbol{n}}$	local surface normal
ρ	fluid density
ν	kinematic viscosity of the fluid
c_0	wave propagation speed in the fluid (for artificial compressibility method only)
Re	Reynolds number
$\vec{\mathbf{u}}$ and $\vec{\mathbf{v}}$	velocity vector (the two different denomination describe the staggered and non-staggered velocity vectors when the distinction is relevant)

p	static pressure
$\mathbf{T}$	shear stress tensor
$\vec{\mathbf{F}}$	external forces
$\vec{\mathbf{F}}_C$	convective fluxes
$\vec{\mathbf{F}}_V$	viscous fluxes
Conv	convective flux derivatives
Visc	viscous flux derivatives
∇	spatial derivative operator.
$\Delta x_m \ (m = 1,2,3)$	grid spacing in the three spatial directions
$[\ ]^n_{(i,j,k)}$	quantity associated with the Cartesian grid cell in *(i,j,k)* at time step *n*
SU	array mapping the structured grid index to its unstructured counterpart
US	array mapping the unstructured grid index to its structured counterpart
$\dot{E}$	power losses (or energy dissipation rate)
$Q_{Hep\rightarrow RPA}$ and $Q_{Hep\rightarrow LPA}$	hepatic flow rate that exits through the RPA and LPA
HFD_{RPA} and HFD_{LPA}	portion (in %) of the hepatic flow rate that exits through the RPA and LPA

SUMMARY

Single ventricle heart defects, where systemic and pulmonary venous returns mix in the single functional ventricle, represent the most complex form of congenital heart defect, affecting 2 babies per 1000 live births. Surgical repairs, termed "Fontan Repairs," reroute the systemic venous return directly to the pulmonary arteries, thus preventing venous return mixing and restoring normal oxygenation saturation levels. Unfortunately, these repairs are only palliative and Fontan patients are subjected to a multitude of chronic complications. It has long been suspected that hemodynamics play a role in determining patient outcome. However, the number of anatomical and functional variables that come into play and the inability to conduct large scale clinical evaluations, due to too small a patient population, has hindered decisive progress and there is still not a good understanding of the optimal care strategies on a patient-by-patient basis.

Over the past decades, image-guided computational fluid dynamics (CFD) has arisen as an attractive option to accurately model such complex biomedical phenomena, providing a high degree of freedom regarding the geometry and flow conditions to be simulated, and carrying the potential to be automated for large sample size studies. Despite these theoretical advantages, few CFD studies have been able to account for the complexity of patient-specific anatomies and *in vivo* pulsatile flows.

In this thesis, we develop an unstructured Cartesian immersed-boundary flow solver allowing for high resolution, time-accurate simulations in arbitrarily complex geometries, at low computational costs. Combining the proposed and validated CFD solver with an interactive virtual-surgery environment, we present an image-based

surgical planning framework that: a) allows for in depth analysis of the pre-operative *in vivo* hemodynamics; b) enables surgeons to determine the optimum surgical scenario prior to the operation. This framework is first applied to retrospectively investigate the *in vivo* pulsatile hemodynamics of different Fontan repair techniques, and quantitatively compare their efficiency. We then report the prospective surgical planning investigations conducted for six failing Fontan patients with an interrupted inferior vena cava and azygous continuation. In addition to a direct benefit to the patients under consideration, the knowledge derived from these surgical planning studies will also have a larger impact for the clinical management of Fontan patients as they shed light onto the impact of caval offset, vessel flaring and other design parameters upon the Fontan hemodynamics depending on the underlying patient anatomy. These results provide useful surgical guidelines for each anatomical template, which could benefit the global surgical community, including centers that do not have access to patient-specific surgical planning interfaces.

CHAPTER 1

INTRODUCTION

1.1 Single Ventricle Heart Defects and Surgical Repairs

Single ventricle congenital heart defects (SHVD) affect about 2 babies per 1000 live births. In these patients, the oxygenated blood coming from the lungs and the deoxygenated blood coming back from the rest of the body mix in the single ventricle leading to acute hypoxia and death if left untreated. The concept of a total right ventricular bypass, first introduced by Fontan and Baudet in 1971 [1], is a palliative surgical procedure aimed at separating the systemic and pulmonary circulations thereby eliminating venous blood mixing. In its current form the Fontan procedure is performed in three stages, ultimately resulting in what is called a total cavopulmonary connection (TCPC) where the inferior (IVC) and superior (SVC) vena cavae are anastomosed directly onto the pulmonary arteries (PAs) thus bypassing the right side of the heart and preventing cyanotic blood mixing in the single ventricle.

1.2 Long-Term Complications

Since its inception, modifications of the Fontan procedure have steadily improved surgical outcomes, reducing the post-operative mortality to the level of simpler congenital heart disease repairs. However, the marked improvement in surgical outcome is balanced by the numerous and serious long-term complications encountered by the Fontan patients, including congestive heart failure, progressive ventricular dysfunction,

atrial arrhythmias, atrioventricular valve regurgitation, pulmonary arteriovenous malformation (PAVMs), diminished exercise capacity, protein losing enteropathy (PLE), somatic growth retardation, thrombotic complications, and poor neurodevelopmental outcomes [2-4]..

1.3 Impact of theTCPC on the Long-Term Patient Outcome

While the etiology of these complications is multi-factorial, the hemodynamics of the TCPC determined by its design and surgical construction have a predominant impact on the patient outcomes. Elevated TCPC resistances have been shown to limit cardiac output and exercise capacity. Orientation and relative position of the IVC and SVC at the center of the connection have a predominant impact upon the distribution of blood flow and nutrients to the lungs, which will in turn dictate whether a patient is prone to PAVMs or not. Flow disturbances within the TCPC construct increase energy dissipation and may yield unphysiologic fluid stresses on blood elements, ultimately resulting in thrombus formation. Optimization of the TCPC hemodynamics via its design is thus a critical step towards alleviating the long term complications observed in SVHD patients and improving long-term clinical outcome.

1.4 Optimization of the TCPC Hemodynamics

Several options have been discussed in literature regarding the optimal TCPC implementation, suggesting the inclusion of IVC-SVC offset [5], vessel curvature[6], flaring of the anastomosis site [7, 8], or the use of Y-shaped IVC grafts [9, 10]. However, with the refinement of the clinical and bioengineering investigation methods, it has now

become clear that the anatomical variability between patients calls for a patient-specific optimization of the TCPC design and hemodynamics. Virtual-reality simulators that reproduce the surgical gesture, coupled with physics-driven computational fluid dynamics (CFD) solvers, offer a unique platform for surgeons to pre-operatively optimize their surgical procedure on a patient-specific basis. Nonetheless, such patient-specific surgical planning approach still requires significant technical innovations on both the virtual modeling and CFD fronts, and its feasibility within clinically practical resources and time-frame has yet to be demonstrated.

1.5 Numerical Modeling Challenges

From the CFD end in particular, a major challenge stems from the complexity of the *in vivo* anatomies, and the number of parameters to be modeled. *In vivo* flows typically take place in multi-connected, tortuous vessels, with moving walls, pulsatile inflows, and feature non-Newtonian behavior and a host of flow regimes ranging from laminar to transient and fully-developed turbulence. Modification of the patient's anatomy during surgery not only affects the local hemodynamics but also often results in remodeling of peripheral organs, which in turn impacts the inflow and outflow boundary conditions of the domain under consideration. Surgical planning CFD simulations thus have to call upon number of simplifications, which ought to be carefully reviewed in order to assess the relevance of the predicted performances and determine the parameters that may or may not be disregarded in favor of faster simulations and increased number of tested virtual-surgery options. In the TCPC realm, simulations have commonly assumed one or several of the following: simplified geometries, rigid walls and steady

inflow/outflow conditions. While idealized geometries obviously cannot account for the diversity of the *in vivo* anatomies the impact of the other parameters is less clear. Preliminary studies have modeled uniformly elastic walls [11] and pulsatile inflow conditions [12, 13], pointing to the latter as having a larger impact upon the predicted TCPC performance. However, the question as to whether modeling pulsatile inflows is critical for the comparative performance of different surgical options remains open.

1.6 Objective of this Thesis Work

This thesis thus seeks to develop a fully-validated numerical flow solver that will allow for pulsatile 3D flow simulations in patient-specific TCPCs to quantify the impact of pulsatility across different TCPC options, and that could be used to conduct patient-specific surgical planning studies within clinical timeframe and resources.

1.7 Summary of Results

In the first specific aim, we devise a novel unstructured Cartesian immersed-boundary approach to tackle the geometrical intricacies of *in vivo* cardiovascular anatomies, and accurately capture the unsteadiness of associated blood flows. The accuracy and computational efficiency of the proposed numerical approach is demsontrated by carrying out systematic mesh refinement studies for several internal flow problems ranging in complexity from flow in a 90 degree pipe bend to flow in patient-specific TCPC anatomies, and comparing our results to experimental measurements obtained in the same geometries under both steady and pulsatile inflow conditions.

This numerical framework is then applied in a two-pronged approach, classified in two independent specific aims: (Aim 2) to probe the pulsatile *in vivo* TCPC hemodynamics and understand the impact of pulsatility on the predicted efficiency metrics; and (Aim 3) to establish of a novel surgical planning approach based on hemodynamic performance and demonstrate its potential benefits to treat patients with complex SVHDs. Finally, by reviewing the experience gained during the patient-specific pulsatile and surgical planning investigations, we seek to derive surgical guidelines for specific anatomical templates, thus expanding the clinical and patient community that may benefit from this study.

CHAPTER 2

BACKGROUND AND SIGNIFICANCE

This chapter provides a brief background on the physiology of the normal heart before focusing on congenital single ventricle heart defects. The efforts made to improve the outcome of patients born with such defects are then discussed in details laying the ground for the current study.

2.1 Normal Cardiovascular System

Blood is a major means of transportation for the nutrients and wastes that travel to and from our tissues. It is pumped through our entire body by the heart and perfuses each single tissue through a complex network of arteries, capillaries and veins, called the cardiovascular circulation. This cardiovascular circulation can be subdivided into two primary circuits: the pulmonary and systemic circulations (Figure 2-1). The pulmonary circuit describes the blood pathway going from the right side of the heart to the lungs and back to the left side heart, while the systemic circulation transports the blood between the heart and the remainder of the body.

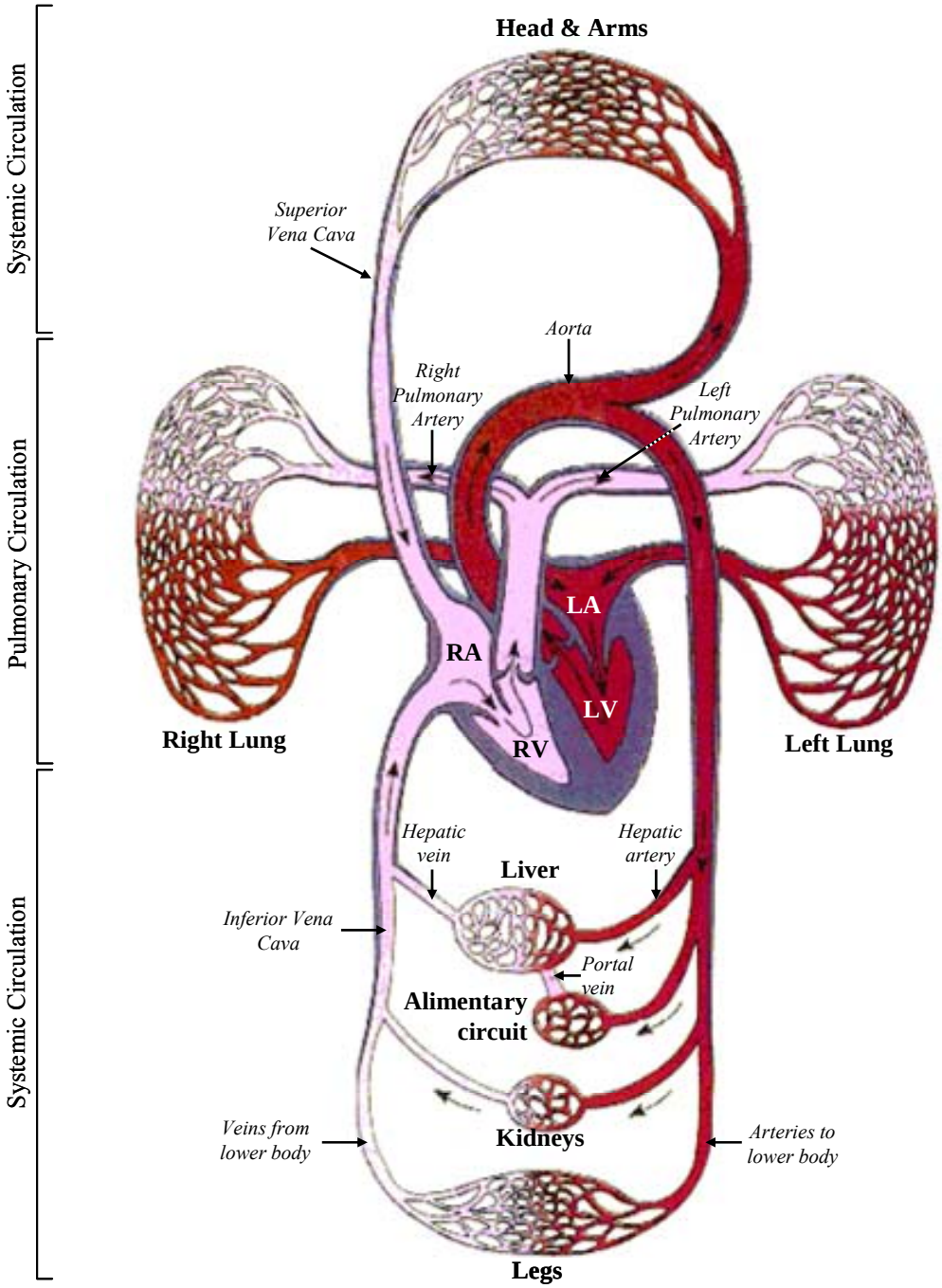

Figure 2-1: Schematic of the two primary circuits of the human blood circulation. The pulmonary circuit drives the blood from the heart to the lungs and back to the heart while the systemic circulation transports the blood to and from the rest of the body. RA and RV: Right atrium and right ventricle. LA and LV: Left atrium and ventricle. (Image courtesy: [1])

In a normal physiology as shown in Figure 2-2, the blood through the systemic circuit is driven by the left side of the heart while the blood through the pulmonary circuit is driven by the right side. The septum separates the right and left sides creating two distinct pumps that function in series (Figure 2-3, left panel). Each side of the heart consists of two chambers, an atrium and a ventricle. This four-chambered structure of the heart is essential to its function. The ventricles provide the pumping force while the atria provide the buffer volume needed to receive the continuous blood flow returning from the body or the lungs. In addition to these four chambers, four valves control the inlet and outlet of both ventricles to prevent blood flow reversal and ensure the efficiency of the ventricular contraction. When the left ventricle (LV) contracts during systole, the increase in ventricular pressure closes the bileaflet mitral valve and forces the trileaflet aortic valve open. Consequently, the blood that was present in the left ventricle before systolic contraction flows from the left ventricle through the open aortic valve into the aorta then to the rest of the body. As pressure builds up in the aorta and decreases in the left ventricle, the aortic valve closes. Meanwhile, the blood returning from the lungs through the pulmonary veins is stored in the left atrium (LA). Left atrium pressure increases and the mitral valve reopens. Blood then flows from the left atrium through the mitral valve into the left ventricle during diastole.

Similarly, the systemic blood coming back from the body flows through the inferior vena cava (IVC) and superior vena cava (SVC) into the right atrium (RA). It then passes through the tricuspid valve into the right ventricle (RV) from where it is discharged through the trileaflet pulmonary valve into the pulmonary circulation towards the lungs for gas exchange.

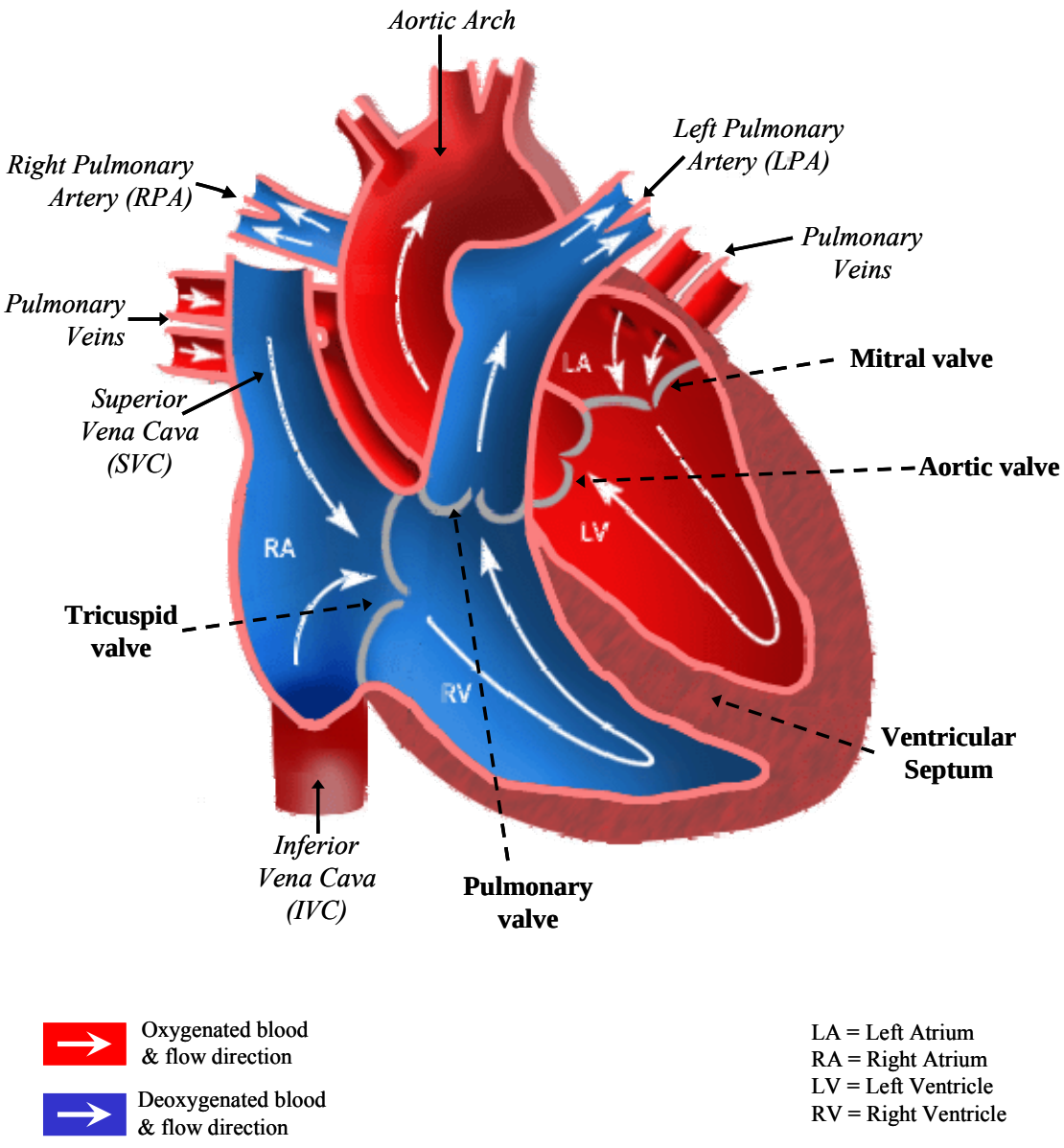

Figure 2-2: Schematic of a normal heart. (Image courtesy: [2])

2.2 Congenital Heart Defects (CHDs)

Congenital heart defects (CHDs) describe all abnormalities of the heart's structure that are present at birth. These may involve defects in the heart muscle, in the heart valves, or in the great arteries and veins that are directly connected to the heart. CHDs arise from faulty embryogenesis between the third and eighth week of gestation, when all the major cardiovascular structures develop, normally going from a simple straight tube to a complex four-chambered heart. Over 40 different forms of CHDs have been reported, ranging from asymptomatic malformations to complex life-threatening defects [3]. The most prevalent forms of CHDs are listed in Table 2-1. The incidence of children born with one or a combination of such defects is about 8 in every 1,000 live births in the United States, making CHDs the most common type of birth defect [4].

Table 2-1: Frequencies of congenital heart defects [5]

CHD	% of all CHD
Ventricular Septal Defects (VSD)	33
Patent Ductus Arteriosus (PDA)	10
Pulmonary Stenosis (VS)	10
Tetralogy of Fallot	9
Aortic Stenosis (AS)	8
Coarctation of the Aorta	5
Atrial Septal Defect (ASD)	5
Transposition of the Great Arteries	5
Atrioventricular Septal Defect	4
Truncus Arteriosus	1
Tricuspid Atresia	1
Total Pulmonary Venous Connection (TPVC)	1
Others	8

Most CHDs are cyanotic in nature, meaning that the heart's ability to pump blood and deliver oxygen to the different tissues in the body is compromised. Typical clinical symptoms include labored breathing, fast heart rate, and a cool and clammy skin. More severe forms may lead to higher degrees of cyanosis with the skin, lips and nailbeds taking a bluish color. Little is known about the cause of most CHDs, and to date, there is no known prevention or cure for any of these diseases. More than half of the children born with a CHD will require at least one invasive surgery in their lifetime [3]. Yet, with the progresses in diagnosis and treatment, most of these CHDs can be treated with an excellent prognosis. Unfortunately, the short and long-term prognosis for the more complex forms of CHDs drastically falls behind that statistic, maintaining CHDs as the number one cause of all infant deaths in the United States, and the number one cause of birth defect related death worldwide [3].

2.3 Single Ventricle Heart Defects (SVHD)

Particularly challenging from a clinical and surgical standpoint are the defects (or combination of defects) observed in about 25% of the CHD patients, which effectively lead to a single-ventricle anatomy and physiology. These defects, which are commonly grouped under the term of single ventricle heart defects (SVHD), result in a cardiovascular configuration where the heart no longer functions as two separate right and left pumps but rather as a single one driving blood to both pulmonary and systemic circuits (Figure 2-3). The ability of the single ventricle to drive blood to both body and lungs depends on the presence of shunts or septal defects allowing for a communication between the pulmonary and systemic circuits. However, these pulmonary to systemic

connections also lead to a significant amount of mixing between the oxygenated and deoxygenated blood causing SVHD patients to be severely cyanotic and for most cases to require surgical interventions within the first years of life. These defects constitute the most complex forms of CHD and mortality rates are quite high despite significant progress in patient treatment and management.

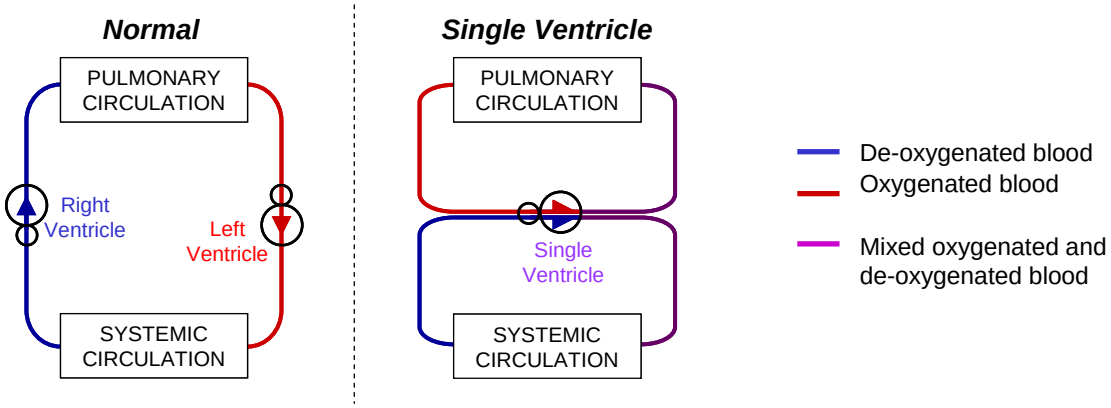

Figure 2-3: Schematic showing the human blood circulation in a single ventricle physiology (right panel) as opposed to the normal physiology (left panel).

The most prevalent forms of CHDs leading to a SV anatomy include hypoplastic left or right heart syndrome, tricuspid or mitral valve atresia, transposition of the great arteries, and a double inlet ventricle. These often occur with other concomitant defects. The tetralogie of Fallot, for example, describes the concurrent presence of a ventricular septal defect, overriding aorta, pulmonary outflow track obstruction and right ventricular hypertrophy. Atrioventricular canal defects or double outlet right ventricle may also lead to a SV anatomy when complicated by an underdeveloped ventricle. While all SVHD yield to common symptoms, such as increased cyanosis, it is important to realize that the

underlying anatomy can drastically differ from patient to patient. The structure of the single ventricle may resemble the normal left or the normal right ventricle, or neither. Surrounding vascular structures may be affected or not. All of these considerations will not only impact the ease with which a surgeon may perform the necessary repairs but also impact the long-term prognosis of these patients. The following sections thus review different forms of SVHD, with a special focus on some of the most complex forms, which are typically where advances in biomedical research are the most needed.

2.3.1 Tricuspid Atresia and Hypoplastic Right Heart Syndrome

Tricuspid atresia accounts for 1-2% of all CHDs [6]. In these patients, the tricuspid valve, which lies between the right atrium and right ventricle, is either inexistent or closed with the three leaflets sealed into a single structure (Figure 2-4). The occlusion of the blood pathway between the right atrium and right ventricle typically results in an underdeveloped right ventricle, and single functional left ventricle. Survival right after birth depends on the presence of other compensatory defects allowing the blood to bypass the malfunctioning right ventricle. This is illustrated in Figure 2-4 where the systemic blood flows from the right to the left atrium through an atrial septal defect. A ventricular septal defect then allows a portion of the mixed oxygenated and de-oxygenated blood to flow back into the right ventricle and pulmonary circulation.

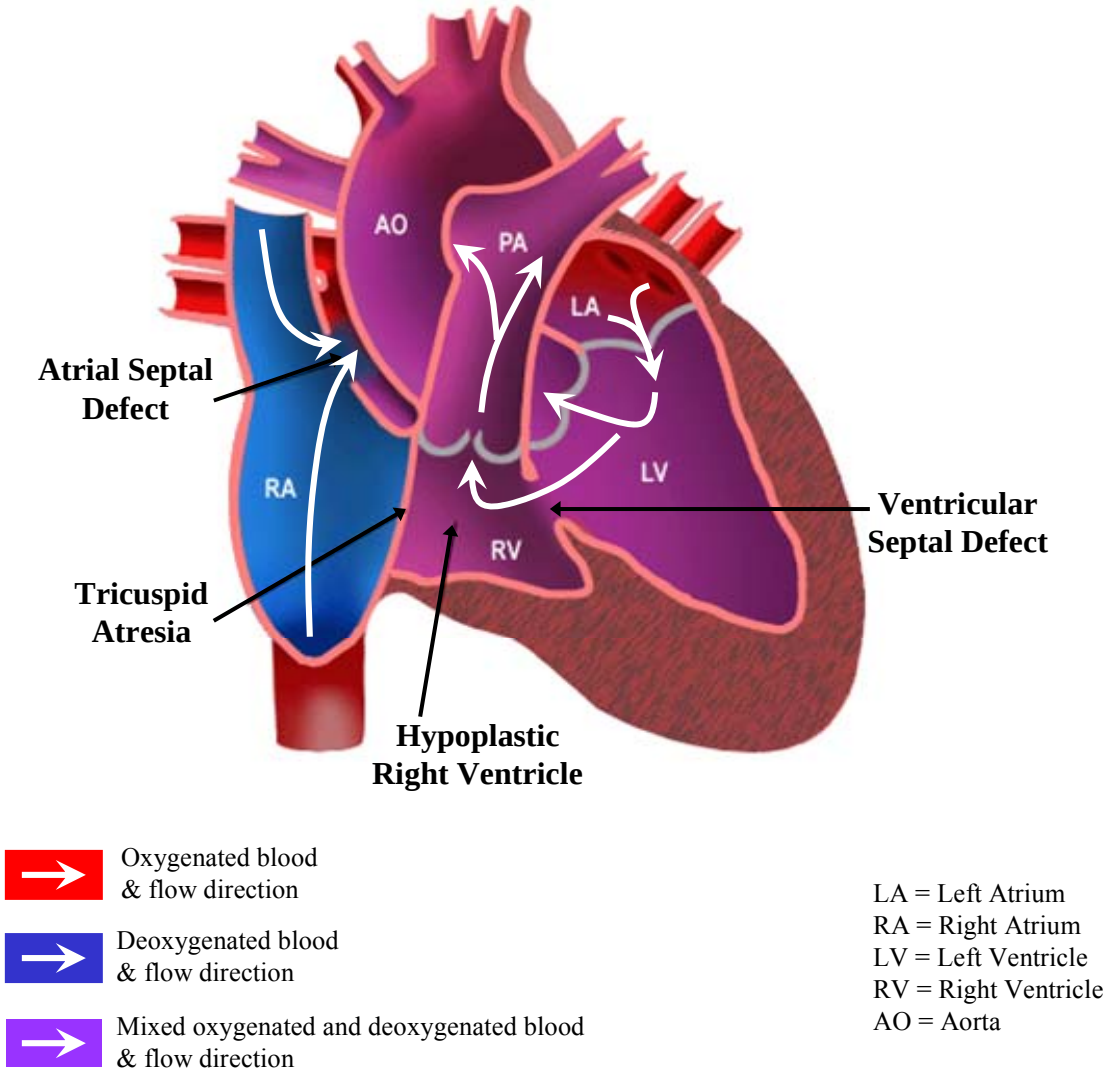

Figure 2-4: Extreme case of tricuspid atresia where the tricuspid valve is inexistent. As a result of the inexistent atrio-to-ventricular flow the right ventricle is hypoplastic, leading to a case of SVHD. Atrial and ventricular septal defects allow the left ventricle to pump to both pulmonary and systemic circuits. (Image courtesy: [6])

2.3.2 Hypoplastic Left Heart Syndrome

Hypoplastic left heart syndrome (HLHS) is one of the most severe forms of single ventricle disease. In this defect, the left side of the heart, including the ventricle, mitral and aortic valves and the aortic root, is under developed. In severe cases of HLHS, the left ventricle is unable to pump blood and survival at birth depends on the existence of other compensatory defects. Such a situation is well illustrated in Figure 2-5. As the left ventricle is unable to fulfill its pumping action, the oxygenated blood returning from the lungs flows from the left atria to the right through an atrial septal defect. A patent ductus arteriosus, shunting the pulmonary arteries to the descending aorta, then allows a portion of the blood pumped by the right ventricle to flow into the systemic circulation.

One of the most detrimental aspects of HLHS compared to other forms of SHVD is that the right ventricle is in charge of pumping blood to the high resistance systemic circuit. In a normal biventricular anatomy, this role is imparted to the left ventricle, which is strong and muscular, while the right ventricle is optimized for the low resistance pulmonary circuit. This makes HLHS the most debilitating form of SHVD, with 100% mortality rate within the first year of birth if left untreated [7].

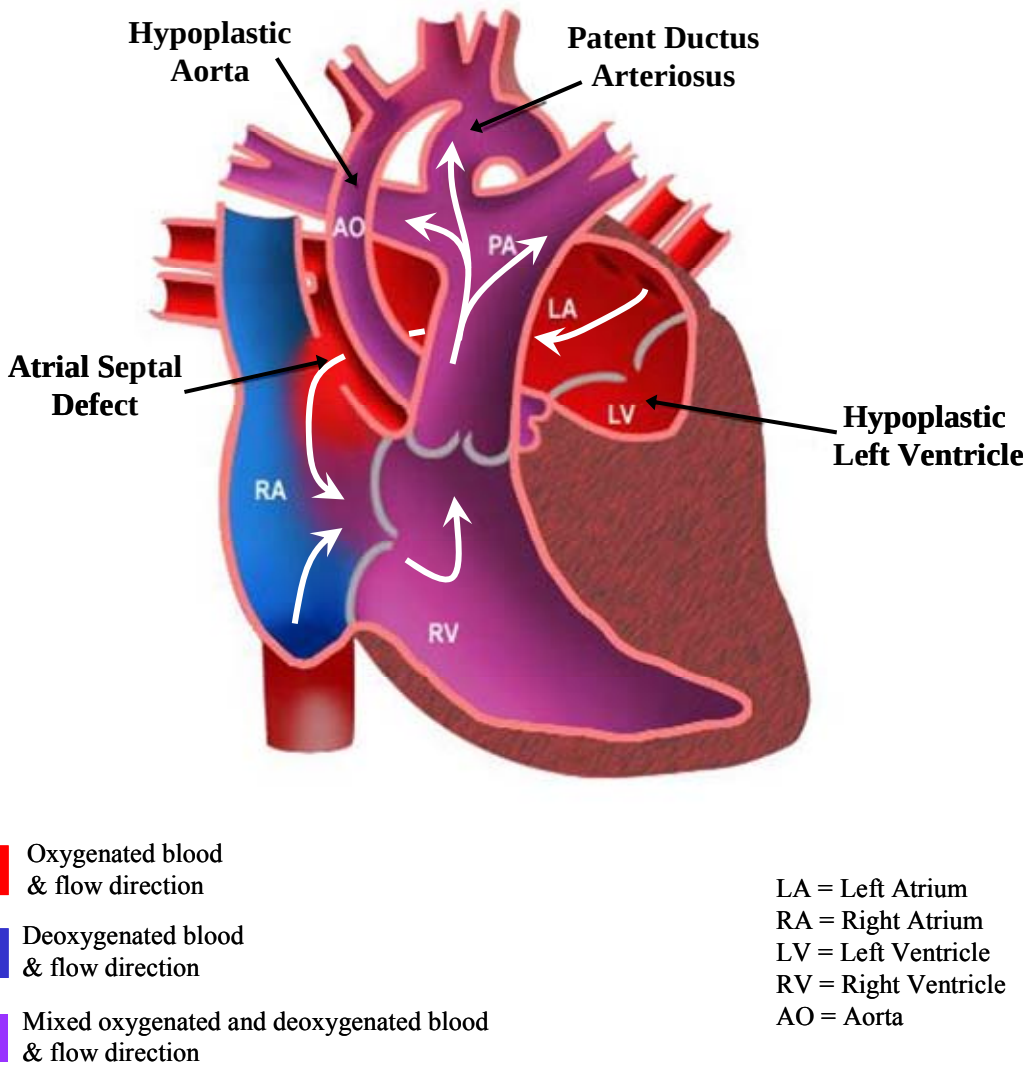

Figure 2-5: Hypoplastic Left Heart Syndrome (HLHS) associated with an atrial septal defect and a patent ductus arteriosus. (Image courtesy: [2])

2.3.3 SVHD Combined with Heterotaxy Syndrome

Heterotaxy syndromes, or situs ambiguous, are rare CHDs, where the configuration of the thoracic and abdominal organs is indeterminate. Though heterotaxy patients actually span the whole spectrum of organ orientations, heterotaxy syndromes tend to fall into two primary subtypes, namely (1) right atrial isomerism, or asplenia syndrome, and (2) left atrial isomerism, or polysplenia syndrome. In right atrial isomerism, the visceral structures tend to resemble the normal right side. The two atrial appendages have the morphologic features of a right atrium (broad-based triangular shape). There usually are two sinus nodes and absence of coronary sinus. The liver is midline, the spleen absent, and both lungs have 3 lobes. The descending aorta and IVC are on the same side of the spine. On the opposite, in left atrial isomerism, the visceral structures tend to resemble the normal left side. The two atrial appendages have the long, tubular appearance with a narrow neck that is typical of the left atrium, and the sinus node may be absent. Patients typically feature two-lobed lungs on both sides, and multiple spleens. Left isomerism is also typically associated with abnormal systemic venous connections. Interruption of the IVC with azygous continuation to the SVC is reported in most cases [8], and more than half of the patients feature persistent left superior vena cava (LSVC).

Both types of isomerisms are almost always associated with complex intra-cardiac CHDs [9]. In a retrospective study on 163 patients with left isomerism, Gilljam and colleagues [8] report that only 22 of them had normal intra-cardiac structures while 141 had concomitant intra-cardiac CHDs, including atrial septal defects (n=135), ventricular septal defects (n=111), and hypoplastic left or right ventricle (n=70). Survival rates at 10

years ranged from approximately 80% for the 22 patients with normal intra-cardiac structures down to 40% for patients with concomitant SVHD. As a result of the large number of cardiovascular and gastro-intestinal abnormalities, SVHD combined with heterotaxy syndromes represent one of the most challenging forms of SVHD to manage.

2.4 Surgical SHVD Repairs

2.4.1 Historical Perspective on SVHD Repairs

Without surgical intervention, survival of SVHD patients once depended on the presence of defects such as a septal defect or a patent ductus arteriosus (Figure 2-4) allowing for the single ventricle to pump blood to both systemic and pulmonary circuits. The first surgical repairs attempted on SVHD patients stemmed from that very observation. Noticing that Tetralogy of Fallot patients with a concomitant patent ductus arteriosus lived longer than those without, Taussig, Blalock and Thomas developed in 1945 a surgical shunt procedure that mimicked the effect of the patent ductus by connecting the subclavian artery to the PAs [10]. However, despite the increased pulmonary blood flow through the shunt, arterial oxygen saturation levels remained low due to blood mixing in the single-ventricle. Furthermore, placing the systemic and pulmonary circulations in parallel subjected the single ventricle to a chronic volume overload, ultimately leading to congestive heart failure.

The advent of the Fontan operation in 1971 [11] brought about a revolution in the management of SVHD. The procedure as it was originally described by Fontan and Baudet consisted in a complete bypass of the right side of the heart achieved by constructing two independent SVC-to-RPA and IVC-to-LPA tracks (Figure 2-6). The

IVC-to-LPA track resulted from the direct anastomosis of the right atrium onto the RPA with two homograft valves placed right upstream and downstream (2a and 2c in Figure 2-6) of the right atrium to prevent flow reversal in the IVC due to gravity and to the regular contraction of the right atrium.

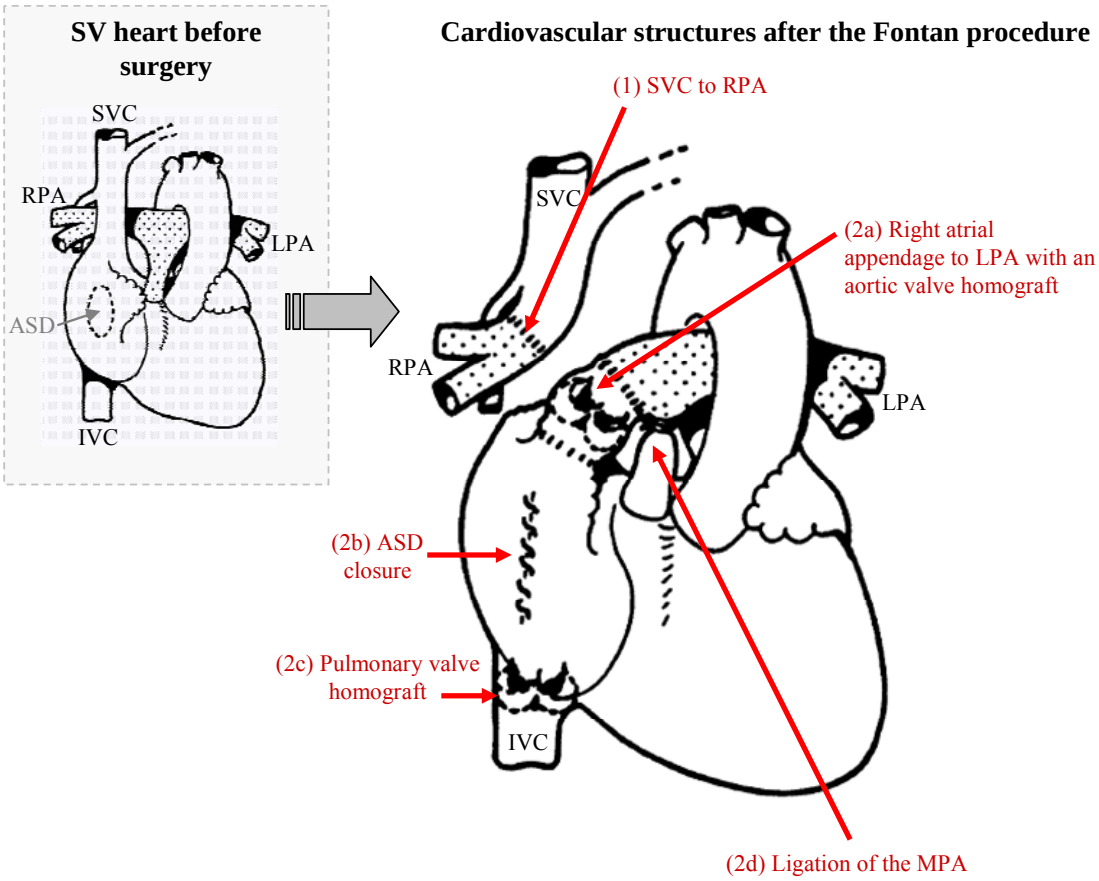

Figure 2-6: Schematic of the five major steps of the Fontan procedure [11]. ASD = Atrial Septal Defect, MPA = Main Pulmonary Artery.

The principle of a complete bypass of the right side of the heart as a result of the Fontan procedure achieved a number of salutary transformations to the SV anatomy (Figure 2-7). It separated the systemic and pulmonary circuits, relieved the volume overloaded ventricle and abolished blood mixing, which in turn ostensibly improved arterial oxygen saturation. On the other hand, the surgical implementation described by Fontan and Baudet yielded number of drawbacks: first, the insertion of the valve homografts obstructed the low-pressure IVC-to-LPA circulation [12]; then, the separation of the IVC-to-LPA and SVC-to-RPA tracks did not allow for any adaptation of the LPA/RPA blood flow ratio, leading to serious complications if one of the lungs became obstructed; and finally, all nutrients and hepatic factors coming through the IVC were excluded from the RPA, yielding pulmonary arteriovenous malformation (PAVMs) in the right lung [13-15].

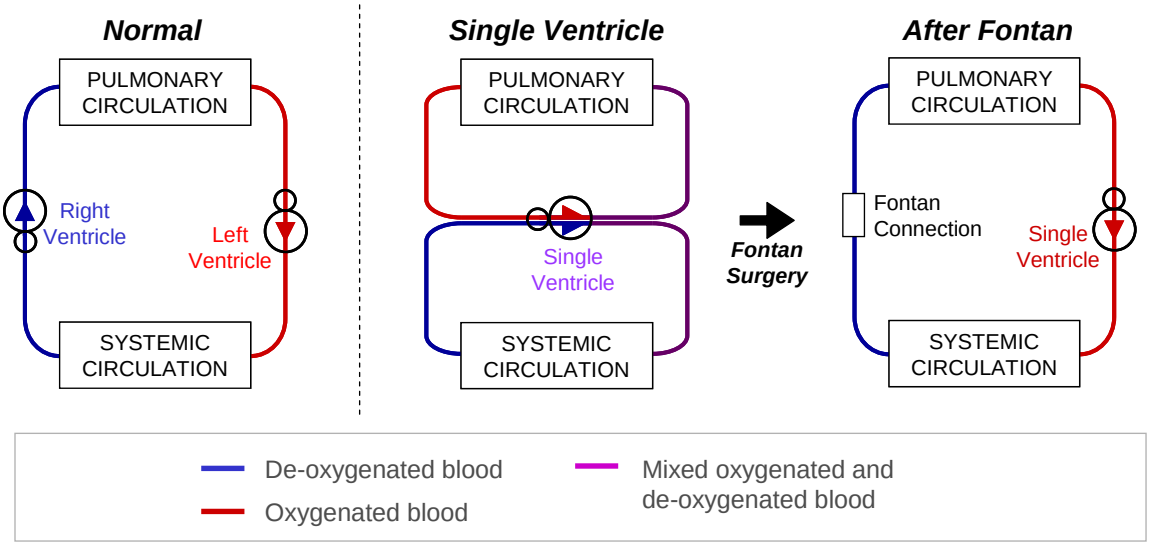

Figure 2-7: Schematic showing net result of the Fontan procedure on the cardiovascular circuit. The total right heart bypass restores the separation of the systemic and pulmonary circuits as in the normal physiology. The single ventricle acts as the left ventricle while the right side is replaced by the passive Fontan connection.

In 1973, Kreutzer et al. [16] described a valveless atrio-pulmonary (AP) connection as an alternative to the Fontan connection. Both SVC and IVC were left in their native configuration, connected to the right atrium. The bypass was simply achieved by an end-to-end anatomosis of the right atrial appendage onto the main pulmonary artery (Figure 2-8). This procedure had the advantages of redistributing the hepatic fluid to both lungs and splitting the pulmonary blood flow depending upon the needs and resistance of either lung. Furthermore, just as in the Fontan procedure, the preservation of the entire atrial appendage was meant to take advantage of the small but non negligible atrial contractions to help drive the flow from the IVC to the PAs.

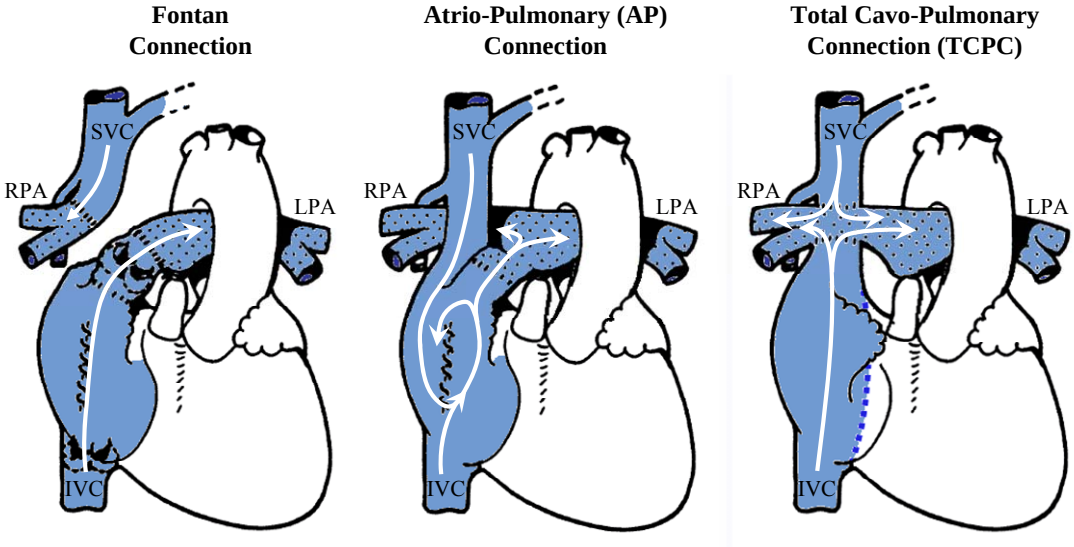

Figure 2-8: Schematic representation of the three main approaches that have been used to bypass the right side of the heart for SVHD repairs. The surgically created connections are colored in blue, while the white arrows depict in a simplistic fashion the global blood flow pathway.

Although the AP connection was quickly endorsed and has had widespread use in many centers, the long-term follow-up indicated that patients with an AP-connection developed supraventricular arrhytmias, right atrial thrombus, exercise intolerance and other symptoms associated with low cardiac output [17-20]. These complications were usually related to a markedly dilated right atrium appendage, which was suspected to be due to the increased pressure load imposed on the atrium [21]. This atrial dilatation was in turn associated with stagnant flows along the dilated right side of the atrium and turbulent flows elsewhere in the AP connection (Figure 2-8), resulting in significant fluid energy dissipation [21].

In 1988, De Leval et al. proposed the total cavopulmonary connection (TCPC) as an alternative to the AP procedure that would no longer make use of the entire atrial chamber [22]. The TCPC was performed by the direct anastomosis of the SVC to the superior wall of the RPA, followed by the creation of a tunnel through the right atrium connecting the IVC to the inferior wall of the RPA (Figure 2-8, right most panel). They demonstrated that such a geometry led to fewer flow disturbances and lower fluid energy losses than the AP connection, and hypothesized that these energy savings would more than compensate the loss of atrial pumping capabilities. This hypothesis was later corroborated by retrospective clinical studies that reported a more favorable course during the postoperative period, lower mortality rates and improved outcomes for patients with a TCPC compared to patients with an AP connection [23-25].

In summary, in an effort to reduce post-operative mortality, improve long-term outcomes and broaden the patient population eligible for single-ventricle repairs, the right heart bypass procedure originally proposed by Fontan and Baudet [11] has considerably

evolved in the past decades. Since the mid-90's, the TCPC has become the procedure of choice for SVHD repairs. It is now performed in multiple stages, allowing the heart, lungs and peripheral vasculatures to progressively adapt to the post-operative physiology. It is worthwhile noting that even though the original Fontan procedure is no longer in use, clinicians still commonly refer to SVHD repairs as the "Fontan procedure". In the remainder of this thesis, "Fontan procedure" will thus be used as a generic term for SVHD repairs, while "Fontan patients" will refer to SHVD patients eligible for these repairs. Specific denomination (TCPC, AP) will be used when the differentiation between the different surgical techniques plays a key role.

2.4.2 Current Approach to SVHD Repairs: The Staged Total CavoPulmonary Connection (TCPC)

A complete right heart bypass is almost impossible to complete at birth. The pulmonary vascular resistance is high, and the vessel sizes are too small for a successful cavopulmonary connection. The three-stage TCPC approach (Figure 2-9) allows the body to gradually adapt to substantially different hemodynamic conditions. The aims of the different stages are as follows:

a) Stage 1: Achieve unrestricted flow from the heart to the aorta and ensure at least a minimal blood flow to the lungs
b) Stage 2: Improve the lung perfusion and begin the separation of systemic and pulmonary circulations
c) Stage 3: Complete the separation of systemic and pulmonary circulations.

Staging the operations has markedly improved surgical outcomes and allowed the TCPC surgery to be applied to a larger range of SVHD patients [26]. It is now an integral part of the methodology for SVHD repairs.

The first stage is not required for all SVHD patients, but only for those featuring an obstructed systemic or pulmonary pathway. Its objective is to establish a viable circulation, allowing neonates to survive until they are eligible for the actual SVHD repairs performed at a minimum of 4 months of age in stages 2 and 3. This first intervention is completed in the first days or weeks after birth using the Norwood procedure [27], which entails the placement of a systemic-to-pulmonary shunt (such as the Blalock-Taussig BT shunt) to increase pulmonary blood flow in patients with blocked pulmonary pathway. In children with HLHS, stage 1 also includes the enlargement of the hypoplastic aortic arch to restore a proper systemic ventricular outflow (Figure 2-9).

The right heart bypass itself is performed in stages 2 and 3 (Figure 2-9). The 2nd stage is typically performed between 4 and 12 months of age. The native patent ductus arteriosus or surgically created systemic-to-pulmonary shunt is removed, and the superior venous return is diverted to the lungs by creating a direct SVC-to-PA anastomosis. This superior cavopulmonary connection is the first step toward the complete separation of the systemic and pulmonary circulations. It alleviates the ventricular overload imposed by the systemic-to-pulmonary shunt, visibly reduces cyanosis via a more efficient lung perfusion [28], and gives the heart some time to adapt to the increase in systemic resistance [29]. The full separation of the systemic and pulmonary pathways is completed in Stage 3 with an IVC-to-PA anastomosis (Figure 2-9). This final stage is performed anywhere between 1 and 5 years of age.

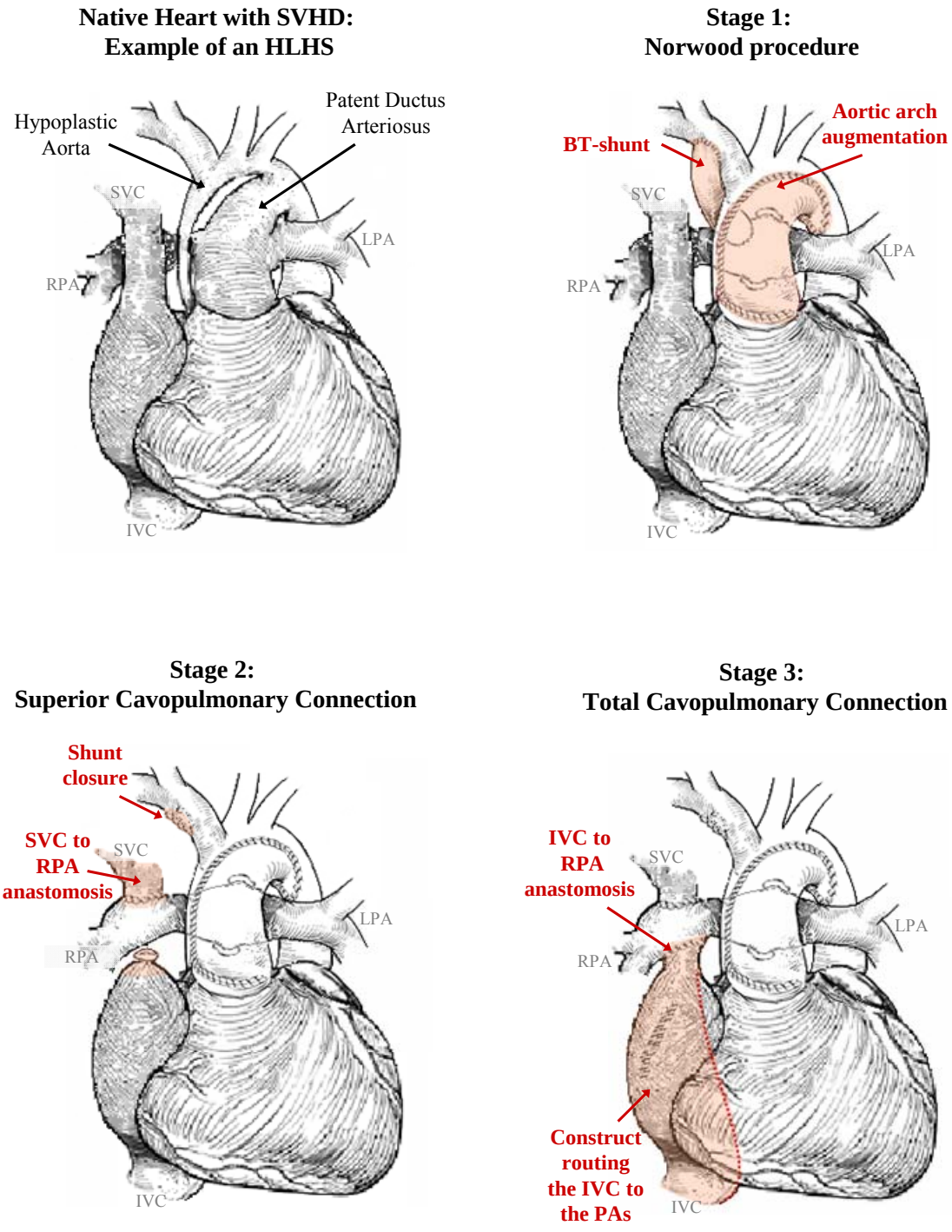

Figure 2-9: Cartoon depicting the different stages of the TCPC procedure as applied to a SVHD patient born with a hypoplastic left heart syndrome. (Images inspired by [30])

2.4.3 Degrees of Freedom in the TCPC Procedure

Although surgeons agree on the staged TCPC as being the procedure of choice for Fontan repairs, number of controversies exist about the exact surgical procedure to follow for each one of the stages, the type of material to use, and the age at which each one of these interventions should be performed.

The 2nd stage for example, is typically performed using either a bidirectional Glenn (BDG) or a Hemi-Fontan (HF) connection (Figure 2-10). Although no clear clinical benefit exists of choosing one procedure over the other, the geometry and hemodynamics of the HF and BDG connections are clearly different. In the BDG procedure, the SVC is disconnected from the atrium and sutured to the RPA in an end-to-side anastomosis, resulting in a T-shaped connection with a flow stagnation point where the SVC flow hits the inferior aspect of the RPA (Figure 2-10(a)). In an HF connection, on the other hand, the SVC remains in its native configuration and it is the right atrial appendage that is connected to the PAs. A patch is inserted into the right atrium to redirect the SVC flow towards the PAs. The SVC flow typically forms a large recirculation in the atrial appendage, prior to flowing into the PAs (Figure 2-10(b)).

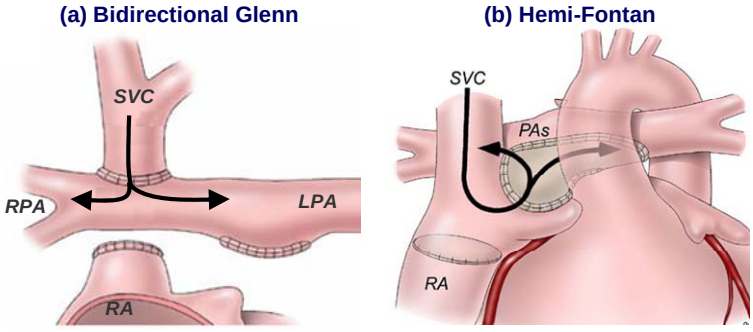

Figure 2-10: The two different approaches typically used to perform the SVC-to-PA anastomosis in the 2nd stage of the TCPC procedure: a) Bidirectional Glenn; b) Hemi-Fontan (Image courtesy: [31]). The black arrows depict the global blood flow pathway.

Similarly, the 3rd stage is mostly done in one of two ways: by constructing an intra-atrial tunnel or using an extra-cardiac connection (Figure 2-11). Intra-atrial tunnels [22] entail the construction of an independent flow pathway going through the right atrium and directing the lower systemic venous return from the IVC up to the superior aspect of the atrial appendage. This construction makes use of the atrial wall on one side and an artificial graft on the other. Intra-atrial tunnels offer the non-negligible advantage of allowing the IVC baffle to grow with the patient. On the other hand, their construction requires opening the right atrium, which carries the risk of disrupting the cardiac electrophysiology and inducing arrhythmias. In addition, they often result in bulgy IVC conduits which have been associated with extensive recirculations, flow disturbances, and energy dissipation [32, 33].

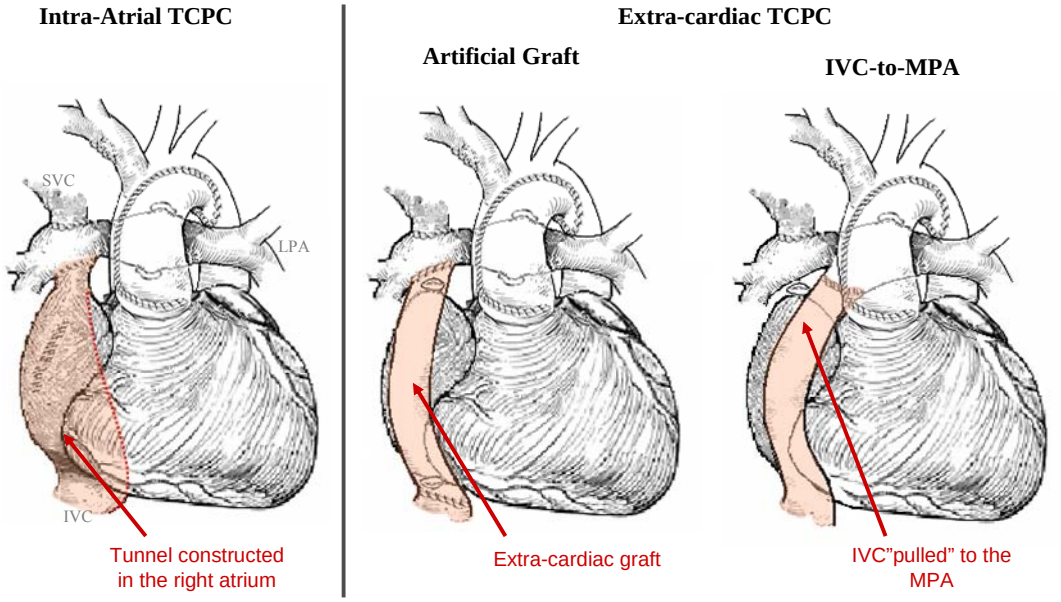

Figure 2-11: Different options available to perform the IVC-to-pulmonary anastomosis in stage 3. (Images inspired by [30])

In contrast to intra-atrial procedures, extra-cardiac approaches [34] do not go through the atrium, but rather use a complete artificial vessel graft (of typically 20 to 24 mm in diameter) to route the IVC around the heart all the way to the PAs (Figure 2-11). As such, extra-cardiac options require fewer suture lines, no incision in the atrial wall, less or no time on the heart-lung machine, and result in almost cylindrical IVC conduits associated with smoother blood flow circulation with limited flow disturbance [35]. However, these advantages are somewhat balanced by the fact that extra-cardiac conduits are typically constructed using artificial vessel grafts (made of Goretex, or Dacron) which do not provide any growth potential and have been associated with conduit stenosis and throboembolism [34, 36, 37]. Direct IVC-to-MPA connections (where the extra-cardiac conduit is constructed by direct end-to-end anastomosis of the IVC to the MPA) have been used as a way to combine the advantages of extra-cardiac conduits with the benefits of using autologous tissues (growth potential and limited thrombogenicity). But such an option requires a particular arrangement of the MPA and IVC and cannot be generalized to all patients. Yalcinbas et al. [38] report of the construction of an extra-cardiac conduit using an autologous pericardium flap with positive short-term outcome (30 months). Longer follow-up data are still needed to assess the robustness of the method.

Some institutions have also advocated in favor of punching a temporary fenestration (or hole) between the IVC conduit and the right atrium to give the heart more time to adapt to the post-operative flow conditions [39]. Including a fenestration in the IVC conduit was demonstrated to lower the systemic venous pressures as well as to improve ventricular filling, consequently leading to improved cardiac output and overall

oxygen delivery [39, 40]. Lemler et al. [41] added that fenestration at the time of the Fontan surgery improved short term outcome in standard-risk patients, with a 41% decrease in the hospitalization duration immediately after surgery, and 67% fewer additional procedures in the postoperative period than for patients without a fenestration. However, while some institutions advocate systematic fenestration, others argue that it should be used more selectively, balancing the potential benefits against the risks and costs of the additional intervention needed to close the fenestration [40].

Finally, the age at which each stage should be completed is still under debate. The mean age at the time of TCPC completion and the mean interval of time separating two consecutive surgeries have significantly decreased over the past decade. While some see this as a beneficial trend [42] that has reduced most of the major complications, others recommend caution pointing out that suture lines significantly limit vessel growth and that vessel size is a major factor for hemodynamic efficiency [43].

In summary, while the TCPC is now accepted as the procedure of choice for SVHD repairs, there are quite a few open-ended questions as to its exact implementation. The geometry of the final surgically created TCPC, the timing of the stages, and the material to use are as many parameters over which surgeons have at least some degree of control. Performing a Hemi-Fontan in the 2nd stage followed by an intra-atrial procedure in the 3rd stage for example, will result in a drastically different geometry than a BDG followed by an extra-cardiac connection. Similarly, the age at which each of these stages is performed will impact vessel diameters. The different geometries resulting from each of these surgical choices will in turn entail different flow features and hemodynamics, but the question as to which is better is still highly controversial.

2.5 Long-Term Complications in SVHD Patients after Fontan Repairs

Modifications to the original Fontan procedure, as well as the improvement in patient management and care, have steadily improved surgical outcomes, bringing the post-operative survival rates up to the level of simpler congenital heart repairs [44-46]. However, while most institutions now report 95% post-operative survival rates, the 10-year survival rate drops to 60-80% [47-49]. The fact is that the Fontan procedure results in a non-physiologic cardiovascular configuration where the single ventricle has to pump blood through both the systemic and pulmonary vascular beds in series (Figure 2-7). The single ventricle experiences an increased afterload (including both systemic and pulmonary vascular resistances) and decreased preload (ventricular filling). In addition, there is a significant increase in central venous pressure due to the lack of pressure step-up typically provided by the right ventricle [50].

In the early post-operative stages, the sudden increase in central venous pressure may lead to ascites, pleural effusions, decreased pulmonary compliance and increased pulmonary vascular resistance. If no remedial action can be taken, then the only real option is to take down the TCPC connection and leave the circulation with a superior cavopulmonary anastomosis [51].

Late failure is typically associated with some of the chronic problems that are a consequence of the abnormal Fontan circulation. Progressive ventricular dysfunction, atrial arrhythmias, atrioventricular valve regurgitation, pulmonary arteriovenous malformations (PAVMs), diminished exercise capacity, protein losing enteropathy (PLE), somatic growth retardation, thrombotic complications, and poor neurodevelopmental outcomes [47] are some of the most commonly reported complications. In their autopsy

review, Kiaffas and colleagues [52] identified congestive heart failure (82% of all deaths), arrythmias (12%) and central venous system dysfunction (6%) as the leading causes for mortality. PLE is reported with a low incidence ranging from 1.5 to 11%, but a 50% mortality rate was reported 5-years from the time of diagnosis [53]. A review of 592 patients showed evidence of thrombus formation in 9% of patients at a mean follow-up time of 22 months [54].

There are two key components to the Fontan circulation, the single pumping ventricle on the one hand and the vascular resistances and compliances on the other. Focusing on the ventricular side, Kirklin et al [55] found ventricular hypertrophy to be a significant risk factor for death. They reported that the survival rate of patients with diminished qualitative ventricular function was only 35% compared to 70% with normal or hyperdynamic function. Senzaki and colleagues argued that increased afterload, decreased preload, and abnormal ventricular-vascular coupling contribute to the decreased cardiac reserve and function in patients with a Fontan circulation [56]. However, this mechanism does not entirely explain the differences in survival and outcome observed among patients receiving sensibly similar procedures. Altmann and colleagues [57] found the native right ventricle function to be the best predictor for operative survival for SVHD patients born with HLHS. Sundareswaran et al. demonstrated that native single right ventricles has a significantly lower power output capacity than native single left ventricles [58]. Accordingly, while the chronic pressure overloaded condition of the single ventricle in a Fontan circulation makes it susceptible for ventricular dysfunction and heart failure, the failure rate is further conditioned by the native configuration and function of the ventricle.

The vascular resistance imposed by the systemic, TCPC and pulmonary circuits in series is another key component of the abnormal Fontan circulation. Clinical studies have shown that, unlike healthy individuals, Fontan patients only respond to exercise by increasing their heart rate, while the stroke volume, which is typically limited by the pre-load, remains approximately constant [56, 59]. On the other hand, PLE and liver dysfunction have been correlated with the high central venous pressures observed in Fontan patients [60, 61]. While seemingly independent, both of these observations stem from the fact that, in the absence of a right pumping chamber, pressure difference between the IVC and the left atrium is the only force left to drive blood through the TCPC and lungs. Therefore, the higher the vascular resistance downstream of the liver, the higher the pressure difference required to achieve a given cardiac output. This observation falls back to Guyton's isolated venous theory [62, 63], which states that the cardiac output in single ventricle patients is highly sensitive to the vascular resistance downstream of the venous compliance. Even though Guyton's theory focused on the effect of pulmonary vascular resistance (PVR), the vascular segment of interest in practice includes both the TCPC and lungs, both of which lie in series downstream of the venous compliance. Accordingly, elevated PVR or TCPC resistance would both result in increased central venous pressures, which have been associated with PLE, and decreased maximum cardiac output, which will limit the patient's exercise capacity.

Vasodilating agents [64] have been utilized successfully to lower PVR. However, in Fontan patients all blood flow has to first travel through the TCPC, such that if the effective resistance of the connection is high, improvements in PVR alone may be insufficient to improve preload and cardiac output, especially under the increased

demands of exercise or other high output states (e.g., illness, pregnancy). The importance of designing the TCPC so as to minimize its resistance was further emphasized by Sundareswaran et al. [65]. Using a combination of *in vivo* Phase Contrast MRI (PC MRI) measurements, CFD results and lumped parameter modeling, the authors established that 1) the TCPC resistances in these patients ranged from 0.1 Wood units (WU) to 1.08WU, with a mean of 0.39+/-0.26 WU, which is non-negligible in front of the PVR (mean of 1.96+/-0.80 WU); 2) there was a negative correlation between the TCPC resistance and the resting cardiac output and a positive correlation between the TCPC resistance and the central venous pressure; and 3) these behaviors were exacerbated under exercise conditions where the TCPC with the highest resistance (1.08 WU) only allowed for a 20.5% increase in cardiac output at 150 beats/min vs. a 50% increase for the TCPC with the lowest resistance, and a 119% increase in the normal biventricular model. This study is an agreement with previous clinical findings, but more importantly it demonstrates that the variations in TCPC designs observed across Fontan patients translates into variations in TCPC resistances that can significantly impact the resting hemodynamics and exercise capacity of these patients. This thus brings forth the question as to how to optimize the design of the TCPC so as to minimize its hemodynamic resistance.

Another major complication that results in Fontan failure and is in part affected by the TCPC design is progressive cyanosis due to the development of unilateral PAVMS [66-70]. PAVMs are intrapulmonary shunts, connecting the pulmonary arteries directly to the pulmonary veins, thus allowing the de-oxygenated blood from the systemic circulation to return to the left atrium without flowing through the gas exchange units. The primary consequence of PAVMS is decreased oxygen saturation. Furthermore, the

intrapulmonary shunts lead to a drop in pulmonary vascular resistance, which tends to direct more flow to the diseased lung creating a positive feedback loop of increasing cyanosis. Although the underlying mechanism leading to PAVMs is unknown, studies have shown that liver derived factors present in the hepatic venous blood prevent their formation [14, 67, 69, 70]. Therefore, an unbalanced hepatic flow distribution to the left and right lungs due to an inadequate design of the IVC-to-PA conduit during the 3rd stage of the TCPC surgery could potentially lead to PAVMs. Clinically, once the extent of PAVMs is such that oxygen saturation is critically low, the only palliative option is to re-operate and re-orient the IVC conduit to achieve a better hepatic flow distribution [14, 71-74]. However, although several palliative options have been discussed in the literature such as the use of a bifurcated extra-cardiac IVC conduit or drainage of the hepatic vein to the persistent azygous vein [72], there is no solution to date that results in the adequate hepatic flow distribution for the cardiovascular configuration of each specific patient.

In summary, while the reasons for Fontan failure are no doubt multi-factorial, a number of the aforementioned complications may be related to the geometric design of the TCPC, would it be via the resulting hemodynamic TCPC resistance or the resulting distribution of blood flow and hepatic nutrients to the lungs. Accordingly, in this study, we chose to focus our attention on the TCPC and its design optimization with respect to key hemodynamic metrics, including energy dissipation, hemodynamic resistance, and the distribution of the cardiac output and hepatic flow to the two lungs.

2.6 *In vivo* Investigations of the TCPC Hemodynamics

The above clinical follow-up studies not only demonstrate the morbidity and decreased functional status of Fontan patients but clearly emphasize the need for improvements in the surgical procedure. Consequently, number of studies have sought to assess the geometrical characteristics of the different options used to perform the TCPC surgery and characterize their impact on the TCPC hemodynamics, the single ventricle performance, and the overall patient outcome. Magnetic resonance imaging (MRI) has emerged as an attractive non-invasive imaging technology to assess TCPC hemodynamics *in vivo* as it allows for the acquisition of both anatomy and flow, and is harmless to the patient thus allowing for frequent repeated scans if needed. With the advents of image segmentation, interpolation, surface fitting and visualization methods, raw magnitude and phase contrast MRI techniques can be used to reconstruct the 3D *in vivo* anatomies and velocity fields, respectively.

MRI has in particular been used by Dr Yoganathan's laboratory at the Georgia Institute of Technology to constitute a large database of Fontan anatomies and flows, which now includes data for over 250 patients recruited at the Children's Healthcare of Atlanta (CHOA), the Children's Hospital of Philadelphia (CHOP), the Children's Hospital Boston (CHB). This wealth of *in vivo* data has provided a unique opportunity to look at the geometrical characteristics of a wide range of TCPC implementations (Figure 2-12). As can readily be anticipated from the diversity of the anatomies displayed in Figure 2-12, it is highly unlikely that there would be one single surgical implementation that will be optimal for all patients. Variations in the geometry of the completed TCPCs depend on the surgical options retained at each one of the TCPC stages (e.g. intra-atrial

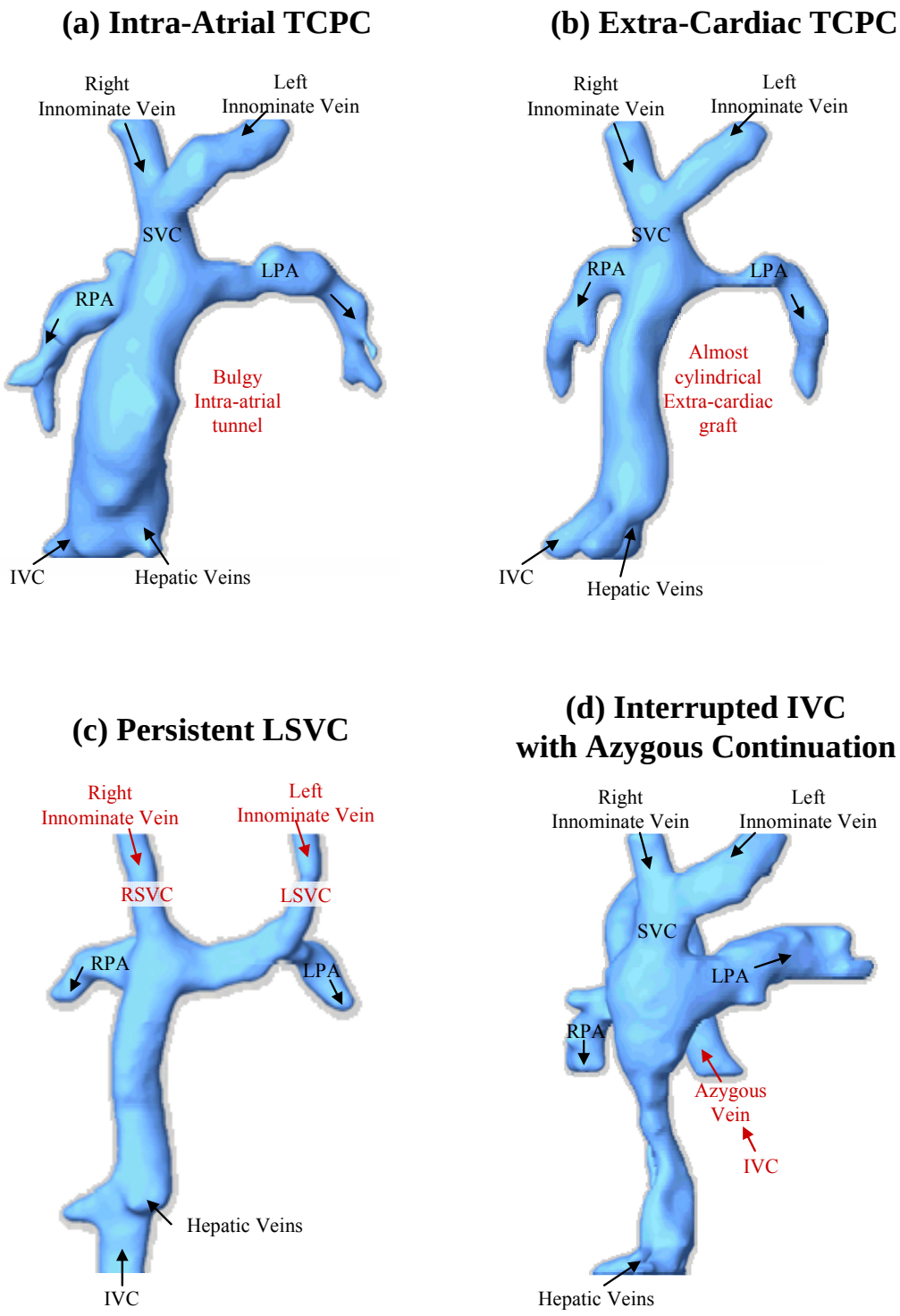

Figure 2-12: Representative sample of *in vivo* TCPC anatomies from the GeorgiaTech MRI database. (a) and (b) show the geometries that may result from different surgical procedures (intra-atrial and extra-cardiac TCPC), while (c) and (d) highlight the different native anatomical configurations.

vs. extra-cardiac) as well as on the native patient anatomy (e.g. presence of a single or bilateral SVC, normal or interrupted IVC, heterotaxy syndrome).

The first study to quantitatively compare TCPC geometries was conducted by Krishnankutty et al. [75]. The analysis process involved the reconstruction of 26 TCPC geometries (13 intra-atrials and 13 extra-cardiacs), the extraction of the TCPC skeleton (or vessel axes), and finally the systematic quantification of the vessel cross-sectional area, vessel curvature, and IVC-SVC offsets. Intra-atrial options were found to have significantly higher area variations than extra-cardiacs, due to the more irregular geometry of intra-atrial baffles when compared to the smooth extra-cardiac grafts. In addition, that study demonstrated that irrespective of the TCPC option, patients born with HLHS were at higher risk of LPA narrowing than those without HLHS. This was attributed to the aortic arch reconstruction done in stage 1 for HLHS patients, during which surgeons tend to oversize the aortic arch, which in turn compresses the LPA and prevents its growth. This study was the first to benchmark the anatomic variability of patient specific TCPCs. Such a quantitative geometric characterization is a critical step to correlate hemodynamic performances with geometric features.

Focusing on the Fontan flow characteristics, Fogel et al. [76] used phase contrast MRI (PC MRI) to measure the IVC and SVC flow rates in ten SVHD patients with an intra-atrial TCPC (1.8$\pm$0.3 years old). By superimposing a pre-saturation pulse on the IVC and the SVC selectively, the authors were able to assess the portion of inferior and superior venous returns that was directed to the LPA and RPA. Distributions of blood to each lung were almost equal for all patients (RPA/LPA blood=0.94+/-0.11), but the LPA received a significantly larger amount of IVC blood (67 +/- 12%) than the RPA [76].

Hjortdal et al. used real-time PC MRI to assess the impact of respiration on the TCPC flow rates [77]. They demonstrated that inspiration facilitated IVC flow under resting conditions, increasing it to 2.99±1.25 L/min/m^2 during inspiration versus 0.83±0.44 L/min/m^2 during expiration. SVC flow was not significantly affected by the respiratory cycle, and under exercise conditions, the peripheral muscular pump seemed to have more influence than respiration on the Fontan circulation.

Be'eri et al. used ECG-gated 3D PC MRI to compare the flow dynamics of five AP and five TCPC connections at multiple time points across the cardiac cycle [78]. The authors selected the orientation of their PC MRI acquisition plane slice so as to include the caval, atrial, and pulmonary components of the Fontan pathway. This study is one of the few studies looking at the velocity fields within the Fontan construct and not only at its inlets and outlets (in cross-sections of the IVC, SVC, LPA and RPA). This may in part be attributed to the prohibitively long PC MRI acquisition time, which have been a limiting factor for adult applications and pose an even greater challenge in pediatrics, where it is difficult to keep infants and young children still for extended periods of time. Interpolation methods [79, 80] are thus gaining interest as a mean to reduce the acquisition time by limiting the number of acquisition plane required, while still providing an appropriate representation of the blood flow field. The continuous representation of the 3D time-dependent blood flow fields opens avenues to the *in vivo* assessment of surrogate markers for TCPC efficiency such as the distribution of hepatic flow to the lungs [80, 81]. Metrics such as energy dissipation should still be handled with caution as PC MRI cannot resolve all length scale, features high noise levels in the vicinity of the vessel walls, and is often associated with signal loss in regions of high

flow disturbances. *In vitro* experiments and numerical modeling have arisen as attractive means to complement these *in vivo* measurements for in depth hemodynamic analyses.

2.7 Experimental and Computational Modeling of the TCPC Hemodynamics

Since the first *in vitro* experiment done by de Leval et al. that demonstrated the superiority of the TCPC over AP connection [22], parametric *in vitro* and computational fluid dynamics (CFD) studies aimed at better understanding the TCPC hemodynamics have flourished. Early *in vitro* or numerical studies investigated the impact of independent geometric parameters on the overall efficiency of highly simplified TCPC geometries with steady flows and rigid walls. In these studies, the simplified TCPCs typically consisted of four cylindrical vessels with varying curvature, diameter, or connection offset (see Figure 2-13).

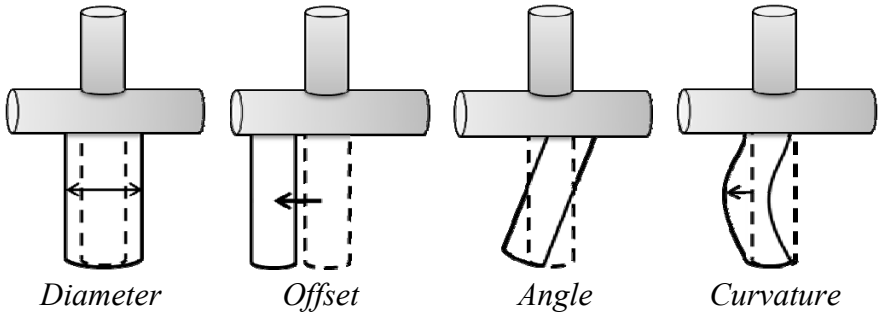

Figure 2-13: Examples of isolated parameters that could define the TCPC geometry (here focused on the variation of the IVC design).

Using such idealized models *in vitro*, Sharma et al. [82] demonstrated that the power dissipated across the connection was significantly reduced when the IVC and SVC were not directly facing each other but rather were offset by 1.0 or 1.5 caval diameters.

Using a similar idealized *in vitro* setting, Gerdes et al. [83] demonstrated that if the IVC baffle was curved such that IVC and SVC flows did not collide, the energy dissipation would be reduced as well. The emphasis set by these studies on the design of the IVC anastomosis was somewhat balanced by DeGroff et al. [43] who argued that vessel diameter was the main determinant of TCPC energy efficiency, while other parameters, such as caval offset, only played a secondary role. Their argument was supported by an *in vitro* analysis of models with varying caval offset and two sets of vessel dimensions. The numerical study of Ryu et al. [84], which compared the performance of idealized TCPCs with straight or curved PAs and with different SVC diameters, reached the same conclusion, pointing to the vessel dimensions as being the primary factor for energy dissipation. The authors also emphasize that oversimplification of the TCPC geometry may bias the conclusions reached by *in vitro* or numerical parametric studies.

An interesting study to understand the mechanisms of energy dissipation in the TCPC is the combined experimental and numerical investigation of Khunatorn et al. [85]. In an effort to understand why their numerical results predicted lower power losses in the idealized no-offset TCPC than the earlier *in vitro* measurements of Sharma et al. [82], Khunatorn et al. conducted an in depth analysis of the *in vitro* and CFD flow fields. They pointed to secondary flow structures in the PAs as an important source of dissipation. Also, while in their simulations the collision of the IVC and SVC streams yielded a stable saddle point, experimental measurements revealed flow instabilities at the collision site. The authors inferred that these flow instabilities could further enhance the secondary structures downstream in a fashion similar to what is illustrated in Figure 2-14.

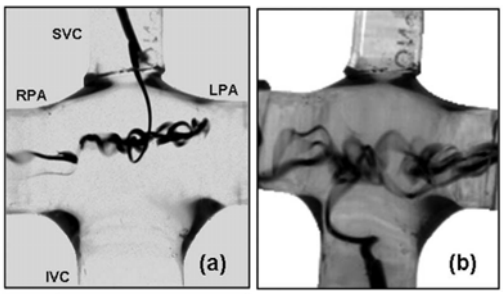

Figure 2-14: Experimental dye flow visualization in an idealized no-offset TCPC at 50/50 LPA/RPA flow split. (a): Dye injected through the SVC. (b): Dye injected through the IVC. (Image courtesy: [33])

Heading towards more comprehensive modeling, recent experimental and computational work has included patient-specific anatomies [33, 86-94]. These studies revealed higher levels of flow disturbances (Figure 2-15) and energy dissipation than in the earlier idealized geometries, as well as a large inter-patient variability. The *in vitro* power losses reported by de Zélicourt et al. for one extra-cardiac [89] and one intra-atrial [33] patient specific TCPC were, respectively, 5 and 70 times higher than those previously reported by Sharma et al. [82] for their idealized one-diameter offset TCPC. The authors pointed to the smaller vessel dimensions as well as the irregular shape of the *in vivo* connections as the main explanation for the high levels of energy dissipation. The argument was supported by a set of parametric studies in idealized geometries, which progressively incorporated the features of the *in vivo* intra-atrial TCPC [95]. Reduction in vessel dimensions increased dissipation, which was even further increased when the central connection area was enlarged to mimick the bulgy IVC intra-atrial tunnel. The sudden expansion of the IVC and SVC into the central connection area favored the development of flow recirculation and instabilities, which turned into an intense and chaotic mixing in the patient-specific intra-atrial case (Figure 2-15).

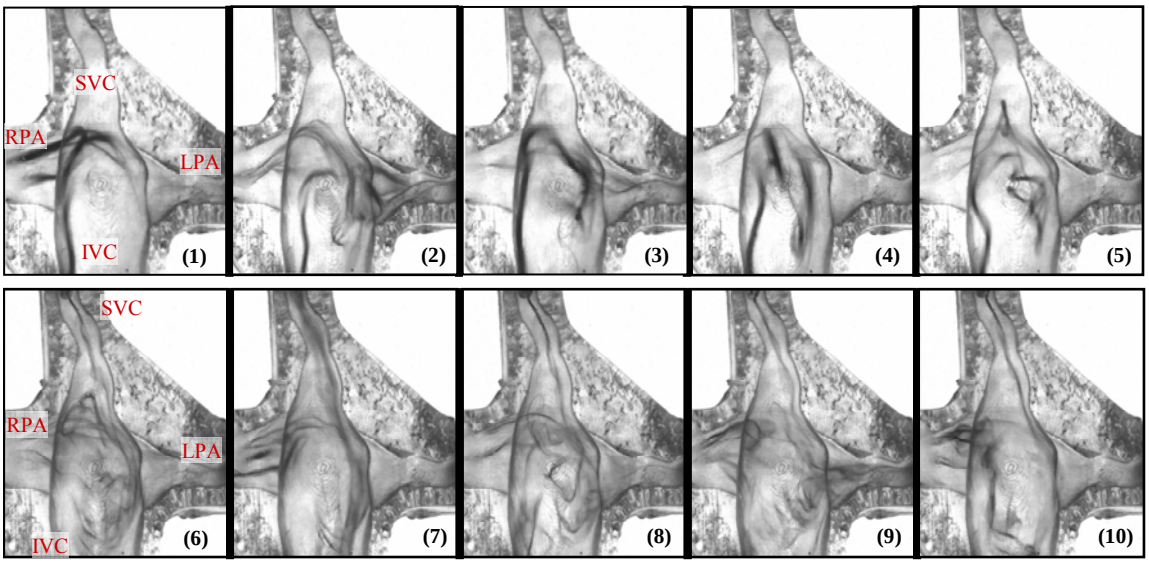

Figure 2-15: *In vitro* dye flow visualization of a patient-specific intra-atrial TCPC [95]. The experiments were conducted with constant inflow rates. The instantaneous time-series demonstrates how the flow instabilities due to the IVC and SVC flow collision develop into an intense and chaotic mixing at the center of the connection. (1) to (5): dye injected in the IVC; (6) to (10): dye injected in the SVC.

Whitehead et al. conducted a larger sample size CFD study of 10 patient-specific TCPCs [92]. Simulations were conducted under the resting, mild and heavy exercise conditions. The results re-emphasize the fact that there *in vivo* configurations span a large range of power losses, especially under exercise conditions. Seeking to identify the main determinants of energy dissipation in patient-specific geometries, Dasi et al. [96] compiled the experimental and numerical power losses obtained across 22 patient-specific anatomies, and confronted them to geometrical metrics obtained from skeletonisation. Results showed that, irrespective of the connection type, the minimum PA cross-sectional area was the strongest correlate for normalized energy dissipation rate (R^2-value of 0.898 and $P<0.0002$), setting the emphasis on the need to i) avoid LPA constriction in stage 1 and ii) dilate any stenosed vessel in later stages. Refining their

analysis further, the same authors [97] derived a simple analytical form of energy dissipation rate which includes the effect of cardiac output, flow split, body surface area, Reynolds number, and pulmonary artery size, and leaves two parameters to be adjusted. The excellent fit provided by this analytical expression re-iterates the fact that the vessel dimensions at the time of TCPC completion play a key role in the magnitude of the TCPC power losses. In that study, the impact of other geometrical parameters, such as vessel curvature, caval offset, bulginess of the IVC conduit, is accounted for in the two parameters to be fit.

Based on the above studies, Soerensen and colleagues suggested the use a bifurcated graft, or Optiflo connection, to avoid blood mixing at the center of the connection, reduce secondary flow structures in the PAs, and ultimately minimize energy dissipation [98]. Proof of concept was provided both experimentally and numerically in highly simplified geometries, revealing energy dissipation levels 50% lower than in any other idealized configuration. The potential benefits of such a bifurcated graft over traditional non-bifurcated ones was further demonstrated in a patient-specific scenario by Mardsen et al. [99]. Using CFD to predict the power losses, the authors reported decreased energy dissipation when splitting the IVC into a Y-shape connection. Both groups also put forth the fact that the bifurcated graft offered an easy control on the blood flow and hepatic factor distribution to the lungs. This last point is of major interest to prevent the formation of PAVMs, but was somewhat balanced by the recent patient-specific study CFD by Sundareswaran et al. [81], where the designed Y-shaped graft failed to achieve a balanced hepatic flow distribution to the lungs. Such a contradiction in

patient-specific applications is not surprising given the wide range of anatomical configurations, but highlights the need for patient-specific modeling.

2.8 Towards Patient-Specific Surgical Planning

Merely looking at the range of anatomical configurations observed *in vivo*, it is apparent that there is not one procedure that would be optimally suited for all Fontan patients. Furthermore, optimizing the TCPC geometry for both minimum energy dissipation and balanced hepatic flow distribution, for example, can lead to contradictory surgical guidelines making the clinical decision more complex rather than helping it. An alternate approach is to take advantage of the advances in clinical imaging, image processing, and numerical methods to perform parametric studies such as the ones listed in Section 2.7 but on a patient-specific basis, thus identifying the optimal surgical strategy for each individual patient. A major milestone for patient-specific optimization and surgical planning is the ability to modify the pre-operative anatomy and model the different post-operative configurations. Early studies have typically employed commercially available computer aided design (CAD) tools to manually modify geometries and generate only a few alternate post-operative options [88, 89]. Such processes are cumbersome and depend on the skill of the operator, especially when applied to complex anatomies. Two main approaches have thus been derived to achieve anatomy modification: (1) parametric representation and modification of the anatomy, (2) advanced anatomy editing tools, with a special focus on easing the human-computer interaction.

The first category of tools includes work such as the one conducted by Mardsen et al. [100], which does not reproduce the surgery per se but is directly focused towards automated shape optimization. Each patient-specific geometry is decomposed into a finite set of parameters, which can then be varied to generate different post-operative anatomies. In their first report for instance, Mardsen et al. [100] sought to optimize the design of an end-to-side anastomoses for bypass surgery. This study used an idealized vessel representation, where the geometry of the end-to-side anastomosis was characterized by three parameters: vessel diameter, graft diameter, and connection angle. Parametric variation of the graft angle and diameter, and automatic generation of the corresponding 3D geometry allowed the authors to conduct an automated optimization of the anatomosis design. The difficulty to generalize such an approach for the systematic investigation of all the options available to the surgeon (including extra-cardiac, intra-atrial and bifurcated Y-grafts for example) lies in the parametric decomposition of complex shapes. In addition, ensuring that the final designs fall within what is surgically feasible (i.e. no main vessel compression or appropriate vessel wrapping around the heart in the case of extra-cardiac options) may represent a challenge in itself.

The second category of tools addresses these difficulties by trying to reproduce the internal patient anatomy and surgical gesture. These may be related to virtual sculpture and make use of the progresses in geometrical handling, image rendering, and human-computer interactions. Pekkan and Rossignac [101] reported a preliminary virtual-surgery framework for cardiovascular surgeries. This virtual surgery interface is exemplified in Figure 2-16 for the performance of a 3rd stage, extra-cardiac TCPC connection. The patient anatomy was reconstructed from MRI, providing a 3D

representation of the vessels involved in the TCPC surgery (IVC, SVC, LPA, and RPA) and surrounding anatomical structures(such as the heart and great vessels), which constrain the surgeon's degrees of freedom. Using two haptic trackers, one in each hand, the user/surgeon may directly interact with the geometry, here placing and deforming an artificial graft to complete the TCPC. Similar frameworks have been developed for applications other than cardiovascular. O'Leary et al. [102] report of an interface with sensitive feedback to mimic bone surgery. Virtual-reality surgical simulators are also gaining interest as training and evaluation tools for surgical trainees [103, 104]. The realism of these virtual surgery environments and the relevance of the surgical options designed therein depend on the extent to which the surrounding structures are represented in the interface, as well as on the realism with which the surgeon may perform a procedure. Contrary to the framework proposed by Marsden et al. [100], these virtual surgery environments are user intensive and do not easily lend themselves to systematic optimization procedures. On the other hand, these tools more easily allow for novel surgical procedures to be designed and tested on realistic patient-specific anatomies rather than simplified representations.

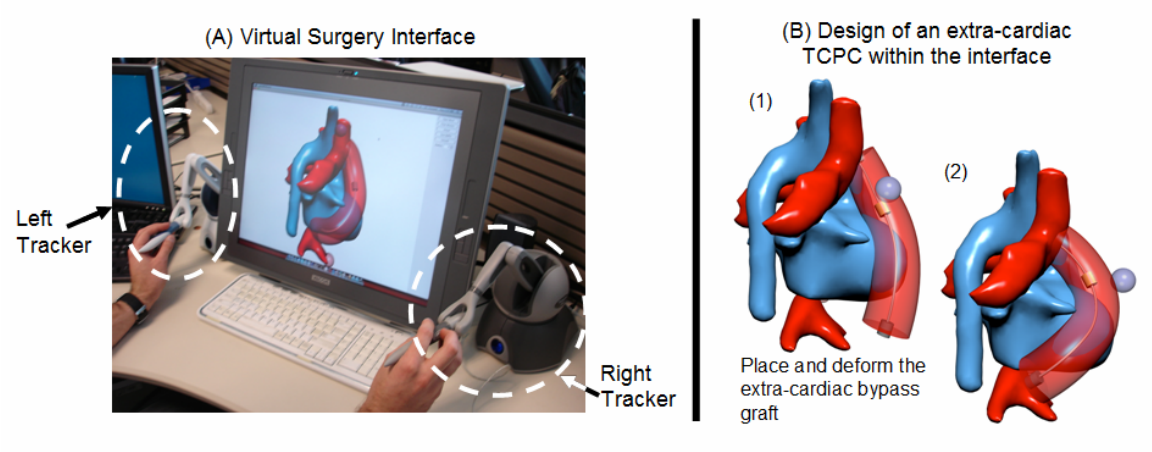

Figure 2-16**:** Virtual surgery environment [101]: Patient TCPC (shown in dark red) and surrounding anatomical structures, such as the heart and great vessels (shown in blue), have been reconstructed from MRI and loaded into the virtual-surgical interface. Using two haptic trackers, one in each hand, the user/surgeon may directly interact with the geometry, here placing and deforming an artificial graft (light transparent red) to complete the TCPC.

Coupled with robust CFD solvers, environments such as the ones developed by Marsden et al. [100] or Pekkan et al. [101] provide a unique opportunity for surgeons to 1) visualize the patient anatomy prior to entering the operating room, 2) envision multiple surgical options, 3) assess the hemodynamics of each option, and finally 4) identify the best surgical scenario (balancing energy dissipation, flow distribution and surgical feasibility) on a patient-specific basis. Such a patient-specific surgical planning approach is especially attractive for diseases such as SVHD, where the small patient population and the diversity of the underlying anatomies make it difficult to draw general guidelines based on clinical studies alone.

2.9 Computational Fluid Dynamics Modeling of the TCPC: Current Status and Limitations

As was highlighted in the previous sections, computational fluid dynamic (CFD) has arisen as an attractive option to model complex biomedical flow patterns, complement clinical *in vivo* data to further the understanding of disease mechanisms, or provide patient-specific surgical recommendations. CFD methods provide distinct advantages over other forms of investigation: a high degree of freedom regarding the geometry and conditions to be simulated, a full 3D representation of the flow field to a level of details that cannot be achieved *in vivo* nor *in vitro*, the possibility to be automated for large sample size studies, and finally the potential to be coupled with virtual surgery environments to investigate novel surgical options and optimize the TCPC procedure on a patient-by-patient basis. However, despite these exciting prospects, it is important to keep in mind that any modeling approach carries simplifications and limitations, which should be carefully assessed prior to drawing any clinical conclusions. Most of the studies listed in Section 2.7 called upon one or several of the following assumptions: simplification of the geometry, rigid walls, constant flow rates at the inlets, constant flow rate or pressure at the outlets, and no feedback mechanism between the local TCPC hemodynamics and the global cardiovascular function. On the other hand, developing a fully-coupled multi-scale model of the whole circulation, including realistic TCPC geometry, wall material properties, detailed fluid mechanics of the TCPC, downstream pulmonary vascular resistance and a closed-loop adaptive model of the whole cardiovascular circuit, if at all feasible, will most likely yield a highly complex numerical scheme, increase convergence times, and ultimately hinder clinical

applicability. The ultimate objective of an investigative numerical flow solver is not so much to capture all *in vivo* intricacies but rather to yield results of clinical relevance within a clinically acceptable timeframe. This section thus reviews the numerical investigations of the TCPC hemodynamics, with a special emphasis on the selected modeling assumptions and their relative impact on the predicted performance of different TCPC options.

2.9.1 Vessel Wall Motion

Orlando et al. looked into the impact of wall compliance on the hemodynamics of an idealized, uniformly elastic TCPC [105]. They reported a 10% increase in power losses when compared to the same simulations conducted using rigid walls. This variation is of small magnitude in front of the variations in power losses that have been observed when altering the interaction of the IVC and SVC streams. Sharma et al. [82] for example, already reported a 50% increase in power loss between an idealized geometry with and without caval offset. De Zélicourt et al. found a 5 fold increase in power loss when allowing the instabilities arising from the IVC and SVC collisions to develop, still in an idealized setting, and up to a 70 fold increase when compared to an anatomical connection of similar dimensions [33, 95]. The rigid wall assumption may thus appear as a reasonable first order assumption in front of other geometrical modifications.

2.9.2 Flow Pulsatility

Due to the absence of a right ventricle, neglecting flow pulsatility in the TCPC was assumed to be an acceptable assumption by most investigators. Yet, pulsatility in both IVC and SVC has been reported clinically in Fontan patients [106, 107] such that the validity of this assumption is questionable. The first pulsatile experiment was described by DeGroff et al. [108], who modeled generic IVC and SVC flow waveforms in a set of idealized TCPCs with varying caval offsets. Comparison to steady flow simulations revealed an increase in power loss under pulsatile conditions for all tested geometries. Pulsatility led to a 67% increase in the average power loss for the 1 diameter offset model, while this increase was of only 25% in the no-offset model. As a result, under pulsatile conditions, including a 1 diameter offset only yielded a 3% reduction in power loss compared to not having any offset, whereas steady flow results had predicted a 28% reduction. The lower sensibility of the no-offset model to the pulsatile flow disturbances could be attributed to the fact that the absence of caval offset already led to significant levels of instability even with constant inflow rates.

Marsden et al. [90] confirmed that flow pulsatility increased the energy dissipation measured in patient-specific geometries. In that study, the authors made use of two patient specific geometries and patient specific flow curves when available. The impact of lower limb exercise was modeled by increasing the heart rate and mean IVC flow rate. Results revealed a significant decrease in energy efficiency (defined as the ratio of the outlet power to the inlet power) under pulsatile conditions for both models and under all simulated exercise levels.

Both of these studies demonstrated a significant impact of pulsatility on energy efficiency, thus raising the question of whether this would alter the relative performance of different TCPC options. The idealized results of DeGroff et al. [108] hint towards the fact that intra-atrial options, which host important levels of instabilities even with steady inflows, might be less sensitive to pulsatile disturbances than extra-cardiac options. On the other hand, analysis of the *in vivo* IVC and SVC flow curves of 62 patients from the Georgia tech database (Table 2-2) revealed that the IVC pulsatility levels are on average 3.2 times higher for intra-atrial TCPCs compared to extra-cardiac options, which would hint towards a higher impact of pulsatility in intra-atrial options. In order to gain a better insight into the intra-atrial and extra-cardiac TCPC hemodynamics, there is thus a need for a detailed study accounting for differences in patient-specific anatomy and pulsatility between intra-atrial and extra-cardiac options.

Table 2-2: Mean pulsatility indices obtained 62 patients selected from the GeorgiaTech patient database

Vessel	IVC (in intra-atrials)	IVC (in extra-cardiacs)	SVC
Pulsatility	2.00 $\pm$ 2.70	0.62 $\pm$ 0.21	0.82 $\pm$ 0.56

2.9.3 Impact of the Surrounding Structures

The most straightforward way of specifying the boundary conditions is to impose the inlet and outlet flow rates based on the measured *in vivo* data, typically obtained from PC MRI. These measured flow data are ideal for reproducing the *in vivo* state, but pose some problems when simulating exercise conditions or altering the geometry. Indeed, reorienting the IVC baffle or dilating an LPA stenosis could alter the flow distribution to

the lungs, such that results obtained using the *in vivo* flow rates may be an erroneous representation of what would happen after modifying the TCPC. Similarly, a modification in TCPC geometry will most likely alter its hemodynamic resistance, which will in turn impact the cardiac output achieved by the single ventricle [65].

Multi-scale approaches, coupling detailed 3D CFD investigations of the TCPC to lower order representation of the rest of the cardiovascular system, are currently under development to model the regulation of the outlet flows by the downstream pulmonary vasculature, as well as the impact of the TCPC upon the rest of the cardiovascular system. Marsden et al. [90] for example prescribed a resistance value to represent the impact of the downstream pulmonary vasculature upon the LPA and RPA outflows. The adequate pulmonary resistance was obtained by fitting the outflow pressures to *in vivo* measurements. Seeking to circumvent the need for these patient specific pressure data, which can only be obtained by invasive catheterization, Clipp et al. [109, 110] suggested using 1D finite element analysis to model blood flow in arterioles large enough to be captured by MRI and imposing an organ specific impedance boundary condition using parameterized fractal trees. Extending the domain even further, lumped parameter models have been used, though not in synergy with 3D CFD, to represent the entire cardiovascular circuit at minimal computational costs [65, 111]. Here again, these models require number of *in vivo* pressure and flow data to fit each one of the organ-specific parameters, which can be difficult to obtain.

In addition to the need for additional patient specific data to fit the different model parameters, extending the simulation domain brings forth one major consideration: increasing the model complexity does not necessarily add to the accuracy if the number

of unknown increases. Is a coupled CFD-lumped parameter model more accurate if generic parameters have been used to fit the vascular compliances? Can the lumped-parameter model predict the post-operative remodeling of the lung and vasculature? Is the gain in accuracy worth the added computational cost? Consider for example a Fontan patient with unilateral PAVMs in the left lung. Due to the venous to pulmonary shunts present in his left lung, this patient will present a far lower PVR on the left side than on the right. The objective of a surgical planning study would thus be to rebalance the hepatic flow distribution, hoping to revert the left PAVMs. This would in turn increase left lung resistance, making the pre-operative model no longer valid. Similarly, venous compliance and resistance is known to vary acutely after the Fontan surgery, such that lumped parameters fit to the pre-operative state may not adequately represent the cardiovascular adaptation even in the acute stage. One approach to overcome this problem would be to develop evolutionary models of the vasculature, such that the pulmonary vascular resistance (PVR) would vary depending on the amount of nutrients distributed to each lung for example. Development of such a model however would require a large amount of clinical data for both parameter fitting and model validation, which are not available to date.

An alternate approach is to characterize the TCPC efficiency of the different surgical options over a wide range of flow conditions [33, 88], thereby providing the necessary information to the engineers and clinicians to try and predict the temporal adaptation of the lungs and flow splits. Similarly, depending on the objective of the study, decoupled CFD and lumped-parameter simulations may represent a viable and more efficient strategy to explore a broad range of “what if” scenarios in a short clinical

time-frame. As an example, Whitehead et al. [92] used 3D CFD simulations to characterize the resistance of different geometries. Sundareswaran et al. [65] then conducted an independent lumped-parameter study to predict the exercise performance of a patient with these TCPC resistances. Similarly, Pekkan et al. [111] made use of CFD-derived TCPC resistances and subsequent lumped-parameter modeling to test the benefit of a ventricular assist device depending on the patient's TCPC resistance.

2.9.4 Solver Accuracy and Need for Validation

Finally, the notion that CFD is a mature technology that can be applied indiscriminately to model any flow physics is becoming *de facto* in the biomedical field. In reality, CFD is an intricate and continuously evolving science that necessitates a close synergy and integration between modeling efforts and *in vitro* experimentation to guide model development and validation. This is of particular importance when dealing with biomedical engineering flows since they exhibit a host of unique modeling challenges and difficulties. Such flows take place in complex, multi-connected domains with compliant walls and flexible immersed boundaries and are dominated, among others, by pulsatile effects, three-dimensional separation and vortex formation, regions of flow reversal, periodic transition to turbulence and laminarization. In spite of these enormous complexities, which pose a formidable challenge to even the most advanced CFD tools available today, only a few of the TCPC studies include an adequate CFD validation. A typical counter-example is the study by Khunatorn et al. [112] that found caval offset to be detrimental from a power loss point of view, contrary to the experimental findings by Sharma et al. in the same geometry [82]. Khunatorn et al. [85] later demonstrated out that

their numerical approach failed to capture the flow instabilities at the center of the connection and secondary flow structures in the PAs, which could explain discrepancies even in global efficiency measures such as energy dissipation rates. Pekkan et al. pointed out that overall 2nd order accuracy was a requirement to capture patient-specific TCPC flow structures, even when considering time-averaged flow fields [87]. The limitations of CFD tools for TCPC simulations have been documented on many occasions [85, 87, 113-115], and all of these studies reinforce the need for high-resolution numerical schemes, comprehensive experimental validation, and careful application [115].

2.10 Summary and Significance of the Proposed Approach

Previous experimental, numerical and *in vivo* studies have all underscored the high sensitivity of the TCPC efficiency, and thus the patient outcome, to the TCPC geometrical design. However, despite a large number of available bioengineering studies, there is still a lack of clear guidelines for the clinical community to best design the TCPC connection during surgery. With the recent convergence of high-resolution medical imaging and processing methods, and the development of virtual surgery environments where the surgeon can reproduce the gestures he would do in the operating room and modify a virtual anatomy, numerical methods present the unique opportunity to provide individualized surgical planning for each incoming patient. As promising though these new technologies may seem, their application in the TCPC realm is still sparse and the clinical relevance of the existing CFD studies remains limited by either too large a number of simplifications, or too small a number of patient cases to draw relevant surgical guidelines. In addition, there is a continuing need for a careful assessment of the

different modeling assumptions, in order to assess the parameters that may or may not be disregarded in favor of faster simulations and increased number of tested options. Finally, it is worthwhile to highlight that while CFD is generally perceived as a well-established and reliable technology, it is in reality a constantly evolving science, calling for thorough validation at each development stages.

The approach proposed in this thesis thus seeks to develop a fully-validated numerical flow solver that will allow for pulsatile 3D flow simulations in patient-specific TCPCs to quantify the impact of pulsatility across different TCPC options, and that could be used to conduct patient-specific surgical planning studies within clinical timeframe and resources. To this end, our numerical approach will be designed to capture the intricacies of *in vivo* anatomies with high accuracy but minimum user-interaction, while the flow solver will ensure overall second order spatial and temporal accuracy to resolve the instabilities and secondary flow structures reported in patient-specific anatomies.

All developments will be validated against controlled *in vitro* experiments to ensure accuracy. Patient-specific pulsatile simulations will be conducted using *in vivo* anatomies and flow curves reconstructed from MRI and PC MRI data available from the Georgia Tech Fontan patient database. To quantify the effect of pulsatility on the TCPC efficiency, each pulsatile simulation will be accompanied by a constant inflow counter-part, conducted using the same *in vivo* anatomy but the mean vessel flow rate rather than *in vivo* flow curve. Comparison between the performance metrics obtained under steady and pulsatile conditions will for the first time quantify the relative impact of flow pulsatility across in patient specific geometries across different TCPC templates.

In addition, the proposed numerical solver will fill in a crucial gap in the array of tools needed for the completion of a surgical planning tool, allowing surgeons to not only virtually perform multiple different surgical options within a virtual-reality simulator, but also compare their hemodynamic efficiency to best plan the TCPC surgeries for each patient. Application and benefits of such an integrated surgical planning will be demonstrated on patients featuring an interrupted IVC with azygous continuation, who represent a particularly challenging clinical scenario. The different surgical options to be investigated will be developed in close synergy with the surgeon in charge of the patient. As this subgroup of patient is especially prone to PAVMs, emphasis will be set on equally distributing the cardiac output and the hepatic nutrients to the left and right lung. Secondary optimization metrics will include minimizing the pressure drops and energy dissipation. In addition to a direct benefit to the patient under consideration, this study will also have a larger impact for the clinical management of SVHD patients with an interrupted IVC. First, the systematic review of the various geometries investigated for each surgical planning case will allow for a better definition of the different "anatomical templates" (e.g. interrupted IVC combined with a single SVC or bilateral SVCs, classification based on the relative position of the azygous and inominate vein). Then, it will shed light onto the impact of caval offset, vessel flaring and other design parameters upon TCPC hemodynamics depending on the underlying patient anatomy. These results will provide useful surgical guidelines for each anatomical template, which could benefit the global surgical community, including centers that do not have access to patient-specific surgical planning interfaces.

CHAPTER 3

NUMERICAL BACKGROUND

The approach proposed in this thesis seeks to develop a fully-validated numerical flow solver that will allow for pulsatile 3D flow simulations in patient-specific total cavopulmonary connections (TCPC), and that could be used to conduct patient-specific surgical planning studies within clinical timeframe and resources. For the purpose of this study, blood will be assumed to be an incompressible Newtonian fluid, which is a fair assumption in large vessels, and the motion of the TCPC walls will be neglected. The main challenges to be addressed are to define a numerical approach that 1) accurately captures the unsteady dynamics of *in vivo* blood flows, and 2) allows for the fine discretization of arbitrarily complex *in vivo* structures with minimum user interaction. The following sections will thus review the computational fluid dynamics (CFD) approaches that have been developed to tackle incompressible Newtonian flows, and the options available to capture the geometrical intricacies of *in vivo* geometries.

3.1 A Brief Review of Incompressible Newtonian Fluid Dynamic

Prior to dwelling into the different modeling options of incompressible Newtonian fluids, this section provides a brief overview of the governing equations of incompressible fluid motion. The motion of a fluid is governed by the conservation laws of mass and momentum. These equations, called the Navier-Stokes equations, can be expressed in their integral form by:

$$\int_V \frac{\partial \rho}{\partial t} dV + \oint_S \rho \vec{\mathbf{u}} \cdot \vec{\mathbf{n}} dS = 0 \tag{3-1}$$

$$\int_V \frac{\partial (\rho \vec{\mathbf{u}})}{\partial t} dV + \oint_S \rho \vec{\mathbf{u}} (\vec{\mathbf{u}} \cdot \vec{\mathbf{n}}) dS = -\oint_S P \vec{\mathbf{n}} dS + \oint_S \mathbf{T} \cdot \vec{\mathbf{n}} dS + \int_V \rho \vec{\mathbf{F}} dV \tag{3-2}$$

where $\vec{n}$ represents the outward normal from the closed surface *S* enclosing the arbitrary volume *V*, $\rho(\vec{\mathbf{x}},t)$ is the fluid density at a given location ($\vec{\mathbf{x}}$) and instant in time (t), $\vec{u}(\vec{\mathbf{x}},t)$ the velocity. $P(\vec{\mathbf{x}},t)$ and $\mathbf{T}(\vec{\mathbf{x}},t)$ represent the normal and anisotropic components of the stress tensor acting on the surface of the fluid element. For fluid applications, $P(\vec{\mathbf{x}},t)$ thus describes the pressure field, while $\mathbf{T}(\vec{\mathbf{x}},t)$ describes the effect of the viscous forces. $\vec{F}(\vec{x},t)$ the force per unit mass due to any external field. Equation II-1 simply states that the change in mass within a given volume *V* is equal to the mass of fluid entering and exiting that same volume. Equation 2-2 is an application of Newton's 2nd law to a continuum rather than to a solid object. It states that the acceleration of a volume of fluid *V* (left hand side of Equation 2-2) is equal to the sum of the forces acting on this element of fluid (right hand side).

The above system of equations contains too many unknowns to be solved directly and modeling assumptions ought to be made in order for the system to have a solution. In our particular case, blood in large vessels is considered to be an incompressible Newtonian fluid and all external body forces will be neglected. These assumptions yield the following simplifications:

(1) As the flow is incompressible, the density, ρ, is constant and uniform.

$$\rho(\vec{\mathbf{x}},t) = \rho \tag{3-3}$$

(2) Then, the shear stresses tensor, $\mathbf{T}(\vec{\mathbf{x}},t)$, of a Newtonian fluid is symmetric and proportional to the shear strains, $\boldsymbol{E}(\vec{\boldsymbol{x}},t)$:

$$\mathbf{T} = 2\mu\left(\mathbf{E} - \frac{1}{3}(\nabla\cdot\vec{\mathbf{u}})I\right) \text{ and } \mathbf{E} = \frac{1}{2}\left(\nabla\vec{\mathbf{u}} + \nabla\vec{\mathbf{u}}^{T}\right) \tag{3-4}$$

where μ is the viscosity of the fluid, **I** is the is the 3x3 identity matrix

(3) Finally, neglecting all body forces yields:

$$\rho\vec{\mathbf{F}} = \vec{0} \tag{3-5}$$

With all these assumptions combined, Equations 2-1 and 2-2 simplify into the following integral form of the incompressible Navier-Stokes equations:

$$\oint_S \vec{\mathbf{u}}\cdot\vec{\mathbf{n}}dS = 0 \tag{3-6}$$

$$\rho\left\{\int_V \frac{\partial(\vec{\mathbf{u}})}{\partial t}dV + \oint_S \vec{\mathbf{u}}(\vec{\mathbf{u}}\cdot\vec{\mathbf{n}})dS\right\} = -\oint_S P\vec{\mathbf{n}}dS + \mu\oint_S\left(\nabla\vec{\mathbf{u}} + \nabla\vec{\mathbf{u}}^{T}\right)\cdot\vec{\mathbf{n}}dS \tag{3-7}$$

Inertia — Surface stresses

Unsteady acceleration — Convective acceleration — Normal pressure stresses — Viscous shear stresses

The above integral form is ideal for finite volume formulations, which assess the force balance over each computational grid cell. Alternatively, finite difference approaches, which establish the force balance at every grid node, will find the discrete reformulation of the above equations more useful. These may be obtained by applying the Gauss–Ostrogradsky theorem to Equations 2-6 and 2-7. This theorem states that the flux of a vector field through a surface *S* is equal to its integral over the enclosed volume *V*, allowing all quantities to be expressed as volume integrals. As the continuity and momentum relations hold for any volume V, it can be deduced that these relationship

hold in any point, yielding the following form for the discrete incompressible Navier-Stokes equations:

$$\nabla\left(\vec{\mathbf{u}}\right) = 0 \tag{3-8}$$

$$\underbrace{\rho\left\{\underbrace{\frac{\partial\left(\vec{\mathbf{u}}\right)}{\partial t}}_{\text{Unsteady acceleration}} + \underbrace{\left(\vec{\mathbf{u}}\cdot\nabla\right)\left(\vec{\mathbf{u}}\right)}_{\text{Convective acceleration}}\right\}}_{\text{Inertia}} = \underbrace{-\nabla\left(P\right)}_{\text{Normal pressure stresses}} + \underbrace{\mu\nabla^2\vec{\mathbf{u}}}_{\text{Viscous shear stresses}} \qquad \text{Surface stresses} \tag{3-9}$$

3.2 Numerical Methods for Incompressible Newtonian Flows

Several numerical schemes have been developed for the simulation of both steady and unsteady incompressible flows. Approaches differ in the way they handle (i) the temporal discretization and time advancement procedure, and (ii) the spatial discretization, both of which are addressed in the following sub-sections.

3.2.1 Temporal Discretization

The specificity of the incompressible Newtonian equations is the absence of an evolutionary equation for pressure that would establish an explicit relationship between the temporal derivative of pressure $\partial P/\partial t$ and other spatial derivatives. A direct consequence is that with the Navier-Stokes equations formulated as in Equations 2-6 through 2-9, the pressure field cannot be calculated by an explicit time-advancement procedure as is used in compressible applications. Nevertheless, velocity and pressure are tightly inter-related, and their synchronization is a compulsory requirement for both the continuity and the momentum equations to be satisfied. The following sections give a

detailed review of the two main approaches that have been derived to enforce this pressure-velocity coupling, namely: 1) the artificial compressibility (AC) method, and 2) fractional step pressure projection (FSPP) method.

3.2.1.1 *Artificial Compressibility Methods*

The AC method for steady incompressible flow simulations was first proposed by Chorin [116]. This method builds on a simple physical observation: in incompressible fluid, information is transmitted from one side of the fluid to the other at infinite speed. This poses an inherent modeling difficulty as numerical schemes cannot replicate infinite propagation speed. The basic idea of the AC approach is thus to perform pseudo-iterations within each physical time step, allowing the information to be propagated at finite speed in the pseudo-time domain. The Navier-Stokes equations with that formulation can be written as follows:

$$\frac{1}{c_0^2}\frac{P^{*l+1}-P^{*l}}{\Delta\tau}+\rho\frac{\partial \mathbf{u}_i^{*l+1}}{\partial x_i}=0 \tag{3-10}$$

$$\frac{\mathbf{u}_i^{*l+1}-\mathbf{u}_i^{*l}}{\Delta\tau}+\frac{\mathbf{u}_i^{*l}-\mathbf{u}_i^{n}}{\Delta t}+\mathbf{u}_j^{*l}\frac{\partial \mathbf{u}_i^{*l}}{\partial x_j}=-\frac{1}{\rho}\frac{\partial P^{*l}}{\partial x_i}-\upsilon\frac{\partial^2 \mathbf{u}_i^{*l+1}}{\partial x_j \partial x_j} \tag{3-11}$$

where t is the physical time, τ the pseudo time and the constant c_0 is equivalent to the speed of sound in the artificially compressible fluid. The superscript n denotes the flow and pressure values after the nth physical time-step, while superscripts $*l+1$ and $*l$ denote the flow and pressure values at the pseudo-time steps l and $l+1$. This formulation restores the elliptic character of the compressible equations, so that any of the time-marching approaches developed for compressible flows can be applied here. The above equations are iterated in pseudo-time until equilibrium is reached for every physical time-step.

Consequently, linearization errors in physical time can be driven to machine zero and the governing equations can be satisfied at the next physical time level. The method therefore has the same order of accuracy for velocity and pressure as that of the discretization of the momentum equations. However, as stated above, equilibrium needs to be reached at every physical time-step. This implies that the entire right hand side of Equation 2-11 needs to be evaluated at every pseudo-iteration until convergence, considerably increasing the CPU time per physical time step.

3.2.1.2 Fractional Step Pressure Projection Methods

The fractional step method, which was first introduced by Harlow and Welch [117], is perhaps the most widely used approach for incompressible flows. The basic idea consists of breaking down the complex Navier-Stokes equations into simpler steps for which efficient time integration procedures can more readily be designed. It typically proceeds into two steps: First an intermediate velocity field $\vec{u}^*$ is computed using the momentum equation only, i.e. without enforcing the continuity equation. Then, since $\vec{u}^*$ doesn't satisfy the continuity equation, and thus is not divergence free, a second step is performed to correct $\vec{\mathbf{u}}^*$ and produce a divergence free field $\vec{\mathbf{u}}^{n+1}$.

Boundary conditions are the major problem of FSPP approaches. Applying physical boundary conditions onto the intermediate velocity field, which has no true physical meaning, brings down the overall scheme accuracy. FSPP approaches that neglect pressure for the first step have been shown to be limited to 1st order temporal accuracy unless very specific boundary conditions are applied [118]. Far more accurate results may be obtained by retaining the best known estimate for pressure in the 1st step

and applying a correction on both velocity and pressures in the second. This approach corresponds to the P2 class of FSPP in [118] and proceeds as follows:

(1) Intermediate velocity step: Considering for simplicity a fully explicit time stepping algorithm, the momentum equation for the intermediate velocity in P2 class methods reads as:

$$\frac{\mathrm{u}_i^* - \mathrm{u}_i^n}{\Delta t} + \mathrm{u}_j^n \frac{\partial \mathrm{u}_i^n}{\partial x_j} = -\frac{1}{\rho}\frac{\partial P^n}{\partial x_i} - \upsilon \frac{\partial^2 \mathrm{u}_i^n}{\partial x_j \partial x_j} \tag{3-12}$$

Note that the pressure field P corresponds to the known pressure field at time step n.

(2) Correction step: The terms omitted from the momentum equation in the first step are then solved together with the continuity equation:

$$\frac{\mathrm{u}_i^{n+1} - \mathrm{u}_i^*}{\Delta t} = -\frac{1}{\rho}\frac{\partial(\delta P)}{\partial x_i} \text{ where } \delta P = P^{n+1} - P^n \tag{3-13}$$

$$\frac{\partial \mathrm{u}_i^{n+1}}{\partial x_i} = 0 \tag{3-14}$$

The incremental pressure δP is obtained using the divergence-free property of the velocity field $\vec{\mathbf{u}}^{n+1}$. Taking the divergence of Equation 2-13 and using the fact that the velocity field $\vec{\mathbf{u}}^{n+1}$ is divergence free, we obtain the Poisson equation for the incremental pressure δP :

$$\frac{\partial^2(\delta P)}{\partial x_i \partial x_i} = \frac{\rho}{\Delta t} \cdot \frac{\partial \mathrm{u}_i^*}{\partial x_i} \tag{3-15}$$

Once δP is know, the velocity u^{n+1} and pressure P^{n+1} fields at time n+1 can be obtained using the expressions given in Equations 2-13.

Since, in the P2 class of FSPP, the intermediate velocity satisfies the full momentum equation, physical boundary conditions can be used on the intermediate

velocity field. The resulting accuracy is of at least second order when using the physical boundary conditions on the intermediate pressure and velocity fields [119] and can be increased even further when using carefully designed boundary methods such as the one proposed by Kim and Moin [120]. While AC methods could yield higher degree of accuracy, this benefit is in practice balanced by the drastically faster computational speed of FSPP approaches. Ge and Sotiropoulos [121], for example, used a Krylov subspace method, namely the restarted Generalized Minimal Residual Method (GMRES) solver, enhanced with a multigrid preconditioner to solve the Poisson equation. The authors report excellent computational performances, and successfully capture the pulsatile blood flow dynamics through a bileaflet heart valve, testifying for the robustness of the method. Such a FSPP approach combines both efficiency and 2nd order temporal accuracy, and thus constitutes an attractive alternative to the AC method.

3.2.2 Spatial Discretization

Accuracy, stability, and ease of implementation should be carefully considered when choosing among different spatial discretization schemes. The most straightforward way to compute 1st and 2nd spatial derivatives is to employ centered differences on a collocated grid (where pressure and velocity information are stored at the same location). Using the artificial compressibility approach for the time-integration for example, central difference operators would yield the following expression for the continuity and momentum equations on the one-dimensional uniform grid shown in Figure 3-1:

$$\frac{1}{c^2}\frac{\partial P_i}{\partial \tau} + \rho \frac{u_{i+1} - u_{i-1}}{2\Delta x} = 0 \tag{3-16}$$

$$\frac{\partial u_i}{\partial \tau} + \frac{\partial u_i}{\partial t} + u_i \frac{u_{i+1} - u_{i-1}}{2\Delta x} = -\frac{1}{\rho} \frac{P_{i+1} - P_{i-1}}{2\Delta x} - \upsilon \frac{u_{i+1} - 2u_i + u_{i-1}}{\Delta x^2} \tag{3-17}$$

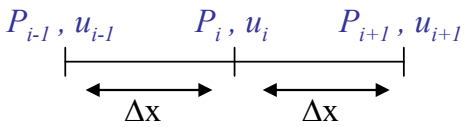

Figure 3-1: Schematic representation of a collocated one dimensional uniform grid. Pressure and velocity values are stored at the same location.

Unfortunately, Equations 2-16 and 2-17 lead to two types of instabilities: 1) oscillations in the velocity fields at high Reynolds numbers and 2) oscillations in the pressure field. The instabilities in the velocity fields are the same as that encountered when solving advection-dominated transport equations or boundary layer equations, and are due to the symmetric nature of the velocity differentiation stencils. The unphysical amplifications of small perturbations in the velocity field can be cured by explicitly introducing an artificial dissipation, or using more dissipative difference operators (such as upwind schemes) to the same effect.

The oscillations in the pressure field find their origin in the combined use of collocated grids and symmetric difference operators. With such a layout, the temporal evolution of the pressure P_i depends on u_{i+1} and u_{i-1}, which in turn depend on P_{i-2}, P_i and P_{i+2}. The pressure values on the odd and even grid lines thus evolve without a direct interaction and may reach a solution independently of one another, leading to what is known as the check-board effect. This issue may be circumvented by either introducing an artificial damping term that will smooth the pressure field and stabilize the solution, or using staggered grids. In the latter option, pressure values are stored at the cell centers

while velocities are stored at the cell faces (see Figure 3-2). Using this alternating pattern, the partially discretized continuity and momentum equations become:

$$\frac{1}{c^2}\frac{\partial P_{i+1/2}}{\partial \tau} + \rho \frac{u_{i+1} - u_i}{\Delta x} = 0 \tag{3-18}$$

$$\frac{\partial u}{\partial \tau} + \frac{\partial u_i}{\partial t} + u_i \frac{u_{i+1} - u_{i-1}}{2\Delta x} = -\frac{1}{\rho}\frac{P_{i+1/2} - P_{i-1/2}}{\Delta x} - \upsilon \frac{u_{i+1} - 2u_i + u_{i-1}}{\Delta x^2} \tag{3-19}$$

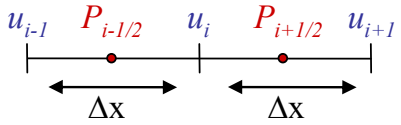

Figure 3-2: Schematic representation of a one dimensional uniform staggered grid arrangement. Velocity values are stored on the cell surface, while pressure values are stored at the cell center.

A limitation of staggered grid arrangement is the difficulty to synchronize the velocity and pressure boundary conditions prescribed at the node and half-node respectively. The hybrid staggered/non-staggered grid arrangement presented by Gilmanov et al. [122] represents an elegant alternative to the problem. The Navier-Stokes equations are solved using the staggered grid arrangement for stability, while the boundary conditions are prescribed on the non-staggered grid layout. This simple reformulation simplifies the implementation of the solution reconstruction algorithm near complex immersed bodies and was shown to increase the accuracy on the vicinity of the boundary.

3.2.3 Summary of the CFD Schemes for Incompressible Flows

In summary, the approach retained for this thesis will build on the methods developed by Gilmanov et al. [122] and Ge et al. [123]. The spatial discretization scheme will be based on the hybrid staggered/non-staggered arrangement proposed by Gilmanov et al. [122], which combines the stability of staggered grid layouts and the simplicity and accuracy of non-staggered grids for the prescription of the boundary conditions. The convective terms will be further discretized using an upwind difference operator to avoid to the development of velocity instabilities. Finally, the solver will incorporate the FSPP approach developed by Ge et al. [123] for its computational expedience. With all these tools at hand the main question to be answered is that of the actual discretization of the computational domain. Irrespective of the numerical scheme retained, the generation of a finely resolved computational mesh of the *in vivo* TCPCs is primordial for the accuracy of the predicted hemodynamics. Identifying the best strategy to capture the *in vivo* geometries will be the object of the following sections.

3.3 Numerical Simulations in Arbitrarily Complex Geometries

A major challenge for the numerical simulation of *in vivo* cardiovascular flows stems from the difficulty to generate computational meshes that properly describe the complexity of real-life anatomies. Unstructured grids with finite-volume or finite-element methods provide a natural choice for tackling such problems and have been used with a great deal of success [124-126]. Such methods, however, typically involve higher computational overhead than finite-difference or finite-volume methods on structured grids. Structured curvilinear body-fitted meshes have also been used but generally need

to be used in conjunction with domain decomposition methods, such as overset Chimera grids [87]. Even when domain decomposition is employed, the generation of good quality composite, boundary-conforming meshes could be cumbersome and time consuming for realistic anatomies [87].

Non-boundary conforming immersed-boundary (IB) approaches have recently attracted considerable attention for the simulation of flows around complex bodies as they circumvent the difficulty of the body-fitted volume mesh generation. The complex geometry is immersed in a background Eulerian grid (Figure 3-3), which will be used to solve the Navier-Stokes equations. Due to the ease with which they can handle complex, moving boundaries, IB methods have been applied to a wide range of problem types ranging from relatively simple flows past cylinders, [122, 127] to flows past swimming animals and organisms, [122, 128]. A review of the different methods used for problems with liquid-solid boundaries is offered by Mittal et al. [129].

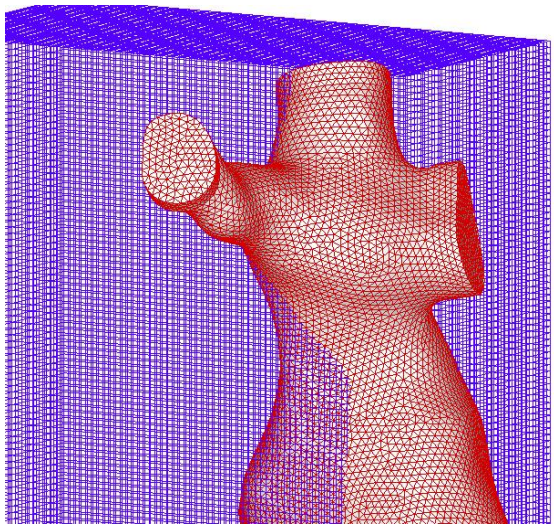

Figure 3-3: Surface mesh of a TCPC (in red) immersed in a background Eulerian grid (in blue).

The quality of the interface tracking and the enforcement of the boundary conditions are two key factors for the overall accuracy of IB methods. In our applications, the TCPC walls will be assumed to be rigid such that tracking of the vessel deformation is of no relevance. On the other hand, enforcement of the boundary conditions, namely of the no-slip boundary conditions along the TCPC walls, should be carefully implemented. Three dominant approaches have been discussed in literature, namely cut-cell methods [130-132], diffuse immersed-boundary methods [133, 134], and sharp interface immersed-boundary methods [121, 122].

Cut-cell methods modify the shape of the computational cells cut by the body to adapt to the exact geometry of the immersed boundary (Figure 2-4) and generate a Cartesian albeit boundary-conforming mesh. Using proper interpolation strategies, the flow variables can be computed on the resulting irregular cell interfaces according to the boundary conditions on the body. A difficulty encountered in the implementation of cut-cell methods arises from the large number of possible geometrical configurations for the interfacial cells, which calls for a large number of special cases when implementing the boundary conditions. Furthermore, in complex geometries, the unavoidable generation of

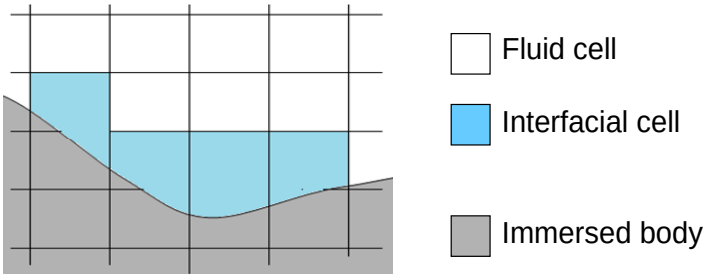

Figure 3-4: Cut-cell approach. Interfacial trapezoidal cells allow the mesh to conform to the shape of the immersed geometry. To avoid having cells of small dimensions, interfacial cells merge with the closest fluid cells.

interface cells with very small volume adversely impacts the conservation and stability properties of the solver. Special treatments are thus also required during the mesh generation step to merge small cells with their closest neighbors [131].

Contrary to the cut-cell approach, diffuse and sharp-interface immersed boundary methods do not modify the geometry of the Cartesian to conform to the immersed body. In diffuse immersed-boundary methods the Navier-Stokes equations are solved on the entire embedding Eulerian grid. The action of the immersed boundary is transmitted to the fluid through an additional source term in the momentum equations. This technique has successfully been applied by Peskin et al. to model the action of a beating heart and the associated intra-cardiac hemodynamics [133, 135]. The cardiac muscle fibers were modeled as a set of elements linked by springs. To avoid numerical instabilities, a delta function was then used to distribute the external forcing of these muscle fibers over 3 to 4 fluid nodes in the vicinity of the boundary. The need for such force distribution poses an inherent limitation to the accuracy of these methods, smearing the location of the immersed boundary over a few grid cells and calling for high resolution grids in order to properly capture the solid-fluid interfaces.

Sharp interface immersed-boundary (SIIB) approaches [136, 137] seek to address that limitation by circumventing the need for discrete force stencils. Similarly to cut-cell approaches the immersed-boundary is treated as a sharp-interface. However, rather than modifying the Eulerian grid cells in the vicinity of the boundary to apply the boundary conditions exactly at the immersed boundary location, SIIB methods use an interpolation strategy to impose the boundary conditions on the fluid elements closest to the boundary. The embedding Cartesian grid is differentiated into three element categories: the

elements that fall outside of the fluid domain, the fluid elements that are in the immediate vicinity of a boundary (IB elements) and the fluid elements that fall strictly inside the fluid domain (fluid elements). The Navier-Stokes equations are solved on the fluid elements without adding any external forcing from the immersed-boundary. The action of the immersed-boundary is accounted for at the IB-elements, whose pressure and velocities are reconstructed by interpolation between the closest immersed-boundary and fluid elements (Figure 3-5). The interpolation procedure is key in the overall SIIB accuracy. Using the quadratic interpolation method exemplified in Figure 3-5, Gilmanov et al. demonstrated that SIIB methods could easily yield overall second order accuracy [122]. Taking advantage of their combined ease of implementation and accuracy, researchers have used SIIB methods for a wide range of problem types ranging from relatively simple flows past cylinders [122, 127], to flows past swimming animals and organisms [122, 128], blood flow past the leaflets of a mechanical prosthetic heart valve [121], and even flows around a walking human [138].

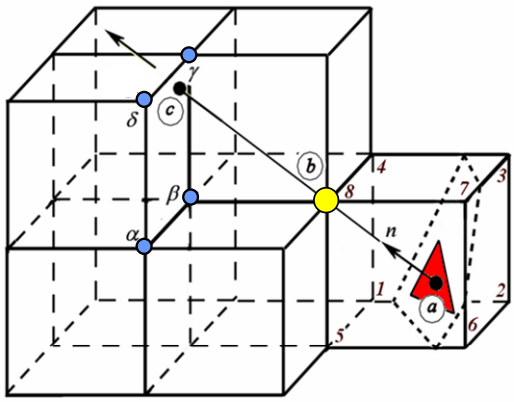

Figure 3-5: Reconstruction of the solution at a boundary node (b) by interpolating between the closest immersed-boundary element (a) and closest fluid element (c) along the local normal to the immersed-boundary. (Image courtesy: [122])

Going back to the modeling of the *in vivo* TCPC anatomies, IB methods seem ideally suited to capture the intricacies of the *in vivo* anatomies without requiring a tedious mesh generation. SIIB methods, in particular, offer a promising route both in terms of implementation simplicity and spatial accuracy. However, with the exception of the pioneering work by Peskin and McQueen, who used the classical diffused-interface IB formulation [134, 139], and the more recent SIIB study of Yokoi *et al.* [140], the use of IB methods in simulating complex anatomical blood flows is not as wide-spread as one would anticipate given the ease with which such methods can handle arbitrarily complex geometries.

One possible explanation for the scarcity of applications of IB methods to anatomical flows lies in the manner in which such methods handle the Cartesian grid nodes that are not part of the flow domain (i.e. the nodes that reside outside of the fluid in the solid side of a fluid/solid interface). The common practice is to retain such non-fluid grid nodes in the grid structure but blank them out of the computation, sacrificing the added memory and computational overhead due to the unused non-fluid nodes for the sake of the overall algorithmic simplicity. Such approach is reasonable when dealing with external flow problems around bodies that only represent a small fraction of the background Eulerian computational box. But a drastically different situation can be encountered in biomedical problems, when IB methods are applied to simulate internal flow problems. Let us consider for example a 90 degree curved pipe immersed into a uniform Cartesian grid as shown in Figure 3-6. Despite the simple geometry under consideration, it is evident that most of the Cartesian grid nodes actually reside outside of the pipe, with no more than 15% of the nodes located within the fluid domain.

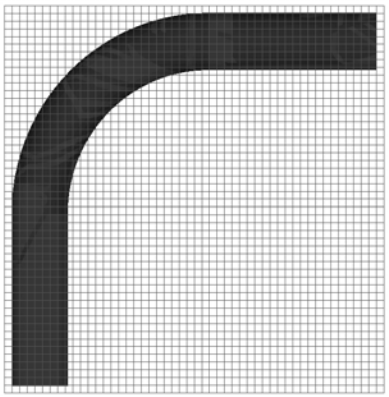

Figure 3-6: 90^{o} curved pipe immersed in a Cartesian grid

This situation will only be exacerbated when one attempts to model arbitrarily complex, multi-connected anatomical TCPC geometries with an IB methodology. As illustrated in Figure 3-7, the ratio of fluid nodes to Cartesian grid nodes does not exceed 10%, and can drop to as low as 1-5% for more tortuous geometries. A clear example of this shortcoming can be found in the recent work of Yokoi *et al.* [140] who employed a SIIB approach to simulate blood flow in a very complex cerebral aneurism anatomy immersed in a Cartesian grid with 160×50×75 nodes. Yokoi *et al.* did not provide any information about the number of nodes lying in the interior of the aneurysm model but given the complexity of their geometry the vast majority of the Cartesian nodes must have resided in the exterior of the flow domain and thus unnecessarily burdened the computation. Furthermore, Yokoi *et al* did not carry out any grid sensitivity studies as they reported results for only one mesh. Therefore, the feasibility of carrying out grid convergence studies for complex anatomical geometries using a SIIB approach has yet to be demonstrated.

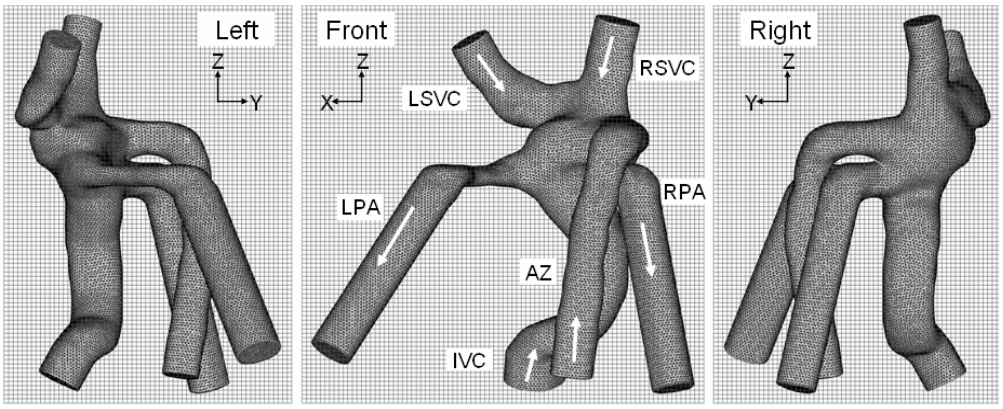

Figure 3-7**:** Patient-specific TCPC geometry immersed in a uniform Cartesian mesh. The curvature of the vessels involved leads to a large number of unused non-fluid nodes around the structure of interest while only a small portion of the nodes (6%) lie within the fluid domain, inside the vessels. IVC and (L or R) SVC: inferior and (left or right) superior venae cavae. AZ: azygous vein. LPA and RPA: left and right pulmonary arteries.

3.4 Optimizing the Data Structure of SIIB Methods

As discussed above, the main challenge confronting SIIB methods when applied to flows in complex, cardiovascular anatomies lies in the excessive memory overhead added by the unused Cartesian grid nodes. In addition SIIB methods are especially sensitive to the mesh refinement in the vicinity of the immersed surface, due to the velocity reconstruction performed at the boundary nodes. This calls for even finer meshes in these boundary regions in order to maintain the overall scheme accuracy. The need for different levels of refinement in different regions of space is not specific to SIIB methods and there is a large core of literature dedicated to the definition of efficient data structures to achieve high spatial resolution in localized regions of space.

Block-structured grids (or multi-block methods) [141] present an attractive option to minimize the overhead imposed by the non-fluid nodes. In such methods, the geometry is embedded in several overlapping Cartesian blocks such that each block offers a better

fit to a section of the immersed body, thus, reducing the number of unwanted non-fluid nodes. However, for such an implementation to be optimal careful attention should be paid to the definition of the blocks. This is far from being straightforward in complex anatomical geometries such as the TCPC geometries shown in Figure 3-7.

Adaptive mesh refinement (AMR) approaches represent another class of methods which seeks to achieve the desired spatial accuracy by embedding the geometry in series of progressively refined grids, providing finer spatial sampling only where needed (Figure 3-8). The basic principle is to define a refinement metrics, such as the velocity gradient or vorticity magnitude, allowing the mesh to be automatically adapted to best capture the flow fields. If the refinement metrics is larger than a preset number, the mesh is refined further. On the opposite, if it is below another preset threshold, the mesh may be coarsened without lowering the overall simulation accuracy. In the context of SIIB methods, AMR has successfully been applied by Collela *et al.* [142-144] and Peskin *et al.* [135, 145] as a mean to maintain the overall scheme accuracy by increasing the resolution in the vicinity of the immersed fluid/solid interface. In both studies, the mesh was refined by patches (Figure 3-8) and a structured grid structure was retained for all refinement levels. Such data structure provides undoubtful advantages for the implementation of the gradient, divergence and Laplacian operators needed to solve the governing Navier-Stokes equations, and allows for an easy correspondence between the different mesh levels at the coarse/fine interfaces. On the other hand, the final data structure retains some dependence on the embedding Cartesian grid size for each one of the refinement levels, which hinders its applicability to internal flow simulations.

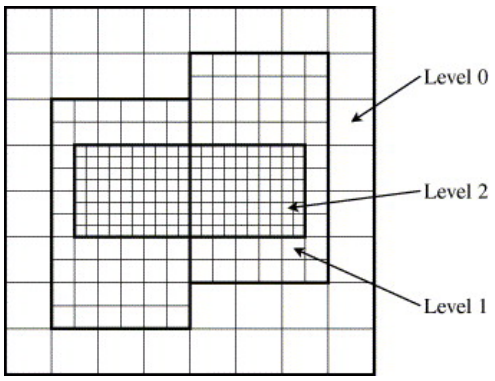

Figure 3-8: Properly-nested locally-refined Cartesian grid. Coarse/fine interfaces are indicated by bold lines. (Image courtesy: [135])

Octree methods have also been used as a more versatile form of AMR [146], allowing for mesh refinement in individual mesh cells rather than in patches and using hierarchical tree structures to store mesh connectivity. The mesh is typically represented starting with a single embedding grid cell that further subdivides until the desired spatial accuracy is achieved. Octree approaches effectively reduce the memory footprint of the data structure but typically result in complicated data structures with relatively slow access and construction times. In an effort to improve data access rates within discrete stencils, Khokhlov *et al.* [146] suggested the use of a fully-threaded tree structure. In addition to the parent/children relationship, direct neighborhood information is stored for each mesh refinement level, thus allowing for faster horizontal spanning of the hierarchical tree. Along the same lines Losasso *et al.* [147] recommended using a uniform block structured grid at the coarsest level, as opposed to a single cell, and defining each grid cell as an octree of its own.

Nielsen *et al.* [148] argued that even with an implementation such as that proposed by Losasso *et al.* [147], the memory footprint still showed some dependency on

the dimensions of the embedding grid. The authors present an interesting alternative where all the Cartesian grid cells that fall outside of the domain of interest are effectively dropped out of the data structure, thus, resulting in a Cartesian albeit unstructured data structure. Unstructured meshes (using tetrahedral or hexagonal elements) have commonly been used in the literature. The particularity of the approach proposed by Nielsen *et al.* [148] lies in the definition of an efficient recursive mapping scheme that restores grid connectivity information, ensures a constant data access time to all points and minimizes data storage. Such data structure is very attractive for TCPC applications, allowing for all non-fluid nodes to be disregarded, while retaining an efficient access to neighboring flow and pressure information. In the study by Nielsen et al., strong emphasis was set on minimizing data storage as the algorithm was mainly meant to be applied to track surfaces (which are one dimension smaller than the embedding Cartesian grid). This problem is less stringent for our applications, since in vivo TCPC geometries still occupy 1-10% of the Cartesian grid. As a result, our implementation could afford a slightly more memory-intensive mapping scheme, in favor of a faster, direct data access rate.

3.5 Approach Retained and Contribution

This thesis seeks to develop an accurate numerical method that will allow for pulsatile flow simulations in *in vivo* cardiovascular geometries. SIIB methods seem ideally suited for that purpose as they can handle geometries of arbitrary complexity, while retaining the accuracy and ease of implementation of Cartesian methods. However, as was highlighted in this chapter, their application to internal flows has been hindered by the memory overhead imposed by the non-fluid nodes, which impose an unnecessary

burden to the computations and limits the spatial accuracy achievable within practical time-frame and computational resources. Making use of an unstructured Cartesian grid formulation, the approach developed in this thesis seeks to extend the application range of SIIB methods, and demonstrate their potential for carrying detailed high-resolution simulations in arbitrarily complex anatomical geometries. In particular, the proposed approach builds on the structured SIIB formulation developed by Sotiropoulos and coworkers [121, 122] for external flows around moving bodies. This SIIB method is recast using an unstructured Cartesian representation similar to that of Nielsen et al. [148], wherein all grid nodes falling outside of the flow domain will be eliminated from the computational domain. However, instead of the recursive formulation described by Nielsen *et al.* to establish the grid connectivity [148], we take advantage of the bijective mapping that exists between the unstructured fluid grid and the underlying structured Cartesian grid. This alternate formulation, though less memory efficient, allows for direct data access thus addressing one of the major limitations of unstructured formulations.

Each numerical development is validated against detailed controlled *in vitro* experiments. To demonstrate the benefits of our approach, the re-formulated SIIB scheme is applied to carry out systematic grid refinement studies for internal flow problems ranging in complexity from a curved pipe to real-life, patient-specific TCPC geometries. The developed numerical solver is then applied to probe the impact of pulsatile inflow conditions upon the hemodynamic performance of different TCPC geometries. Finally, we demonstrate how such a versatile unstructured SIIB approach could benefit the clinical community, allowing for the performance of patient-specific surgical planning studies within a clinically practical timeframe.

CHAPTER 4

HYPOTHESIS AND SPECIFIC AIMS

The introduction of a complete right heart bypass procedure [11] brought in a revolution in the management and care of children born with single ventricle heart defects (SVHD). Over the years this procedure has evolved from the original single-stage Fontan surgery to the multi-stage total cavopulmonary connection (TCPC) procedure, in which the superior vena cava (SVC) and the inferior vena cava (IVC) are directly connected to the pulmonary arteries bypassing the right side of the heart. Despite marked improvements in overall survival, these patients still present with numerous severe long-term complications such as ventricular dysfunction, pulmonary arteriovenous malformation (PAVMs), diminished exercise capacity, protein losing enteropathy (PLE), and thrombotic complications [47, 149, 150]. While the etiology of these complications is multi-factorial, the hemodynamics of the TCPC determined by its design and surgical construction have a predominant impact on the patient outcomes. Elevated TCPC resistances have been shown to limit cardiac output and exercise capacity. Orientation and relative position of the IVC and SVC at the center of the connection have a predominant impact upon the distribution of blood flow and nutrients to the lungs, which will in turn dictate whether a patient is prone to PAVMs or not. Flow disturbances within the TCPC construct increase energy dissipation and may yield unphysiologic fluid stresses on blood elements, ultimately resulting in thrombus formation. Optimization of the TCPC hemodynamics via its design is thus a critical step towards alleviating the long

term complications observed in SVHD patients and improving long-term clinical outcome.

Several options have been discussed in literature regarding the optimal TCPC implementation, suggesting the inclusion of IVC-SVC offset [82], vessel curvature[84], flaring of the anastomosis site [83, 151], or the use of Y-shaped IVC grafts [99, 152]. However, with the refinement of the clinical and bioengineering investigation methods, it has now become clear that the anatomical variability between patients calls for a patient-specific optimization of the TCPC design and hemodynamics. Virtual surgery interfaces coupled with physics-driven computational fluid dynamics (CFD) solvers offer a unique platform for surgeons to pre-operatively optimize the surgical procedure on a patient-by-patient basis. Nonetheless, such patient-specific surgical planning still requires significant technical innovations on both the virtual modeling and CFD fronts, and its feasibility within clinically practical resources and time-frame has yet to be demonstrated.

From the CFD end in particular, a major challenge stems from the complexity of the *in vivo* anatomies, and the number of parameters to be modeled. *In vivo* flows typically take place in multi-connected, tortuous vessels, with moving walls, pulsatile inflows, and feature non-Newtonian behavior and a host of flow regimes ranging from laminar to transient and fully-developed turbulence. Modification of the patient's anatomy during surgery not only affects the local hemodynamics but also often results in remodeling of peripheral organs, which in turn impacts the inflow and outflow boundary conditions of the domain under consideration. Surgical planning CFD simulations thus have to call upon number of simplifications, which ought to be carefully reviewed in order to assess the relevance of the predicted performances and determine the parameters

that may or may not be disregarded in favor of faster simulations and increased number of tested virtual-surgery options. In the TCPC realm, simulations have commonly assumed one or several of the following: simplified geometries, rigid walls and steady inflow/outflow conditions. While idealized geometries obviously cannot account for the diversity of the *in vivo* anatomies the impact of the other parameters is less clear. Preliminary studies have modeled uniformly elastic walls [105] and pulsatile inflow conditions [90, 108], pointing to the latter as having a larger impact upon the predicted TCPC performance. However, the question as to whether modeling pulsatile inflows is critical for the comparative performance of different surgical options remains open. This question is especially relevant when comparing extra-cardiac and intra-atrial approaches, which host very different levels of instabilities and mixing even under non-pulsatile conditions.

Accordingly, the hypothesis of this thesis is two folds: we first hypothesize that ***immersed-boundary CFD methods are ideally suited to conduct patient-specific surgical planning within a clinical setting***, and then that ***a thorough understanding of the in vivo pulsatile hemodynamics of intra-atrial and extra-cardiac options is a critical step towards more refined post-operative modeling***. These hypotheses will be addressed in three steps:

1) Tailor existing immersed boundary methods to achieve high resolution simulations at low computational costs in arbitrarily complex geometries, under both steady and pulsatile conditions
2) Investigate the pulsatile hemodynamics of extra-cardiac and intra-atrial TCPCs using *in vivo* anatomies and flow curves

3) Conduct pre-operative surgical planning studies for SVHD patients with an interrupted IVC

The structure followed for each of these specific aims is detailed in the subsequent paragraphs.

Specific Aim 1. ***Achieve high resolution simulations at low computational costs in arbitrarily complex geometries by optimizing the data structure of sharp-interface, immersed boundary (SIIB) methods***. The main challenges to be addressed in this specific aim are to define a numerical approach that 1) allows for the fine discretization of arbitrarily complex *in vivo* structures with minimum user interaction; 2) accurately captures the unsteady dynamics of *in vivo* flows. To this end, the approach retained builds upon an existing sharp interface immersed boundary (SIIB) method [122, 123], whose accuracy has previously been demonstrated for external flow applications around a swimming fish [122] or around a moving heart valve leaflet [153-156]. SIIB approaches are ideally suited for our application as they circumvent the mesh generation difficulties: the complex geometry is immersed in a background Cartesian grid, and the Navier-Stokes equations are solved only for the Cartesian grid nodes that fall within the fluid domain. However, in the context of the TCPC these approaches face the challenge that most of the Cartesian grid nodes fall outside of the flow domain. These "non-fluid" nodes impose an unnecessary memory and computational overhead without enhancing the numerical resolution in the region of interest, and ultimately limit the maximum achievable accuracy. To remedy this situation, we will recast the original structured SIIB formulations into an unstructured Cartesian grid layout, which will solely retain the fluid

Cartesian nodes and drop all non-fluid nodes, and take advantage of the bijective mapping that exists between the unstructured fluid grid and the underlying structured Cartesian grid to prescribe the unstructured connectivity.

The efficiency of our method will be demonstrated by carrying out systematic mesh refinement studies for several internal flow problems ranging in complexity from flow in a 90 degree pipe bend to flow in patient-specific TCPC anatomies. Accuracy will be assessed by comparing the computed flow fields to experimental measurements obtained in the same geometries under both steady and pulsatile inflow conditions.

Specific Aim 2. ***Investigate the effect of pulsatility in intra-atrial and extra-cardiac patient-specific TCPCs.*** The objective of this aim is to gain insights into the pulsatile *in vivo* TCPC hemodynamics, assess whether neglecting pulsatility affects the predicted performance ranking of different options, and if so determine whether pulsatility should be accounted for in all options or only in intra-atrial ones. To achieve this specific aim, extra-cardiac and intra-atrial patients will be selected from the Georgia Tech Fontan database of magnetic resonance images (MRI) based on the availability of anatomical reconstruction, inflow/outflow flow curves, and 3D *in vivo* flow reconstruction [80]. Simulations will be conducted using the patient-specific geometries and flow curves, with rigid boundaries. Comparison with controlled *in vitro* experiments under the same conditions will testify for the accuracy of the flow solver, while comparison to the reconstructed *in vivo* flow fields will test for the validity of the modeling assumptions, namely rigid wall and prescribed flow boundary conditions. Finally, to quantify the effect of pulsatility on the TCPC efficiency, each pulsatile simulation will be accompanied by a

constant inflow counter-part, conducted using the same *in vivo* anatomy but with the mean vessel flow rate rather than *in vivo* flow curve. Comparing the flow structures, pressure drops, power losses and hepatic flow distribution predicted by the steady inflow simulations to those obtained by averaging the pulsatile simulations over a cardiac cycle will for the first time quantify the relative impact of flow pulsatility in patient specific geometries across different TCPC templates. This knowledge will then determine whether efforts should be placed in designing statistical models of the flow pulsatility in virtual-surgery options to further refine post-operative modeling.

Specific Aim 3. ***To pre-operatively determine the TCPC geometry that will optimize hepatic flow distribution and energy dissipation for patients featuring an interrupted IVC with azygous continuation.*** One of the most challenging SVHD subgroups from a clinical and surgical prospective is SVHD patients featuring an interrupted IVC with azygous continuation. Clinical studies [67, 69] report an especially high incidence of unilateral PAVMs in these patients, due to a mal-distribution of the hepatic nutrients through the TCPC to the diseased lung. The fact is that, in these patients, the distribution of hepatic flow to the lungs is even more sensitive to the design of the TCPC than in patients without interrupted IVC, while the large number of anatomical and flow abnormalities make it even more difficult for surgeons to identify the best-suited surgical approach based on anatomical observations alone. This is the exact setting where fluid dynamics and associated flow distributions could make or break the surgery, and virtual surgical planning make a significant clinical impact.

The feasibility of such a surgical approach will be demonstrated by the combined use of the virtual surgery interface developed by Dr Jarek Rossignac and the flow solver presented in SA1. The pre-operative anatomy and flows will be obtained from magnetic resonance images. Virtual surgeries will be designed within the virtual surgery interface in close synergy with the surgeon assigned to the patient. CFD simulations will then be conducted on each designed option to predict the associated hemodynamics performance. Emphasis will be set on optimizing the TCPC design for an even distribution of blood flow and hepatic nutrients to the left and right lungs. Secondary optimization metrics will include power losses and pressure drops across the connection. Whenever such information will be available, the recommended option will be compared to the one actually performed *in vivo*, and predicted performance will be contrasted to clinical follow-up data.

In addition to a direct benefit to the patient under consideration, this study will also have a larger impact for the clinical management of SVHD patients with an interrupted IVC. First, the systematic review of the various geometries investigated for each surgical planning case will allow for a better definition of the different "anatomical templates" (e.g. interrupted IVC combined with a single SVC or bilateral SVCs, classification based on the relative position of the azygous and inominate vein). Then, it will shed light onto the impact of caval offset, vessel flaring and other design parameters upon TCPC hemodynamics depending on the underlying patient anatomy. These results will provide useful surgical guidelines for each anatomical template, which could benefit the global surgical community, including centers that do not have access to patient-specific surgical planning interfaces.

CHAPTER 5

STUDY DESIGN AND PROTOCOLS

In this chapter, we describe the methods and protocols used for the two arms of our study, namely the investigation of the pulsatile hemodynamics of the total cavopulmonary connection (TCPC), and the pre-operative surgical planning studies. We first present the overall study design of these two investigations, followed by a description of each technical milestone, from patient data acquisition, to numerical modeling and extraction of the clinically relevant metrics. The mathematical formulation of the computational fluid dynamic (CFD) solver developed for these studies is addressed separately in Chapter 6.

5.1 Study Design and Methodology Overview

Prior to delving into the different methodologies used, it is important to recall the goals of the pulsatile and surgical planning studies and outline the overall processes required to achieve them. The study design of the pulsatile study is illustrated in Figure 5-1. This study investigates the impact of pulsatility on the hemodynamics of different of TCPC connection types. To this end, we compare the hemodynamics obtained using the pulsatile *in vivo* flow curves to the ones obtained using the mean *in vivo* flow rates in a controlled idealized TCPC representation first, and then for three patients having each undergone a different TCPC procedure. The comparison of the pulsatile and non-pulsatile results for the same patient will demonstrate whether pulsatility has strong impact on the

clinical end-points for that patient, whereas the comparison across the four different patients will highlight whether some procedures are more sensitive to pulsatility than others. We will also compare the pulsatile CFD results to the 3D *in vivo* flow fields obtained from magnetic resonance imaging (MRI). This last comparison will provide preliminary insights into the impact of some of our numerical modeling assumptions, notably neglecting wall motion, upon the range of validity of our simulations.

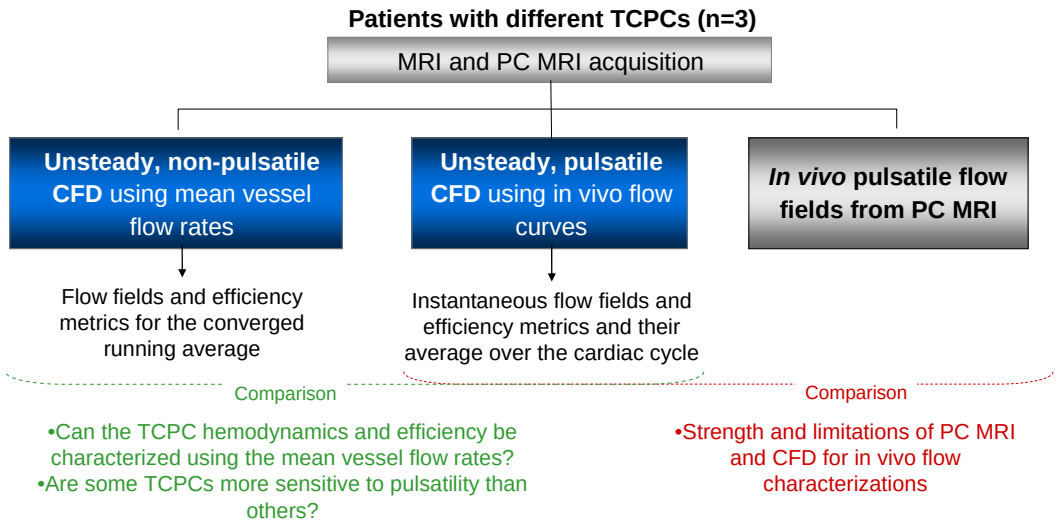

Figure 5-1: Study design of the pulsatile investigations. The gray boxes depict steps that were performed by collaborators, while the blue boxes highlight the core of our work.

The surgical planning study makes use of the image processing tools developed in our laboratory and of the flow solver developed in this thesis, to help surgeons identify the best-suited TCPC implementation on a patient-by-patient basis. The overall framework is presented in Figure 5-2. The first step is the acquisition of clinical images (preferably MRI) to obtain the patient's pre-operative anatomy and flow rates. The pre-operative anatomy is loaded into a virtual surgery interface, where the user or surgeon

can virtually perform multiple different surgical procedures and compare their hemodynamic performance, as predicted by the in-house CFD solver developed in the course of the present thesis. This patient-specific surgical planning framework is applied to six patients who were referred for the completion or redo of the final stage of the TCPC, i.e. to connect the hepatic veins to the pulmonary arteries. A subset of the surgical planning patients (4 out of 6) already had a completed TCPC at the time of referral, but suffered from severe complications due to an improper TCPC design in the first round. For these four patients, an additional set of simulations was conducted prior to the surgical planning to investigate the hemodynamics of the failing connection, and use that knowledge to guide the design of possible corrective procedures in the subsequent steps.

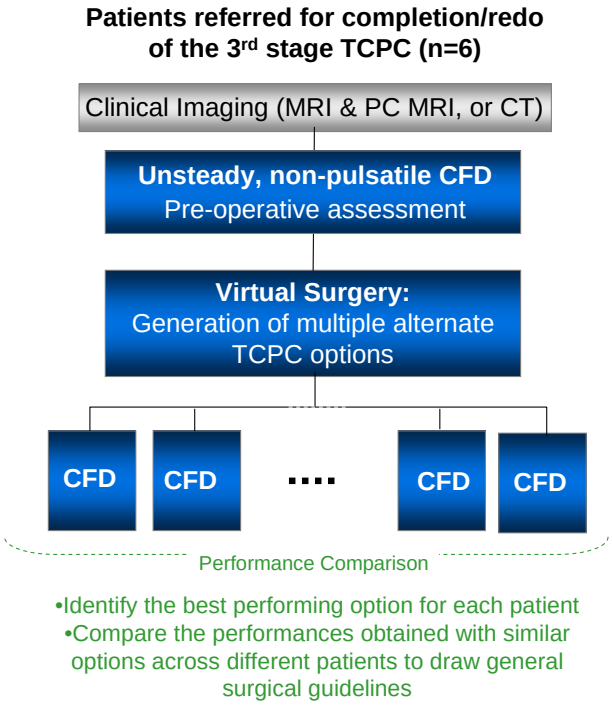

Figure 5-2: Study design of the surgical planning investigations. The gray boxes depict steps that were performed by collaborators, while the blue boxes highlight the core of our work.

Finally, by reviewing the results obtained across all six patients, we draw general guidelines and identify cases for which individualized surgical planning remains the only recommendable approach.

Although seeking to answer different questions, both the pulsatile and surgical planning investigations use the same array of tools and methods, including: clinical image acquisition, image processing to extract the *in vivo* anatomies and flows, computer aided design (CAD) to manipulate the *in vivo* geometries, image-based numerical modeling, and finally extraction of the clinically relevant metrics. The general organization of each one of these steps is best illustrated by the flow chart shown in Figure 5-3. Similarly to the color-scheme used in Figure 5-1, the work conducted by our collaborators, namely the clinical imaging and image processing, is shown in gray to be differentiated from our contribution. Each point is addressed in turn in the following sections. We first describe our patient selection criteria, followed by a brief background on the clinical imaging modalities used. We then detail every technical step, lumped into five main categories: (1) the handling of the anatomies would they be patient-specific or virtual surgical options, (2) the extraction of the vessel flow curves and mean flow rates, (3) the reconstruction of the 3D *in vivo* flow fields (for the pulsatile study only), (4) the set-up of the CFD simulations, and (5) the extraction of the clinically relevant metrics.

5.2 Patient Selection

The four patients recruited as part of the pulsatile study were retrospectively selected from the Georgia Tech database of Fontan patients. These patients were recruited based on the availability of the following three sets of *in vivo* information: a)

3D reconstruction of the TCPC geometry, b) flow curves through each one of the TCPC vessels, and c) 3D reconstruction of the *in vivo* velocity fields. For the surgical planning study, the patients were enrolled on a surgical-need basis. In an effort to address as large a patient population as possible, the enrollment criteria for these patients were less stringent than for the pulsatile study, and only the 3D reconstruction of the pre-operative anatomy and mean vessel flow rates were required.

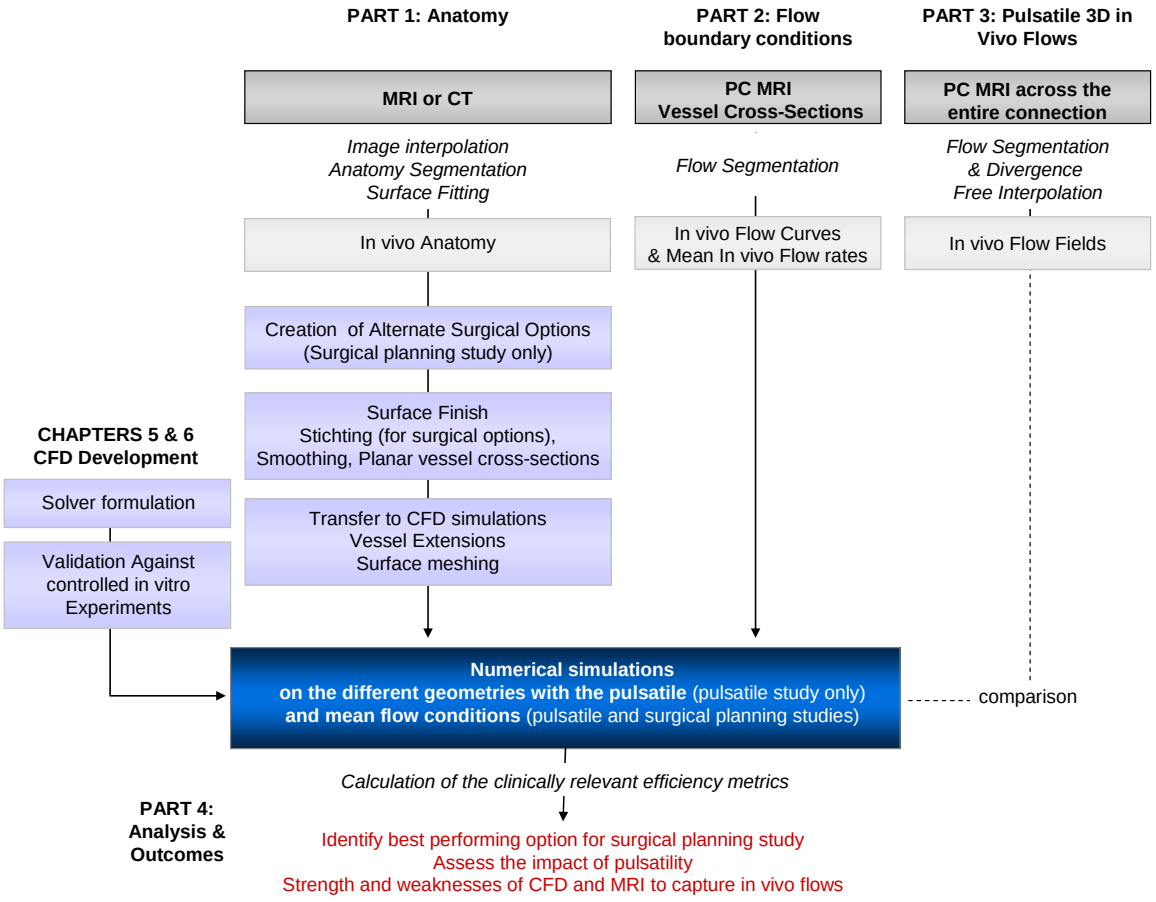

Figure 5-3: Methodology overview. The gray boxes depict steps that were performed by collaborators, while the blue boxes highlight the core of our work.

5.3 Imaging Modalities Used

Magnetic resonance imaging (MRI) was the clinical imaging modality of choice for this study, as it has the unique ability to non-invasively provide both anatomical and velocity measurements. MRI uses a powerful magnetic field to align the nuclear magnetization of the free-precessing hydrogen protons, typically found in water inside the body. Radio frequency (RF) fields are used to systematically alter the alignment of this magnetization, causing the hydrogen nuclei to produce a rotating magnetic field detectable by the scanner. This signal can be manipulated by additional magnetic fields to build up enough information to construct an image of the body.

Anatomical MR images provide a density map of the free-precessing hydrogen protons. Cardiovascular applications typically make use of a True-FISP sequence (true fast imaging with steady state precession), an example of which is provided in Figure 5-4. True-FISP sequences are encoded such that high proton densities (such as blood) appear in white, whereas lower densities (such as the pulmonary airways or soft tissues) appear in black. This sequence thus optimizes the contrast between the blood stream and the surrounding structures, which is ideally suited for the reconstruction of the TCPC blood vessels needed for our applications. Furthermore, True-FISP MRI is fast and relatively motion insensitive, which makes it a reliable technique, even in patients who have difficulties holding their breath as is often the case in young subjects such as the Fontan patients.

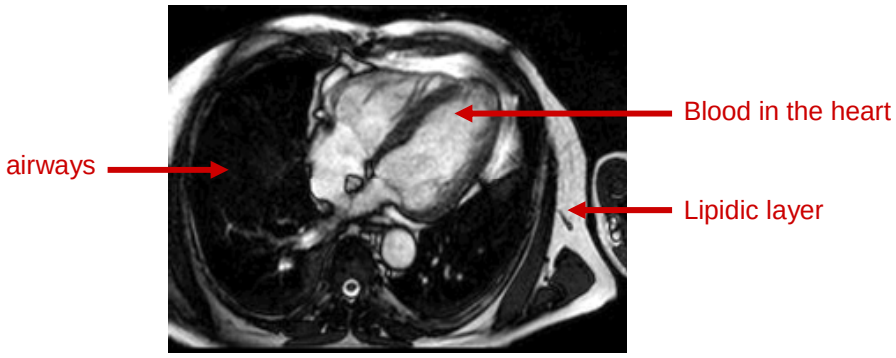

Figure 5-4: Example of a True-FISP anatomical MRI of the heart in a four chamber view. The heart, blood vessels and the lipidic layer under the skin, all of which are rich in water, appear in white, whereas the pulmonary airways appear in black.

Beyond anatomical features, MRI can also non-invasively quantify blood velocities. The basic principle is to subject the free-precessing hydrogens protons to two consecutive magnetic gradient pulses of opposite signs, G_x and -G_x. For static protons, the two pulses will cancel out. However, for protons moving at a velocity V_x in the direction of the magnetic gradient, this will translate into a phase shift, ϕ_x, in the measured signal. This phase shift is directly proportional to the velocity of the protons, and can be expressed as:

$$\phi_x = 2\gamma\, \tau^2 G_x \cdot V_x \qquad (5\text{-}1)$$

where γ is the gyromagnetic ratio of protons, and τ is the length of the magnetic gradient pulse G_x. The image created as a result of these phase shifts constitute what is called a phase-contrast MRI (PC MRI) acquisition. 3D velocity vectors can be obtained by performing three consecutive PC MRI acquisitions encoded for three orthogonal spatial directions, as exemplified in Figure 5-5. The velocities in each direction can be recovered from the pixel intensity by a simple linear transformation, the white pixels corresponding to the maximum positive velocity along the encoding direction, the black pixels the

maximum negative velocity, and the gray pixels a zero velocity. The signal in the pulmonary airways and surrounding atmosphere is characterized by salt-and-pepper noise.

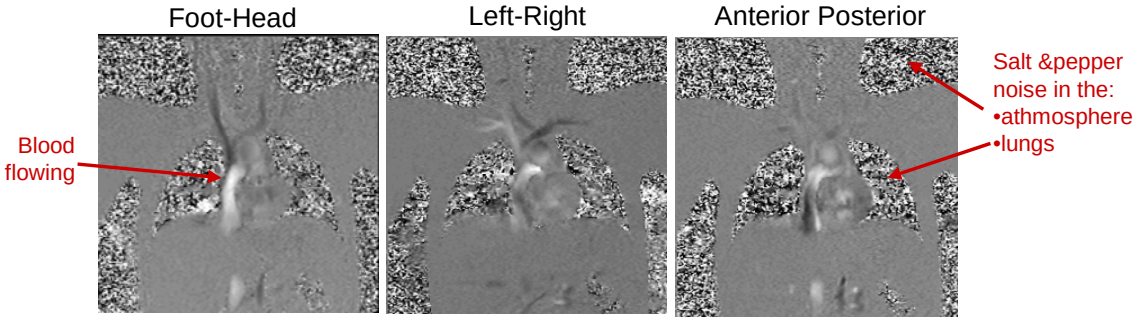

Figure 5-5: Example of a 3D PC MRI acquisition. All three images are acquired in the same plane, but with the velocity encoded in three orthogonal directions, namely in the Foot-Head, Left-Right, and Anterior-Posterior directions.

A drawback of MRI is that it requires the exposition of the patient to a strong magnetic field. While this is not harmful per se, it is totally counter-indicated if the patient has metallic implants, such as coils or pacer wires. Two of the patients enrolled in the surgical planning study featured such devices and were imaged using X-ray computed tomography (CT). Similarly to the anatomical MRI images, CT images capture the blood stream with a pixel intensity different from those of the surrounding organs. Similar image processing techniques can thus be applied to both types of images to extract the anatomical information. However, CT does not allow for velocity measurements. As will be discussed in the corresponding results section (Chapter 9), flow conditions for these two patients were obtained from invasive catheterization measurements, or from mean flow values in patients of similar age and weight when no other measurement was available.

5.4 Preparation of the *In Vivo* and Surgical Planning Anatomies

This section details the processes leading from the anatomical images to a surface mesh readily usable in the CFD simulations.

5.4.1 Imaging Protocol

A stack of anatomical (MRI or CT) images was acquired in the axial direction spanning the entire thorax (Figure 5-6). The anatomical images were acquired at a single time-point in the cardiac cycle, providing a static representation of the TCPC geometry, with a typical in-plane resolution of 0.5 to 1 mm per pixel and a slice thickness of 3 to 5 mm. Depending on the size of the patient 40 to 50 True-FISP MRI images and 100 to 150 CT images were required to cover the thorax, spanning from the confluence of the hepatic veins into the inferior vena cava (IVC) to the top of the aortic arch.

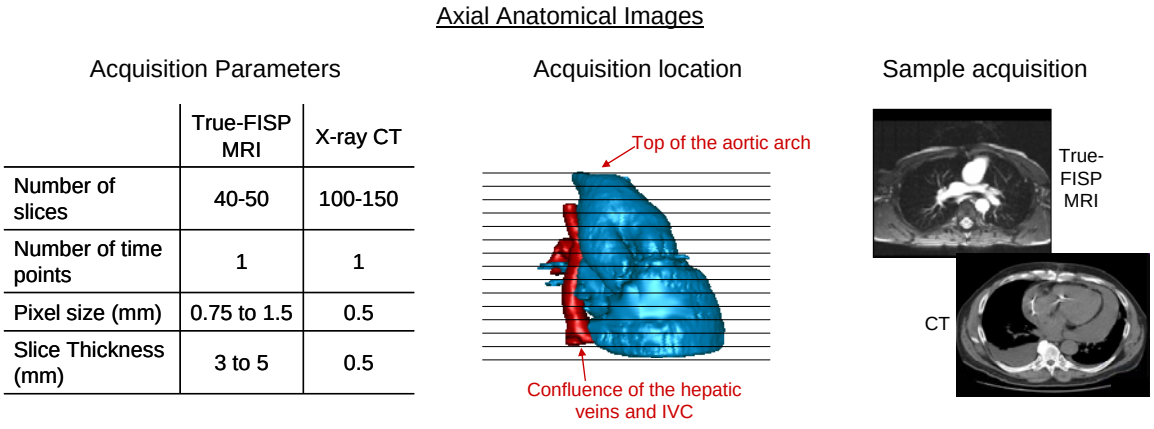

	True-FISP MRI	X-ray CT
Number of slices	40-50	100-150
Number of time points	1	1
Pixel size (mm)	0.75 to 1.5	0.5
Slice Thickness (mm)	3 to 5	0.5

Figure 5-6: Anatomical acquisition protocol. The location of the acquisition planes is shown by the black lines overlaid on the TCPC and heart.

5.4.2 Reconstruction of the TCPC Geometry

The 3D geometry of the TCPC is reconstructed from the anatomical images, using a methodology previously developed in our laboratory [157, 158] and illustrated in Figure 5-7. Since the in-plane resolution of the MRI or CT images is typically three to five times finer than the out-of-plane resolution due to MRI constraints, these images are first interpolated to an isotropic voxel size in order to improve the overall accuracy of the anatomical reconstruction[157]. This interpolation is achieved using the adaptive control grid interpolation technique developed by Frakes and co-workers[157]. The TCPC flow domain is then interactively segmented in each one of the interpolated slices using a bouncing ball algorithm[158] (Figure 5-7 a). The segmented contours are finally imported into Raindrop Geomagic Studio 9.0 (Geomagic Inc., NC, USA) and a surface is fitted to the contours to create a 3D reconstruction of the geometry (Figure 5-7 b and c).

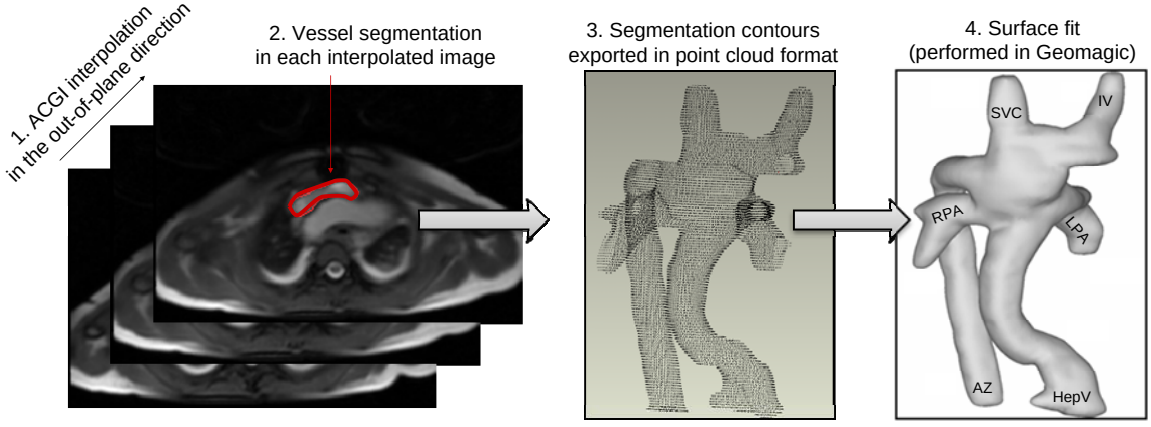

Figure 5-7: Main steps for the reconstruction of a TCPC anatomy from a stack of axial MRI, performed using a combination of in-house interpolation and segmentation software and Geomagic Studio 9.0 (Geomagic Inc., NC, USA) for the surface fit.

5.4.3 Surface Finish: Smoothing and Creation of Planar Vessel Cross-Sections

The reconstructed anatomies typically feature number of surface irregularities, which stem from slight deviations in the MRI segmentation process but are not representative of what is seen *in vivo*. In regard of the upcoming CFD simulations, it should also be ensured that all surface elements follow the same orientation, with their normal pointing towards the vessel lumen. Accordingly, after their reconstruction the TCPC anatomies are imported into a CAD software, Geomagic Studio 9.0 (Geomagic Inc., NC, USA), for further smoothing and post-processing. The main surface processing steps are illustrated in Figure 5-8. Surface irregularities are smoothed out using the "sand-paper" option offered by the software. The element orientation can be readily visualized in Geomagic Studio, as elements pointing towards the vessel lumen should appear in blue, while inverted elements should appear in yellow. Inverted elements are deleted and the holes filled based on the surface curvature. Finally, the prescription of the CFD flow boundary conditions at each inlet and outlet requires planar vessel cross-sections. These vessel cross-sectional cuts are created by intersecting the TCPC surface with a plane oriented perpendicularly to the vessel axis. For consistency across datasets, the inlet and outlet cross-sections are systematically taken at the following locations:

- Just downstream of the confluence between the hepatic veins and the IVC
- Just downstream of the confluence between the innominate vein and the SVC
- And just upstream of the point where the LPA and RPA branch into smaller vessels

For the surgical planning options, these cuts are taken on the pre-operative anatomy, prior to any virtual surgery modifications, so as to ensure that all the options designed for a

given patient considered the same vessel configurations. A detailed protocol for the surface processing steps performed in Geomagic Studio 9.0 (Geomagic Inc., NC, USA) is provided in Appendix A.1.

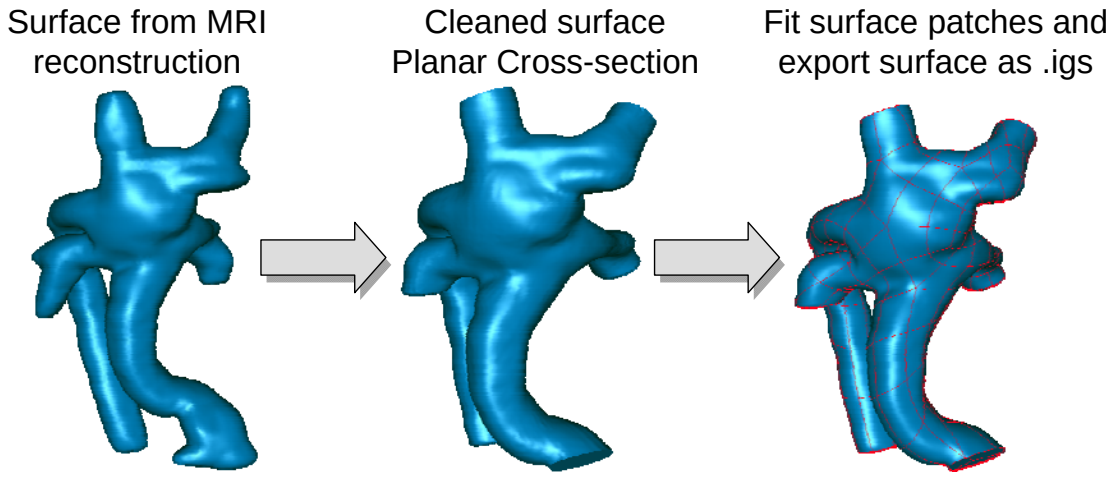

Figure 5-8: Surface finish operations performed in Geomagic Studio 9.0 (Geomagic Inc., NC, USA): (a) TCPC surface as obtained from PC MRI, (b) after surface smoothing, (c) after the creation of planar inlet/outlet cross sections.

5.4.4 Creation of Virtual Surgical Options

A major milestone for the planning of surgical procedures is the ability to modify the pre-operative anatomy and design different post-operative configurations. Studies limited to only a few cases have typically employed commercially available CAD tools to manually modify geometries[88, 89]. Such processes are cumbersome and depend on the skill of the operator, especially when applied to complex anatomies. In this thesis, we thus used the virtual-surgery interface developed by Rossignac and co-workers[159-162] to easily design a large number of options for each patient. This interface makes use of

the recent advances in 3D geometrical morphing, image rendering and human-computer interaction to provide an environment where the user can easily interact with the reconstructed anatomy.

Performance of a virtual surgery within that interface is illustrated in Figure 5-9. For surgical planning applications, the anatomical reconstruction procedure described in Section 5.4.2 is not only applied to the TCPC (shown in red in Figure 5-9) but also to the surrounding cardiovascular structures, such as the heart, aorta and pulmonary veins (shown in blue in Figure 5-9), to better represent the constraints faced by the surgeon. The semi-transparent tube features an artificial extra-cardiac graft to be placed. Using two 3D magnetic trackers, one each hand, the user can precisely set the graft in place and deform it to follow the curvature of the heart and avoid the surrounding vessels.

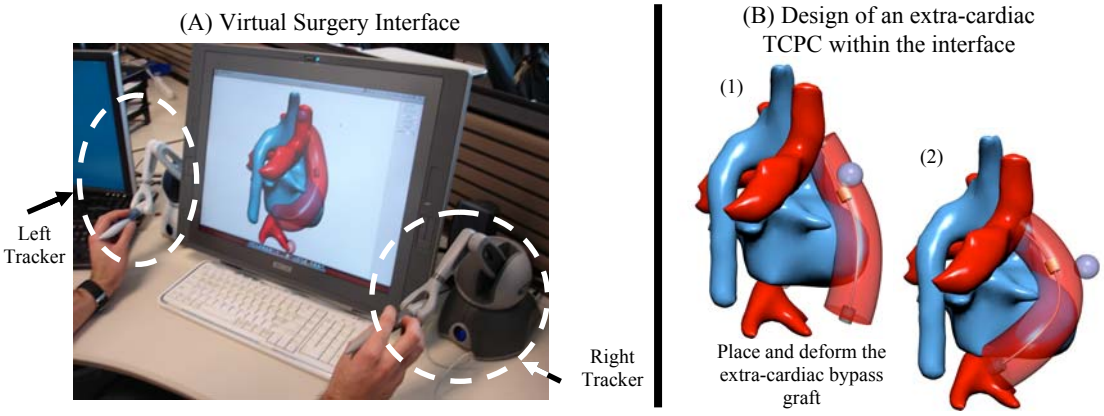

Figure 5-9**:** Performance of a virtual surgery within the interface developed by Rossignac and co-workers [101, 161]. The vessels involved in the TCPC (shown in red) and surrounding anatomical structures, such as the heart and great vessels (shown in blue), have been reconstructed from MRI and loaded into the virtual-surgical interface (A). Using two haptic trackers, one in each hand, the user/surgeon may directly interact with the geometry, here placing and deforming an artificial graft to complete the TCPC (B).

The above interface allows for the fast design of a large number of possible grafts, varying the point of connection, degree of curvature, using intra-atrial or extra-cardiac approaches, or even bifurcated Y-shaped grafts. However, in its current state, that interface does not allow for the thus-created graft variations to be stitched to the patient's anatomy. All stitching or cutting operations are thus performed off-line using the Geomagic Studio 9.0 (Geomagic Inc., NC, USA), as illustrated in Figure 5-10. The *in vivo* anatomy and virtual graft are first united using the Boolean operation toolkit. The anastomosis site is then smoothed to better represent what would be seen *in vivo*. For patients who had a completed TCPC but required a new baffle to be designed, the original baffle was deleted and the two ends filled based on the vessel curvature.

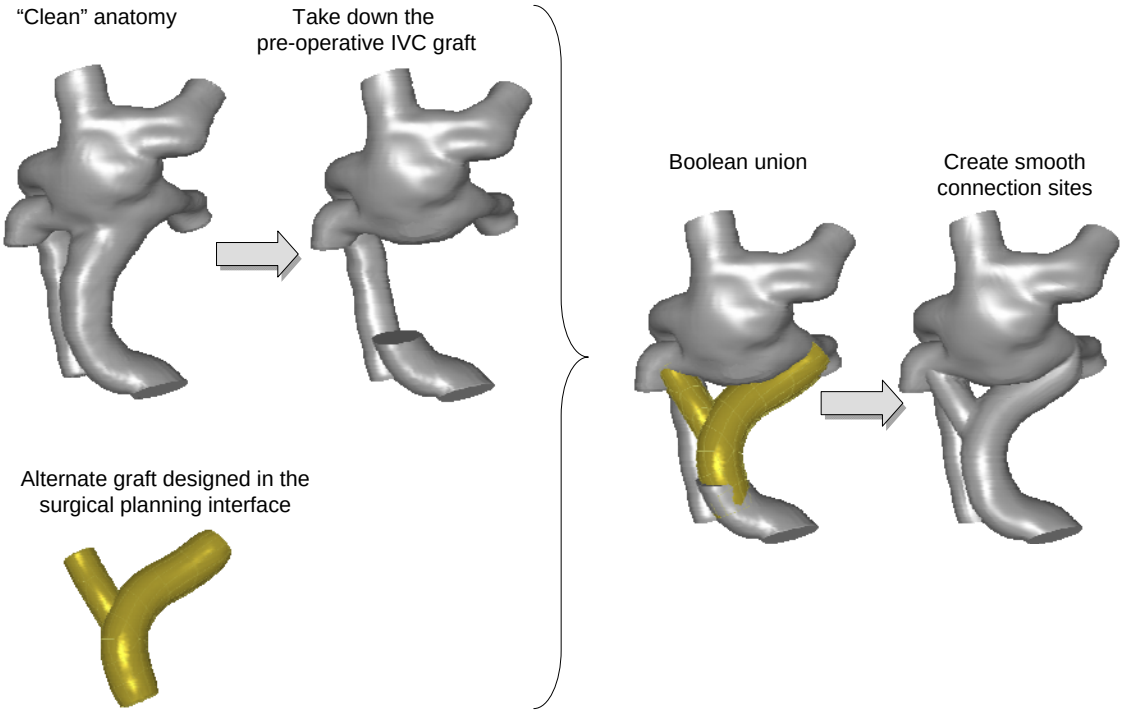

Figure 5-10: Stitching and cutting operations performed in Geomagic Studio 9.0 (Geomagic Inc., NC, USA)

5.4.5 Surface Mesh Generation for CFD

Having prepared the *in vivo* or surgical planning geometries, the final step consists in discretizing the TCPC with an unstructured triangular surface mesh to be imported into the CFD flow solver. This is achieved using the commercial meshing software Gambit 2.4 (ANSYS Inc., PA, USA). To increase the stability of the CFD simulations, the pulmonary arteries are extended by approximately 5 vessel diameters, allowing the swirling pulmonary flows to reattach prior to reaching the outlet of the domain. Similarly, the inlets are extended by approximately one diameter to avoid any spurious effect of the boundary condition prescription on the flow dynamics within the connection itself. The extended geometry is discretized with an unstructured triangular surface mesh using a typical resolution of 1 to 1.5 mm. The surface mesh is exported using the FIDAP file format, which is readily usable by the CFD flow solver. A detailed protocol for the surface mesh generation is provided in Appendix A.2. This step completes the anatomy preparation section.

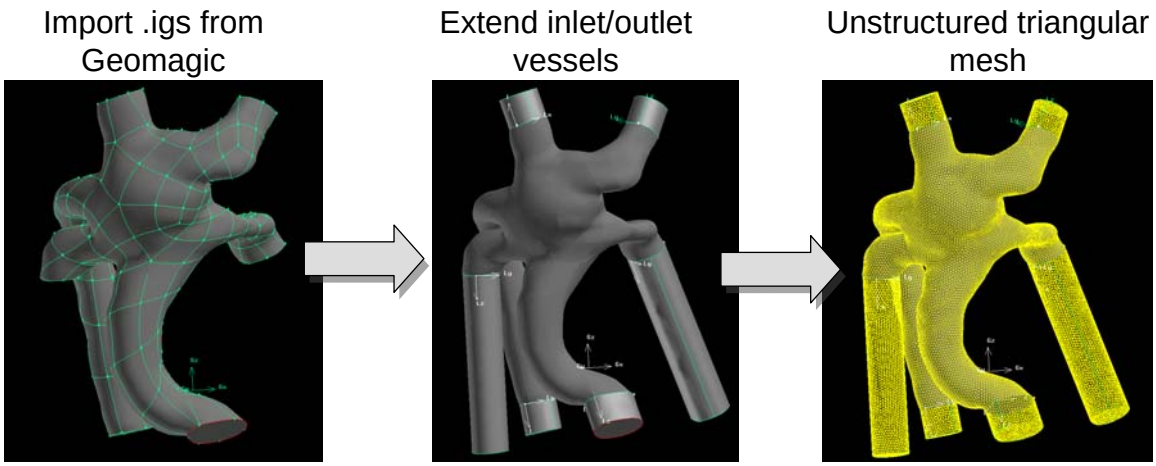

Figure 5-11: Vessel extension and surface meshing in Gambit 2.4 (ANSYS Inc., PA, USA).

5.5 Vessel Flow Rates

After meshing the *in vivo* or surgical planning anatomies, the second requirement for patient-specific simulations is to obtain the patient-specific flow conditions. Here, we detail the imaging modality and acquisition protocol used to measure the TCPC flow rates *in vivo*, and the subsequent image processing and analysis required to extract the necessary information.

5.5.1 Imaging Protocol

In order to provide flow boundary conditions at each inlet and outlet of the TCPC, one PC MRI slice was acquired across each one of the TCPC vessels. The slices were oriented normally to the vessel axis, and only the through-plane velocity was captured (Figure 5-12). For consistency across patients, the PC MRI cross-sections were acquired:

- Just downstream of the confluence between the hepatic veins and the IVC
- Just downstream of the confluence between the innominate vein and the SVC
- And just upstream of the point where the LPA and RPA branch into smaller vessels

Through-Plane PC MRI for flow boundary conditions

Acquisition Parameters

Number of slices	4 to 6 (depending on anatomy)
Number of time points	20 to 30
Pixel size	0.7to 1.5 mm
Slice Thickness	3 to 6 mm

Acquisition locations

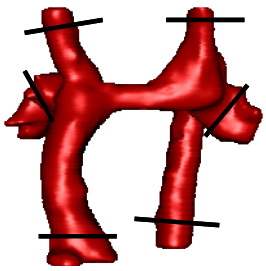

Sample acquisition

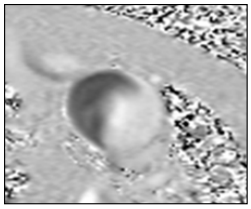

Figure 5-12: PC MRI acquisition protocol for the vessel flow rate characterization. The location of the acquisition planes is shown by the black lines overlaid on the TCPC.

For each cross-sectional slice, data were acquired at 20 to 30 evenly-spaced time points in the cardiac cycle depending on the heart rate of the patient (a slower heart rate allowing for more acquisitions than a fast one).

5.5.2 Extraction of the TCPC Vessel Flow Rates

The pixel intensity in each one of the through-plane PC MRI acquisitions is linearly proportional to the through-plane velocity component, so that the velocity field within a region of interest can be quantified with a simple linear transformation. The key is to properly isolate the vessel cross-section of interest, namely one of the TCPC inflows or outflows. This segmentation is performed using the approach developed by Sundareswaran et al. [163], which combines gradient flow, parametric active contours to identify the vessel borders and an adaptive median filtering to remove the spurious noise vectors close to the vessel walls. Once the vessel is segmented, the vessel flow rate is simply obtained by integrating the out-of-plane velocity component over the cross-section. The process is iterated over the 20 to 30 acquisition time points, yielding a characteristic flow curve for each vessel, as exemplified in Figure 5-13. For the non-pulsatile simulations, these flow curves were then averaged over the cardiac cycle, yielding a single mean flow rate value per vessel.

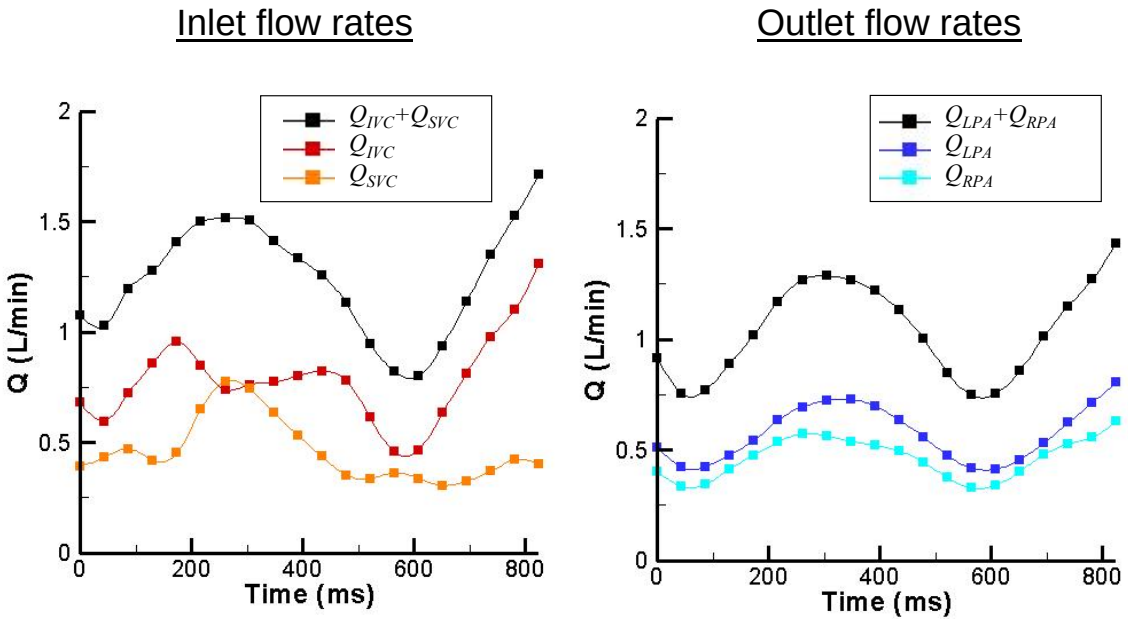

Figure 5-13: Example of the inflow and outflow curves as computed from PC MRI. The black lines depict the sum of the inflow or outflow rates.

5.5.3 Flow Corrections for the CFD Boundary Conditions

As can be observed from Figure 5-13, the sum of the incoming flow rates as computed from PC MRI was generally not equal to the sum of the outgoing flows through the left and right pulmonary arteries. This might be attributed to the small dimensions of the pulmonary arteries, which leads to a larger error in the PC MRI measurements. Irrespective of the underlying reason for this discrepancy, the flow conditions to be prescribed in the CFD simulations should ensure a global mass conservation. Accordingly, the *in vivo* PC MRI measurements are corrected as follows. Assuming the incoming flow rates to be more accurate, the flow conditions at the TCPC inlets are prescribed using the *in vivo* flow measurements. The outflow boundary conditions on the other hand are prescribed using the *in vivo* LPA/RPA flow ratios.

The resulting flow conditions for non-pulsatile simulations will thus read as follows:

$$\overline{Q}_I^{\,CFD} = \overline{Q}_I^{\,PC\,MRI} \tag{5-2}$$

$$\overline{Q}_{RPA}^{\,CFD} = \frac{\overline{Q}_{RPA}^{\,PC\,MRI}}{\overline{Q}_{RPA}^{\,PC\,MRI} + \overline{Q}_{LPA}^{\,PC\,MRI}} \cdot \sum_{I \in \text{inflow}} \overline{Q}_I^{\,PC\,MRI} \tag{5-3}$$

$$\overline{Q}_{LPA}^{\,CFD} = \frac{\overline{Q}_{LPA}^{\,PC\,MRI}}{\overline{Q}_{RPA}^{\,PC\,MRI} + \overline{Q}_{LPA}^{\,PC\,MRI}} \cdot \sum_{I \in \text{inflow}} \overline{Q}_I^{\,PC\,MRI} \tag{5-4}$$

where $\overline{Q}_I$ denotes the mean flow rate through the inlet *I*, $\overline{Q}_{RPA}$ and $\overline{Q}_{LPA}$ indicate the mean flow rates through the RPA and LPA outlets, respectively, the PC MRI superscript denotes the values obtained from the PC MRI measurements and the CFD superscript denotes the values used for the CFD boundary conditions.

The same approach is propagated to the pulsatile simulations, where the *in vivo* flow curves are prescribed at the inlets, while the time varying *in vivo* flow ratios are used at the outlets. An additional step is, however, required to more finely discretize the flow rate and flow ratio curves than the 20 to 30 time points provided by the PC MRI measurements. These curves were thus first decomposed into a Fourier series of sine waves, from which the signal could be reconstructed with a higher temporal resolution.

5.6 *In Vivo* 3D TCPC Velocity Fields

With the recent progresses in acquisition and post-processing techniques, PC MRI now constitutes an attractive approach to characterize the *in vivo* velocity fields on a full volumetric dataset (and not only in a few acquisition slices). All four patients retained for the pulsatile investigation were selected based on the availability of reconstructed 3D *in vivo* velocity fields, to compare the CFD predictions and *in vivo* measurements. The

subsequent sections briefly describe the acquisition parameters and velocity reconstruction.

5.6.1 Imaging Protocol

Compared to anatomical MRI, PC MRI requires a long acquisition time, which limits its application for detailed hemodynamic investigations, especially in young or diseased subjects who may not be able to stay in the magnet for the necessary amount of time. Accordingly, for the velocity reconstructions, the 3D PC MRI slices were acquired in the coronal direction, allowing the entire TCPC to be covered with 6 to 10 slices rather than the 40-50 axial slices used for the anatomical acquisition. The slice orientation and typical acquisition parameters are given in Figure 5-14. It might be noted that the spatial resolution in every direction is two to three times coarser than in the anatomical MRIs.

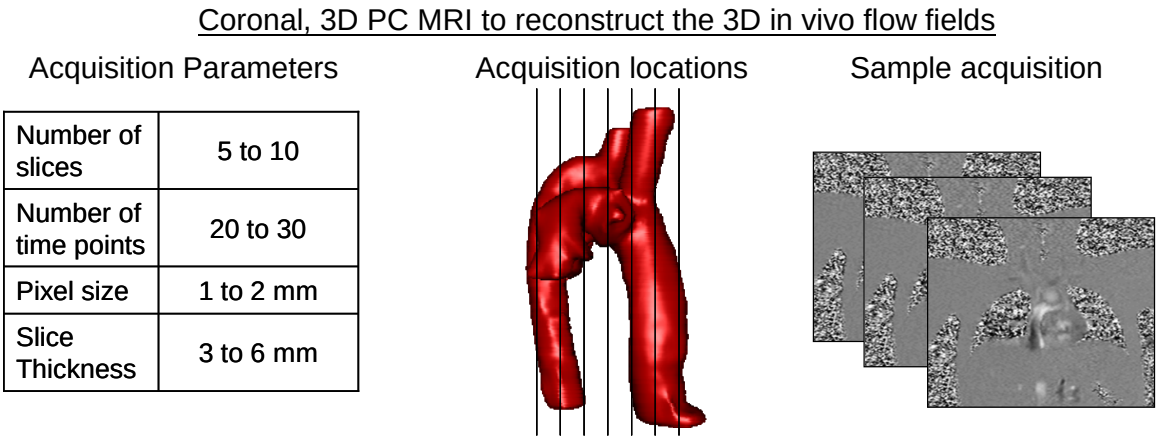

Figure 5-14: PC MRI acquisition protocol for the reconstruction of the 3D in vivo velocity fields.

5.6.2 Reconstruction of the 3D Velocity Fields

Obviously, characterizing the TCPC with only a limited number of slices comes at the cost of spatial resolution. In order to visualize the detailed in vivo 3D flow structures, the coronal PC MRI measurements were thus interpolated to an isotropic voxel size of 1 to 2mm. Scalar interpolation methods, where each velocity component is interpolated individually, do not perform well on 3D PC MRI data-sets and are especially sensitive to the high levels of noise present in the vicinity of the vessel walls. The divergence-free interpolation developed by Sundareswaran et al. [80] takes advantage of the incompressible properties of blood to interpolate all three velocity components in conjunction. In addition, Sundareswaran et al. [80] impose a no-slip boundary condition along the vessel walls, which constrains the velocities to be null at the vessel boundaries and efficiently filters the noise in the vicinity of the walls. Recursively applying this divergence-free interpolation to the 20 to 30 acquisition time points yields a time-dependent representation of the 3D in vivo velocity fields. For the four patients selected for the pulsatile study, the time-dependent velocity reconstructions were readily available as per the work of Sundareswaran and Haggerty.

5.7 CFD Simulations

With the surface meshes of the *in vivo* or surgical planning anatomies created in Section 5.4 and the patient-specific flow conditions obtained from Section 5.5, detailed hemodynamic evaluations can now be performed using the flow solver developed as part of the first specific aim of this thesis. For the clarity of our presentation, the mathematical formulation of the solver is addressed separately in Chapter 6, and only the set-up of the

CFD simulations is treated in this section. Detailed instructions regarding the input parameter prescription are provided in Appendix A.3 and Appendix B.

5.7.1 Non-Dimensionalization

In our solver formulation, we solve the incompressible Newtonian Navier-Stokes equation in their non-dimensional form, using one of the TCPC inlets as the reference for normalization. Assuming that the vessel of reference is the inferior vena cava (IVC), the velocities are normalized by the mean velocity at the IVC inlet, $\overline{U}_{IVC}$, and the distances by the equivalent IVC diameter, D_{IVC}, defined as $D_{IVC} = 2\sqrt{A_{IVC}/\pi}$, where A_{IVC} is the area of the IVC inlet cross-section. Time is normalized by the characteristic time scale defined as $D_{IVC}/\overline{U}_{IVC}$, and pressure by $\rho\overline{U}_{IVC}^{2}$, where $\rho = 1060$ kg·m^{-3} is the density of blood. Finally, we define the characteristic Reynolds number to be $\mathrm{Re} = \left(\rho\overline{U}_{IVC} \cdot D_{IVC}\right)/\mu$, where $\mu = 3.71$ kg·m^{-1}·s^{-1} is the viscosity of blood.

5.7.2 Volume Mesh Generation

Resolution of the Navier-Stokes equations requires both a robust flow solver, and an adequate discretization of the fluid domain. This last point constitutes a major challenge for *in vivo* applications due to the difficulty to generate computational volume meshes that can adequately describe the complexity of real-life anatomies. Unstructured grids provide a natural choice for tackling such problems and have been used with a great deal of success [124-126], but typically involve higher computational overhead than structured grids. Structured curvilinear body-fitted meshes have also been used for this purpose but in conjunction with overset Chimera grids [87]. Even when domain

decomposition is employed, the generation of good quality, composite, boundary-conforming meshes could be cumbersome and time consuming for realistic anatomies [87]. The formulation retained for this thesis effectively addresses these difficulties using an immersed-boundary approach. The Navier-Stokes equations are solved on a structured Cartesian grid, which can easily be generated, and the location of the TCPC vessel wall is carefully tracked to appropriately prescribe the boundary conditions.

Accordingly, provided with the unstructured surface meshes generated in Section 5.4, the only parameters required to generate the volume mesh are 1) the characteristic distance used to normalize the TCPC geometry, and 2) the non-dimensional spatial resolution for each one of the Cartesian grid directions. The spatial resolution used in this thesis typically was of 0.02 D_{IVC}, but finer grids were employed in cases were severe vessel stenoses were present, for example. A detailed mesh refinement study supporting this parameter setting is provided in Chapter 7.

5.7.3 Boundary Conditions

Flow boundary conditions are prescribed using the corrected time-averaged flow rates or corrected flow curves from Section 5.5. Since all computations are conducted in non-dimensional form, caution should be paid to appropriately normalize the vessel flow rates and cardiac cycle duration. All flow simulations reported in this thesis use one of two types of inlet velocity profiles: 1) a flat velocity profile where the velocity is uniform across the inlet cross-section; or 2) a parabolic velocity profile based on the equivalent hydraulic diameter of the inlet under consideration. The velocity profile at the outflows is extrapolated from the fluid domain and rescaled to enforce global mass conservation.

Finally, the immersed TCPC vessel wall is treated as a rigid, no-slip wall. Details on the formulation of these boundary conditions may be found in Chapter 6, Section 6.2.

5.7.4 Convergence Criteria

For all simulations, convergence at each time-step is ensured by constraining the mean divergence to reduce by 3 orders of magnitude or more, and the maximum non-dimensional divergence to fall below 0.001. Non-pulsatile flow simulations are iterated until convergence of the running average, which is assessed by tracking the pressure and velocity time histories at selected points within the computational domain. These trackers are typically set at the center of the connection and within the pulmonary outflow tracks. Pulsatile simulations are iterated over a minimum of 3 cardiac cycles. The first cardiac is systematically discarded as it does not account for the unsteady effects imparted by the earlier cycles.

5.8 Clinical Metrics Extraction

As highlighted in the clinical background (Section 1.5), the postulated pathways through which a given TCPC impacts the long-term outcome of a patient include:

- the pressure drops across the connection, which in turn impact the pressure levels in the gastro-intestinal track, higher pressures being correlated with a higher risk for protein losing enteropathy
- the power lost across the connection, which increases the workload imposed on the single ventricle by an equal amount

- and the distribution of the hepatic nutrients to the left and right lung, which condition their development, a low supply in hepatic nutrients being correlated with the development of pulmonary arterio-venous malformations.

The above metrics will thus be the central focus of our analyses. When deemed necessary, qualitative visualization of the flow structures or pressure drops will also be provided in order to elucidate the mechanisms leading to an increased energy dissipation, or a given hepatic flow distribution. Unless otherwise specified in the corresponding chapters, all non-pulsatile flow fields, pressures or hepatic flow distributions shown in this thesis are obtained using the converged running average, while the pulsatile results correspond to the instantaneous flow fields. Extraction of the velocity and pressure fields, power loss calculation, and hepatic flow distribution quantification are addressed in turns in each one of the following subsections.

5.8.1 Extraction of the Flow and Pressure Fields

The first step for all subsequent post-processing is to remove the vessel extensions, which were solely added for computational purposes but do not correspond to any *in vivo* structures. This is achieved using an in-house code that reads in the unstructured Cartesian grid used for the computations and a triangular surface mesh of the TCPC geometry without extensions created in Gambit 2.4 (ANSYS Inc., PA, USA). All points falling outside of the domain delimited by the surface mesh without extension are discarded. Distances, velocities and pressures are re-dimensionalized to cm, cm/s and mmHg units providing clinically meaningful information, and written into an ASCII file format to be read by any visualization software. All visualizations performed herein used

Tecplot 360 (Tecplot Inc., WA, USA). Finally, velocities and pressure are averaged over each inlet and outlet of the TCPC domain with no extensions, providing the pressure drops and velocity values needed for the power loss calculations.

5.8.2 Power Loss Calculations

The power losses, $\dot{E}$, across the TCPC are computed using the following control volume expression

$$\dot{E} = \int_S \left(P(\vec{x}) + \frac{1}{2}\rho \|\vec{u}(\vec{x})\|^2 \right) \vec{u}(\vec{x}) \cdot \vec{n} dS \tag{5-5}$$

Where $\rho = 1060$ kg/m^3 is the density of blood, P is the static pressure, $\vec{u}$ is the velocity vector, S is the TCPC surface, including inlets and outlets, dS is the surface element, and $\vec{n}$ is the inward surface normal. The instantaneous and mean power losses are computed the in-house code depicted above during the removal of the vessel extensions, avoiding the need to perform additional integrations.

5.8.3 Hepatic Flow Distribution Quantification

Quantification of the hepatic flow distribution to the left and right lung first requires the knowledge of the path followed by these nutrients. For the purpose of this study, all diffusion effects are neglected and the hepatic nutrients are considered as weightless point particles, passively advected by the flow. The method used to compute the particle pathways differ depending upon whether the particles are tracked through a single flow field, as is the case for the non-pulsatile simulations, or through successive

instantaneous flow fields, as in the pulsatile simulations. Those two methods are described in turn below.

5.8.3.1 *Hepatic Flow Distribution in Non-Pulsatile Simulations*

For the quantification of the hepatic flow distribution on the converged running average, one to two thousand particles are uniformly seeded over a cross-section of the hepatic veins and the corresponding streamtraces are generated using Tecplot 360 (Tecplot Inc., WA, USA). These streamtraces serve separate the particles into two groups: $\Omega_{Hep\to RPA}$, which regroups all particles exiting through the RPA, and $\Omega_{Hep\to LPA}$ for the particles exiting through the LPA. The amount of hepatic flow going to the RPA and LPA, $Q_{Hep\to RPA}$ and $Q_{Hep\to LPA}$, respectively, is then quantified as:

$$Q_{Hep\to RPA} = \sum_{p\in\Omega_{Hep\to RPA}} u_p^0 dA_p \tag{5-6}$$

$$Q_{Hep\to LPA} = \sum_{p\in\Omega_{Hep\to LPA}} u_p^0 dA_p \tag{5-7}$$

where u_p^0 the velocity of the particle p at its seeding point and dA_p is the area represented by that particle. Since the particles are uniformly seeded $dA_p = A/Np$ where A is the cross-sectional area of the hepatic or IVC inlet, and N_p is the number of particles seeded over that cross-section. In the subsequent chapters, hepatic flow distribution is typically expressed as the percentage of hepatic flow going to each lung, obtained as:

$$HFD_{RPA} = \frac{Q_{Hep\to RPA}}{Q_{Hep\to RPA} + Q_{Hep\to LPA}} \tag{5-8}$$

$$HFD_{LPA} = \frac{Q_{Hep\to LPA}}{Q_{Hep\to RPA} + Q_{Hep\to LPA}} \tag{5-9}$$

5.8.3.2 Particle Tracking and Pulsatile Hepatic Flow Distribution

For the pulsatile simulations, the particle pathways were computed using an in-house particle tracking code. Since the hepatic nutrients are considered as weightless passively advected particles, their velocity is equal to that of the surrounding fluid and their displacement is governed by the following equation:

$$\left.\frac{\partial \vec{x}_P^{\,n}}{\partial t}\right|_{t^n} = \vec{u}\left(\vec{x}_P^{\,n}, t^n\right) \tag{5-10}$$

where $\vec{x}_P^{\,n}$ denotes the spatial location a particle *P* at the instant t^n, and $\vec{u}\left(\vec{x}_P^{\,n}, t^n\right)$ is the fluid velocity obtained from the CFD simulations at the point $\vec{x}_P^{\,n}$ and instant t^n. The main components of the particle tracking algorithm are thus a spatial and temporal interpolation scheme to reconstruct $\vec{u}\left(\vec{x}_P^{\,n}, t^n\right)$ from the available CFD results, and a time-integration scheme to advance the particle position in time.

The temporal interpolation is performed using a second-order accurate linear formulation given by:

$$\vec{u}\left(\vec{x}, t^n\right) = \frac{\left(T_2 - t^n\right)\cdot \vec{u}\left(\vec{x}, T_1\right) + \left(t^n - T_1\right)\cdot \vec{u}\left(\vec{x}, T_2\right)}{T_2 - T_1} \tag{5-11}$$

where t^n is the time point at which the information is needed, and T_1 and T_2 are the two closest instants where CFD results were obtained, verifying $T_1 \le t^n \le T_2$.

The spatial interpolation is performed using a third order-accurate parabolic scheme, applied in turn in each spatial direction. To simplify our explanations, let us consider a one-dimensional problem, with one velocity component *u* and one spatial direction *x* as exemplified in Figure 5-15. Let x_P be the *x* coordinate of the particle *P* for which *u* is needed. Let *i* be the index of the computational grid cell containing x_P. Since

all the simulations reported in this thesis are conducted on uniform Cartesian grids, the index i can simply be obtained by $i = (x_P - x_{\min})/\Delta x + 1$, where $x_{\min}$ is the x coordinate of the first Cartesian grid cell center, and Δx is the grid spacing in the x direction.

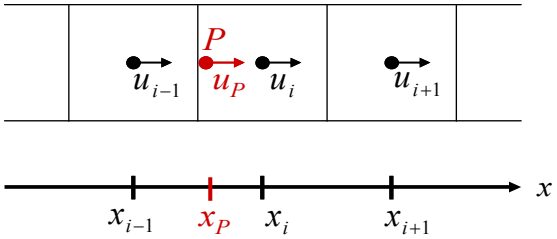

Figure 5-15: One dimensional example of the interpolation stencil for the third-order accurate spatial interpolation used in the particle tracking algorithm.

Knowing the velocity at the grid closest grid cell center, $u(x_i) = u_i$, we can express $u(x_P)$ as follows:

$$u(x_P) = u_i + \int_{x_i}^{x_P} \frac{\partial u}{\partial x} dx \tag{5-12}$$

Equation 4-12 is approximated with a centered Riemann integral as:

$$u(x_P) = u_i + \left.\frac{\partial u}{\partial x}\right|_{\frac{x_P - x_i}{2}} \cdot (x_P - x_i) \tag{5-13}$$

where the first derivative $\partial u/\partial x$ is evaluated at the mid-point between x_i and x_P. Using the same approach as in Equation 4-8, this derivative can be further expressed as:

$$\left.\frac{\partial u}{\partial x}\right|_{\frac{x_P - x_i}{2}} = \left.\frac{\partial u}{\partial x}\right|_{x_{i-1/2}} + \int_{x_{i-1/2}}^{\frac{x_P - x_i}{2}} \frac{\partial^2 u}{\partial x^2} dx \tag{5-14}$$

u is assumed to follow a locally parabolic profile, such that the second derivative $\partial^2 u/\partial x^2$ is constant across our interpolation stencil, and can be evaluated in x_i. All

required spatial derivatives are evaluated using a second order-accurate central scheme, as follows:

$$\left.\frac{\partial u}{\partial x}\right|_{x_{i-1/2}} = \frac{u_i - u_{i-1}}{\Delta x} \tag{5-15}$$

$$\left.\frac{\partial^2 u}{\partial x^2}\right|_{x_i} = \frac{u_{i+1} - 2\cdot u_i + u_{i-1}}{\Delta x^2} \tag{5-16}$$

Combining Equations 4-13 through 4-16 we obtain the following expression for $u(x_P)$:

$$u(x_P) = u_i + \left(\frac{u_{i+1} - 2u_i + u_{i-1}}{\Delta x^2} \cdot \left(\frac{x_P - x_i}{2} + \frac{\Delta x}{2} \right) + \frac{u_i - u_{i-1}}{\Delta x} \right) \cdot (x_P - x_i) \tag{5-17}$$

Finally, the time integration is performed using an approximate 4th order accurate Runge-Kutta scheme as follows:

$$\vec{x}_P^{(1)} = \vec{x}_P^n + \frac{\Delta t}{2} \cdot \vec{u}\left(\vec{x}_P^n, t^n\right) \tag{5-18}$$

$$\vec{x}_P^{(2)} = \vec{x}_P^n + \frac{\Delta t}{2} \cdot \vec{u}\left(\vec{x}_P^{(1)}, t^n\right) \tag{5-19}$$

$$\vec{x}_P^{(3)} = \vec{x}_P^n + \Delta t \cdot \vec{u}\left(\vec{x}_P^{(2)}, t^n\right) \tag{5-20}$$

$$\vec{x}_P^{n+1} = \vec{x}_P^n + \frac{\Delta t}{6} \cdot \left\{ \vec{u}\left(\vec{x}_P^n, t^n\right) + 2\cdot\vec{u}\left(\vec{x}_P^{(1)}, t^n\right) + 2\cdot\vec{u}\left(\vec{x}_P^{(2)}, t^n\right) + \vec{u}\left(\vec{x}_P^{(3)}, t^n\right) \right\} \tag{5-21}$$

where each one of the velocity values are reconstructed using the above temporal and spatial interpolation schemes. For the sake of computational speed, the temporal interpolation is only performed once at the beginning of the time integration, in $t = t^n$.

One to two thousand particles are released at the inlet cross-section of the hepatic veins, at 200 evenly spaced time points per cardiac cycle. These particles are advected through the pulsatile TCPC flow fields using the above described particle tracking

algorithm. Similarly to the non-pulsatile approach the particles are then classified into two groups depending on the pulmonary artery through which they exit. The final hepatic flow distribution is quantified as:

$$HFD_{RPA} = \frac{N_{Hep \rightarrow RPA}}{N_{Hep \rightarrow RPA} + N_{Hep \rightarrow LPA}} \tag{5-22}$$

$$HFD_{LPA} = \frac{N_{Hep \rightarrow LPA}}{N_{Hep \rightarrow RPA} + N_{Hep \rightarrow LPA}} \tag{5-23}$$

where $N_{Hep \rightarrow RPA}$ and $N_{Hep \rightarrow LPA}$ are the number of particles exiting through the RPA and LPA, respectively.

This concludes the description of the methods and protocols used in this thesis to numerically simulate blood flow in patient-specific TCPC anatomies and extract the clinically-relevant efficiency metrics, ultimately allowing us to identify the most performing option(s) during the surgical planning investigations, and understand the impact of neglecting or including pulsatility on the accuracy of our predictions.

CHAPTER 6

NUMERICAL METHODS

In this chapter, we present the numerical methods used to simulate flows within complex cardiovascular anatomies. The formulation employed is an extension of the methodology developed by Sotiropoulos and co-workers [123, 164], which has been successfully applied to flow simulations around swimming fishes, and through mechanical heart valves under pulsatile flow conditions. This formulation is here recast onto a hybrid structured/unstructured layout to best tackle internal flows within arbitrarily complex cardiovascular structures. This chapter is organized as follows: First, we restate the governing equations and present the flow solver formulation retained for their discrete integration. Next, we describe the structured sharp-interface immersed-boundary method and, last, the hybrid structured/unstructured formulation developed to optimize the computational efficiency of immersed-boundary methods for internal flow applications. The chapter closes with a few remarks on code parallelization.

6.1 Solver Formulation

6.1.1 Governing Equations for Incompressible Newtonian Flows

For the purpose of this study, blood will be assumed to be an incompressible Newtonian fluid, which is a fair assumption in large vessels. Under these assumptions, blood motion is governed by the unsteady, incompressible, Newtonian Navier-Stokes equations. Using a vectorial notation these equations may be expressed as follows:

$$\nabla(\vec{\mathbf{u}}) = 0 \tag{6-1}$$

$$\frac{\partial(\vec{\mathbf{u}})}{\partial t} = -\nabla(p) - \nabla(\vec{\mathbf{u}} \cdot \vec{\mathbf{u}}) + \nabla\left\{\frac{1}{\mathrm{Re}}\left(\nabla\vec{\mathbf{u}} + (\nabla\vec{\mathbf{u}})^T\right)\right\} \tag{6-2}$$

where $\vec{\mathbf{u}}$ is the three-dimensional velocity vector, p is the pressure, t is time, Re the Reynolds number and ∇ is the spatial derivative operator. It should be noted that the above equations depict the Navier-Stokes equations in their non-dimensional form. The characteristic scales of the problem were chosen to be the equivalent IVC diameter, D_{IVC} ($D_{IVC} = 2\sqrt{A_{IVC}/\pi}$, with A_{IVC} the area of the IVC inlet cross-section) and the mean velocity at the IVC inlet, $\overline{U}_{IVC}$. In addition, the density and molecular viscosity of blood were assumed constant, given by $\rho = 1060$ kg·m^{-3} and $\mu = 3.71$ kg·m^{-1}·s^{-1}, respectively.

6.1.2 Variable Layout & Notations

To simplify the presentation of the temporal and spatial discretizations used in our flow solver, we will first present the layout adopted to store the pressure and velocity variables and the notations used in the subsequent sections.

As discussed in details in the numerical background (Section 1.2.2), the straightforward implementation of a three-point central difference scheme on top of a non-staggered grid (where pressure and velocities are both stored at the cell centers) may lead to non-physical pressure oscillations, the well-known odd-even decoupling problem. This problem can be effectively resolved using a staggered storage of the flow variables, where the velocity components are stored at the cell interfaces while the pressure is stored at the cell centers. Such staggered arrangement, originally proposed by Harlow and Welch in 1965 [165], removes the pressure oscillations without the requirement for

special treatments on the pressure field or for the addition of artificial dissipation terms to stabilize the computations. However, as the pressure and each one of the velocity components are stored in different locations, adequate prescription of the boundary conditions is a stringent problem for staggered grid approaches. Based on these observations, Gilmanov and Sotiropoulos [164, 166] developed a hybrid staggered/non-staggered grid approach, which combines the versatility and convenience of implementation of the non-staggered grids with the stability and accuracy of staggered mesh approaches. This hybrid formulation has been successfully applied to a wide range of flow simulations, such as flows around fishes and planktonic copepod, or blood flow through artificial heart valves [123, 164, 166, 167].

Given the successful simulations of complex flows achieved using the staggered/non-staggered arrangement of the variables [123, 164, 166, 167], the numerical methodology developed and employed in this thesis builds upon this algorithm. To help the discussion, Figure 6-1 demonstrates the data storage locations using this hybrid layout for one Cartesian grid cell. For the remainder of this method section, integer indices, such as (i, j, k) in Figure 6-1, will denote the cell centers. In counterpart, half integer indices, such as $(i+1/2, j, k)$, $(i, j+1/2, k)$ and $(i, j, k+1/2)$ in Figure 6-1, will denote the centers of cell surfaces in each one of the grid directions.

Similarly to a staggered grid arrangement, the pressure p is stored at the cell center, while the velocity components $(u_m \text{ with } m \in \{1,2,3\})$ are stored at the surface centers. In addition to the staggered variables, the hybrid arrangement also makes use of non-staggered velocities $(v_m \text{ with } m \in \{1,2,3\})$ to ease the computation of the governing equations and the prescription of the boundary conditions. Away from the boundaries,

these non-staggered velocities are reconstructed from the surface-centered velocities with a QUICK interpolation scheme, as exemplified below for the v_1 velocity component:

$$v_{1\,(i,j,k)} = \frac{3 \cdot u_{1\,(i-1/2,j,k)} + 6 \cdot u_{1\,(i+1/2,j,k)} - u_{1\,(i+3/2,j,k)}}{8} \tag{6-3}$$

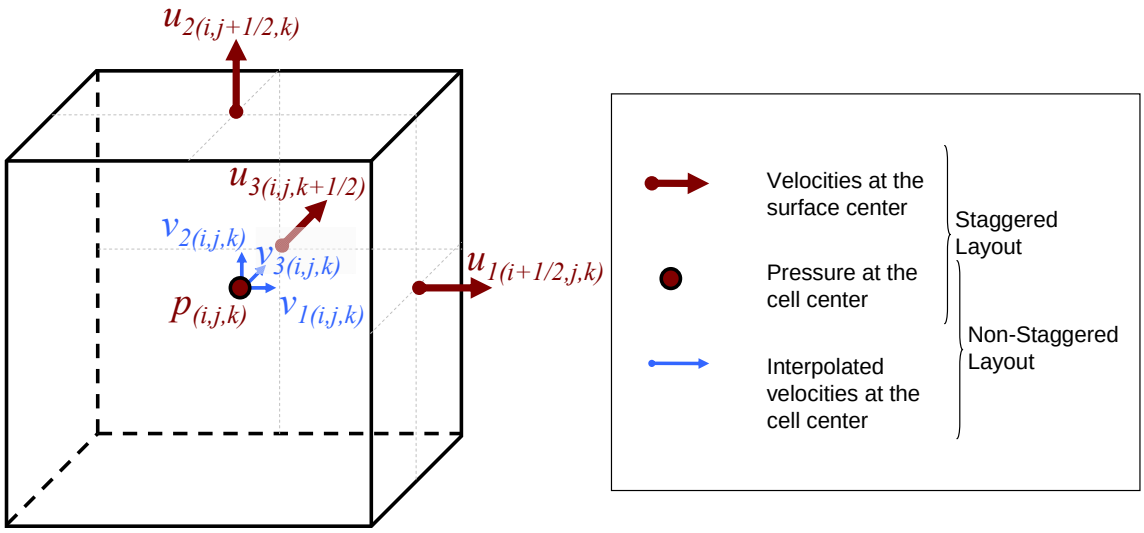

Figure 6-1: Schematic representation of a hybrid staggered/non-staggered layout. The light gray lines are provided as a mere visual help, to help localize the centers of the cell surface.

6.1.3 Temporal Discretization - Fractional-Step Formulation

The governing equations are integrated in time using a fractional-step method, which comprises two steps: a prediction step, where the momentum equations are solved without enforcing continuity; and a correction step, which enforces the divergence free constraint and advances both pressure and velocities in time.

1- Prediction step: In the prediction step, we solve the momentum equations (Equation 5-2) using a second-order accurate backward Euler scheme for the time derivative and a semi-implicit formulation for the right hand side of the equation. The partially discretized momentum equation reads as follows:

$$\frac{1}{2\Delta t}\left(3\vec{\mathbf{u}}^{*}-4\vec{\mathbf{u}}^{n}+\vec{\mathbf{u}}^{n-1}\right)=-\nabla\left(p^{n}\right)-\nabla\left(\vec{\mathbf{u}}^{*}\cdot\vec{\mathbf{u}}^{*}\right)+\nabla\left\{\frac{1}{\mathrm{Re}}\left(\nabla\vec{\mathbf{u}}^{*}+\left(\nabla\vec{\mathbf{u}}^{*}\right)^{T}\right)\right\} \qquad (6\text{-}4)$$

where $\vec{\mathbf{u}}^{n}$ and $\vec{\mathbf{u}}^{n-1}$ are the velocity field at time step *n* and *n-1*, and $\vec{u}^{*}$ describes intermediate non-divergence free velocity field. Note that $\vec{u}^{*}$ satisfies the momentum equation with the pressure p^{n} and not p^{n+1}.

2- Correction step: The intermediate field $\vec{\boldsymbol{u}}^{*}$ is in general not divergence free, so that in the second step, a correction is applied to produce a velocity field $\vec{\mathbf{u}}^{n+1}$ that satisfies both the divergence free constraint and the momentum equations expressed with p^{n+1}. These conditions may be formulated as follows:

$$\nabla\left(\vec{\mathbf{u}}^{n+1}\right)=0 \qquad (6\text{-}5)$$

$$\frac{1}{2\Delta t}\left(3\vec{\mathbf{u}}^{n+1}-4\vec{\mathbf{u}}^{n}+\vec{\mathbf{u}}^{n-1}\right)=-\nabla\left(p^{n+1}\right)-\nabla\left(\vec{\mathbf{u}}^{*}\cdot\vec{\mathbf{u}}^{*}\right)+\nabla\left\{\frac{1}{\mathrm{Re}}\left(\nabla\vec{\mathbf{u}}^{*}+\left(\nabla\vec{\mathbf{u}}^{*}\right)^{T}\right)\right\} \qquad (6\text{-}6)$$

By subtracting Equation 5-4 to Equation 5-6, we obtain the following equation for the incremental pressure, $\delta p = p^{n+1} - p^{n}$:

$$\frac{3}{2\Delta t}\left(\vec{u}^{n+1}-\vec{u}^{*}\right)=-\nabla\left(\delta p\right) \qquad (6\text{-}7)$$

Taking the divergence of Equation 5-7 and applying the fact that the divergence of $\vec{u}^{n+1}$ is zero, we obtain the Poisson equation for the incremental pressure:

$$\nabla^2(\delta p) = \frac{3}{2\Delta t}\nabla(\vec{u}^*) \tag{6-8}$$

Having solved Equation 5-8 for δP, $\vec{u}^{n+1}$ and p^{n+1} can be simply obtained as:

$$p^{n+1} = p^n + \delta p \tag{6-9}$$

$$\vec{u}^{n+1} = \vec{u}^* - \frac{2\Delta t}{3}\nabla(\delta p) \tag{6-10}$$

6.1.4 Resolution of the Prediction Step

Given the temporal discretization described above, the key point for the prediction step is the computation of the convective, viscous and pressure terms at the surface centers for the resolution of the three momentum equations. It is important to recall here that all variables are stored on a hybrid staggered/non-staggered layout, where p and $\vec{\mathbf{v}}$ depict the collocated pressure and velocity variables, while $\vec{\mathbf{u}}$ depicts the velocities at the surface centers. For the sake of simplicity, the momentum equations given in 4-2 will be recast as follows:

$$\left.\frac{\partial u_1}{\partial t}\right|_{i+1/2,j,k} = -\left.\frac{\partial p}{\partial x_1}\right|_{i+1/2,j,k} - Conv_1(\vec{\mathbf{u}})_{i+1/2,j,k} + Visc_1(\vec{\mathbf{u}})_{i+1/2,j,k} \tag{6-11}$$

$$\left.\frac{\partial u_2}{\partial t}\right|_{i,j+1/2,k} = -\left.\frac{\partial p}{\partial x_2}\right|_{i,j+1/2,k} - Conv_2(\vec{\mathbf{u}})_{i,j+1/2,k} + Visc_2(\vec{\mathbf{u}})_{i,j+1/2,k} \tag{6-12}$$

$$\left.\frac{\partial u_3}{\partial t}\right|_{i,j,k+1/2} = -\left.\frac{\partial p}{\partial x_3}\right|_{i,j,k+1/2} - Conv_3(\vec{\mathbf{u}})_{i,j,k+1/2} + Visc_3(\vec{\mathbf{u}})_{i,j,k+1/2} \tag{6-13}$$

where $Conv_m(\vec{\mathbf{u}})$ and $Visc_m(\vec{\mathbf{u}})$ with $m = 1,2,3$ denote the three components of the convective and viscous terms. These relate to the convective and viscous fluxes, $\vec{\mathbf{F}}_C^m$ and $\vec{\mathbf{F}}_V^m$ ($m = 1,2,3$), as follows:

$$\overrightarrow{\mathbf{Conv}}(\vec{u}) = \frac{\partial \vec{\mathbf{F}}_C^m}{\partial x_m} \tag{6-14}$$

$$\overrightarrow{\mathbf{Visc}}(\vec{u}) = \frac{\partial \vec{\mathbf{F}}_V^m}{\partial x_m} \tag{6-15}$$

where the fluxes at the surface centers of each control volume are expressed as:

$$\vec{\mathbf{F}}_C^m = \begin{pmatrix} u_m u_1 \\ u_m u_2 \\ u_m u_3 \end{pmatrix} \tag{6-16}$$

$$\vec{\mathbf{F}}_V^m = \frac{1}{\mathrm{Re}} \begin{pmatrix} \frac{\partial u_m}{\partial x_1} + \frac{\partial u_1}{\partial x_m} \\ \frac{\partial u_m}{\partial x_2} + \frac{\partial u_2}{\partial x_m} \\ \frac{\partial u_m}{\partial x_3} + \frac{\partial u_3}{\partial x_m} \end{pmatrix} \tag{6-17}$$

As can be seen from the above equations, using a purely staggered grid would require the evaluation of the viscous and convective terms on the three different control volumes (centered on each one of the surface centers), which can quickly burden the speed of the numerical simulations. The staggered hybrid/non-hybrid approach circumvents that difficulty by first evaluating the viscous and convective terms at the cell centers and then reconstructing them at each one of the surface centers. The method employed for the flux calculations and their derivatives are treated in the following subsections.

6.1.4.1 Evaluation of the Viscous Fluxes

The viscous fluxes through each one of the cell interfaces are evaluated with a second-order accurate central difference scheme applied to the cell-centered velocity values, $\vec{\mathbf{v}}$. Let us consider the viscous flux $F^1_{V(i+1/2,j,k)}$ that is applied on the x_2-x_3 interface centered on the point $(i+1/2, j, k)$:

$$F^1_{V(i+1/2,j,k)} = \frac{1}{\mathrm{Re}} \begin{pmatrix} 2\left.\dfrac{\partial u_1}{\partial x_1}\right|_{i+1/2,j,k} \\ \left.\dfrac{\partial u_1}{\partial x_2}\right|_{i+1/2,j,k} + \left.\dfrac{\partial u_2}{\partial x_1}\right|_{i+1/2,j,k} \\ \left.\dfrac{\partial u_1}{\partial x_3}\right|_{i+1/2,j,k} + \left.\dfrac{\partial u_3}{\partial x_1}\right|_{i+1/2,j,k} \end{pmatrix} \tag{6-18}$$

The evaluation of $F^1_{V(i+1/2,j,k)}$ requires the evaluation of the derivatives of all three velocity components in the direction normal to the interface (i.e. along x_1), and the derivatives of the u_1 velocity component along the two directions tangential to the interface (i.e. along x_2 and x_3). The derivatives normal to the interface are evaluated using a second-order accurate central difference scheme as follows:

$$\left.\frac{\partial u_m}{\partial x_1}\right|_{i+1/2,j,k} = \frac{v_{m(i+1,j,k)} - v_{m(i,j,k)}}{\Delta x_1} \text{ with } m = 1,\ 2,\ 3 \tag{6-19}$$

The derivatives in the two tangential directions are first evaluated in (i, j, k) and $(i+1, j, k)$ using a central difference, and then interpolated in $(i+1/2, j, k)$:

$$\left.\frac{\partial u_1}{\partial x_2}\right|_{i+1/2,j,k} = \frac{1}{2}\left\{\frac{v_{1(i+1,j+1,k)} - v_{1(i+1,j-1,k)}}{2\Delta x_2} + \frac{v_{1(i,j+1,k)} - v_{1(i,j-1,k)}}{2\Delta x_2}\right\} \tag{6-20}$$

$$\left.\frac{\partial u_1}{\partial x_3}\right|_{i+\frac{1}{2},j,k} = \frac{1}{2}\left\{\frac{v_{1(i+1,j,k+1)} - v_{1(i+1,j,k-1)}}{2\Delta x_3} + \frac{v_{1(i,j,k+1)} - v_{1(i,j,k-1)}}{2\Delta x_3}\right\} \tag{6-21}$$

The viscous fluxes are only evaluated on valid cell interfaces, i.e. at cell interfaces such that both (i,j,k) and $(i+1,j,k)$ fall within the fluid domain. Accordingly, the normal derivatives given by Equation 5-19 are always defined. On the other hand, the tangential derivatives given by Equations 5-20 and 5-21 use a larger stencil, and special cases may arise in the vicinity of the immersed boundary where some of the required cell-centers do not belong to the fluid domain. In such case, the differential stencil is modified from a three-point central difference to a differential stencil biased towards the fluid domain, as illustrated in Figure 6-2 for a 2D grid layout. Accounting for these special cases, Equation 5-20 reads as follows:

$$\begin{aligned}
&\text{if } \{(\mathrm{i},\mathrm{j}+1,\mathrm{k}) \text{or } (\mathrm{i}+1,\mathrm{j}+1,\mathrm{k}) \text{ does not belong to the fluid domain}\} \\
&\qquad \left.\frac{\partial u_1}{\partial x_2}\right|_{i+\frac{1}{2},j,k} = \frac{1}{2}\left\{\frac{v_{1(i+1,j,k)} - v_{1(i+1,j-1,k)}}{\Delta x_2} + \frac{v_{1(i,j,k)} - v_{1(i,j-1,k)}}{\Delta x_2}\right\} \\
&\text{else if } \{(\mathrm{i},\mathrm{j}-1) \text{or } (\mathrm{i}+1,\mathrm{j}-1) \text{ does not belong to the fluid domain}\} \\
&\qquad \left.\frac{\partial u_1}{\partial x_2}\right|_{i+\frac{1}{2},j,k} = \frac{1}{2}\left\{\frac{v_{1(i+1,j+1,k)} - v_{1(i+1,j,k)}}{\Delta x_2} + \frac{v_{1(i,j+1,k)} - v_{1(i,j,k)}}{\Delta x_2}\right\} \\
&\text{else if all neighboring cell centers fall wihtin the fluid domain} \\
&\qquad \left.\frac{\partial u_1}{\partial x_2}\right|_{i+\frac{1}{2},j,k} = \frac{1}{2}\left\{\frac{v_{1(i+1,j+1,k)} - v_{1(i+1,j-1,k)}}{2\Delta x_2} + \frac{v_{1(i,j+1,k)} - v_{1(i,j-1,k)}}{2\Delta x_2}\right\} \\
&\text{end if}
\end{aligned} \tag{6-22}$$

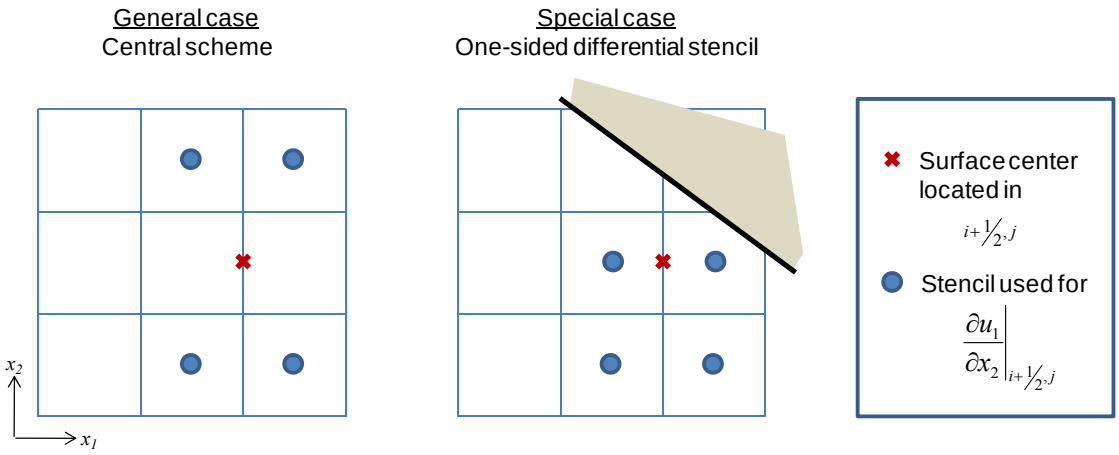

Figure 6-2: Stencil used for the evaluation of the tangential derivatives required for the viscous flux calculations, exemplified on a 2D Cartesian grid.

6.1.4.2 Evaluation of the Convective Fluxes

Similarly to the viscous fluxes, the computation of the convective fluxes through each one of the cell interfaces is conducted using the reconstructed cell-centered velocities, $\vec{\mathbf{v}}$. To increase the stability of the momentum equations, the convective fluxes at the surface centers are approximated using a second-order accurate upwind-biased QUICK scheme expressed as:

$$\vec{\mathbf{F}}^{1}_{(i+1/2,j,k)} = u^{+}_{(i+1/2,j,k)}\vec{\mathbf{U}}^{+}_{(i+1/2,j,k)} + u^{-}_{(i+1/2,j,k)}\vec{\mathbf{U}}^{-}_{(i+1/2,j,k)} \tag{6-23}$$

where the forward flux $u^{+}_{(i+1/2,j,k)}\vec{\mathbf{U}}^{+}_{(i+1/2,j,k)}$ is evaluated as:

$$u^{+}_{(i+1/2,j,k)} = \frac{v_{1(i,j,k)} + v_{1(i+1,j,k)} + \left\| v_{1(i,j,k)} + v_{1(i+1,j,k)} \right\|}{4} \tag{6-24}$$

$$\vec{\mathbf{U}}^{+}_{(i+1/2,j,k)} = \frac{3\vec{\mathbf{v}}_{(i+1,j,k)} + 6\vec{\mathbf{v}}_{(i,j,k)} - \vec{\mathbf{v}}_{(i-1,j,k)}}{8} \tag{6-25}$$

and the backward flux $u^{-}_{(i+1/2,j,k)}\vec{\mathbf{U}}^{-}_{(i+1/2,j,k)}$ is evaluated as:

$$u^{-}_{(i+1/2,j,k)} = \frac{v_{1(i,j,k)} + v_{1(i+1,j,k)} - \left\| v_{1(i,j,k)} + v_{1(i+1,j,k)} \right\|}{4} \tag{6-26}$$

$$\vec{\mathbf{U}}^{-}_{(i+1/2,j,k)} = \frac{3\vec{\mathbf{v}}_{(i,j,k)} + 6\vec{\mathbf{v}}_{(i+1,j,k)} - \vec{\mathbf{v}}_{(i+2,j,k)}}{8} \tag{6-27}$$

Similarly to the viscous fluxes, convective fluxes are only evaluated on valid cell interfaces, i.e. at cell interfaces such that both (i,j,k) and $(i+1,j,k)$ fall within the fluid domain. In cases where $(i-1,j,k)$ or $(i+2,j,k)$ fall outside of the forward and backward flux evaluations revert to first order as:

$$\vec{\mathbf{U}}^{+}_{(i+1/2,j,k)} = \vec{\mathbf{v}}_{(i,j,k)} \tag{6-28}$$

$$\vec{\mathbf{U}}^{-}_{(i+1/2,j,k)} = \vec{\mathbf{v}}_{(i+1,j,k)} \tag{6-29}$$

6.1.4.3 *Evaluation of the Flux Derivatives*

From the above surface-centered fluxes, $\vec{\mathbf{F}}^{m}_{C}$ and $\vec{\mathbf{F}}^{m}_{V}$ ($m = 1,2,3$), the convective and viscous terms can be directly obtained at the cell centers using central differencing:

$$\begin{aligned} Conv(\vec{\mathbf{u}})_{(i,j,k)} \quad = \quad & \frac{\vec{\mathbf{F}}^{1}_{C(i+1/2,j,k)} - \vec{\mathbf{F}}^{1}_{C(i-1/2,j,k)}}{\Delta x_1} + \frac{\vec{\mathbf{F}}^{2}_{C(i,j+1/2,k)} - \vec{\mathbf{F}}^{2}_{C(i,j-1/2,k)}}{\Delta x_2} \\ + \quad & \frac{\vec{\mathbf{F}}^{3}_{C(i,j,k+1/2)} - \vec{\mathbf{F}}^{3}_{C(i,j,k-1/2)}}{\Delta x_3} \end{aligned} \tag{6-30}$$

$$\begin{aligned} Visc(\vec{\mathbf{u}})_{(i,j,k)} \quad = \quad & \frac{\vec{\mathbf{F}}^{1}_{V(i+1/2,j,k)} - \vec{\mathbf{F}}^{1}_{V(i-1/2,j,k)}}{\Delta x_1} + \frac{\vec{\mathbf{F}}^{2}_{V(i,j+1/2,k)} - \vec{\mathbf{F}}^{2}_{V(i,j-1/2,k)}}{\Delta x_2} \\ + \quad & \frac{\vec{\mathbf{F}}^{3}_{V(i,j,k+1/2)} - \vec{\mathbf{F}}^{3}_{V(i,j,k-1/2)}}{\Delta x_3} \end{aligned} \tag{6-31}$$

The surface-centered viscous and convective terms are then reconstructed from the above cell-centered values using a QUICK interpolation scheme applied in each one

of the grid dimensions. The expression for the viscous and convective flux derivatives in $(i+1/2, j, k)$ thus reads as:

$$\overline{Conv}(\vec{\mathbf{u}})_{1(i+1/2,j,k)} = \frac{3 \cdot Conv(\vec{\mathbf{u}})_{1(i+1,j,k)} + 6 \cdot Conv(\vec{\mathbf{u}})_{1(i,j,k)} - Conv(\vec{\mathbf{u}})_{1(i-1,j,k)}}{8} \tag{6-32}$$

$$\overline{Visc}(\vec{\mathbf{u}})_{1(i+1/2,j,k)} = \frac{3 \cdot Visc(\vec{\mathbf{u}})_{1(i+1,j,k)} + 6 \cdot Visc(\vec{\mathbf{u}})_{1(i,j,k)} - Visc(\vec{\mathbf{u}})_{1(i-1,j,k)}}{8} \tag{6-33}$$

Finally, since the pressure is stored at the cell centers, the pressure gradient is directly obtained at the surface centers by applying a central differencing as follows:

$$\left.\frac{\partial p}{\partial x_1}\right|_{(i+1/2,j,k)} = \frac{p_{(i+1,j,k)} - p_{(i,j,k)}}{\Delta x_1} \tag{6-34}$$

Having discretized the pressure, convective and viscous terms at each one of the surface centers, $\vec{\mathbf{u}}$ can readily be advanced in time, yielding the intermediate non divergence free velocity field, $\vec{\mathbf{u}}^*$.

6.1.5 Resolution of the Pressure-Correction Step

The overall efficiency of a fractional step method largely depends on the approach adopted to solve the Poisson equation in the correction step (Equation 5-8). All spatial derivatives are discretized using central differencing, and Equation 5-8 in its discrete form reads as follows:

$$\begin{aligned}
&\frac{\delta P_{(i+1,j,k)} - 2\delta P_{(i,j,k)} + \delta P_{(i-1,j,k)}}{\Delta x_1{}^2} \\
&+ \frac{\delta P_{(i,j+1,k)} - 2\delta P_{(i,j,k)} + \delta P_{(i,j-1,k)}}{\Delta x_2{}^2} \\
&+ \frac{\delta P_{(i,j,k+1)} - 2\delta P_{(i,j,k)} + \delta P_{(i,j,k-1)}}{\Delta x_3{}^2}
\end{aligned} = \frac{3}{2\Delta t} \cdot \left(\begin{aligned}
&\frac{u^*_{1\,(i+1/2,j,k)} - u^*_{1\,(i-1/2,j,k)}}{\Delta x_1} \\
&+ \frac{u^*_{2\,(i,j+1/2,k)} - u^*_{2\,(i,j-1/2,k)}}{\Delta x_2} \\
&+ \frac{u^*_{3\,(i,j,k+1/2)} - u^*_{3\,(i,j,k-1/2)}}{\Delta x_3}
\end{aligned} \right) \qquad (6\text{-}35)$$

The above system may be re-written as $A \cdot \varphi = B$, where A is the discrete 3D Laplacian operator, B can be computed from the intermediate velocity field $\vec{\mathbf{u}}^*$, and φ is the solution vector containing the incremental pressure values for each grid cell. If one seeks to solve the Poisson equation in simple coordinates, such as a rectangular structured Cartesian grid for example, then A is a sparse symmetric matrix and the solution can be efficiently obtained through direct solvers [168, 169]. However, as will be detailed later in this chapter, the domain considered for our applications is limited to the Cartesian grid cells inside the fluid domain, resulting in an effectively unstructured grid. With such data-structure, the discrete 3D Laplacian operator, *A*, is still sparse (with at most 7 non-zero elements per row), but no-longer symmetric. Iterative methods thus represent the only feasible alternative to solve the discrete Poisson equation in our unstructured grid system.

The mathematical description of the different iterative methods available to date is beyond the scope of this thesis and the interested reader is referred to [170] for a detailed review on iterative approaches to linear and non-linear systems of equations. Briefly, rather than computing A^{-1}, the exact inverse of the matrix *A*, and solving φ as

$\varphi = A^{-1}b$, iterative methods seek to devise a linear operator S that approximates A^{-1} and iterate the solution vector φ until convergence. The iterative procedure proceeds as:

$$\varphi^{n+1} = \varphi^n + S \cdot r^n \tag{6-36}$$

where φ^n is the solution vector computed at the n^{th} iteration, and $r^n = b - A\varphi^n$ is the corresponding residual. The system is iterated until r^n is smaller than a set convergence criterion. The difference between alternate iterative methods resides in the approach retained to construct the approximate inverse operator S.

The most efficient iterative solvers available today include Krylov subspace methods, such as the flexible general minimal residual (FGMRES) [171] and stabilized bi-conjugate gradient (BiCGSTAB) [172] formulations, and multi-grid methods, where the equation is first solved on a coarse grid and then refined onto a finer grid level. An additional option is to pre-condition the solution by first using a fast iterative method to formulate an initial guess, and then using a higher accuracy scheme to refine the solution. Combining the above approaches, Ge and Sotiropoulos [123] demonstrated that using a multigrid-preconditioned FGMRES method to solve the Poisson equation yielded a robust and computationally efficient fractional step formulation.

Accordingly, in this work, we employ an FGMRES solver with a cell-centered multi-grid preconditioner to solve the Poisson equation. To better explain the multi-grid procedure, let us denote by $\ell+1$ the Cartesian grid on which the Navier-Stokes are solved, and by ℓ a coarser grid level, embedded in grid $\ell+1$. The grid for the coarser level ℓ is generated by coarsening the level $\ell+1$ by a factor two in each direction. This process is illustrated in Figure 6-3 for a two-dimensional Cartesian grid.

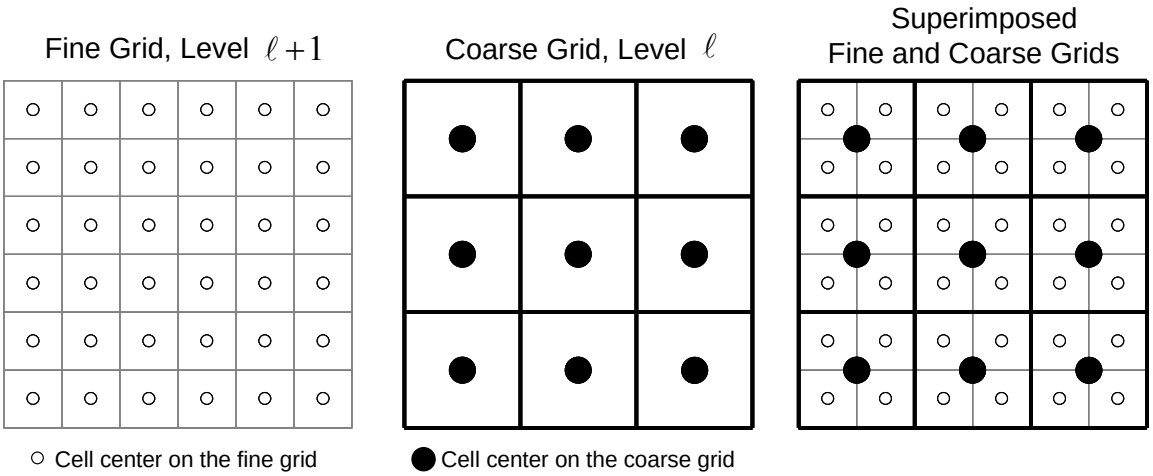

Figure 6-3: Two embedded grid levels

We then define two multi-linear interpolation operators, $R_{\ell+1\to\ell}$ and $R_{\ell\to\ell+1}$, which will be used to interpolate variables from the finer level $\ell+1$ onto the coarser level ℓ, and reciprocally to restrict variables from ℓ to $\ell+1$ (see Appendix C for implementation details). With these notations in mind, the iterative procedure at level $\ell+1$ reads as:

$$\varphi_{\ell+1}^{n+1} = \varphi_{\ell+1}^{n} + \left(A_{\ell+1}\right)^{-1} \cdot r_{\ell+1}^{n} \tag{6-37}$$

and may be recast as follows:

$$\varphi_{\ell+1}^{n+1} = \varphi_{\ell+1}^{n} + R_{\ell\to\ell+1} \cdot \left(A_{\ell}\right)^{-1} \cdot R_{\ell+1\to\ell} \cdot r_{\ell+1}^{n} \tag{6-38}$$

where $A_\ell = R_{\ell+1\to\ell} A_{\ell+1} R_{\ell\to\ell+1}$ is the Jacobian matrix restricted to the level ℓ. If we now define S_ℓ as the solution procedure used to approximate A_ℓ^{-1} on the level ℓ, the Poisson equation can be solved as:

$$\varphi_{\ell+1}^{n+1} = \varphi_{\ell+1}^{n} + R_{\ell\to\ell+1}\left\{S_\ell\left\{R_{\ell+1\to\ell} \cdot r_{\ell+1}^{n}\right\}\right\} \tag{6-39}$$

The solution at the fine grid level $\ell+1$ can be obtained by solving the equation at the level ℓ, which is less computationally expensive than on the finer grid $\ell+1$, and then interpolating the coarse solution onto level $\ell+1$. A two level multi-grid procedure will thus proceed as follows:

1. Solve the equation on the fine grid as $\varphi^0_{\ell+1} = S_{\ell+1} \cdot b$, to obtain the initial residual: $r^0_{\ell+1} = b - A_\ell \varphi^0_{\ell+1}$
2. Restrict the residual from the finer to the coarser level: $r^0_\ell = R_{\ell+1 \to \ell} r^0_{\ell+1}$
3. Solve the equation on the coarser level: $\Delta\varphi_\ell = S_\ell \cdot r^0_\ell$
4. Interpolate the solution $\Delta\varphi_\ell$ from the coarser to the finer level and update the solution at the finer level: $\varphi^1_{\ell+1} = \varphi^0_{\ell+1} + R_{\ell \to \ell+1} \cdot \Delta\varphi_\ell$
5. Compute the corresponding residual and solve the equation at the finer level one more time to smoothen the interpolated solution.

As illustrated in Figure 6-4, the same process is repeated recursively when more than two levels are employed. It may be noted that the Poisson equation is solved after each interpolation or restriction to smoothen the reconstructed fields. The key to an efficient multi-grid implementation is thus to use fast iterative methods to smoothen the finer levels (levels 1 to 3 in Figure 6-4), and a high accuracy scheme to solve the Poisson equation on the coarsest level (level 0 in Figure 6-4). To this end, we employ a Block Jacobi decomposition for the finer levels, and the FGMRES method at the coarsest level.

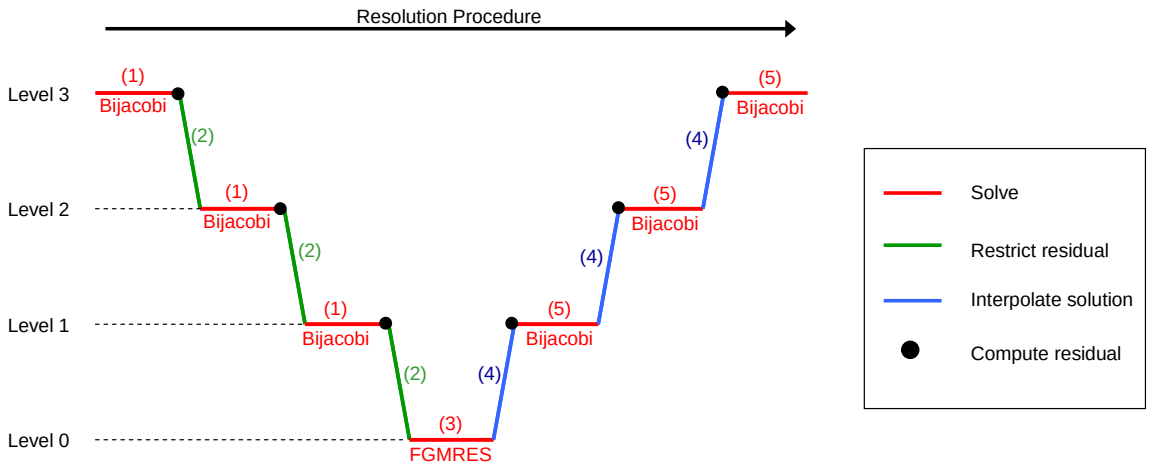

Figure 6-4: Schematic representation of the multi-grid solution procedure with four grid levels. Numbers in parenthesis refer to the itemized list given above. The iterative procedures used for each "Solve" step are provided in red.

In summary, our Poisson solver combines an FGMRES method with a multi-grid preconditioner. The solution procedure is characterized by the following parameters:

1. multiple embedded grid levels, which are iteratively coarsened by a factor two in all directions
2. tri-linear restriction and interpolation operators between two consecutive grid levels
3. discrete 3D Laplacian operators, A_ℓ, for each grid levels, which are constructed at the first time step, and stored in memory for improved computational speed in the subsequent time iterations
4. solution procedures S_ℓ at each grid level, which use the FGMRES method to solve the Poisson equation at the coarsest level and a Block Jacobi decomposition to serve as a smoother at the finer levels.

This Poisson solver was implemented using the Krylov Subspace libraries offered by PETSC [173, 174], where the FGMRES and multi-grid methods were readily available.

The interested reader is thus referred to the PETSC manual [174] for more details on the implementation of these iterative solvers.

6.2 Sharp Interface Immersed-Boundary Method

The fractional step method described above is implemented together with the sharp interface immersed-boundary approach of Gilmanov and Sotiropoulos [164]. This approach distinguishes itself from other immersed boundary implementations in the treatment of the Cartesian nodes closest to the immersed boundary. In this section, we thus first present the classification of the Cartesian grid nodes, depending on their location with respect to the immersed boundary, followed by a detailed description of the boundary condition prescription.

6.2.1 Node Classification

The surface of the immersed boundary, here the TCPC vessel wall, is discretized with an unstructured triangular mesh and immersed in a background Cartesian grid. With reference to Figure 6-5, the cells of the Cartesian grid are sorted as follows: 1) *external* cells that are outside of the fluid domain; 2) *immersed boundary (IB)* cells that are located in the interior of the flow domain but in the immediate vicinity of the immersed boundary; and 3) *fluid* cells that are located strictly inside the fluid domain. In the flow solver presented above, the Navier-Stokes equations are discretized and solved on the *fluid* cells only, with boundary conditions prescribed at the *IB* cell centers. Only the cell-centered velocity components need to be reconstructed at these *IB* cell centers because the hybrid staggered/non-staggered grid approach of Gilmanov and Sotiropoulos [164] eliminates the need for explicitly specifying boundary conditions for the pressure.

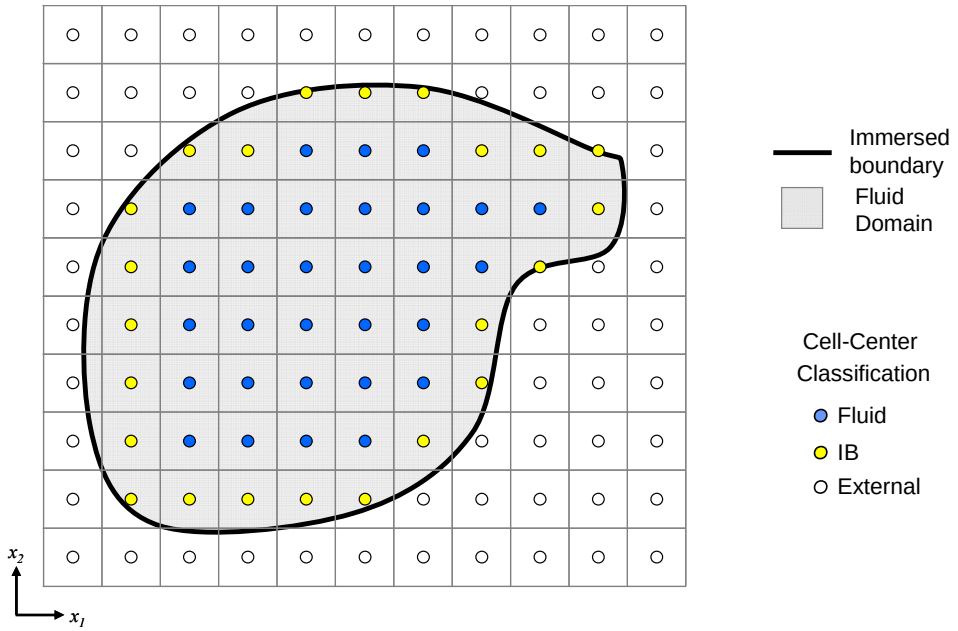

Figure 6-5**:** Schematic representation of a 2D immersed-boundary layout. The fluid domain is immersed in a background Cartesian grid. The Cartesian grid cells are sorted into three categories based on the position of their cell center relative to the immersed boundary.

6.2.2 Velocity Reconstruction along the Vessel Walls

The TCPC vessel walls are treated as rigid, no-slip surfaces. The velocity variables at the *IB* cell centers closest to these wall surfaces are reconstructed via quadratic interpolation along the local normal direction to the vessel wall. Using the notations defined in Figure 3-5, let G be the IB cell center to be treated, and *s* the triangular element of the immersed-boundary that is the closest to G. $\vec{n}_F$ is the unit normal to element s, and F is the projection of G along $\vec{n}_F$ onto the surface element s. Symmetrically, H represents the projection of G along the wall normal direction $\vec{n}_F$ onto the closest fluid elements (defined by the fluid cell centers h_1, h_2, h_3 and h_4).

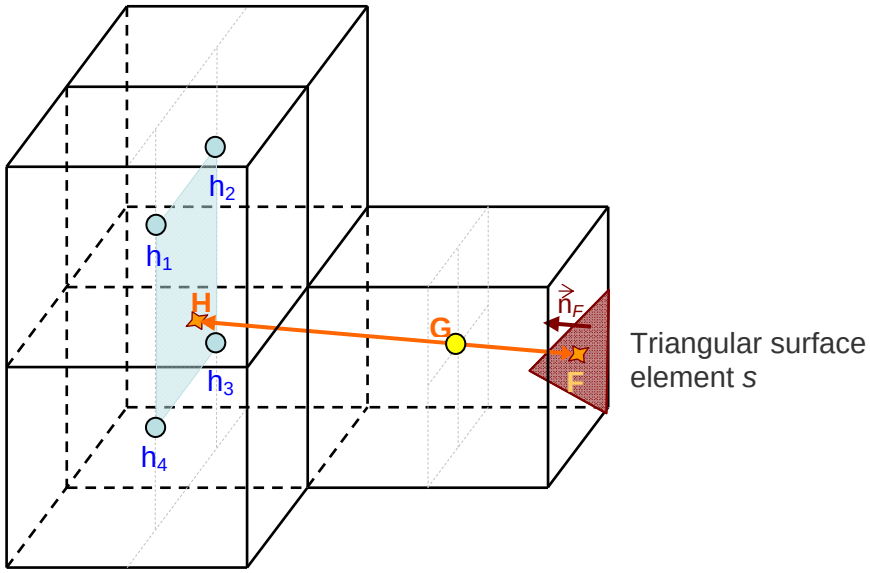

Figure 6-6: Reconstruction of the solution at an IB-cell center (G) by interpolating between its projection onto the closest immersed-boundary and fluid elements (points F and H, respectively) along the local normal to the immersed-boundary. The light gray lines are provided for sole visual display to help localize the centers of the fluid and IB cells.

In the present study, the walls of the TCPC are considered rigid and the velocity at point F, $\vec{\mathbf{v}}_F$, is known and equal to zero at any point in time. The velocity at point H, $\vec{\mathbf{v}}_H$, is reconstructed from the velocities at the four neighboring fluid cell centers using an inverse distance interpolation, as depicted below:

$$\vec{\mathbf{v}}_H = \frac{\sum_{\ell=1}^{4} \vec{\mathbf{v}}_{h_\ell} \cdot \left\| \overrightarrow{Hh_\ell} \right\|^{-1}}{\sum_{\ell=1}^{4} \left\| \overrightarrow{Hh_\ell} \right\|^{-1}} \tag{6-40}$$

With $\vec{\mathbf{v}}_F$ and $\vec{\mathbf{v}}_H$ known, the velocity at the IB cell center, $\vec{\mathbf{v}}_G$, can now be reconstructed by interpolation. We employ the quadratic interpolation procedure detailed by Gilmanov and Sotiropoulos [164], which was found to increase the overall accuracy of

the flow solver when compared to a linear interpolation procedure. To simplify the notation in the subsequent equations, v will describe one of the three cell-centered velocity components. The quadratic interpolation assumes that every component of the velocity vector varies in a quadratic manner with respect to the normal distance to the wall, as depicted by the following equation:

$$v(d) = C_1 d^2 + C_2 d + C_3 \tag{6-41}$$

where C_1, C_2, and C_3 are coefficients to be determined, and d is the normal distance to the wall. There is thus a total of four unknowns: the three afore-mentioned coefficients and the velocity value at the IB node, v_G. These four unknowns can be fully determined by solving the following system of equations:

$$v(0) = C_3 = v_F \tag{6-42}$$

$$v(d_{FG}) = C_1 {d_{FG}}^2 + C_2 d_{FG} + C_3 = v_G \tag{6-43}$$

$$v(d_{FH}) = C_1 {d_{FH}}^2 + C_2 d_{FH} + C_3 = v_H \tag{6-44}$$

$$\left.\frac{\partial v}{\partial d}\right|_{d_{FG}} = 2C_1 d_{FG} + C_2 \tag{6-45}$$

where d_{FG}, d_{FH} and d_{GH} denote the distances between the specified points. To close the above system of equations, the derivative of the velocity in G is approximated by first computing the velocity derivatives in the middle of the segments FG and GH by central differencing, and then reconstructing the derivative in G by linear interpolation. The approximation to the velocity derivative in G thus reads as follows:

$$\left.\frac{\partial v}{\partial d}\right|_{d_{FG}} = \alpha \frac{v_G - v_F}{d_{FG}} + (1-\alpha)\frac{v_H - v_G}{d_{GH}} \tag{6-46}$$

where $\alpha = d_{GH}/d_{FH}$. Combining Equations 4-37 through 4-41, we now have a closed system of equations, which can be solved to determine v_G. The solution with the above notations reads as:

$$v_G = \frac{\frac{v_H - v_F}{d_{FH}}\left(d_\beta + d_{FG}\right) + \frac{v_F}{d_{FG}}\left(\alpha d_\beta + d_{FG}\right) - \frac{v_H}{d_{GH}}\left(1-\alpha\right)d_\beta}{1 + \alpha\frac{d_\beta}{d_{FG}} - \left(1-\alpha\right)\frac{d_\beta}{d_{FH}}} \tag{6-47}$$

where $d_\beta = d_{GH}d_{FG}/\left(d_{GH} - d_{FG}\right)$. This quadratic interpolation procedure is applied to all three components of the velocity vector. The overall accuracy of the solver with the above reconstruction algorithm has been shown to be second-order in space [166].

6.2.3 Other Boundary Conditions

6.2.3.1 *Inflow Boundary Conditions*

The cell centered velocities at IB cells closest to one of the inlets of the immersed boundary are imposed so to achieve the desired flow rate and velocity profile. Depending on the problem treated, two types of velocity profiles are used in this study, namely flat and parabolic velocity profiles. Using the same notation as in Figure 3-5, the prescription of a flat velocity profile at an IB cell center, G, simply reads as follows:

$$\vec{v}_G = \overline{U} \cdot \vec{n}_F \tag{6-48}$$

where $\vec{n}_F$ is the local normal to the inlet surface, and $\overline{U} = Q/A$ is the mean velocity across the inlet, Q defining the desired flow rate and A the inlet cross-sectional area. For a fully developed parabolic profile, $\vec{v}_G$ would read as:

$$\vec{v}_G = 2\overline{U}\left(1-\left(\frac{r_G}{R}\right)^2\right)\cdot\vec{n}_F \tag{6-49}$$

where $R=\sqrt{A/\pi}$ is the radius of the inlet cross-section and r_G is the distance between the normal projection of G onto the inlet surface, point F in Figure 3-5, and the center of that inlet.

6.2.3.2 *Outflow Boundary Conditions*

For the IB cells closest to an outlet surface of the immersed boundary, the reconstruction of the cell-centered velocities is performed in two steps. First the velocities are reconstructed at all the IB cells pertaining to that outlet by extrapolation. Using the same notations as in Figure 3-5, the extrapolation procedure for an outlet IB cell, G, reads as follows:

$$\vec{v}_G = \vec{v}_H \tag{6-50}$$

where H is the projection of G along the normal to the outlet cross-section and onto the closest fluid element, and $\vec{v}_H$ is obtained by inverse distance interpolation as in Equation 5-39. These extrapolated values are then corrected to enforce global mass conservation across the fluid domain, as follows:

$$\vec{v}_G = \vec{v}_G + \Delta Q\cdot\vec{n}_F \tag{6-51}$$

where ΔQ is the difference between the mass flow rate obtained after the extrapolation and the desired mass flow rate, Q_O, computed as:

$$\Delta Q = Q_O - \sum_{G\in Outlet}\vec{v}_G\cdot\vec{n}_F \tag{6-52}$$

6.2.3.3 Pressure Reconstruction along all Boundaries

Finally, although not required to solve the Navier-Stokes equations, the pressure values at the IB cell centers are reconstructed as well, so as to avoid any perception bias when visualizing the computed pressure fields. Using the same notations as in Figure 3-5, the pressure at an IB cell center G, p_G, is extrapolated from the pressure at point H, p_H, by assuming a zero pressure gradient in the direction normal to the boundary, leading to:

$$p_G = p_H \tag{6-53}$$

where p_H is reconstructed by inverse distance interpolation as was done for the velocity in Equation 5-39:

$$p_H = \frac{\sum_{\ell=1}^{4} p_{h_\ell} \cdot \left\| \overrightarrow{Hh_\ell} \right\|^{-1}}{\sum_{\ell=1}^{4} \left\| \overrightarrow{Hh_\ell} \right\|^{-1}} \tag{6-54}$$

The same pressure reconstruction procedure is applied to all IB cells irrespective of the type of boundary condition. If this approach might be questionable from a physical stand point, it should be kept in mind that the reconstructed pressures only serve to improve the display, but in no case impact the flow resolution itself.

6.3 The Unstructured Cartesian Grid Paradigm

The original immersed-boundary method of Sotiropoulos and co-workers [123, 164] is implemented on a structured Cartesian grid. Regardless of the shape and size of the immersed boundary to be handled by the method, the entire background Cartesian grid is retained in the data-structure and the *external* cells, which do not need to be included in the computations, are "blanked out" of the calculations. To facilitate our

subsequent discussion and the presentation of an alternate formulation, we illustrate the structured implementation in the following pseudo-code in terms of the discretization of the velocity divergence, as required for the right hand side of the Poisson equation (Equations 5-8 and 5-34):

do $k = 2, KM$

do $j = 2, JM$

do $i = 2, IM$

if $\{$ $(\mathrm{i, j, k})$ is a fluid cell center $\}$ *then*

if $\{$ $(\mathrm{i-1, j, k})$, $(\mathrm{i, j-1, k})$ and $(\mathrm{i, j, k-1})$ are not external cells $\}$ *then*

$$D(i,j,k) = \frac{uh_1(i,j,k) - uh_1(i-1,j,k)}{\Delta x_1} + \frac{uh_2(i,j,k) - uh_2(i,j-1,k)}{\Delta x_2} + \frac{uh_3(i,j,k) - uh_3(i,j,k-1)}{\Delta x_3} \qquad 6\text{-}55$$

end if

end if

end do

end do

end do

where Δx_m with m=1, 2, 3 are the grid increments in three directions, *IM*, *JM*, and *KM* are the maximum number of grid nodes along the respective Cartesian coordinate lines, D is the discrete divergence operator, and uh_m with m=1, 2, 3 is the array storing the three surface-centered velocity components. uh_m relates to the former notation, u_m, in the following manner: $uh_1(i,j,k) = u_1(i+1/2, j, k)$, $uh_2(i,j,k) = u_2(i, j+1/2, k)$ and $uh_3(i,j,k) = u_3(i, j, k+1/2)$. We shall refer to this straightforward and quite common implementation as the *structured Cartesian* (SC) grid formulation.

For flow problems, such as those considered in [164] and [123], for which the volume of the immersed body is typically a small fraction of the background Cartesian domain, the standard SC approach is the method of choice. On the other hand, for internal flow problems involving even moderately complex, multi-connected conduits the most commonly encountered situation is for the *external cells* to constitute the vast majority of the overall grid nodes. For the TCPC shown in Figure 6-7 for example, only 7% of the Cartesian grid cells fall within the fluid domain, while the 93% remaining are *external* cells that do not contribute to the numerical solution. For such problems, the implementation of a sharp interface Cartesian grid methodology in conjunction with the SC approach could be very inefficient and in many cases totally impractical. Indeed, in the SC formulation all flow variables are stored in arrays of the size $IM \times JM \times KM$, and the large proportion of *external cells* leads to a large memory overhead allocated to store information in cells that are never being used. In addition, even though no computations are actually carried at the *external cell centers*, every do-loop in the code still has to go through them and exclude them using an *if*-statement (see above pseudo-code). This extra computational cost, which is hardly detectable when the *external cells* are few, can grow significantly with increasing number of *external cells*.

To remedy the aforementioned difficulties of the SC data indexing scheme, we have developed an *unstructured Cartesian* approach. The key idea, illustrated in Figure 6-8, is to replace the SC grid structure with the grid structure that arises when all grid nodes in the exterior of the flow domain are eliminated from the computational domain. The resulting grid is an unstructured grid system since the number of grid nodes along a certain grid direction is no longer constant and changes arbitrarily from line to line. The

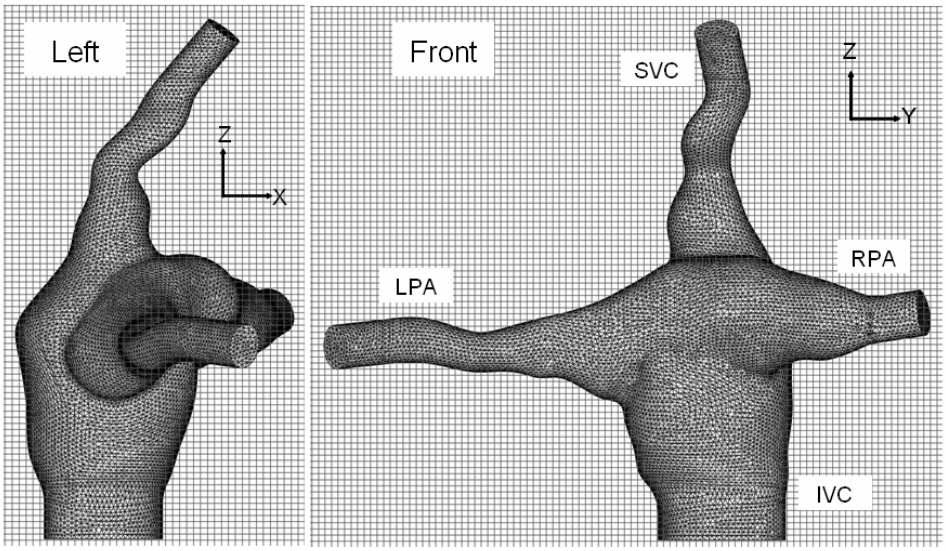

Figure 6-7: Example of a TCPC geometry embedded in a Cartesian grid. The multiple, interconnected vessels span a large 3D domain but occupy only a small portion of it, resulting in only 7% of the Cartesian grid cells falling within the fluid domain.

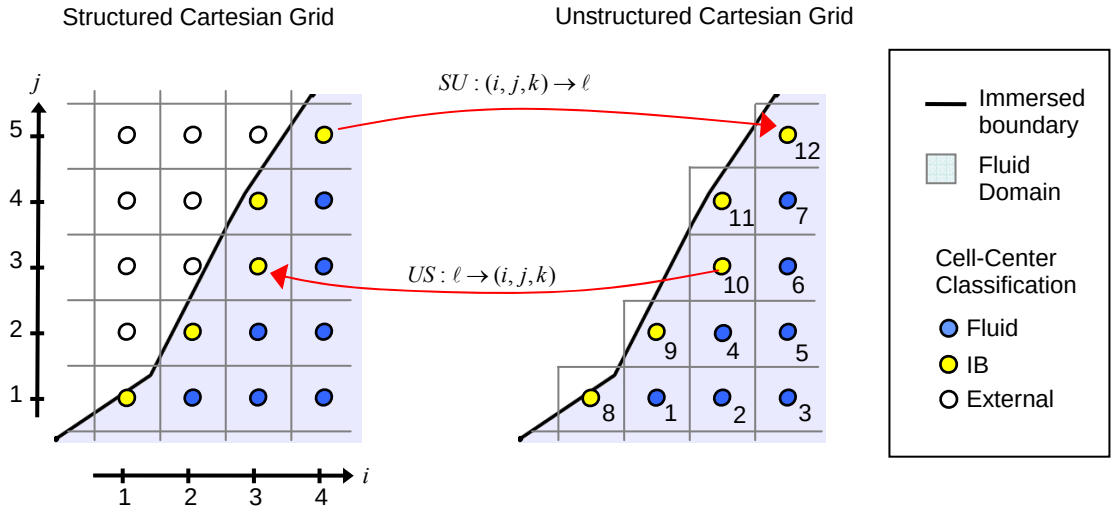

Figure 6-8: Schematic of a structured and unstructured Cartesian layout

simple indexing scheme of the complete Cartesian mesh is thus lost and a critical prerequisite for the successful implementation of the UC data structure is the development of an efficient indexing scheme for specifying the connectivity of the resulting unstructured mesh. We achieve this by taking advantage of the fact that each *active* grid cell (i.e. each cell of the unstructured Cartesian grid) can be referred to using two indexing systems: 1) the structured system $(i,j,k) \in [1, IM] \times [1, JM] \times [1, KM]$, and 2) the unstructured system, $\ell \in [1, N_a]$, where N_a is the total number of *active* grid cells—$N_a = N_f + N_{IB}$, where N_f and N_{IB} denote the number of *fluid* and *IB cells*, respectively. We define two mapping arrays, *SU* and *US*, respectively, which map the two indexing systems onto each other as follows:

$$\begin{aligned} SU &: (i,j,k) \rightarrow \ell \\ US &: \ell \rightarrow (i,j,k) \end{aligned} \qquad \text{6-56}$$

The *SU* array maps the structured grid index to its unstructured counterpart $\ell = SU(i,j,k)$ and has dimensions *IM*×*JM*×*KM*. The *US* array accomplishes the inverse mapping and has dimensions $3 \times N_a$:

$$\begin{aligned} i &= US(1,\ell) \\ j &= US(2,\ell) \\ k &= US(3,\ell) \end{aligned} \qquad \text{6-57}$$

In order to optimize programming and memory allocation, the *active cells* of the unstructured Cartesian mesh are numbered serially depending on their type. Accordingly, the N_f *fluid cells*, where the Navier-Stokes equations are discretized and solved, are assigned an index $\ell = 1, N_f$, while indices $\ell = N_f + 1, N_a$ are assigned to the remaining active *IB cells* where boundary conditions are applied. Using these notations and the two mapping arrays, the pseudo-code shown in 5-54 can now be implemented as follows:

$$
\begin{aligned}
&do \;\; \ell = 1, N_f \\
&\quad i = \mathrm{US}(1,\ell) \\
&\quad j = \mathrm{US}(2,\ell) \\
&\quad k = \mathrm{US}(3,\ell) \\
&\quad RHS(\ell) = \frac{uh_1(\mathrm{SU}(i,j,k)) - uh_1(\mathrm{SU}(i-1,j,k))}{\Delta x_1} + \frac{uh_2(\mathrm{SU}(i,j,k)) - uh_2(\mathrm{SU}(i,j-1,k))}{\Delta x_2} \\
&\qquad\quad + \frac{uh_3(\mathrm{SU}(i,j,k)) - uh_3(\mathrm{SU}(i,j,k-1))}{\Delta x_3} \\
&end \;\; do
\end{aligned}
\qquad \text{6-58}
$$

It should be noted that since the loop is only performed on the fluid cells, i.e. cells that fall strictly inside the fluid domain and are neighbored by active cells only, no specific condition needs to be added to assess whether the neighboring cells fall within the fluid domain.

The obvious advantage of the UC data structure when compared to its SC counterpart arises from the use of one-dimensional arrays of dimension N_a which ensures that no memory resources are wasted to store the useless *external cells*. Furthermore, the above-explained numbering procedure simplifies programming significantly since all computations that should be carried out solely at *fluid cells* may be performed in a single loop running from index 1 through N_f without the need for an "*if* statement". Similarly all *IB cells* can be treated by looping through indices $\ell = N_f + 1, N_a$. Moreover, this sequential indexing ensures that the flow information at grid nodes of similar type are allocated a consecutive memory address, which improves the cache hit rate and saves time in transferring data between the memory and processor.

6.4 Concluding Remarks on the Flow Solver

An overview of the solver implementation is provided in Appendix C. The numerical solver, which comprises a fractional step formulation for the Navier-Stokes equations coupled with an unstructured sharp-interface immersed-boundary method, is written in Fortran 90, and is thus platform independent and portable. The Poisson solver for the pressure correction step is implemented using Petsc libraries [173, 174], a suite of data structures and routines for the parallel solution of scientific applications modeled by partial differential equations. It includes support for parallel vectors, parallel matrices but also Krylov subspace approaches such as the FGMRES method employed in the current Poisson solver.

Furthermore, the present numerical solver has been parallelized using the Message Passing Interface (MPI) standard for all communications between processors during the computations. A particularity of our system for parallelization stems from the unstructured grid layout. Merely dividing the underlying Cartesian grid into even blocks will in practice lead to a highly uneven distribution of the active cells between the different processors. Accordingly a specific domain-splitting subroutine was implemented that divides the Cartesian grid such that the number of active nodes is evenly distributed across all processors involved. The subroutine proceeds recursively as depicted in the following pseudo-code:

SPLIT($N_0, \mathrm{I_m}, \mathrm{I_M}, \mathrm{J_m}, \mathrm{J_M}, \mathrm{K_m}, \mathrm{K_M}, \mathrm{NP_m}, \mathrm{NP_M}$)

$$DP = \frac{NP_M - NP_m}{2}$$

$$N_{target} = \frac{N_0}{NP_M - NP_m + 1} \cdot DP$$

do $i = I_m, I_M$

$cnt_{-1} = cnt$

$cnt = cnt + \text{number of active cells in } [i] \times [J_m, J_M] \times [K_m, K_M]$

$if\left(cnt_{-1} < N_{target} \le cnt\right)\{\ I_S = i;\ \text{exit loop}\ \}$

end do

6-59

update the domain spanned by the processors:

processors $\mathrm{NP_m}$ to $\mathrm{NP_m}$+DP : $[I_m, I_S] \times [J_m, J_M] \times [K_m, K_M]$

processors $\mathrm{NP_m}$+DP+1 to $\mathrm{NP_M}$: $[I_S{+}1, I_M] \times [J_m, J_M] \times [K_m, K_M]$

and iterate:

$if\left(\mathrm{NP_m} < (\mathrm{NP_m}{+}\mathrm{DP})\right)$ call SPLIT$\{cnt, \mathrm{I_m}, \mathrm{I_S}, \mathrm{J_m}, \mathrm{J_M}, \mathrm{K_m}, \mathrm{K_M}, \mathrm{NP_m}, (\mathrm{NP_m}{+}\mathrm{DP})\}$

$if\left((\mathrm{NP_m}{+}\mathrm{DP}{+}1) < \mathrm{NP_M}\right)$ call SPLIT$\{(\mathrm{N_0} - cnt), (\mathrm{I_S}{+}1), \mathrm{I_M}, \mathrm{J_m}, \mathrm{J_M}, \mathrm{K_m}, \mathrm{K_M}, (\mathrm{NP_m}{+}\mathrm{DP}{+}1), \mathrm{NP_M}\}$

where $\mathrm{NP_m}$ and $\mathrm{NP_M}$ denote the starting and ending indices of the processors over which the grid should be distributed, $[I_m, I_M] \times [J_m, J_M] \times [K_m, K_M]$ depict the size of the domain covered by these processors and $\mathrm{N_0}$ the number of active nodes in that domain. For the sake of simplicity, the above pseudo-code only splits the Cartesian grid along the *i* direction. In practice the splitting direction is chosen to be the longest side of the domain to be split. If $(J_M - J_m + 1) = \max\left((I_M - I_m + 1), (J_M - J_m + 1), (K_M - K_m + 1)\right)$, for example, then the Cartesian block under consideration will be split along the *j* direction.

CHAPTER 7

FLOW SOLVER VALIDATION

In this chapter, we apply the hybrid unstructured Cartesian (UC) immersed-boundary flow solver developed as part of our first specific aim to simulate various internal flow problems of progressively increasing complexity. Our objectives are to validate our implementation and demonstrate that, when combined with appropriate data storage, immersed-boundary methods can be used to carry out grid refinement studies for complex anatomical geometries, which would simply be impractical using the standard structured Cartesian (SC) implementation. We first assess the relative performance of the SC and UC formulations in terms of storage and computational speed. Next, we report simulations and grid refinement studies for the three following test cases: 1) flow through a 90 degree curved pipe, 2) flow in an idealized TCPC geometry, 3) highly unsteady flow in a patient-specific TCPC geometry. Pulsatile flow simulations in idealized and patient-specific TCPC geometries are reported in Chapter 8.

7.1 Performance Assessment of the SC and UC approaches

In this section, we carry out a series of numerical experiments aimed at quantifying the computational speed and memory requirements of the UC and SC approaches as a function of the ratio *active* grid nodes to the total number of Cartesian grid nodes, defined as:

$$r = N_a / (IM \times JM \times KM) \tag{7-1}$$

where $N_a = N_f + N_{IB}$ is the number of *active* nodes defined as the sum of the *fluid* nodes, N_f, and of the boundary (or *IB*) nodes, N_{IB}. *IM*, *JM* and *KM* are the number of Cartesian grid cells in the three spatial directions. By definition *r* varies between 0 and 1. The SC formulation is expected to be optimal when $r \to 1$, while the UC formulation is expected to be the best suited approach when $r \to 0$.

To design a numerical experiment for which *r* can be easily varied across a broad range of values, we consider a straight circular pipe of radius *R* and length *R*, embedded in a background Cartesian domain of dimensions $L \times 2.1R \times 2.1R$, where L is the streamwise extent of the domain (see Figure 7-1). The Cartesian domain is discretized with a constant grid spacing *h* along all three spatial directions. To systematically vary the ratio parameter *r*, we maintain the pipe dimension *R* and the grid increment *h* constant, but we gradually vary the streamwise grid dimension, *L*, from 1.1*R* to 54.1*R*. As shown in Figure 7-1, this procedure results in a pipe of fixed volume (N_a remains

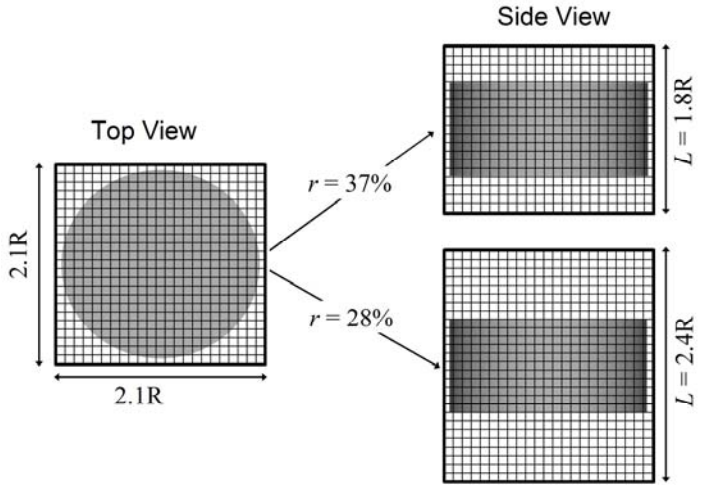

Figure 7-1**:** Test case to evaluate the performance of the various approaches as a function of the active-to-total grid nodes ratio *r*. The ratio *r* is artificially decreased by increasing the dimensions of the surrounding Cartesian grid, while keeping the grid spacing and hence the number of *active nodes*, N_a, constant.

constant) embedded in gradually larger Cartesian domains (*IM* linearly increases with *L*), allowing us to vary *r* over nearly two orders of magnitude from 0.7 down to 0.01.

Calculations are carried out on 11 different grid sizes by initializing all flow variables in the interior of the pipe with zero and prescribing the fully-developed parabolic velocity solution as boundary condition at the inlet of the pipe. The computational time (CT) and memory allocation (MA) are recorded and averaged over 80 iterations. All simulations are conducted on a single 1.6 GHz 64 bit AMD Opteron processor with 2.0 GB RAM. The memory requirement for a given *r* is assessed based on the operating system requirements. Even though this metric does not provide an exact measure of the amount of allocated memory, it still provides a measure of the code footprint on the overall system.

The comparative performance of the SC and UC approaches is shown in Figure 7-2, expressed as the ratio of the SC computational time or memory allocation to that of the UC approach. The MA_{SC}/MA_{UC} and CT_{SC}/CT_{UC} ratios are greater than one for all tested configurations, demonstrating that the UC formulation requires a lower memory allocation and allows for faster simulations than the SC method even for *r* values as high as 0.7. More precisely, when $r = 0.7$, the computational time per iteration and the memory allocation are approximately equivalent for the two methods, with a slight advantage of the UC approach ($CT_{SC}/CT_{UC} = 1.09$ and $MA_{SC}/MA_{UC} = 1.24$). However, these ratios increase exponentially with decreasing *r*. When the number of active nodes represent only 5% of the embedding Cartesian grid (i.e. $r = 0.05$), the performance ratios are of $CT_{SC}/CT_{UC} = 5.97$ and $MA_{SC}/MA_{UC} = 9.87$, meaning that the SC approach is about 5 times more expensive and requires one order of magnitude more memory than

the UC method. The SC implementation is seen to be 10 and 20 times more expensive than the UC method for r = 0.025 and 0.012, respectively.

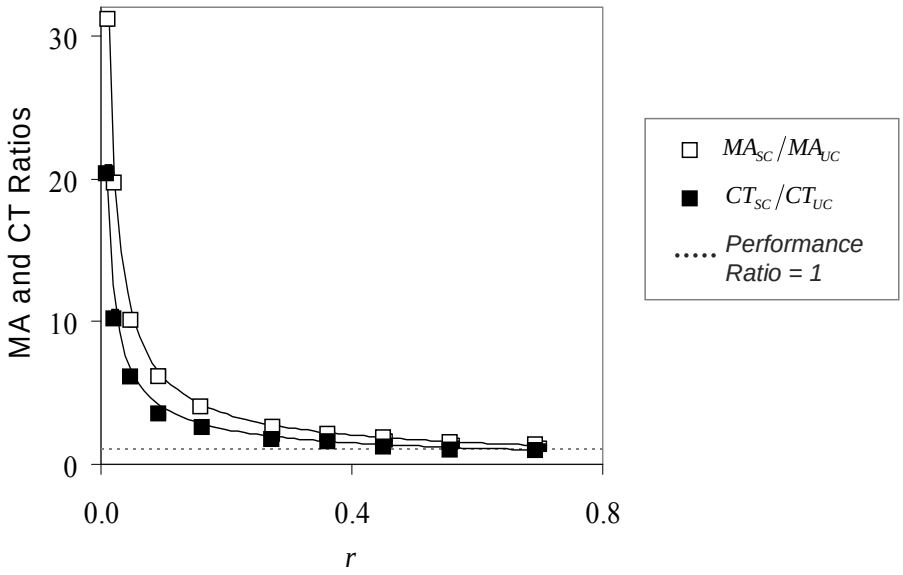

Figure 7-2: Comparison of the memory allocation (MA) and computational times (CT) of the structured Cartesian (SC) formulation vs. the unstructured formulations UC as a function of *r*. Numbers are expressed as the ratio of the SC quantity (either MA or CT) over the corresponding UC quantity.

As was discussed in the numerical methods (Chapter 6), the rapidly decreasing performance of the SC implementation as *r* decreases stems from the fact that, in that formulation, the *external nodes* are blanked out of the computation but are retained in the data structure. Accordingly, all variables are stored in arrays of dimension *IM*×*JM*×*KM* and an "*if*-statement" is required within each *do*-loop in order to blank out the *external nodes* from the simulation.

In the UC approach, on the other hand, memory allocation is optimized in that only the *active nodes* are retained in the data structure and all variables are stored in

arrays of dimension N_a. The price for this optimal allocation, however, is that the simple connectivity of the Cartesian grid is lost and additional data structures and thus additional memory space are required to explicitly store the connectivity information. Obviously, if all Cartesian grid nodes are *active* grid nodes (r = 1) the UC method requires more storage space than the SC approach. However, as $r \to 0$ the amount of extra memory required to store the connectivity information is quickly outweighed by that saved by eliminating from the data structure the unused *external nodes*. Furthermore, serial indexing of the fluid nodes, removes the need for an "*if* statement" in the *do*-loops. In counterpart, the connectivity of the grid is no longer implicit and every differencing operation requires looking up a connectivity matrix in order to identify the neighborhing nodes. As was seen in Figure 7-2, the cost of looking up the connectivity information only at the *fluid nodes* is outweighed by that of the "*if* statement" required for all nodes of the Cartesian grid, even for r as high as 0.7.

In summary, the numerical experiments reported in this section clearly show the superiority of the UC approaches over the SC implementation especially for small values of r. As we will subsequently show, complex cardiovascular anatomies often result in a grid structure with r as low as r = 0.05 (see Section 7.4 below). The results reported in this section showed that for such low percentage of *active* grid nodes the standard SC implementation of the method of Gilmanov and Sotiropoulos [164] would require approximately one order of magnitude more memory for storage and 5 times more computational time than the UC formulation. Clearly such excessive computational overhead renders the SC approach impractical to use especially when very fine grids are required within the flow domain to obtain accurate results.

7.2 Steady Flow in a 90° pipe bend

The geometry and flow conditions for this first case correspond to the experimental work of Bovendeerd et al. [175] who carried out experiments for steady fully-developed flow in a 90° curved pipe of diameter D and radius of curvature $3\times D$ (see Figure 7-3). The inlet and outlet sections are placed $3\times D$ upstream and downstream of the bent section, respectively. A fully-developed parabolic velocity profile with a Reynolds number of 700 (based on the mean inflow velocity and the pipe diameter) is prescribed at the inflow to match experimental conditions. The pipe surface is discretized with an unstructured triangular mesh (3,924 nodes) and immersed in rectangular Cartesian box of dimensions $6.6D\times 6.6D\times 1.1D$, which is discretized with a uniform and isotropic Cartesian grid. Simulations are carried out for two different mesh resolutions, which are summarized in Table 7-1. For both grids the dimensions of the Cartesian box remains fixed.

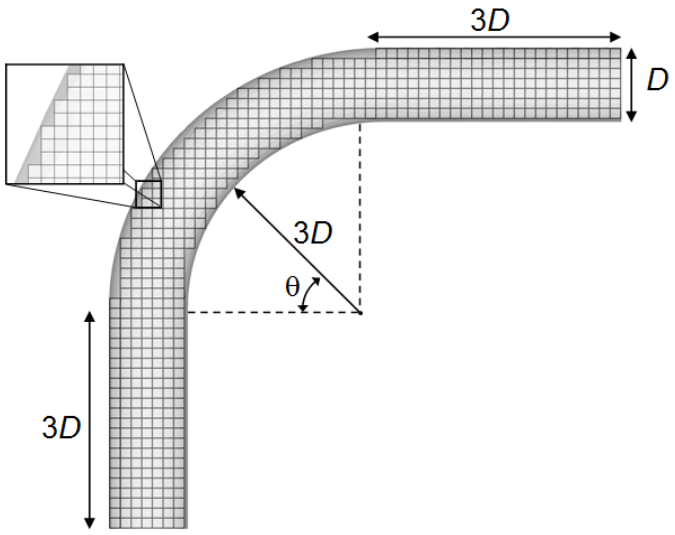

Figure 7-3**:** Dimensions and geometry of the 90° curved pipe. Θ denotes the angle between the inlet plane of the bend and a given cross-section in the bend. The zoomed-in region shows the layout of the unstructured Cartesian mesh.

Table 7-1**:** Mesh resolutions used for the 90º curved pipe (*D* is the pipe diameter).

.	h	$IM \times JM \times KM$	N_a	r
Mesh A1	0.03D	2,032,800	1,648,656	0.174
Mesh A2	0.02D	6,860,700	5,427,200	0.181

Steady-state streamwise velocity profiles on the symmetry plane of the pipe are compared with the laser Doppler velocimetry data from Bovendeerd et al. [175] at seven streamwise locations located at angles Θ = 0.0°, 4.6°, 11.7°, 23.4°, 39.8°, 58.5° and 81.9° in Figure 7-4 (see Figure 7-3 for definition of the angle Θ). Apart from a slight velocity overshoot for the peak velocity at the location Θ = 81.9°, the results obtained with both meshes A1 and A2 are in excellent agreement with each other and the experimental data.

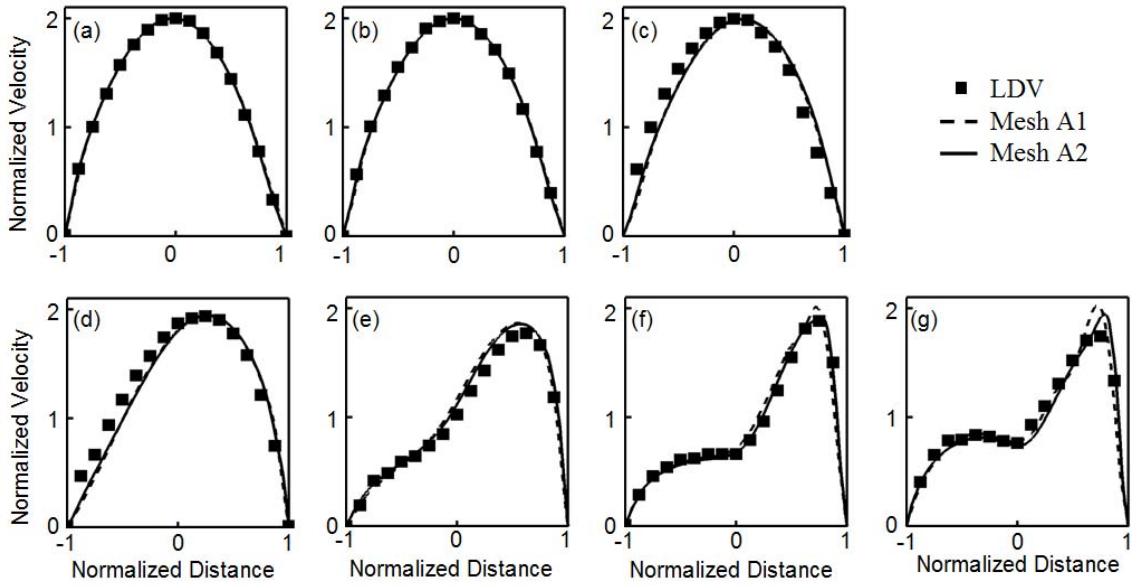

Figure 7-4**:** Comparison of measured and computed time steady-state velocity profiles at seven locations on the symmetry plane of the 90º curved pipe: from (a) Θ = 0, (b) Θ = 4.6, (c) Θ = 11.7, (d) Θ = 23.4, (e) Θ = 39.8, (f) Θ = 58.5 and (g) Θ = 81.9º, respectively. Velocities are normalized by the mean inflow velocity. Distances are normalized by *D/2*.

7.3 Flow in an idealized TCPC geometry

The second test-case is an idealized representation of a total cavopulmonary configuration and corresponds to the experimental study by Ensley *et al.* [176]. As shown in Figure 7-5, the geometry consists of four pipes of equal diameter *D=14mm*, representing the inferior and superior venae cavae (IVC and SVC, respectively) and the right and left pulmonary arteries (RPA and LPA). The axes of the IVC and SVC are offset by one pipe diameter. Entrance and exit lengths spanned 7.15*D* between the inlet or outlet boundaries and the closest pipe axis. The complete (no symmetry assumption is invoked) surface of the pipe junction geometry is discretized with an unstructured triangular grid (22,145 nodes) embedded in a rectangular Cartesian box of dimensions *16.5D×15.5D×1.1D*, which is discretized with a uniform and isotropic Cartesian mesh. Three different grid sizes are used ranging from 200,000 to 1.3 million *active* grid nodes, (see Table 7-2). All subsequent results are shown at the symmetry plane of the connection.

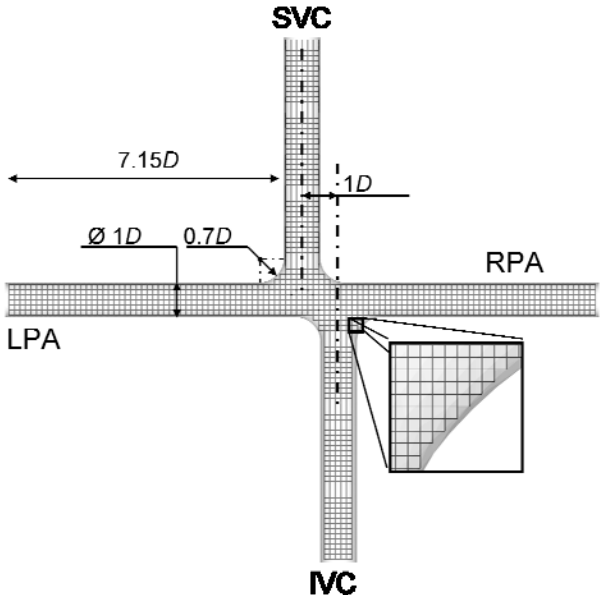

Figure 7-5**:** Geometry of the pipe junction geometry, which is an idealized representation of anatomic TCPC configurations.

Table 7-2**:** Mesh resolutions used for the pipe junction geometry (*D* is the pipe diameter).

	h	$IM \times JM \times KM$	N_a	$\frac{N_a}{IM \times JM \times KM}$
Mesh B1	0.05D	2,367,643	198,330	0.084
Mesh B2	0.03D	7,858,624	651,727	0.084
Mesh B3	0.025D	16,195,872	1,353,083	0.084

The experiments were conducted at 4 L/min, with 60% of the flow coming through the IVC, 40% through the SVC, and a 50/50 RPA/LPA mass flow ratio at the outlets. For the computations and in the subsequent results, all quantities are normalized by the pipe diameter *D* and the mean velocity at the IVC inlet. The corresponding Reynolds number is Re = 1040. Time-dependent calculations are carried out using a non-dimensional physical time step $\Delta t = 0.01$. Flat flow velocity profiles (plug flow) are prescribed at both inlets. Comparisons with the experimental measurements in the IVC 1.25*D* upstream of the junction region show that the calculated velocity profiles are in good overall agreement with the measurements, which supports the use of a plug velocity profile at the inlet sections.

As indicated in the vorticity snapshots shown in Figure 7-6 and Animation 7-1, the flow in the connection region is unsteady as it is characterized by weak, albeit persistent and sustainable over the entire simulation interval, unsteady fluctuations of the shear layers that emanate from the walls of two inlet pipes and collide in the junction region. The flow entering from the IVC is seen to impinge on the upper junction region where it extracts wall vorticity of opposite sign and interacts with vorticity from the SVC. After impinging on the wall, the IVC shear layer ("red" vorticity in Figure 7-6) bends to the left and curves downward to impinge onto the lower wall of the LPA where it

interacts with the negative vorticity coming from the wall of the SVC. The interaction of the two shear layers results in seemingly aperiodic vortex shedding events when shear layer vorticity is injected into the LPA. Since the experimental measurements reported only time-averaged results all subsequent presented comparisons between experiments and simulations are reported for time-averaged flow quantities.

As shown in Figure 7-7, the main flow features are captured on all three meshes used in the mesh refinement study. These flow features are identified with the letters A through D in Figure 7-7 as follows: (A) the flow separation at the junction region of the SVC; (B) the saddle of attachment at the upper wall of outlet 2 pipe due to the impingement of the IVC flow; (C) the stream from the IVC flow going around the central recirculation region and merging with the deflected SVC flow to form a strong shear layer; and (D) the recirculating flow region at the center of the junction region. The vorticity plots also shown in Figure 7-7 demonstrate that even though most features of the flow are adequately resolved even on the coarser mesh, the shear layers emanating from the IVC and SVC walls and their merging dynamics in the junction region do become sharper and somewhat more intense as the mesh is refined. Overall all three meshes, and especially the two finest meshes B2 and B3, yield results that are in good agreement with each other and the experimental measurements.

A characteristic of this test case compared to the 90 degree curved pipe reported earlier is that, here, only 8 to 9 percent of the total Cartesian grid nodes are *active* grid nodes. Based on numerical experiments comparing our code performance with the SC and UC implementation, conducting the same simulations with the SC formulation would have required about 6 to 7 times the allocated memory and 3 times the computational

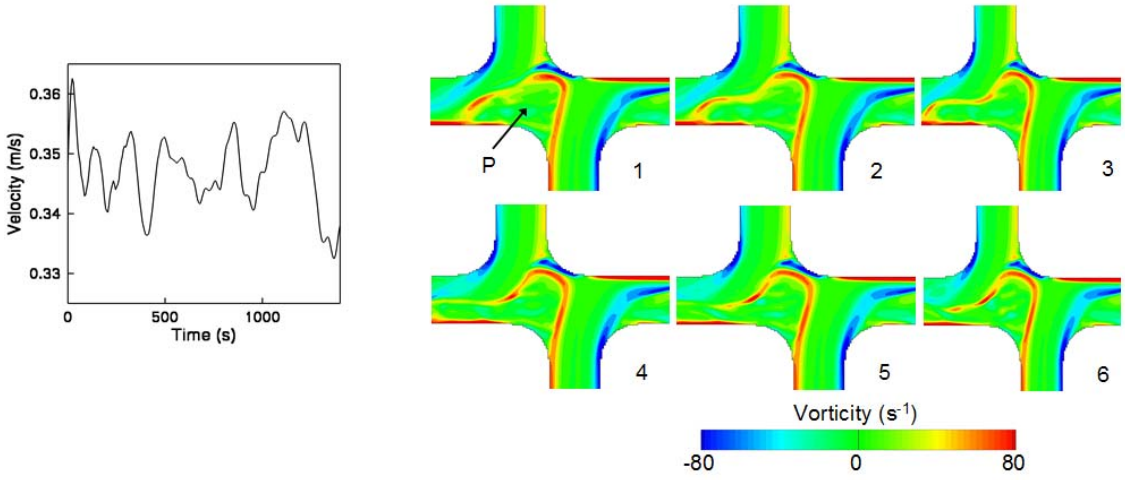

Figure 7-6**:** Time series on the symmetry plane of the idealized TCPC geometry obtained on grid B2. Left: Instantaneous U velocity at point P at the center of the connection. Right: Out of plane vorticity field at 6 instants in time.

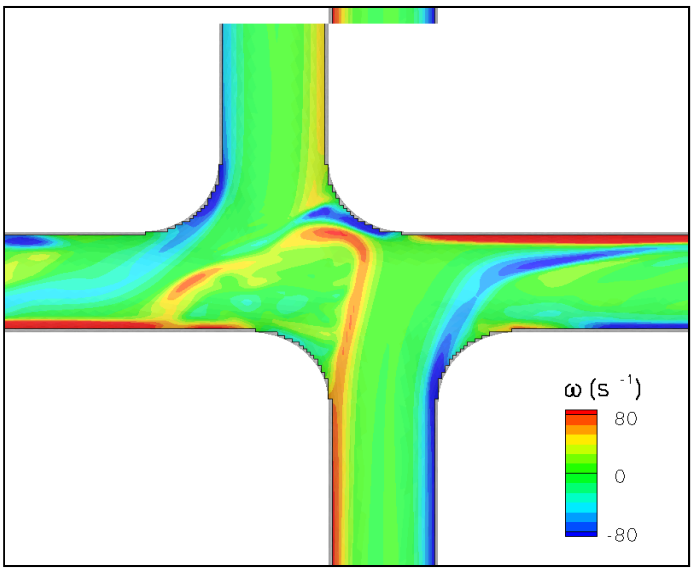

Animation 7-1: Out-of-plane vorticity field on the symmetry plane of the idealized TCPC geometry obtained on grid B2. Note the intermittent vortex shedding at the center of the connection.

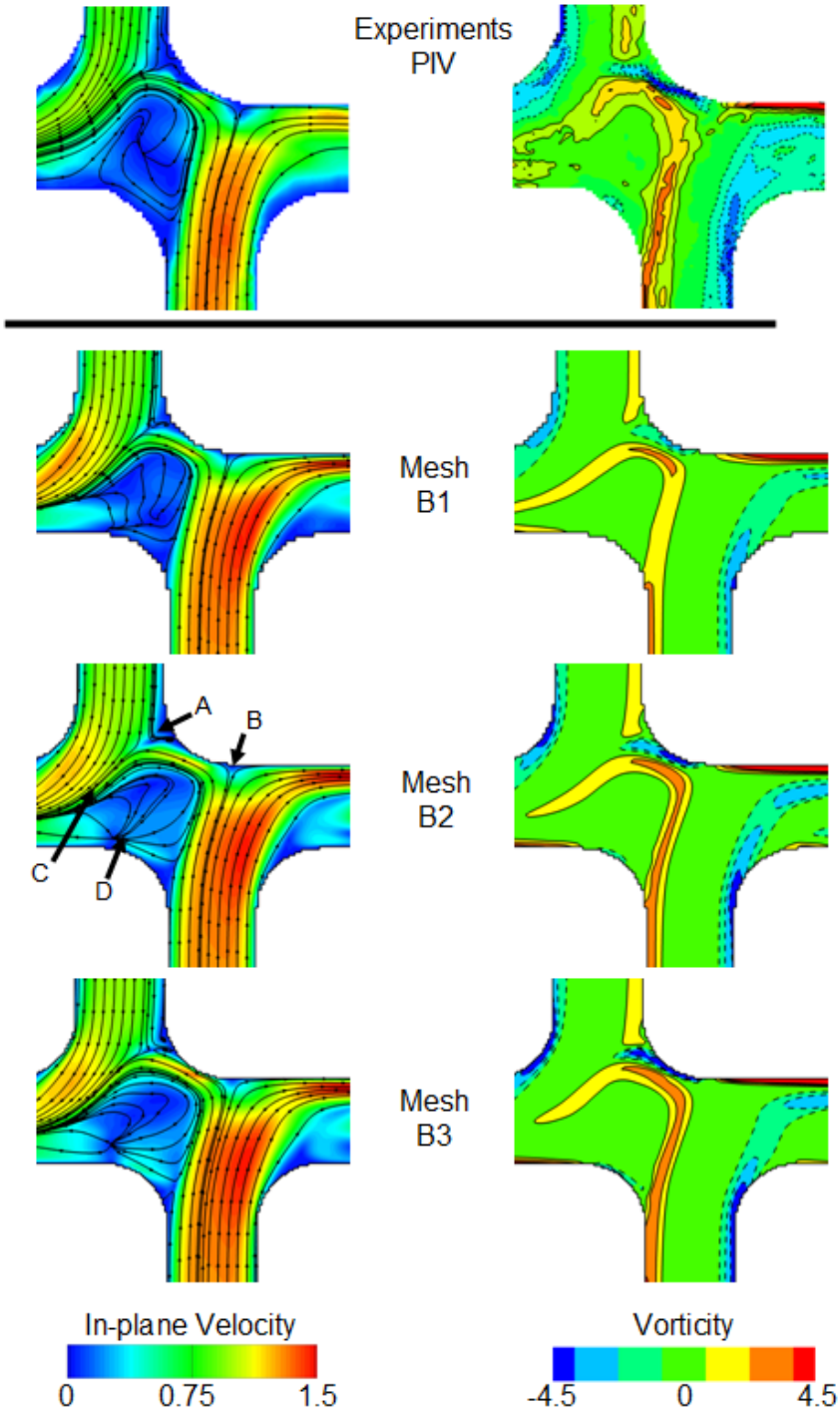

Figure 7-7**:** Comparison of the measured and computed time-averaged velocity (magnitude and streamlines) (Left) and vorticity (Right) fields in the symmetry plane of the pipe junction geometry.

time required by the UC approach. Furthermore, as was also the case for the curved pipe test-case (Sections 7.2), the size of the Cartesian grid required to achieve the *active* node spatial resolution of the two finest meshes, B2 and B3, is excessive especially for the finest mesh for which more than 16 million grid nodes are required.

7.4 Non-Pulsatile Flow in a Patient-Specific Intra-Atrial TCPC Anatomy

The last test-case reported in this section seeks to demonstrate the potential of the UC approach as a powerful tool to simulate complex anatomical configurations by considering flow through patient specific TCPC anatomies. The anatomy under consideration is an intra-atrial connection with a single SVC for which previous experimental studies revealed high levels of flow unsteadiness in the central connection region. This test-case is included here to demonstrate the complexity of the flow structures observed in *in vivo* anatomies and the level of mesh refinement required for obtaining grid insensitive results. The patient-specific geometry shown in Figure 7-8 was reconstructed from magnetic resonance images of a 13 year old single-ventricle patient. Details on the model generation and experimental study are provided by de Zélicourt *et al.* [177]. Inflow and outflow boundary conditions are prescribed in the calculations to match the experimental flow conditions [177] with a constant total volume flow rate of 4 L/min and mass flow splits of 60/40 between the IVC and SVC inflows and 50/50 between the LPA and RPA outflows. Plug (flat) flow profiles were prescribed at the IVC and SVC inflow planes for all subsequent results unless explicitly indicated otherwise. All quantities are normalized based on mean velocity and equivalent hydraulic diameter of the IVC. The corresponding Reynolds number is Re=294.

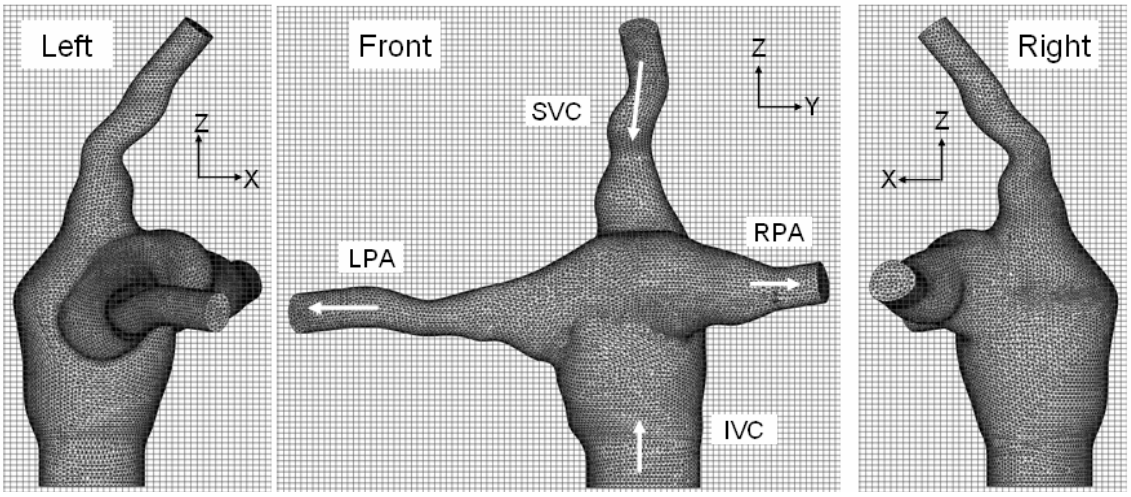

Figure 7-8**:** Patient-specific intra-atrial TCPC anatomy immersed in a Cartesian grid. The curvature of the vessels leads to a large number of unused *external cells*, and only 7% of the Cartesian grid cells are *active cells* and fall within the fluid domain. The arrows indicate the main flow directions in the various branches.

The computational domain is illustrated in Figure 7-8. The surface of the TCPC anatomy is immersed in a uniform and isotropic Cartesian grid of dimensions $2.5D_{IVC} \times 5.5D_{IVC} \times 5.0D_{IVC}$, where D_{IVC} is the equivalent hydraulic diameter of the IVC inlet cross-section. The TCPC surface is discretized with an unstructured triangular mesh with 15,110 nodes. Three different spatial resolutions are used to discretized the background Cartesian domain and carry out a systematic mesh refinement study. The coarsest mesh used in these simulations (Mesh C1 in Table 7-3) was set so that its spatial resolution ($h = 0.03D_{IVC}$) was equal to the spatial resolution of the experimental particle image velocimetry (PIV) data acquired by Zélicourt et al. [177]. Time-dependent calculations were carried out using a non-dimensional physical time step of $\Delta t = 0.005$. Running-averages of the velocity components converged after simulating about 200 units of non-dimensional physical time.

Table 7-3**:** Mesh resolutions used for the anatomical intra-atrial geometry (D_{IVC} is the equivalent hydraulic diameter of the IVC cross-section at the inflow)

	h	$IM \times JM \times KM$	N_a	r
Mesh C1	$0.03D_{IVC}$	3,029,400	219,030	0.072
Mesh C2	$0.02D_{IVC}$	10,032,624	740,103	0.074
Mesh C3	$0.016D_{IVC}$	17,116,140	1,260,841	0.074

In spite of the steady inflow conditions and flow rates well within the laminar regime, highly unsteady vortical motion were observed within the connection region. This unsteadiness is illustrated in Figure 7-9, which shows the velocity time series at a point in the SVC connection. It should be noted that such unsteadiness was observed in our simulations throughout the connection. The complex three-dimensional structure of the instantaneous flow in this region is further illustrated in Figure 7-10 and Animation 7-2, which visualizes instantaneous coherent structures using the *q*-criterion [178]. The unsteadiness seems to originate at the unstable saddle point where the IVC and SVC streams collide and manifests itself as a seemingly chaotic meandering and flapping of the flow. Even though *in vitro* experiments in the identical TCPC configuration reported only time-averaged in-plane velocity measurements, the flow unsteadiness was documented using dye flow visualization [177]. These experiments revealed very complex and highly unsteady transport of the dye in the connection region characterized by intense stretching and folding processes, which are the hallmarks of chaotic transport and mixing.

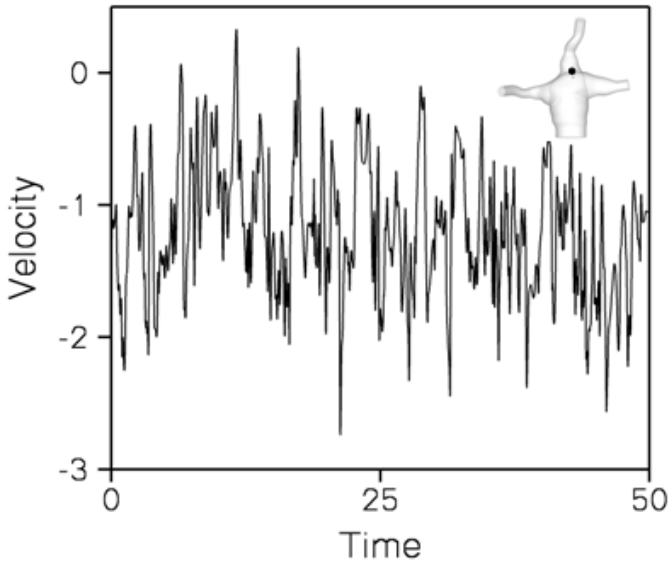

Figure 7-9**:** Calculated time series of the U velocity component at the point of the anatomical intra-atrial geometry marked with a dot in the top right inset.

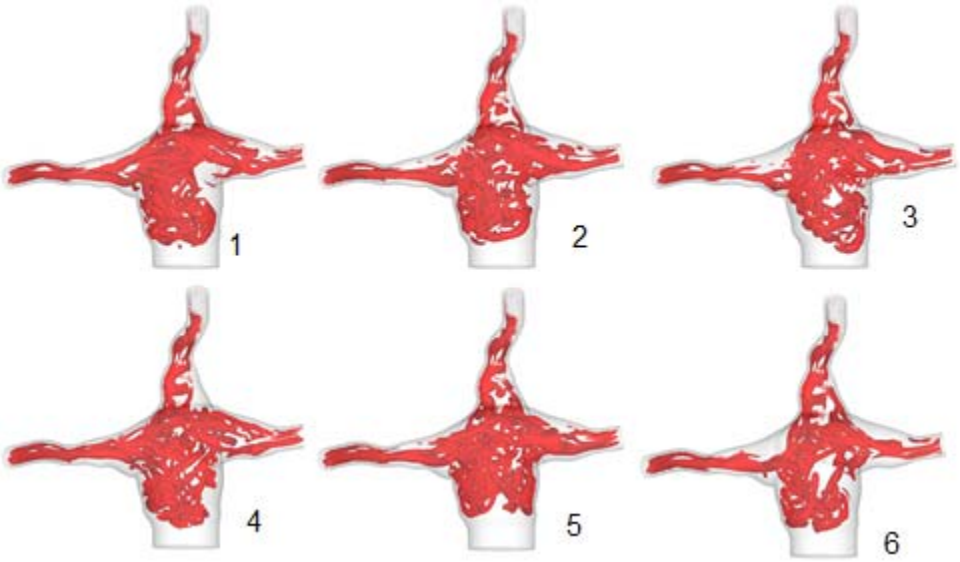

Figure 7-10**:** Instantaneous coherent structures in the connection region of the anatomical intra-atrial geometry visualized with q-criterion for 6 instants in time separated by 1.2 non-dimensional time units.

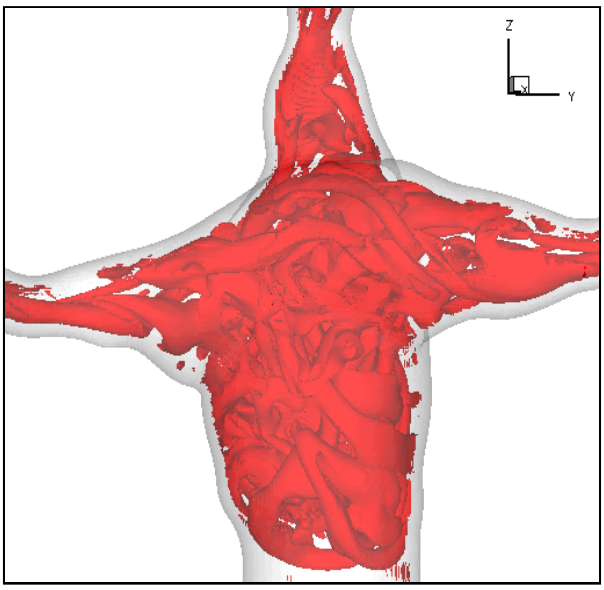

Animation 7-2: Instantaneous coherent structures in the connection region of the anatomical intra-atrial geometry visualized with the q-criterion.

From a clinical standpoint, the intense flow unsteadiness revealed by both simulations and experiments is extremely important as it results in regions of high velocity gradients and increased energy dissipation within the TCPC region. This in turn increases the workload of the heart and could have serious long term effects on the patient's health and quality of life. As such, surgeons strive to design the TCPC connection such that flow unsteadiness and energy dissipation rates are minimized. Clearly, being able to systematically refine the mesh for such complex unsteady flow is a critical prerequisite for establishing the potential of any CFD algorithm as a reliable surgical planning and optimization tool.

Figure 7-12 to Figure 7-13 show the results of the mesh refinement study. Figure 7-11 displays the velocity and vorticity fields for a plane taken across the connection

perpendicular to the X-axis. As can be observed from Figure 7-11, essentially all the dominant flow features (identified with letters A through E) on this plane are captured on all three meshes. These include the low velocity region with its small recirculation and flow separation patterns at the opening of the SVC (regions A and B) and the double vortex structure at the center of the connection (zones D and E), both of which were captured on all three meshes. The location of the vortex centers (points D and E) shifts between the meshes C1 and C2 but remains exactly the same between the meshes C2 and C3. Similarly, the low velocity recirculation points A and B and the shear layer between the incoming streams (zone C) are present in Mesh C1 but it is only on meshes C2 and C3 that they converge to the same location. The overall features of the vorticity field are also captured even on the coarsest mesh C1 but significant quantitative discrepancies become evident as the mesh is refined. Changes are mainly dictated by the refinement of the wall boundary layers such as in regions F through I in Figure 7-11 or along the LPA and RPA vessel walls in Figure 7-12. The structure and intensity of the boundary layers do not change significantly on meshes C2 and C3. Even though the vorticity iso-contours obtained with those two finer meshes do not exactly coincide, peak and low vorticity magnitudes are found in identical regions as shown in Figure 7-11 and Figure 7-12. A more quantitative comparison among the solutions on the different meshes is provided in Figure 7-13, which shows the profiles of the through-plane velocity magnitude along the two sections indicated in the figure. The profiles obtained with meshes C2 and C3 are essentially indistinguishable. The results shown in Figure 7-11 to Figure 7-13 collectively suggest that, even though the solution on the finest mesh may not be grid independent in the strict sense, it is certainly insensitive to further grid refinement insofar as all major

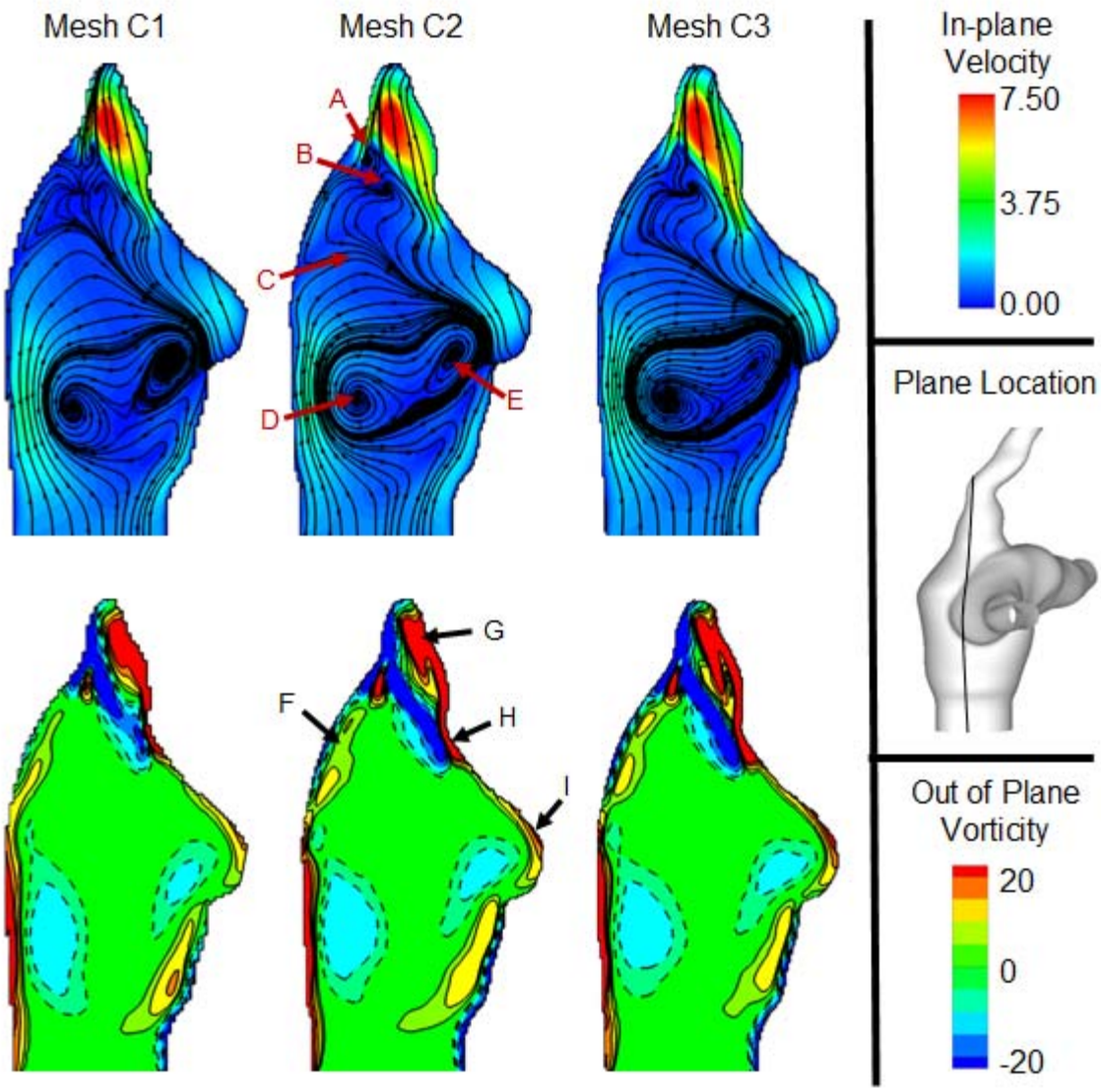

Figure 7-11**:** Comparison of the time-averaged velocity magnitude and in-plane streamlines (top row) and out-of-plane vorticity (bottom row) fields obtained with the three different mesh refinements used for the anatomical intra-atrial geometry.

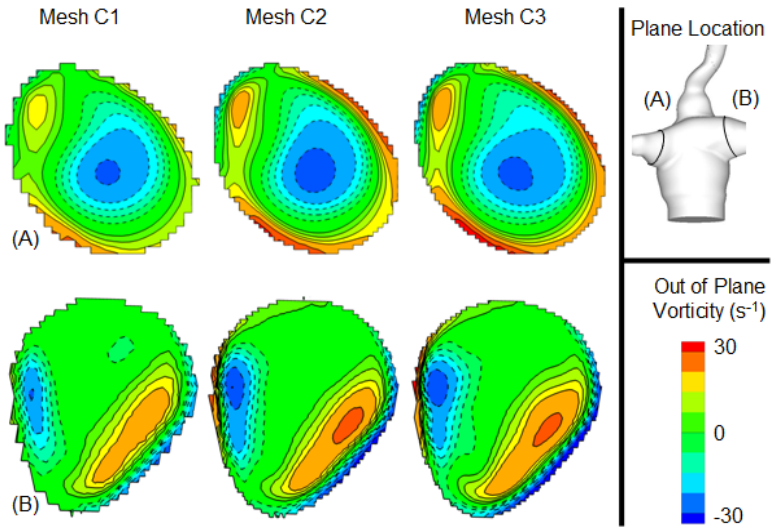

Figure 7-12**:** Comparison of the time-averaged out-of-plane vorticity fields obtained with the three different mesh refinements in cross-sections of the left (section A, top row) and right (section B, bottom row) outflow tracks of the anatomical intra-atrial geometry.

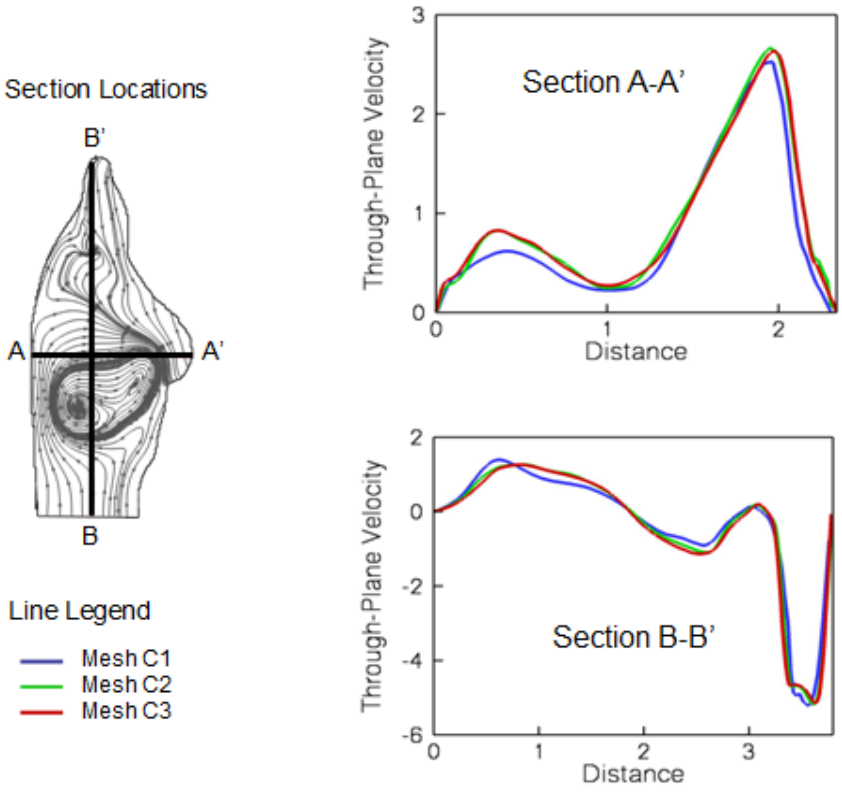

Figure 7-13**:** Comparison of the time-averaged through-plane velocity profiles on the three successively finer meshes for the anatomical TCPC geometry on two cross-section of the mid-plane. The horizontal axis is the distance along segment AA′ (BB′) measured from point A (B).

features of the flow are concerned. We believe that reaching strictly grid independent solutions for such a complex flow would require increasing the resolution of the boundary layers, which could be accomplished by combining the UC method with an local mesh refinement strategy.

Finally, Figure 7-14 compares measured and calculated time-averaged velocity magnitude contours and streamlines at the previously defined plane through the TCPC region. Though the experimental set-up was designed so as to try and ensure a fully-developed profile at the inflows, [177], the precise state of the flow at the entrance of the IVC and SVC was not documented. To explore the sensitivity of the simulated flow patterns to the state of the incoming boundary layers, we carried out three simulations using different sets of inflow velocity profiles (see Figure 7-14) including combinations of fully developed and plug inflow velocity profiles for the SVC and IVC. Due to the smaller dimensions and more tortuous configuration of the SVC when compared to the IVC, varying the SVC inflow profile only induced minor variations in the flow fields, whereas varying the IVC inflow profile had a drastic effect on the overall flow structures. The results obtained using a fully-developed and a plug velocity profiles at the IVC and SVC, respectively, are found to be in good overall agreement with the measurements especially in light of the fact that the uncertainties regarding the exact state of the inflow velocity profiles cannot be conclusively resolved from the available experimental data.

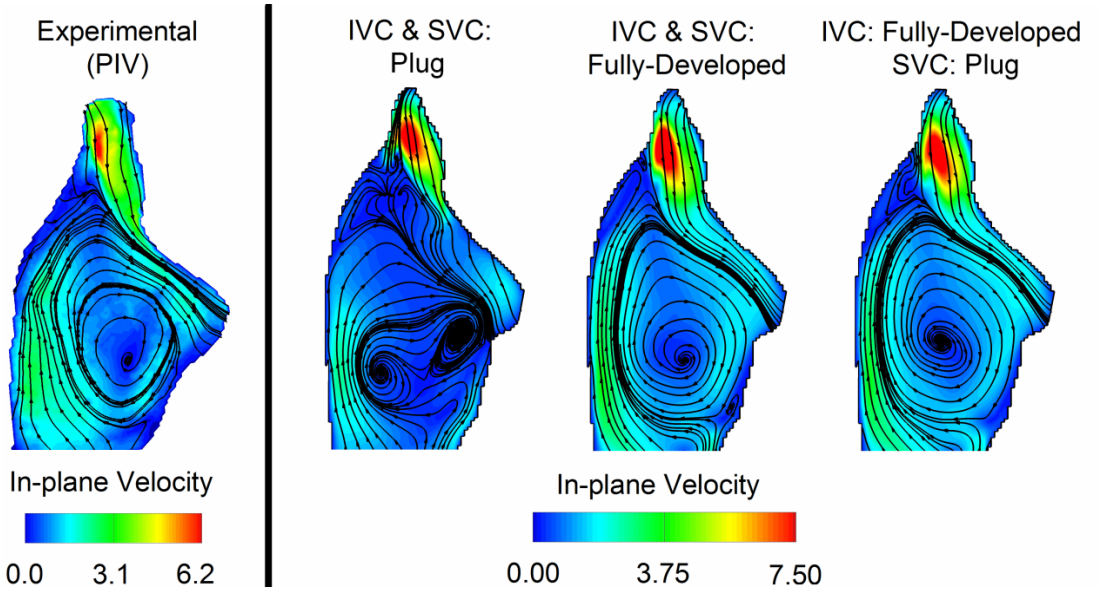

Figure 7-14**:** Comparison of the time-averaged experimental and calculated velocity magnitude and in-plane streamlines for the same plane of the anatomical intra-atrial geometry as in Figure 13. All numerical results are obtained on Mesh C1 using three scenarios for the IVC and SVC inflow boundary conditions (fully developed and plug velocity profile combinations).

7.5 Conclusion

The results presented in this chapter demonstrate the robustness and accuracy of our flow solver implementation, even for cases as complex as the reported *in vivo* anatomy, which featured complex dynamics, including regions of transition to turbulence and re-laminarization. In an era when computational simulations for clinical applications are becoming widespread, these results underscore the need for careful numerical simulations on fine computational meshes in order to properly capture all dynamic features of the *in vivo* flow structures. IB methods are inherently suited to tackle the geometrical complexity of *in vivo* anatomies. However, the fact that often in internal flow

applications involving complex, multi-connected geometries only a small fraction of the embedding Cartesian grid is located in the interior of the flow domain (typically between 5 – 10 percent) renders the use of classical structured IB methods impractical for cardiovascular applications. Any attempt to carry out grid refinement studies for such configurations using standard structured Cartesian approaches would quickly lead to excessively high memory and computational time requirements. The proposed unstructured immersed-boundary paradigm effectively alleviates this difficulty and strikes a balance between computational efficiency and memory requirements.

CHAPTER 8

PULSATILE TCPC SIMULATIONS

In this chapter, we apply the computational fluid dynamics (CFD) solver developed and validated in the previous chapters to investigate the impact of pulsatility on the hemodynamics and efficiency metrics of the total cavopulmonary connection (TCPC). Four cases are considered herein: first, the theoretical scenario of an idealized TCPC geometry subjected to sinusoidal inlet flow waveforms; then, the patient-specific pulsatile TCPC hemodynamics of three patients having each undergone a different TCPC procedure. Each test-case is investigated under both pulsatile conditions and non-pulsatile mean flow conditions. Streamtrace and particle tracking animations are provided for each one of the four cases to best visualize the pulsatile dynamics and are included as an addendum to this thesis. Comparison of the pulsatile and non-pulsatile results for the same patient will demonstrate whether pulsatility has strong impact on the clinical end-points for that patient, whereas the comparison across the three different patients will highlight whether some procedures are more sensitive to pulsatility than others. The chapter closes with a summary of the main findings.

8.1 Study Objective and Parameters of Interest

The objective of this study is to gain insights into the pulsatile *in vivo* TCPC hemodynamics, assess whether neglecting pulsatility affects the predicted performance ranking of different options, and if so determine whether pulsatility should be accounted

for in all options or only under specific conditions. To this end, we first investigate the impact of flow pulsatility in a carefully controlled idealized TCPC configuration and in three patient-specific scenarios. The patients were selected from the Georgia Tech Fontan database of magnetic resonance images (MRI) based on the availability of anatomical reconstruction, inflow/outflow flow curves, and 3D *in vivo* flow reconstruction [80]. These three cases were further chosen to constitute a representative sample of the geometrical and flow configurations observed across the database. The first two patients have a normal vascular configuration, with an inferior vena cava (IVC) and single superior vena cava (SVC), and similar pulsatility levels, but feature two different types of TCPC configurations, namely an extra-cardiac TCPC for the first patient and an intra-atrial TCPC for the second. The third patient features a highly abnormal systemic venous return with an interrupted IVC and persistent left superior vena cava (LSVC), and is here studied as a representative example of the upper range of geometrical complexity and flow pulsatility levels that may be expected in the *in vivo* TCPC configurations.

For all four case-studies, pulsatile CFD simulations are conducted using the experimental or patient-specific geometries and flow curves, with rigid vessel boundaries. In addition, in order to quantify the effect of pulsatility on the TCPC efficiency, each pulsatile simulation is accompanied by a non-pulsatile counter-part, conducted using the same geometry but with the mean vessel flow rate rather than the pulsatile flow curves. The relative impact of flow pulsatility is assessed by comparing the flow structures and efficiency metrics predicted by the non-pulsatile simulations to those obtained by averaging the pulsatile results over multiple cardiac cycles and to the departure of the instantaneous pulsatile data points from their time-averaged value.

Efficiency metrics of interest are the pressure drops and power losses across the connection, the hepatic flow distribution and the particle residence times. Pressure drops and power losses constitute surrogate measures for the workload imposed on the single ventricle and the pressure build-up in the gastro-intestinal track. Hepatic flow distribution to the two lungs is taken as a surrogate measure for the risk of developing pulmonary artero-venous malformations (PAVMs), which have been correlated with a low supply in humoral hepatic factors[67]. Finally, particle residence time provides a quantitative measure for the differences in the pulsatile and non-pulsatile particle pathways, as well as an indicator for the risk of thrombus formation.

Each case study follows the same structure: first, we describe the experimental or *in vivo* geometry and flows and the numerical set-up; next, we compare the pulsatile CFD hemodynamics to the experimental or *in vivo* measurements, as well as to their non-pulsatile CFD counter-part, followed by a quantitative comparison of the pressure drop and power loss levels; finally, we perform a particle tracking analysis to visualize the pathways followed by blood borne particles in the pulsatile environment and quantify the hepatic flow distribution and particle residence times.

8.2 Idealized TCPC

The first test-case is an idealized TCPC representation and corresponds to the experimental study conducted in our laboratory by Christopher Haggerty and Jessica Kanter [179]. This test-case was retained to assess the impact of flow pulsatility in a carefully controlled environment and further assess the accuracy of our pulsatile simulations in a problem representative of the TCPC flows.

8.2.1 Experimental Set-Up

As shown in Figure 7-5, the geometry consists of four pipes of equal diameter *D*=14mm, representing the inferior and superior venae cavae (IVC and SVC, respectively) and the right and left pulmonary arteries (RPA and LPA). The axes of the IVC and SVC are offset by 21mm.

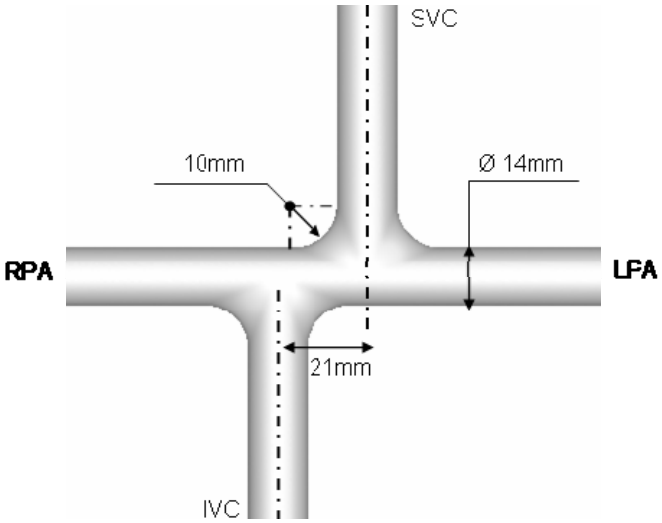

Figure 8-1**:** Geometry of the pipe junction geometry, which is an idealized representation of anatomic TCPC configurations.

The experimental pulsatile flow waveforms are shown with full symbols in Figure 8-2. A steady submersible pump and programmable piston pump were used in conjunction to produce a mean flow rate superimposed with sinusoidal oscillations. Flow rates were measured in the IVC, SVC and RPA at 500Hz. The period of the oscillations was 860 ms, which is equivalent to a heart rate of 70 beats per minute. The IVC flow rate, $Q_{IVC}^{\exp}$, ranged from 1.88 L/min to 3.38 L/min with a mean of 2.66 L/min. The SVC

flow rate, $Q_{SVC}^{\exp}$, ranged from 0.93 L/min to 1.76 L/min with a mean of 1.34 L/min. The pulsatility index (PI), defined as:

$$PI = \frac{Q_{\max} - Q_{\min}}{2\overline{Q}} \tag{8-1}$$

where $Q_{\max}, Q_{\min}, \overline{Q}$ are the maximum, minimum and average vessel flow rate, respectively, was 28.3% for the IVC and 31.1% for the SVC. Outflow conditions were set using ball valves to impose a constant downstream resistance. 52.5% $\pm$ 4.4% of the total flow rate exited through the RPA and 47.5% $\pm$ 4.4% through the LPA.

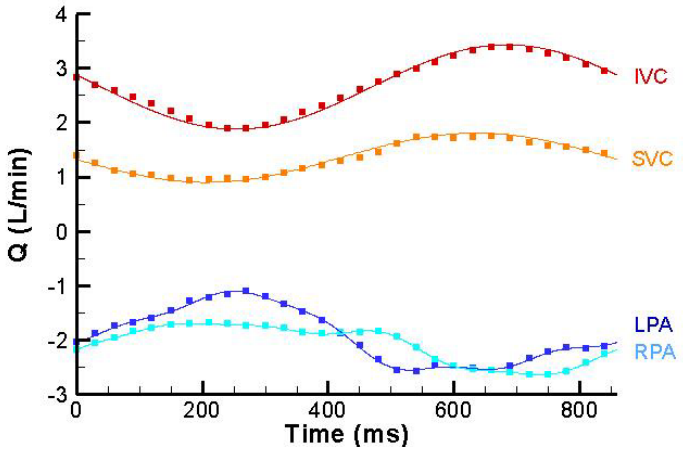

Figure 8-2: Experimental (full symbols) and numerical (continuous lines) flow curves. To ease the comparison, the experimental flow measurements are down-sampled to a frequency of 33.3Hz.

8.2.2 Numerical Set-Up

The characteristic length and velocity scales used to non-dimensionalize the problem are the pipe diameter, *D*, and the time- and space-averaged velocity across the IVC inlet cross-section, $\overline{U}_{IVC}$. The corresponding mean IVC Reynolds number is Re = 1155. The Womersley number for the problem is $\alpha = 10.1$. The flow wave-forms at the

IVC and SVC inlets are specified from the Womersley solution of a fully developed pulsatile flow within a circular pipe [180]:

$$u_{inlet}(r,t) = K_1 \cdot 2\left[1-\left(\frac{r}{R}\right)^2\right] - i\frac{K_2}{\omega}e^{i\omega t}\left[1-\frac{J_0\left(r\sqrt{\frac{-i\omega}{\nu}}\right)}{J_0\left(R\sqrt{\frac{-i\omega}{\nu}}\right)}\right] \tag{8-2}$$

where J_0 denotes the Bessel function of the first kind and order zero, r is the radial distance from the center of the pipe, t is the instant in time, $R = D/2$ is the radius of the pipe, ω represents the angular frequency of the flow oscillation, which is 7.3 rad/s, and $\nu = 3.5 \cdot 10^{-6}$ m^2/s is the fluid viscosity. In order to generate the sinusoidal flow waveform that varies in accordance with the experiments, the constant K_1 and K_2 are set to K_1=1 and K_2=0.125 for the IVC, and K_1=0.51 and K_2=0.073 for the SVC. We use Matlab 7.4 (The MathWorks Inc., Natick, MA, USA) to solve Equation 7-2 and the resulting solutions are stored and fed into the flow solver to specify the time-varying inlet velocity profile. The outflow conditions are prescribed using the time-varying experimental global flow distributions to the LPA and RPA (GFD_{RPA} and GFD_{LPA}), defined as:

$$GFD_{RPA}(t) = \frac{Q_{RPA}^{\exp}(t)}{Q_{IVC}^{\exp}(t) + Q_{SVC}^{\exp}(t)} \tag{8-3}$$

$$GFD_{LPA}(t) = 1 - GFD_{RPA}(t) \tag{8-4}$$

where $Q_{IVC}^{\exp}$, $Q_{SVC}^{\exp}$ and $Q_{RPA}^{\exp}$ are the instantaneous experimental flow rates through the IVC, SVC and RPA, respectively. The so-computed inflow and outflow waveforms are shown by the continuous lines in Figure 8-2 and are in good overall agreement with the experimental flow conditions.

The complete (no symmetry assumption is invoked) surface of the pipe junction geometry is discretized with an unstructured triangular grid (22,145 nodes) embedded in a rectangular Cartesian box of dimensions *16.5D×15.5D×1.1D*, which is discretized with a uniform and isotropic Cartesian mesh. The Cartesian grid resolution is set to h=0.3D, which was shown to appropriately resolve all vortical structures in the mesh sensitivity study conducted in Section 6.4. Each pulsatile flow cycle is divided into 2000 time steps, corresponding to a non-dimensional time step dT = 0.0089.

In order to quantitatively assess the impact of pulsatility on the retained efficiency metrics, namely power losses and hepatic flow distribution, non-pulsatile flow simulations are conducted as a control. These simulations are carried using the same spatial and temporal resolution as the pulsatile simulations, h=0.3D and dT = 0.0089, respectively. Inflow and outflow conditions are set to match the experimental flow rates averaged over the cardiac cycle, with $Q_{IVC} = 2.66\,\text{L/min}$, $Q_{SVC} = 1.34\,\text{L/min}$, $GFD_{RPA} = 47.5\%$ and $GFD_{LPA} = 52.5\%$. The mean IVC Reynolds number for the non-pulsatile problem is the same as in the pulsatile simulations, namely Re=1155. Parabolic fully-developed velocity profiles are prescribed at both IVC and SVC inlets, using the non-fluctuating part of Equation 7-2 as follows:

$$u_{inlet}(r) = K_1 \cdot 2\left[1 - \left(\frac{r}{R}\right)^2\right] \tag{8-5}$$

8.2.3 Pulsatile Flow Fields

The experimental pulsatile flow fields in the symmetry plane of the idealized TCPC were measured by particle image velocimetry (PIV) at 10 evenly spaced time-

phases across the cardiac cycle, seven of which are shown in Figure 8-3. Instantaneous CFD flow fields for the same seven instants in time are shown in Figure 8-4 (and animated in Animation 8-1), together with the time-averaged pulsatile flow and the non-pulsatile results. To better visualize the experimental flow structures, the color-scale used to display the in-plane velocity magnitude in Figure 8-3 is optimized for each time-phase, while the velocity vectors are shown using the same scaling factors for all time-phases thus providing an easy comparison of the relative velocity magnitudes. It may be noted that the experimental velocity magnitudes in phases P3 and P5 of Figure 8-3 are abnormally lower than in other phases. This is best illustrated by noting that the velocity scale used in P5 is about half of that used in P1 despite identical inlet flow rates. The discrepancy in the measured magnitudes might be attributed to an inadequate optimization of the imaging frequency, but should not alter the captured flow structures, which will be the focus of our discussion.

Similar flow structures are observed in both the PIV and CFD flow fields. In the early acceleration phase (P5 and P7), the IVC flow is directed almost exclusively towards the RPA. This is due to the fact that in these phases, the RPA flow rate exceeds that of the LPA. The LPA and RPA flow curves cross-over at phase P5 and the IVC flow is seen to progressively switch to a "vertical" orientation in the late acceleration phase (P8) and maintain that orientation throughout the peak and deceleration (phases P9 to P3). In these phases, the IVC flow hits the superior aspect of the RPA and a portion of the IVC stream splits towards the left, and recirculates around the central connection region into the LPA (see CFD results for phases P9 to P3 in Figure 8-4).

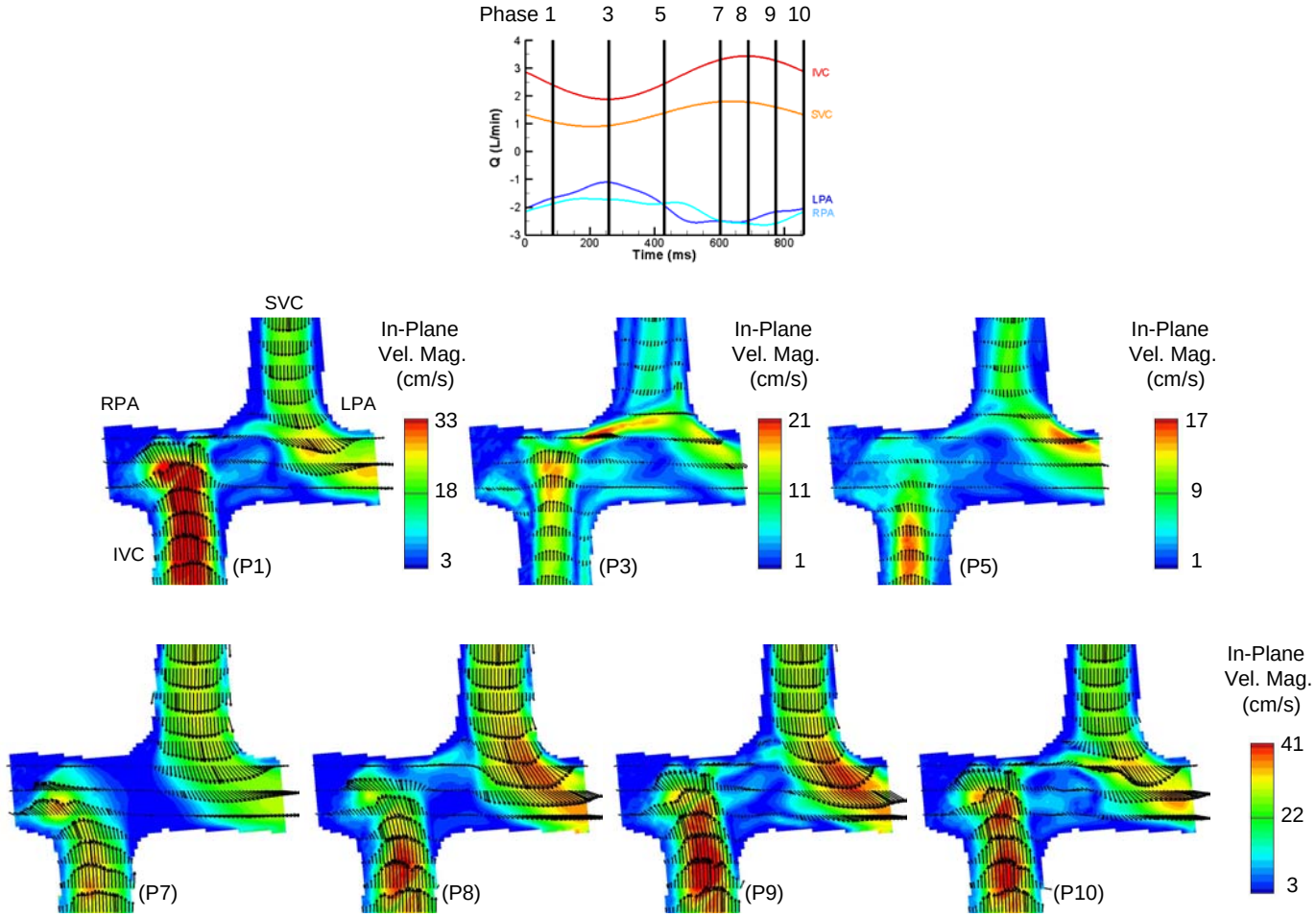

Figure 8-3: Experimental pulsatile velocity fields as measured by particle image velocimetry (PIV) on the central plane of the idealized TCPC connection. The color-contours display the in-plane velocity magnitude, with a color-scale optimized for each of the displayed time phases. The velocity vectors (in black) maintain the same scaling factors for all time phases.

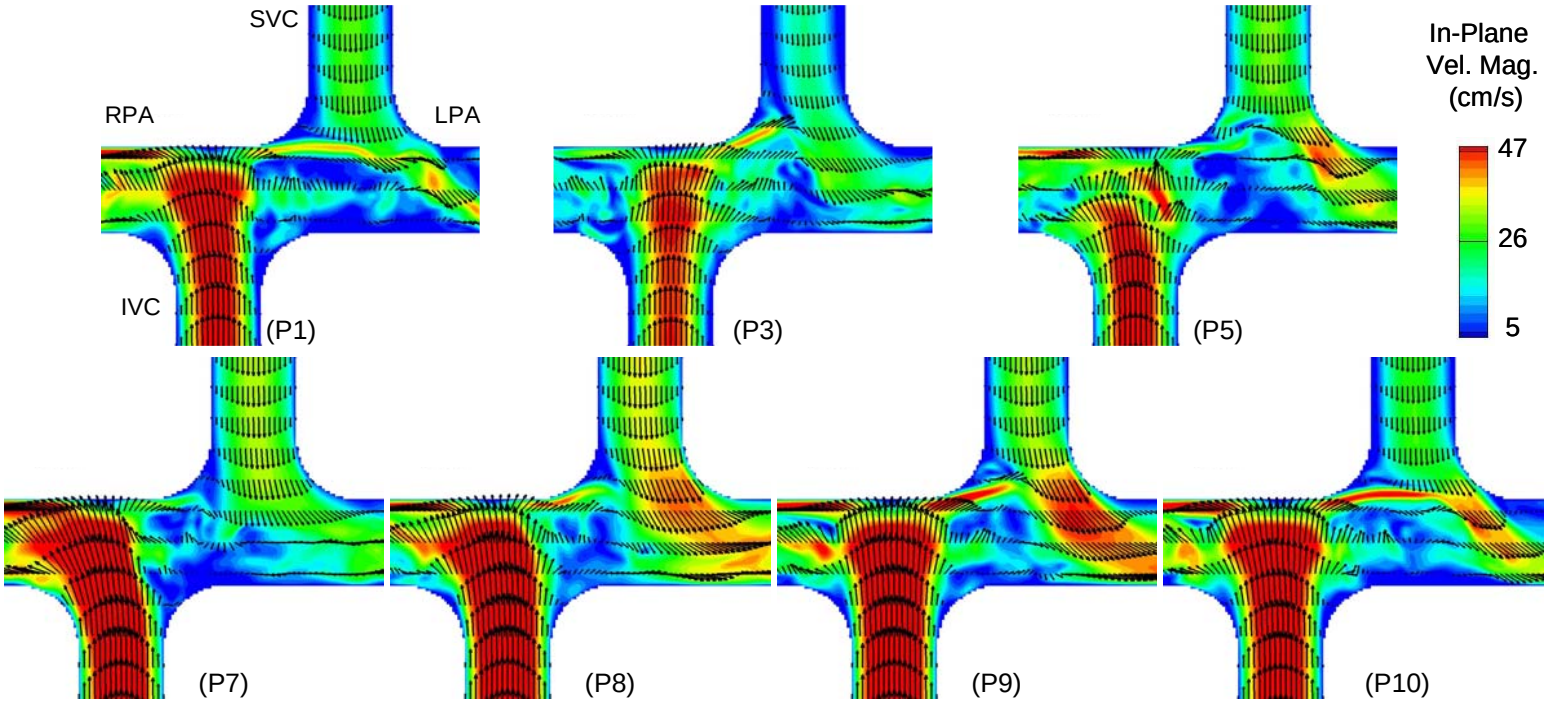

Figure 8-4: Pulsatile CFD velocity fields on the symmetry plane of the idealized TCPC connection. The color-contours display the in-plane velocity magnitude, while the flow structures are illustrated by the in plane velocity vectors (in black). See Animation 8-1 for a dynamic visualization of the displayed flow structures.

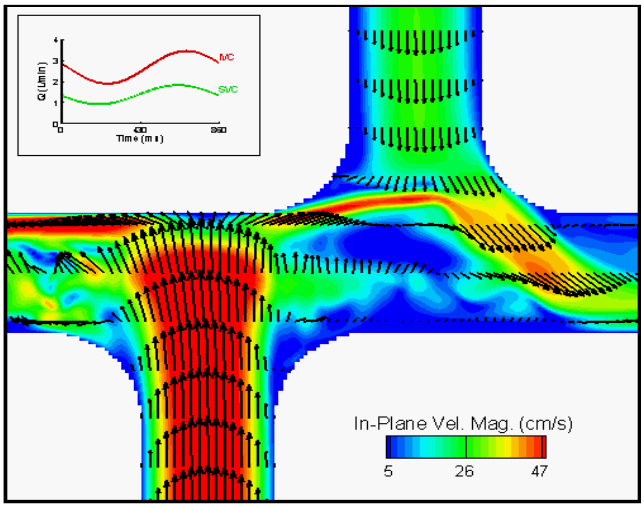

Animation 8-1: Pulsatile CFD velocity fields on the symmetry plane of the idealized TCPC connection. The color-contours display the in-plane velocity magnitude, while the flow structures are illustrated by the in plane velocity vectors (in black).

The SVC flow remains exclusively directed to the LPA throughout all time phases, turning towards the left branch directly upon entrance in the central connection region. The SVC velocity magnitude progressively increases from time-phase P3 to P9, in accordance with the measured SVC flow rate. The peak SVC velocities are systematically noted just downstream of the connection site, where the SVC flow accelerates and turns into the LPA. In phase P5, the SVC stream is confined in the left corner of the SVC anastomosis, resulting in a strong transient flow acceleration, which disappears in phase P7 as the SVC jet becomes larger with lower velocity values than in P5. The SVC velocities then increase again in phases P8 and P9 as the SVC flow rate reaches its peak. The SVC flow deceleration gives rise to complex unstable flow structures in phase P1, and local flow reversal in phase P3. Flow reversal is apparent along the right aspect of the SVC wall in the CFD results and on both the left and right side of the SVC in the PIV results. Such flow reversal in the vicinity of the vessel walls is

consistent with the flow structures typically observed in a Womersley pipe flows. Flow reversal on the right side of the SVC is further enhanced by the competition with the fast stream of IVC flow that recirculates around the center of the connection.

The center of the connection is characterized by low velocities (blue and light green) and highly unsteady flow structures. In phases P7 to P9, where the flow acceleration leads to two stable SVC and IVC streams oriented towards the closest PA, this low flow region is confined to the area lying between the two vessels. During deceleration, on the other hand, the low flow region progressively increases, extending further below the SVC anastomosis site. It appears to be the largest in phase P3 in the experimental PIV measurements and in phase P1 in the CFD flow fields. The complexity of the dynamics at the center of the connection is best visualized with the vorticity contours shown in Figure 8-5 and Animation 8-2. The portion of the IVC that splits towards the LPA leads to the formation of a strong narrow shear layer that interacts with the "red" vorticity from the SVC, with an intermittent vortex-shedding into the LPA. The center of the connection is characterized by number of small, transient and apparently random eddies.

Overall, the computed pulsatile velocity fields are in good agreement with the experimental observations. Differences in the reported magnitudes are mostly believed to originate from an erroneous scaling of the measured PIV displacements. Local differences in the dynamics of the center of the connection mostly stem from the fact that this region is prone to high level of non-periodic unsteadiness. These transient unsteady structures are apparent in the instantaneous CFD flow fields but smoothed out in the PIV measurements, which represent the time-bin averages over multiple cardiac cycles.

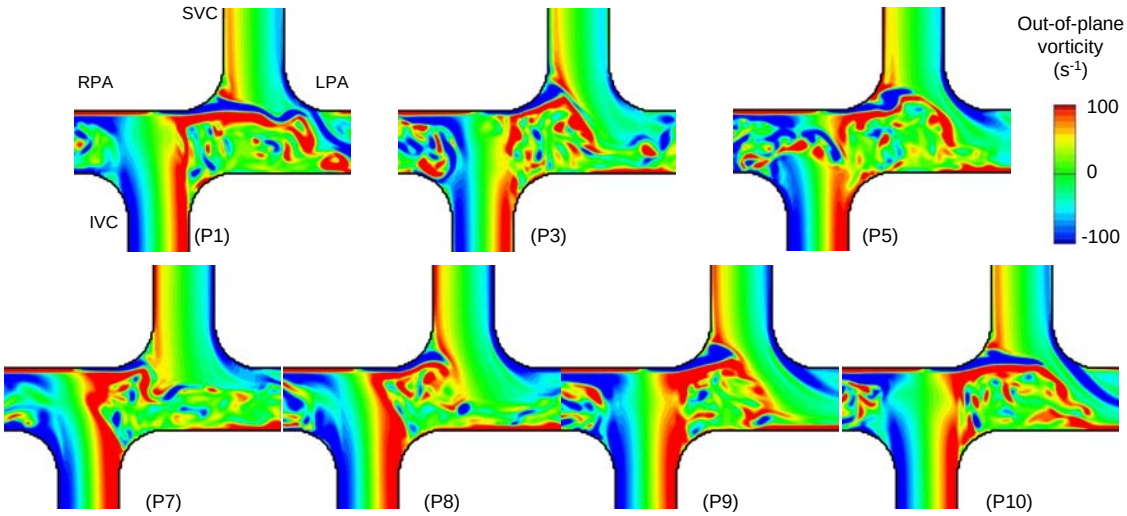

Figure 8-5: CFD vorticity fields on the symmetry plane of the idealized TCPC connection (see Animation 8-2 for the corresponding dynamic visualization). The instantaneous vorticity plots correspond to the same seven instants in time as in Figure 8-4.

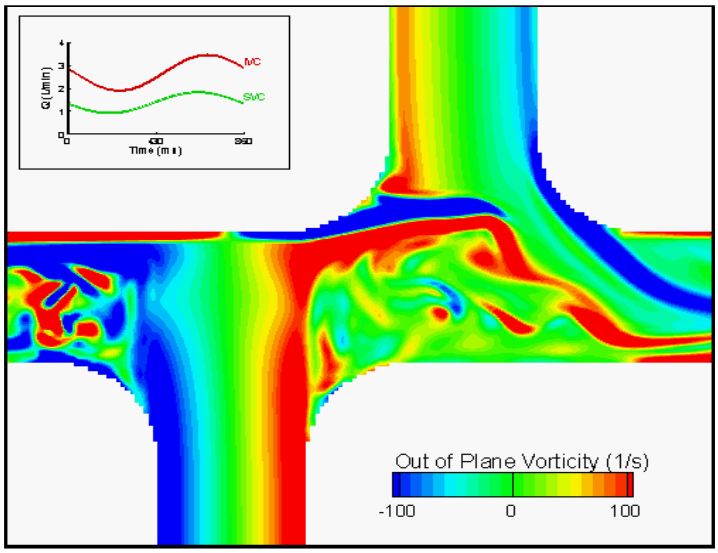

Animation 8-2: CFD vorticity fields on the symmetry plane of the idealized TCPC connection.

8.2.4 Comparison of the Time-Averaged Pulsatile and Non-Pulsatile Flow Fields

Figure 8-6 shows the time-averaged pulsatile velocity and vorticity fields, and compares them to the results obtained under non-pulsatile conditions using the same mean inlet and outlet flow rates. All transient structures are smoothed out in the pulsatile time-average resulting in an almost zero vorticity (green) at the center of the connection and blunter shear layer boundaries than in the instantaneous vorticity fields. It is interesting to note the high degree of similarity between the time-averaged pulsatile and non-pulsatile results. The main difference between the two flow fields resides at the center of the connection, and is best visualized with the vorticity contours. In the non-pulsatile results, the IVC consistently splits between the LPA and RPA, leading to a well defined shear layer (in red) that extends far into the central connection region. This red IVC shear layer gives rise to a small flow separation and slow counter-clockwise recirculation in the right corner of the SVC, apparent as a patch of blue, almost stagnant, velocities, and a confined patch of blue vorticity.

In the pulsatile simulations on the other hand, the IVC flow alternates between the RPA and a more "vertical" orientation (see Figure 8-4), and the patch of counter-clockwise blue vorticity in the right corner of the SVC anastomosis shifts from being more upstream in phases P3 and P5 of Figure 8-5 to a more downstream position in phases P1 and P7. As a result, in the time-averaged pulsatile vorticity field, the red IVC shear layer rapidly fades out as it goes around the central connection region, and the patch of blue vorticity in the right SVC corner averages to a smaller recirculation region than in the non-pulsatile flow field.

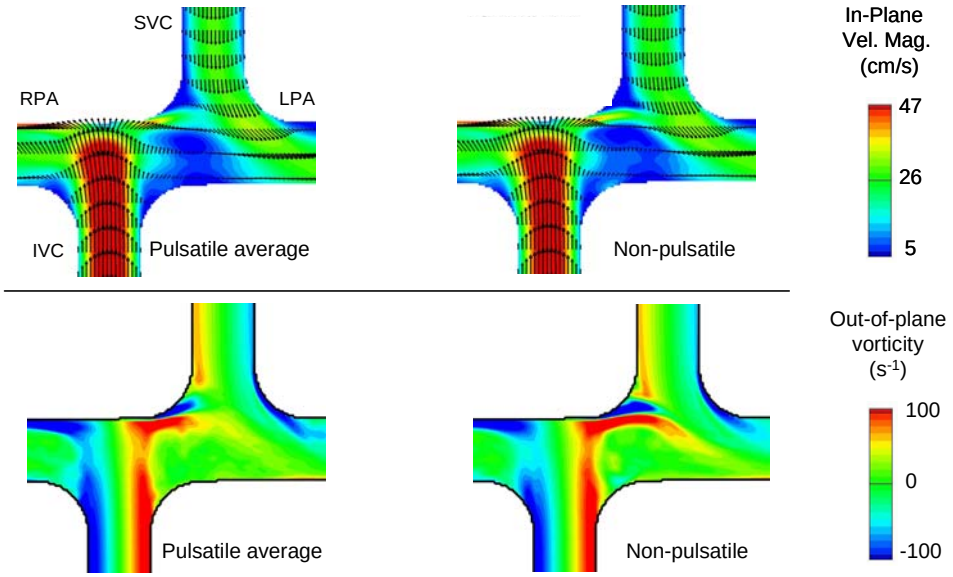

Figure 8-6: Comparison of the velocity and vorticity fields obtained by averaging the pulsatile simulations over 4 cardiac cycles, and in the non-pulsatile simulations conducted under the same mean inflow and outflow conditions.

8.2.5 Energy Dissipation

Table 8-1 provides the pulsatile and non-pulsatile power losses averaged over the cardiac cycle, as well as the maximum deviations from the mean values recorded in the pulsatile simulations. The mean pulsatile pressures fall within a remarkably close range of the non-pulsatile values, the maximum difference between the two settings being of only 0.03 mmHg in the SVC. The mean pulsatile power losses are 20% higher than their non-pulsatile counter-part, which might be attributed to the higher levels of flow unsteadiness at the center of the connection.

The fact that the time-averaged pulsatile pressures and power losses fall within the same range as the non pulsatile results is in line with the similarities observed between the time-averaged and the non-pulsatile velocity and vorticity fields. However, as can be noted from the maximum pressure drops and power loss values reported in

Table 8-1, it is apparent that the mean values do not suffice to tell the whole story. The pulsatile RPA and LPA pressure drops fall as low as -3.94 mmHg and -4.65 mmHg, while power losses reach up to 28.19 mW, i.e. close to four times the mean. The pressure fluctuations stem from both the inlet pulsatility and the variations in RPA/LPA flow ratios. The maximum power losses are recorded during the flow acceleration phase (phases P3 to P9) when the pressure drops are the largest. Symmetrically, the flow deceleration hosts the lowest power losses, as the pressure gradient temporarily reverses to slow down the flow throughout the connection.

Table 8-1: Pulsatile and non-pulsatile power losses for the idealized TCPC connection

		Pressure in reference to the IVC (mmHg)				Power Loss (mW)
		IVC	SVC	LPA	RPA	
Pulsatile	Average	0	-0.05	-0.57	-0.52	7.90
	Max	*0*	*1.56*	*-4.65*	*-3.94*	*28.19*
Non Pulsatile		0	-0.08	-0.59	-0.53	6.58

8.2.6 Particle Tracking

In order to assess the impact of pulsatility on the IVC flow distribution (taken as a surrogate measure of the hepatic flow distribution) and particle residence times, a Lagrangian particle tracking analysis is performed using three sets of data, namely the instantaneous pulsatile flow fields, the pulsatile time-average and the non-pulsatile results. For each data set, 700 new particles are released in the IVC and SVC every 2.15 ms for four consecutive cardiac cycles and passively advected by the flow according to the method described in Chapter 5 (Section 5.8.3.2).

The particle trajectories associated with the instantaneous pulsatile flow fields are shown in Figure 8-4 for six evenly spaced time points and animated in Animation 8-3. The IVC particles are color-coded based on the time at which they were seeded, while the SVC particles are color-coded in black to ease the distinction of the IVC and SVC streams. In phases P3, P5 and P7, the flow at the center of the connection is mostly dominated by the IVC, which confines the black SVC particles towards the left-side of the SVC anastomosis and into the LPA. The constriction of the SVC stream leads to the local flow acceleration noted at the SVC connection site for these time-phases (Figure 8-4). In phase P3, some blue IVC particles are also observed to engulf in the local flow reversal on the right side of the SVC anastomosis. Phases P7 and P1 present a larger degree of IVC and SVC mixing at the center of the connection than the other phases. In phase P1, this may be attributed to the RPA/LPA flow ratio, which is largely in favor of the RPA, so that most of the IVC particles flow towards the RPA, opening up the central connection region for the SVC flow. In phase P7, the increased mixing stems both from the RPA/LPA flow distribution and from the fact that the SVC reaches its peak flow rate and thus peak momentum energy.

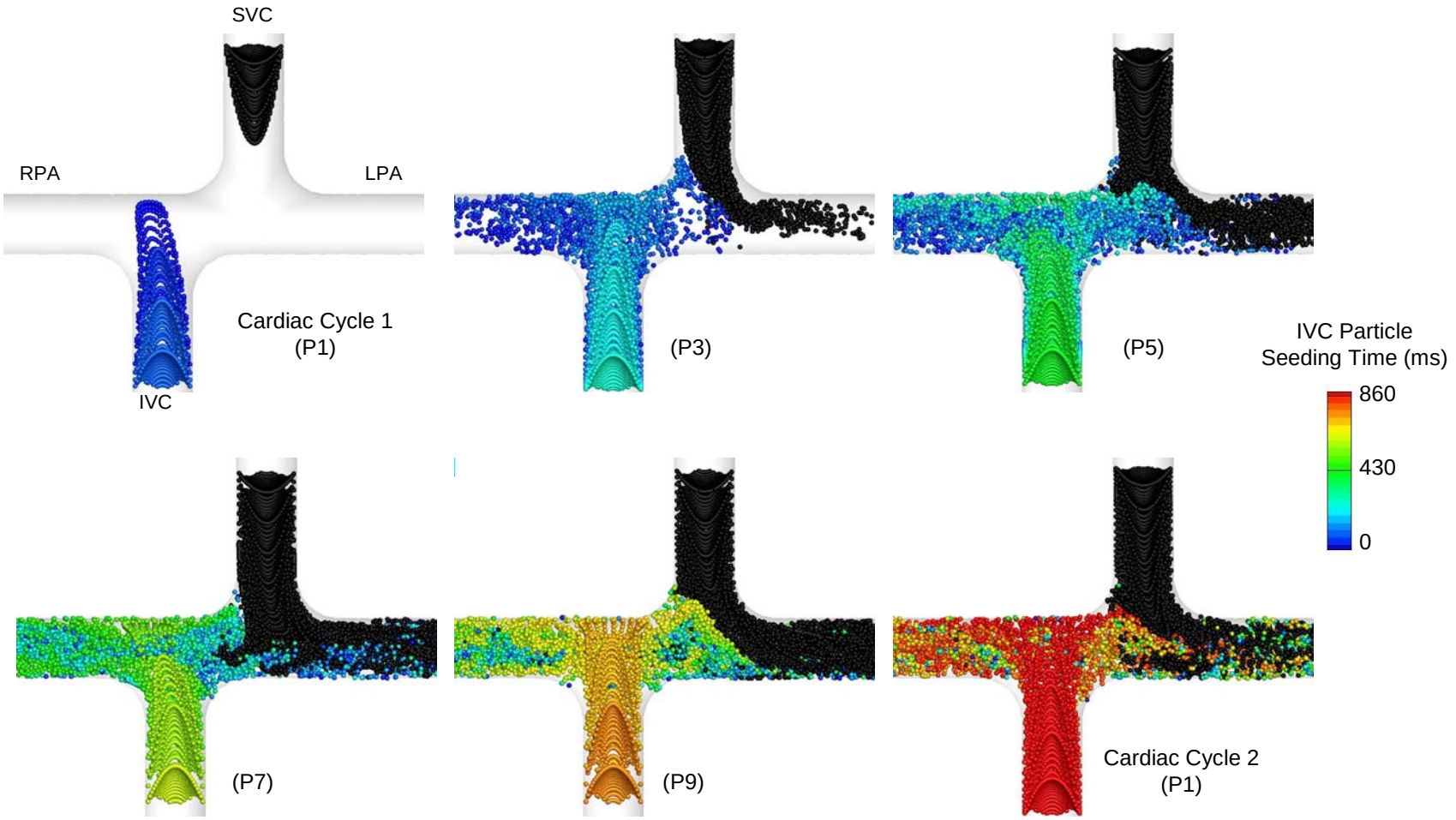

Figure 8-7: Particle positions at six time points separated by 172 ms (corresponding to phases P1, P3, P5, P7 and P9 shown in Figure 8-4). Phase P1 is shown for both the first and second cardiac cycle to better highlight the dynamics at the center of the connection. The IVC particles are color-coded by their release time. Blue particles thus denote particles that were seeded early in the cardiac cycle, while orange and red particles denote particles seeded towards the end of the cardiac cycle. The SVC particles are shown in black. Animation of the particles is included in Animation 8-3.

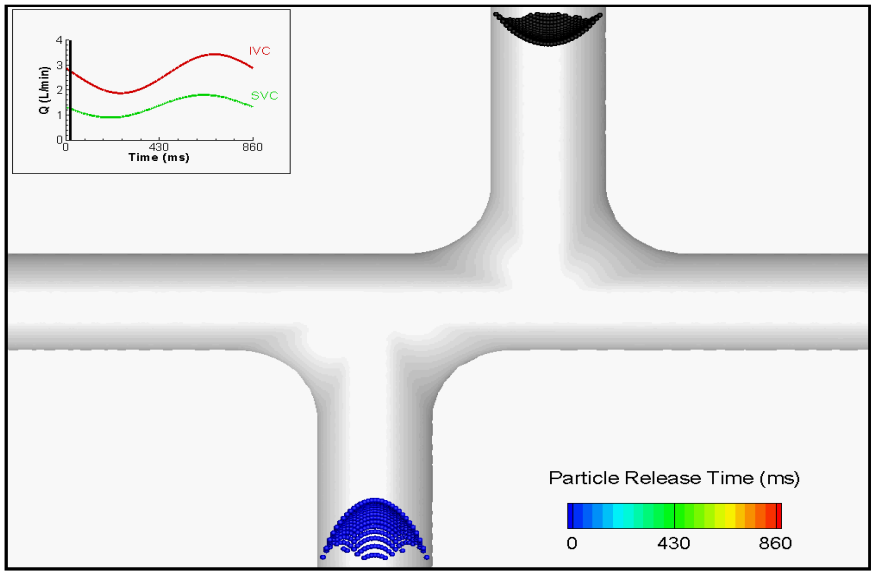

Animation 8-3: Dynamic particle visualization. The particle color coding is the same as in Figure 8-7.

8.2.6.1 Particle Residence Time

Looking at the color-coding of the IVC particles in Figure 8-7, it may be noted that only very few blue or light green particles remain at the beginning of the second cardiac cycle (P1b). This implies that most IVC particles exit the connection in less than a heart beat. The quantitative distribution of the IVC particle residence time is shown in Figure 8-8 and compared to the values obtained by applying the same approach to the time averaged pulsatile flow field and non-pulsatile results.

Time-average and non-pulsatile results display very similar distributions, with a narrow peak at 344 ms and 360 ms for the time-averaged and non-pulsatile results, respectively. As is best seen from the cumulative distribution shown in Figure 8-9, 80% of the IVC particles exit the domain in 250 to 560 ms. The increase rate of the cumulative

distribution for both time-averaged and non-pulsatile results, slows down beyond 560 ms, which corresponds to the relatively uniform distribution of the particle residence times between 560 and 970 ms in Figure 8-8. These longer residence times are mostly associated with IVC particles evolving at a low velocity in the boundary layers of the IVC or PAs.

In comparison with the time-averaged results, the distribution of the IVC particle residence times under pulsatile conditions shows a peak at shorter residence times (272 ms), but that peak is of smaller amplitude and followed by a slower decay than for the time-averaged results. This translates into the fact that the cumulative distribution shown in Figure 8-9 rises earlier than the time-averaged one, but increases at a slower rate. It is also interesting to note that beyond 560 ms, the residence time distribution in the pulsatile simulations keeps decreasing unlike in the time-averaged results where it became more uniform. This might be attributed to the flow pulsatility, which increases the flow disturbances and, in turn, the chances of the particles in the wall boundary layers to be re-directed towards the bulk of the flow.

The cumulative pulsatile and time-averaged curves shown in Figure 8-9 fall back on top of each other for residence times of 750 ms or higher. Overall, 94% of the IVC particles take less than one cardiac cycle (860 ms) to exit the connection domain in the pulsatile simulations, which is in close range to the values of 96% and 95% predicted for the time-average and non-pulsatile flow fields.

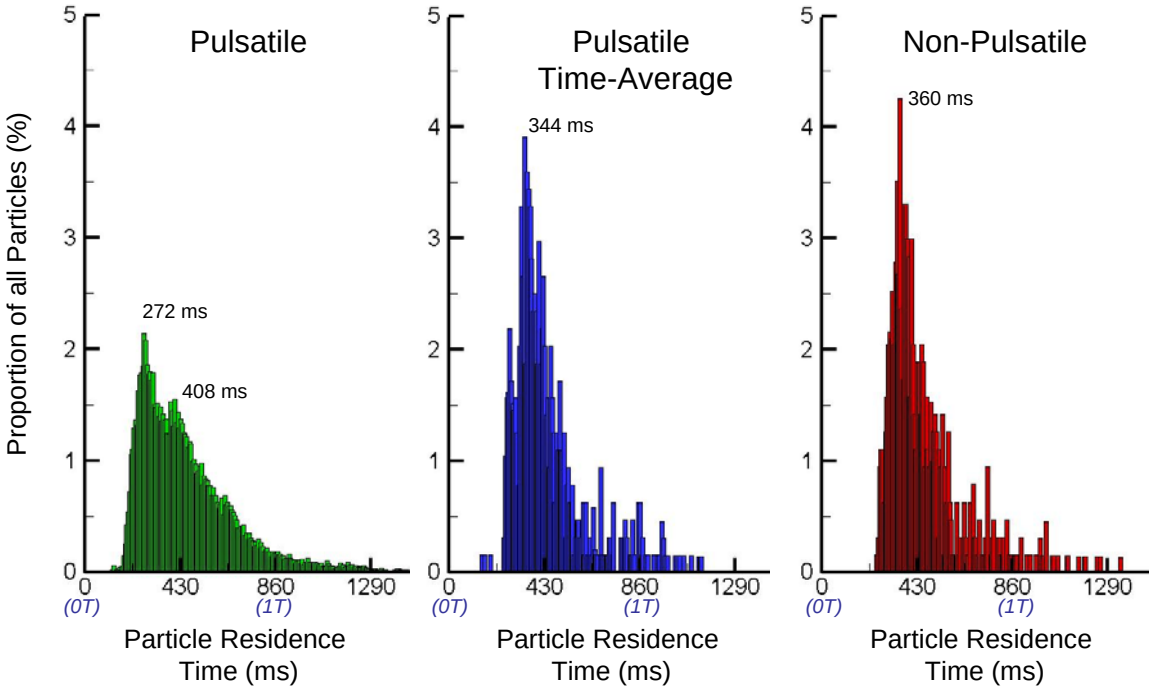

Figure 8-8: Distribution of the IVC particle residence times for the pulsatile, time average and non-pulsatile results.

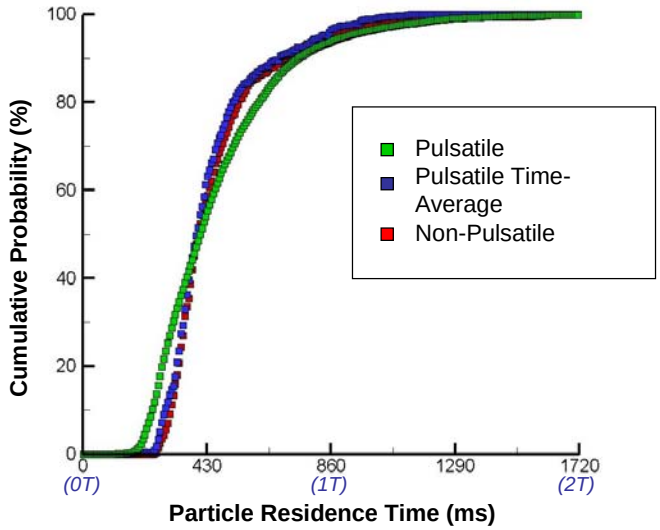

Figure 8-9: Cumulative distribution of the IVC particle residence times for the pulsatile, time average and non-pulsatile results.

8.2.6.2 IVC Flow Distribution

Throughout all phases shown in Figure 8-7, almost no SVC particles are seen to reach the RPA, and it is the IVC particles that divide between the left and right branch to match the desired time-varying RPA/LPA flow ratio. The cumulative distribution of IVC particles exiting through the RPA or LPA is depicted in Figure 8-10 as function of the time elapsed since the first particle release. The results obtained by applying the same approach to the pulsatile time-average and non-pulsatile flow fields are shown as well for comparison.

The flow distributions to the RPA or LPA start to rise at approximately 430 ms, which corresponds to the time needed by the first particles to flow across the domain. The pulsatile distribution follows the same trendline as the time-averaged or non-pulsatile results. The pulsatile IVC distribution to the LPA falls below the mean at the beginning of each cardiac cycle, which also corresponds to the phases were the global flow distribution to the LPA is the lowest. As flow to the LPA increases in the later part of the cardiac cycle, the pulsatile IVC flow distribution reaches the same values as the time-averaged or non-pulsatile results. The impact of the instantaneous fluctuations attenuates as more cardiac cycles are taken into account. Results stabilize after four cardiac cycles. At the end of the fifth cardiac cycle, the distribution of the IVC particles is computed to be 75.7/24.3 RPA/LPA for the pulsatile simulations vs. 74.3/25.3 and 74.9/25.1 when using the pulsatile time-average and the non-pulsatile results, respectively.

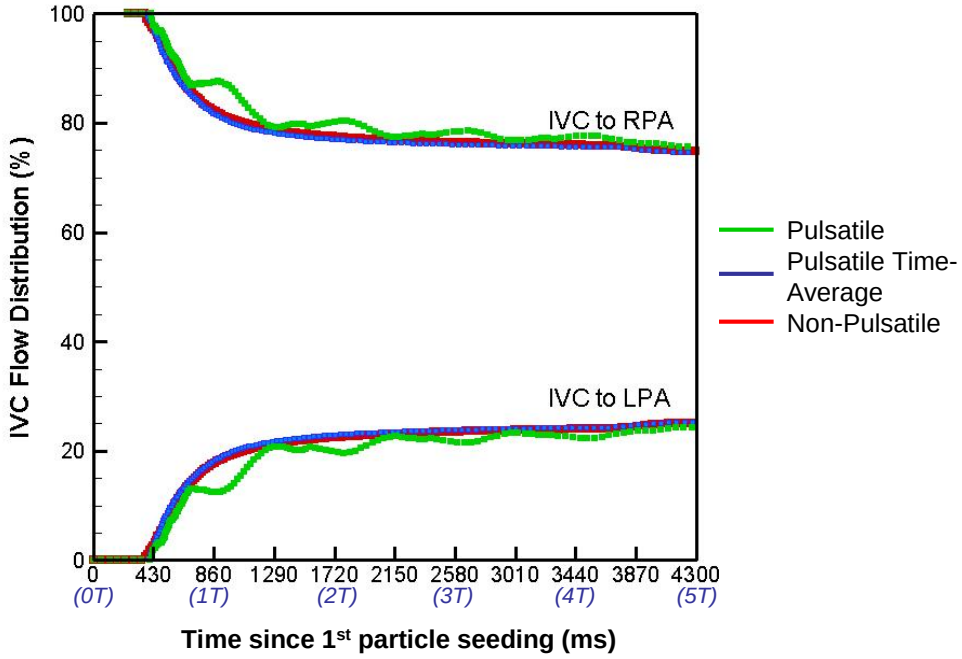

Figure 8-10: Comparison of the IVC flow distribution associated with the pulsatile flow fields, the pulsatile time-average and the non-pulsatile simulations. The number of cardiac cycles is indicated in blue below the x-axis for an easier reading.

8.2.7 Summary

Overall, the time-averaged pulsatile and the non-pulsatile results for the idealized TCPC geometry were in very close match. Slight differences were observed in the velocity and vorticity fields at the center of the connection, where the impact of the pulsatile flow instabilities is the highest. However, these small discrepancies did not translate into significant variations in the reported pressure drops, IVC flow distributions or particle residence times. On the other hand, the pulsatile fluctuations lead to 1) increased flow disturbances at the center of the connection with a number of small local eddies, which were unseen in the non-pulsatile results, 2) large variations in the LPA and RPA pressure drops, whose maximum values deviate by as much as 4 mmHg from the mean, to accommodate for the repeated flow accelerations and decelerations, 3) large

variations in power losses, the maximum value being close to four times the mean. The cumulated effect of the flow instabilities and pressure translated into a 20% increase in power losses for the pulsatile results compared to the non-pulsatile ones.

8.3 Patient 1 (CHOP 095): Extra-Cardiac TCPC

The first *in vivo* anatomy retained for this study is an extra-cardiac TCPC with a single SVC and normal systemic venous return. The patient-specific anatomy, shown in Figure 8-11, was reconstructed from anatomical MR images of an 8 year-old female Fontan patient. *In vivo* flow rates were assessed by phase-contrast MRI (PC MRI) acquired through each one of the vessel cross-sections at 23 evenly spaced time-points across the cardiac cycle. The 3D *in vivo* flow structures were reconstructed from a stack of coronal PC MRI acquired at the same frequency. Details on the model generation, flow condition extraction and 3D velocity field reconstruction are provided in Chapter 5.

8.3.1 In Vivo Flows Conditions and Numerical Set-Up

The *in vivo* inlet and outlet flow conditions as measured by PC MRI are illustrated by the square symbols in Figure 8-12, in terms of the time-dependent cardiac output (computed as the sum of the instantaneous IVC and SVC flow rates) and time dependent inlet and outlet flow distributions. The patient's heart rate was 91 beats per minute, corresponding to a cardiac cycle duration of 659 ms. The mean cardiac output over the cardiac cycle was 2.7L/min, with an average mass flow splits of 62/38 between the IVC and SVC and 43/57 between the RPA and LPA. The geometric and flow characteristics of the problem are summarized in Table 8-2.

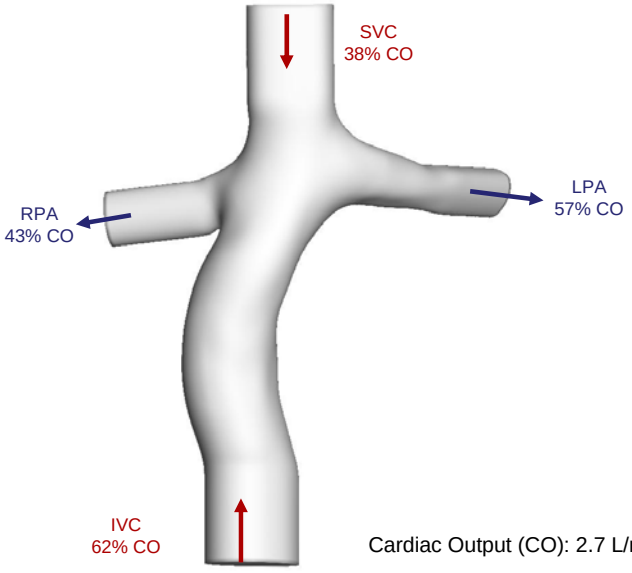

Figure 8-11: Patient-specific anatomy of the extra-cardiac test-case. The arrows indicate the main inflow/outflow directions. The mean in vivo flow rates, averaged over the PC MRI phases are reported next to each one of the vessels expressed as a percentage of the mean cardiac output.

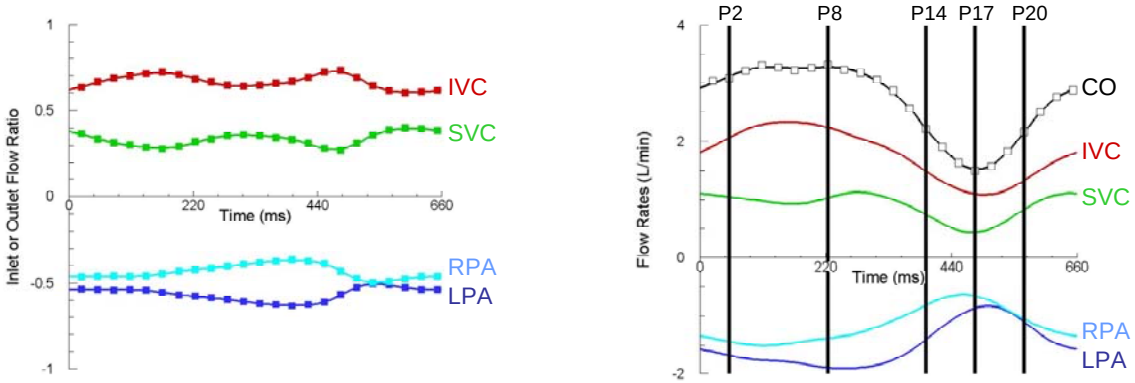

Figure 8-12: Inlet and outlet flow rates as obtained from the in vivo PC MRI measurements (symbols) and as prescribed for the CFD simulations (continuous lines). The CFD flow conditions are imposed using the in vivo flow ratios (Left) at the outlets and in vivo flow rates (Right) at the inlets. The vertical black lines depict the five time-phases for which the PC MRI and CFD flow fields will be discussed in details.

Table 8-2: Geometric and CFD flow characteristics at the two inlets (IVC and SVC) and outlets (RPA and LPA) of the extra-cardiac TCPC.

Vessel		IVC	SVC	LPA	RPA
Area (cm^2)		2.91	1.91	0.57	0.64
Flow Rate (L/min)	Mean	1.79	0.92	1.54	1.17
	Max	2.51	1.26	2.25	1.63
	Min	0.78	0.37	0.25	0.61
Pulsatility index		48.5%	48.5%	64.6%	43.3%

As discussed in Chapter 5, the *in vivo* flow rate measurements could not be used directly for the CFD simulations because the sum of the *in vivo* inflows (IVC and SVC) did not match the sum of the *in vivo* outflows (LPA and RPA). Accordingly, the CFD inlet boundary conditions are prescribed to match the *in vivo* flow rates, while the outlet boundary conditions are computed based on the time-varying *in vivo* mass flow ratios. The inlet and outlet flow distributions and flow curves used in the CFD simulations are shown by the continuous lines in Figure 8-12. The IVC and SVC flow curves are almost exactly in phase, reaching their minimum flow rate at t = 500 ms and t = 476 ms, respectively. A slightly larger phase shift is observed between the RPA and LPA flow curves, which reach their minimum at t = 455 ms and t = 505 ms, respectively.

In the simulations, all quantities are normalized based on mean velocity and equivalent hydraulic diameter of the IVC, D_{IVC}, yielding a characteristic Reynolds number Re=565, a Womersley number α=15.9 and a non-dimensional cardiac cycle duration T=3.52. The pulsatility indices associated with the CFD inflow and outflow curves are 48.5% for both IVC and SVC, 43.3% for the RPA and 64.6% for the LPA. Plug (flat) flow profiles are prescribed at the IVC and SVC inflow planes and scaled to match the instantaneous flow rate.

The TCPC surface is discretized with an unstructured triangular mesh with 11,498 triangular elements. The background Cartesian domain is discretized with a resolution $h = 0.02D_{IVC}$. Pulsatile calculations are carried out using a non-dimensional physical time step of $\Delta t = 0.001$, corresponding 3520 time steps per cardiac cycle, and iterated over 10 cardiac cycles. Finally, the non-pulsatile time-dependent simulations are carried using the time-averaged inflow and outflow conditions and the same temporal and spatial accuracy as in the pulsatile simulations.

8.3.2 3D Flow Structures

The 3D *in vivo* flow structures reconstructed from the coronal PC MR images are shown in the top panels of Figure 8-13 and Figure 8-14 for five selected time phases out of the 23 that were acquired. The lower panels of these two figures display the pulsatile CFD results obtained for the same five instants in time, as well as the non-pulsatile flow fields obtained under the mean inflow and outflow conditions. Both figures display the instantaneous flow structures using 3D ribbons seeded in the IVC and SVC. In Figure 8-13, these 3D ribbons are color-coded by their vessel of origination (in orange for IVC streamtraces and green for SVC streamtraces) to best illustrate the interaction between the two incoming caval flows. In Figure 8-14, the ribbons are color-coded by velocity magnitude and the anterior half of the TCPC is blanked out of the image to gain better insights into the flow structures at the center of the connection. The dynamic visualization of these streamtraces across the cardiac cycle is provided in Animation 8-4 and Animation 8-5 for the *in vivo* PC MRI and pulsatile CFD results, respectively.

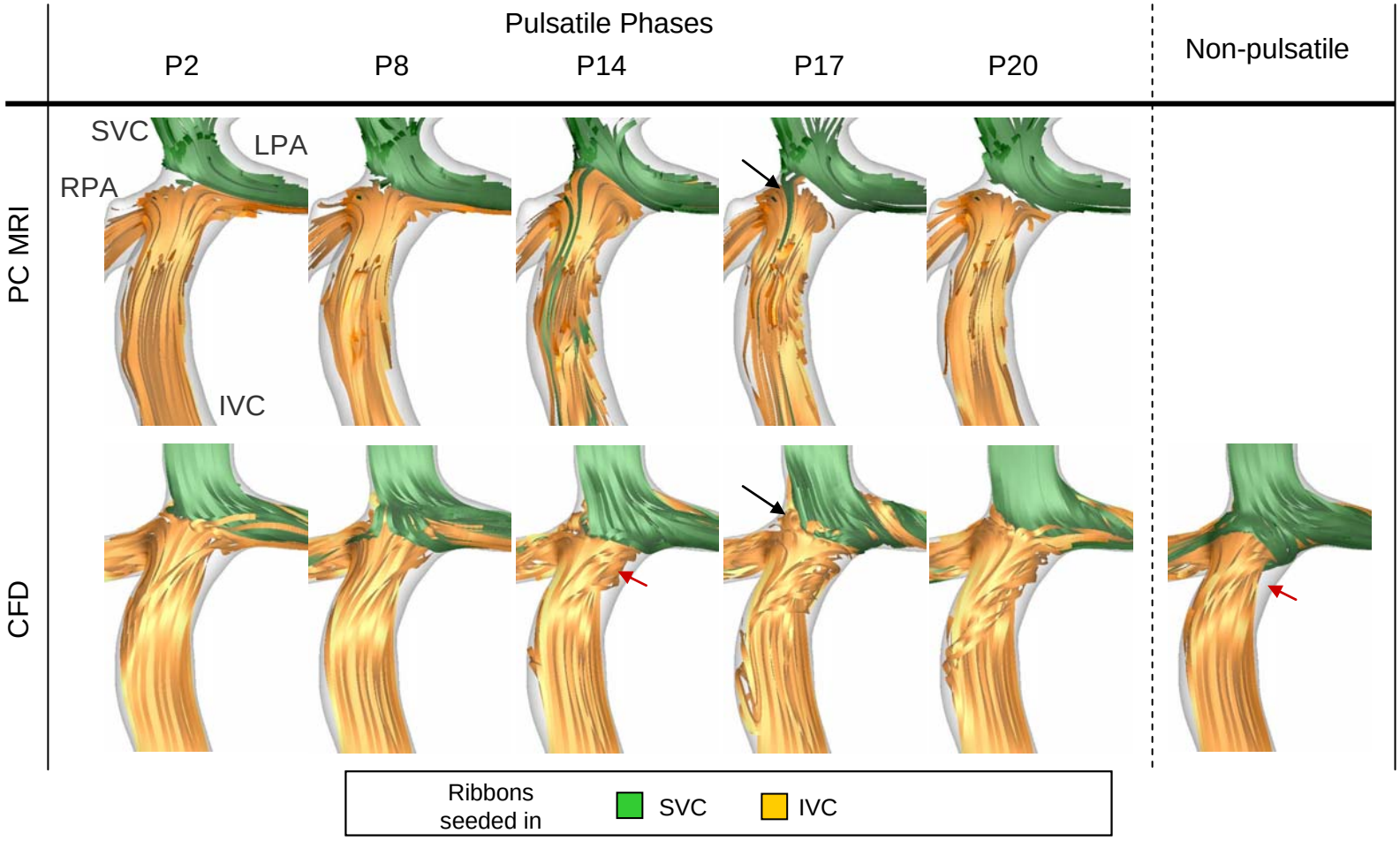

Figure 8-13: Global flow structures as reconstructed from the coronal PC MRI images (Top) and as computed by CFD (Bottom) for five time phases across the cardiac cycle. The non-pulsatile CFD flow structures are provided as well for comparison. The IVC and SVC interactions are illustrated by 3D streamtraces color-coded by their vessel of origin (IVC: orange; SVC: green). Animation of the PC MRI and CFD streamtraces are included in Animation 8-4 and Animation 8-5, respectively.

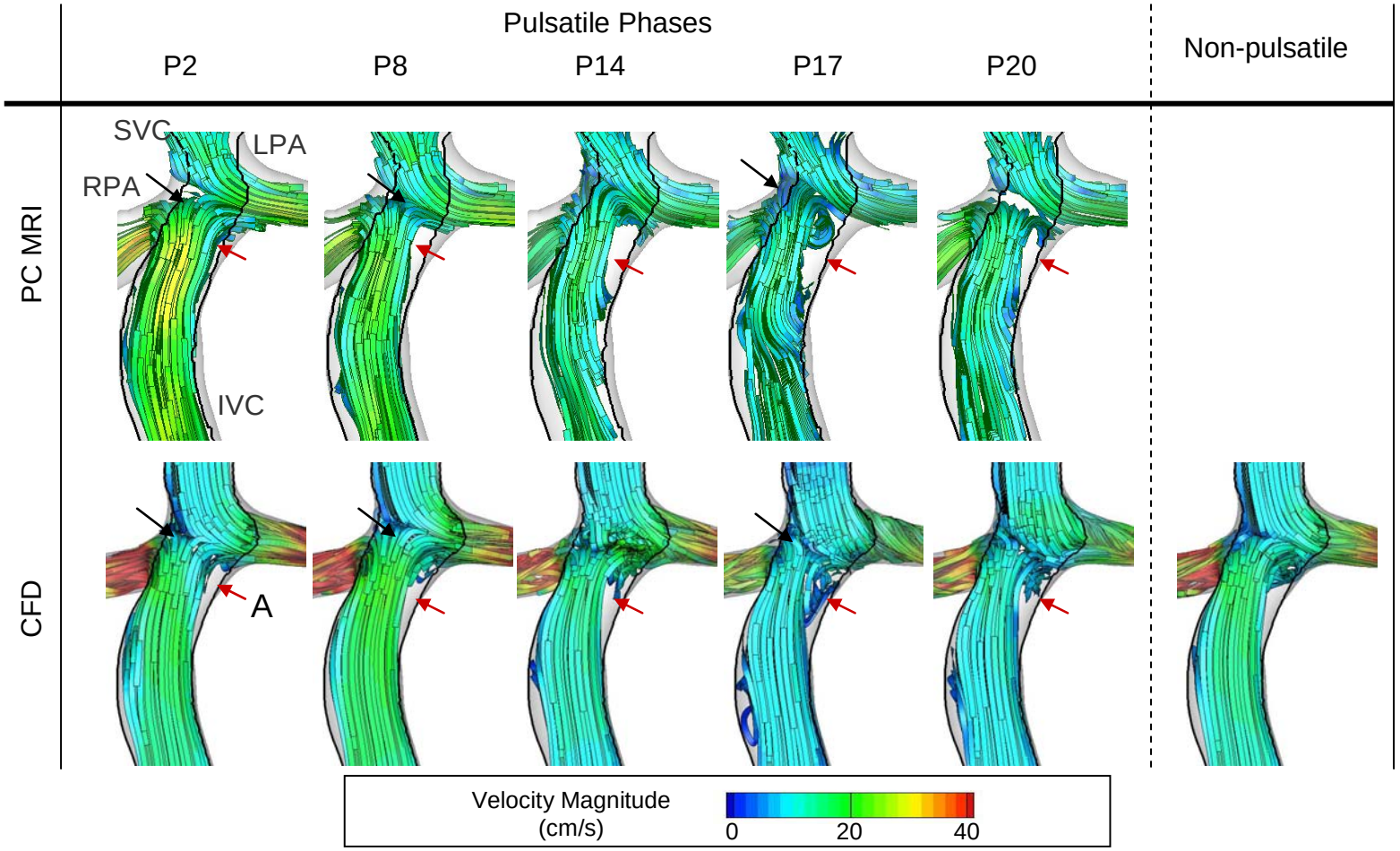

Figure 8-14: Global flow structures as reconstructed from the coronal PC MRI images (Top) and as computed by CFD (Bottom) for five time phases across the cardiac cycle. The non-pulsatile CFD flow structures are provided as well for comparison. The 3D streamtraces are color-coded by velocity magnitude and the anterior half of the domain is blanked out for a better visualization of the inner flow structures.

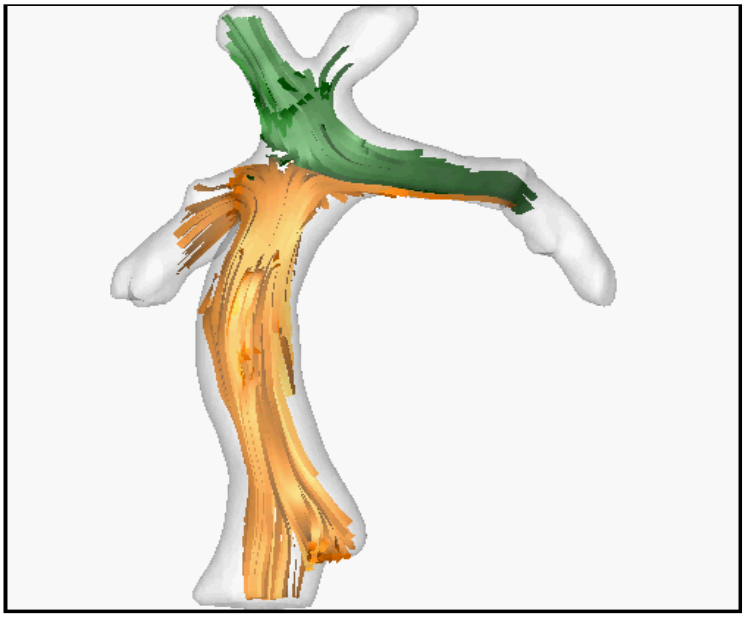

Animation 8-4: Dynamic visualization of the *in vivo* flow structures as reconstructed from the coronal PC MRI images. The 3D streamtraces color-coded by their vessel of origin (IVC: orange; SVC: green).

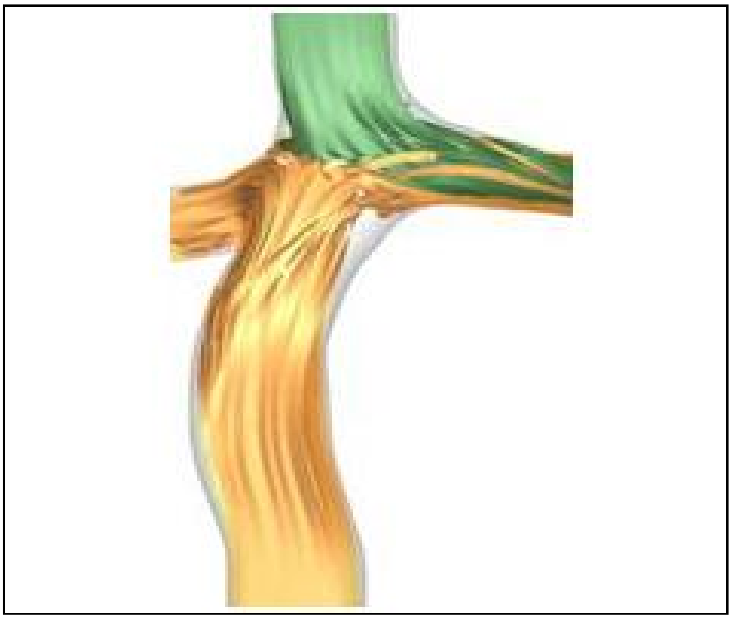

Animation 8-5: Dynamic visualization of the pulsatile CFD flow structures. The 3D streamtraces color-coded by their vessel of origin (IVC: orange; SVC: green).

8.3.2.1 General Considerations

Looking at the velocity magnitudes reported in Figure 8-14, it is noteworthy that the PC MRI and CFD values fall within the same range at the center of the connection but drastically differ in the pulmonary outflow tracks. As was mentioned above, the sum of the PC MRI outflow rates is systematically lower than the sum of the inflows, leading to inconsistent *in vivo* measurements. This discrepancy, which is consistently observed across our patient database, has been attributed to larger measurement errors in the PAs than in the VCs due to the smaller dimensions of the former vessels [181]. It should also be pointed out that the *in vivo* velocities measured in the IVC are less uniform than in the CFD results, although falling within the same range. This is most likely due to the flat inlet velocity profiles used in this study, and results could be further improved by smoothing and interpolating the *in vivo* velocity profiles onto the CFD inlet cross-sections.

Despite this assumption at the inlets, the agreement between the measured and computed flow structures is quite remarkable. As is best visualized from Figure 8-13, the IVC streamtraces occupy most of the central connection area in both the PC MRI and CFD flow fields, constraining the SVC streamtraces towards the left side of the SVC anastomosis site. This behavior is similar to what was observed in the idealized TCPC case, and results in an almost exclusive distribution of the SVC flow to the LPA throughout the cardiac cycle. The flow pulsatility mostly impacts the flow structures in the IVC and at the center of the connection, which will be the focus of the subsequent section.

8.3.2.2 Phase-by-Phase Analysis

The temporal location of the five selected time phases is illustrated by the thick black lines in the right panel of Figure 8-12. Phase P2 corresponds to the late acceleration, P8 lies in the plateau of the cardiac output curve, P14 is located mid-way through the deceleration, P17 corresponds to the lowest cardiac output and P20 to the early acceleration.

In the late acceleration and peak flow phases (P2 and P8), the IVC features stable flow structures, its streamtraces being nicely aligned with the vessel axis. A small flow separation can be noted on the left side of the IVC anastomosis due to the curvature of the IVC baffle (red arrows in Figure 8-14). The collision of the IVC and SVC streamtraces leads to the formation of a flow stagnation point in the IVC (black in Figure 8-14), around which the IVC streamtraces divide into those going towards the RPA and those going towards the LPA. The CFD and PC MRI flow structures for those two time phases are in remarkable agreement. A slight difference can be noted in phase P8 of Figure 8-13 where some of the SVC streamtraces are seen to travel close to the anterior wall of the connection and follow a helical flow pattern into the PAs in the CFD results but not in the PC MRI flow fields. This difference can for the most part be attributed to the low resolution and poor signal-to-noise ratio of the PC MRI measurements in the vicinity of the vessel walls.

The flow separation region noted in phases P2 and P8 is present throughout the cardiac cycle and can also be clearly identified in the non-pulsatile flow fields. It is least pronounced in the late acceleration phase (P2) and most pronounced in phase P14 during the flow deceleration. As the flow decelerates towards the minimum cardiac output

(phases P14 and P17), flow instabilities develop half-way through the baffle, resulting in tortuous 3D streamlines in the upper half of the IVC baffle (red arrow in Figure 8-13). At the connection site, the decreasing kinetic energy of the SVC, allows the IVC to penetrate further into the central connection region along the right side of the SVC anastomosis location (black arrows in Figure 8-13 and Figure 8-14). Penetration of the IVC into the SVC pathway is more pronounced in the PC MRI measurements than in the CFD results, especially in phase P14. This might here again be due to the choice of flat inlet velocity profiles. The use of Womersley velocity profiles in the idealized TCPC led to the development of a local flow reversal at the SVC anastomosis site, which allowed for a deeper penetration of the IVC stream. A similar phenomenon might be at stake here. As the analytical Womersley solution only applies for circular pipes, a possible alternative would be to interpolate the *in vivo* inflow conditions, or further extend the entrance length to allow a wall boundary layer to develop. Finally, as the flow starts accelerating again in phase P17, the flow structures re-stabilize and strongly resemble those reported for P2.

Results obtained under the non-pulsatile mean flow conditions demonstrate flow structures that closely resemble those of phases P2 and P8, where the IVC flow was most stable. Similarities include presence of the flow separation at the IVC anastomosis, stagnation point at the center of the connection and a highly preferential distribution of the SVC flow to the LPA. In absence of any destabilizing pulsatile effects, the flow recirculation (red arrows) is better defined in the non-pulsatile flow field than in any of the pulsatile time phases. In addition, slightly more SVC streamtraces succeed to reach the RPA by flowing along the anterior wall of the connection, than in the pulsatile flow

fields. However, these differences are minor overall and the non-pulsatile flow fields are in good agreement with the global pulsatile flow structures.

8.3.3 Power Losses

The average pulsatile pressure and power losses over the cardiac cycle and the maximum deviations from these mean values are given in Table 8-3, together with the corresponding values obtained in the non-pulsatile simulations. The mean pulsatile pressures and power loss values fall remarkably close to the non-pulsatile values. The largest difference in terms of pressures is seen in the LPA, where the pulsatile pressure drop is 0.15 mmHg or 7% larger than in the non-pulsatile simulations. The mean pulsatile power losses are 2 mW larger than their non-pulsatile counterpart, which represents less than a 5% increase. Under both flow conditions, the maximum pressure drops are recorded in the LPA, which may be attributed to the fact that the LPA featured both a smaller diameter and a larger flow rate than the RPA (see Table 8-2).

Table 8-3: Pulsatile and non-pulsatile power losses for the extra-cardiac TCPC

		Pressure in reference to the IVC (mmHg)				Power Loss
		IVC	SVC	LPA	RPA	(mW)
Pulsatile	Average	0	-0.01	-2.08	-1.28	48.51
	Max	*0*	*0.21*	*-3.24*	*-2.03*	*70.65*
Non Pulsatile		0	-0.01	-1.95	-1.26	46.50

The largest PA pressure drops recorded in the pulsatile simulations are -3.24 mmHg for the LPA and -2.03 mmHg in the RPA, which represents a maximum deviation of 56% and 59% from the corresponding time-averaged values. The highest pulsatile

power losses are recorded during the first 350 ms of the cardiac cycle, corresponding to the plateau observed in the cardiac output waveform. The maximum pulsatile power loss is 70.65 mW representing a 46% increase compared to the time-averaged value. Overall, the fluctuations of the instantaneous pressure and power loss values are less marked in this anatomical case than in the idealized setting. This may be attributed to the lower flow rates measured in this patient, compared to the idealized test-case, and to the smaller PA dimensions, which reinforce the stabilizing viscous effects.

8.3.4 Particle Tracking

For the assessment of the Lagrangian particle pathways and efficiency metrics, 1800 new particles were released at the IVC inlet cross-section every 33 ms for ten consecutive cardiac cycles. The computed IVC and SVC particle trajectories are illustrated in Animation 8-6. Figure 8-15 shows the IVC particle trajectories only, for the two last cardiac cycles (cycles 9 and 10). The IVC particles are color-coded based on the cardiac cycle during which they were seeded. Particles seeded during cardiac cycle 9 appear in dark orange, while other colors (light orange, yellow or green) denote particles that were seeded in earlier cardiac cycles. To better visualize the progression of the IVC particles as they exit the TCPC domain, particles seeded in the last cardiac cycle (cycle 10) are not displayed. Few of the dark orange particles reach the PAs by the end of the cardiac cycle in which they were seeded (namely cycle 9), and quite a large proportion of them remain within the IVC and the center of the connection even after the following cardiac cycle. It may also be noted that in phase P2 of the cardiac cycle 9, some green particles (which were seeded three cardiac cycles prior to the one visualized) are still

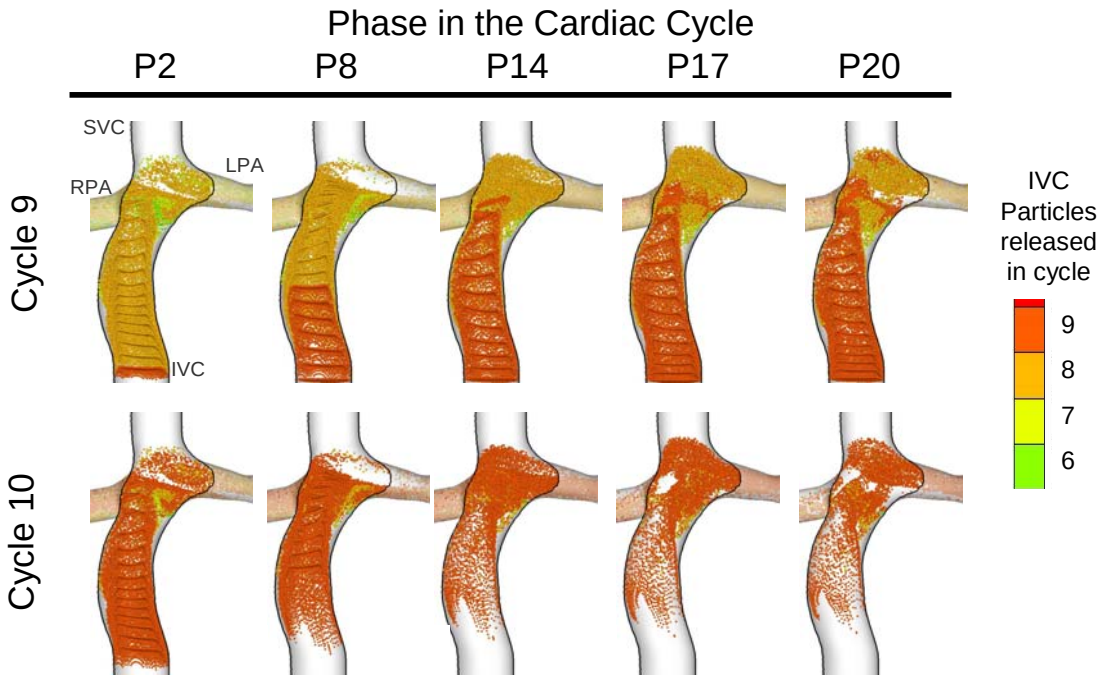

Figure 8-15: Progression of the particles seeded at the IVC inlet of the extra-cardiac anatomy for two consecutive cardiac cycles. The IVC particles are color-coded by their seeding time. Particles seeded in cardiac cycle 9 appear in dark orange, while the lighter orange, yellow or green particles were seeded in earlier cardiac cycles.

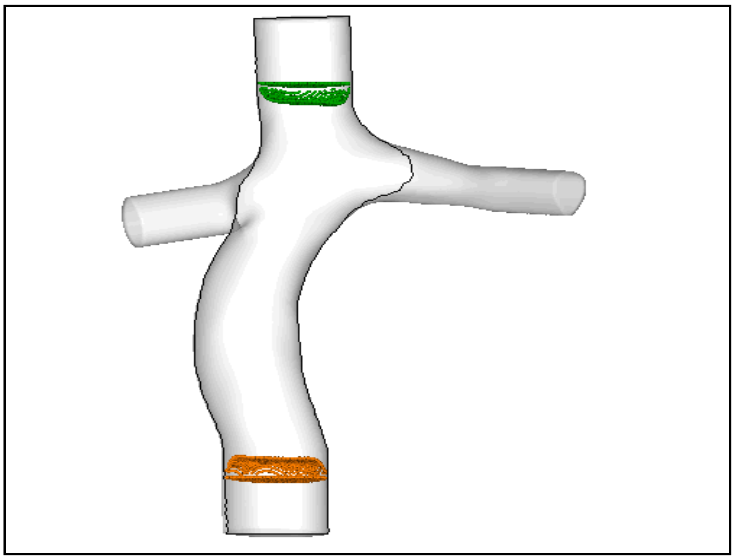

Animation 8-6: IVC and SVC particle pathways. The particles are color-coded by their vessel of origin (IVC: orange; SVC: green)

present in the flow separation region on the left side of the IVC anastomosis. These green particles are washed out in the later part of cardiac cycle 9, and are replaced by yellow particles (seeded in cycle 7) in phase P2 of cardiac cycle 10. These results demonstrate that particles that get entrapped in the IVC flow separation region remain within the TCPC domain for about 3 cardiac cycles.

8.3.4.1 Particle Residence Time

The quantitative distribution of the IVC particle residence time is shown in Figure 8-16 and compared to the values obtained by applying the same approach to the time averaged pulsatile flow field and non-pulsatile results. The associated cumulative distributions are shown in Figure 8-17. The distribution of the particle residence times under pulsatile conditions displays a main peak at 497 ms followed by a second peak of lower amplitude at 759 ms. As can be seen from Figure 8-15, particles seeded at the beginning of a cardiac cycle, while the IVC flow rate is high, reach the connection site by P14 (which corresponds to t = 400 ms) and flow into the RPA. Most of these particles thus correspond to the first peak in Figure 8-16. Particles seeded later in the cardiac cycle take a little longer to flow across the TCPC domain, due to the IVC flow deceleration between phases P14 and P19, spreading the first peak towards higher particle residence times. The secondary peak corresponds to the particles that re-circulate around the connection region prior to reaching either one of the PAs. As is best illustrated in the cumulative distribution shown in Figure 8-17, no IVC particle exits the TCPC in less than 367 ms, and only 46% of them exit the domain in one cardiac cycle or less. The 95% probability of an IVC particle reaching either one of the PAs corresponds to t = 1377 ms, which is to say a little over two cardiac cycles.

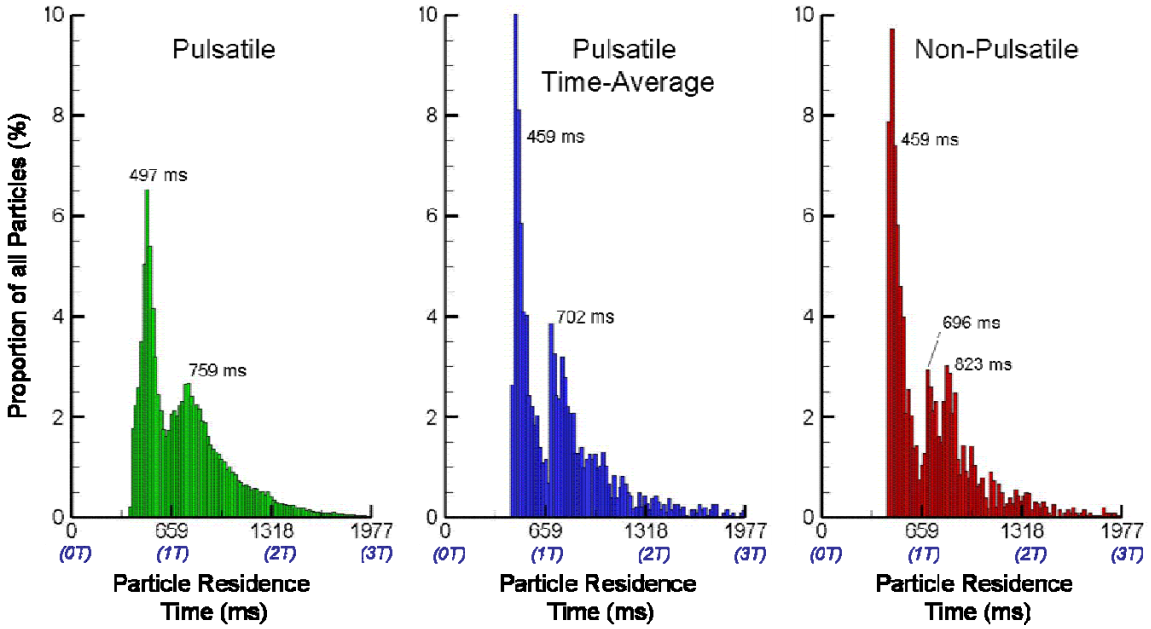

Figure 8-16: Distribution of the IVC particle residence times for the pulsatile, time average and non-pulsatile results in the extra-cardiac anatomy. The number of cardiac cycles is indicated in blue below the x-axis for an easier reading.

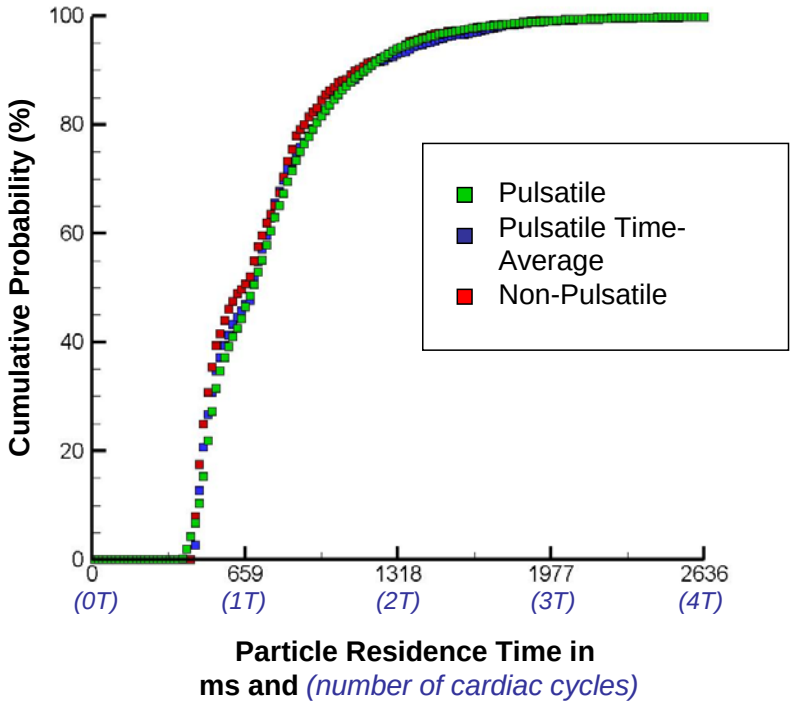

Figure 8-17: Cumulative distribution of the IVC particle residence times for the pulsatile, time average and non-pulsatile results in the extra-cardiac anatomy. The number of cardiac cycles is indicated in blue below the x-axis for an easier reading.

The distribution of the particle residence times computed using the non-pulsatile flow fields closely match the pulsatile time-average, and follow the same overall trends as the pulsatile results. A first narrow peak is observed at 459 ms that reaches up to 10%, followed by a secondary peak of lower amplitude around 700 ms. Both these peaks are higher and narrower than their pulsatile counterpart. This stems from the fact that the time-average or non-pulsatile results correspond to a single flow configuration leading to a lower spread in the possible residence times. However, these differences remain small and have little impact on the cumulative distributions reported in Figure 8-17, where the pulsatile, time-average and non-pulsatile curves fall within 5% of each other.

8.3.4.2 IVC Flow Distribution

The distribution of the IVC particles between the left and right lung is illustrated in Figure 8-18. The distribution of IVC particles to the RPA rises to 100% at t = 367 ms and remains at 100% until t = 621 ms. All particles exiting the TCPC domain between 367 and 621 ms are thus directed towards the RPA, which is in line with the longer residence times reported earlier for particles that had to flow across the central connection region prior to reaching the LPA. Time-averaged and non-pulsatile data points are almost indistinguishable from one another, and converge towards a 70/30 RPA/LPA distribution of the IVC flow. This IVC flow distribution may be contrasted to the 43/57 RPA/LPA global flow distribution, reflecting a highly preferential distribution of the IVC to the RPA.

The pulsatile measurements closely follow the non-pulsatile trend. It may be noted that the pulsatile distribution to the RPA consistently falls above the non-pulsatile

measurements at the beginning of a new cardiac cycle. This overshoot corresponds to the high flow phase (P2 and P8). As was observed from the 3D streamtraces shown in Figure 8-13, the SVC flow occupies most of the central connection region during these first time phases, leading to the formation of a flow stagnation point in the IVC. As a result, the IVC particles shown in Figure 8-15 do not penetrate into the central connection region and flow almost exclusively to the RPA in phases P2 and P8. As the flow decelerates in later part of the cardiac cycle, the mixing between the IVC and SVC increases, and the IVC distribution re-equilibrates to the same values as for the non-pulsatile simulations. The pulsatile IVC flow distribution converges to 69/31 RPA/LPA after 5 cardiac cycles.

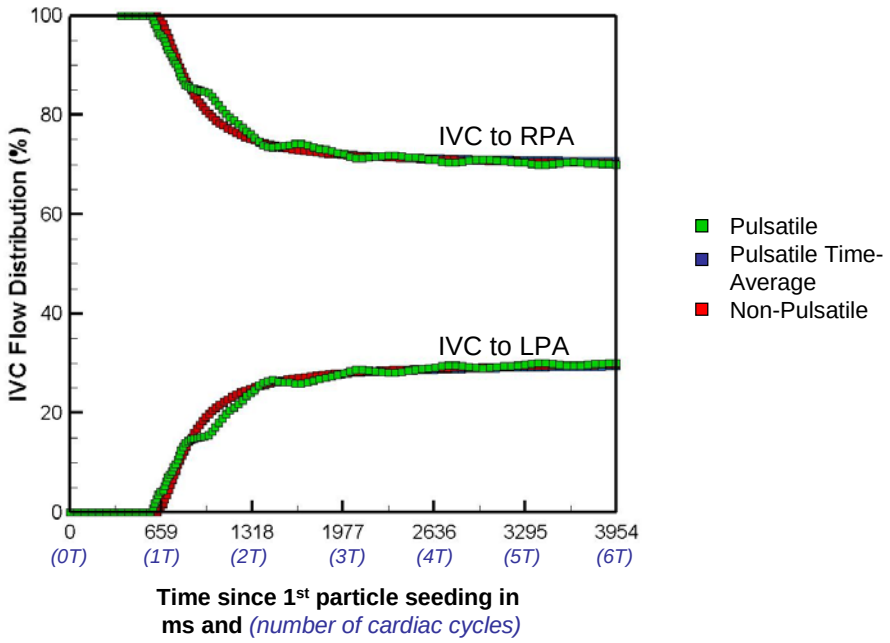

Figure 8-18: Comparison of the IVC flow distribution associated with the pulsatile flow fields, the pulsatile time-average and the non-pulsatile simulations in the extra-cardiac anatomy. The number of cardiac cycles (0T, 1T, etc) is indicated in blue below the x-axis for an easier reading.

8.3.5 Summary

In summary, in this subsection we studied a patient-specific extra-cardiac configuration designed with almost no-offset between the IVC and SVC anastomosis sites. The caval inflow curves were almost exactly in phase and had a pulsatility index of 48.5%. The computed pulsatile flow dynamics were in very good agreement with the *in vivo* flow fields reconstructed from PC MRI. The SVC flow was almost exclusively directed to the LPA throughout all cardiac phases. Pulsatility mostly affected the fluid dynamics in the IVC baffle and at the center of the connection, transiently opening and shutting off the access of the IVC particles to the LPA. Overall, the non-pulsatile flow simulations provided an excellent representation of the mean pulsatile efficiency metrics, especially in terms of particle residence times and IVC flow distribution. The largest differences between the two were observed in the pressure and power loss measurements. The unsteady flow features in the IVC and central connection region lead to slightly higher power losses under pulsatile conditions (48.51 mW) compared to those obtained under the non-pulsatile conditions (46.50 mW). However, this difference was less than 5% of the non-pulsatile losses, which might be deemed reasonable. Furthermore, the maximum recorded pressure drops and power losses across the cardiac cycle remained within 50% of the time-averaged values, and were associated with the early phases of the cardiac cycle when both pressure drops and inflow rates were the highest.

8.4 Patient 2 (CHOP 068): Intra-Atrial TCPC

The second Fontan patient retained for this study was a 6 year old female with a normal systemic venous return and pulsatility levels of the same order of magnitude as Patient 1. This patient test-case was retained to assess the impact of flow pulsatility in a typical intra-atrial configuration, which typically results in more irregular TCPC geometries and more flow mixing at the connection site than extra-cardiac TCPCs.

8.4.1 *In Vivo* Data

Patient 2 had undergone a hemi-Fontan connection in stage 2 followed by an intra-atrial completion of the TCPC in stage 3. The *in vivo* TCPC anatomy as reconstructed from the anatomical MRI data is shown in Figure 8-19. The patient's heart rate was 68 beats per minute corresponding to a cardiac cycle duration of 883 ms. The *in vivo* inlet/outlet flow rates and the 3D *in vivo* velocity field reconstructions were obtained from PC MRI measurements acquired at 25 time points in the cardiac cycle. The time-dependent *in vivo* flow measurements are illustrated by the full symbols in Figure 8-20, where they are expressed in terms of the time-dependent cardiac output (computed as the sum of the instantaneous IVC and SVC flow rates) and flow distributions. The mean cardiac output was 1.08L/min, with an average mass flow split of 68/32 IVC/SVC and 58/42 RPA/LPA. All geometric and flow characteristics are summarized in Table 8-4.

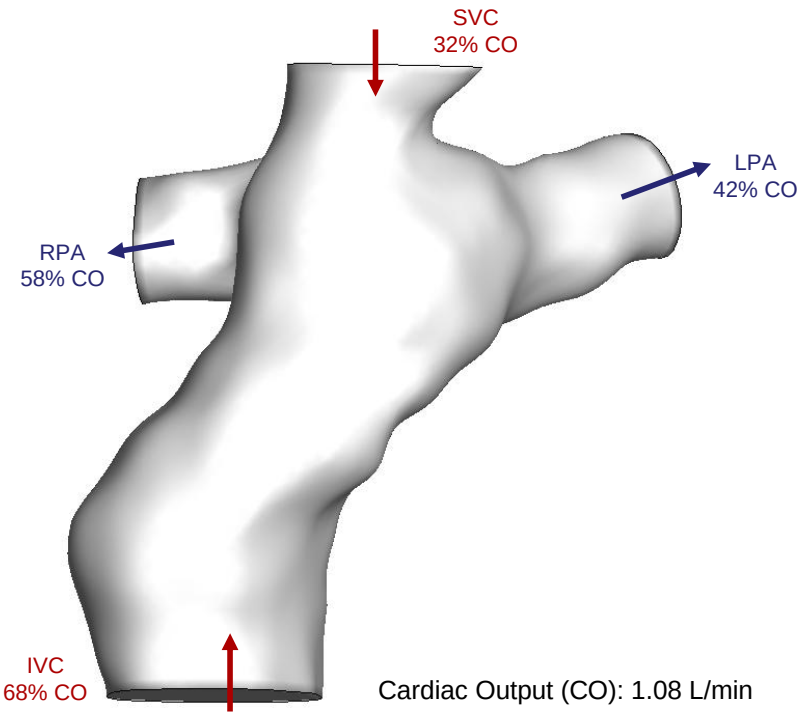

Figure 8-19: Intra-atrial TCPC geometry of the second patient test-case retained for the pulsatile investigation.

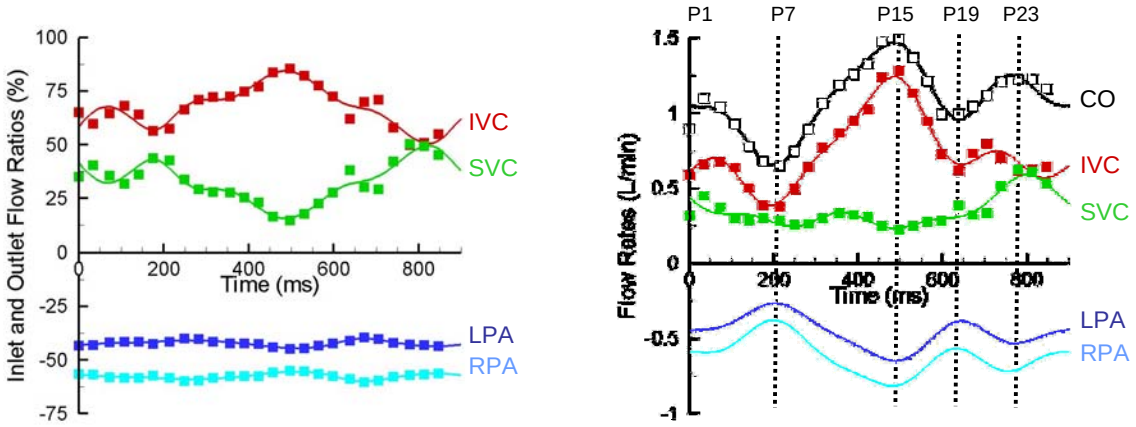

Figure 8-20: Inlet and outlet flow conditions for the patient-specific extra-cardiac anatomy. The full symbols denote the *in vivo* PC MRI measurements, while the continuous lines denote the boundary conditions imposed on the CFD simulations. The dotted vertical lines indicate the time-points retained in the subsequent figures.

Table 8-4: Geometric and CFD flow characteristics at the two inlets (IVC and SVC) and outlets (RPA and LPA) of the patient-specific intra-atrial TCPC.

Vessel		IVC	SVC	LPA	RPA
Area (cm^2)		3.37	1.61	0.75	0.77
Flow Rate (L/min)	Mean	0.74	0.34	0.46	0.62
	Max	1.28	0.62	0.27	0.38
	Min	0.37	0.22	0.67	0.83
Pulsatility index		61.0%	58.3%	43.5%	36.0%

8.4.2 Numerical Set-Up

Following the same procedure as for Patient 1, the CFD inlet boundary conditions are prescribed to match the *in vivo* IVC and SVC flow rate measurements, while the outlet boundary conditions are computed based on the *in vivo* RPA/LPA mass flow ratios. The inlet and outlet flow distributions and flow curves used in the CFD simulations are shown by the continuous lines in Figure 8-20. It may be noted that the amplitude of the flow rate variations are about twice larger in the IVC than in the SVC or any of the PAs. However, since the IVC is also the vessel that has the largest mean flow rate, the IVC pulsatility index (61.0%) is of the same order as that of the SVC (58.3%). The IVC flow rate reaches its peak at t = 497 ms, which also corresponds to the minimum SVC flow rate. The peak SVC flow rate occurs towards the end of the cardiac cycle at t = 795 ms. The flow distribution to the LPA and RPA is almost uniform through the cardiac cycle, varying between 40-45% for the LPA and 55-60% for the RPA. As a result, the two outlet flow curves closely follow the trend of the cardiac output flow curve.

In the simulations, all quantities are normalized based on mean velocity and equivalent hydraulic diameter of the IVC, D_{IVC}, yielding a characteristic Reynolds

number Re=217, a Womersley number α=14.8 and a non-dimensional cardiac cycle duration T=1.56. The TCPC surface is discretized with 12,666 triangular surface elements, and the background Cartesian mesh with a resolution $h = 0.02D_{IVC}$. Calculations are conducted using a non-dimensional time step $\Delta t = 0.000782$, which corresponds to 2,000 time steps per cardiac cycle. Non-pulsatile simulations are conducted as well, using the time-averaged cardiac output and flow distributions, and the same spatial and temporal resolution as above.

As will be discussed below, the inlet velocity profiles in the *in vivo* 3D PC MRI measurements were not aligned with the vessel axis but rather significantly skewed towards the RPA at the SVC inlet and towards the left at the IVC inlet. In order to improve the correspondence between the CFD and *in vivo* measurements, the mean *in vivo* flow direction was computed by averaging the PC MRI measurements over a slice at the IVC and SVC inlets and over the cardiac cycle, and used as the main flow direction for the CFD inlet boundary conditions.

8.4.3 3D Flow Structures

The *in vivo* flow structures as reconstructed from the coronal PC MR images are shown in the top row of Figure 8-21, using 3D streamtraces color-coded by their vessel of origin. These flow structures are shown for five time-phases, corresponding to the time-points indicated in Figure 8-20. Phase P7 corresponds to the first local minimum in the IVC flow curve, phase P15 to the peak IVC flow rate, phase P19 to the second local minimum in the IVC flow curve and phase P23 to the peak SVC flow rate.

The *in vivo* flow structures (top row in Figure 8-21) are characterized by: a large vortex along the right aspect of the connection site (region A), a large flow separation region in the intra-atrial baffle with hardly any IVC streamtraces (region B), and finally a preferential distribution of the green SVC streamtraces to the RPA, while the orange IVC streamtraces split between the LPA and RPA in region C. The flow separation region in the intra-atrial baffle finds its roots in both the local expansion of the intra-atrial conduit, which bulges out at that location, and the skewed IVC profile at the entrance of the connection, which is preferentially oriented towards the left. The SVC flow, on the other hand, enters the TCPC with a preferential orientation towards the right. As a result, even though the intra-atrial baffle appears not to have any significant offset, the two IVC and SVC flows do not enter the connection region along the same axis for a head-on collision, but rather on two parallel axes, the IVC flow more to the left and the SVC more to the right, resulting in the formation of the large counter-clockwise vortex in region A. The size of this vortex varies across the cardiac cycle, depending on the relative velocities of the IVC and SVC streams. It expands from phases P1 to P15, going through the local minimum of the IVC flow curve and the peak IVC flow rate. It seems to almost disappear during the strongest flow deceleration phase (P19) and re-appears towards the end of the cardiac cycle (P23) as the IVC flow rate starts to increase again.

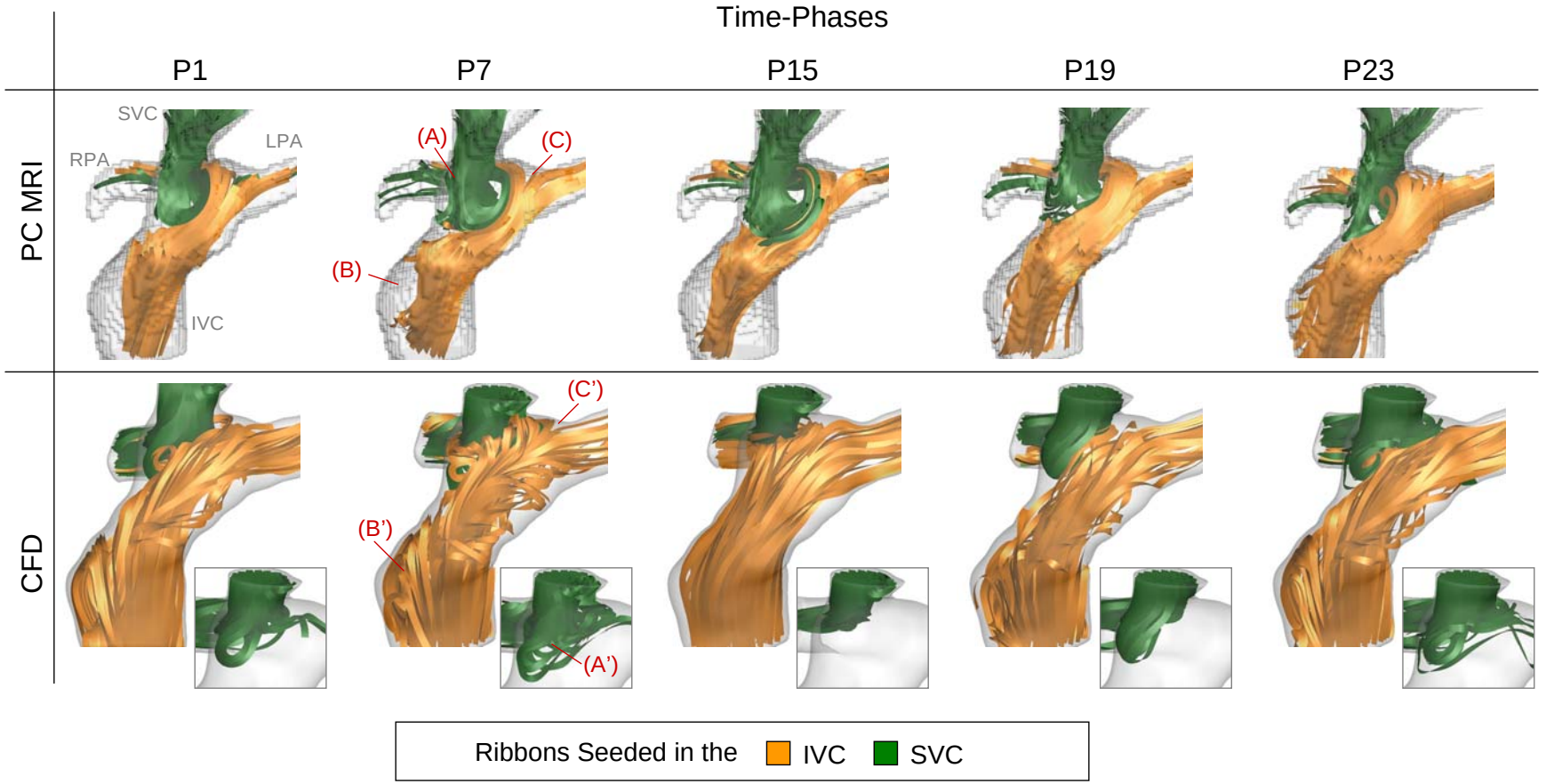

Figure 8-21: Global flow structures as reconstructed from the coronal PC MRI images (Top) and as computed by CFD (Bottom) for five time phases across the cardiac cycle. The 3D streamtraces color-coded by their vessel of origin (IVC: orange; SVC: green). Letters A, B and C point to the flow structures discussed in the text. The dynamic PC MRI and CFD flow structures may also be visualized in Animation 8-7 and Animation 8-8, respectively.

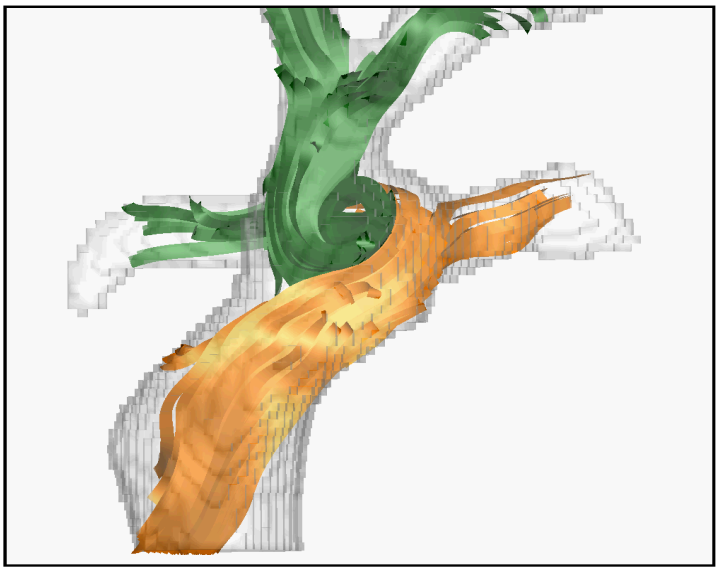

Animation 8-7: Dynamic visualization of the global *in vivo* flow structures as reconstructed from the coronal PC MRI images. The 3D streamtraces color-coded by their vessel of origin (IVC: orange; SVC: green).

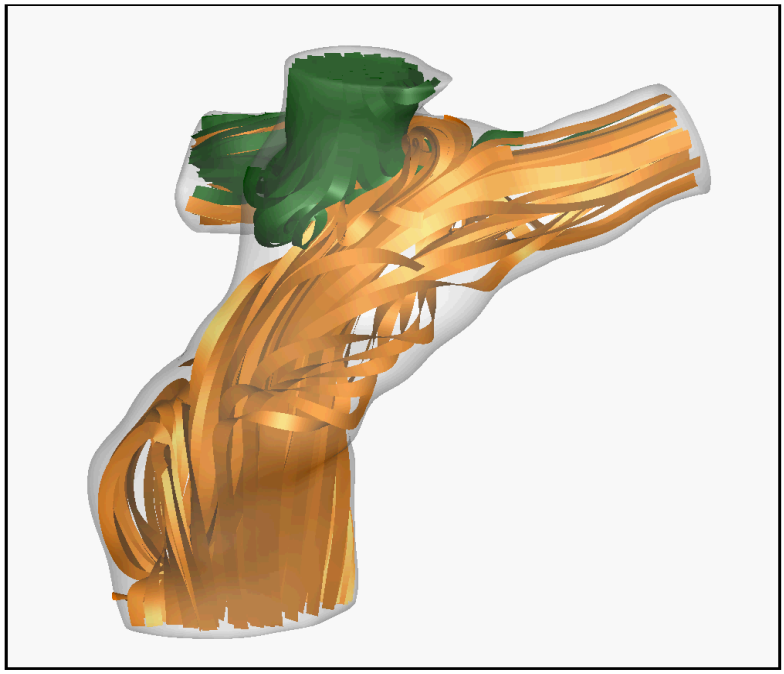

Animation 8-8: Dynamic visualization of the pulsatile CFD flow structures. The 3D streamtraces color-coded by their vessel of origin (IVC: orange; SVC: green).

The 3D flow structures obtained from the pulsatile CFD simulations for the same five instants in time are illustrated in the bottom row of Figure 8-21 (animation included). For each time phase, an insert shows the SVC streamtraces alone to better visualize the dynamics at the center of the connection. The dominant CFD flow patterns are in good agreement with the PC MRI measurements, including: 1) a region of flow recirculation at the center of the connection (region A'), where the SVC streamtraces recirculate prior to exiting towards the RPA (see inserts for phases P1, P7, P19 and P23); 2) a flow separation region on the right side of the IVC baffle, in which IVC streamtraces get entrapped and recirculate (region B'); and 3) a flow stagnation point on the posterior wall of the LPA, from which the IVC streamtraces split between the right and left pulmonary branches (region C').

On the other hand, the maximum expansion of the central recirculation is significantly smaller in the CFD simulations (A') than in the PC MRI flow fields (A). In addition, in the CFD simulations, this vortical region is the largest in phase P7 when the IVC flow rate is the lowest, and tends to disappear as the IVC flow increases towards its peak (P15), whereas the opposite trend is observed in the PC MRI measurements. The extent of this central recirculation region is dictated by the competition between the IVC and SVC streams, which is turn dictated by the main IVC and SVC flow direction and velocity profiles. The choice of inlet velocity profiles is a key determinant for the computed velocity fields, especially for the SVC whose inlet fell close to the domain of interest. Efforts were made in the present simulations to match the global orientation of the flow at the IVC and SVC inlets. However, the inlet velocity profile in the PC MRI data was highly non-uniform, showing two local peaks, which most likely correspond to

the independent contribution of the right SVC and innominate veins to the global superior venous return. The contribution of each one of these two vessels varies across the cardiac cycle, impacting the global flow direction and its spatial distribution. Further refinement of the CFD simulations could thus entail extending the computational domain so as to include the main vascular branches upstream of the region of interest, or interpolating the PC MRI velocity profiles.

Figure 8-22 compares the time-averaged pulsatile flow structures to the results obtained in the non-pulsatile simulations, conducted under the mean inflow and outflow conditions. The time-averaged pulsatile results display all the major features identified in the instantaneous pulsatile flow fields, namely a flow separation on the right side of the IVC baffle, a preferential orientation of the IVC flow towards the LPA and a preferential orientation of the SVC flow towards the LPA. The non-pulsatile results very closely reproduce the time-averaged flow fields, hinting towards a small impact of the flow pulsatility on the global hemodynamic performance of the connection.

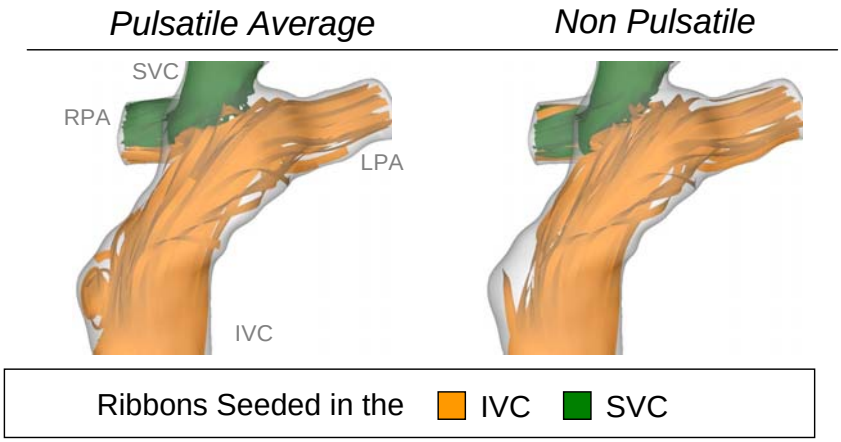

Figure 8-22: Comparison of the time-averaged pulsatile flow structures to the results obtained in the non-pulsatile simulations conducted under the mean flow conditions. Streamtraces are color-coded by their vessel of origin (orange: IVC; green: SVC).

8.4.4 Power Losses

Table 8-5 summarizes the pressure measurements at the inlets and outlets of the intra-atrial geometry and the associated power losses, for both the pulsatile and non-pulsatile flow fields. The non-pulsatile values are in remarkable agreement with the mean pulsatile measurements. This observation is in line with the similarities observed in the previous section between the time-averaged pulsatile flow structures and their non-pulsatile counter part. The maximum pulsatile pressure drops in the LPA and RPA are of less than 0.4 mmHg, which is well within the clinically accepted range for a successful Fontan. The maximum power loss is 7.893 mW and is associated with the peak flow rate.

Table 8-5: Pulsatile and non-pulsatile power losses for the intra-atrial TCPC

		Pressure in reference to the IVC (mmHg)				Power Loss (mW)
		IVC	SVC	LPA	RPA	
Pulsatile	Average	0	0.004	-0.100	-0.125	1.291
	Max	*0*	*0.173*	*-0.354*	*-0.310*	*7.893*
Non Pulsatile		0	0.003	-0.097	-0.121	1.292

8.4.5 Particle Tracking

In order to better visualize the flow pathways followed by blood-borne elements and quantify the IVC flow distribution and particle residence time, particles were released at the IVC and SVC inlet cross-sections every 55 ms for ten consecutive cardiac cycles. The number of particles released was 1,900 in the IVC and 800 in the SVC. In order to assess the impact of flow pulsatility on the metrics of interest, this particle tracking approach was applied to the instantaneous pulsatile flow fields as well as to the pulsatile time-average and to the non-pulsatile results.

The particle pathways under pulsatile conditions are shown in Figure 8-23 and Animation 8-9. Their non-pulsatile counterpart is shown in Figure 8-24. In both figures, the SVC particles are color-coded in black, while the IVC particles are color-coded by their seeding-time. To ease the comparison, the same color-scale is used in the two figures, where particles seeded before t = 883 ms (which corresponds to the first cardiac cycle for the pulsatile simulations) appear in dark blue, and particles seeded around 1,700 to 1,766 ms (which corresponds to the end of the second cardiac cycle in the pulsatile simulations) appear in red. A large number of similarities can be observed between the pulsatile and non-pulsatile results. Particles released in the IVC first flow along the left aspect of the IVC baffle until they reach the LPA anastomosis location, where a portion of them goes into the LPA (light blue particles in P25) while the others turn towards the RPA. This corresponds to the splitting point observed with the instantaneous streamtraces (region C' in Figure 8-21). However, it is interesting to note, that the portion of IVC particles that turn towards the right do not flow directly into the RPA as was predicted by the instantaneous streamtraces but rather get entrapped in the recirculation region located below the SVC anastomosis site. IVC particles that get entrapped in that recirculation tend to stay within the TCPC fluid domain for a longer period of time than others, as is best illustrated by the large number of dark blue particles that remain in that region even towards the end of the second cardiac cycle in P25. In both pulsatile and non-pulsatile results, the light blue particles that were seeded at the beginning of the second cardiac cycle are only seen to exit the fluid domain in P25, which suggests that most particles remain within the fluid domain for at least one cardiac cycle.

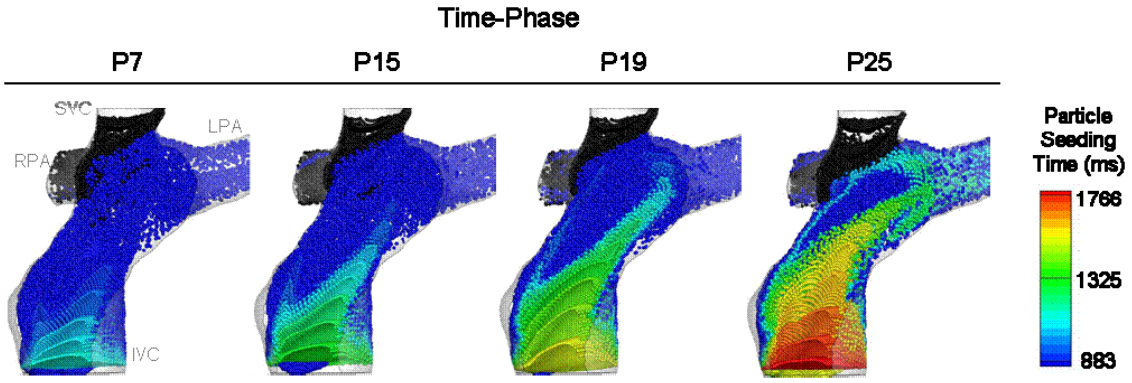

Figure 8-23: Pulsatile particle trajectories in the second cardiac cycle (t = 883 ms to 1766 ms). The SVC particles are color-coded in black, while the IVC particles are color-coded based on their seeding time. Dark blue particles thus denote particles seeded in the first cardiac cycle that are still in the fluid domain during the cardiac cycle shown here. In order to better visualize the dynamics at the center of the connection, the anterior half of the domain is blanked out of the image. An animation of the pulsatile particle pathways is included in Animation 8-9.

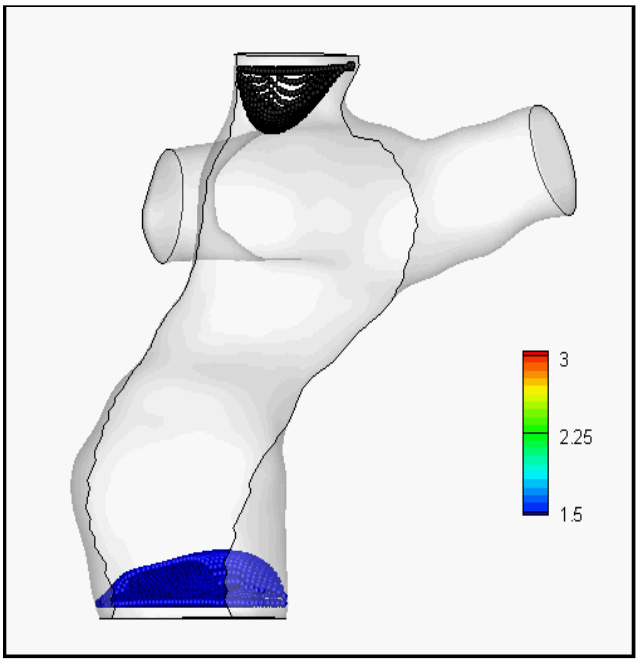

Animation 8-9: Dynamic visualization of the pulsatile particle trajectories using the same color-coding as in Figure 8-23.

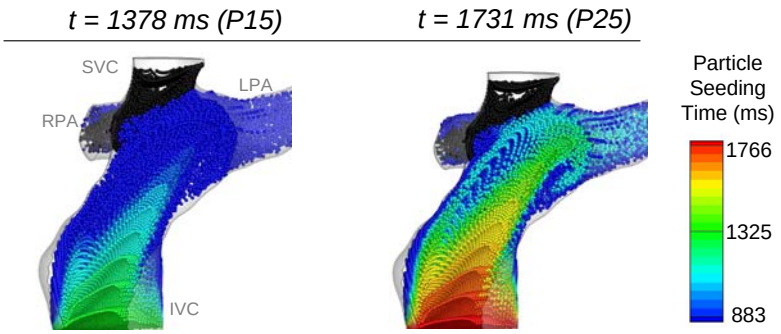

Figure 8-24: Particle trajectories through the non-pulsatile velocity fields. The SVC particles are color-coded in black, while the IVC particles are color-coded based on their seeding time. Dark blue particles thus denote particles seeded before 883 ms that are still in the fluid domain at the instants shown in this figure. P15 and P25 indicate the correspondence for the pulsatile results. In order to better visualize the dynamics at the center of the connection, the anterior half of the domain is blanked out of the image.

The main difference between the pulsatile and non-pulsatile results resides in the right side of the IVC baffle. The color-contours formed by particles released at the same time are more irregular in the pulsatile results than in the non-pulsatile ones. This reflects the fact that pulsatile flow variations do not uniformly affect the flow through a given cross-section. In addition, in the non-pulsatile simulations, the absence of pulsatile flow disturbances allows a larger portion of the light blue and green particles, seeded early in the cycle, to exit the fluid domain within the same cardiac cycle than was the case under pulsatile conditions.

8.4.5.1 Particle Residence Time

The quantitative distribution of the IVC particle residence time under pulsatile conditions is shown in Figure 8-25 and compared to the results obtained using the time-averaged pulsatile flow field and non-pulsatile results. The associated cumulative distributions are shown in Figure 8-26. As can be seen from Figure 8-25, the distribution

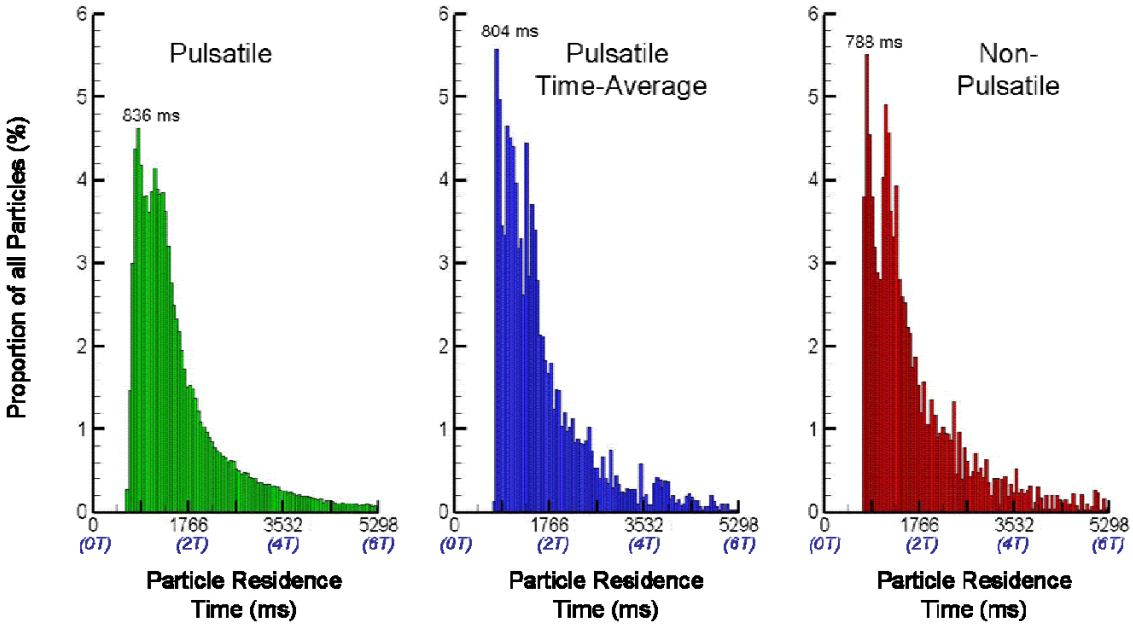

Figure 8-25: Distribution of the IVC particle residence times for the pulsatile, time average and non-pulsatile results in the intra-atrial anatomy. The number of cardiac cycles is indicated in blue below the x-axis for an easier reading.

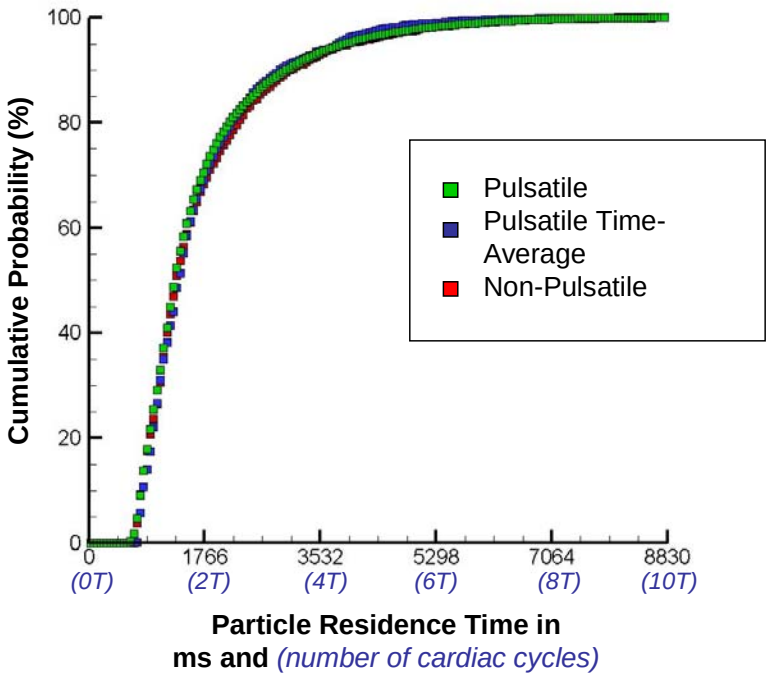

Figure 8-26: Cumulative distribution of the IVC particle residence times for the pulsatile, time average and non-pulsatile results in the intra-atrial anatomy. The number of cardiac cycles is indicated in blue below the x-axis for an easier reading.

of the particle residence times under pulsatile conditions is very similar to that obtained using the pulsatile time-average or the non-pulsatile flow fields. A main peak is observed around one cardiac cycle followed by a progressive decay until 6 cardiac cycles. The main peak corresponds to the particles flowing along the left-most aspect of the IVC baffle that enter directly into the LPA, without mixing in the center of the connection. In the pulsatile results, this peak occurs for residence times of 836 ms, with a probability of 4.6%. The non-pulsatile results predict a higher occurrence of 5.5% at slightly short residence time (788 ms). However, as can be noted from Figure 8-26, these differences are small and only have a minor impact on the cumulative distribution. The 95% probability of an IVC particle reaching either one of the PAs corresponds to t = 3,932 ms or about 4.5 cardiac cycles. Such extended residence time is worthwhile noting, especially since the particles that remain the longest in the fluid domain are the ones that get entrapped in slow recirculating fluid regions. Assuming that such particle pathway could be representative of the trajectories followed by blood cells, such extended residence time could in practice translate into higher risks of thrombus formation, allowing activated platelets to come in contact and aggregate.

8.4.5.2 IVC Flow Distribution

The distribution of the IVC particles between the LPA and RPA is illustrated in Figure 8-27 for the pulsatile, pulsatile time-average and the non-pulsatile particle tracking analyses. The LPA and RPA distributions start to rise towards the end of the first cardiac cycle, in accordance with the shortest particle residence times reported above. For all cases, the IVC flow is predominantly directed to the LPA as could be anticipated from

the flow structures and particle pathways. The non-pulsatile results over-estimate the IVC distribution to the LPA with an LPA/RPA ratio of 65/35 vs. 58/42 under pulsatile conditions. This difference stems from the differences in IVC and SVC mixing between the two flow settings. The bulgy aspect of the intra-atrial geometry favors the appearance of flow disturbances or recirculation at the center of the connection, which are further enhanced under pulsatile conditions as was noted in the particle tracking visualization (Figure 8-24). The increased mixing under pulsatile conditions allows for an IVC flow distribution that is in closer match with the global flow distribution of 42/58 LPA/RPA.

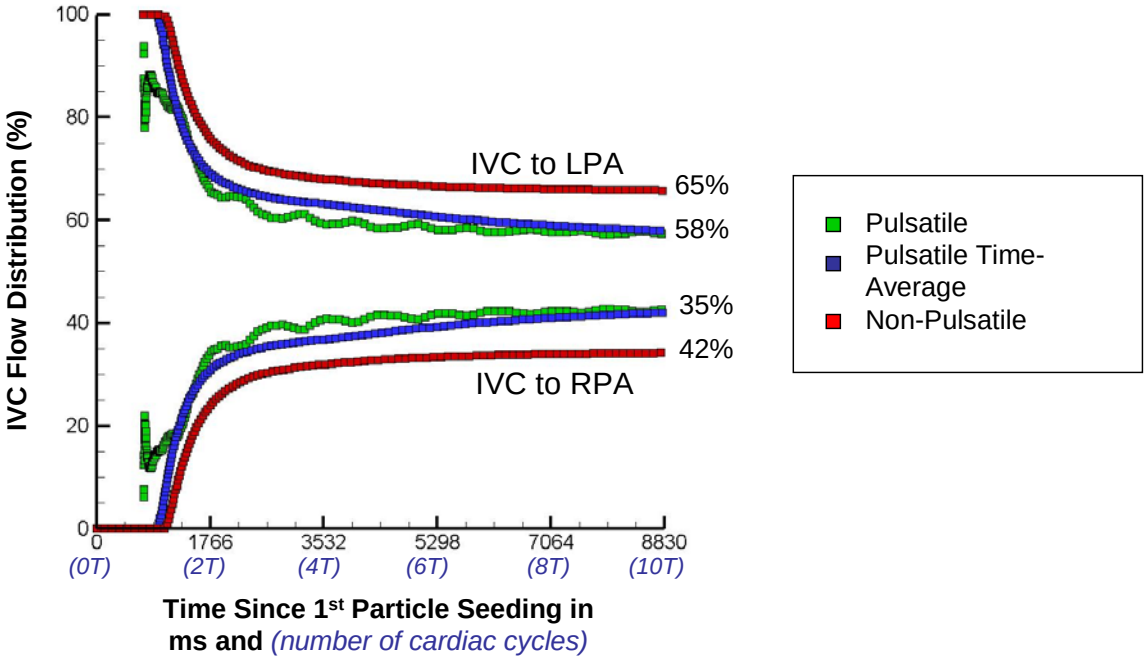

Figure 8-27: Comparison of the IVC flow distribution associated with the pulsatile flow fields, the pulsatile time-average and the non-pulsatile simulations for Patient 2. The number of cardiac cycles is indicated in blue below the x-axis for an easier reading.

8.4.6 Summary

In summary, the non-pulsatile flow fields in Patient 2 captured most of the dominant pulsatile flow structures, including the region of flow separation in the IVC conduit, the almost exclusive distribution of the SVC flow towards the RPA and the preferential orientation of the IVC flow towards the LPA. The non-pulsatile pressure drops and power losses for Patient 2 were also in excellent agreement with the mean pulsatile values. While it is evident that the non-pulsatile losses cannot provide a representation of the dynamic range covered by the pulsatile power losses over the cardiac cycle, matching the mean pulsatile power losses provides a good representation of the power requirements imposed by the TCPC on the single ventricle.

On the other hand, the use of non-pulsatile boundary conditions under-estimated the amount of flow mixing at the center of the connection, resulting in a more biased IVC flow distribution than was the case under pulsatile conditions. Such difference in IVC flow distribution was not observed in the extra-cardiac TCPC of Patient 1, which featured comparable pulsatility levels but only a very limited amount of IVC-SVC flow interactions under both non-pulsatile and pulsatile conditions. Beyond the pulsatility index, a parameter of importance for the estimation of the impact of pulsatility upon the Lagrangian metrics (namely the hepatic flow distribution) might thus be the amount of IVC-SVC flow interactions, which are naturally favored in intra-atrial connection, due to the large and bulgy baffle.

8.5 Patient 3 (CHOP M8): Abnormal Systemic venous Return and High Hepatic Flow Pulsatility

The last patient-specific case retained for our pulsatile investigation was a 6 year old male, with an interrupted IVC with azygous (AZ) continuation, a persistent LSVC, and significant flow reversal in the hepatic veins. This patient test-case was retained as a representative example of the highest levels of geometrical complexity and flow pulsatility that may be expected in an *in vivo* Fontan configuration.

8.5.1 In Vivo Data

Patient 3's TCPC anatomy is shown in Figure 8-28 together with the mean inlet and outlet flow distributions obtained from the *in vivo* PC MRI measurements. The time-dependent *in vivo* flow measurements are displayed by the full symbols in Figure 8-29. All flow and geometric characteristics are summarized in Table 8-6.

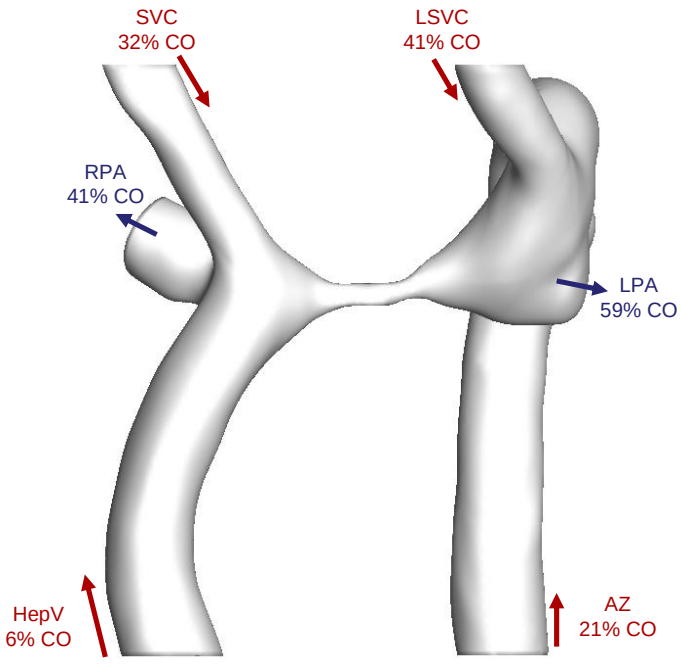

Figure 8-28: In vivo anatomy and mean flow distribution for Patient 3

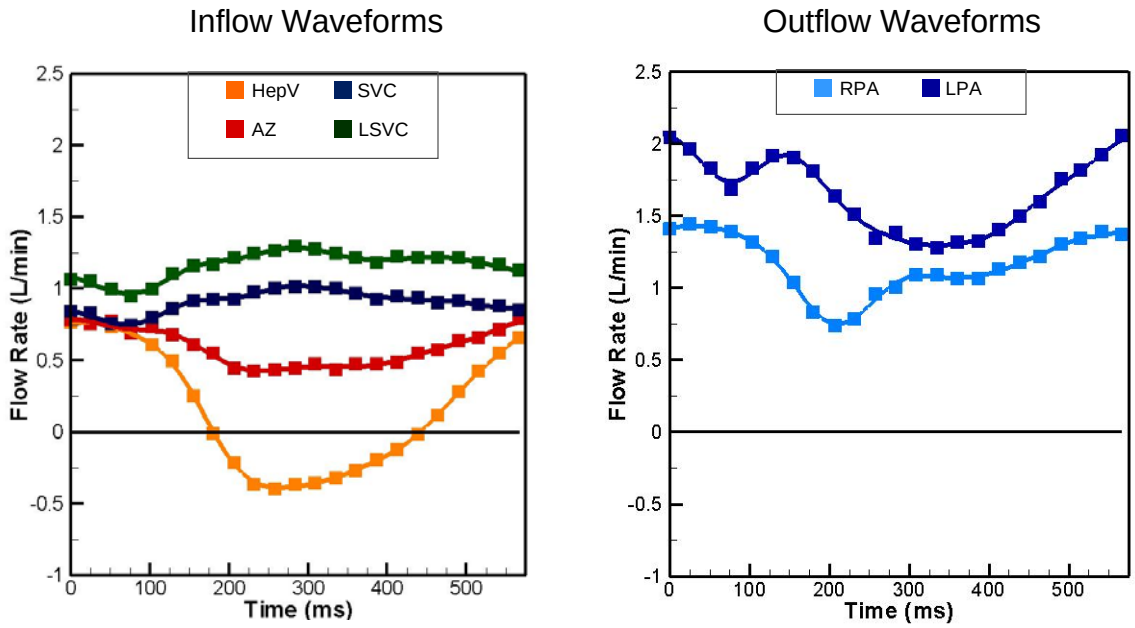

Figure 8-29: Inflow and outflow waveforms as measured by PC MRI (full symbols) and as prescribed for the CFD simulations (continuous lines).

Table 8-6: Geometric and CFD flow characteristics at the four inlets (HepV, SVC, AZ and SVC) and two outlets (RPA and LPA) of Patient 3's TCPC anatomy.

Vessel		HepV	SVC	AZ	LSVC	LPA	RPA
Area (cm^2)		1.40	0.46	1.22	0.70	0.94	0.81
Flow Rate (L/min)	Mean	0.16	0.91	0.59	1.16	1.66	1.16
	Max	0.77	1.01	0.79	1.29	2.05	1.44
	Min	-0.39	0.75	0.43	0.95	1.27	0.74
Pulsatility index		361%	15%	31%	15%	24%	30%

The patient's heart rate was 101 heart beats per minute, corresponding to a cardiac cycle duration T = 593 ms. The mean systemic venous return (i.e. the sum of the hepatic, azygous, SVC and LSVC flow rates) was 2.82 L/min distributed as follows: 6% coming through the extra-cardiac baffle, 32% through the SVC, 21% through the azygous, and 41% through the LSVC. A distinctive feature of a patient with an interrupted IVC is that the TCPC baffle only carries the hepatic venous return, while the rest of the inferior venous return is carried by the azygous vein into one of the SVCs. As a result the mean flow rate carried by the TCPC baffle is typically low (here only 6% on average), and flow fluctuations can easily translate into high pulsatility indices. For the patient case considered here, the hepatic flow rate varied by as much as 0.6 L/min around its mean value leading to a pulsatility index of 361% and hepatic flow reversal (negative flow rates in the left panel of Figure 8-29) for 232 ms out of the 593 ms of the cardiac cycle duration.

It is also interesting to note that the two lower systemic venous returns (namely the HepV and AZ) decreased concurrently, while the superior venous returns (the SVC and LSVC) followed the exact opposite pattern, increasing when the AZ and LSVC decreased. Finally, the mid-PA segment was severely stenosed with an average cross-sectional area of only 0.16 cm^2 (compared to 0.46 cm^2 for the SVC, which was the next smallest vessel), and only little flow was measured by PC MRI through that section. Looking at the flow distributions on the left side of the connection it may be noticed that the LSVC and AZ combined represent 62% of the cardiac output, which almost exactly matches the 59% exiting through the LPA. It might thus be inferred that, on average, only 3% of the cardiac output travels through the mid-PA.

8.5.2 Numerical Set-Up

For the CFD simulations, all distances are normalized by the equivalent hydraulic diameter of the HepV inlet cross-scetion, D_{HepV}. The surface of the TCPC is discretized with 69,918 triangular surface elements progressively refining the mesh towards the narrow mid-PA section. The background Cartesian grid is discretized with a resolution of $0.015D_{HepV}$, yielding a computational mesh size of 2.8 million grid cells and ensuring a minimum of 22 grid cells across the mid-PA diameter.

The characteristic velocity for the pulsatile simulations is set to be the mean HepV velocity at its peak flow rate, yielding a characteristic Reynolds number Re=344.6 and a non-dimensional cardiac cycle duration T=4.01. The Womersley number based on the hepatic baffle diameter is α=11.6. Pulsatile simulations are conducted using a non-dimensional time-step $\Delta t = 0.002$, which corresponds to 2,005 time steps per cardiac cycle. For the non-pulsatile simulations, the characteristic velocity is set to be the mean IVC velocity over the cardiac cycle, resulting in a characteristic Reynolds number Re=73.3. The non-pulsatile simulations are conducted using a non-dimensional time-step $\Delta t = 0.005$. For both sets of simulations, plug (flat) velocity profiles are prescribed at the four inflow planes and scaled to match the desired instantaneous or mean flow rates.

The inlet and outlet flow waveforms prescribed in the pulsatile simulations are shown by the continuous lines in Figure 8-29. The PC MRI measurements obtained in the LPA featured high levels of data loss, which is typically the hallmark of important flow disturbances. The measurements at that outlet were thus substituted with the LPA flow waveform was computed as:

$$Q_{LPA}(t) = \sum_{I \in \text{inflow}} Q_I(t) - Q_{RPA}(t) \tag{8-6}$$

where $Q_{LPA}(t)$, $Q_{RPA}(t)$ and $Q_I(t)$ describe the flow rates through the LPA, RPA and the inflows (namely the HepV , SVC, AZ and LSVC) at any given instant *t*. The global flow distribution favored the LPA with a 41/59 RPA/LPA flow split. Flow pulsatility in the pulmonary arteries was of the similar levels as in the AZ, LSVC and SVC with 30% pulsatility in the RPA and 24% in the LPA.

8.5.3 3D Flow Structures

The instantaneous pulsatile flow structures as obtained from the PC MRI measurements and CFD simulations are shown in Figure 8-30 for five time-points across the cardiac cycle. The flow structures are illustrated using 3D streamtraces color-coded by their vessel of origin (animation included).

As can readily be seen from Figure 8-30, PC MRI measurements in Patient 3 were discontinuous and characterized by large areas of missing data. Such PC MRI data loss is typically associated with regions of turbulent flows or important mixing, where the random directions and interactions of the moving protons results in dephasing and loss of signal coherence. Nonetheless, it is interesting to note that the regions of PC MRI data loss are in remarkable agreement with the regions of flow disturbances observed in the pulsatile CFD results. The first such region is the center of the Kawashima connection on the left, where the AZ and LSVC flow structures are illustrated by short discontinuous streamtraces in the PC MRI flow fields. In the pulsatile CFD results, this region is associated with a complex mixing of the LSVC and AZ flows, as is illustrated by the intertwined red and green streamtraces at the left connection site in phase P3, P6 and P21. In phases P12 and P18, where the AZ flow rate reaches its minimum and the LSVC its

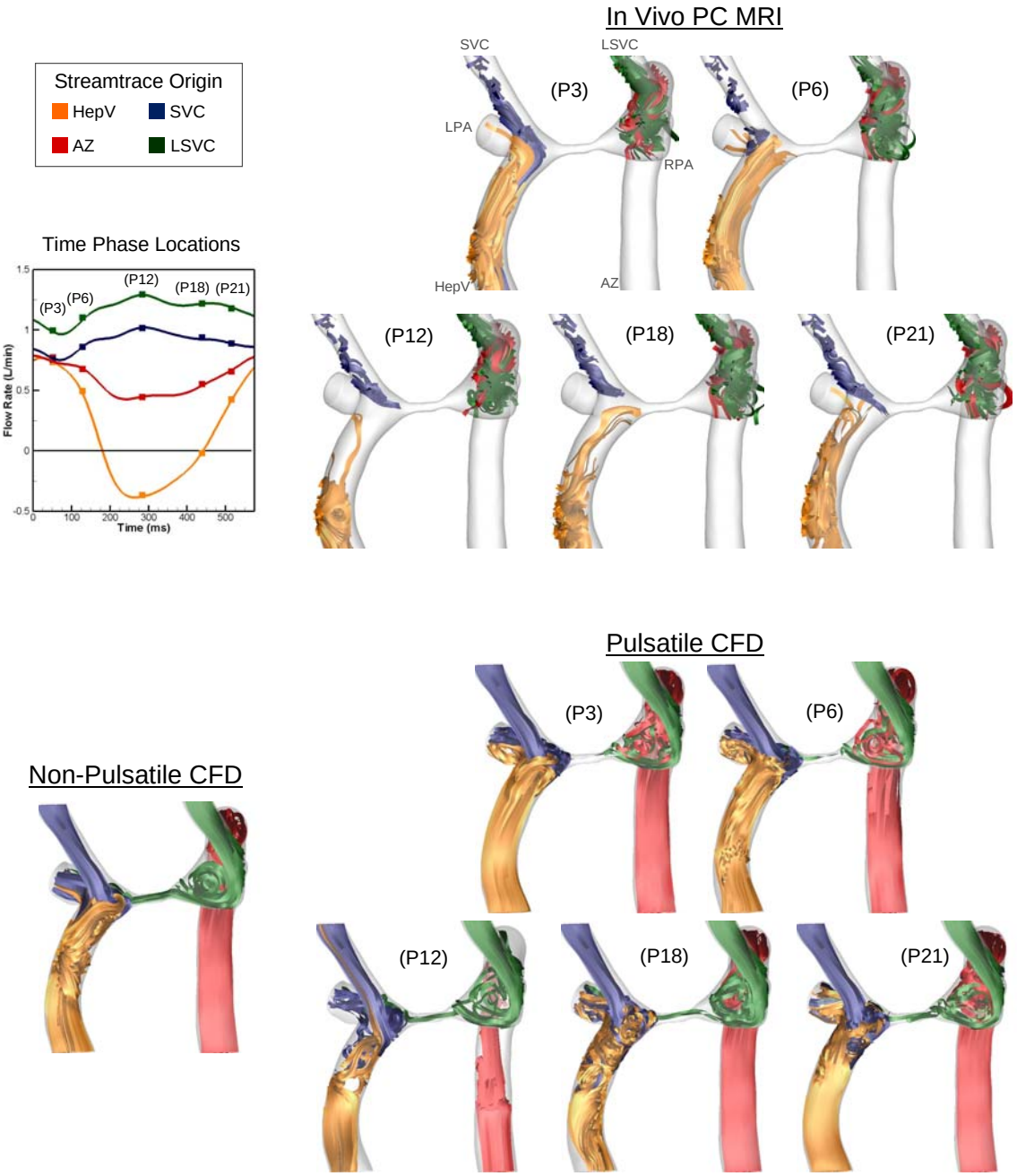

Figure 8-30: Instantaneous 3D streamtraces in the 3D PC MRI reconstruction and pulsatile CFD simulations for five time points across the cardiac cycle. 3D streamtraces in the non-pulsatile simulations are provided as a ground of comparison. For all results, the 3D streamtraces are color coded by their vessel of origin. Dynamic visualizations of the PC MRI and CFD flow structures are provided in Animation 8-10 and Animation 8-11, respectively.

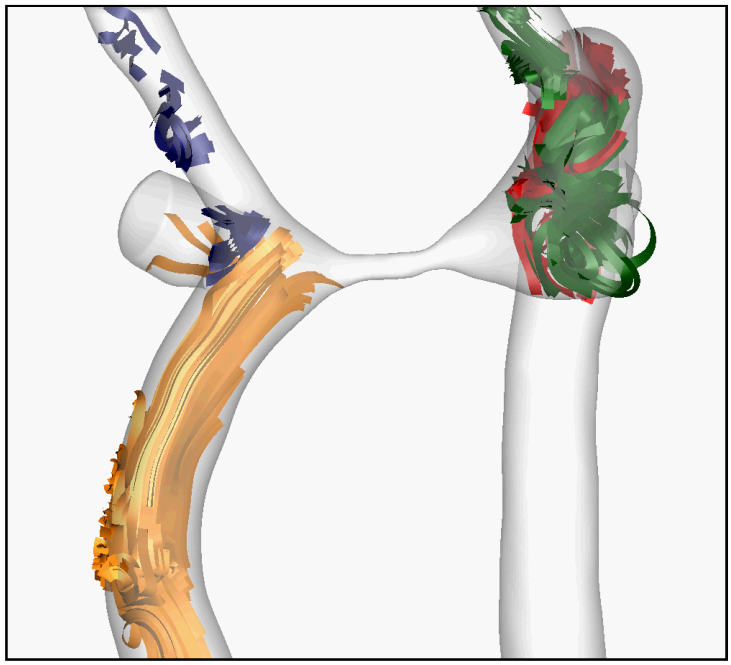

Animation 8-10: Dynamic visualization of the *in vivo* 3D flow structures as reconstructed from PC MRI.

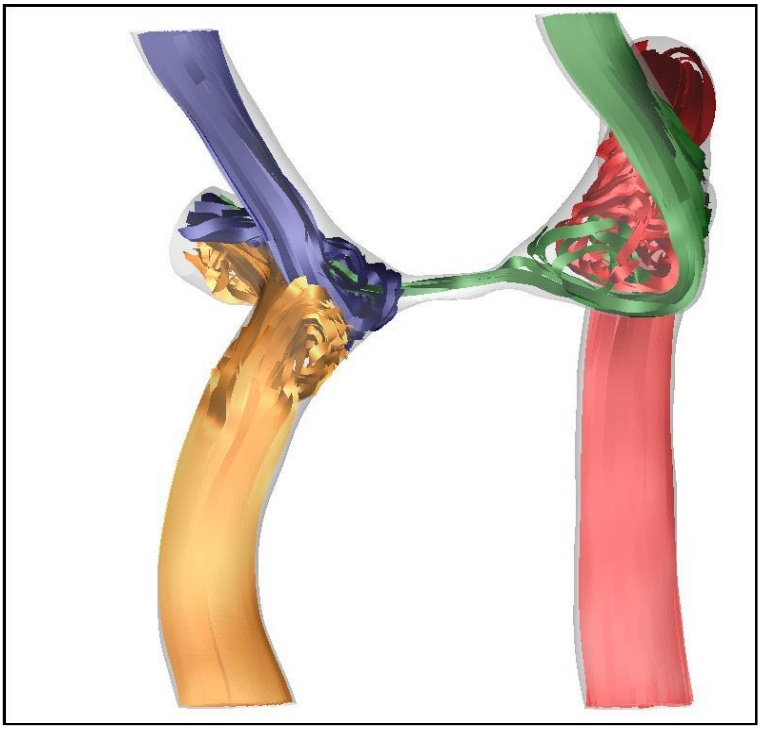

Animation 8-11: Dynamic visualization of the pulsatile CFD flow structures.

maximum, the red azygous streamtraces have little interaction with the LSVC streamtraces and flow directly into the LPA. The LSVC flow is still observed to follow a complex recirculation pattern at the center of the Kwashima connection.

The second region of major PC MRI data loss is the hepatic baffle at time phases P12 and P15, during the hepatic flow reversal, but less so in phases P3, P6 or P21. In phase P3, when the hepatic flow rate is the highest, the PC MRI hepatic streamtraces are well defined and smoothly follow the vessel axis, turning towards the RPA at the connection site. The CFD hepatic streamtraces at the same instant in time follow a very similar flow pattern with little flow disturbances at the SVC and HepV collision site. Similar quality in the PC MRI signal is observed in the early hepatic flow deceleration phase (P6), although the CFD results reveal the onset of flow instabilities halfway through the hepatic baffle. As the hepatic flow reverses in phases P12 and P15, the upper half of the hepatic baffle is the host of important flow disturbances as is illustrated by the disappearance of any coherent streamtrace in the PC MRI data, and the intertwined blue and orange streamtraces in the CFD results. These flow disturbances are due to both the destabilizing effects of flow deceleration and the deep penetration of the SVC flow (blue streamtraces) almost halfway into the hepatic baffle. It should be pointed out here, that the orange streamtraces represent the instantaneous forward and backward pathway followed by streamtraces seeded at the hepatic inlet, which should not be mistaken for the pathway followed by the hepatic nutrients. As the hepatic flow accelerates and the SVC flow decelerates (phase P21), the PC MRI hepatic streamtraces extend further into the baffle than in previous phases, flowing along the right side of the baffle towards the RPA. In the corresponding CFD results, the hepatic streamtraces recover an overall coherence,

and follow a smooth path until slightly downstream of the connection site. The SVC streamtraces still penetrate into the hepatic baffle but to a lower extent than in the previous phases. Throughout all time-phases, only little LSVC flow travels through the mid-PA segment towards the RPA, which is coherent with the global mass flow distribution between the LPA and RPA.

The non-pulsatile CFD flow structures are shown in the bottom left panel of Figure 8-30 for comparison with the instantaneous pulsatile CFD flow fields. The non-pulsatile flow fields show some of the characteristics of the pulsatile results under the low hepatic flow rates. The common features include an intense flow recirculation in the left connection site, penetration of the blue SVC streamtraces into the hepatic baffle, and flow instabilities in the extra-cardiac conduit. The recirculation in the left connection site is uniquely composed of green LSVC streamtraces, the azygous streamtraces flowing directly into the LPA with minimal interaction with the LSVC flow. The penetration of the SVC into the hepatic baffle is due to the low mean hepatic flow rate, and resultant low hepatic kinetic energy, which does not allow for the hepatic flow to compete against the SVC flow. While these flow structures do share some common traits with the pulsatile ones, they oversee the richness of the pulsatile dynamics, notably the intense flow instabilities that develop in the hepatic baffle during the reversed flow phase.

8.5.4 Power Losses

The mean pulsatile pressures and power losses over the cardiac cycle and the maximum deviations from these mean values are given in Table 8-7, together with the corresponding values obtained in the non-pulsatile simulations. In both sets of results the

left-sided pressures, namely the AZ, LSVC and LPA pressures, are more than 1 mmHg higher than the right-sided pressures in the HepV, SVC and RPA. This phenomenon is illustrated in Figure 8-31 for the non-pulsatile flow fields, where the left side of the connection is color-coded in orange and red, denoting high pressure values, while the right side of the connection is color-coded in shades of blue denoting low pressure values. The elevated left-to-right pressure gradient results from the high hydrodynamic resistance imposed by the stenosed mid-PA segment, which requires a large pressure head to ensure the desired left-to-right flow rate.

The most distinctive characteristic of this patient-case compared to the other three configurations studied in this chapter is that the non-pulsatile power losses fail to capture the mean pulsatile energy dissipation levels. Due to the highly unstable pulsatile dynamics, the mean pulsatile power loss is 18.33 mW, which is 10 mW higher than the non-pulsatile value. Maximum power losses fall significantly above that range with a peak at 45.57 mW, which coincides with the peak reversed flow in the hepatics. The pulsatile pressures significantly deviate from their mean values across the cardiac cycle, as well, with a maximum pressure difference of over 2 mmHg in the azygous. The non-pulsatile results for Patient 3 thus appear as an inadequate representation of the pulsatile dynamics.

Table 8-7: Pulsatile and non-pulsatile power losses for the TCPC with an interrupted IVC

		Pressure in reference to the IVC (mmHg)						Power Loss (mW)
		HepV	SVC	AZ	LSVC	RPA	LPA	
Pulsatile	Average	0	0.60	1.15	1.75	-1.08	0.54	18.33
	Max	*0*	*1.80*	*3.17*	*2.90*	*-2.06*	*-0.39*	*45.57*
Non Pulsatile		0	0.39	2.42	3.00	-0.91	1.81	8.54

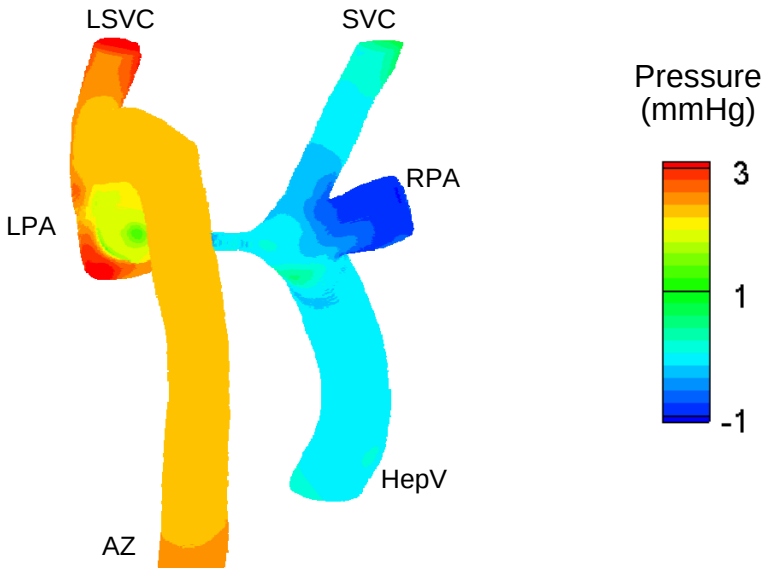

Figure 8-31: Pressure levels in the non-pulsatile flow field. Contrary to all other figures shown in this chapter, the anatomy is shown from the posterior side so as to best visualize the pressure contours in the two PAs.

8.5.5 Particle Tracking

Given the high level of flow pulsatility in the hepatic baffle, the instantaneous streamtraces visualized above only provide limited insights into the pathways followed by blood borne elements. Particle tracking was thus performed by seeding particles not only in the hepatic baffle, but also in the SVC, AZ and LSVC to better visualize the dynamic interactions and mixing between the different inflows. For the pulsatile simulations, 2535, 2015, 118 and 832 new particles were released every 15 ms for ten consecutive cardiac cycles in the HepV, AZ, LSVC and SVC cross-sections, respectively. HepV particle tracking was also performed in the non-pulsatile simulations to provide a ground of comparison for the hepatic flow distribution and particle residence times.

8.5.5.1 Dynamic Pulsatile Particle Pathways

The dynamic particle pathways as computed in the pulsatile flow fields are illustrated in Figure 8-32 and Figure 8-33 (and Animation 8-12). Figure 8-32 displays the pathways followed by particles seeded at all four inlets, with the particles color-coded by their vessel of origin, while Figure 8-33 displays the hepatic particles only, color-coded by their seeding time.

Looking at the dynamics in the left side of the connection (Figure 8-32), the mixing of the azygous and LSVC flow is illustrated by patches of red particles among the green ones in phases P12 to P21 of the second cardiac cycle. Some blue SVC particles penetrate halfway into the mid-PA segment in phases P3 to P9 (cycle 1), but do not reach the left connection site before the flow direction inverses and green LSVC particles start flowing into the mid-PA. In the second cardiac cycle, once the particle distributions start stabilizing, the particles in the mid-PA segment mostly appear in green (LSVC), which is consistent with the mean left-to-right flow direction in that section.

On the right side of the connection, the dark-blue SVC particles are seen to penetrate deep down into the hepatic baffle during the reversed flow period (P9 to P18). During the hepatic flow acceleration (from phase P21 in the first cardiac cycle to phase P6 in the second cardiac cycle), the SVC particles are expelled from the baffle but a significant proportion of them remains present in the hepatic baffle throughout the cardiac cycle. Looking at the hepatic particles (in orange), it may be noted that none of the particles seeded in the first cardiac cycle succeed in reaching beyond the first half of the hepatic conduit. The reversed flow phase results in a highly skewed particle profile (which can be taken as representative of the local velocity profile) in phases P15 and P18,

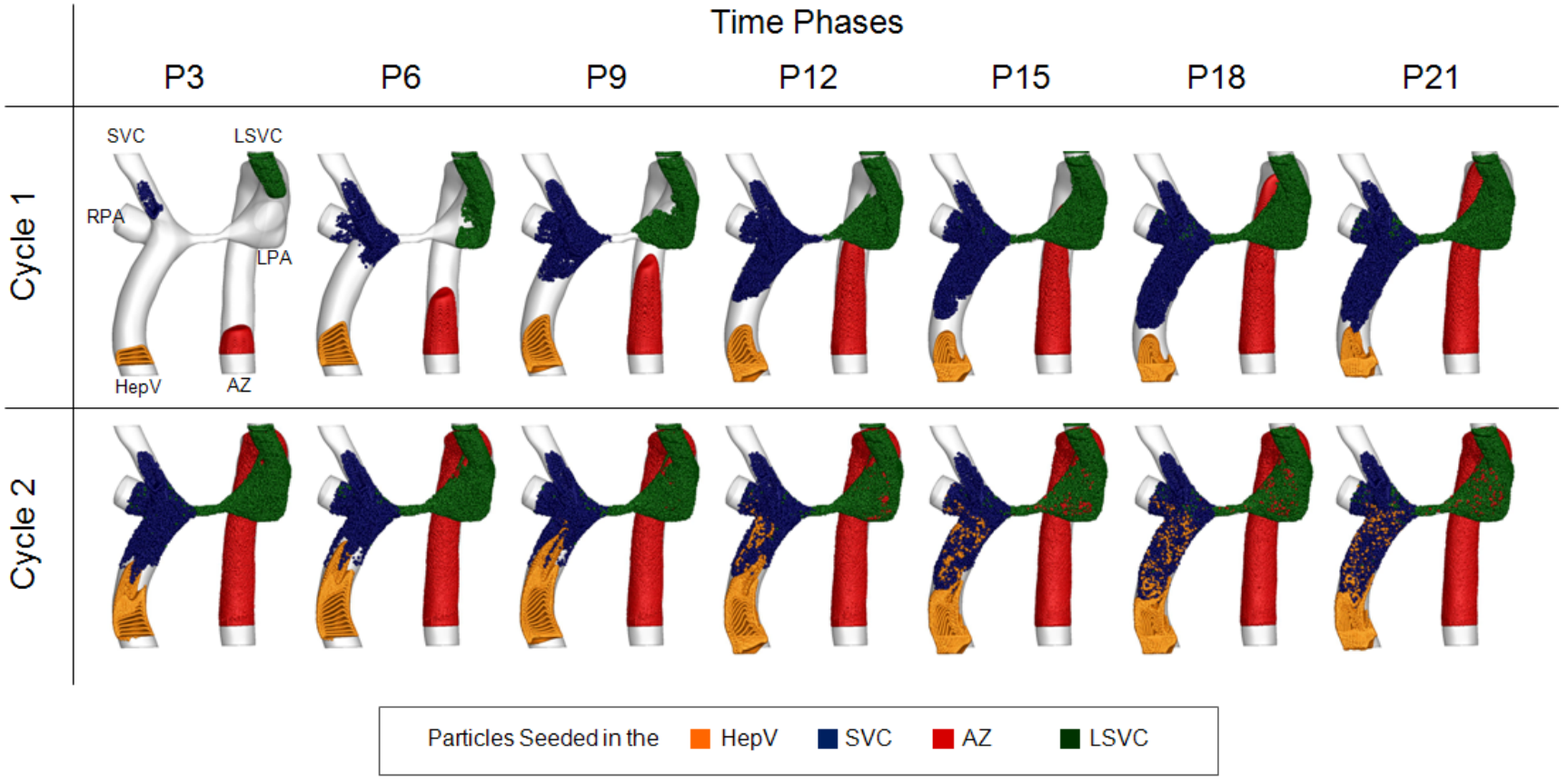

Figure 8-32: Particle positions at seven time points separated by 77 ms. The corresponding phases in the PC MRI acquisition (P3 to P21) are provided to better locate the displayed particle fields on the inflow and outflow curves. The particles are color coded by their vessel of origin to better elucidate the inflow interactions.

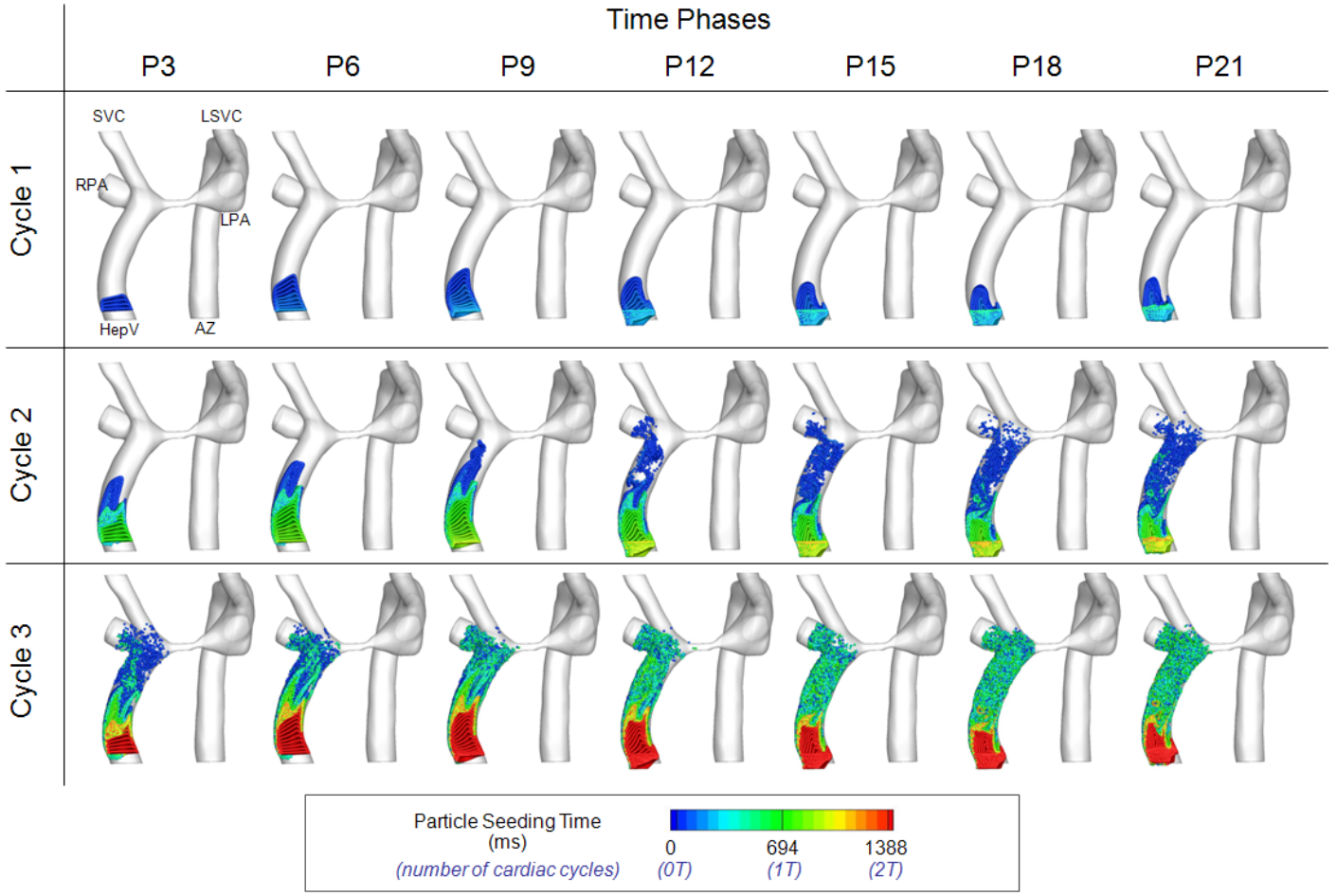

Figure 8-33: Hepatic particle positions at seven time points separated by 77 ms. The corresponding phases in the PC MRI acquisition (P3 to P21) are provided to better locate the displayed particle fields on the inflow and outflow curves. The hepatic particles are color coded by their seeding time to visualize their residence time and evolution across the cardiac cycle. An animation of the particle pathways is provided in Animation 8-12.

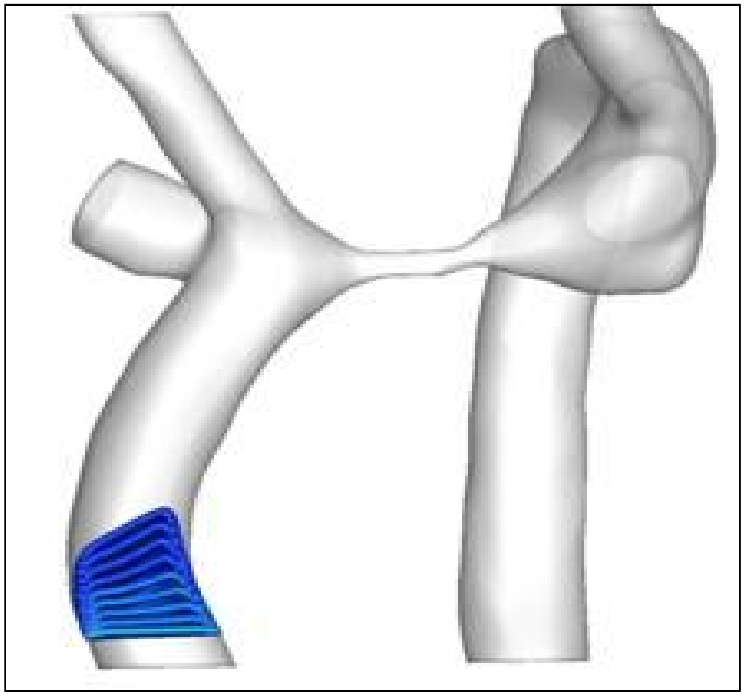

Animation 8-12: Dynamic visualization of the hepatic particle pathways. The particles are color coded by their seeding time using the same color scheme as in Figure 8-33.

with a slower particle progression rate along the inner side of the baffle curvature. In the second cardiac cycle, the first seeded particles flow up to the two third of the hepatic baffle before the hepatic flow starts reversing in P9. The hepatic particles that are the furthest up into the baffle get caught into the SVC recirculation region and are continuously ejected towards the RPA even during the reversed flow phase.

The temporal evolution of the HepV particle location is best visualized in Figure 8-33, where they are color-coded based on their seeding time. The dark blue hepatic particles seeded at the beginning of the first cardiac cycle only reach the RPA towards the middle of cycle 2, pointing to a particle residence time of 1.5 cardiac cycle or more. During the reversed flow phase, the particles closest to the inlet of the extra-cardiac conduit backflow into the hepatic veins (P12 to P18 of cycle 1). Further along the extra-

cardiac conduit, the reversed flow gives rise to high levels of instabilities and mixing which is best visualized in phases P12 to P18 of cycle 2, where the dark blue hepatic particles spread in all directions and occupy the entire upper half of the extra-cardiac baffle. Due to the low mean hepatic flow rate and alternate forward and backward flow motion, some particles remain within the extra-cardiac baffle for over two cardiac cycles, and a significant proportion of HepV particles seeded in cycle 1 can still be observed up until phase P9 in cycle 3.

8.5.5.2 Hepatic Particle Residence Time

The distribution of the hepatic particle residence times is quantified in Figure 8-34 for both pulsatile and non-pulsatile flow conditions. The pulsatile distribution (left panel in Figure 8-34) peaks around t = 1204 ms, meaning that most hepatic particles remain within the fluid domain for a little over two cardiac cycles. The residence times under steady conditions show a peak distribution for slightly longer times, around t = 1476 ms. More importantly the non-pulsatile distribution decay at a slower rate after the first peak than their pulsatile counterpart. The important mixing occurring under pulsatile conditions randomizes the pathways followed by particles seeded at different locations, yielding more uniform residence times across the particles.

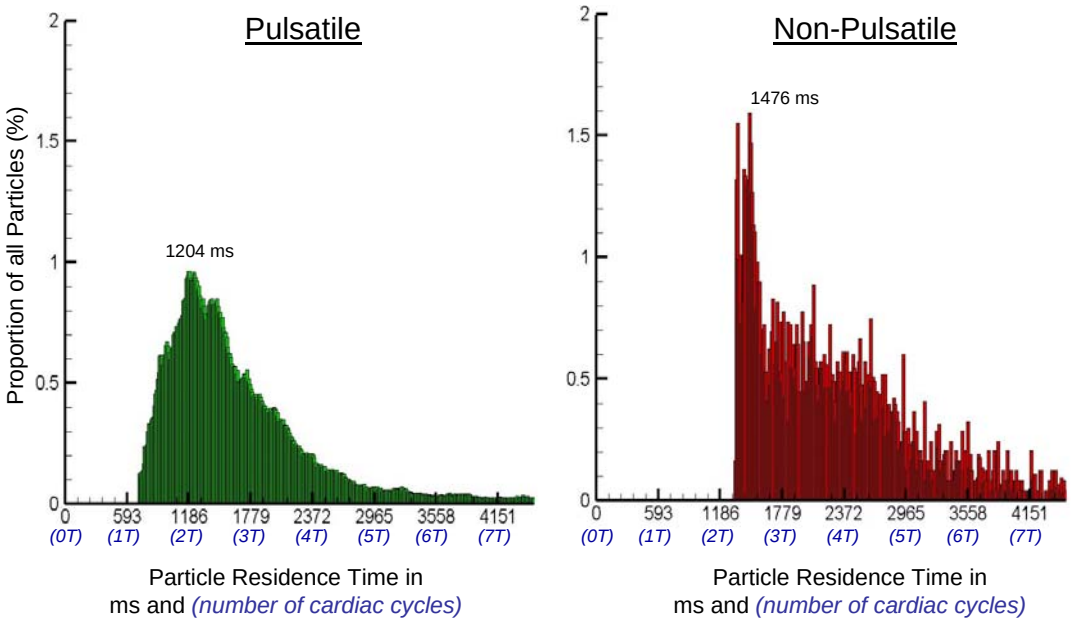

Figure 8-34: Distribution of the hepatic particle residence times for Patient 3, under pulsatile and non-pulsatile flow conditions. The number of cardiac cycles is indicated in blue below the x-axis for an easier reading.

8.5.5.3 Hepatic Flow Distribution

As could be anticipated from the fact that only very little flow was observed to travel through the high resistance mid-PA segment, the hepatic flow distribution for Patient 3 was of a 100% to the RPA under both pulsatile and non-pulsatile conditions. The perfect agreement between the pulsatile and non-pulsatile results stems from the absence of any flow going from the right to the left side of the connection, but does not imply that the non-pulsatile results provide an adequate description of the pulsatile hepatic flow distribution under pulsatility levels as high ass 631%. Indeed, as was observed in the particle tracking visualizations (Figure 8-32 and Figure 8-33), the high pulsatility of the hepatic flow leads to a thorough mixing of the hepatic and SVC streams, so that the distribution of the hepatic nutrients will follow the distribution of the combined HepV and SVC flows. This mixing is underestimated under non-pulsatile

conditions, and it might be anticipated that, in a geometry with a more balanced right and left resistance, hepatic pulsatility levels as high as the ones reported here (PI=361%) would lead to a more balanced hepatic distribution than predicted under steady conditions.

8.5.6 Summary

In summary, Patient 3 represented the most complex *in vivo* scenario considered in this study both in terms of its geometrical complexity and hemodynamics, with high levels of unsteadiness and mixing. A specificity of this patient compared to Patients 1 and 2 was that the hepatic flow was reversed for almost half of the cardiac cycle, resulting in an especially low mean flow rate through the baffle, which accounted for only 6% of the cardiac output. Hepatic flow reversal led to a deep penetration of the SVC flow down into the hepatic baffle, highly unstable dynamics, and intense mixing between the hepatic and SVC flows, all of which were significantly underestimated under non-pulsatile conditions. Although pulsatile and non-pulsatile results both predicted a peak in the hepatic particle residence time around two cardiac cycles, the thorough mixing of the hepatic and SVC flows under pulsatile conditions limited the occurrence of even longer residence times (5 or 6 cardiac cycles) that were otherwise seen in the non-pulsatile results. Furthermore, the mean pulsatile power losses were about twice those obtained under non-pulsatile conditions, unlike all three previous cases where the non-pulsatile losses appeared as a good representation of the mean pulsatile ones. Based on all of these observations, the non-pulsatile assumption does not appear acceptable when pulsatility indices reach levels as high as 361%, as was the case for Patient 3. Finally, since almost no-flow was seen to travel through the stenosed mid-PA segment, both pulsatile and non-

pulsatile results predicted that the entirety of the hepatic nutrients would flow to the RPA and into the right lung. From a clinical standpoint, such unilateral hepatic distribution sets Patient 3 at high risk for the development of pulmonary arteriovenous malformations in the contra-lateral lung (i.e. in the left lung).

8.6 Conclusion

This chapter presented a detailed comparison of the pulsatile and non-pulsatile TCPC hemodynamics and their impact on the surrogate markers for TCPC efficiency, namely power losses, hepatic (or IVC) flow distribution and particle residence time. The first test-case presented was an idealized representation of the TCPC, followed by three patient-specific studies. Although this patient pool is far too small to draw any clear-cut conclusion, non-pulsatile simulations appear to provide an adequate representation of the mean pulsatile power losses and pressure drops for moderate pulsatility indices as in the idealized geometry, Patient 1 and Patient 2. The impact of the pulsatile forcing on HFD not only depended upon the pulsatility index but also on the amount of IVC-SVC interaction. The error in the non-pulsatile HFD predictions was thus higher in the intra-atrial anatomy, which naturally favored flow unsteadiness and IVC-SVC mixing due to its irregular geometry, than in the idealized or extra-cardiac geometries for which the IVC-SVC interactions were very limited. Finally, when flow pulsatility reaches levels as high as 361% (as was the case for Patient 3), the non-pulsatile assumption clearly fails to represent the pulsatile dynamics, significantly underestimating the amount of flow mixing, unsteadiness and energy dissipation. A detailed discussion of the impact of pulsatility on the TCPC efficiency metrics is provided in Section 10.2.

CHAPTER 9

PATIENT-SPECIFIC SURGICAL PLANNING

In this chapter, we present a novel surgical planning approach based on hemodynamic performance and underscore the potential benefits of such an approach to treat patients with complex single-ventricle heart defects (SVHD). We focus our attention on SHVD patients with an interrupted inferior vena cava (IVC). The chapter is divided into three main sections. The first section presents the clinical problem and the patient groups retained for the study. The two subsequent sections present the surgical planning results for our two groups of patients, namely patients with a single SVC and patients with persistent LSVC. The chapter closes with a summary of the main findings.

9.1 Patient Selection

9.1.1 Clinical Problem

SVHD patients featuring an interrupted inferior vena cava (IVC) with azygous vein (AZ) continuation are one of the most challenging subgroups of SVHD patients from a clinical and surgical perspective. These patients feature a highly abnormal systemic venous return where all systemic blood flow from the lower limbs is directed to the AZ instead of the IVC. Furthermore, an interrupted IVC is often associated with complex heterotaxy syndromes where the vascular structures and bowels do not follow their normal orientation. These patients thus combine complex intra-cardiac SVHDs with

a large number of anatomical and flow abnormalities, making it even more difficult for surgeons to identify the best-suited surgical approach.

This patient subgroup has been reported with an especially high incidence of pulmonary arterio-venous malformations (PAVMs) after completion of the total cavopulmonary connection (TCPC) [182]. PAVMs are intrapulmonary arterial to venous shunts, which bypass the pulmonary gas exchange units, resulting in a net decrease in oxygen saturation. PAVMs also lead to a drop in pulmonary vascular resistance, which tends to direct more flow to the diseased lung, creating a positive feedback loop of increasing hypoxemia.

Although the underlying mechanism leading to PAVMs is unknown, studies have shown PAVMs to be correlated with an insufficient supply in liver derived factors present in the hepatic venous blood [14, 67, 69, 70]. Appearance of PAVMs after TCPC completion is thus attributed to an unbalanced hepatic flow distribution (HFD) to the left and right lungs due to an inadequate design of the hepatic baffle. Once the extent of PAVMs is such that oxygen saturation is critically low, the only palliative option is to re-operate and re-orient the hepatic baffle to achieve a better HFD [67]. Although several approaches for this palliative surgery have been proposed and discussed in the literature, there is still no consensus as to the best surgical approach to adopt for a specific patient. The small patient population and the large number of anatomical and functional variations pose a severe obstacle to the establishment of surgical guidelines from clinical studies alone. This is the exact setting where hemodynamics, via the HFD to the left and right lung, could make or break the surgery, and where virtual surgical-planning could make a significant clinical impact.

9.1.2 Patient Groups

Six single-ventricle patients with interrupted IVC and severe PAVMs were enrolled in the study. All six patients were recommended for surgical planning in order to identify the TCPC option that would best distribute the hepatic flow to the two lungs and lead to the disappearance of the existing PAVMs. The TCPC geometries at the time of PAVM diagnosis are shown in Figure 9-1. For clarity, each TCPC geometry is identified by three key parameters: the location of the PAVMs as per clinical diagnosis, the patient code name in the Georgia Tech Fontan patient database (CHOP M1 for instance), and the imaging modality used to capture the anatomy (magnetic resonance imaging, MRI, or X-ray computed tomography, CT).

The TCPC anatomy comprises the left and right pulmonary arteries (LPA and RPA, respectively) and the systemic veins, namely the hepatic veins (HepV), the azygous vein (AZ), the superior vena cava (SVC) and the innominate vein (IV). In a normal systemic venous configuration, the venous return from the lower limbs is carried by the IVC and the AZ only drains the deoxygenated blood from the posterior walls of the abdomen and the thorax into the SVC. The AZ is thus normally of small dimensions, and minimally contributes to the total systemic venous return. In patients with an interrupted IVC, on the other hand, the AZ is the carrier of all lower systemic venous return. As can be observed in Figure 9-1, the dimension of the AZ in these patients is comparable to that of the other systemic veins. For SVHD patients with an interrupted IVC, the staged

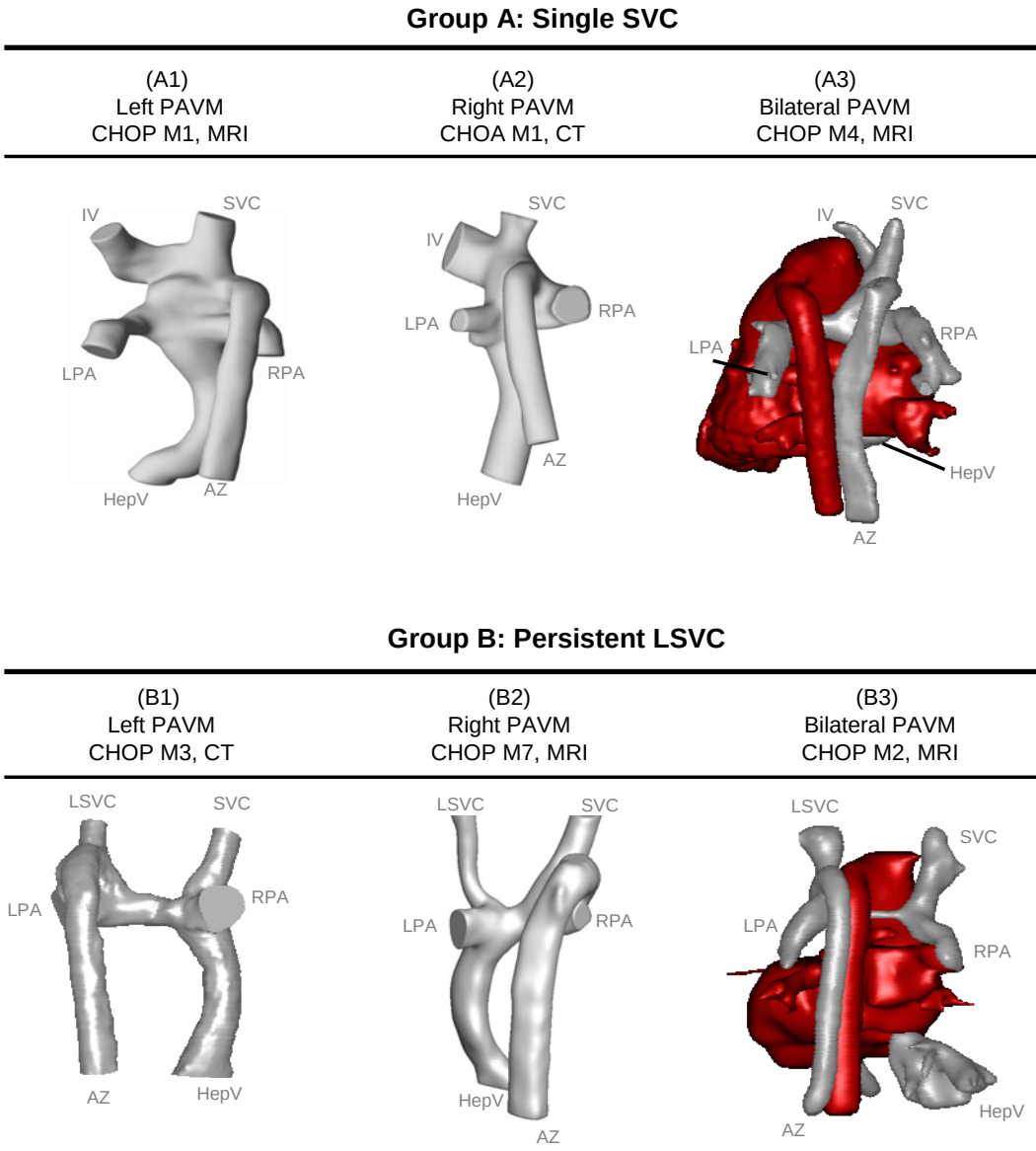

Figure 9-1: Patient TCPC anatomies. The geometries are identified with the location of the PAVMs as per clinical diagnosis, the patient code name in the Georgia Tech Fontan patient database, and the imaging modality used to capture the anatomy. The right most-column shows the heart anatomy in red.

TCPC procedure entails first the connection of the all superior venous returns (including the IV, SVC and AZ) to the PAs, and then the connection of the HepV. The superior cavopulmonary connection in presence of a large AZ is typically called the Kawashima connection.

The six enrolled patients are separated into two groups. Group A, or single SVC group, includes the three patients for whom the SVC, AZ and IV merge together before connecting to the PAs. Group B includes the three patients who feature an additional systemic venous abnormality in the form of a persistent left superior vena cava (LSVC). The corresponding anatomies (B1 through B3 in Figure 9-1) are characterized by the fact that, first, the IV is absent and then, the left superior venous return drains into the LSVC, which is connected to the PAs at a different location than the SVC.

9.1.3 Patient Data

The clinical and anatomical characteristics of the six patients enrolled in the study are summarized in Table 9-1. Patients A1, A2, B1 and B2 had a completed TCPC and were diagnosed with severe unilateral PAVMs. Patient A3 was still at the Kawashima stage. Patient B3 had previously undergone a TCPC that had been taken down due to a clot in the hepatic baffle. Accordingly, the anatomical reconstructions shown in Figure 9-1 for Patients B3 and A3 do not feature a hepatic baffle. Both A3 and B3 were diagnosed with bilateral PAVMs.

Table 9-2 summarizes the *in vivo* velocity information available for each patient. For patients A1, A3, B2 and B3 flow information was available from MRI for all TCPC vessels. Patients A2 and B1 had coils or pacer wires and could not be exposed to

Table 9-1: Summary of the clinical and geometrical characteristics of the six patients enrolled in the study. EC TCPC: completed TCPC with an extra-cardiac baffle. IA TCPC: completed TCPC with an intra-atrial baffle.

		Group A: Single SVC			Group B: Persistent LSVC		
		A1	**A2**	**A3**	**B1**	**B2**	**B3**
GT codename		CHOP M1	CHOA M1	CHOP M4	CHOP M3	CHOP M7	CHOP M2
Sexe		Female	Male	Female	Female	Male	Female
Age		4	6	3	12	11	4
Anatomy		Heterotaxy, Dextrocardia	Heterotaxy	Heterotaxy, Levocardia	Heterotaxy	Heterotacy, Dextrocardia	Heterotaxy
TCPC Stage		EC TCPC	IA TCPC	Kawashima	EC TCPC	EC TCPC	Kawashima (TCPC taken down)
PAVM		Left	Right	Bilateral	Left	Right	Bilateral
BSA		0.61 m^2	0.75 m^2	0.635 m^2	0.73 m^2	1.22 m^2	0.64 m^2
Vessel Dimensions (cm^2)	HepV	1.96	2.46	1.91	3.67	2.76	4.62
	IV (or LSVC)	1.09	1.83	n/a	1.94	0.57	1.01
	AZ	1.03	1.31	0.58	1.01	1.81	0.86
	SVC	1.13	1.26	1.34	1.46	1.16	1.29
	LPA	1.56	0.81	0.76	2.68	1.78	1.21
	RPA	1.06	2.41	1.28	3.55	0.98	0.84

Table 9-2: Flow boundary conditions. Patient specific data are denoted in black, while the gray figures denote missing flow information that was taken to be identical to patient A1.

		Group A: Single SVC			Group B: Persistent LSVC		
		A1	**A2**	**A3**	**B1**	**B2**	**B3**
Q_S		3.43 L/min	3.43 L/min	3.86 L/min	3.25 L/min	3.95 L/min	2.93 L/min
Flow distribution	HepV	21%	21%	32%	21%	10%	21%
	IV (or LSVC)	22%	22%	n/a	22%	19%	26%
	AZ	24%	24%	17%	24%	31%	15%
	SVC	33%	33%	51%	33%	40%	38%
	LPA	70%	n/a	49%	72%	65%	39%
	RPA	30%	n/a	51%	28%	35%	61%

the magnetic field. The anatomy was acquired using CT but the flow information was missing. For patient B1, cardiac catheterization measurements of the LPA flow rate and cardiac output in the ascending aorta (which was assumed to be equal to Q_S, the sum of all systemic venous return) partly compensated for the lack of MRI flow data. No such catheterization information was available for Patient A2. The missing flow data, namely the inlet flow distribution for Patient B1, and both the inlet flow distribution and Q_S for Patient A2, were defined based on other patient data that were available when Patients A2 and B1 were enrolled, which, at the time, were mostly limited to the flow measurements obtained for Patient A1. In Table 9-1, these extrapolated values are distinguished from the patient-specific measurements using a gray-colored font.

9.1.4 Performance Assessment and Optimization Metrics

A critical step for surgical planning is to define the clinically relevant optimization metrics, and their relative importance to ultimately determine the optimal surgical option on a patient-by-patient basis. For the patients considered in this study, the primary objective of the surgery was to revert the existing PAVMs and enable proper lung development, via a balanced hepatic flow distribution (HFD) and lung perfusion. The goal is to achieve an HFD close to 50/50 RPA/LPA when the GFD is close to 50/50 RPA/LPA as well. The hepatic flow distributions to the right and left lung (HFD_{RPA} and HFD_{LPA}, respectively) are defined as:

$$HFD_{RPA} = \frac{Q_{Hep \to RPA}}{Q_{Hep \to RPA} + Q_{Hep \to LPA}} \tag{9-1}$$

$$HFD_{LPA} = \frac{Q_{Hep \to LPA}}{Q_{Hep \to RPA} + Q_{Hep \to LPA}} \tag{9-2}$$

where $Q_{Hep \to RPA}$ and $Q_{Hep \to LPA}$ represent the amount of hepatic flow going to the RPA and LPA, respectively, which are quantified by uniformly seeding weightless point particles across an HepV cross-section and passively advecting them across the computed flow fields (see Section 4.8.3.1 for more details).

However, as discussed in the clinical background (Section 1.5), a balanced HFD distribution is not the only parameter of importance. The ideal TCPC should also 1) minimize pressure drops to minimize the increase in central pulmonary resistance, 2) minimize power losses, to minimize the workload imposed on the heart, 3) feature no regions of elevated shear stresses nor flow recirculation to minimize the thromboembolic potential of the connection, and, and above all 4) be surgically feasible.

The power losses, $\dot{E}_{Loss}$, are computed for each corrective anatomy envisioned using an integrated control volume energy balance:

$$\dot{E}_{Loss} = \sum_{\substack{i \in Inlets \\ Outlets}} \left(P_i + \frac{1}{2} \rho \left(\frac{Q_i}{A_i} \right)^2 \right) . Q_i \tag{9-3}$$

where $\rho = 1060$ kg/m^3 is the density of blood, and P_i, Q_i and A_i represent the pressure, flow rate and cross-sectional area of the inlet or outlet i. Q_i is positive if i corresponds to an inlet and negative for an outlet. By taking into account the pressure differences between the inlets and outlets, power losses constitute a surrogate measure for the global pressure drop and hemodynamic resistance associated with each surgical option. They may also be interpreted as a measure of the energy lost by viscous dissipation in shear layers along the vessel walls or at the center of the connection, or in turbulent flow structures. Finally, surgical feasibility is accounted for at the design stage by including the surrounding organs within the virtual-surgery interface, so that the surgeons or user

can ensure that the options considered fall within the constraints imposed by the surrounding structures and do not impinge on the pulmonary veins, for example.

The surgical options designed for each patient are closely reviewed with all of the above parameters in mind. However, it is very likely that no option will fulfill all optimization conditions at the same time. For the purpose of this study, priority will thus be set on surgical feasibility and HFD. Power losses and flow structures will be used as secondary measures to discriminate between equal performing options.

9.2 Surgical Planning Results for Patients with a Single SVC (Group A)

The results of the surgical planning campaign conducted for patients with a single SVC are here described. For each patient, we first present the clinical case report, followed by a detailed analysis of the pre-operative hemodynamics. We then describe the envisioned surgical options, and discuss their hemodynamic performance in terms of hepatic flow distribution and power losses.

The hepatic flow distribution is expressed in terms of HFD_{RPA}, which represents the HFD to the RPA. Similarly, the lung perfusion is expressed in terms of GFD_{RPA}, which represents the global flow distribution (GFD) to the RPA. The objective of the surgical planning campaign is thus to identify the option that yields 1) a balanced HFD and lung perfusion to enable proper pulmonary development, i.e. achieve HFD_{RPA}=50% when GFD_{RPA} is close to 50% as well, and 2) low vascular resistance (i.e. low power losses or pressure drops) to minimize the workload imposed on the heart.

9.2.1 Patient A1 (CHOP M1)

9.2.1.1 Pre-operative Clinical diagnosis

Patient A1 was a 4 year-old Fontan patient, female, who presented to the Children's Hospital of Philadelphia (CHOP) with an oxygen saturation of 72% in the ascending aorta. The patient had complex heterotaxy syndrome, single-ventricle, dextrocardia, total anomalous pulmonary venous connection to the right atrium, and an interrupted IVC with AZ continuation. Dye injection X-ray angiography revealed the formation of severe left lung PAVMs, responsible for the observed hypoxemia.

The patient anatomy at the time of diagnosis is shown in Figure 9-2 from three view angles. The geometric and flow characteristics at each one of the inflows and outflows are summarized in Table 9-3. Patient A1 had undergone a Kawashima procedure followed by an extra-cardiac connection of the HepV to the PAs. The extra-cardiac conduit was a 16 mm graft (cross-sectional area of 1.96cm^2) curved towards the LPA. The AZ adjoined the Kawashima connection on the right hand side, just above the RPA. The LPA exhibited a severe stenosis, possibly due to a compression by the over-riding aorta. The LPA cross-sectional-area at the point of highest constriction was 0.37 cm^2 vs. 1.56 cm^2 for the outlet cross-section. As will be discussed in subsequent paragraphs, this stenosis and the large vessel curvature of the two pulmonary arteries introduced large disturbances in the flow giving rise to a very complex unsteady flow. For that reason, the PAs in the numerical model were extended by 5 vessel diameters to ensure that outflow boundary conditions were applied sufficiently far downstream to avoid spurious wave reflections that could lead to numerical instability.

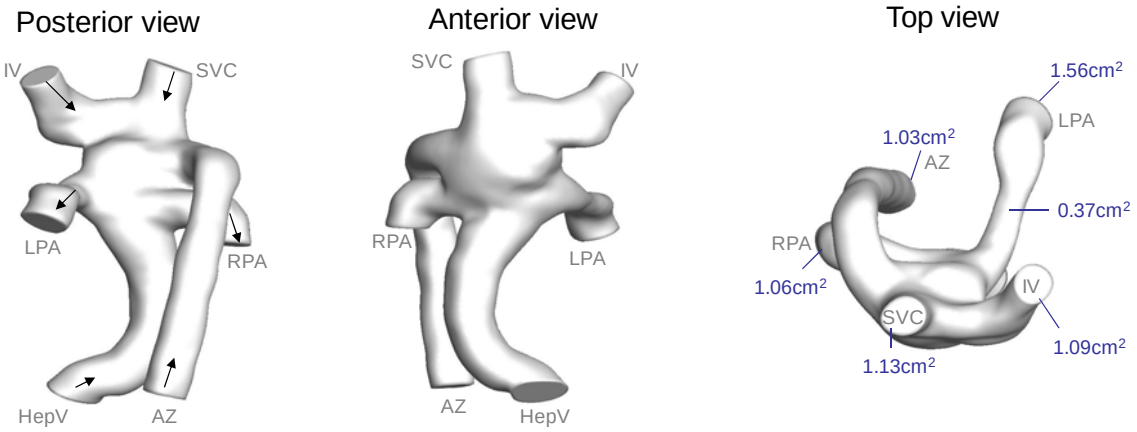

Figure 9-2: Patient A1's pre-operative TCPC geometry. The black arrows depict the global flow direction for each inlet and outlet. The inlet/outlet cross-sectional areas as well as the smallest LPA cross-sectional area are indicated in blue.

Table 9-3: Geometric and flow characteristics of Patient A1 at the time of PAVM diagnosis, and flow boundary conditions used for the CFD simulations. Q_S: sum of the systemic inflows. Q_P: sum of the pulmonary outflows.

	Cross-sectional Area (cm^2)	MRI Flow measurements		CFD Flow Conditions		
		Q (L/min)	Q (%)	Q (L/min)	Q (%)	Characteristic Velocity (cm/s)
Systemic Venous Return						
HepV	1.96	0.72	21%	0.72	21%	6.15
LSVC	1.09	0.75	22%	0.75	22%	11.49
AZ	1.03	0.82	24%	0.82	24%	13.31
SVC	1.13	1.13	33%	1.13	33%	16.67
Q_S		3.43		3.43		
Pulmonary Flows						
LPA	1.56	2.52	70%	2.39	70%	25.57
RPA	1.06	1.09	30%	1.04	30%	16.24
Q_P		3.61		3.43		

9.2.1.2 Pre-Operative Hemodynamics

Dominant flow structures: Figure 9-3 illustrates the dominant flow structures and pressure variations observed within the pre-operative anatomy. The pressures reported in the right panel are expressed with respect to the mean pressure at the HepV inlet. The pressure at any given point in the geometry thus corresponds to the pressure differential between that point and the HepV. The left panel demonstrates the main flow structures using 3D streamtraces color-coded by velocity magnitude. As can be observed from Figure 9-3, velocities within the connection remain low, on the order of 10 to 20 cm/s. A sudden flow acceleration is noted as flow enters into the LPA. This is in part due to the fact that the LPA is the vessel that conveys the largest share of the flow (Q_{LPA}=70%Q_S), and is worsened by the LPA stenosis just downstream of the connection. At the center of the LPA stenosis, the average velocity magnitude is of 160 cm/s, and is accompanied by a mean pressure drop of 6.2 mmHg. A slight pressure recovery can be noted downstream of the stenosis, as the LPA expands and the flow slows down.

To better understand the interaction between the four inflows, Figure 9-4 shows the same 3D streamtraces as in Figure 9-3, but color-coded by their point of origination rather than by velocity magnitude. Streamtraces from all inlets mix in the center of the connection where they are tangled together. A portion of the SVC flow goes along the anterior wall of the connection down into the hepatic baffle, resulting in an intense recirculation at the opening of the baffle (structure A in Figure 9-3). The flow structures in the LPA are dominated by a large-scale helical structure, which is consistent with what is typically observed in pulmonary arteries downstream of the TCPC [84, 85, 183]. A similar helical flow, though of lower intensity, is observed in the RPA.

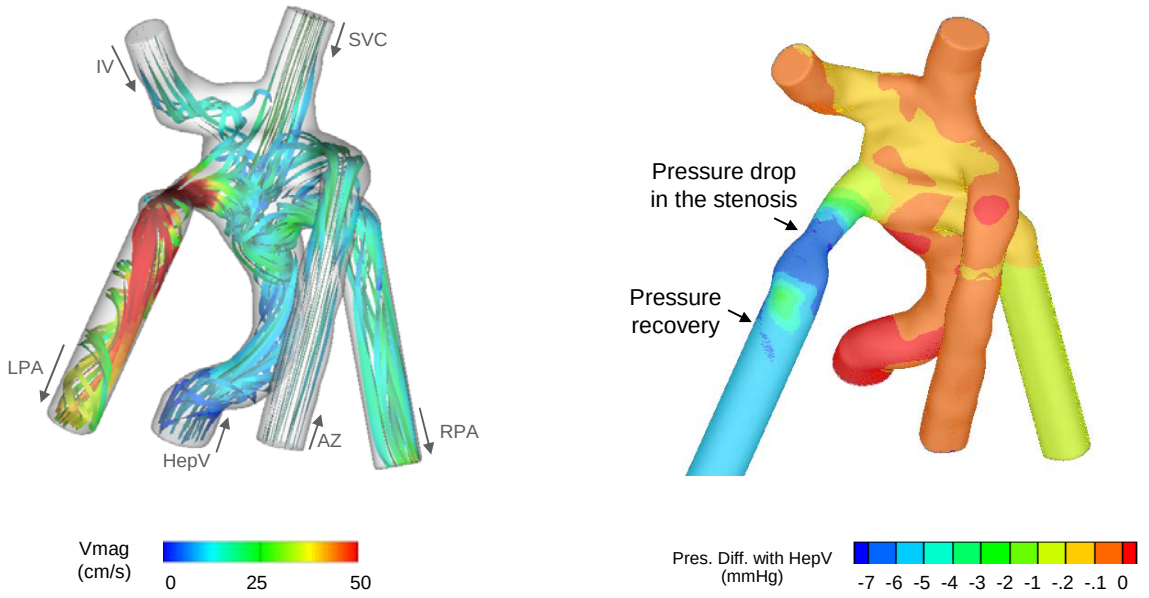

Figure 9-3**:** Global flow structures and pressure fields in the pre-operative anatomy of Patient A1. Left: Time-averaged 3D streamtraces color-coded by velocity magnitude (Vmag). The color-scale is optimized to show velocity variations in the body of the connection. Right: Corresponding pressure field expressed with reference to the mean pressure at the HepV inlet. A non-linear color-scale is used to show the small pressure variations within the connection as well as the pressure drop across the stenosis.

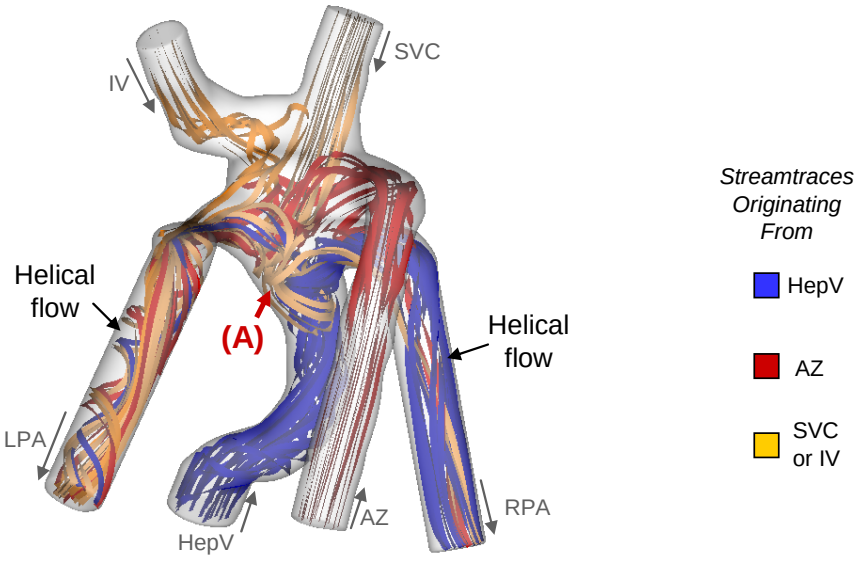

Figure 9-4**:** Time-averaged flow structures within the pre-operative anatomy for patient A1. Streamtraces are color-coded based on their vessel of origination.

It is noteworthy that, despite the noted mixing at the center of the connection, streamtraces in the LPA mostly originate from the AZ, SVC and IV (in red and orange in Figure 9-4) , while almost all HepV streamtraces (in blue in Figure 9-4) exit through the RPA outlet. The AZ, which is oriented towards the LPA, constrains the IV and SVC streams towards that vessel. The HepV is also oriented towards the LPA but cannot sustain the flow competition at the center of the connection and is forced into the RPA. The flow recirculation within the baffle (region A in Figure 9-4) further constrains the HepV towards the RPA. A detailed HFD quantification reveals that 91% of the hepatic flow goes to the RPA while only 9% goes to the LPA. Such preferential HFD to the RPA is consistent with the presence of PAVMs in the left lung.

Impact of the instantaneous flow instabilities: All of the above analysis was conducted using the converged running average of the CFD simulations. However, given the level of mixing observed within the baffle, the question may arise as to whether the time-averaged results smooth out some of the instantaneous characteristics. To investigate this point, Figure 9-5 and Figure 9-6 compare the coherent flow structures in the time-averaged flow fields to the instantaneous ones. The coherent flow structures are captured using the Q-criterion, which isolates regions where the vorticity dominates the shear. The iso-surfaces displayed thus correspond to independent vortex cores.

The collision of the HepV inflow with the combined azygous, SVC and IV inflows leads to the formation of a stable elongated vortex core (structure H) that spans the entire connection region and penetrates into both PAs. Nearly perpendicular to structure H is another stable and elongated structure (structure V) that emanates from the

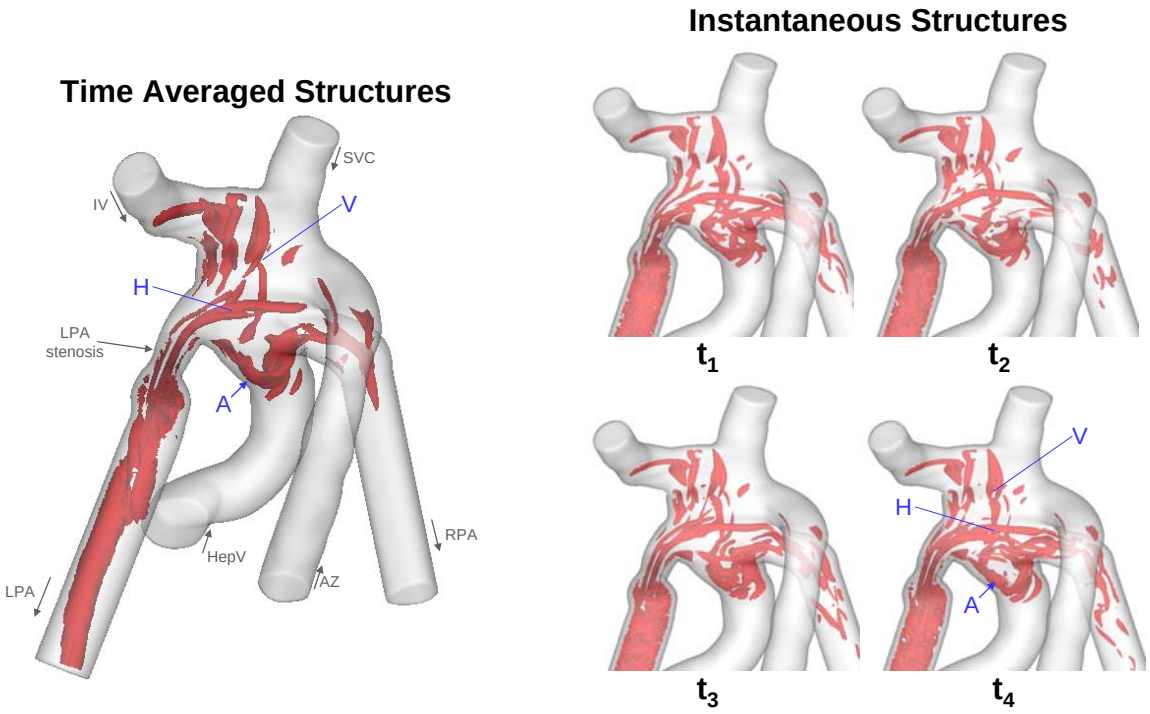

Figure 9-5: Coherent structures visualized with Q-criterion. (left) Time-averaged velocity structures. (right) instantaneous structures at 4 consecutives instants in time (Right). The stable elongated vortex core (structure H) results from the collision of the HepV flow with the AZ, SVC and IV flows. Structure V emanates from the shear layer between the AZ and SVC flows and then dives into the hepatic baffle (region A). An animation of these flow structures is provided in Animation 9-1.

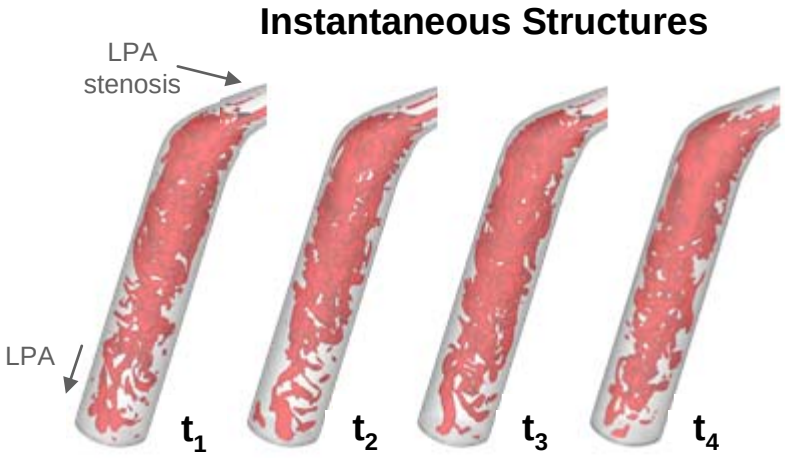

Figure 9-6**:** Instantaneous coherent structures in the LPA visualized with Q-criterion for the same 4 instants in time as in Figure 9-5. The flow is characterized by chaotic flow structures just after the stenosis and relaminarization towards the vessel outlet.

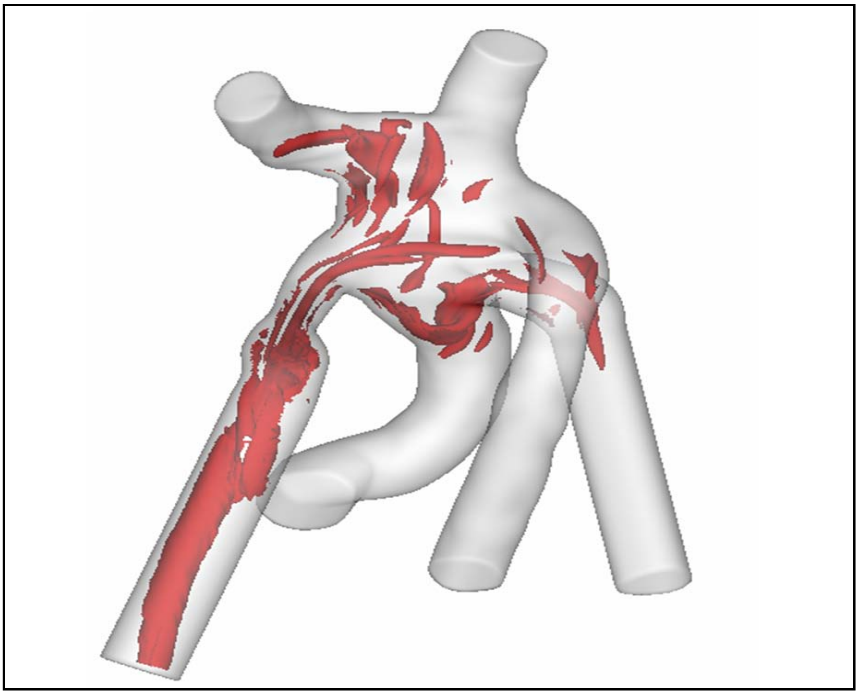

Animation 9-1: Dynamic visualization of the coherent structures visualized with Q-criterion. Note that the structures within the center of the connection remain fairly stable in time, while the flow downstream of the stenosis is characterized by chaotic flow structures followed by a progressive relaminarization towards the vessel outlet.

shear layer between the AZ and SVC inflows and then dives into the hepatic baffle (region A). The vortices created in region A are ejected towards the RPA anastomosis where they interact with the structure H again. This second interaction results in seemingly aperiodic vortex shedding events causing smaller vortical cores to be ejected further down the RPA. These instantaneous structures (in particular structure H and those at the opening of the hepatic baffle) are also present in the time-averaged flow field, which demonstrates their quasi-steady character. Despite the intense mixing noted within the baffle, the flow structures in the connection and in the RPA thus demonstrate low levels of unsteadiness.

The enormous complexity of the flow in the LPA region is best visualized in Figure 9-6, which shows the instantaneous coherent structures in the LPA extended vessel for the same time instants as those shown in Figure 9-5. The flow is characterized by chaotic flow structures and the emergence of intense velocity fluctuations. The instabilities observed in the LPA outflow track stem from the presence of a severe LPA stenosis just downstream of the connection. As highlighted above, the flow entering the LPA is already unsteady and three-dimensional due to the complex vortical structures created in the connection center. As the flow accelerates in the constriction these large-scale vortical structures stretch and intensify. The sudden increase in the diameter of the LPA downstream of the stenosis imposes an adverse streamwise pressure gradient (Figure 9-3), which destabilizes the flow and causes the rapid breakdown of the LPA jet into a seemingly chaotic, turbulent-like state. Downstream of the stenosis, the small-scale vortical structures start to decay and larger vortices begin to emerge, which suggests that the flow begins to re-laminarize again due to the stabilizing effect of viscosity.

Pre-Operative Summary: The main clinical symptom of this patient is severe hypoxemia due to the presence of left-sided PAVMs. Analysis of the pre-operative hemodynamics reveals that 91% of the hepatic blood flows through the RPA towards the right lung, while only 9% reach the left lung. This highly preferential HFD to RPA stems from the fact that 1) the orientation of the AZ at its connection site directs the AZ blood towards the LPA, which entrains the two other superior inflows in its wake towards the left, 2) the HepV stream is of low velocity and low energy and cannot sustain flow competition with the superior inflows. The preferential distribution of the superior inflows to the LPA presents a

hemodynamic barrier to the HFD to LPA, constraining the hepatic flow to the RPA. This is re-inforced by the curvature of the HepV baffle. Moreover, it is apparent that the severe LPA stenosis just downstream of the vessel anastomosis results in number of detrimental hemodynamic features, including elevated pressure drops, a drastic increase in velocity as the flow goes through the stenosis, and a transition in flow regimes immediately downstream of the stenosis. The rise of small turbulent vortex cores downstream of the stenosis increases the shear forces that will be imposed on traveling platelets and red blood cells.

Accordingly, surgical recommendations include 1) dilating the LPA stenosis to decrease the power loss and stresses on the blood elements, and 2) redesigning the hepatic baffle to improve HFD. Dilation of the LPA stenosis may be performed by the trans-catheter insertion of a balloon-dilated stent. It is expected that such dilation will primarily result in lower pressure drops and power losses but will not significantly affect HFD. Accordingly, since the primary symptom of Patient B1 is hypoxemia, we will focus our attention on modifying the baffle design to improved HFD. The strategies designed should seek to either minimize the head-on collision between the HepV and the other inflows, or increase the energy of the stream coming through the baffle for it to better resist flow competition at the center of the connection.

9.2.1.3 Surgical Planning Options

Based on the analysis of the pre-operative hemodynamics conducted above, four re-operative strategies are investigated herein. These four options were designed using the virtual surgery framework described in Chapter 5, and the resulting geometries are displayed in Figure 9-7 together with the pre-operative anatomy. Option 1 makes use of an extra-cardiac baffle similar to the pre-operative one, but shifted further towards the left. Option 2 consists of using a 'Y' shaped graft similar to the Optiflo proposed by Soerensen et al. [98]. The right and left branches are connected on either side of the Kawashima connection (i.e. on either side of the point of convergence of all the superior inflows) to prevent any head-on collision with the superior inflows and avoid mixing at the center of the connection. The right branch is set to a smaller diameter than the left to increase the resistance of the HepV-to-RPA pathway, and hopefully decrease the HFD to RPA. Option 3 seeks to increase the energy of the flow coming through the extra-cardiac conduit by connecting the azygous vein to the hepatic veins, and merging the AZ and HepV flows within the extra-cardiac conduit. Finally, Option 4 seeks to both increase the energy of the HepV pathway and avoid head-on flow collisions by merging the AZ and HepV flows together in the azygous vein. The hepatic flow is routed through a HepV-to-AZ shunt into the azygous vein and the extra-cardiac conduit is taken down.

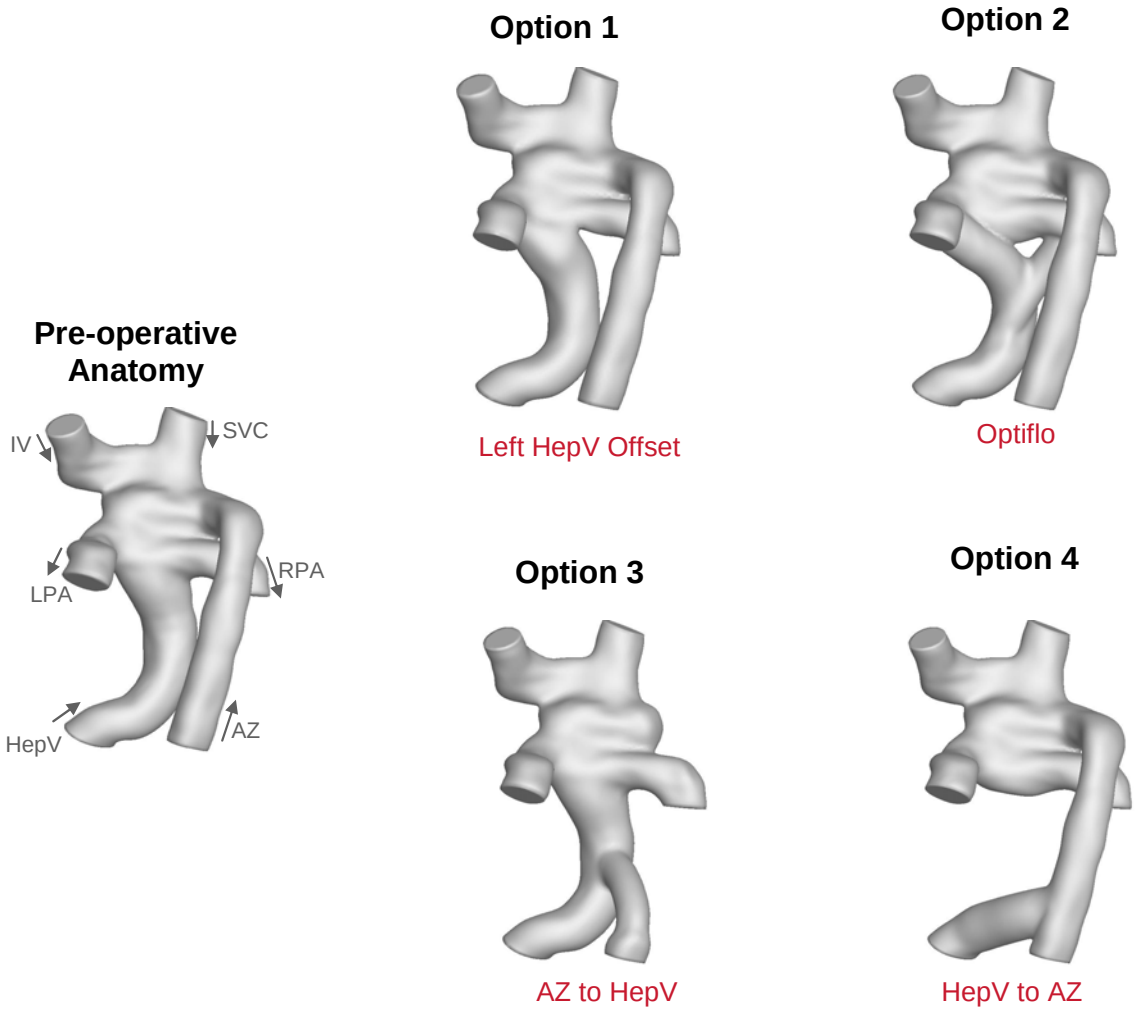

Figure 9-7: The four surgical planning options investigated for patient A1 viewed from the posterior side. The pre-operative anatomy is provided for comparison. The surgical procedure associated with each one of these options is briefly described by the red annotations.

CFD simulations are conducted for each of the surgical options to compare their hemodynamic performance. Emphasis is set on achieving a balanced HFD to the two lungs. Because the post-operative outflow conditions are likely to differ from the pre-operative conditions, two outflow distributions are investigated:

- the pre-operative GFD of 30/70 RPA/LPA to represent the acute post-operative state, before any PAVM resorbtion and changes in pulmonary vascular resistance
- and a GFD of 50/50 RPA/LPA to model the global flow distribution that would be achieved in long-term if the left-sided PAVMs resorbed and the pulmonary vascular resistances rebalanced.

The results for each of these flow conditions are provided hereafter. The CFD results are displayed in the anatomy without the numerical vessel extensions. To better visualize the flow dynamics at the center of the connection, all displayed flow fields are viewed from the posterior side. In the figures shown for Patient A1, the LPA is thus on the left and the RPA on the right.

9.2.1.4 Hemodynamic Performance at a GFD of 30/70 RPA/LPA

As previously mentioned, the parameters of interest to select the optimal surgical option are the HFD and hemodynamic resistance. Figure 9-8 compares the hemodynamic performance of all four surgical options in the acute post-operative stage, in terms of HFD and static pressure drops. HFD is reported in terms of HFD_{RPA} and HFD_{LPA}, which represent the percentage of the hepatic flow going to RPA and LPA, respectively. The global flow structures are illustrated as well to better understand the reported HFD values.

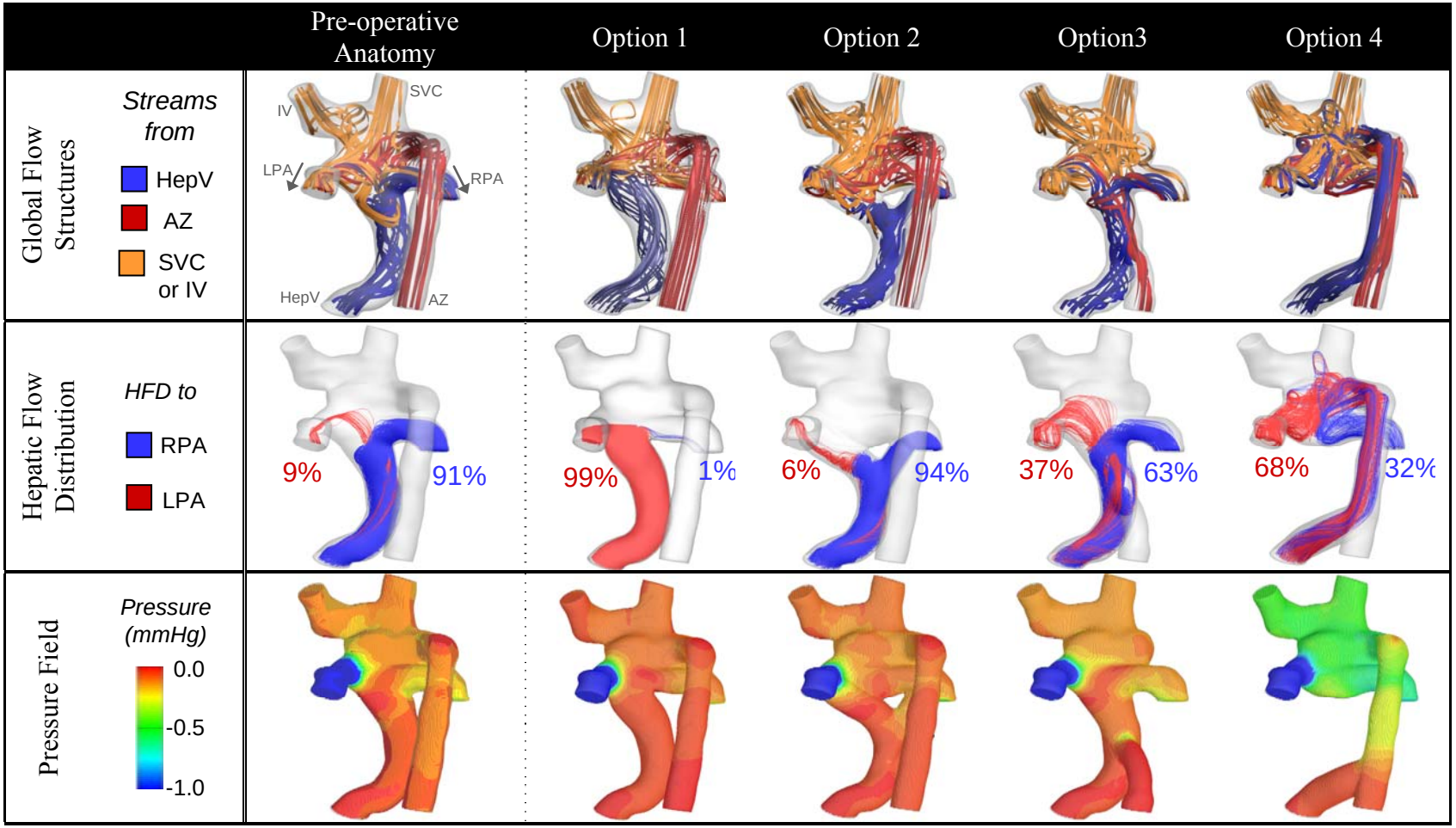

Figure 9-8**:** Comparison of the hemodynamic performance of the four surgical planning options at GFD_{RPA}=30%. The objective is to reduce HFD_{RPA} down to a level that is in closer match to GFD_{RPA}, and to minimize the pressure drops across the connection. The pressure scale is optimized to show differences in the body of the connection and not for the pressure drops across the LPA stenosis. The pre-operative hemodynamics are provided for reference.

Option 1: The extra-cardiac baffle in Option 1 is shifted to the left, avoiding a direct head-on collision between the HepV flow and the superior inflows. Looking at the top row of Figure 9-8, it can be observed that, thanks to the offset, none of the superior inferior inflows penetrate into the baffle. The HepV streamtraces (in dark blue in Figure 9-8) are free to occupy the entire baffle and not constrained towards the right side as was the case in the pre-operative anatomy. However, as the HepV streamtraces exit the baffle, they are caught by the superior inflows that seek to reach the left lung and forced into the LPA. As a result, Option 1 leads to a complete inversion of the HFD compared to the pre-operative flow distribution. HFD goes from 91/9 RPA/LPA in the pre-operative anatomy to 1/99 in Option 1. Such an increase in HFD_{LPA} will definitely lead to the disappearance of the left-sided PAVMs, but carries the risk to yield right-sided PAVMs if the HFD does not rapidly reach a more balanced 50/50 distribution as the lungs remodel. The pressure field of Option 1 is similar to that of the pre-operative anatomy, indicating comparable energy losses.

Option 2: The flow structures observed in Option 2 show number of similarities with the pre-operative ones. The AZ flow forces the IV and SVC flows towards the LPA, and part of the SVC flow penetrates into the left branch of the Y-graft constraining the HepV flow towards the right branch. As a result, this option fails to improve the hepatic flow distribution, with only 6% of the HepV flow reaching the LPA.

Option 3: In Option 3, the AZ flow is directed to the HepV baffle. The SVC and IV streamtraces (in orange in Figure 9-8) come straight down into the connection site, rather than being forced towards the LPA by the azygous flow, as was the case in the pre-operative anatomy. This results into a head-on collision between the IV+SVC streams

and the combined AZ and HepV streams, but is not accompanied by the superior IV and SVC inflows penetrating into the baffle. Combining the AZ and HepV flows increases the velocity and kinetic energy in the extra-cardiac baffle, allowing those two combined flows to sustain the competition with the IV and SVC. As a result, HFD to the left lung increases from 9% in the pre-operative anatomy up to 37% in Option 3. A potential drawback of combining the AZ and HepV flows is increasing the overall resistance of the TCPC. However, the pressure drops associated with this option are of the same order as those of the original anatomy.

Option 4: Finally, in Option 4, the HepV and AZ flow merge together into the azygous vein. All the superior venous returns thus enter the connection from its superior aspect, which avoids the competitive head-on collision observed in the pre-operative anatomy. An intense mixing can be observed at the center of the connection, with streamtraces of all colors entangled together (Figure 9-8). Thanks to this intense mixing Option 4 is the option that has the best performance from an HFD distribution stand-point, achieving a 32/68 RPA/LPA ratio, which is in close match with the global cardiac output distribution of 30/70 RPA/LPA to the lungs. On the other hand, Option 4 features the highest pressure drops of all tested options. The pressure difference between the HepV and the center of the connection is of about 0.50 mmHg compared to less than 0.20 mmHg for the pre-operative anatomy and Options 1 to 3. Combining the hepatic and azygous streams into the azygous vein increases the viscous friction along the AZ vessel walls, which in turn increases the hemodynamic resistance and pressure drop required to drive the HepV and AZ flows up towards the connection site.

9.2.1.5 Hemodynamic Performance at a GFD of 50/50 RPA/LPA

Results under the pre-operative flow conditions demonstrated that Option 2 would result in an HFD similar, if not worse, to that of the pre-operative anatomy. This option is thus not expected to improve patient outcome, and is therefore not retained as a potential candidate for the surgery nor is it retained for subsequent investigation. Options 1, 3 and 4, on the other hand, represent potential candidates, as they were seen to increase HFD_{LPA} under the pre-operative flow conditions. Nonetheless, the pre-operative GFD can at best represent the acute post-operative stage, and the question arises as to how these options would perform in the long-term. In order to discriminate between Options 1, 3 and 4, we thus compare their hemodynamic performance at a GFD of 50/50 RPA/LPA, to emulate the flow conditions after the left PAVM have resorbed and the left pulmonary resistance has increased. The corresponding flow structures, HFD and pressure fields are displayed in Figure 9-9 using the same conventions as in Figure 9-8.

Option 1: Overall, the flow structures and relative HFD performance of Options 1, 3 and 4 are similar to what was noted under the pre-operative flow conditions. Option 1 still yields a highly biased HFD to the LPA, which only decreases to 96% from the 99% measured with the pre-operative flow splits. The left-sided HepV offset favors HFD to the LPA. In addition, the IV and SVC flows (orange streamtraces in the top row of Figure 9-8) constitute a barrier that prevents the HepV from reaching the RPA. Based on the flow behaviors observed at GFD_{RPA}=30% and 50%, it might be expected that Option 1 will provide only little hepatic flow to the right lung unless all of the AZ, IV and SVC flows are directed to the RPA. Accordingly, Option 1 will most likely lead to right-sided PAVMs and does not appear as a suitable candidate for the surgery.

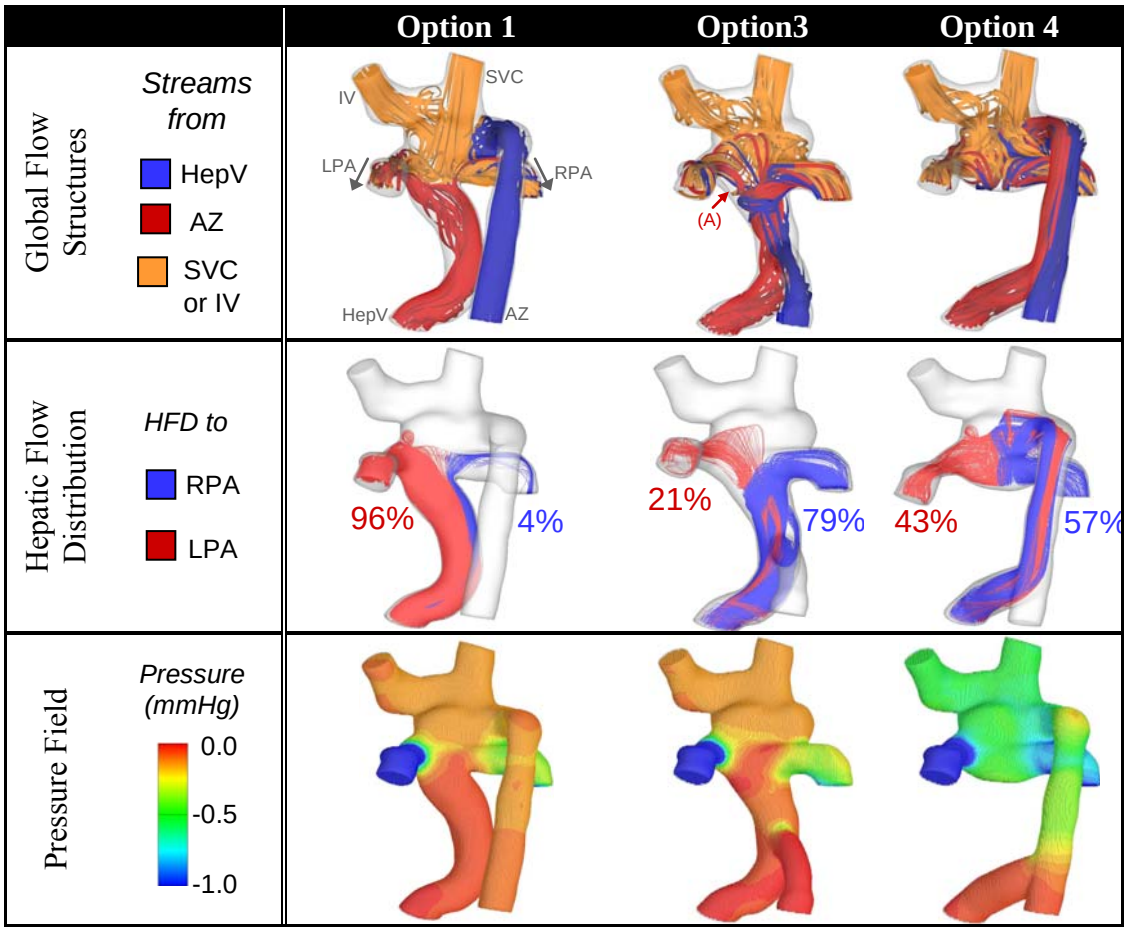

Figure 9-9**:** Comparison of global performance measures at a GFD of 50/50 RPA/LPA. Only the three options that yielded a higher HFDLPA than the pre-operative anatomy when the GFD was of 30/70 RPA/LPA are considered here.

Option 3: Option 3 (second column in Figure 9-9) allows for some mixing between the superior and inferior inflows. This is manifested by the intertwined red, blue and orange streamtraces at the center of the connection. However, due to the curvature of the extra-cardiac baffle, the AZ and HepV streamtraces (in blue and red in the top row of Figure 9-9) detach from the left side of the baffle (region A). The IV flow further constrains the AZ and HepV flows towards the right and into the RPA. As a result,

despite some mixing at the center of the connection, this option only provides 21% of the hepatic flow to the left lung when GFD_{RPA}=50%.

Option 4: Finally, Option 4 (last column in Figure 9-9) is here again the host of an intense mixing at the center of the connection. HFD_{LPA} goes from 68% to 43% when GFD_{LPA} decreases from 70% to 50%. The intense mixing of all inflows at the center of the connection ensures that the HFD closely follows the GFD. It may thus be assumed that Option 4 would lead to the disappearance of the left-sided PAVMs in the acute stage, and still maintain a normal left and right lung function as the GFD rebalances from 30/70 to 50/50 RPA/LPA in the long term. This option is hindered by higher pressure drops than the others even at GFD_{RPA}=50%, but this is deemed acceptable in view of the improvements in HFD.

9.2.1.6 Surgical Planning Summary

Four surgical planning options were created based on the pre-operative hemodynamics assessment of Patient A1. Each of these options was investigated under the acute post-operative conditions (simulated using the pre-operative CFD of 30/70 RPA/LPA) and after a possible disappearance of the left-sided PAVMs (simulated using a GFD of 50/50 RPA/LPA). The HFD for Patient A1 was shown to be highly dependent upon the interaction between the superior and hepatic inflows. Options 1 and 2, which maintained the four inflows separated, did not show major improvement in the distribution of the hepatic flow. Varying the HepV offset towards the LPA, as demonstrated with Option 1, led to a complete switch of the HFD from 91% HFD to the RPA in the pre-operative anatomy to 4%. This points to a very high sensitivity of the

HFD to the HepV offset due to a limited mixing between the low energy HepV flow and the combined superior inflows. Similarly, splitting the HepV baffle as in Option 2 failed to improve HFD to the left lung.

Merging the AZ and HepV was observed to be the best strategy for Patient A1. Combining the two flows into the baffle, as in Option 3, increased the energy of the inferior venous return and in turn the mixing of the inferior (AZ and HepV) and superior (IV and SVC) inflows. Although Option 3 did improve HFD, this improvement was not deemed sufficient to completely heal the PAVMs. Optimal results from an HFD standpoint were obtained by redirecting the HepV flow into the AZ (Option 4). Though coming at a slightly higher cost in terms of pressure drops, this option led to a complete mixing of all venous inflows (namely the AZ, IV, SVC and HepV flows) and an apparent linear relationship between the global and hepatic flow distributions. This suggests that Option 4 would lead to the disappearance of the left-sided PAVMs in the acute stage, and still maintain a normal left and right pulmonary function as the GFD rebalances from 30/70 to 50/50 RPA/LPA.

The corrective surgery was eventually performed with Option 4. Five month follow-up data support this choice with a clear improvement in the overall clinical condition and an increase of oxygen saturation levels 72 to 94%, implying regression of the PAVMs.

9.2.2 Patient A2 (CHOA M1)

9.2.2.1 *Pre-Operative Anatomy and Clinical Diagnosis*

Patient A2 was a 6-year old male referred by the Children Hospital of Atlanta (CHOA). This patient had a heterotaxy syndrome, SVHD, and an interrupted IVC. He had undergone a Kawashima procedure followed by an intra-atrial procedure to complete the HepV-to-PA conduit. The patient showed signs of increasing hypoxemia, with an arterial oxygen saturation below 83% at the time of examination. He was diagnosed with severe right lung PAVMs. Angiogram examination revealed that most of the dye injected into the hepatic veins flowed into the left lung, re-instating the correlation between the presence of PAVMs and a poor supply in hepatic blood.

Patient A2 featured number of coils, which prevented regular MRI acquisition, so that CT images had to be used to reconstruct the *in vivo* TCPC geometry. The coils still induced imaging artifacts in the images of the intra-atrial baffle, whose geometry had to be reconstituted using the virtual surgery environment. Three landmarks were used to guide the virtual design and ensure that the re-created HepV baffle accurately represented the *in vivo* pre-operative anatomy. These were: 1) the location of the HepV stump, which could be identified in the CT images, 2) the location of a stump on the PAs, which was taken to be the location of the HepV to PA anastomosis, and 3) the angiogram images used for PAVM diagnosis, where the dye clearly illustrated the hepatic blood flow pathway. The resulting anatomy is shown in Figure 9-10. The cross-sectional areas of each of the inlet and outlet vessels are listed in Table 9-4. The LPA, with a cross-sectional area of only 0.81 cm^2, was significantly smaller than the RPA (2.41cm^2).

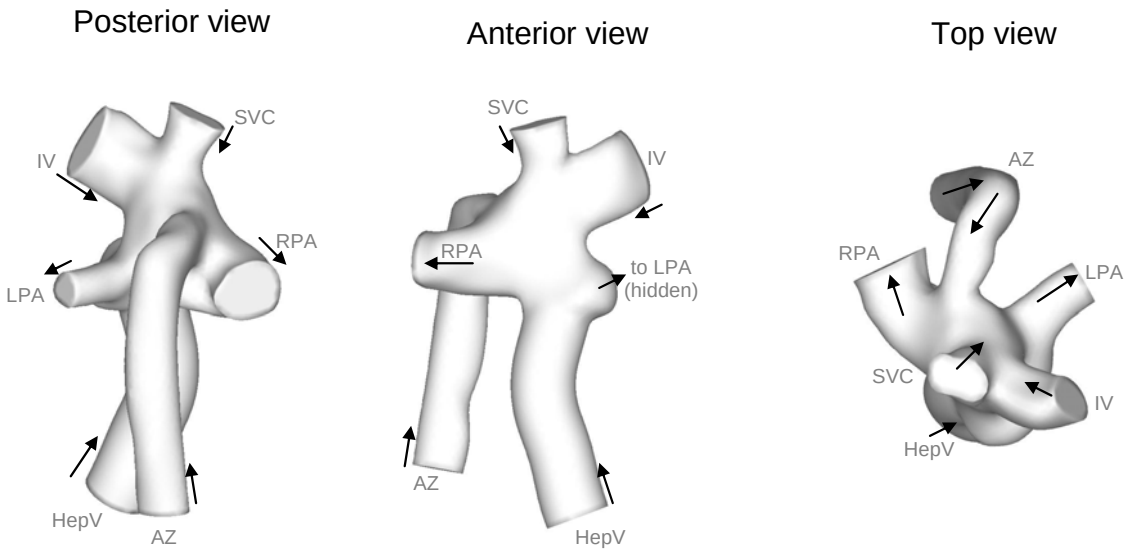

Figure 9-10: Patient A2's pre-operative TCPC anatomy. The geometry was reconstructed from CT and the hepatic baffle added using the virtual surgery interface. The black arrows depict the global flow direction for each inlet and outlet.

Table 9-4: Geometric characteristics of Patient A2 at the time of PAVM diagnosis, and flow boundary conditions used for the CFD simulations. *In vivo* flow measurements were unavailable since the patient was imaged by CT. Inflow conditions for the CFD simulations were taken to be the same as for Patient A1. Outflow conditions were varied, but the flow rates and characteristic velocities at a 50/50 RPA/LPA flow split are provided as an example. Q_S: sum of the systemic inflows. Q_P: sum of the pulmonary outflows.

	Cross-sectional Area (cm^2)	*In Vivo* Flow measurements		CFD Flow Conditions		
		Q (L/min)	Q (%)	Q (L/min)	Q (%)	Characteristic Velocity (cm/s)
Systemic Venous Return						
HepV	2.46	n/a	n/a	0.72	21%	4.89
IV	1.83	n/a	n/a	0.75	22%	6.84
AZ	1.31	n/a	n/a	0.82	24%	10.49
SVC	1.26	n/a	n/a	1.13	33%	14.92
Q_S		n/a		3.43		
Pulmonary Flows						
LPA	0.81	n/a	n/a	1.71	50%	35.22
RPA	2.41	n/a	n/a	1.71	50%	11.86
Q_P		n/a		3.43		

Table 9-4 also provides the flow conditions used for the CFD simulations. No pre-operative flow measurements were available as he had only undergone a CT evaluation. The CFD inflow conditions were thus taken to be the same as for Patient A1 and the global flow distribution at the outlet was varied over a wide range of RPA/LPA mass flow ratios for both the pre-operative anatomy and the surgical planning options. From the characteristic velocities listed in Table 9-4, it is noteworthy that that the mean velocity across the HepV baffle was two to three times lower than that across the AZ and SVC. The HepV stream for Patient A2 will thus show a low kinetic energy compared to the other two inlets. Based on the experience gained from Patient A1, the HFD can thus be expected to be very sensitive to the flow competition between the HepV stream and the other three inflows.

9.2.2.2 Pre-operative Hemodynamics

Based on the observation that both the right-sided PAVMs and the larger RPA diameter will tend to decrease the resistance of the pathway to the right lung compared to the left lung, the pre-operative hemodynamics were assessed for GFDs that favored flow to the RPA, ranging from 50/50 RPA/LPA up to 80/20 RPA/LPA.

Flow structures and pressures: The results obtained at the two extremities of the tested range, namely 50/50 and 80/20 RPA/LPA, are displayed in Figure 9-11, in terms of pressure, velocity and flow structures. All pressures are expressed in reference to the mean pressure at the HepV inlet. For both reported flow conditions, the IV and HepV flows were associated with low velocities (on the order of 5 to 7 cm/s) and low pressure drops. Velocities in the azygous vein were slightly higher (on the order of 10 cm/s) due to

the smaller diameter of that vessel compared to the IV and HepV. The pressures in that vessel are also slightly higher than in the other two, because a higher pressure head is required to drive the azygous flow to the center of the connection. The SVC was the fastest of all inflows, due to the fact that it carried one third of the systemic return and featured the smallest of the inflow cross-sections. At GFD_{RPA}=50% (top row in Figure 9-11), the velocities in the RPA fall within the same range as in the SVC. The mean RPA velocity is of 11.8 cm/s, with a peak around 18 cm/s. The associated pressure drop from the HepV is of only 0.15 mmHg. In contrast, the mean velocity at the LPA outlet is of 35 cm/s, accompanied by a mean pressure drop of 0.88 mmHg. These higher values compared to the RPA find their origin in the smaller dimension of the LPA, whose outlet cross-section is about three times smaller than the RPA, thus opposing a higher resistance to the flow. Figure 9-12 displays the pressures recorded through the connection in relation to the control volume power losses. It may be noticed that the high pressure drops in the LPA correspond to elevated power losses. The mean LPA pressure shows a strong dependency on the global flow distribution, dropping rapidly when the LPA flow rate increases (decreasing GFD_{RPA}). The fast decrease in LPA pressures translates into a fast decrease in the control volume power losses. The power loss curve reaches its minimum around GFD_{RPA}=75%, which is in close match to the point where the LPA and RPA pressure curves intersect. When GFD_{RPA} is lower than 75%, the increase in power losses is thus imparted by the LPA. Symmetrically, when GFD_{RPA} is larger than 75%, the power losses are dominated by the energy dissipation rate in the RPA. At GFD_{RPA}=80%, the mean RPA velocity and pressure drop are of 19 cm/s and 0.31 mmHg, respectively, compared to 14 cm/s and 0.20 mmHg in the LPA (Figure 9-11).

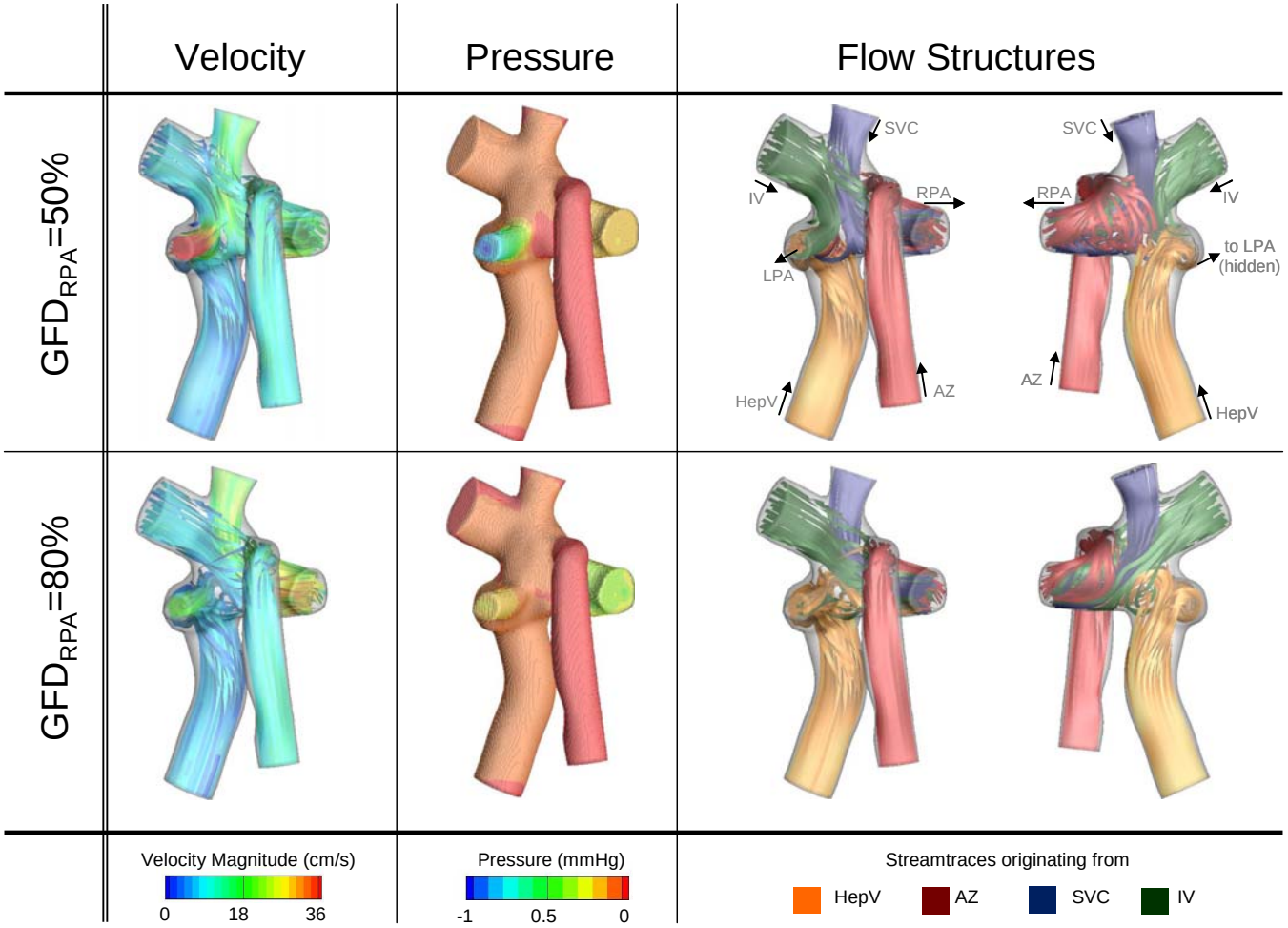

Figure 9-11: Hemodynamics of the Patient A2's pre-operative anatomy at a GFD of 50/50 RPA/LPA and 80/20 RPA/LPA. The velocities and pressure fields are shown from the posterior view to better visualize the changes in the PAs. The flow structures are shown from both the posterior and anterior views.

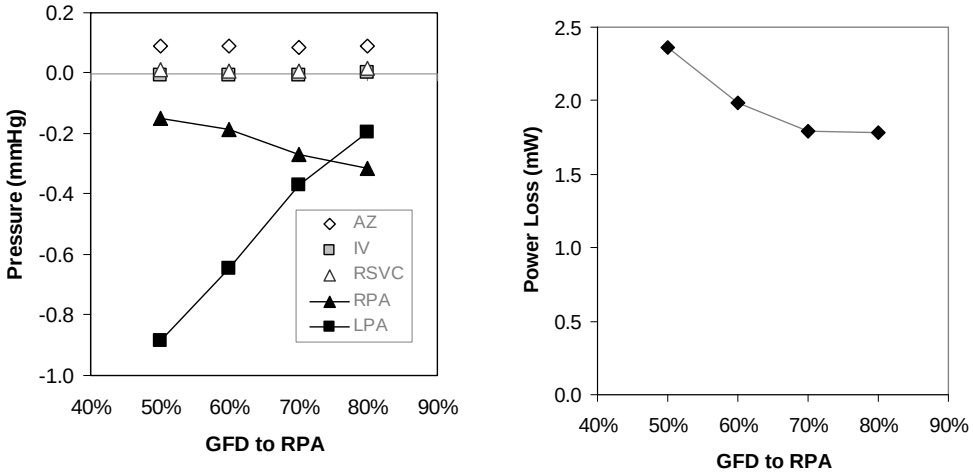

Figure 9-12: Dependence of the pressure (left) and power loss (right) to the flow distribution for the pre-operative anatomy of patient A2. The pressure corresponds to the average pressure values computed across each inlet/outlet. Note that the pressure in the HepV was taken as the pressure of reference and thus has a zero pressure value for all flow conditions.

Hepatic flow distribution: Figure 9-13 depicts the computed hepatic flow distribution to the right lung (HFD_{RPA}) as a function of the global flow distribution to that lung (GFD_{RPA}). The HFD_{RPA}=GFD_{RPA} line represents the ideal scenario where the lungs receive hepatic nutrients in proportion with the amount of blood flow. In a normal physiology, this is ensured by a complete mixing of all systemic venous returns in the right atrium and ventricle prior to their redistribution to the pulmonary arteries. For Fontan patients, the HFD will solely depend on the design of the TCPC and resultant interaction of the inflows at the center of the connection. For Patient A2, all HFD_{RPA} measurements fall far below the HFD_{RPA}=GFD_{RPA} line, testifying for a highly preferential HFD to the left lung.

The mechanism behind this preferential HFD to LPA can be better understood by going back to the flow structures shown in Figure 9-11. For all tested flow conditions, the

AZ streamtraces (in red), which enter the connection the farthest to the right, flow into the RPA. The SVC (in blue) and IV (in green) inflows split sequentially to adjust for the desired GFD. At GFD_{RPA}=50%, only the SVC splits between the RPA and LPA, while the IV streamtraces are exclusively directed to the LPA. When GFD_{RPA} increases to 80%, the SVC streamtraces switch completely towards the RPA, and it is the IV streamtraces that split between the LPA and RPA. The HepV (in orange) remains almost exclusively directed to the LPA for all tested flow conditions. From the point of view of the hepatic flow distribution, the pre-operative anatomy thus behaves the same way as a connection with a large offset towards the LPA, even though the offset was only of small magnitude in the pre-operative anatomy. Such sensitivity to even a small left-sided offset might be attributed to the low velocities and resultant low kinetic energy of the HepV flow, which prevents it from mixing with the other inflows.

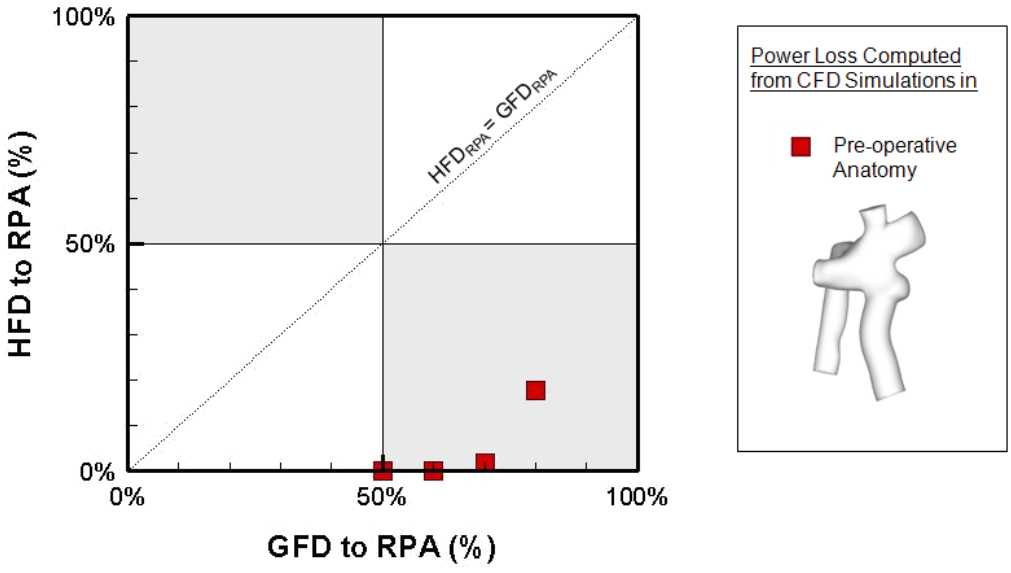

Figure 9-13: Hepatic flow distribution obtained by CFD in the pre-operative anatomy. The plot is split in four quadrants to help the visual interpretation.

9.2.2.3 Surgical Planning Options

Eight options are considered for the surgical planning campaign conducted for Patient A2. The corresponding anatomies are shown in Figure 9-14. The investigated parameters include 1) the HepV offset, progressively shifting the HepV from the right to the left of the connection, 2) the surgical procedure used, namely comparing intra-atrial and extra-cardiac approaches, 3) splitting the HepV in two branches using a Y-shaped Optiflo graft, and 4) merging the AZ and HepV streams together, either in the hepatic baffle or in the azygous vein.

Options 1 through 3 use an intra-atrial baffle of similar dimension as the pre-operative anatomy, but vary the position of the HepV anastomosis site to identify the HepV offset that would best split the hepatic flow between the two lungs. Option 1 connects the HepV the furthest towards the RPA. In Option 2, the HepV faces the AZ vein, while, in Option 3, it faces the SVC. To investigate if the procedure used made a significant impact on the associated HFD, Option 4 connects with an offset similar to Option 2, but using an extra-cardiac baffle.

In Options 5 and 6, the HepV is split in two branches following the Optiflo concept proposed by Soerensen et al. [98]. The objective of such a design is to split the hepatic flow to the left and right lung while avoiding head on flow collision of the HepV flow with the superior inflows. Both options make use of the existing intra-atrial graft thereby limiting the surgical procedure to the addition of a HepV-to-RPA branch, which is brought further to the RPA in Option 5 than in Option 6.

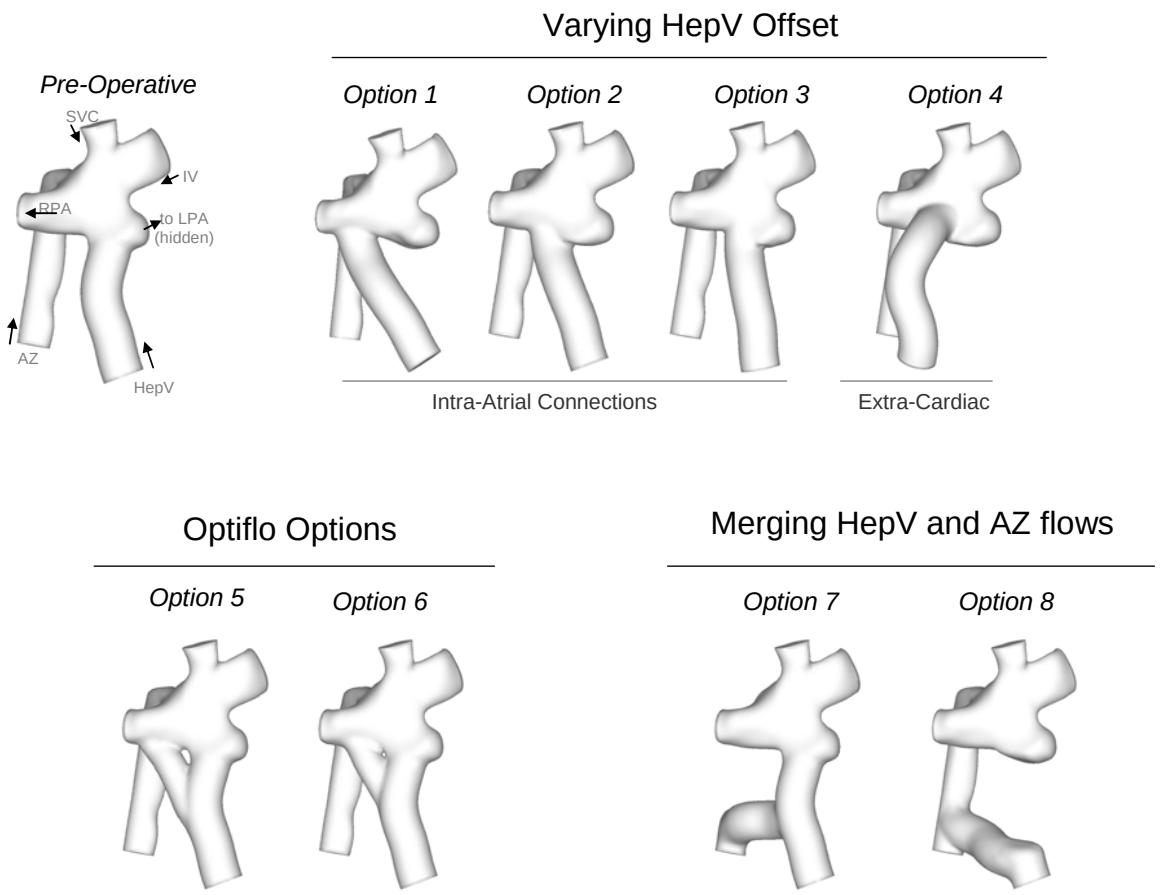

Figure 9-14: Geometry of the eight surgical planning options designed for Patient A2. The first four options vary the location of the HepV anastomosis site with respect to the superior inflows (HepV offset). Options 5 and 6 investigate the benefits of a Y-shaped Optiflo graft to avoid head-on collision. Options 7 and 8 seek to improve mixing by the redirecting either the AZ blood into the HepV baffle (Option 7) or the hepatic blood into the AZ vein (Option 8).

Finally, Options 7 and 8 aim at improving the hepatic flow distribution by including either an AZ-to-HepV (Option 7) or a HepV-to-AZ (Option 8) connection. In Option 7, the objective is to increase the momentum of the flow coming through the intra-atrial baffle, and thereby allow the HepV flow (in combination with the AZ flow) to compete with the superior inflows at the center of the connection. In Option 8, the intra-atrial baffle is taken down and the HepV flow is routed through a HepV-to-A shunt into the azygous vein. All venous returns enter the connection from the superior aspect of the PAs. The objective is to suppress all head-on collision and force flow mixing at the center of the connection. Options 7 and 8 are similar to Options 3 and 4 proposed for patient A1.

9.2.2.4 HFD Performance

The performance of the eight surgical planning options is assessed through series of numerical simulations using the same inflow conditions as for the pre-operative hemodynamics. The outflow conditions are adjusted so as to best predict the point at which an equal HFD to both lungs would be achieved. The performance at equal lung perfusion, i.e. when the global flow distribution is 50/50 RPA/LPA, is assessed for all options. Figure 9-15 shows the hepatic flow performance the surgical planning options over all tested flow conditions. The results are split into two graphs for clarity. The left panel shows the HFD_{RPA} achieved by Options 1 to 4, while the right panel shows the performance of Option 5 to 8. The pre-operative performance is provided as well in order to visualize the improvement brought in by the different options. As a reminder, the HFD_{RPA}=GFD_{RPA} curve (black dashed line) represents the best scenario where the hepatic flow distribution directly aligns itself to the global flow distribution.

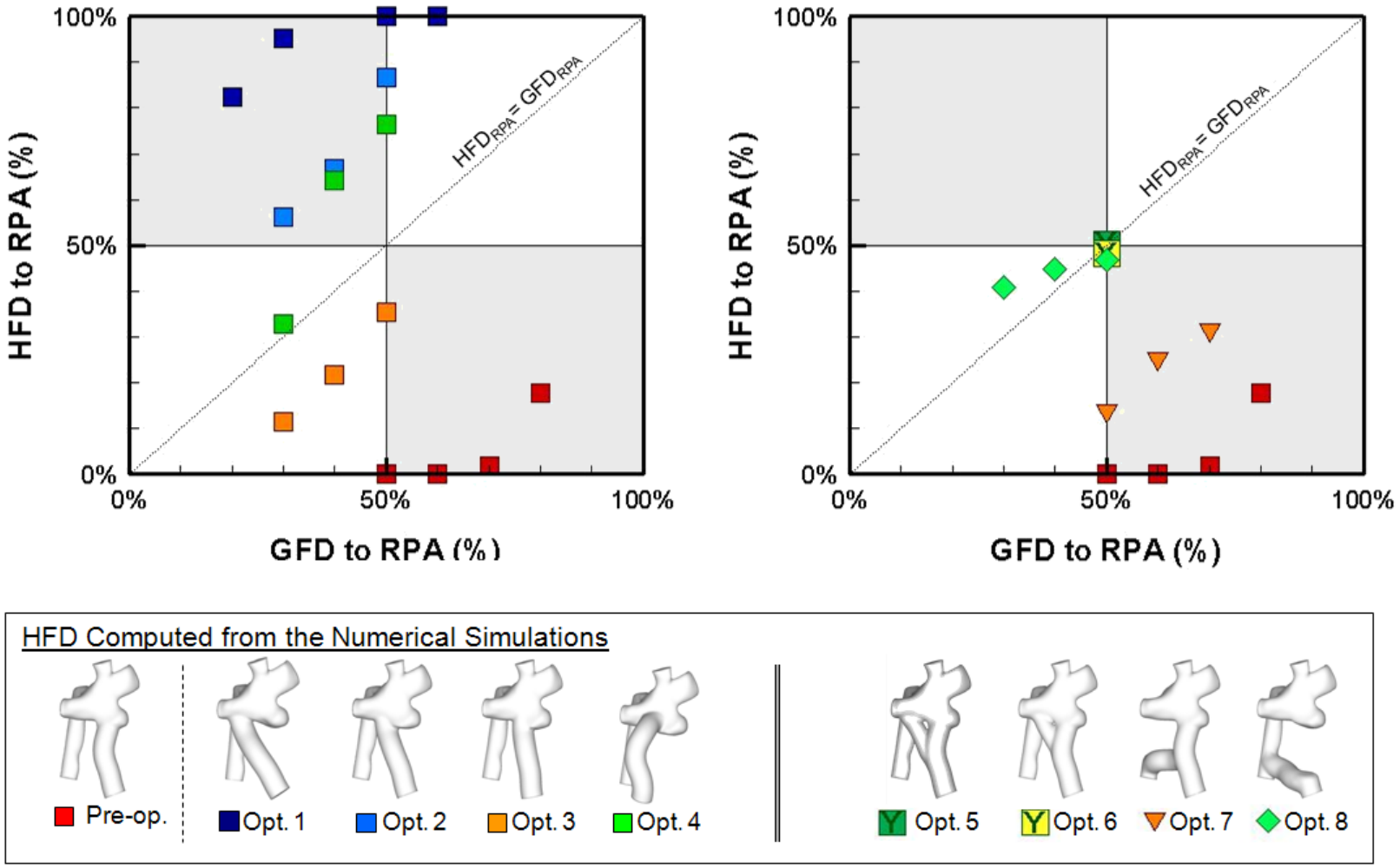

Figure 9-15: Comparison of the hepatic flow distribution achieved by the eight surgical planning options over the whole range of tested flow conditions. The results are separated in two graphs for clarity. The pre-operative anatomy is provided in the left panel to visualize the improvement brought in by the different options.

Options 1 to 4: The left panel of Figure 9-15 compares the HFD performance of the pre-operative anatomy and Options 1 through 4. The curves can be distinguished between those that fall above the $HFD_{RPA} = GFD_{RPA}$ line, which is indicative of a favorable HFD to the RPA, and those that fall below, indicating a favorable HFD to the LPA. The former category includes Options 1, 2 and 4, for which the HepV connects opposite to the aygous vein or further to the RPA. Symmetrically, Option 3 and the pre-operative anatomy, where the HepV connects opposite to the SVC or further to the LPA, favor HFD to the LPA. The worst performers are the pre-operative anatomy and Option 1, which fall the farthest away from the central line. Option 1, which has the largest offset towards the RPA, demonstrates an almost exclusive distribution of the hepatic flow to the RPA. This behavior is symmetric to what was observed for the pre-operative anatomy, indicating a very limited level of mixing between the hepatic blood and the other inflows. Options 2, 3, and 4, which were connected to the center of the connection more closely followed the central $HFD_{RPA} = GFD_{RPA}$ curve. However, it is striking to note that even a slight variation in the HepV anastomosis site leads to large changes in the measured HFD at all tested conditions.

To better understand the mechanism behind the observed HFD, Figure 9-14 compares the path followed by the hepatic flow in the eight surgical planning options at 50/50 RPA/LPA since this flow condition was tested for all geometries. The hepatic streamtraces going to the RPA and LPA are color-coded in blue and red, respectively. HFD_{RPA} and HFD_{LPA} are reported next to each option using the same color-coding. The dashed axis superimposed on Option 2 indicates the HepV stagnation point, which corresponds to the point where the superior inflows (IV, SVC and AZ combined) collide

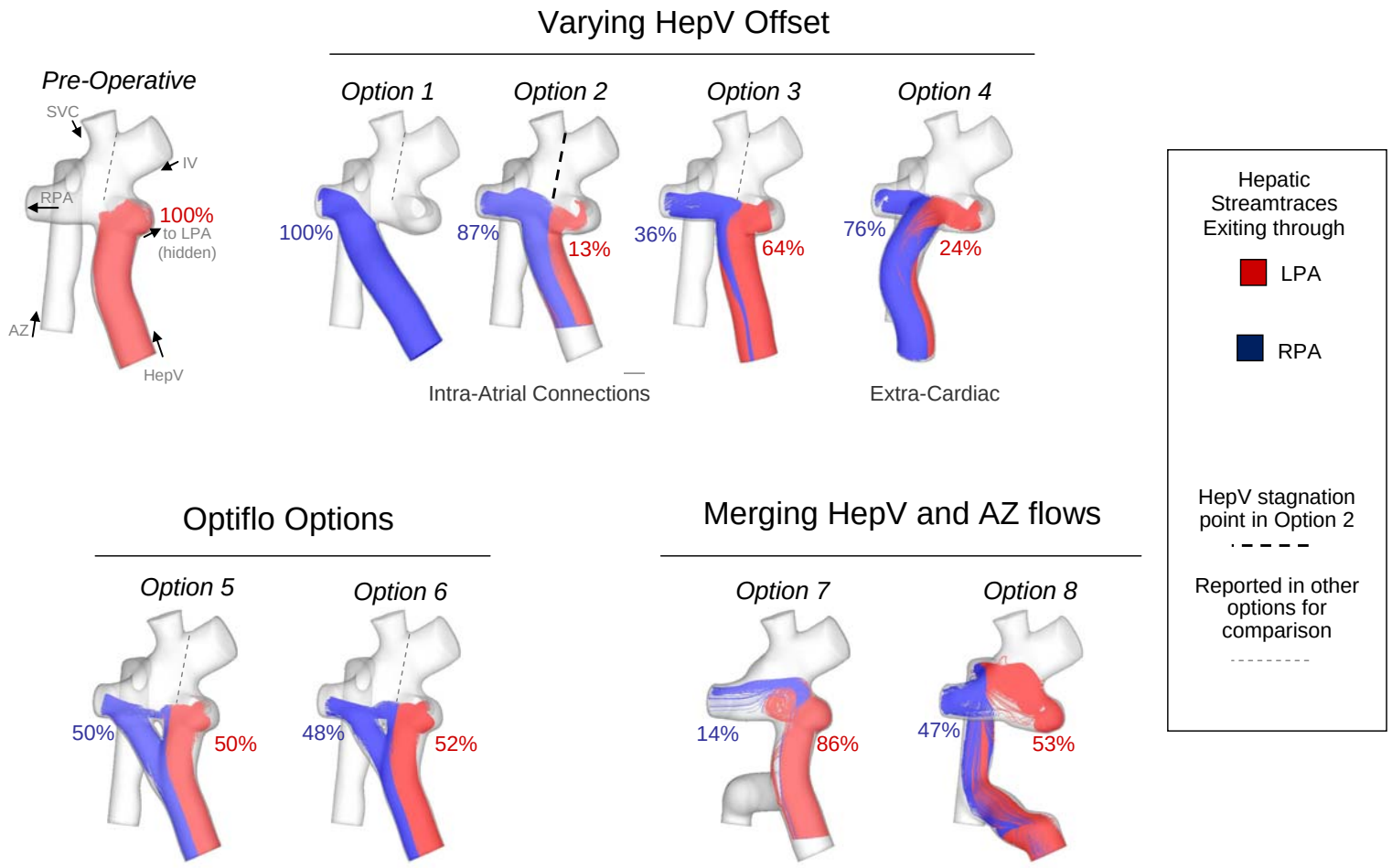

Figure 9-16: Hepatic flow splits in the pre-operative anatomy and the eight surgical planning options at a global flow distribution of 50/50 RPA/LPA. The location of the HepV stagnation point in Option 2 is reported on the other configurations that made use of an intra-atrial baffle to compare their locations.

into the HepV stream dividing it between the LPA and RPA. This axis is reported in the other intra-atrial geometries to compare the position of their flow stagnation point to that of Option 2. It is striking to note that the dashed axis points almost exactly to the flow stagnation point of Options 3, 5 and 6, demonstrating that the HepV flow splits in the same location in these three options as in Option 2. The fact that the location of the stagnation point is insensitive to the HepV offset demonstrates that, in these options, the HepV has little to no impact on the superior inflows. Rather, it is the superior inflows that dictate its distribution. Options 1 connects far to the right of the stagnation point and leads an exclusive HFD to RPA. Option 2 is slightly offset to the right of the stagnation and directs 87% of its flow to the RPA. Symmetrically, Option 3, which includes a slight offset to the left of the stagnation point, directs 64% of its flow to the LPA, while the pre-operative anatomy which lies almost entirely to the left of that point leads to an exclusive HFD-to-LPA. The hepatic flow distribution in the intra-atrial options appears to be related to the area of the baffle that lies to the left and right of the stagnation point.

The dynamics of Option 4, which uses an extra-cardiac approach, are slightly different. The baffle does not connect on the inferior aspect of the PAs but rather on its anterior side. This approach slightly improves mixing within the connection, resulting in HFD_{RPA} measurements (light green symbols in Figure 9-15) that are close to the center line at GFD_{RPA} = 30%. When GFD_{RPA} increases, the HFD measurements for Option 4 tend towards the ones obtained for Option 2, which has a similar HepV offset but uses an intra-atrial approach. This points to the HepV offset as being the main determinant for the hepatic flow distribution in Patient A2, while the type of procedure used (i.e. extra-cardiac vs. intra-atrial) only is a second order factor. The optimal HepV anastomosis site

appears to be related to the stagnation point of the superior inflows. The fact that such location does not depend only on geometric considerations, but also on the flow rates going through the different vessels, makes it difficult to identify and even more to generalize. Furthermore, the very high sensitivity of the HFD to the exact HepV location makes the classic intra-atrial and extra-cardiac options dangerous to implement *in vivo* for this patient.

Options 5 and 6: The Optiflo approaches (Option 5 and 6) provide an attractive alternative to this difficulty. As can be seen from the right panel of Figure 9-15, both of these options yield a close to 50/50 HFD, when the global flow distribution is of 50/50 RPA/LPA. This represents an ideal situation where the two lungs can be both properly perfused and receive a sufficient amount of hepatic nutrients. It is interesting to note that in Figure 9-16 the stagnation point for those two options falls at the exact same location as in Option 2. The Optiflo options are thus subjected to the same constraint as the classic intra-atrial approaches, but the advantage is that they circumvent the difficulty of identifying the best suited connection location. The only thing to ensure is that the two branches reach far enough into the PAs to seat on either side of the inflow splitting point.

Option 7: The HFD measurements for Option 7 in Figure 9-15 are notably closer to the centerline than those of the pre-operative anatomy, reflecting an improvement in HFD despite the fact that Option 7 used the same intra-atrial design as the pre-operative anatomy. Looking at Figure 9-16, it can be noticed that, the HepV streamtraces are not flattened by the superior inflows at the exit of the HepV baffle. On the opposite, they cross the entire diameter of the LPA, impinge on the superior wall, and then split between the left and right. Combining the AZ and HepV flows without changing the baffle

diameter increases the velocity and kinetic energy of the flow coming through the intra-atrial conduit, thus allowing it to resist the superior inflows. Despite the noted improvement, the HFD_{RPA} curve for Option 7 still falls far below the HFD_{RPA}=GFD_{RPA} line in Figure 9-15, which indicates a preferential HFD to the LPA. As such this option does not seem indicated for Patient A2. Using a more centered baffle design would most likely improve the performance of this option, but was not attempted for Patient A2.

Option 8: Results for Option 8 closely follow the central line in Figure 9-15. The streamtraces in Figure 9-16 span the entire connection area, reflecting an increased mixing between the different inflows. As was observed for Patient A1, this mixing leads to an almost perfectly balanced HFD at GFD_{RPA}=50%. For lower GFD_{RPA} values, results slightly depart from the central curve in favor of left lung, but remain within reasonable bounds with an HFD_{RPA} of 40.8% at GFD_{RPA}=30%.

9.2.2.5 Power Loss Performance

Considering the power loss behavior over a wide range of operating conditions is also an important factor in the clinical decision process. For a given set of flow conditions, higher power losses reflect a higher TCPC resistance, leading to increased central venous pressures and workload imposed on the heart. The power losses computed for the pre-operative anatomy and the surgical planning options are provided in Figure 9-17.

Options 1 to 4: The power losses associated with the "offset variation" options (Options 1 through 4) and the pre-operative anatomy collapse onto a single curve, indicating that the LPA-RPA offset only has little impact on power losses. The absence of difference between the extra-cardiac approach (Option 4) and the intra-atrial options (Options 1 to

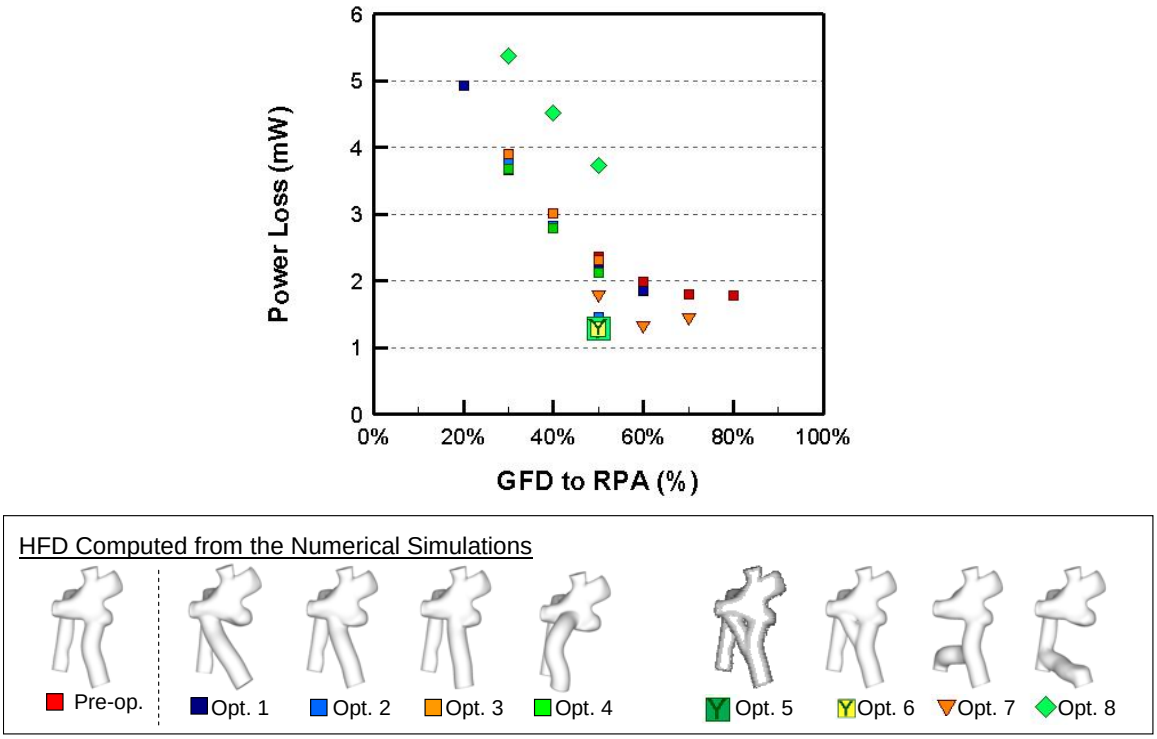

Figure 9-17: Power losses for all options tested for patient A2.

3), also suggests that HepV curvature is only a small contributor to the overall energy dissipation rate. Accordingly, power losses are not a strong discriminator between Options 1 and 4.

Options 5 and 6: From a power loss point of view, the best performance is achieved with the two Optiflo options (Options 5 and 6), which yield the lowest power losses of all tested options at GFD_{RPA}=50%. The adjunction of the HepV-to-RPA branch to the existing intra-atrial baffle increases the total cross-section area offered to the hepatic flow compared to the pre-operative anatomy or to Options 1 through 4. This increase in area leads to a reduction in the mean hepatic velocity, which in turn decreases the friction losses in the hepatic baffle. In addition, splitting the hepatic flow between the LPA and

RPA avoids flow mixing at the center of the connection, further reducing the amount of energy dissipation within these two options.

Options 7 and 8: Option 7 (orange triangles in Figure 9-17) is another attractive option from a power loss point of view, leading to a decrease in power losses compared to the pre-operative anatomy. This stems from the fact that the AZ is the smallest of the four inflows and, in the pre-operative anatomy, was associated with higher pressure drops than the HepV. By diverting the azygous flow away from this narrow vessel and into the hepatic baffle, Option 7 brings down the net energy balance, though not as low as Options 5 and 6. Option 8 (light green diamonds in Figure 9-17), on the contrary, features the highest power losses of all tested options, with values that are consistently 1.4mW to 1.5mW higher than those measured in the pre-operative anatomy or in Options 1 through 4. This increase may be attributed to the fact that, in this option, both the HepV and AZ flows go up the narrow azygous vein, resulting in an increased viscous dissipation along the azygous vessel walls. Finally, it is interesting to note that the power losses in Options 7 and 8 follow a trend similar to that of the pre-operative anatomy and Options 1 through 4, quickly increasing when GFD_{RPA} decreases below 70%. As was established during the pre-operative hemodynamic analysis, this trend finds its origin in the small dimension of the LPA, which makes it more expensive to drive flow through the LPA than through the RPA.

9.2.2.6 Surgical Planning Summary

In summary, eight re-operative options were examined for Patient A2, which mayy be grouped into three broad categories: the HepV offset variations using either

intra-atrial or extra-cardiac grafts (Options 1 through 4), the Optiflo options (Options 5 and 6) and the options combining HepV and AZ flows (Options 7 and 8). HFD appeared to be highly sensitive to the offset between the HepV anastomosis site and the center of the Kawashima connection. Such a high sensitivity makes the traditional intra-atrial and extra-cardiac options dangerous to implement *in vivo*, leaving very little error margin during their actual surgical implementation. An AZ-to-HepV shunt, as in Option 7, slightly reduced the sensitivity to the offset. However, Option 7 made use of the pre-operative intra-atrial baffle and thus still resulted in a preferential HFD to the LPA. It might be inferred that and AZ-to-HepV shunt combined with a more centrally connected baffle would yield better performance but this would require two procedures (designing an AZ-to-HepV shunt and shifting the intra-atrial baffle) which would prolong the time spent during the surgery. The two Optiflo options (Options 5 and 6) and the HepV-to-AZ shunt (Option 8) yielded very satisfactory results in terms of HFD. However, due to the small dimension of the Patient A2's azygous vein, Option 8 came at an elevated energy cost. As a result, an Optiflo approach appeared better suited for Patient A2 and was the option recommended for surgery.

9.2.3 Patient A3 (CHOP M4)

9.2.3.1 Pre-Operative Anatomy and Clinical Diagnosis

The third patient of the single SVC group, Patient A3, was a 3 year old female patient born with a heterotaxy syndrome, SVHD, interrupted IVC, and a malaligned atrioventricular canal to the right ventricle. This patient had previously undergone a Kawashima procedure and was awaiting TCPC completion. She was diagnosed with bilateral PAVMs, which were attributed to the absence of any hepatic flow to the lungs due to the incomplete TCPC. The patient was referred for an MRI examination to enable a surgical planning investigation and identify the best TCPC completion procedure.

Patient A3's pre-operative anatomy at the time of diagnosis is shown in the left panel of Figure 9-18. The right panel also displays the heart and great vessels to better represent the spatial constraints faced by the surgeon. The inlet and outlet cross-sections are listed in Table 9-6, together with the available *in vivo* MRI flow measurements and CFD flow conditions. It should be pointed out that the MRI flow measurements for the superior inflows were acquired downstream of the IV and SVC confluence. Accordingly, only the common SVC trunk was considered in the CFD simulations and not the individual IV and SVC branches. The SVC was oriented almost perpendicularly to the pulmonary arteries with no visible preferential direction, while the AZ vein came in at an angle, its axis oriented towards the LPA. Due the young age of Patient A3 compared to Patient A2 (3 vs. 6 years of age), the vessel cross-sectional areas reported here are significantly smaller than in the last case. As an example, the cross-sectional area offered to the superior venous returns in Patient A3 was limited to the SVC cross-sectional, i.e. to 1.34 cm^2, whereas for Patient A2 the cross-sectional area offered to the superior venous

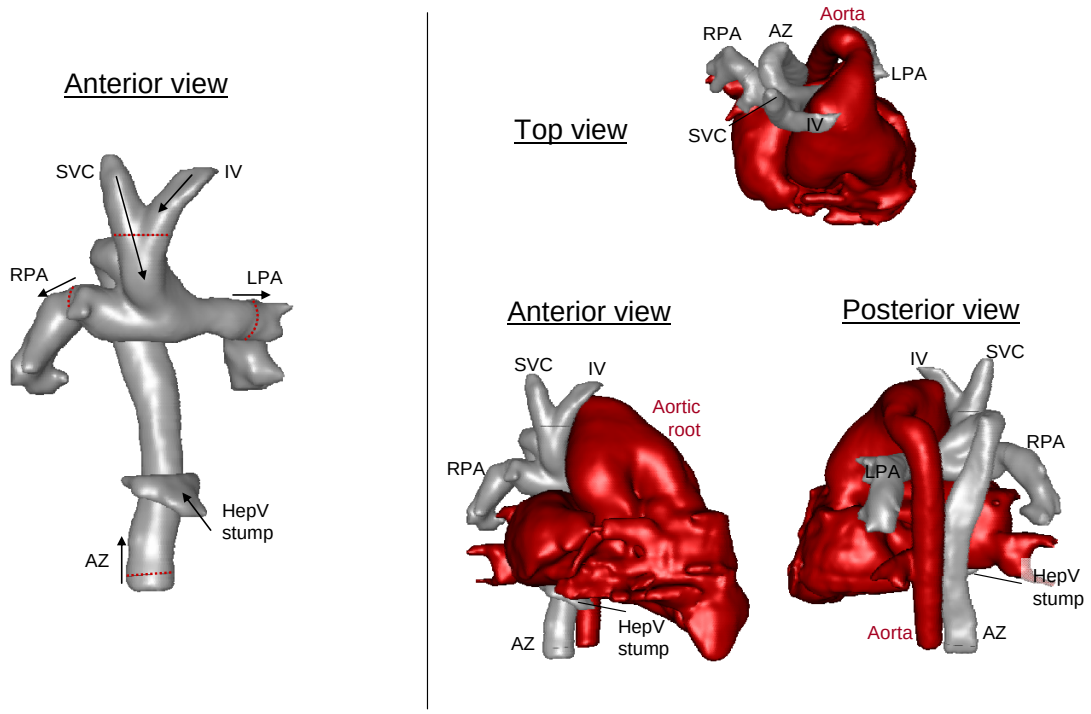

Figure 9-18: On the left, Patient A3's pre-operative TCPC anatomy is shown as a stand alone structure. The dotted red liens show the point where the vessels were cut for the CFD simulations. On the right, the TCPC (in gray) is shown with the heart (in red) to better represent the spatial constraints faced by the surgeons.

Table 9-5: Geometric and flow characteristics of Patient A3 at the time of PAVM diagnosis, and flow boundary conditions used for the CFD simulations. Q_S: sum of the systemic inflows. Q_P: sum of the pulmonary outflows.

	Cross-sectional Area (cm^2)	In Vivo Flow measurements		CFD Flow Conditions		
		Q (L/min)	Q (%)	Q (L/min)	Q (%)	Characteristic Velocity (cm/s)
Systemic Venous Return						
HepV	1.91	1.23	32%	1.23	32%	10.75
AZ	0.58	0.64	17%	0.64	17%	18.44
SVC	1.34	1.98	51%	1.98	51%	24.65
Q_S		3.85		3.85		
Pulmonary Flows						
LPA	0.76	1.22	49%	1.89	49%	41.38
RPA	1.28	1.26	51%	1.96	51%	25.46
Q_P		2.48		3.85		

returns by the SVC and IV combined amounted to of 2.27 cm^2. In addition, the AZ was compressed in the anterior-posterior direction, resulting in a cross-sectional area of only 0.58 cm^2 compared to more than 1 cm^2 in the earlier patient cases. The LPA cross-sectional area was only about half that of the RPA. Based on the experience gained with Patient A2, it might thus be expected that the power losses will show a strong dependency on the LPA flow rate.

Finally, a few points a worth noting regarding the pre-operative *in vivo* flow distributions. First, the SVC carried a significantly higher share of the flow (51% Q_S) than previous patients, while the AZ carried a significantly lower share of the flow (17% Q_S). This is consistent with Patient A3's younger age, since the systemic venous return has been shown to progressively switch from the upper to the lower limbs as children grow [76]. The hepatic veins carried a non-negligible share of the venous return with 32% Q_S. Finally, unlike Patients A1 and A2, Patient A3 featured an almost balanced global flow distribution, with 51% and 49% Q_p going to the RPA and LPA, respectively. This stemmed from the fact that both lungs had PAVMs, so that there was no major imbalance in the right and left pulmonary vascular resistances.

9.2.3.2 Surgical Planning Options

Figure 9-19 shows the eight surgical options that were designed for Patient A3. Options 1 through 6 vary the anastomosis location of the HepV baffle, progressively shifting the HepV offset from the right to the left of the Kawashima connection. Option 1 is an extra-cardiac baffle that is connected onto the anterior aspect of the SVC anastomosis, to the right of the AZ vein. Option 2 and 3 connect with a similar offset, but

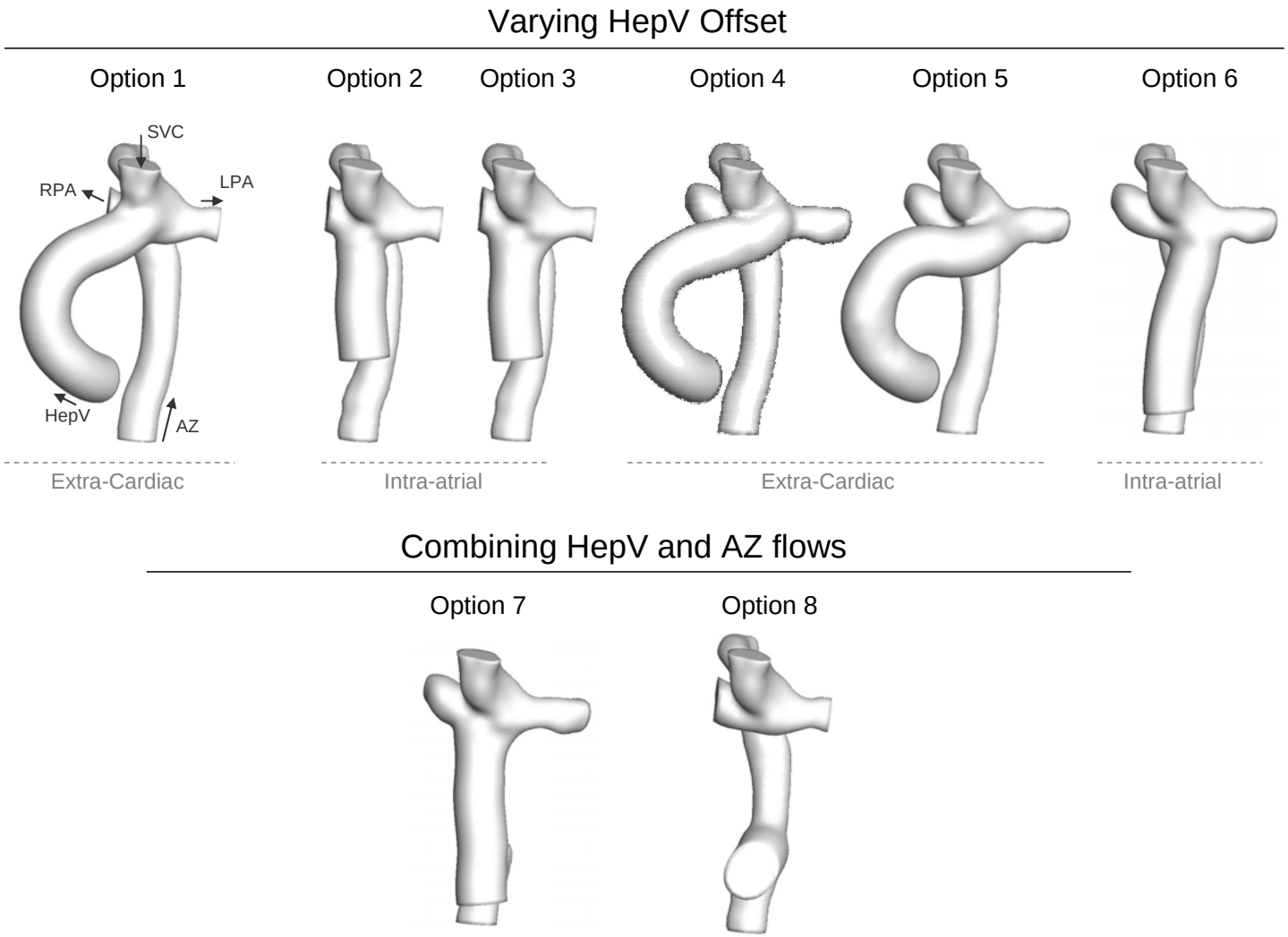

Figure 9-19: Surgical planning options implemented for Patient A3. All geometries are viewed from the anterior side.

onto the inferior aspect of the SVC anastomosis site using an intra-atrial approach. Option 3 also includes a slight flaring towards the LPA, so as to open up the connection on its left side, and promote hepatic flow distribution to the LPA. Option 4 uses an extra-cardiac graft to reach the PAs slightly on the left of the SVC, opposite to the AZ connection site. Finally, Options 5 and 6 reach to the left of the AZ vein, using an extra-cardiac graft in Option 5 and an intra-atrial graft in Option 6.

Based on the positive results obtained for Patients A1 and A2, Options 7 and 8 seek to promote mixing between the superior and inferior inflows by combining the HepV and AZ flows. In Option 7 the azygous flow is routed towards the hepatic baffle through an AZ-to-HepV shunt. This option then makes use of the same flared intra-atrial baffle design as in Option 3. Option 8 performs the opposite combination, routing the hepatic flow through a HepV-to-AZ shunt into the AZ vein.

9.2.3.3 HFD Performance

The performances of the eight surgical planning options are assessed through series of numerical simulations using the pre-operative *in vivo* flow rates at the inflows. The performance under the pre-operative outflow boundary conditions, i.e. when the global flow distribution is 51/49 RPA/LPA, is assessed for all options to predict the behavior in the acute post-operative stage. The outflow conditions are then varied so as to best predict the point at which an equal HFD to both lungs would be achieved. The hepatic flow distributions associated with the eight surgical planning options are displayed in Figure 9-20 for all tested flow conditions. For better readability, the results are split in two graphs. The left panel shows the results obtained for Options 1 through 6, while the right panel displays the results obtained for Options 7 and 8.

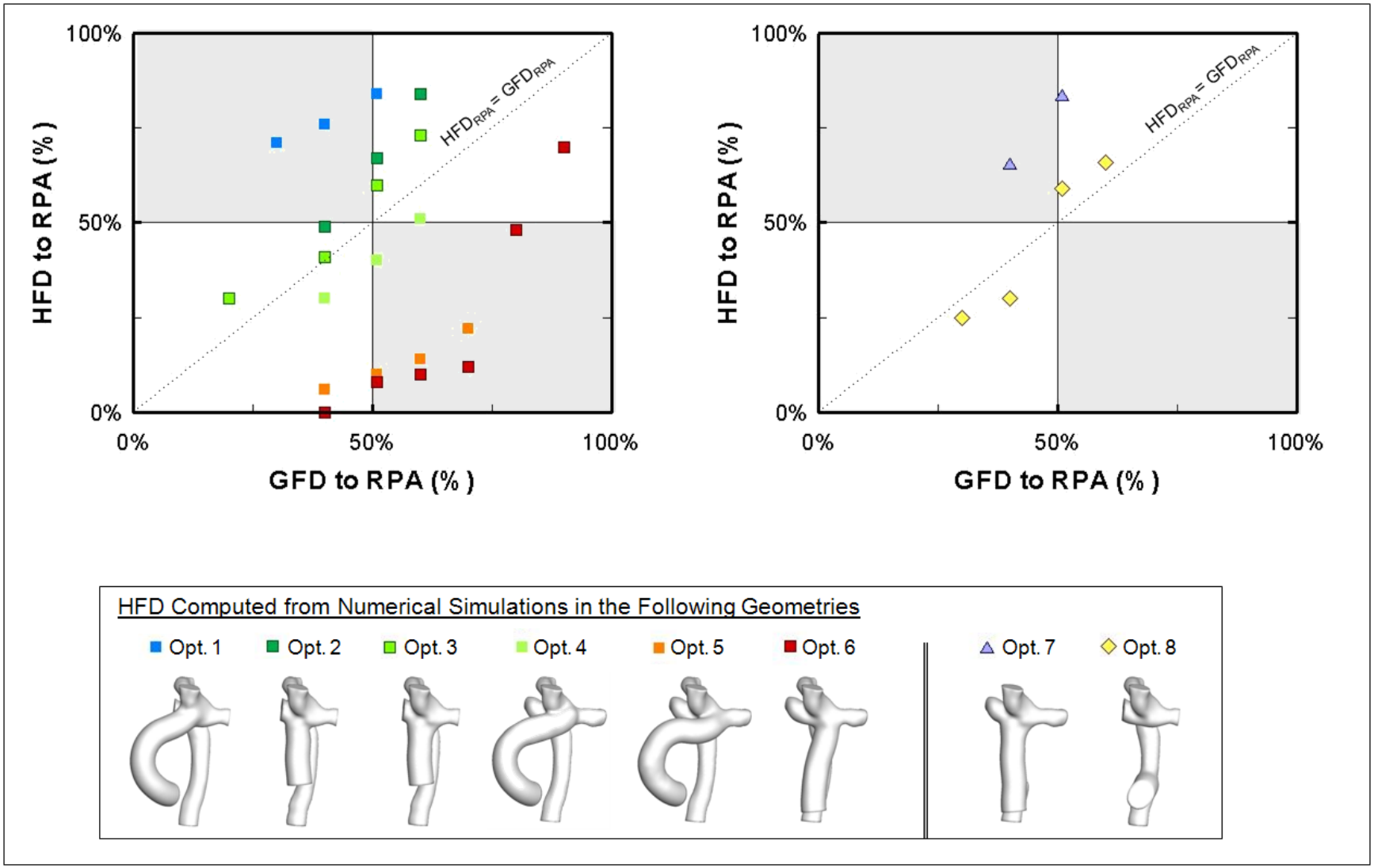

Figure 9-20: Hepatic flow distribution in the eight surgical planning options tested for Patient A3.

Options 1 to 6, offset variations: Focusing on the right panel of Figure 9-20, it may be noticed that the HFD_{RPA} measurements for Option 1 (blue symbols) fall far above the HFD_{RPA}=GFD_{RPA} line, testifying for a preferential HFD to the RPA. HFD_{RPA} measurements for the intra-atrial options 2 and 3, and the extra-cardiac option 4 fall within close range of the HFD_{RPA}=GFD_{RPA} line, testifying for an HFD that closely follows the global flow distribution to the right and left lung. Finally, the two options connected to the left of the Kawashima (i.e. Options 5 and 6) show a highly preferential HFD to the LPA, with HFD_{RPA} measurements that fall far below the HFD_{RPA}=GFD_{RPA} line. From these results it is apparent that the HepV offset is a key determinant for the hepatic flow distribution. In addition, the HFD_{RPA} measurements of Options 2, 3 and 4 follow a trend almost parallel to the HFD_{RPA}=GFD_{RPA} line, showing a lower dependency of HFD_{RPA} on the global flow distribution than what was observed for Patient A2. This stems from the fact that Patient A3 had a higher proportion of the systemic venous return coming through the hepatic veins than Patient A2, so that the HepV flow could more readily oppose the superior venous returns.

It is also interesting to note that the intra-atrial option 2 had a significantly better HFD performance than the extra-cardiac option 1, even though both connected with a similar HepV offset. To elucidate the dynamics leading to these HFD, Figure 9-21 and Figure 9-22 compare the flow structures associated with the three extra-cardiac and three intra-atrial options under the pre-operative GFD of 51/49 RPA/LPA. The flow structures are displayed as 3D streamtraces color-coded by their vessel of origination. From Figure 9-21, it can be observed that, in Option 1, the hepatic streamtraces (orange) come in with a preferential orientation towards the LPA due to the

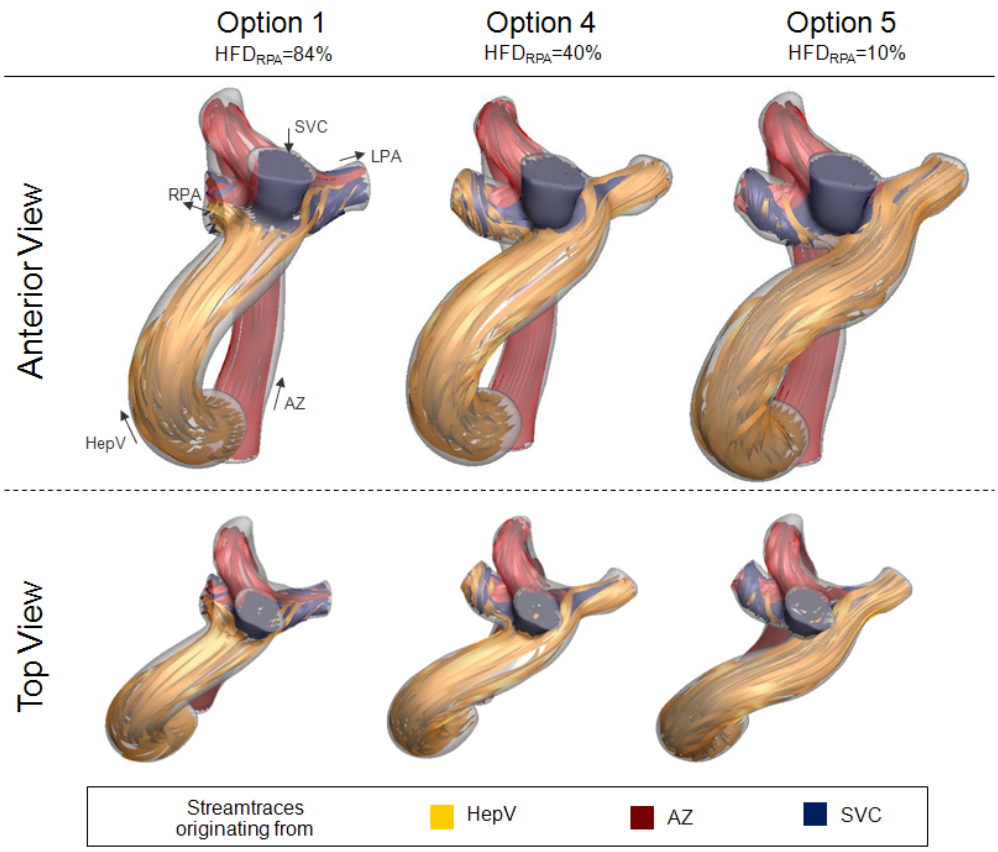

Figure 9-21: Flow structures and HFD associated with the three extra-cardiac options (Options 1, 4 and 5) at the *in vivo* GFD of 51/49 RPA/LPA.

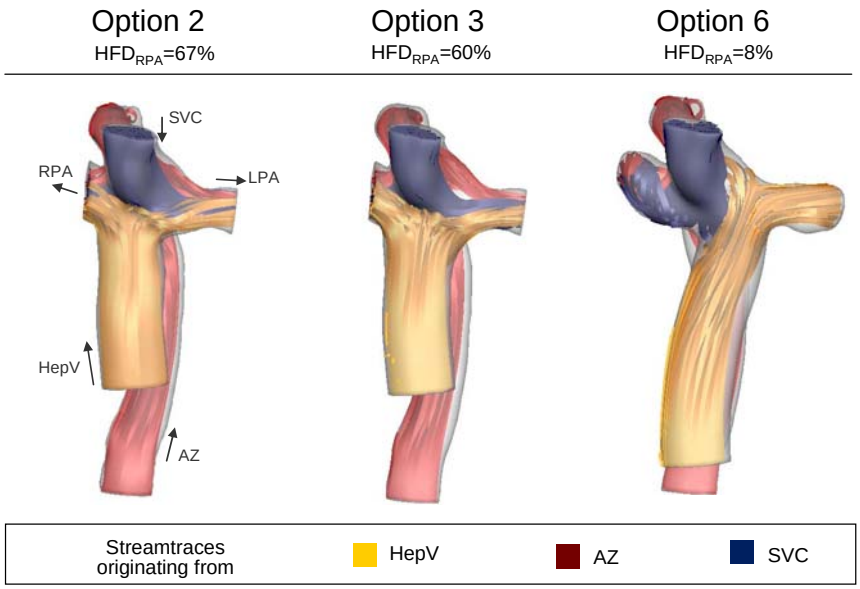

Figure 9-22: Flow structures and HFD associated with the three intra-atrial options (Options 2, 3 and 6) at the *in vivo* GFD of 51/49 RPA/LPA. All options are viewed from the anterior side.

curvature of the extra-cardiac baffle. These streamtraces then collide with the SVC flow (in blue), which prevents their entry into the LPA. As a result, despite the curvature of the extra-cardiac graft, most hepatic flow turns towards the RPA, leading to the high HFD_{RPA} values reported in Figure 9-20.

The dynamics of the intra-atrial options (illustrated in Figure 9-22) are drastically different. In Option 2, the hepatic flow also collides with the SVC flow, but in a head-on manner, where both SVC and HepV streams come in opposite directions. This leads to the formation of a stagnation point at the center of the connection, from which both SVC and HepV streams split towards the LPA and RPA. As a result, even though Option 2 has an offset similar to the extra-cardiac Option 1, significantly more hepatic flow goes to the LPA than in the extra-cardiac implementation. Flaring the HepV baffle towards the left allows a better splitting of the HepV stream and further improves hepatic flow distribution. Options 5 and 6 both reach too far to the left, so that the HepV streamtraces flow directly into the LPA without interacting with the SVC and AZ streams, leading to the small HFD_{RPA} values reported in Figure 9-20.

Options 7 and 8: The HFD performance of the two options combining AZ and HepV flows (Options 7 and 8) are shown in the right panel of Figure 9-20, while the associated flow structures are illustrated in Figure 9-23 under the pre-operative GFD of 51/49 RPA/LPA. Option 7 seeks to reduce the sensitivity to the HepV offset by combining the AZ and HepV streams into the same intra-atrial baffle as in Option 3. However, for this patient, the AZ stream (red streamtraces in Figure 9-23) flows along the left side of the baffle, thus forcing more of the hepatic flow into the RPA than was the case in Option 3. As a result, the HFD_{RPA} measurements for Option 7 (blue triangles in

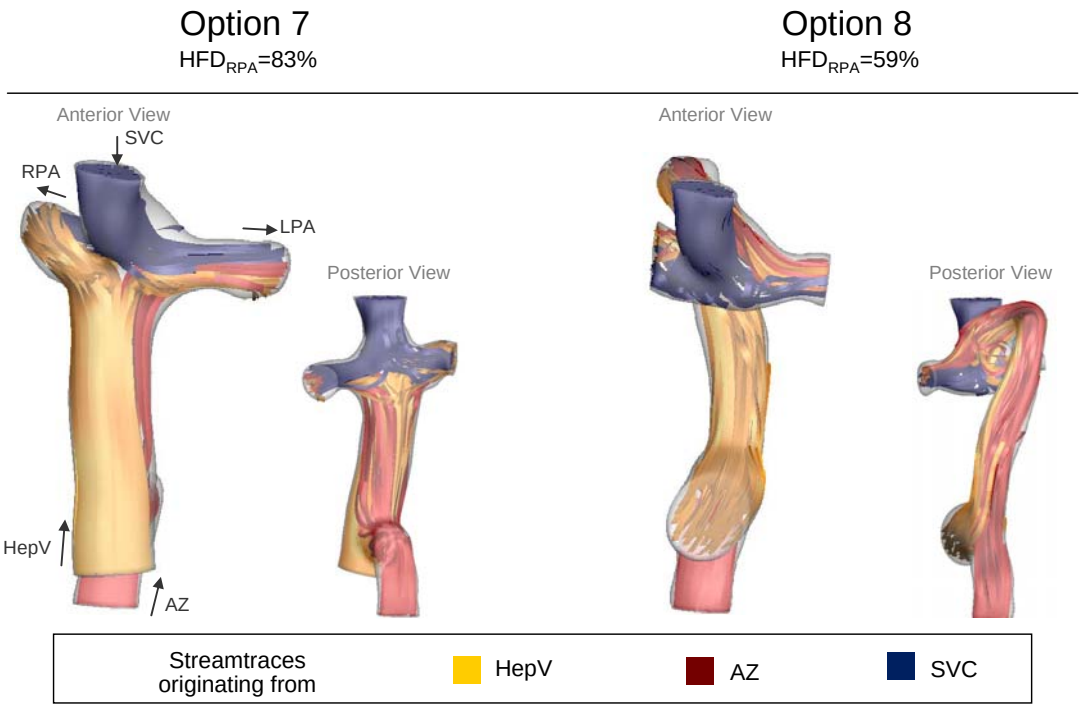

Figure 9-23: Flow structures and HFD associated with the two options combining AZ and HepV flows (Options 7 and 8) at the *in vivo* GFD of 51/49 RPA/LPA. Both anterior and posterior views are provided for a better understanding of the AZ and HepV interactions.

Figure 9-20) fall above the $HFD_{RPA}=GFD_{RPA}$ line, demonstrating a preferential HFD to the RPA at all tested flow conditions. Due to the smaller dimensions and less regular shape of the AZ, routing the HepV to the AZ (Option 8) forces the AZ and HepV streams to mix thoroughly as is testified by the entangled red and orange streamtraces in Figure 9-23. The mixed streams then collide with the SVC and split between the two lungs. As a result, HFD_{RPA} measurements for Option 8 fall within close range to the $HFD_{RPA}=GFD_{RPA}$ line, testifying for a proper hepatic flow distribution. Option 8 thus led an HFD performance comparable to that of Options 2, 3 and 4 but with drastically different hemodynamics.

9.2.3.4 Power Loss Performance

Beyond HFD another parameter of interest is the amount of energy dissipated through the connection. The power losses associated with the eight surgical planning options are displayed in Figure 9-24. For clarity, the results are separated into two graphs, the left panel focusing on the offset variation options (Options 1 through 6) and the right panel showing the results for the two options combining AZ and HepV flows (Options 7 and 8). Both graphs use the same scale for ease of comparison.

Options 1 to 6: In the right panel of Figure 9-24, the power losses measured for the first six options almost overlap, demonstrating that for intra-atrial or extra-cardiac baffles of the same diameter, the baffle design and HepV offset have only little impact on the amount of energy dissipation. All six options follow a trend of decreasing power losses as GFD_{RPA} increases from 20% to 70%. Measurements for Option 6 then reveal a steep increase in power losses as GFD_{RPA} increases to 80% and 90%. The mechanism for decreasing and subsequently increasing power losses is best illustrated by looking at the measured pressure drops, as illustrated in Figure 9-25 for Option 6. Due to the smaller LPA cross-sectional area (0.76 cm2) compared to the RPA (1.28 cm2), the former vessel is the highest source of resistance to the blood flow. As a result, the highest pressure drops are recorded in the LPA until the flow to that vessel drops below 40% of the cardiac output (i.e. until GFD_{RPA} exceeds 60%). While part of the potential energy is transformed into kinematic energy to accelerate the flow through the LPA, part of it is also dissipated in friction along the vessel walls. At GFD_{RPA}=60-70%, the LPA and RPA pressures are almost equal, which corresponds to the minimum observed in the power

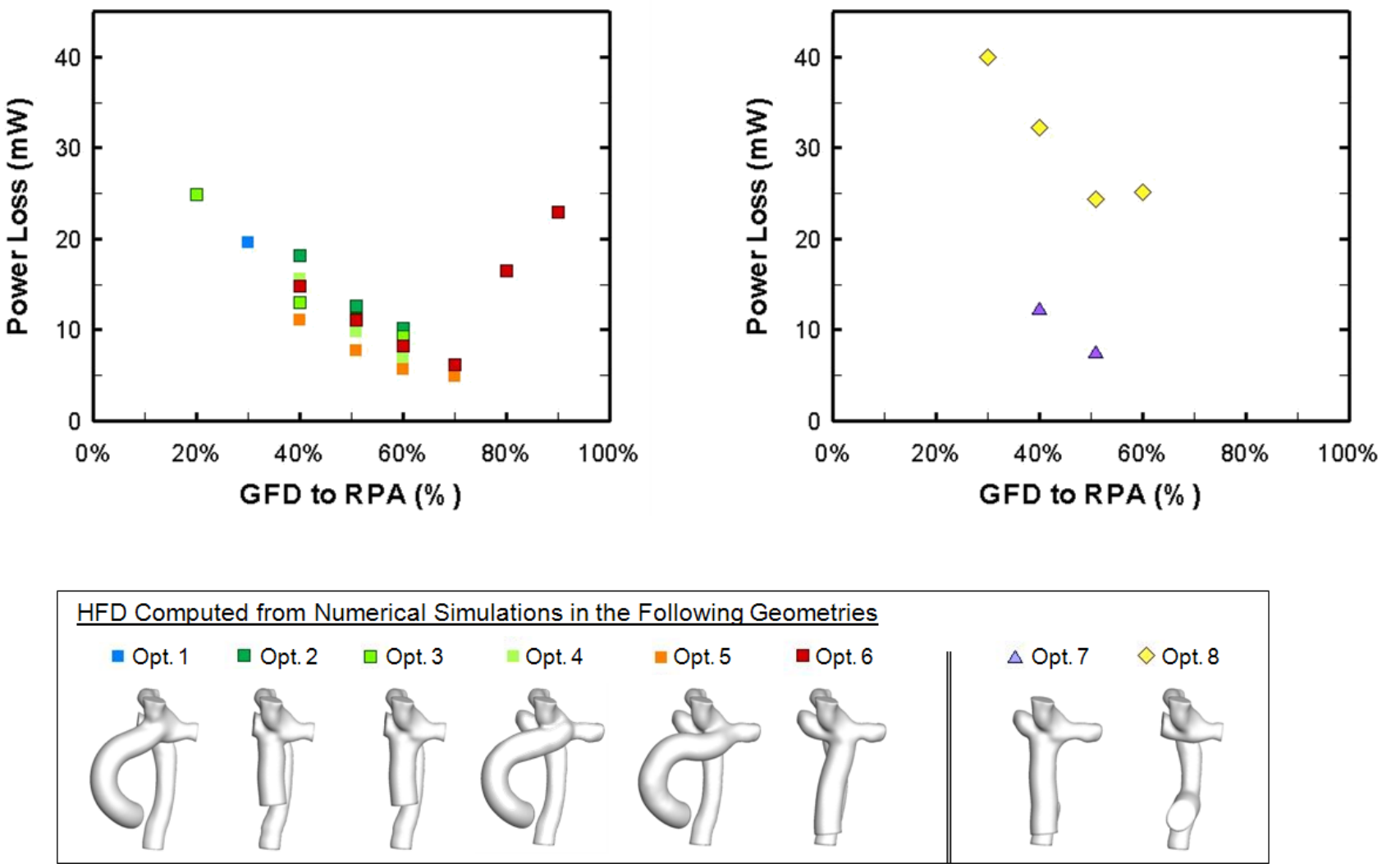

Figure 9-24: Power Loss measured across the eight surgical planning options attempted for Patient A3 for all tested GFD conditions.

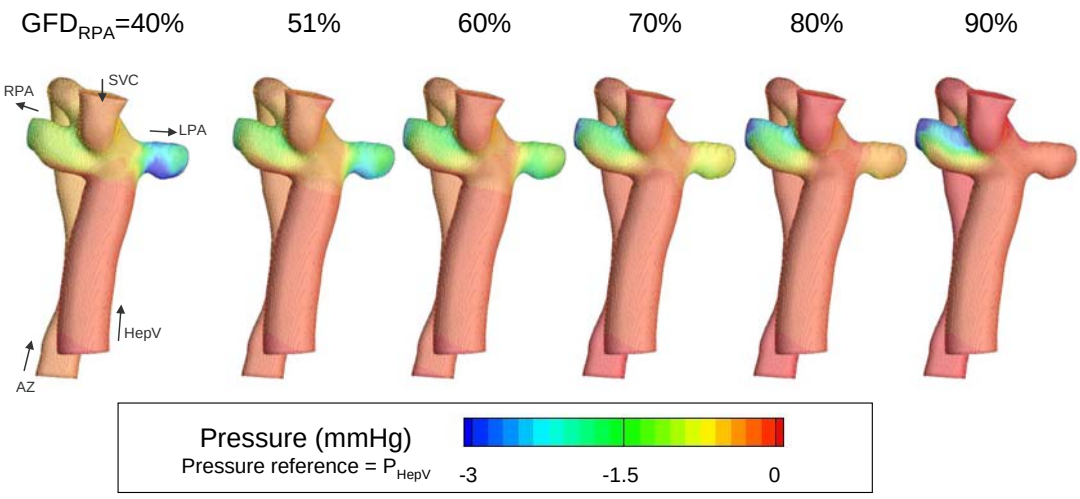

Figure 9-25: Pressure fields associated with Option 6 for a GFD varying between 40/60 and 90/10 RPA/LPA. All pressures are expressed taking the mean pressure across the HepV inlet as a reference.

.

loss curves. As GFD_{RPA} increases beyond 70%, it may be noticed that it is the RPA that features the highest pressure drops, reflecting both a stronger flow acceleration and higher energy dissipation.

Options 7 and 8: The left panel of Figure 9-24 displays the power losses associated with the two options that combine HepV and AZ flows. Option 7, where the combined flows are directed to an intra-atrial baffle, leads to energy dissipation levels comparable to those of Options 1 to 6. Adding the AZ flow to the HepV flow increases the energy dissipation through the baffle, but this increase is compensated by the absence of energy dissipation through the AZ vein. Option 8, on the other hand, is associated with significantly higher power losses than Options 1 through 7. From the velocity and pressure fields displayed in Figure 9-26, a sudden flow acceleration can be noted in the azygous vein after the AZ and HepV flow have merged together. This flow acceleration is here again associated

with a sudden pressure drop and increased energy dissipation by wall friction, leading to a higher baseline energy dissipation than in the seven former options. The dependency on the global flow distribution is then similar to that of Option 1 through 7, reaching a minimum between GFD_{RPA}=60% and 70%. Apart from this latter option, which yielded significantly higher energy dissipation than Options 1 through 7, power losses did not significantly discriminate between the different surgical options.

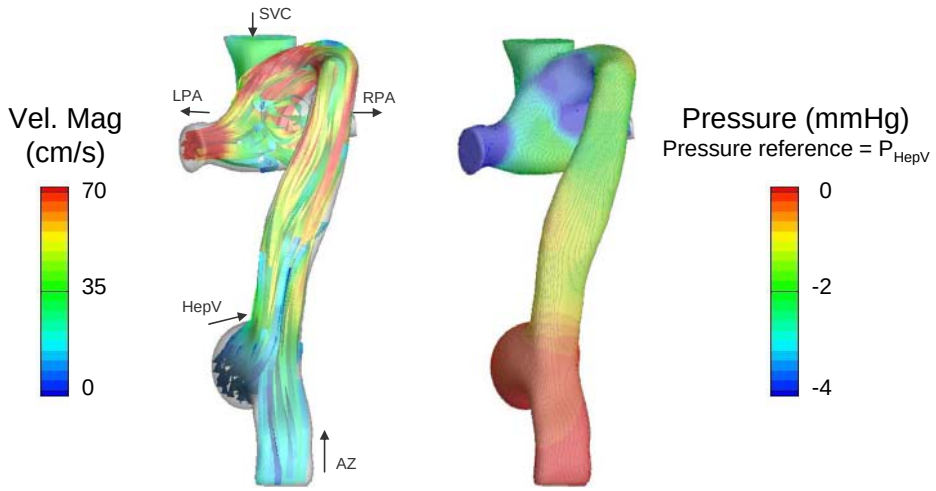

Figure 9-26: Velocity and pressure fields associated with Option 8 at the pre-operative GFD of 51/49 RPA/LPA. The anatomy is viewed from the posterior side to better visualize the flow acceleration and pressure drops in the AZ vein.

9.2.3.5 Surgical Planning Summary

A total of eight options were investigated for Patient A3, looking into the impact of the HepV offset (Options 1 through 6), the choice of baffle design (intra-atrial options 2, 3 and 6 vs. extra-cardiac options 1, 4 and 5), and different combination of HepV and

AZ flows (Options 7 and 8). A particularity of Patient A3 stemmed from a higher hepatic flow rate compared to A1 and A2. As a result, HFD showed a lower sensitivity to HepV offset, especially when using an intra-atrial design. The intra-atrial baffles that connected directly opposite to the SVC and AZ anastomosis site (Options 2 and 3) lead to a close to ideal HFD. The extra-cardiac options, on the other hand, were more sensitive to HepV offset, as the interaction between the HepV and SVC flows resulted from a combination between the angle of incidence (governed by the extra-cardiac baffle curvature) and the connection site (governed by the HepV offset). Such sensitivity leaves little margin for error and as such extra-cardiac options were not recommended for Patient A3. Merging the AZ flow into the hepatic baffle (Option 7) did not appear as a satisfactory option either, as the azygous flow constrained the hepatic flow towards the right side of the baffle and into the RPA. The opposite approach, merging the HepV flow into the AZ (Option 8), lead to an increased mixing of the venous returns and achieved satisfactory HFD to both lungs. From an HFD stand-point both the intra-atrial options 2 and 3 and the HepV-to-AZ option 8 appeared as suitable candidates. However, while power losses did not discriminate between the first seven options, they were significantly higher in Option 8 than in Options 2 and 3. Based on the above observations, the recommendation for Patient A3 was thus to perform an intra-atrial connection with no or minimal HepV offset as in Options 2 and 3.

9.2.4 Summary of the Single SVC Cases

A few conclusions and trends can be derived from the three patient cases studied in this section. All three patients demonstrated a high sensitivity of the HFD to the offset between the HepV connection site and the Kawashima connection. For the two first patients, the sensitivity to HepV offset was such that the traditional intra-atrial or extra-cardiac procedures did not appear as suitable surgical options. Due to the fact that the intra-atrial or extra-cardiac baffles only carried the hepatic blood flow (instead of the combined hepatic and lower limb venous returns in patients without an interrupted IVC), the velocities in the baffle were typically lower than in all the other inflows, resulting in a lower kinetic energy and an incapacity of the HepV flow to sustain the competition with the superior inflows. The optimal offset thus appeared to be governed by the superior inflows, their relative contributions to the total systemic venous return and their main flow directions. All of these considerations make it difficult to identify the best baffle design and anastomosis site, pointing to traditional extra-cardiac or intra-atrial connections as suboptimal approaches for patients with an interrupted IVC and a single SVC. Patient A3 presented a notable exception as the recommended option was to perform an intra-atrial connection. However, it should be pointed out that this patient featured a higher HepV flow rate than the other two, which allowed the HepV flow to better resist the superior inflows and reduced the sensitivity to offset. In such cases, the optimal solution was to minimize the HepV offset, so as to maximize the interaction and mixing between the different inflows.

Optiflo options, which divide the hepatic flow into a left and right branch and seek to avoid the direct collision and competition with the superior inflows, could appear

as an attractive alternative. The key design parameter appeared to be design the graft such that the point where it would split into two branches would be aligned with the flow axis, effectively dividing the HepV flow into a left and right stream. This was difficult to ensure with an extra-cardiac graft (as for Patient A1) due to the baffle curvature which tended to favor hepatic flow to one branch over the other. An intra-atrial implementation as was suggested for Patient A2 appeared as more efficient, even though it may be more challenging to perform surgically. An added weakness of the Optiflo options is that they do not solve the problem of the low HepV energy, such that the HepV flow is still subjected to the influence of the superior inflows. In cases such as Patient A1, where the superior inflows have a strong preferential orientation to one lung (the left lung for Patient A1), the HepV flow might still be forced towards the contra-lateral branch of the graft (the right branch for Patient A1). As a result, even though using an Optiflo appeared as the optimal solution for Patient A2, these results may not be generalized to all patients.

Increasing the energy of the blood flowing through the baffle (would it be an extra-cardiac, intra-atrial or Optiflo) by merging the AZ and HepV flows into the baffle was attempted for all patients. For Patients A1 and A2, such approach lead to significant improvements in HFD, but the HFD was still highly dependent on the HepV offset. In addition in some cases, such as Patient A3, the AZ flow effectively constrained the HepV to one side of the baffle, leading to suboptimal HFD performance. As such, merging the AZ flow into the HepV baffle does not appear as a general approach. Furthermore, for all three patients considered in this section, this option never stood out as the best approach.

Re-routing the HepV flow into the azygous vein appeared as a well performing option from an HFD stand point for all three patients. This approach maximized the

mixing between all systemic venous returns, thus ensuring that the HFD closely followed the global flow distribution. However, this option was plagued by higher energy losses than all other alternatives. Accordingly, while merging the HepV flow into the AZ vein might be the best option by default, individualized surgical planning studies might help identify better performing alternatives.

Finally, it is worth pinpointing that within each patient case, there was no notable difference in pressure drops and power losses among the surgical options, apart for the HepV-to-AZ option which systematically increased the pressure drops and energy dissipation rate across the AZ vein. The largest pressure drops were observed in the PAs and the power loss dependence upon GFD was governed by the relative RPA and LPA cross-sectional areas. Comparing across different patients, it might be noticed that the power losses for Patient A3 spanned a significantly higher range (between 5 and 40 mW) than for Patient A2 (between 1 and 6 mW). This stemmed from Patient A3's smaller vessel dimensions but similar cardiac output, which translated into higher velocities and higher energy dissipation rate across all vessels. All of these results point to the vessel cross-sectional areas and the mass flow rates through each vessel as being the main predictors for energy dissipation, while other parameters such as the HepV offset or type of baffle used (intra-atrial vs. extra-cardiac) play a secondary role. The primary mechanism for energy dissipation in the TCPC is thus the viscous friction along the vessel walls, while the disturbances at the center of the connection (which will be impacted by the baffle design and offset) are only second order parameters. Accordingly, apart for the HepV-to-AZ options, power losses did not significantly discriminate between the different surgical options and HFD was the main optimization parameter.

9.3 Group B: Patients with a Persistent LSVC

This section covers the surgical planning investigations that were carried for the three patients with a persistent LSVC. These patients differ from the former patient group in that the left and right superior venous returns reach the PAs in two different locations, leading to drastically different interactions between the different inflows. Results are organized in a similar fashion as for Group A. The clinical diagnosis and pre-operative anatomy are provided first, followed by a review of the associated flow structures. We then present the different surgical planning options and compare their relative performance in terms of hepatic flow distribution (expressed as HFD_{RPA}) and energy efficiency (expressed as power losses).

9.3.1 Patient B1 (CHOP M3)

9.3.1.1 Pre-Operative Clinical Diagnosis and Data

The first patient of the persistent LSVC group, Patient B1, was a female patient born with a heterotaxy syndrome, SVHD, coarctation of the aorta, persistent LSVC, and an interrupted IVC. She had undergone a staged TCPC procedure, but presented to the Children's Hospital of Philadelphia (CHOP) at the age of 12 years with symptoms of increasing hypoxemia. Dye injection X-ray angiography revealed the formation of severe left lung PAVMs, responsible for the observed hypoxemia.

Patient B1 featured number of pacer wires, which prevented regular MRI acquisition, so that CT images had to be used to reconstruct the *in vivo* TCPC geometry. The anatomical data was supplemented by cardiac catherization flow measurements in the aorta and LPA, which were used as a basis for the CFD boundary conditions. The pre-

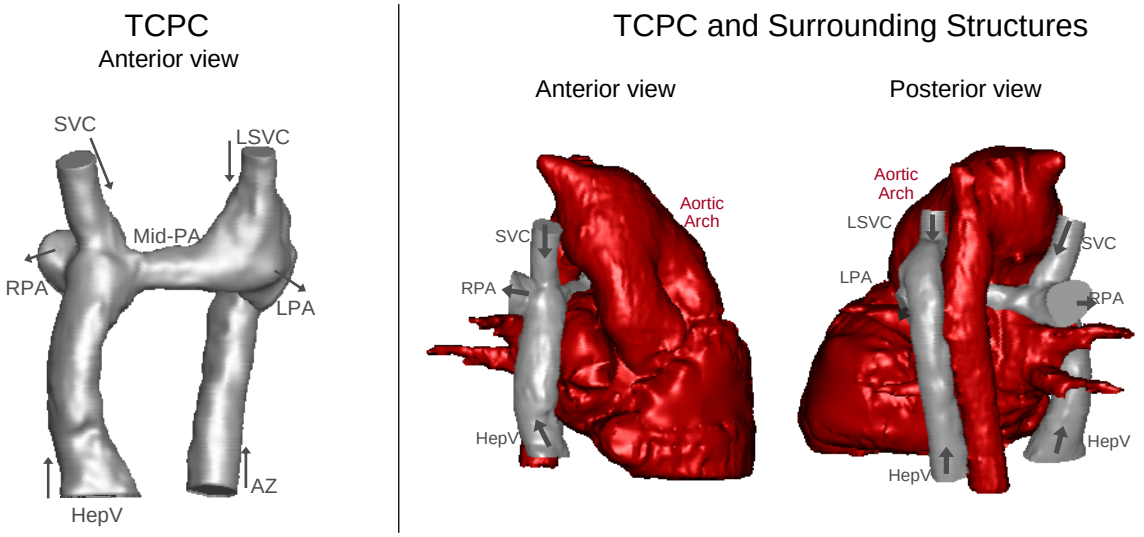

Figure 9-27: On the left, Patient B1's pre-operative TCPC anatomy is shown as a stand alone structure. On the right, the TCPC (in gray) is shown with the heart (in red) to better represent the spatial constraints faced by the surgeons.

Table 9-6: Geometric and flow characteristics of Patient B1 at the time of PAVM diagnosis, and flow boundary conditions used for the CFD simulations. *In vivo* flow measurements were limited to the aortic cardiac output and LPA flow rate obtained from catheterization. Q_S and Q_P were taken to be equal to the measured cardiac output, while the inflow distributions (in %) were defined based on other patient data available at the time of the study, which were mostly limited to Patient A1. These extrapolated values are denoted in purple. Q_S: sum of the systemic inflows. Q_P: sum of the pulmonary outflows.

	Cross-sectional Area (cm^2)	In Vivo Flow measurements		CFD Flow Conditions		
		Q (L/min)	Q (%)	Q (L/min)	Q (%)	Characteristic Velocity (cm/s)
Systemic Venous Return						
HepV	3.67	n/a	n/a	0.68	*21%*	3.10
LSVC	1.94	n/a	n/a	0.78	*22%*	6.70
AZ	1.01	n/a	n/a	0.71	*24%*	11.79
SVC	1.46	n/a	n/a	1.07	*33%*	12.24
Q_S		3.25		3.25		
Pulmonary Flows						
LPA	2.68	2.34	n/a	2.34	72%	14.55
RPA	3.55	n/a	n/a	0.91	28%	4.28
Q_P		n/a		3.25		

operative anatomy at the time of diagnosis is shown in Figure 9-27. The right panel also displays the heart and great vessels to better represent the spatial constraints faced by the surgeon. The inlet and outlet cross-sections are listed in Table 9-6, together with the available *in vivo* flow measurements and the flow conditions used in the CFD simulations.

The SVC and LSVC were connected to the PAs with a bidirectional Glenn in stage 2, followed by an extra-cardiac connection in stage 3 to route the hepatic flow to the pulmonary arteries. The extra-cardiac conduit was wrapped around the anterior side of the heart, reaching the PAs just opposite the SVC. The LSVC connected to the PAs on the left of the aortic arch. The segment of the pulmonary arteries that lies between the SVC and LSVC is referred to as the "mid-PA" in the remainder of this section. The over-riding aortic arch was of especially large dimensions, limiting the access to the mid-PA segment and thus imposing a severe constraint for the surgical planning options to be designed.

As mentioned above, *in vivo* flow measurements were for the most part unavailable for Patient B1, due to coils that prevented MRI flow acquisition. The pre-operative flow conditions listed in Table 9-6 were derived from the available catheterization flow measurements and from the flow distributions observed in other patients. The pre-operative *in vivo* flow measurements included a cardiac output of 3.25 L/min and an LPA flow rate of 2.34 L/min. The inflow boundary conditions for the CFD simulations were obtained by distributing the cardiac output to each one of the TCPC inlets according to the flow distribution measured for Patient A1. The RPA flow rate was obtained by subtracting Q_{LPA} to the cardiac output. The resultant flow distribution at the

outlet was of 28/72 RPA/LPA. Such unbalanced flow distribution is in accordance with the diagnosed left PAVMs, which reduce left lung resistance and thereby increase the total amount of flow going through the LPA. It is important to recall here that a large global flow distribution (GFD) to the LPA does not necessarily imply that a large portion of the hepatic flow goes to the LPA. On the opposite, the presence of left-sided PAVMs indicates that, in the pre-operative anatomy, the hepatic flow distribution (HFD) was most likely biased towards the RPA.

9.3.1.2 Pre-operative Hemodynamics

Prior to designing surgical planning options for Patient B1, it is important to understand the mechanisms that lead to the formation of left-sided PAVMs in the pre-operative anatomy. The flow simulations were conducted using the flow conditions derived from the catheterization measurements. The corresponding flow structures, velocity and pressure fields are illustrated in Figure 9-28. The results are shown from the posterior view to better visualize the interaction between the SVC and HepV on the right side of the connection. The distribution of the different venous returns is best visualized from the left panel of Figure 9-28, where the 3D streamtraces are color-coded by their vessel of origination. Both LSVC and AZ streams (green and red streamtraces) are directed exclusively towards the LPA. It is important to note that those two streams combined already contribute 46% Q_S to the LPA. The SVC and HepV flows combined can thus only reach the LPA if that vessel receives more than 46% of the cardiac output. However, it might be noted that despite the fact 72% of the cardiac output goes to the LPA, almost none of the HepV streamtraces (orange) flow towards that vessel. This stems from the competition between the SVC and HepV flows on the right side of the

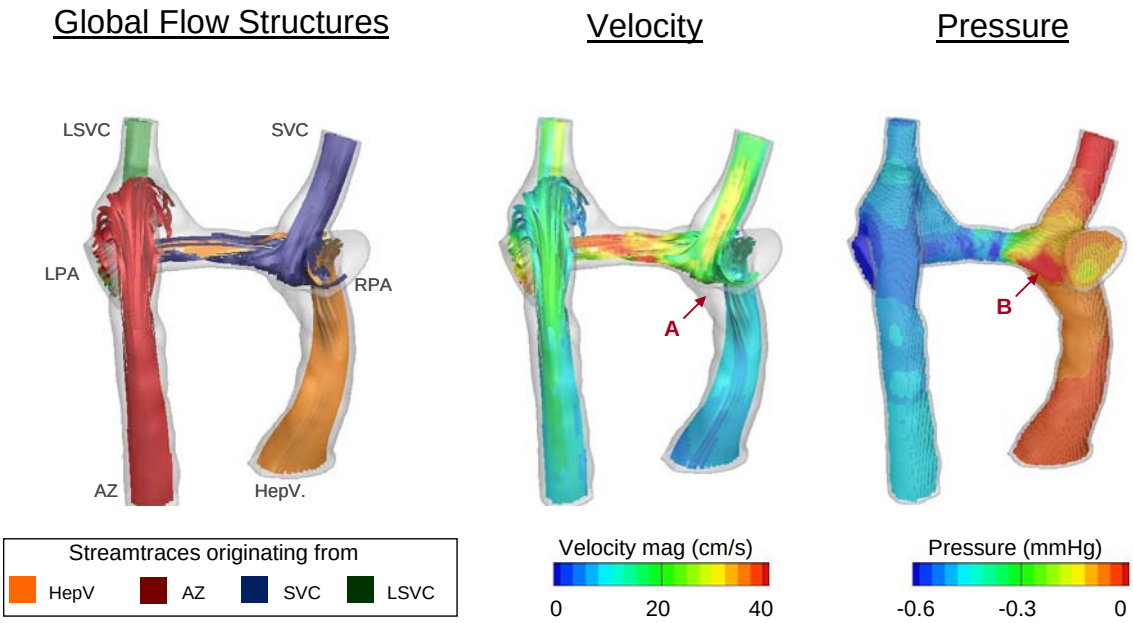

Figure 9-28: Hemodynamics in the Patient B1's pre-operative anatomy. From left to right: Global flow structures shown using 3D streamtraces color-coded by their vessel of origin; the same 3D streamtraces color-coded by velocity magnitude; pressure field. The pressures are expressed relative to the mean pressure at the HepV inlet. Region A: the HepV flow detaches from the left side of the baffle. Region B: high pressures at the point where the SVC flow impinges on the vessel wall.

connection. The SVC is connected with a slight angle towards the mid-PA, which favors SVC flow distribution to the LPA. In counterpart, velocities in the HepV are three to for times smaller than those in the SVC, leading to a lower kinetic energy, which poses a barrier to a proper mixing between the two streams and forces the HepV stream away from the SVC into the RPA. In addition, due to the curvature of the extra-cardiac graft, the HepV flow detaches halfway through the baffle (region A in Figure 9-28) and concentrates on the right side of the baffle. This flow detachment combined with the preferential distribution of the SVC towards the LPA yields most of the HepV to go towards the RPA. As a result, the pre-operative HFD_{RPA} was computed to be of 85.3 %

vs. only 14.7% for HFD_{LPA}. Such uni-lateral hepatic flow distribution towards the right PA is in good agreement with the diagnosed left-sided PAVMs and the decreasing oxygen saturation levels.

The right panel of Figure 9-28 shows the pressure distribution in the pre-operative anatomy. A local pressure rise can be observed on the right side of the connection, directly opposite the SVC anastomosis, at the point where the SVC flow impinges on the pulmonary vessel wall (region B in Figure 9-28). The mean pressure difference between the HepV inlet and the RPA cross-section is -0.05 mmHg. However, this difference is negligible in front of the pressure drop recorded across the mid-PA segment. Due to its small dimensions, the mid-PA segment leads to a sudden flow acceleration, with velocities two to three times higher than in the rest of the connection (central panel). This sudden acceleration yields a sudden pressure drop, with the pressure field suddenly changing from red to blue. The mean pressure differential between the HepV and LPA cross-section is -0.39 mmHg, i.e. about eight times that between the HepV and RPA. The mid-PA segment thus represents the highest source of energy dissipation in the pre-operative anatomy.

In summary, the analysis of the pre-operative hemodynamics points to the curvature of the hepatic baffle, its position relative to the SVC as the two most detrimental features from an HFD point of view. Additional detrimental factors include the low HepV velocities and the fact that the AZ and LSVC combined already account for 46% Q_S. Finally, the narrow mid-PA segment stands as the major source of energy dissipation.

9.3.1.3 Surgical Planning Options

Based on the knowledge gained from the pre-operative analysis, nine surgical planning options were designed (Figure 9-29) that seek to re-equilibrate HFD to the left and right lungs, and if possible to reduce the dissipation through the mid-PA segment. The approaches retained include 1) shifting the HepV connection site away from the SVC, 2) using surgical approaches other then a posterior extra-cardiac to reduce the baffle curvature, 3) combining the AZ and HepV flows, and 4) splitting the HepV between the LPA and RPA.

Options 1 through 5 vary the surgical procedure used (intra-atrial vs. extra-cardiac) and the HepV anastomosis site, shifting it away from the SVC. Options 1 and 2 reach the mid-PA segment using an extra-cardiac baffle routed along the anterior side of the heart as in the pre-operative anatomy. Option 1 connects to the mid-PA slightly closer to the SVC anastomosis than Option 2. Due to the presence of the atrium and pulmonary veins, reaching the mid-PA segment with either of these two options requires a high degree of curvature, as is best evidence from the top view of these two options. Option 3 connects approximately at the same location as Option 2 but using an extra-cardiac conduit routed along the posterior side of the heart. The posterior design might pose some difficulties for its surgical implementation, but is still investigated as it circumvents the difficulties posed by the aortic arch and avoids having a large curvature in the baffle just before the anastomosis. Along the same lines, Options 4 and 5 make use of an intra-atrial approach, which allows for a direct access to the mid-PA with minimum vessel curvature. Option 4 connects the HepV to the center of the mid-PA, while Option 5 connects slightly further toward the LSVC.

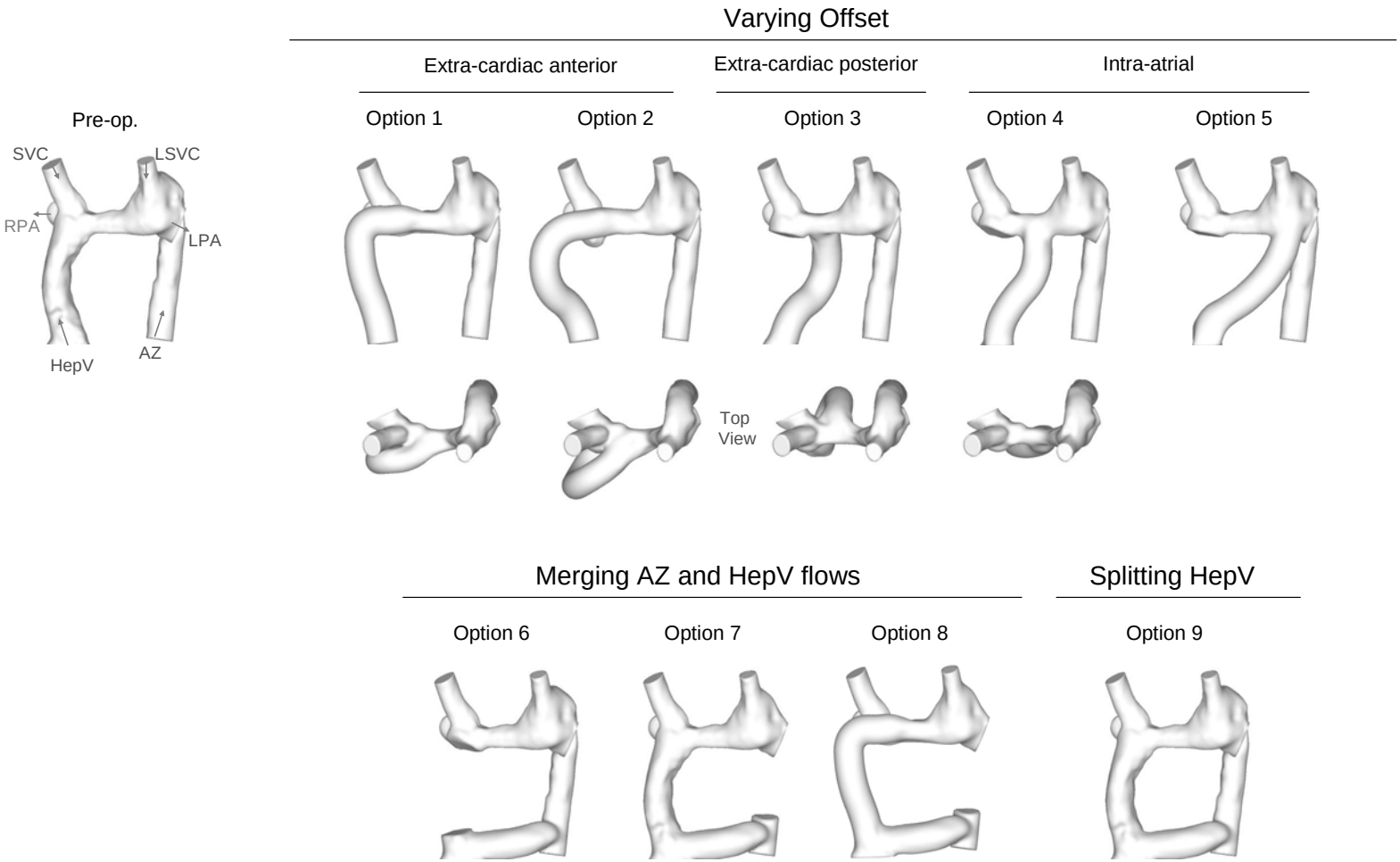

Figure 9-29: Surgical planning options implemented for Patient B1. The pre-operative anatomy is provided as a reference. All geometries are view from the anterior side. A top view is provided for Options 1 through 4 to highlight the differences in the curvature and angle of incidence of the different hepatic baffles.

Options 6 through 8 seek to address the difficulties posed by the low velocities in the hepatic baffle by merging the azygous and hepatic flows. In Option 6, it is the hepatic flow that is directed towards the azygous vein. This is achieved by adding a shunt between the hepatic and azygous veins and ligating the HepV baffle. Attention was paid to avoid the descending aorta during design of the HepV-to-AZ shunt. Options 7 and 8 use a similar shunt, but the objective in these options is to direct the azygous flow into the hepatic baffle. The hepatic baffle is thus left open and the azygous vein is ligated just downstream of the shunt. The two options differ in the graft used to route the combined AZ and HepV flows to the pulmonary arteries. Option 7 makes use of the existing extra-cardiac baffle whereas Option 8 uses a more central extra-cardiac baffle (identical to the one used for Option 1). Finally, Option 9 splits the hepatic flow between the pre-operative extra-cardiac baffle and the azygous vein. This option makes use of the same shunt as the Options 6 through 8, but neither the HepV nor the azygous vein are ligated, allowing the hepatic and azygous blood to freely take one path or the other.

9.3.1.4 HFD Performance

The performance of the nine surgical planning options is assessed through series of numerical simulations using the same inflow conditions as for the pre-operative hemodynamics. In order to predict the behavior in the acute post-operative stage, all options are first tested under the pre-operative outflow conditions, i.e. when the global flow distribution is 28/72 RPA/LPA. The outflow conditions are then varied so as to best predict the point at which an equal HFD to both lungs would be achieved. The hepatic flow distributions associated with the nine surgical planning options are displayed in

Figure 9-30 for all tested conditions. For better readability, the results are split in two graphs. The left panel shows the results obtained for Options 1 through 5, while the right panel displays the results obtained for Options 6 through 9. The pre-operative operating point (dark blue symbol in the upper left quadrant of the graphs) is showed in both graphs as a reference.

Options 1 to 4: Focusing on the left panel, it can be noticed that Options 1 through 4 show very similar trends, following a close to linear behavior between the point where HFD_{RPA} rises from 0% and the point where it reaches 100%. Upon investigation of the associated flow structures, all four options demonstrated similar dynamics and inflow interactions. Figure 9-31 shows the evolution of the global flow structures associated with Option 4 as a typical example of what was observed. In that option, the AZ and LSVC streams (in red and green, respectively) go almost exclusively to the LPA, while the SVC (in blue) goes the RPA. The hepatic blood distribution is seen to closely depend on the flow split, adjusting its contribution to the left and right lung to match the global flow distribution. At a GFD of 28/72 RPA/LPA, the HepV streamtraces (orange) are solely directed to the LPA. They progressively switch towards the RPA as the amount of flow going to that vessel increases, and exclusively directed to the RPA when GFD_{RPA} reaches 50%. Looking more precisely at the HFD_{RPA} values shown in Figure 9-30 for Option 4 (yellow circles), it may be noticed that the HFD_{RPA} measurements start rising at a GFD_{RPA} close to 30%. This value is in close match to the SVC flow rate of 33% Q_S. This means that Option 4 only demonstrates a minimal amount of mixing between the SVC and hepatic flow, and that the hepatic flow only goes towards the RPA when the SVC does not suffice to match the desired RPA flow rate. On the other side of the

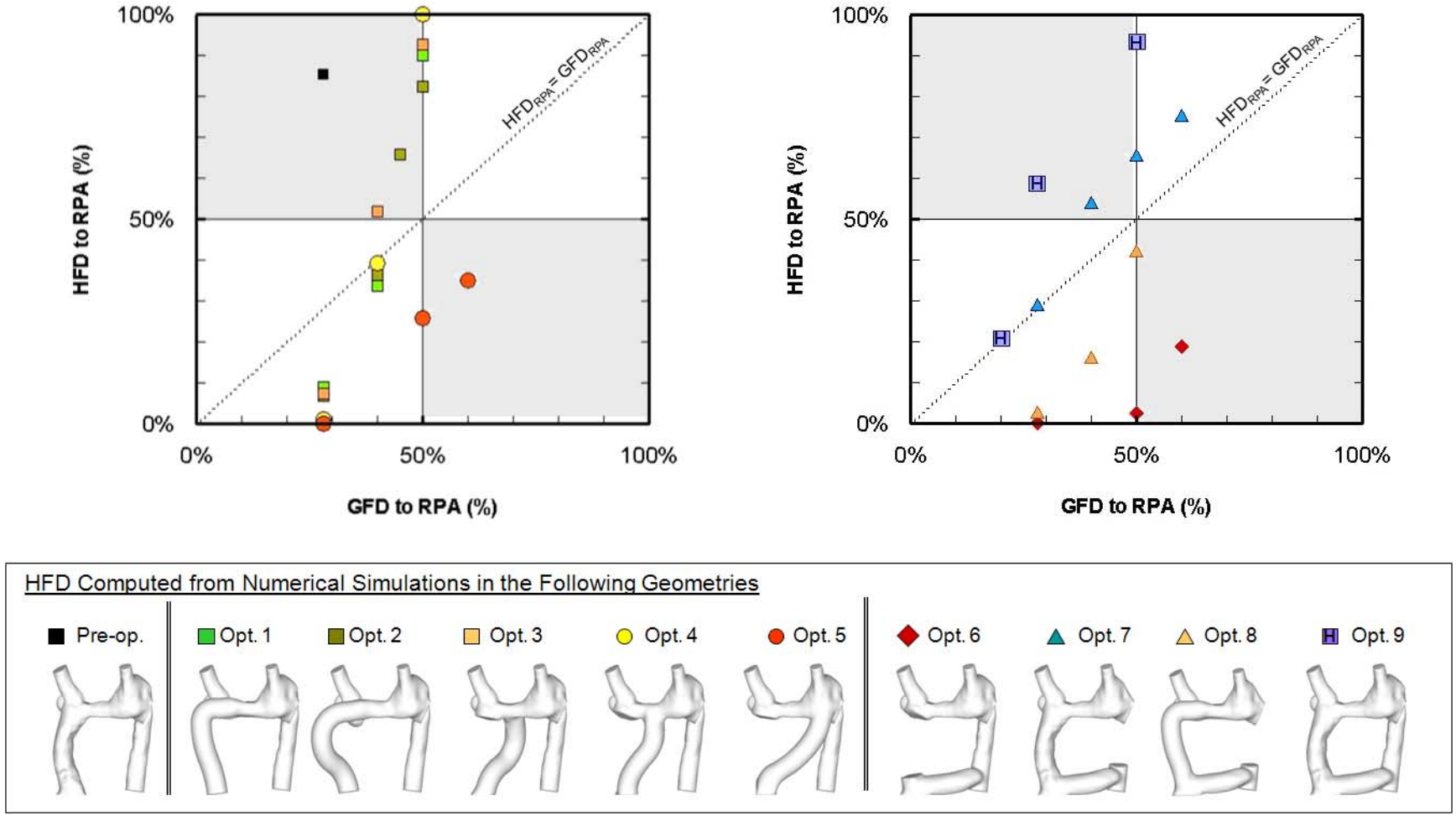

Figure 9-30: Hepatic flow distribution in the nine surgical planning options tested for Patient B1. The pre-operative HFD is provided as a reference.

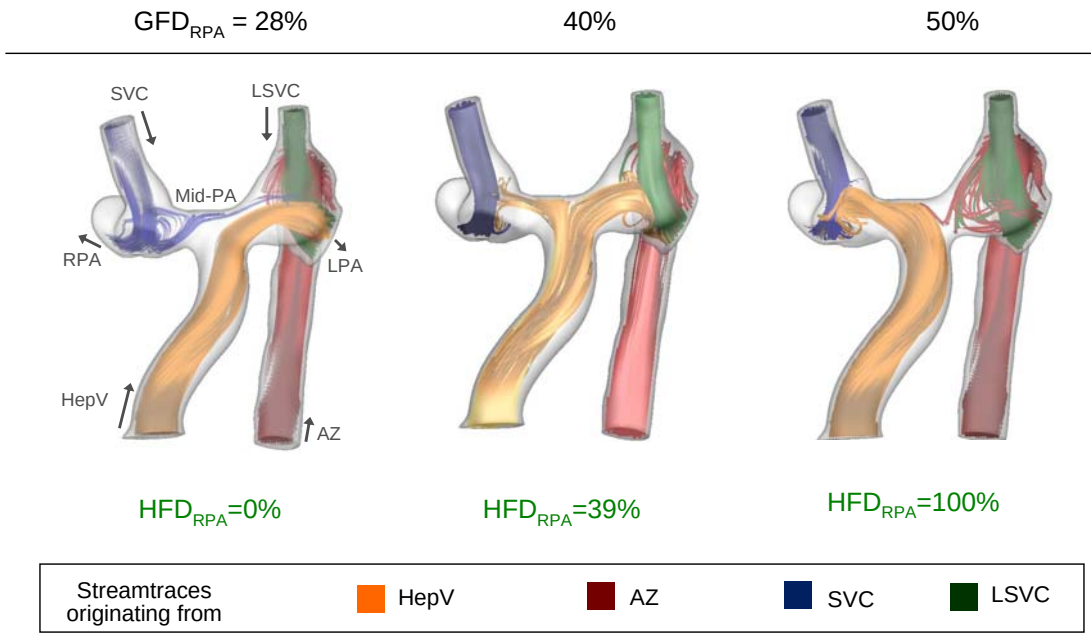

Figure 9-31: Global flow structures observed in Option 4 for a global flow distribution varying between the pre-operative flow split of 28/72 RPA/LPA and 50/50 RPA/LPA. This option is shown as a representative example of what was observed in Options 1 through 4.

spectrum, HFD_{RPA} for Option 4 reaches 100% at GFD_{RPA}=50%. This point is in close match to the sum of the SVC and HepV flows, which is 54% Q_S, meaning that the AZ and LSVC streams only start to contribute to the RPA flow once the SVC and HepV alone do not suffice to match that demand. This in turn reflects the absence of mixing between the hepatic flow and the left venous returns (AZ and LSVC). Based on a linear regression, Option 4 is expected to distribute hepatic flow equally to both lungs for GFD_{RPA} = 42%. This is a drastic improvement compared to the performance of the pre-operative anatomy. The only concern could be that the RPA/LPA flow distributions where both lungs receive at least some amount of hepatic flow is limited to a narrow range between GFD_{RPA}=30% and 50%.

Option 5: The HFD_{RPA} measurements for Option 5 (orange circles in Figure 9-30) drastically deviate from those of Option 1 through 4, falling below the HFD_{RPA}=50% line for all tested conditions. This demonstrates a preferential HFD to the right lung. The HFD curve for that option appears to rise at a GFD_{RPA}=29% as was the case for Options 1 through 4, but to grow at a slower rate. Looking at the evolution of the global flow structures (Figure 9-32) provides a better understanding of the slower growth rate. The AZ, LSVC and HepV flows mix thoroughly prior to dividing between the LPA and RPA. For every percent increase in its flow rate, the RPA flow rate receives a combined contribution from the AZ, LSVC and HepV. This explains the slower growth rate, which could be advantageous as it will spread the range of flow conditions over which this option will provide hepatic flow to both lungs. On the other hand, this results in an HFD that is highly biased towards the right lung. By extrapolating the measurement curve, Option 5 is expected to yield an even hepatic flow distribution around GFD_{RPA}=66%, which appears too far from the ideal 50% value.

To summarize the knowledge gained on the "offset variations", all options connected to the mid-PA (Option 1 through 4) resulted in very similar HFD. Reaching too far to the left as in Option 5 favored HFD to the LPA. These results combined demonstrate that the exact position of the anastomosis site on the mid-PA or the degree of curvature has only little impact on HFD. The only parameter of importance is to ensure that the HepV anstomosis is offset away from both the SVC and the LSVC. In addition, HFD_{RPA} for the first five options followed a linear behavior which appeared to be dictated by simple mass balance considerations.

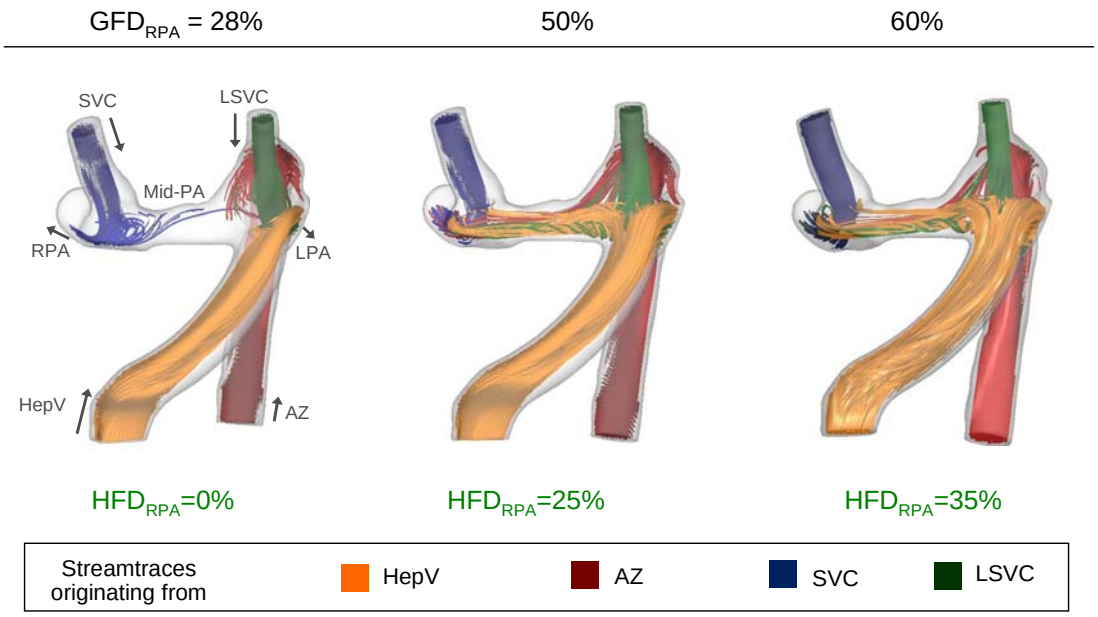

Figure 9-32: Global flow structures observed in Option 5 for a global flow distribution varying between the pre-operative flow split of 28/72 RPA/LPA and 60/40 RPA/LPA.

The HFD results for the second set of options, combining AZ and HepV flows (Options 6 through 9), are shown in the right panel of Figure 9-30.

Option 6: The HFD_{RPA} results for Option 6 (red diamonds in Figure 9-30) fall below those reported for Option 5, indicating a higher bias of the HFD towards the LPA than in the former option. The mechanism behind this biased flow distribution is best understood by looking at the flow structures shown in Figure 9-33 for GFD_{RPA} =50%. Merging of the HepV to the AZ veins results in a helical pattern in the AZ, with red and orange streamtraces intertwined. When both flows reach the left connection site, the orange HepV streamtraces are clustered along the left aspect of the AZ vein, while the red AZ streamtraces flow along the right side of the vessel. Both AZ and HepV streams split between the LPA and RPA to adjust for the desired GFD, but due to their spatial repartition within the vessel, it is mostly the red AZ streamtraces that are directed to the

RPA, while the HepV flow goes to the LPA. Option 6 thus appears to be equivalent, from an HFD standpoint, to placing the HepV between the AZ and LSVC, the LSVC being on its right and the AZ on its left. It can thus be expected that as long as the sum of the SVC and LSVC flows suffices to match Q_{RPA}, all of the HepV flow will go to the LPA, and that the hepatic flow will only split towards the RPA when $Q_{RPA} > Q_{SVC}+Q_{LSVC}$, which is 57% Q_S. This observation is in accordance with the trend followed by the HFD_{RPA} measurements for Option 6, which only start to rise when more than 50% of the flow goes to the RPA. Extrapolating the existing points, it might be predicted that Option 6 would require a global flow distribution of 67/33 RPA/LPA to achieve an HFD_{RPA}=50%. If Option 6 performs better than the pre-operative anatomy, it still has too large of a bias in HFD to be recommended for surgery.

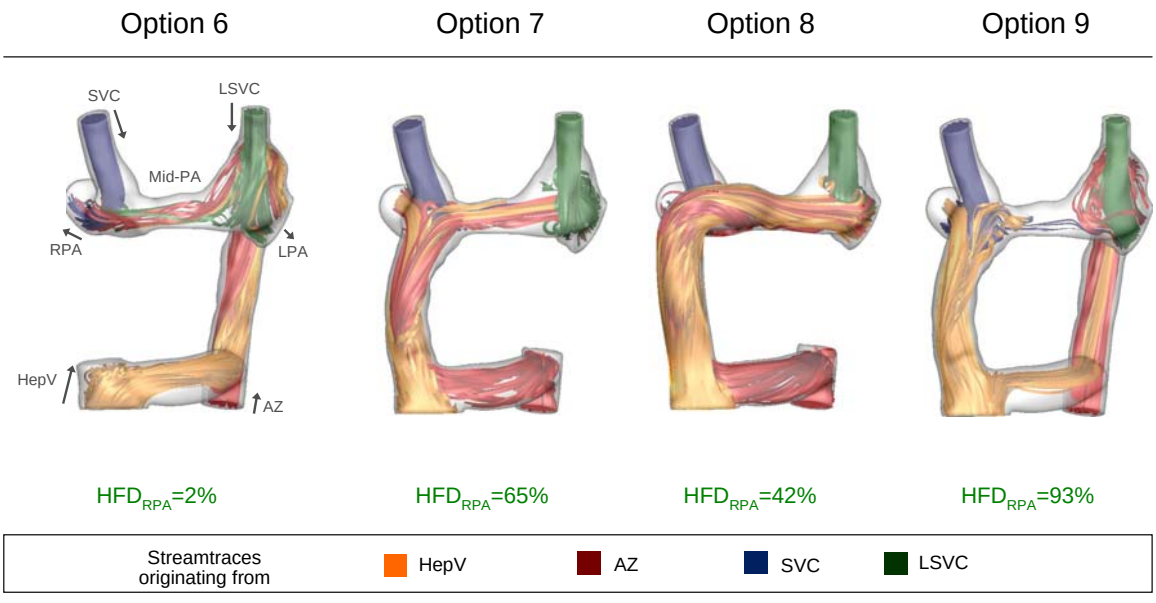

Figure 9-33: Flow structures and HFD for the four the four options combining azygous and hepatic flows (Options 6 through 9) at a GFD_{RPA} of 50%. This flow condition was chosen as representative of the relative performance of Options 6 through 9.

Option 7: Option 7 uses the same baffle design as the pre-operative anatomy, but has the combined AZ and HepV blood flowing through it. As can be observed from Figure 9-33, this leads to an intense mixing between the SVC, AZ and HepV streamtraces in the right connection site. Due to the mixing observed within the right connection, each percent increase in RPA flow is provided by the AZ, HepV and SVC flows in combination, reducing the relative contribution of the HepV. As a result, the HFD_{RPA} measurements for Option 7 rise at a lower rate than what was observed in Options 1 through 4 or in Option 6. Merging the AZ flow into the pre-operative baffle thus had the two following advantages: 1) by increasing the momentum of the flow through the extra-cardiac baffle, it increases mixing at the center of the connection, and 2) by leading to a complete mixing of the AZ, HepV and SVC inflows, it reduces the sensitivity of the HFD to the global flow distribution. However, due to the right-sided position of the pre-operative extra-cardiac baffle, Option 7 favors HFD to the RPA, with its measurement points falling above the ideal $HFD_{RPA}=GFD_{RPA}$ line.

Option 8: Option 8 uses a similar approach but directs the combined AZ and HepV flows towards the mid-PA segment via the same extra-cardiac baffle as in Option 1. The corresponding flow structures are displayed in Figure 9-33. The SVC and LSVC flows are exclusively distributed to the closest PA, while the AZ and HepV flows split between the LPA and RPA to match the desired GFD. Accordingly, the HFD_{RPA} measurements for Option 8 (orange triangle in Figure 9-30) remain at 0% until GFD_{RPA} exceeds 30%, which corresponds to the contribution of the SVC. HFD_{RPA} then increases with GFD_{RPA}, as the amount of flow to the RPA exceeds what can be provided by the SVC alone. This behavior is similar to what was observed in Options 1 through 4. However, the HFD_{RPA}

growth rate is slower for Option 8 than in the four former options, since both AZ and HepV flows contribute equally to increase the RPA flow. Extrapolating the measurements, Option 8 might be predicted to yield an HFD_{RPA} of 50% at a GFD of 56/44 RPA/LPA. To provide a ground of comparison, the extra-cardiac Option 4 yielded an HFD_{RPA} of 50% at a GFD of 42/58 RPA/LPA. Both types of options thus appear to yield similar performance. However, the lower growth rate of Option 8 compared to Option 4, for which HepV and AZ were not combined, should ensure a liberty from PAVMs over a broader range of GFD_{RPA}. As an example, Option 8 ensures that both lungs receive a minimum of 40% of the hepatic nutrients ($HFD_{RPA} \in [40\%, 60\%]$) for a GFD_{RPA} varying between 51.0% and 60.0%, while this range is reduced to $GFD_{RPA} \in [41.3\%, 45.6\%]$ for Options 1 through 4.

Option 9: Option 9 is the last option that was investigated for Patient B1. It combines the pre-operative extra-cardiac graft, which was shown to favor HFD to the RPA, and the HepV-to-AZ shunt of Option 6, which was shown to favor HFD to the LPA. The resulting HFD_{RPA} are shown by the light blue H symbols in Figure 9-30. HFD_{RPA} was of 58.7% under the pre-operative flow conditions (GFD_{RPA}=28%), which was a drastic improvement compared to HFD_{RPA}=85.3% measured in the pre-operative anatomy. However, these values rapidly increased and, despite an improvement compared to the pre-operative anatomy, Option 9 was still seen to highly favor HFD to the RPA (with measurement points far above the centerline). The reason for the inefficient splitting of the hepatic flow between the shunt on the left and the extra-cardiac baffle on the right is best visualized in Figure 9-33. The HepV-to-AZ shunt departs from the HepV axis with a close to 90 degree angle. As a result, a large flow separation region forms at the entrance

of the shunt. Only a small portion of the flow impinges on the shunt wall and diverts away from the extra-cardiac baffle towards the HepV-to-AZ. The decrease in RPA pressure when GFD_{RPA} increases further only worsens the phenomenon, making the HepV path through the extra-cardiac baffle more favorable, and shifting all hepatic blood away from the shunt. When GFD_{RPA} reaches 60%, all of the hepatic flow goes through the extra-cardiac baffle, and the shunt actually carries a small portion of the AZ flow towards the RPA.

9.3.1.5 Energetic Performance and Power Loss Measurements

Beyond HFD another parameter of interest is the amount of energy dissipated through the connection. The power losses associated with the nine surgical planning options is shown in Figure 9-34. For clarity, the results are separated into three different graphs grouping the options based on their HFD behavior: (i) the options that were connected to the mid-PA segment and left the azygous flow track untouched (Option 1 through 4); (ii) the options that favored HFD to LPA (Options 5 and 6); and finally (iii) all remaining options (Options 7, 8, and 9). All graphs also display the pre-operative performance as a reference, and use the same scale for ease of comparison.

Option 1 to 4: In Figure 9-34(a) the power losses measured for the first four options almost overlap and only cover a narrow range, going from 0.76mW to 1.16mW. These options appear to reach a minimum power loss around 40-45% GFD_{RPA}, which corresponds to the point where the hepatic flow is equally distributed to the LPA and RPA.

Option 5: Figure 9-34(b) shows that, at GFD_{RPA}=30% and 50%, the power losses measured for Option 5 fall within 6% of those measured for Option 4, demonstrating that

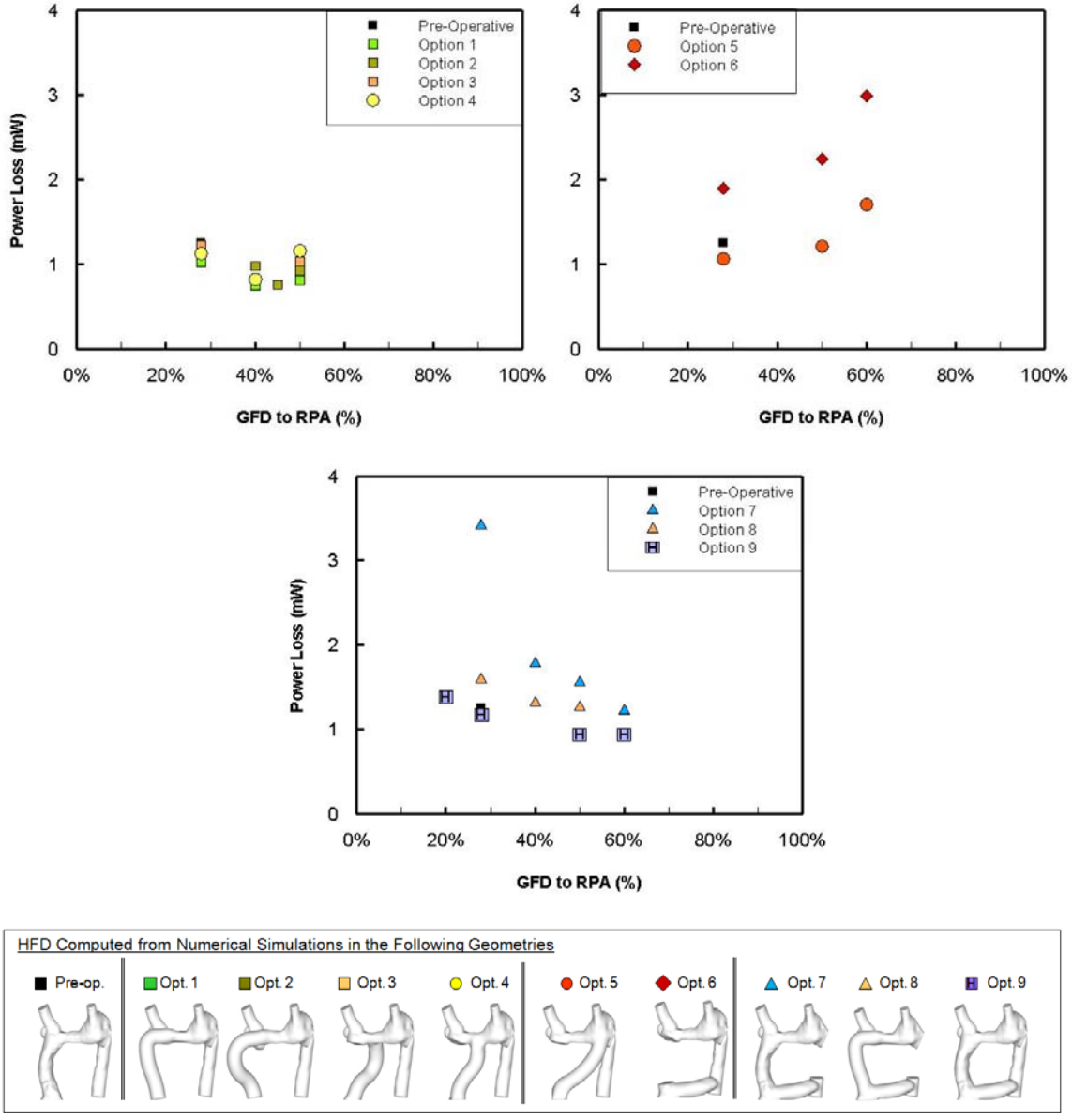

Figure 9-34: Power Loss measured across the pre-operative anatomy and surgical planning options for all tested GFD conditions. The surgical planning options are separated in three groups based on the trends observed in the power losses. The pre-operative power loss is provided in all graphs as a reference point.

the HepV offset only had little impact on the energy dissipation in the 30% to 50% range. However, as GFD_{RPA} increases to 60%, the power losses for Option 5 suddenly increase to 1.7mW. This change in power loss behavior in Option 5 is due to the left-sided offset of the HepV. As was pointed out during the pre-operative hemodynamic analysis, the mid-PA is a major source of energy dissipation. Due to the left-sided offset of Option 5 (and Option 6), more flow has to travel through the mid-PA segment at a given GFD_{RPA} than in Options 1 through 4, and this flow has to travel through the entire segment vs. only half of it in Options 1 through 4. Both of these mechanisms lead to a sudden rise in power losses as GFD_{RPA} increases beyond 50%.

Option 6: The power losses computed for Option 6 show a dependency on GFD_{RPA} similar to Option 5, increasing quickly as GFD_{RPA} increases beyond 50%. This behavior is consistent with the fact that both surgical options result in a similar distribution of the inflows, with the LSVC, AZ and HepV flows merging on the left side and only the SVC on the right side (see streamtraces shown in Figure 9-33). It is also noteworthy that the power losses in Option 6 fall consistently 1 to 1.5mW above those of Option 5. Combining the azygous and hepatic streams into the azygous vein leads to elevated friction losses against the AZ vessel walls, increasing the overall level of energy dissipation in the connection.

Option 7: The power losses for Option 7 (Figure 9-34(c)) follow a trend opposite to that observed for Options 5 and 6, drastically decreasing as GFD_{RPA} increases. This inversion in power loss trends stems form the fact that Option 7 results in a distribution of the inflows that is opposite to that of Options 5 and 6, with a vast majority of the blood flow (SVC, AZ and HepV) entering through the right side of the connection, and only the

LSVC flow entering through the left. Accordingly, in Option 7, power losses are minimum when a majority of the flow exits through the RPA, minimizing the flow rate through the mid-PA segment. They increase quickly as GFD_{RPA} decreases and flow through the mid-PA segment increases.

Option 8: Option 8, shown in Figure 9-34(c), follows a flatter profile than Options 5,6 and 7, indicating a lower dependency of the power losses upon GFD_{RPA}. This might be attributed to the fact that, similarly to Options 1-4, the baffle is connected to the mid-PA segment. However, since Option 8 routes both AZ and HepV streams through the baffle, the energy dissipated by friction in the baffle is higher than in Options 1-4, and consequently, the power loss levels are also higher than in Options 1-4. Power losses for Option 8 appear to tend towards a minimum around GFD_{RPA}=50%, which corresponds the point where the combined AZ and HepV flows are almost equally distributed to the LPA and RPA.

Option 9: Finally Option 9 is the option that leads to the lowest power losses overall. Losses under the pre-operative flow conditions (GFD_{RPA}=28%) are of the same order as in the pre-operative anatomy and Options 1-5, but they keep decreasing beyond GFD_{RPA}=50%. This might be attributed to the fact that, when flow to the RPA increases beyond the contribution of the SVC and HepV flows combined, part of the azygous flow reaches the RPA through the Hep-to-AZ shunt and extra-cardiac baffle rather than by flowing across the mid-PA section. This bypass reduces the flow rate through the narrow mid-PA section, and thereby the amount of energy dissipated by friction in that section. As GFD_{RPA} increases power losses for Option 9 tend towards the same value as Option 7, for which all of the azygous flow is forced through the extra-cardiac baffle.

9.3.1.6 Summary

A total of nine options were investigated for Patient B1, looking into the impact of the HepV offset (Options 1 through 5), the baffle curvature (Options 1 through 4), and different combination of HepV and AZ flows (Options 6 through 9). Among the options that left the AZ unaltered (Options 1 through 5), HepV offset was observed to be the strongest determinant for HFD. The best performance was obtained when connecting the hepatic baffle to the mid-PA segment (Option 1-4). When the hepatic baffle was connected to the mid-PA, the HFD was more or less insensitive to the baffle curvature as well as to the exact HepV connection point along the mid-PA section.

Merging AZ and HepV flows into the azygous vein (Option 6) was equivalent to a left-sided offset, and thus not recommended from an HFD point of view since it resulted in the HepV flow totally bypassing the RPA, and only going to the LPA. Such option is thus expected to heal the left-sided PAVMs, but yield right-sided PAVMs in the long term. Option 9, which sought to split the hepatic flow between the pre-operative baffle and the azygous vein, was not recommended either as it effectively resulted in a biased HFD to RPA distribution. Using the same shunt but ligating the azygous vein to merge the AZ and HepV flows into the hepatic baffle (Options 7 and 8) provided promising results. Combining the AZ and HepV flows reduced the sensitivity of the HFD to the baffle offset and widened the range of LPA/RPA flow splits that could be achieved while still maintaining a proper supply in hepatic nutrients to both lungs. The optimal HFD results were obtained with Option 8 where the combined AZ and HepV flows were directed to the mid-PA segment.

The power losses were observed to be relatively insensitive to the design of the hepatic baffle, and mostly dictated by the laminar friction along the different vessels. Due to the small dimensions of the mid-PA segment, power losses in Options 5, 6 and 7 showed a very strong dependency on the global flow distribution. Connecting the baffle to the mid-PA segment appeared to be an efficient strategy to reduce power loss levels. An alternate solution might be to dilate the mid-PA segment using a stent, thus reducing the friction losses in that region. Finally, Options 6 through 8 came at a slightly higher energy cost than Options 1-4 due to the HepV and AZ flow combination into a single vessel, but these power loss values remained low so that this added cost in Option 8 was discarded in view of the better HFD performance.

Based on the above observations, it was recommended to either modify the extra-cardiac connection to reach the mid-PA segment or to shunt the azygous flow towards the hepatic baffle, or if time allowed to perform both of the above.

9.3.2 Patient B2 (CHOP M7)

9.3.2.1 Pre-Operative Clinical Data and Diagnosis

Patient B2 was an 11 year-old male born with a single ventricle, a heterotaxy syndrome with dextrocardia, an interrupted IVC and a persistent LSVC. This patient had undergone a Kawashima operation followed by an extra-cardiac connection of the hepatic veins to the pulmonary arteries. The patient reportedly had right PAVMs.

The patient anatomy at the time of diagnosis is shown in Figure 9-35, with and without the surrounding cardiovascular structures. Since the patient had dextrocardia the apex of the heart is pointed towards the right. The Kawashima connection was performed on the right hand side, merging AZ and SVC flows. The extra-cardiac baffle was wrapped around the left side of the heart and connected opposite to the LSVC. Both the SVC and LSVC were angled towards the mid-PA segment.

Table 9-7 summarizes the characteristic dimensions and flow rates of each one of the inflows and outflows. The LSVC was notably smaller than the other vessels with a cross-sectional area of only 0.57 cm^2, compared to 2.75 cm^2 for the hepatic baffle. The LPA was the smaller of the two PAs with a cross-sectional area of 0.98 cm^2 vs. 1.78 cm^2 for the RPA. The clinical report also mentions the presence of a kink or narrowing further downstream in the RPA.

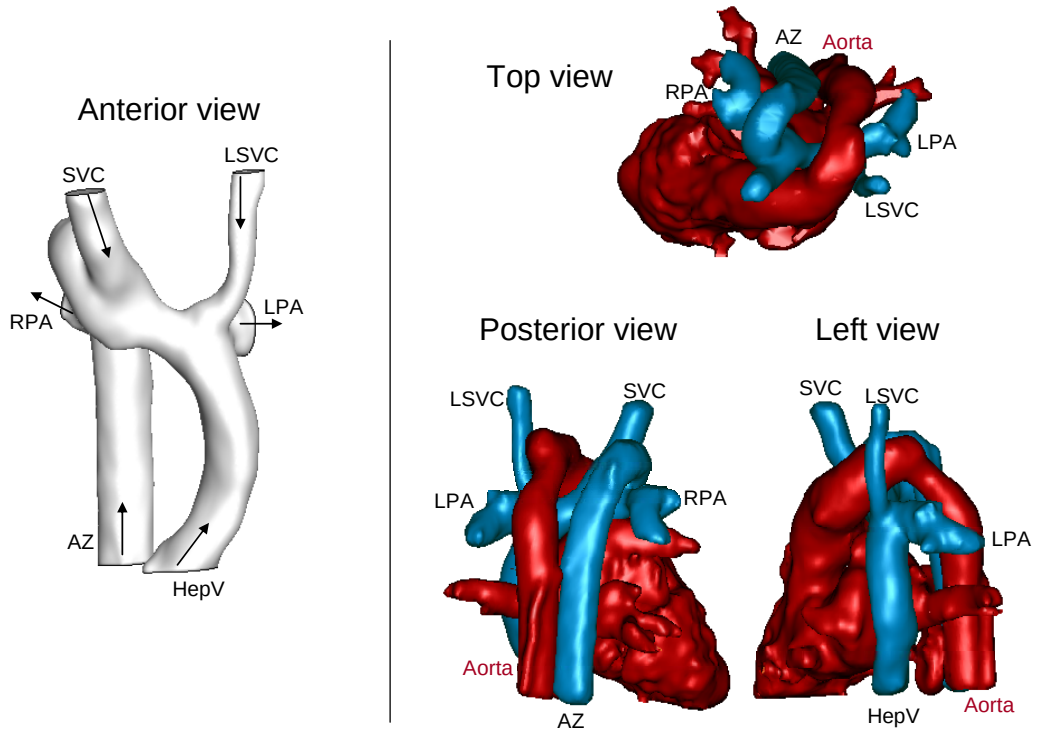

Figure 9-35: Pre-operative anatomy for Patient B2. Left: TCPC geometry, with arrows indicating the main flow direction at each inflow and outflow. Right: TCPC geometry (in blue) and surrounding cardiovascular structures (in red).

Table 9-7: Geometric and flow characteristics of Patient B2 at the time of PAVM diagnosis, and flow boundary conditions used for the CFD simulations. Q_S: sum of the systemic inflows. Q_P: sum of the pulmonary outflows.

	Cross-sectional Area (cm^2)	MRI Flow measurements		CFD Flow Conditions		
		Q (L/min)	Q (%)	Q (L/min)	Q (%)	Characteristic Velocity (cm/s)
Systemic Venous Return						
HepV	2.76	0.41	10%	0.41	10%	2.49
LSVC	0.57	0.77	19%	0.77	19%	22.47
AZ	1.81	1.20	31%	1.20	31%	11.05
SVC	1.16	1.57	41%	1.57	40%	22.53
Q_S		3.95		3.95		
Pulmonary Flows						
LPA	1.78	2.30	65%	2.57	65%	24.08
RPA	0.98	1.23	35%	1.38	35%	23.35
Q_P		3.54		3.95		

9.3.2.2 Pre-Operative Hemodynamics

MRI assessment of the pre-operative flow rates revealed two notable features: first, the HepV only accounted for 10% of the systemic venous return, which is about half of what was noted in the other patients; then, the pre-operative GFD_{RPA} was of only 35% despite the presence of right PAVMs. This low flow distribution to the RPA might be attributed to the kink noted downstream, which increases the resistance of the right pulmonary pathway. The first question that arises is whether dilating the distal RPA stenosis, and thereby increasing GFD_{RPA}, would suffice to increase HFD_{RPA} to normal levels. The hemodynamics of the pre-operative anatomy where thus assessed for global flow distributions varying from 40/60 RPA/LPA up to 60/40 RPA/LPA.

Figure 9-36 displays the global flow structures and HFD observed in the pre-operative anatomy for GFD_{RPA}=40% to 60%. The flow structures are displayed as 3D streamtraces color-coded by their vessel of origination. For all tested conditions, HepV (orange) and LSVC (green) flows are directed to the LPA, maintaining HFD_{RPA} at 0%. This uni-sided distribution of the HepV and LSVC flows even at GFD_{RPA}=60% stems from the fact that the AZ and SVC flows combined account for 70% Q_S. Thus, unless GFD_{RPA} exceeds 70%, the AZ and SVC suffice to provide all the blood needed in the RPA. The AZ flow, which enters the connection the furthest to the right, is almost exclusively directed to the RPA. For the tested range of GFD_{RPA}, it is the SVC that splits between the LPA and RPA to match the desired GFD.

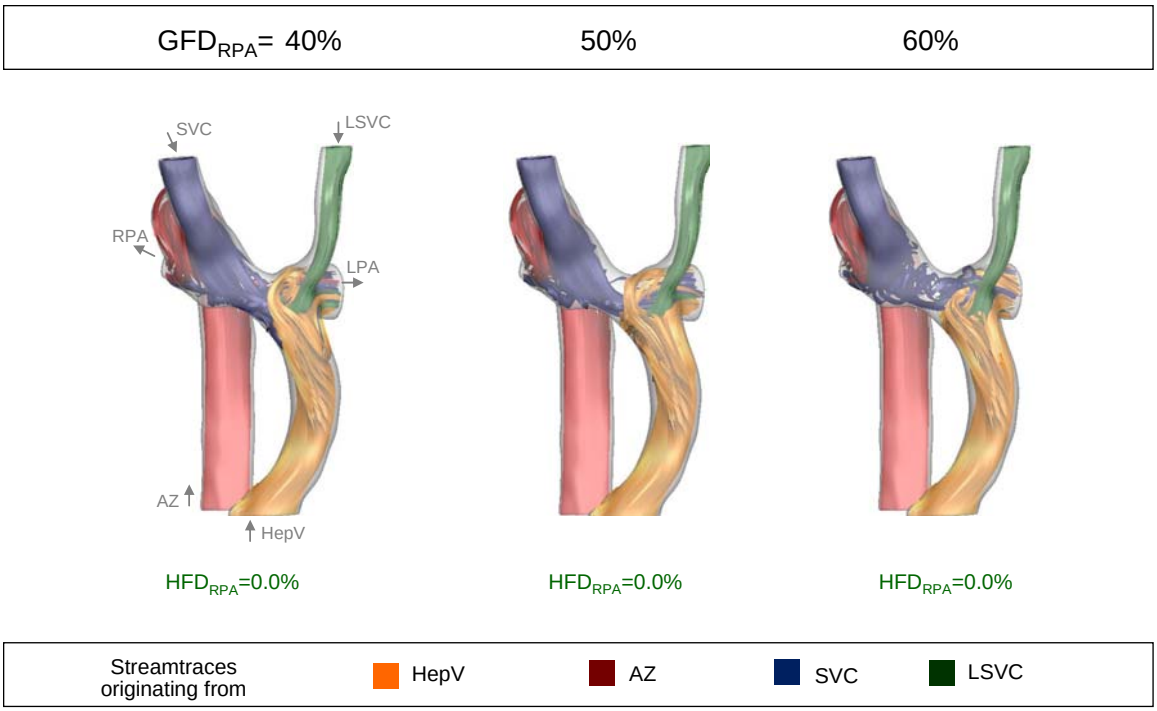

Figure 9-36: Flow structures and HFD in the pre-operative anatomy of Patient B2, for GFD_{RPA} ranging from 40% to 60%.

9.3.2.3 <u>Surgical Planning Option</u>

Seven surgical planning options were envisioned and tested for Patient B2. The corresponding geometries are displayed in Figure 9-37. Based on the knowledge gained from Patient B1, it can be predicted that an equal distribution of the hepatic flow to the left and right lung (HFD_{RPA}=50%) would correspond to a GFD_{RPA} of 5% if the HepV was connected to the right of the AZ, 75% if it was connected between the SVC and LSVC, and 95% if it was connected to the left of the LSVC. None of these conditions appear as being acceptable. On the other hand, complete mixing of the SVC and HepV inflows could yield to an HFD_{RPA} of 50% at GFD_{RPA}=55.5%, which would be an ideal configuration. Accordingly, Option 1 is the only option that varies the HepV offset,

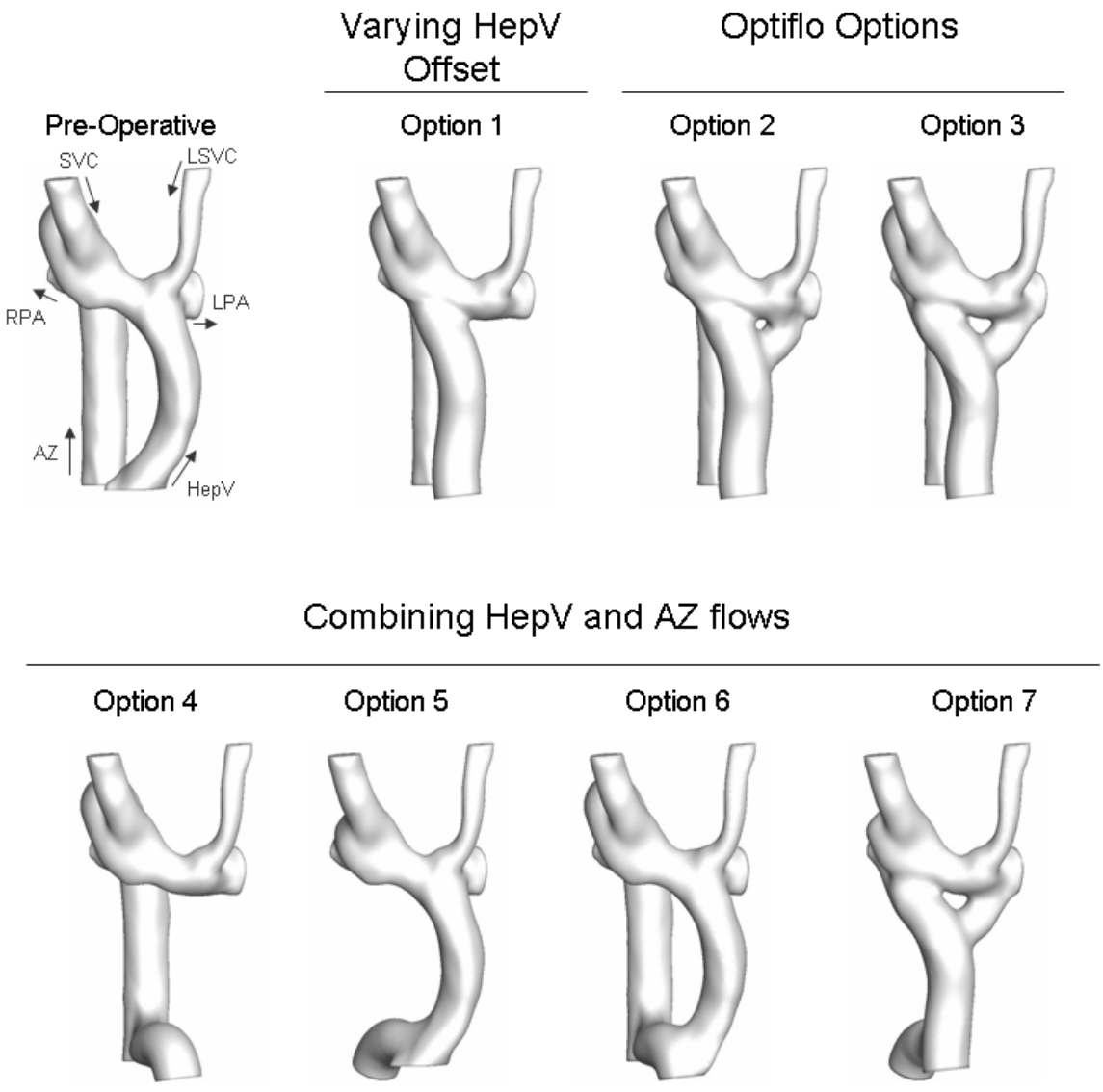

Figure 9-37: Geometries of the seven surgical planning options attempted for Patient B2. The pre-operative anatomy is shown as well for comparison.

setting the baffle right opposite the SVC in an effort to increase mixing. The pre-operative extra-cardiac baffle is taken down and replaced by an intra-atrial approach to reach far enough towards the SVC.

Options 2 and 3 try to prevent all competitive mixing between the HepV and the superior inflows using Y-shaped Optiflo baffles. In order for the right branch of the Y to reach far enough towards the SVC, both options require an intra-atrial approach. Option 2 makes use of the same intra-atrial baffle as Option 1, with the addition of an HepV-to-LPA branch. Option 3 reaches further towards the RPA and LPA.

Since the HepV flow only accounts for 10.4%Q_S it can be anticipated that even if one of the above options succeeds to achieve a balanced HFD for a GFD_{RPA} close to 50%, the operative range for that option will remain very narrow. Options 4 through 7 thus combine the AZ and HepV flows in an effort to both improve mixing and widen the operative range. In Option 4, the hepatic flow is routed to the azygous vein using a HepV-to-AZ shunt. The hepatic baffle is ligated and removed from the computational domain. Option 5 makes use of the same HepV-to-AZ shunt, but the HepV baffle is left open, allowing the HepV flow to split between the extra-cardiac graft and the azygous vein. Finally, in Options 6 and 7, it is the AZ flow that is routed to the hepatic baffle via an AZ-to-HepV shunt. The azygous vein is ligated and removed from the computational domain. In Option 6 the combined AZ and HepV flows are routed through the pre-operative extra-cardiac baffle, while Option 7 makes use of the Optiflo baffle designed for Option 3.

9.3.2.4 HFD Performance

Figure 9-38 displays the HFD_{RPA} associated with the seven surgical planning options envisioned for Patient B2. The HFD_{RPA} performance of the pre-operative anatomy is shown as well as a reference. For ease of understanding, the results are spread over two graphs. The left panel displays the HFD_{RPA} measurements obtained for Options 1 through 3, while the right panel shows the results associated with Options 4 through 7.

Global considerations for Options 1 through 3: As can be seen from the left panel of Figure 9-38, Option 1, where the HepV was shifted towards the center of the connection, and Option 2, where the HepV was split using an Optiflo graft, do not yield any significant improvement compared to the pre-operative anatomy. Even when 70% of the systemic venous return is directed to the RPA (GFD_{RPA} = 70%), HFD_{RPA} remains close to 0% in Option 1 and 13% in Option 2. Option 3, which uses an Optiflo as in Option 2 but reaching further to the RPA and LPA, yields a better performance. At GFD_{RPA}=50%, the hepatic flow distribution is close to ideal with an HFD_{RPA} of 45.7%. However, this only corresponds to a local maximum and HFD_{RPA} for Option 3 falls back to 22.7% at GFD_{RPA}=70%. The presence of local maxima in the HFD_{RPA} measurements of Options 1 and 3 is one of the most notable features of the results obtained for Patient B2. To better elucidate the reason for this non-monotonous behavior, Figure 9-39 displays the flow structures associated with these three first options across all tested flow conditions.

Option 1: Focusing on Option 1 (top row in Figure 9-39), it can be noticed that the flow patterns of AZ (in red) and LSVC (in green) streams do not evolve significantly between GFD_{RPA}=40% and 60%. Both streams are exclusively distributed to the closest

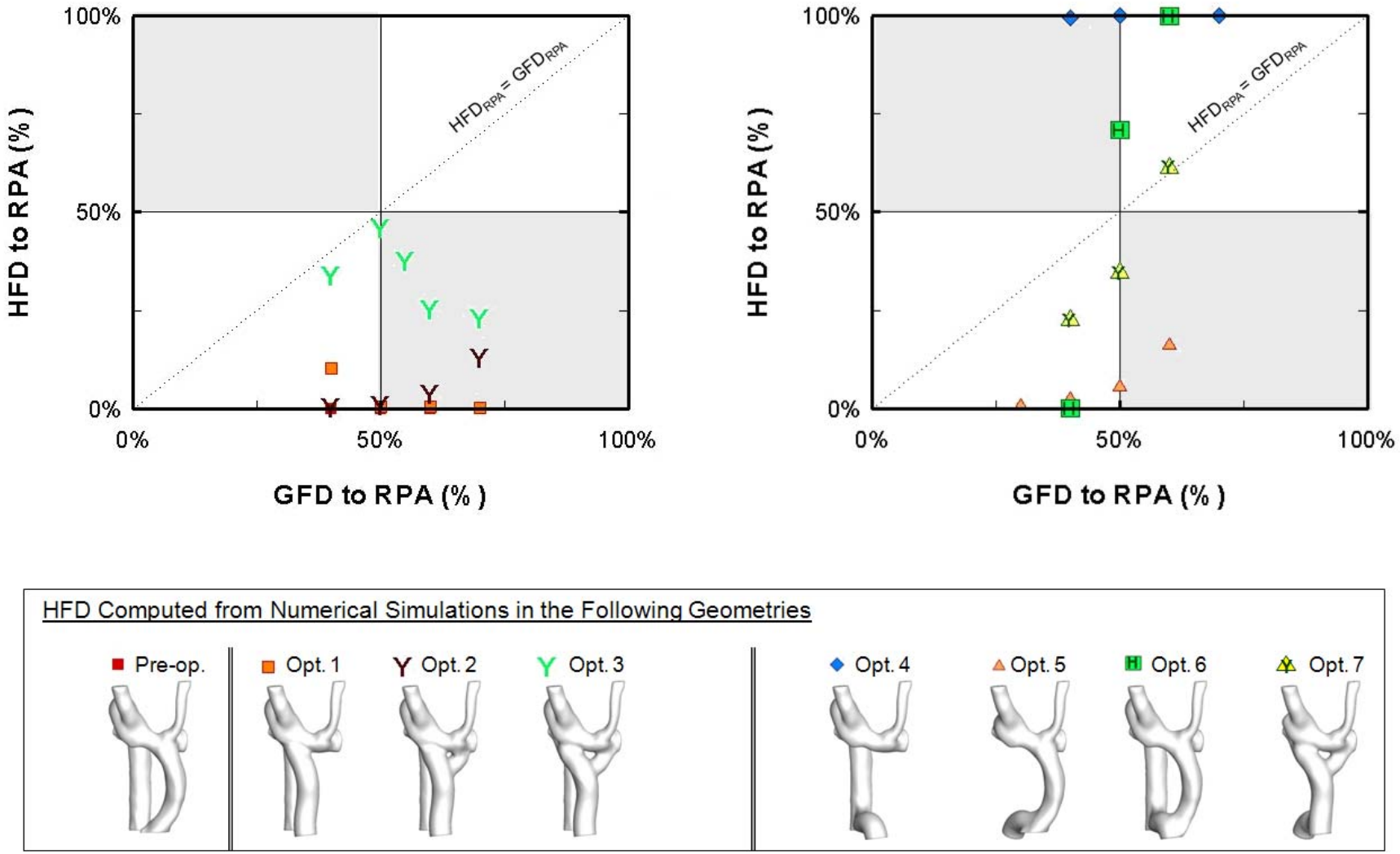

Figure 9-38: Hepatic flow distribution measured in the seven surgical planning options implemented for Patient B2. The dotted central diagonal serves as a reference, indicating the ideal scenario where $HFD_{RPA} = GFD_{RPA}$.

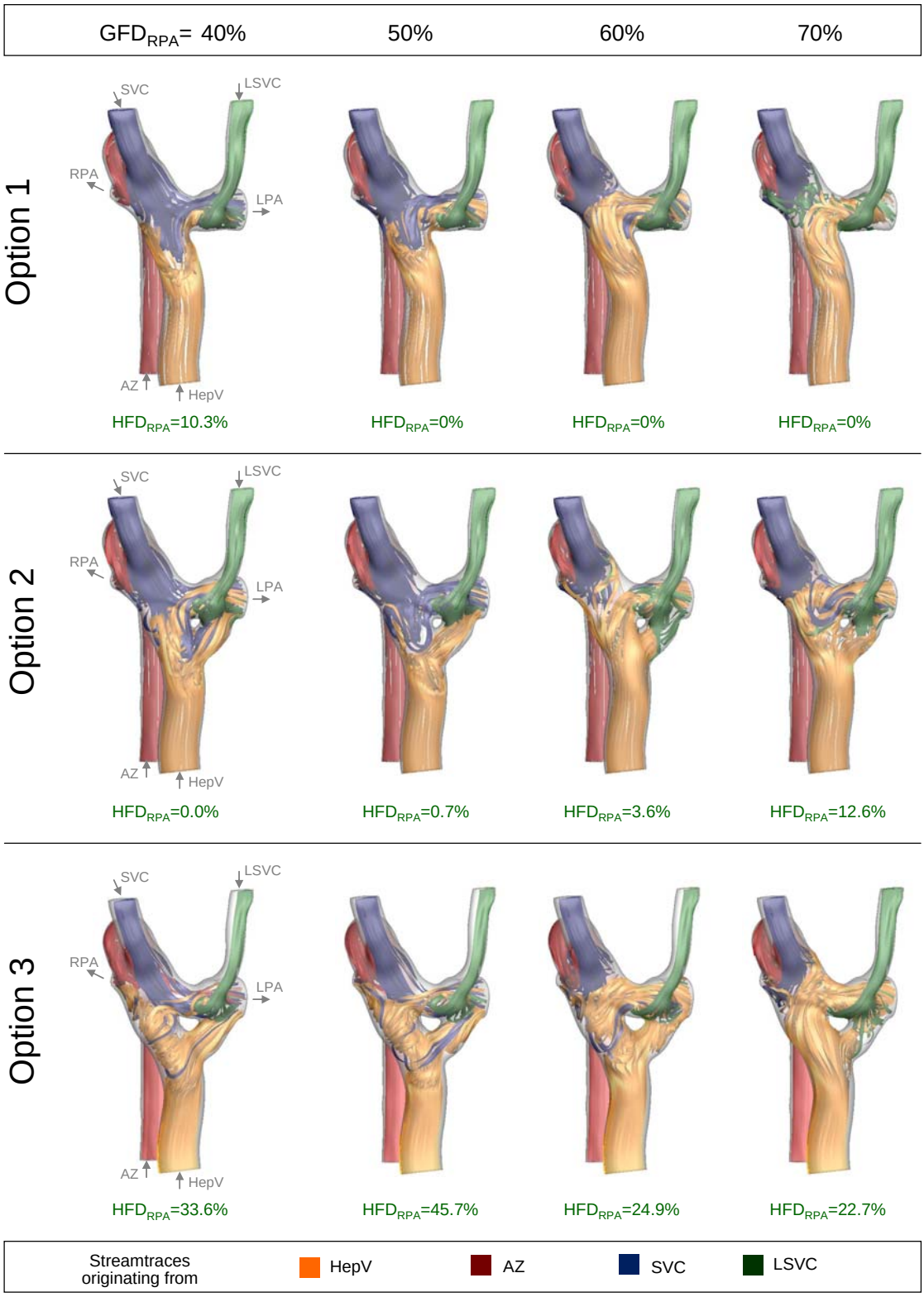

Figure 9-39: Flow structures observed in Options 1, 2 and 3 for Patient B2. The associated HFD_{RPA} are provided below each flow field in green.

pulmonary artery, the LSVC flowing to the LPA and the AZ to the RSVC. On the other hand, significant changes can be noticed in the interaction between the SVC and HepV flows. At GFD_{RPA}=40%, a large proportion of the SVC flow is directed towards the LPA to match the desired GFD. The SVC and HepV streams thus directly face one another. This feature was intended and meant to increase the mixing between the two streams. However, the low HepV flow rate and large HepV diameter result in a low kinetic energy for that inflow. The HepV is unable to sustain the momentum of the SVC, resulting in a high penetration of the SVC into the hepatic baffle. Most of the SVC flow entering the hepatic baffle exits towards the LPA, forcing a larger proportion of the HepV towards the RPA. This corresponds to the local maximum of 10.3% observed in the HFD_{RPA} curve of Option 1 for GFD_{RPA}=40%. As GFD_{RPA} increases to 50%, part of the SVC flow turns towards the RPA within the connection itself. This results in a lower penetration of the SVC into the HepV baffle, but also creates a large recirculation region within the connection that prevents the HepV from reaching the RPA. This blockage results in an exclusive distribution of the hepatic flow to the LPA, and thus to an HFD_{RPA} of 0%. It is interesting to note that at GFD_{RPA}=70%, part of the LSVC stream actually flows in a direction opposite to that of the HepV, crossing the mid-PA segment towards the RPA. This is due to the angulated orientation of the LSVC towards the mid-PA.

Option 2: The interaction between the four different inflows in Option 2 (middle row in Figure 9-39) follows a similar dynamics as in Option 1. The HepV distribution is strongly dominated by the SVC flow. A major difference compared to Option 1 is the presence of the left branch of the Optiflo, which allows the HepV flow to reach to the LPA. As a result, when GFD_{RPA} is below or equal to 50% and the SVC penetrates into the HepV

baffle, most of the HepV flow exits via the left branch rather than mixing with the SVC. This explains why, despite the fact that Options 1 and 2 featured the same intra-atrial baffle, no local maximum was observed at GFD_{RPA}=40% in Option 2. Another distinctive feature of Option 2 compared to Option 1, is that at GFD_{RPA} values of 60% or more, the LSVC flow gets entrapped into the left branch of the Optiflo. This prevents the LSVC from competing with the HepV to go towards the RPA. As a result, HFD_{RPA} continuously increases with increasing GFD_{RPA}.

Option 3: Option 3 (bottom row in Figure 9-39) differs from Option 2 in that the two branches of the Optiflo reach further towards the RPA and LPA. The right branch is not exactly aligned with the SVC axis, but rather slightly shifted to the right. As a result at the lower GFD_{RPA} values, the SVC flow does not penetrate into the baffle, allowing the HepV flow to reach for the RPA when GFD_{RPA}=40% and 50%. However, when GFD_{RPA} increases beyond 50%, the large portion of the SVC flow that turns towards the RPA opposes a high resistance to the HepV flow and restricts its access to the RPA. Furthermore, as the left branch lies further to the left than in Option 2, the LSVC flow does not get entrapped at GFD_{RPA}=60 and 70%. Accordingly when GFD_{RPA} increases beyond 50%, the competition between the SVC, LSVC and HepV flows pushes the lowest energy stream, i.e. the HepV, towards the LPA, leading to a temporary decrease in HFD_{RPA}.

Based on the above observations, it is apparent that the low HepV flow rate in Patient B2 represents an obstacle to a proper hepatic flow distribution to the left and right lung. Combining the HepV and AZ flows to try and improve the momentum of the combined stream and thereby improve mixing might provide a solution to that problem.

The right panel of Figure 9-38 displays the HFD_{RPA} curves obtained for the four different combinations of the HepV and AZ streams tested in Options 4 through 7.

Option 4: In Option 4, where the HepV is directed to the AZ vein, HFD_{RPA} (blue diamonds in Figure 9-38) is of 100% even at GFD_{RPA}=40%, demonstrating a highly preferential HFD to RPA. The mechanism behind such uni-sided flow distribution can be better visualized from Figure 9-40, which displays the 3D flow structures associated with Option 4 through 7 at a GFD_{RPA}=50%. In Option 4, the combined AZ and HepV streams (in red and orange, respectively) enter the connection on the far right and flow exclusively to the RPA. Since, the AZ is the vessel that lies the furthest to the right, merging the HepV stream into the AZ vein is the equivalent of a right-sided HepV offset.

Option 5: In Option 5, where the AZ flow is merged into the pre-operative extra-cardiac graft, the HFD_{RPA} measurements (light red triangles in Figure 9-38) demonstrate a clear improvement compared to the pre-operative anatomy. As can be observed from Figure 9-40, combining the HepV and AZ streams allows the flow coming through the extra-cardiac baffle to compete with the LSVC, resulting in a better distribution of the combined HepV and AZ streams to the two lungs. However, this option still results in a highly preferential HFD to the LPA due the left-sided offset of the pre-operative extra-cardiac graft. In addition, the AZ stream constrains the HepV towards the left side of the baffle further shifting the HFD towards the LPA.

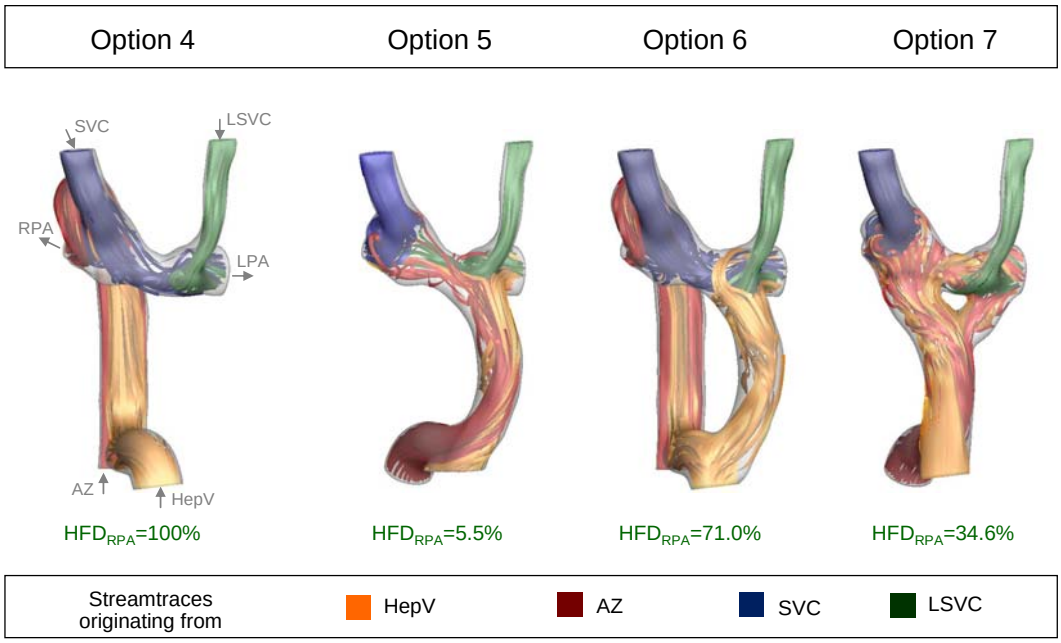

Figure 9-40: Flow structures in Options 4 through 7 at GFD_{RPA}=50%. The associated HFD_{RPA} are provided below each flow field in green.

Options 6 and 7: Both Options 6 and 7 (H and Y symbols in Figure 9-38) succeed in achieving a balanced HFD at a close to balanced GFD. Option 6 uses a HepV-to-AZ shunt similar to Options 4 and 5 but both the AZ vein and the pre-operative extra-cardiac graft are kept opened. This design allows the HepV flow to reach the LPA through the extra-cardiac baffle at low GFD_{RPA}, and reach the RPA through the AZ vein at high GFD_{RPA}. The success of Option 7, which combines the AZ and HepV streams into the Optiflo graft designed for Option 3, resides in an intense mixing of the lower and superior inflows within the connection area (Figure 9-40). Such mixing was impossible in the pre-operative anatomy and in Options 1-3 due to the low momentum of the HepV, and only limited in Option 5 due to the left-sided offset of the extra-cardiac graft. Merging the AZ flow to the HepV and using a Y-shaped Optiflo graft to distribute the combined flows to the two sides of the connection addresses both of these issues.

9.3.2.5 Power Loss Performance

The power losses associated with the seven investigated options are displayed in Figure 9-41. Power losses in the pre-operative anatomy are included as well for comparison. Results for Options 1-3 and Options 4-7 are displayed in two separate graphs for clarity, but both graphs are displayed using the same scale to ease the comparison between the different options. No notable difference in energetic performance may be noted across the different options. This is due to the fact that the flow dynamics in these options mostly differ in the path followed by the HepV flow, which is only a small contributor to the overall energy dissipation.

Options 1 to 3: Power losses in Option 1, where the HepV baffle connects towards the center, are slightly higher at lower GFD_{RPA} than those measured in the pre-operative anatomy. For these low GFD_{RPA} values, more flow has to travel through the mid-PA segment to reach the LPA than in the pre-operative anatomy due to the fact that HepV is connected further to the right in Option 1 than in the pre-operative anatomy. This increased flow through the mid-PA in turn increases the energy dissipation in that segment, yielding the observed increase in power losses. The Optiflo options (Options 2 and 3) slightly deviate from Option 1 at lower GFD_{RPA} values. The HepV-to-LPA branch increases the effective cross-sectional area available to reach the LPA, which in turn translates in a measurable decrease in power losses when GFD_{RPA} is lower than 50%.

Options 4 and 6: Options 4 and 6 featured the highest power losses of all investigated options, due to the presence of the HepV-to-AZ shunt that directs at least part of the HepV flow to the azygous vein. The noted increased in energy dissipation through the azygous vein in both of these options is consistent with what was observed for other

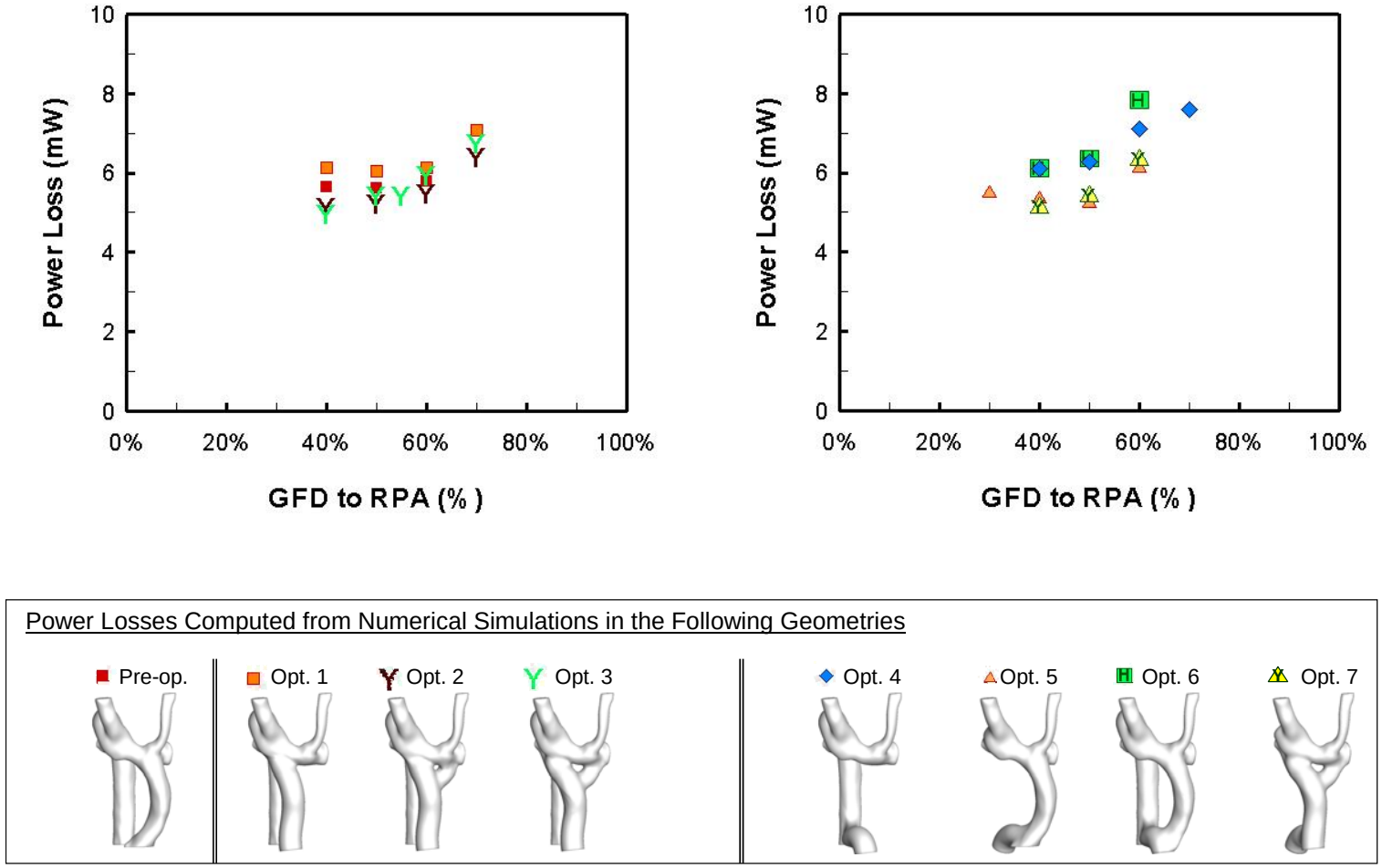

Figure 9-41: Power losses measured across the pre-operative anatomy and the first four surgical planning options (Left), and across the options that combined azygous and hepatic flows (Right).

patients, even though the magnitude of the increase is smaller than for other patients due to the small HepV rate.

Options 5 and 7: The power losses obtained for Options 5 and 7, which merge the AZ flow into the HepV baffle, are almost overlaid onto one another, restating the fact that vessel diameters and flow rates are the two predominant factors for energy dissipation, while the exact baffle geometry is only a second order parameter. At GFD_{RPA}=40%, Options 5 and 7, respectively, lead to a 5.7% and 8.9% decrease in energy dissipation compared to the pre-operative anatomy. Redirecting the AZ flow towards the HepV baffle, which has a larger diameter than the azygous vein, reduces the amount of energy lost in wall friction by the AZ flow prior to entering the connection. This translates into a net energy gain at low $GFD_{RPA.}$ However, at GFD_{RPA}=60%, those two options are observed to yield a 5 to 9% increase in energy dissipation. The right-sided position of the azygous vein in the pre-operative anatomy provides an advantage at higher GFD_{RPA}, reducing the distance traveled by the AZ flow as well as the mixing in the connection. Both of these features are lost when connecting the AZ to the HepV as in Options 5 and 7. As a result, the power losses in these two options rise faster when GFD_{RPA} exceeds 50% than they did in the pre-operative anatomy.

Finally, it should be noted that, apart for Options 4 and 5, the reported increase or decrease in power losses do not exceed 0.5mW. As such power losses do not appear as a stringent optimization constraint for Patient B2.

9.3.2.6 <u>Summary</u>

A total of seven options were investigated for Patient B2. The first three options sought to optimize the shape and connection location of the HepV baffle without

modifying the course of the other inflows. However, these three first options failed to increase HFD_{RPA} and were thus not recommended for surgery. The failure of Options 1 through 3 finds its roots in the especially low HepV flow rate recorded in Patient B2, which only accounts for 10% of the systemic return, resulting in a very low kinetic energy compared to the other inflows. As a consequence, the HepV flow could not sustain any competition with the superior inflows, and its distribution in Options 1-3 was mostly imposed by the SVC and LSVC. This resulted in an irregular behavior of the HFD_{RPA}, with local maxima followed by steep decreases.

Combining the AZ and HepV streams as in Options 4 through 7 was an efficient measure to restore a monotonous HFD_{RPA} behavior and increase HFD_{RPA}. Combining HepV and AZ flows into the azygous vein as in Option 4 led to too drastic of an increase, resulting in an exclusive HFD to RPA, and thus did not constitute a recommendable surgical option. The best results were obtained when using either Option 5 or Option 7. Option 5 divided the HepV stream between the azygous vein and the pre-operative extra-cardiac baffle, which were connected to the right and left of the connection, respectively. This allowed the hepatic flow to linearly switch extra-cardiac conduit to the azygous, i.e. from the LPA to the RPA, as GFD_{RPA} increased from 40% to 60%. Option 7 merged the AZ and HepV flows into a Y-shaped Optiflo connection. The two branches of the Y were designed so as to reach to beyond the LSVC on the left side, and beyond the SVC on the right. The HFD for that option more gradually switched from the left to the right, spreading the range over which both lungs receive some amount of hepatic flow.

Based on these observations, Option 7 was selected as the best possible option for Patient B2. This option might, however, pose some difficulties during the surgical

performance as it would entail converting the pre-operative extra-cardiac baffle into an intra-atrial Optiflo. An alternate option could be to keep an extra-cardiac approach but displace the baffle towards the mid-PA segment thus achieving the same levels of mixing as in Option 7. Finally, all of the above options seek to achieve a balanced HFD when flow to the lungs is balanced as well (GFD_{RPA}=50%). However, it should be restated that in the pre-operative anatomy a GFD_{RPA}=50% could not be achieved due to a stenosis in the RPA downstream of the segment considered in the surgical planning study. For optimal HFD to the two lungs, it might thus be critical to also alleviate the RPA stenosis, either during the surgery or by deploying a stent via catheter.

9.3.3 Patient B3 (CHOP M2)

9.3.3.1 Pre-Operative Clinical Diagnosis

The last patient, Patient B3, was a 4 year-old female Fontan patient who was born with a single ventricle, an interrupted IVC and a persistent LSVC. This patient had undergone a Kawashima operation followed by an extra-cardiac connection of the hepatic veins to the pulmonary arteries. The extra-cardiac connection was later taken down due to a clot in the hepatic baffle. After removal of the extra-cardiac connection, Patient B3 was diagnosed with severe bilateral PAVMs. She was recommended for a second TCPC to restore hepatic flow to the pulmonary arteries.

The patient anatomy at the time of diagnosis is shown in Figure 9-42, and its characteristic dimensions are summarized in Table 9-7. Since the former extra-cardiac connection had been taken down, the hepatic veins are routed to the right atrium. All

hepatic veins merge together just upstream of the atrium, resulting in a large total cross-sectional area of 4.62 cm^2. The azygous vein ascends along the left side of the aorta and connects to the LSVC. The aorta is thus located between the azygous and hepatic veins, which is a constraint to keep in mind for the design of HepV-to-AZ or AZ-to-HepV shunts. The mid-PA segment is narrow, with a cross-sectional area of only 0.24 cm^2 compared to 1.21 cm^2 for the LPA and 0.84 cm^2 for the RPA. Only little flow was noted through that segment during the MRI examination.

No pre-operative hemodynamics evaluation was conducted for Patient B3, since this patient did not feature a completed TCPC at the time of diagnosis. However, a few points are worthwhile noting from the pre-operative *in vivo* flow rates listed in Table 9-7. First, since the hepatic veins are not connected to the PAs, the sum of the *in vivo* LPA and RPA flow rates do not add up to Q_S but rather to the sum of the AZ, LSVC and SVC flow rates. The situation will be different in the surgical planning simulations where the HepV flow will be adjoined to the other systemic venous returns and distributed to the two lungs as well. To emulate the acute post-operative stage, it will be assumed that Q_S will be distributed in the same proportions as the pre-operative Q_P. All surgical planning options will thus be investigated at a 61/39 RPA/LPA flow ratio. The outflow conditions will then be varied to best predict the point at which each option will yield a balanced HFD. The next point of interest is that the AZ and LSVC flows combined

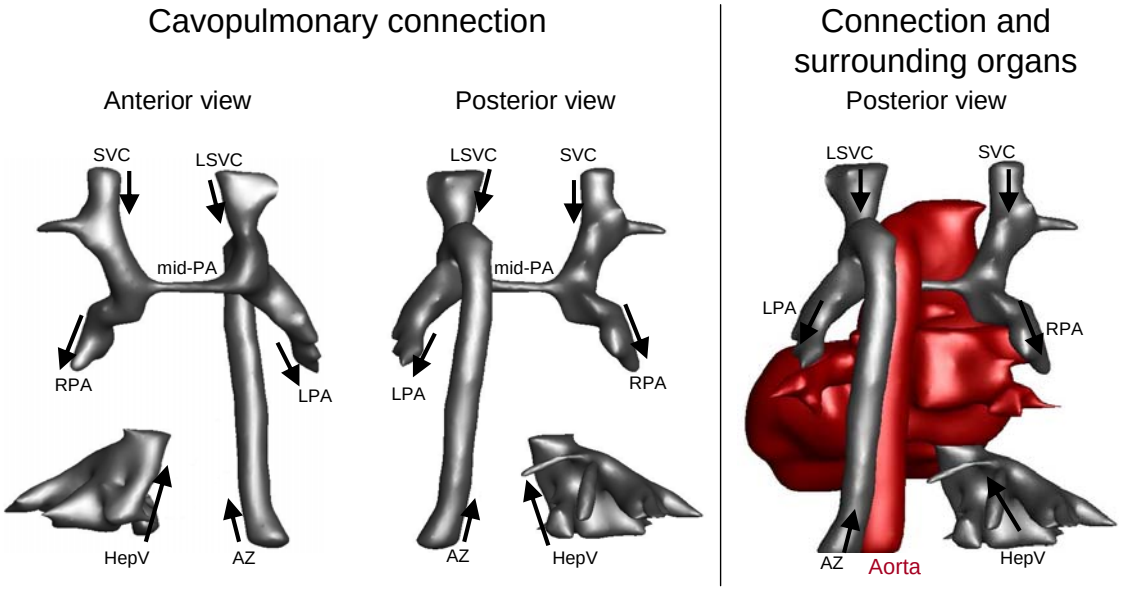

Figure 9-42: Pre-operative anatomy of Patient B3 with and without the surrounding cardiovascular structures. The superior cavopulmonary connection and hepatic veins are shown in grey, while the surrounding structures are shown in red. The black arrows indicate the main flow direction at each one of the inflows and outflows.

Table 9-8: Geometric and flow characteristics of Patient B3 at the time of PAVM diagnosis. Q_S: sum of the systemic inflows. Q_P: sum of the pulmonary outflows.

	Cross-sectional Area (cm^2)	MRI Flow measurements		CFD Flow Conditions		
		Q (L/min)	Q (%)	Q (L/min)	Q (%)	Characteristic Velocity (cm/s)
Systemic Venous Return						
HepV	4.62	0.63	21%	0.63	21%	2.26
LSVC	1.01	0.77	26%	0.77	26%	12.73
AZ	0.86	0.43	15%	0.43	15%	8.39
SVC	1.29	1.10	38%	1.10	38%	14.28
Q_S		2.93		2.93		
Pulmonary Flows						
LPA	1.21	0.90	39%	1.15	39%	15.84
RPA	0.84	1.40	61%	1.78	61%	35.33
Q_P		2.30		2.93		

balanced HFD. The next point of interest is that the AZ and LSVC flows combined account for 41% Q_S, while the SVC flow accounts for 37.6% Q_S. The left (i.e. the LSVC and AZ) and right (i.e. the SVC) superior inflows are thus almost perfectly balanced. Setting the HepV between the left and right superior inflows might thus constitute an efficient surgical planning option.

9.3.3.2 Surgical Planning Options

An exhaustive parametric investigation was conducted for Patient B3 during the surgical planning phase. Fourteen virtual surgeries were generated. The corresponding anatomies are shown in Figure 9-43 viewed from the anterior side. A top view is also provided for the anterior extra-cardiac options to better visualize changes in the curvature of the hepatic baffle. The investigated parameters include 1) offset of the HepV anastomosis site, 2) curvature of the HepV baffle, 3) combinations of the hepatic and azygous flows, and 4) splitting of the hepatic flow in two branches.

In Options 1 through 9, the HepV anastomosis site is progressively shifted from the RPA to the LSVC. Options 1 to 3 are considered to have a right-sided offset. Option 1 is connected approximately one diameter to the right of the SVC, Option 2 half a diameter to the right of the SVC and Option 3 is connected onto the SVC with a slight offset to the left compared to the SVC axis. Options 4 to 8 are considered to be centered. These options are connected to the mid-PA segment, their anastomosis location progressively shifting from right to left. Option 4 is connected one diameter away from the SVC. Options 5, 6 and 7 attach to the center of the mid-PA segment, and Option 8 reaches the mid-PA only one diameter away from the LSVC. Finally, Option 9 connects opposite to the LSVC anastomosis, and is considered to have a left-sided offset.

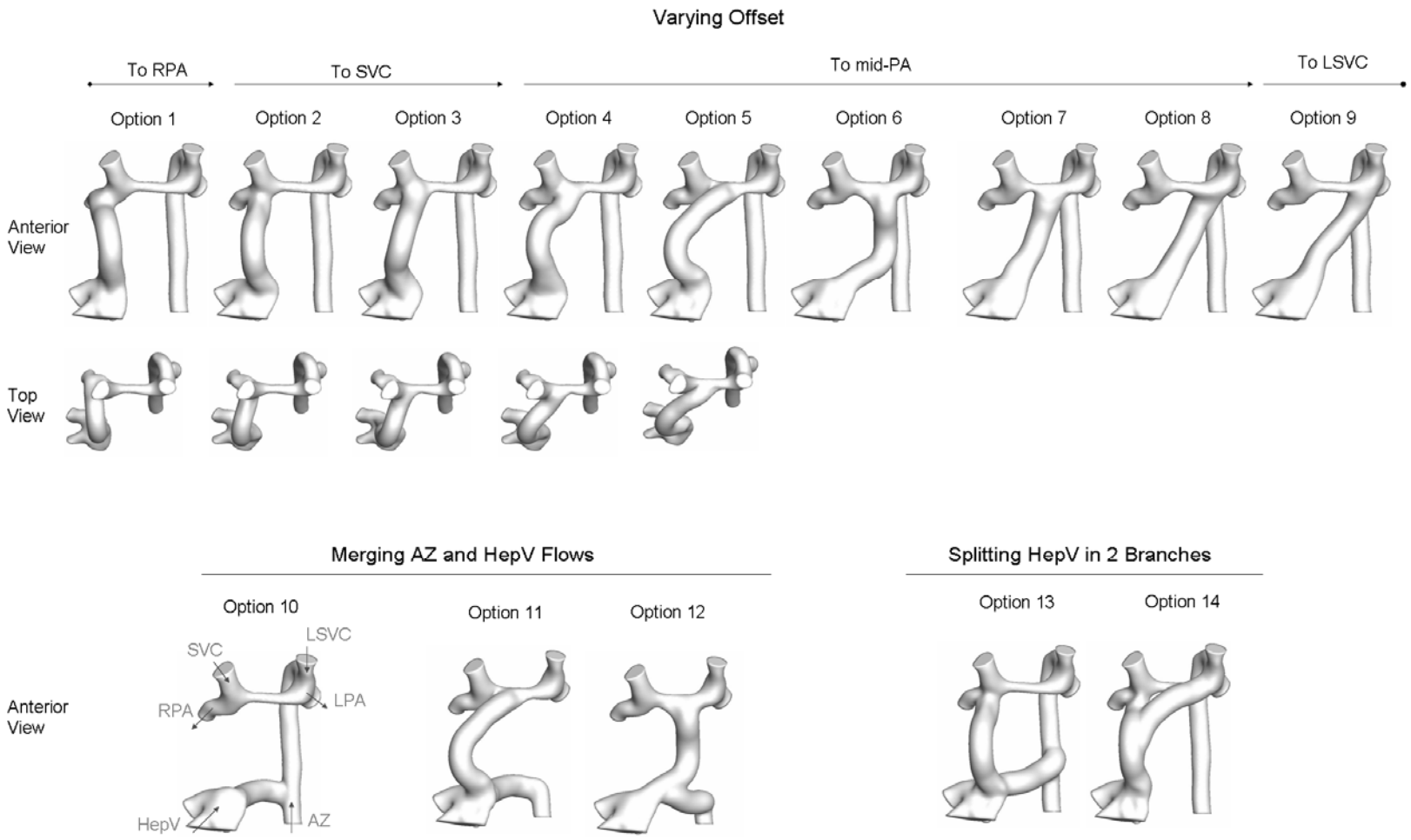

Figure 9-43: Virtual surgical planning options tested for Patient B3. All anatomies are viewed from the anterior side. A top view is also provided for the extra-cardiac options 1 to 5 to better visualize changes in the curvature of the HepV baffle. The nomenclature of the different vessels and the main flow directions are shown on Option 10.

In addition to the offset variation, Options 1 to 9 also differ in the type of surgical procedure used. Options 1 to 5 use an extra-cardiac graft wrapped along the anterior side of the heart. These options result in a highly curved hepatic baffle. The curvature is best visualized in the top views provided in Figure 9-43. To reach the mid-PA with a lower curvature in the vicinity of the anastomosis, Option 6 uses an extra-cardiac graft wrapped along the posterior side of the heart. The aortic arch and descending aorta impose a limit to the offset that may be reached with extra-cardiac grafts. Options 7 to 9 thus use an intra-atrial approach to reach further towards the LSVC.

Options 10 to 12 merge the hepatic and azygous flows into a common vessel. In Option 10, the hepatic flow is routed to the azygous vein via a HepV-to-AZ shunt. In Options 11 and 12, it is the azygous flow that is routed through an AZ-to-HepV shunt towards the hepatic baffle. Option 11 uses the same anterior extra-cardiac graft as in Option 5, while Option 12 uses the same posterior extra-cardiac graft as in Option 6.

Finally, in Options 13 and 14, the HepV baffle is split into two branches directed towards the LPA and RPA, respectively. In Option 13, this is achieved using the anterior extra-cardiac graft of Option 2 for the right branch, and a HepV-to-AZ shunt for the left branch. Option 14 makes use of a Y-shaped extra-cardiac graft, wrapped around the anterior side of the heart. The right branch of the graft is connected to the SVC, while the left branch reaches under the aortic arch towards the LSVC.

9.3.3.3 HFD Performance

Figure 9-44 displays the hepatic flow distribution, HFD_{RPA}, as a function of the global flow distribution, GFD_{RPA}, for all fourteen options. For clarity, the results are distributed over four different graphs based on the option types.

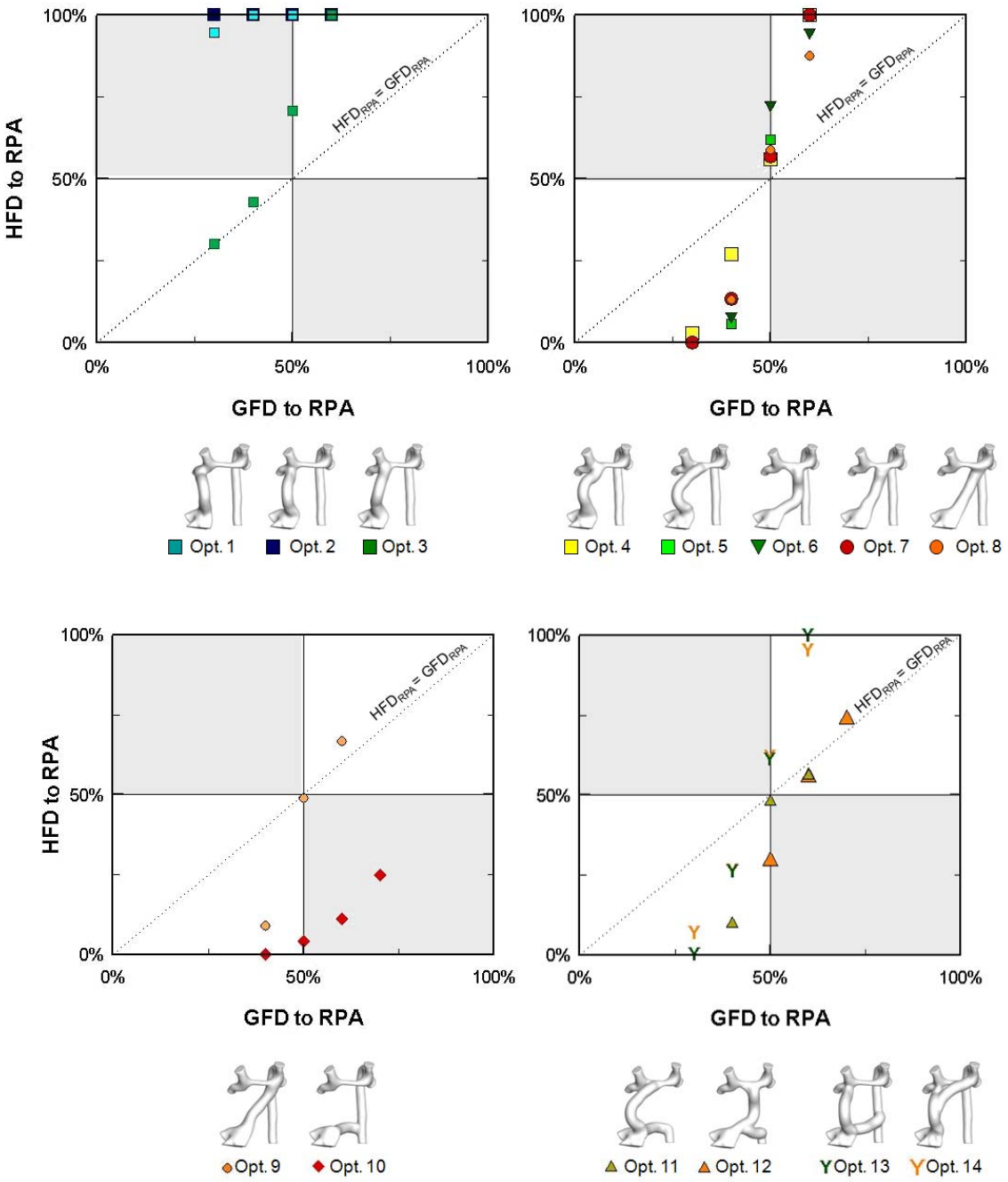

Figure 9-44: HFD performance across for the fourteen surgical options designed for Patient B3. Top Left: Results for the Options 1-3 with a right-sided offset. Top Right: Results for Options 4-8 connected to the mid-PA segment. Bottom Left: Results for Options 9 and 10 with a left-sided offset or equivalent. Bottom Right: Results for Options 11-14, which either merge the AZ into the HepV (Options 11 and 12) or split the HepV in two branches (Options 13 and 14).

Options 1 to 3: The top left panel of Figure 9-44 shows the performance of the three right-sided options, Options 1 to 3. Options 1 and 2, which were connected to the right of the SVC, result in a highly preferential HFD to the RPA, with all measurement points falling close to HFD_{RPA}=100% even when GFD_{RPA} is as low as 30%. In contrast, HFD_{RPA} measurements for Option 3 only reach 100% at GFD_{RPA}=60% and fall almost on top of the HFD_{RPA}=GFD_{RPA} line between GFD_{RPA}=30% and 40%. To better understand the underlying hemodynamic mechanisms and inflow interactions, Figure 9-45 displays the 3D streamtraces associated with Options 2 and 3 at GFD_{RPA} = 50% and 61%. In Option 2, the HepV streamtraces (in orange) are exclusively directed to RPA for all tested flow conditions. Due to the lower velocities and kinetic energy of the HepV stream compared to the SVC flow, the HepV cannot sustain the competition against the SVC and the right-sided offset, even though small, leads to a complete switch of the HepV streamtraces

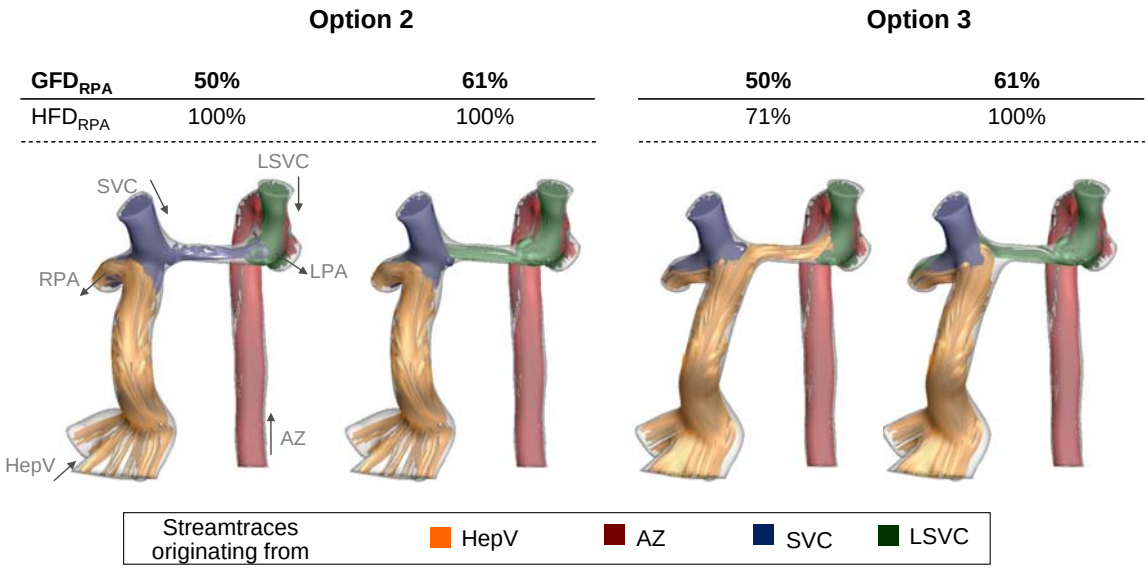

Figure 9-45: Comparison of the flow structures and HFD associated with the right-sided options 2 and 3 under the pre-operative outflow conditions (GFD_{RPA}=61%) and an equal blood flow distribution to the two lungs (GFD_{RPA}=50%). The streamtraces are color-coded by their vessel of origin.

towards the RPA. This opens up a flow separation on the left-side of the HepV anastomosis, into which the SVC streamtraces (in blue) engulf further constraining the hepatic flow towards the right. For lower GFD_{RPA} values, the SVC streamtraces (in blue) split between the RPA and LPA to match the global flow distribution, while at higher GFD_{RPA} values it is the LSVC streamtraces (in green) that split between the two outflows. It might be thus expected that, when the HepV baffle is connected to the right of the SVC axis as in Options 1 and 2, the hepatic flow only splits between the left and right lung when the flow to the LPA increases beyond the contribution of the SVC, AZ and LSVC flows combined, which is to say when flow to the LPA exceeds 79% Q_S and GFD_{RPA} falls below 21%.

In Option 3, the HepV flow axis falls slightly to the left of the SVC axis. As a result, when GFD_{RPA}=50%, it is the orange HepV streamtraces that split to adjust for the global flow distribution, while all of the SVC flow goes to the RPA. When GFD_{RPA}=60%, the RPA flow exceeds what can be provided by the SVC and HepV alone (Q_{HepV}+Q_{SVC}=59%Q_S) and it is the LSVC that splits between the RPA and LPA as was the case in Option 2. It might also be noted that, in Figure 9-44, the HFD_{RPA} for Option 3 increased at a slower rate for GFD_{RPA} values below 50%. This reflects the fact that at small GFD_{RPA} values the SVC does not uniquely flow to the RPA, but that both SVC and HepV streams split between the left and right lung. Based on a linear regression it might be predicted that Option 3 would yield a balanced hepatic flow distribution (HFD_{RPA} = 50%) for GFD_{RPA} = 42%.

Options 4 to 8: The top right panel of Figure 9-44 shows the HFD performances of the five centered options (Options 4 to 8). It is striking to note that, irrespective of the baffle

design and exact anastomosis location, the HFD_{RPA} curves described by these five options are almost overlaid onto one another. It may be noted that all of these measurements start to rise above the HFD_{RPA}=0% line around GFD_{RPA}=35%, which corresponds almost exactly to the contribution of the SVC of 38% Q_S. Unlike Option 3, the SVC flow in these options is thus exclusively directed to the RPA for all tested flow conditions. As long as the SVC flow suffices to match the desired RPA flow rate (i.e. as long as $GFD_{RPA} < 30\%$), all of the HepV flow is thus directed to the LPA. As GFD_{RPA} increases beyond 35%, HFD_{RPA} measurements for Options 4 to 8 increase almost linearly and reach HFD_{RPA}=100% for a global flow distribution of about 60/40 RPA/LPA. The HepV thus splits between the RPA and LPA until the RPA flow rate exceeds the sum of the HepV and SVC flows, which account for 59% Q_S combined. Option 8, which is only one diameter away from the LSVC, slightly deviates from Options 4 to 7 at GFD_{RPA}=60%, reflecting some mixing between the HepV and LSVC. Finally, the point at which Options 4 to 8 cross the HFD_{RPA}=50% line varies between GFD_{RPA}=46% and GFD_{RPA}=48%. All five options thus achieve a balanced HFD for a close to balanced GFD. Furthermore, the very low sensitivity of the HFD performance to the exact baffle geometry and implementation location makes them attractive for the surgery, allowing for some degree of freedom to adjust to unforeseen constraints *in vivo*.

Options 9 and 10: The HFD performance for left-sided options (Options 9 and 10) is shown in the bottom left panel of Figure 9-44. Option 9 connects opposite to the LSVC, using an intra-atrial baffle. Until GFD_{RPA}=50%, the HFD_{RPA} measurements for that option follow a pattern similar to what was observed in Options 4 to 8. HFD_{RPA} starts increasing around GFD_{RPA}=37% and reaches 50% at GFD_{RPA}=50%. This implies that,

similarly to Options 1 through 4, the SVC is exclusively directed towards the RPA and that, between GFD_{RPA}=37% and 50%, the HepV is the only inflow to be split between the RPA and LPA to adjust for the desired flow split. Beyond GFD_{RPA}=50%, the HFD_{RPA} measurements for Option 9 increase at a slower rate than what was observed for Options 4 through 8. Looking at the flow structures shown in Figure 9-46, it might be observed that at GFD_{RPA}=61%, the flow through the mid-PA segment of Option 9 is composed of a mixture of green and orange streamtraces, originating from the LSVC and HepV, respectively. The LSVC thus starts to contribute to the RPA flow rate earlier in Option 9, than in Options 4 to 8, explaining the slower increase rate of the HFD_{RPA} measurements beyond GFD_{RPA}=50%.

In Option 10, the HepV flow reaches the pulmonary arteries via the azygous vein and through the left Kawashima connection. This option results in a strong bias of the HFD towards the LPA, with all HFD_{RPA} measurements falling far below the HFD_{RPA}=GFD_{RPA} line. HFD_{RPA} starts rising around GFD_{RPA}=40% to 45% at a much slower rate than the previous options. As can be observed from Figure 9-46, at GFD_{RPA}=61% all SVC (blue) and LSVC (green) streamtraces are directed to the RPA, while only a small portion of the mixed AZ and HepV streamtraces (in red and orange) flow across the mid-PA segment towards the RPA. This biased distribution stems from the fact that the azygous vein is the left-most vessel in the connection, so that the combined AZ and HepV flows are the last ones to switch from the LPA to the RPA.

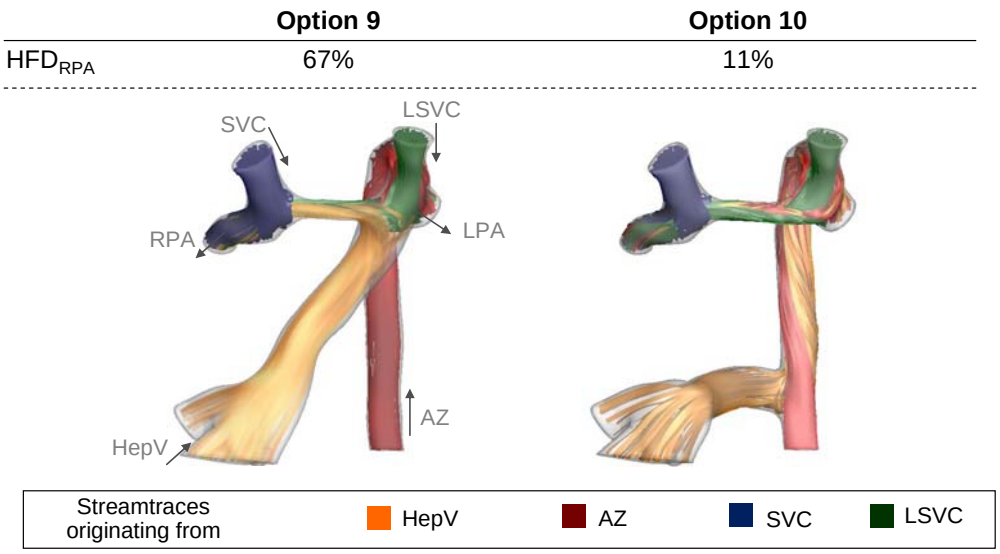

Figure 9-46: Comparison of the flow structures and HFD associated with the two left-sided options (Options 9 and 10) under the pre-operative outflow conditions (GFD$_{RPA}$=61%). The streamtraces are color-coded by their vessel of origin.

Options 11 and 12: Options 11 and 12 re-route the AZ flow through an AZ-to-HepV shunt and into one of the centrally connected extra-cardiac baffles (baffles from Options 5 and 6). Similarly to Options 5 and 6, the HFD$_{RPA}$ measurements for Options 11 and 12 (bottom left panel of Figure 9-44) rise above the HFD$_{RPA}$=0% line for a global flow distribution of about 35/65 RPA/LPA. This indicates that similarly to the former options, the hepatic flow is exclusively directed to the LPA until the RPA flow exceeds what can be provided by the SVC alone. The difference between the two classes of options resides in the range of GFD$_{RPA}$ values over which the hepatic flow switches from being exclusively directed to the LPA (HFD$_{RPA}$ = 0%) to going exclusively to the RPA (HFD$_{RPA}$ = 100%). For Options 5 and 6, this range is confined to GFD$_{RPA}$ values between 35% and 60%, while in Options 11 and 12 it extends to 70% or beyond. This larger transition range stems from the addition of the AZ flow to the HepV baffle, which allows

both streams to concurrently split between the left and right lung. Based on a linear interpolation, Options 11 and 12 are expected to achieve a balanced HFD (HFD_{RPA}=50%) for a close to balanced GFD, between GFD_{RPA} = 54% and 57%. The wider transition range might provide an additional advantage, allowing both lungs to receive hepatic nutrients even if the global flow distribution deviates from a 50/50 flow split.

Options 13 and 14: The two last options (Options 13 and 14) divide the HepV flow into two branches, directed to the LPA and RPA, respectively. Both options result in an even distribution of the hepatic flow, with HFD_{RPA} measurements that closely follows the trend previously observed in Options 4 through 8 (Figure 9-44). However, as can be visualized from Figure 9-47, the underlying hemodynamics drastically differ from those observed in the former options. In Option 13, the HepV flow progressively switches from the HepV-to-AZ shunt to the extra-cardiac conduit. At low GFD_{RPA} values, only little HepV flow goes through the extra-cardiac baffle, and the SVC streamtraces (blue) are seen to penetrate deep down into the baffle. On the other end of the spectrum, when GFD_{RPA} = 61%, a portion of the AZ flow is diverted through the HepV-to-AZ shunt towards the RPA, thus bypassing the mid-PA segment. Similarly, in Option 14, the HepV flow progressively switches from the left to the right branch of the Y-shaped graft. At GFD_{RPA} = 30%, a few SVC streamtraces penetrate deep down into the right branch of the graft and flow back up the left branch, thus bypassing the mid-PA segment. A symmetric behavior is observed with the LSVC streamtraces at high GFD_{RPA} values. These two options achieve a balanced HFD for a close to balanced GFD of 47/53 RPA/LPA.

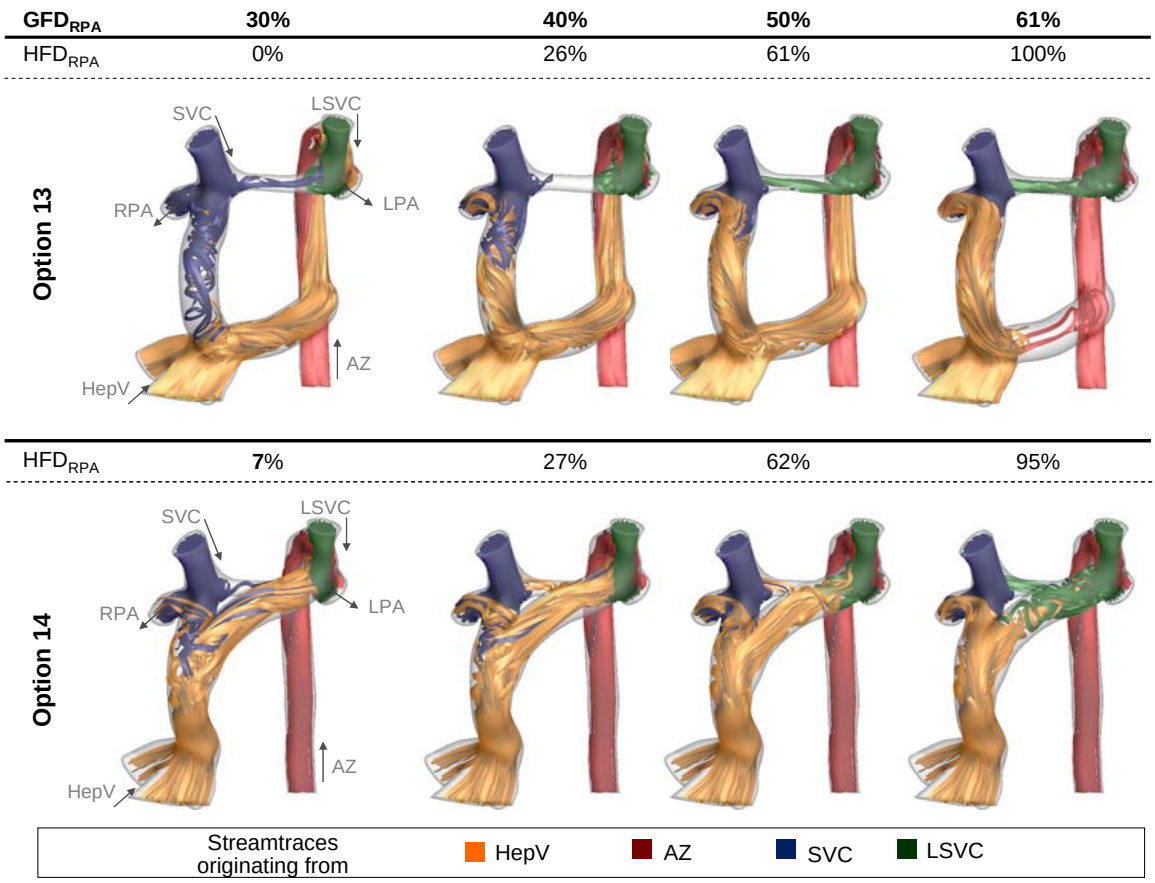

Figure 9-47: Comparison of the flow structures and HFD associated with Options 13 and 14 across all tested flow conditions. The streamtraces are color-coded by their vessel of origin.

9.3.3.4 Power Loss Performance

Figure 9-48 shows the power loss measurements obtained across all fourteen surgical planning options. For clarity, the results are separated into three graphs, based on the trends followed by the power losses. All options apart from the HepV-to-AZ connection (Option 10) yield power losses of the same order of magnitude, ranging between 2.6mW and 6.4mW. The trends mostly differ in the location of their minimum, and in their dependence on GFD_{RPA}.

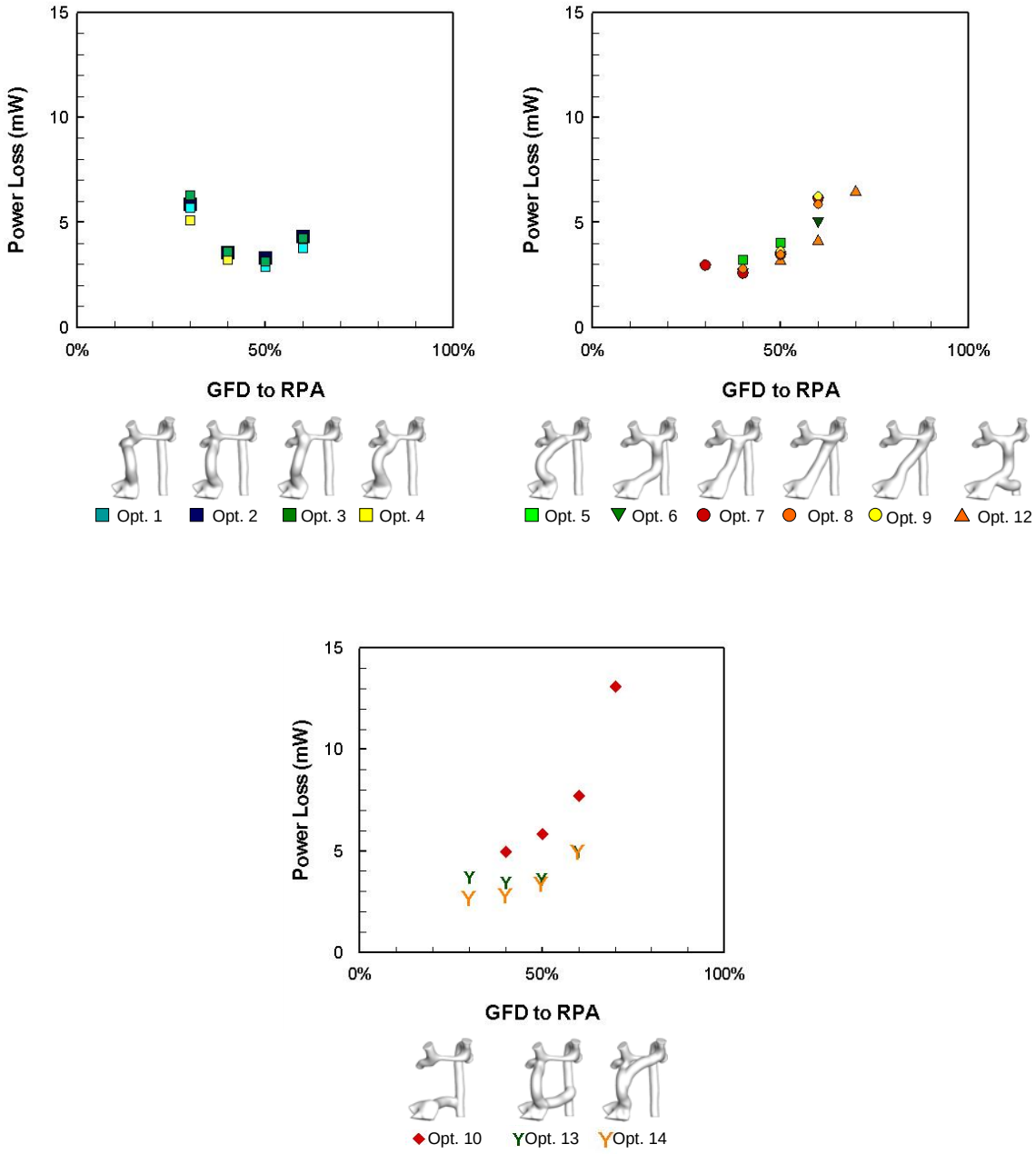

Figure 9-48: Power losses measured across all surgical planning options for Patient B3. For clarity, the results are separated based on the trends followed by the power loss curves. Top Left: baffles connected within one diameter of the SVC (Options 1 to 4). Top Right: baffles connected more than one diameter away from the SVC (Options 5 to 9 and 12). Bottom: the HepV-to-AZ (Option 10) and the two Y-grafts (Options 13 and 14).

Options 1 to 4: The top left panel of Figure 9-48 displays the results that show a stronger dependence to low GFD_{RPA} values. This includes the four first extra-cardiac options, which are all connected within one diameter of the SVC. In these options, 59% of the systemic venous return (i.e. $Q_{HepV} + Q_{SVC}$) comes in through the right side of the connection. When GFD_{RPA} is lower than 59%, some of the SVC or HepV flow has to travel across the narrow mid-PA segment towards the LPA. Power losses reach their minimum at GFD_{RPA}=50% when only 9% Q_S travels across the mid-PA.

Options 4-9 and 11-12: The top right panel of Figure 9-48 displays the results that show a stronger dependence to high GFD_{RPA} values and reach their minimum at GFD_{RPA}=40%. This includes Options 5 to 9, all of which use a baffle connected more than one diameter away from the SVC. The AZ-to-HepV options (Options 11 and 12) also fall in this category, as they make use of the same baffles as Option 5 and 6, respectively. Power losses in these six options are here again dominated by the dissipation occurring in the mid-PA segment. The minimum observed at GFD_{RPA}=40% corresponds to the point where less than 10% of the left-sided inflows (HepV, AZ and LSVC combined) travels across the mid-PA segment, towards the RPA. The power loss curves slightly deviate from one another at higher GFD_{RPA} values. Power losses in the left-sided Option 9 show a higher dependency on GFD_{RPA} than in the centrally located options. The left-sided offset increases the distance that the left inflows have to traveled through the mid-PA. This in turn increases the amount of dissipation in the mid-PA, resulting in a higher sensitivity to GFD_{RPA}. Options 11 and 12, on the other hand, display a slightly lower dependency on GFD_{RPA}, with power losses that are lower than those measured in the other options. Here again the difference in power losses finds its origin in the amount of

energy dissipation occurring in the mid-PA segment. Connecting the AZ flow in the center of the mid-PA segment reduces the distance that the AZ flow has to travel through that narrow section and thus the energy dissipation.

Options 10, 13 and 14: The bottom panel of Figure 9-48 displays the power loss results for the three remaining options, namely the HepV-to-AZ connection (Option 10) and the two options that divided the HepV into two branches (Options 13 and 14). Power losses in Option 10 are higher than in any other option for all tested conditions. This results from the increased blood flow through the azygous vein, which increases the dissipation along the azygous vessel walls. These power losses reach there minimum for GFD_{RPA} below 40% and rapidly increase as GFD_{RPA} increases beyond 40%. As was the case in the left-sided Option 9, this rapid power loss increase is due to an increasing dissipation in the mid-PA segment when the flow to the RPA increases. Options 13 and 14, where the HepV flow is distributed to the LPA or RPA through two different branches, yield the lowest power losses of all tested options. The left and right branches allow the HepV flow to reach the LPA or RPA without going through the mid-PA segment, reducing the flow rate and dissipation in the mid-PA segment. However, the performance gain does not exceed 0.3mW, and thus does not constitute a decisive parameter per se.

9.3.3.5 Summary

A total of fourteen surgical planning options were investigated for Patient B3. The first nine options investigated the impact of the HepV offset, and the curvature of the HepV baffle. Options 10 through 12 explored different combinations of the AZ and HepV flows, and the two last options looked into the potential benefit of splitting the

hepatic pathway into two branches. The parametric variations of the HepV offset revealed that, when the HepV was connected beyond the SVC (as in Options 1 and 2) or beyond the LSVC (as in Option 10), the resultant HFD was highly biased to the closest lung. On the other hand, all options where the HepV connected to the mid-PA segment (Options 3 to 9) yielded similar HFD performance, irrespective of the exact HepV anastomosis location, or the procedure used to perform the surgery. HFD_{RPA} typically increased from 0% to 100% between GFD_{RPA}=35% and 60%, achieving an HFD_{RPA} of 50% for an almost balanced global flow distribution. Option 3, where the HepV was connected to the SVC anastomosis site, slightly favored HFD to the RPA compared to Option 4 through 9. Symmetrically, Option 9, where the HepV faced the LSVC anastomosis site, slightly favored HFD to the LPA. However, both of these differences were of small magnitude compared to the variations observed when the HepV was connected beyond the SVC or LSVC. This in practice implies that even a slight offset towards the mid-PA suffices to equilibrate the HFD to the left and right lung. This finding is of critical importance since it is often difficult in these patients to reach the center of the mid-PA segment due to the presence of the overriding aorta. It should be emphasized that the success of Option 3 to 9 relied on the fact that the Q_{SVC} was almost equal to $Q_{LSVC}+Q_{AZ}$ allowing for the hepatic flow to transition from the LPA to the RPA over a range of GFD_{RPA} values centered around 50%.

Merging the AZ and HepV flows into one of the centrally connected baffles (as in Options 11 and 12) widened the range of GFD conditions for which both lungs received some hepatic nutrients. This presents the advantage of allowing for a greater tolerance to the global flow distribution. However, such approach would require two consecutive

procedures, creating an extra-cardiac baffle connection on the one hand and an A-to-HepV shunt on the other, which may not be necessary in view of the good performance of the centrally connected baffles alone. Finally, Options 13 and 14, where the HepV was split into an RPA and an LPA branch, resulted in the same HFD trends as the centrally connected baffles (Options 4 to 8). As these two options bypassed the mid-PA segment, they also resulted in slightly lower power losses than the other options. However, the energy gain recorded in Options 13 and 14 was only of small amplitude and did not appear as a major decision criterion.

Based on these observations, the surgical planning recommendation was to either connect the HepV baffle between the SVC and LSVC (as in Options 3 through 9), or to split the HepV into a right and a left branch (as in Options 11 and 12). The surgical procedure was performed using an anterior extra-cardiac graft connected to the SVC anastomosis site as in Option 3.

9.3.4 Summary of the Persistent LSVC Case Studies

Reviewing the three case studies conducted in this section, a few trends and guidelines might be drawn. Similarly to the single SVC group, HFD was predominantly dictated by the location of the HepV anastomosis site relative to the superior inflows. Connecting the HepV to the right or to the left of all other systemic venous returns (namely the SVC, AZ and LSVC) led to a highly preferential HFD to the closest lung. However, while trying to avoid any right or left-sided offset presented a major challenge in patients with a single SVC, the presence of a persistent LSVC drastically simplified the problem. Provided that the right and left superior venous returns were almost equal,

the equivalent of a no-offset design was to connect the hepatic baffle between the SVC and LSVC. The resultant HFD was then more or less insensitive to the exact anastomosis location along the mid-PA segment and to the type of connection used (intra-atrial vs. extra-cardiac, anterior vs. posterior grafts). From a surgical standpoint, this finding is of importance as it provides surgeons with some degree of freedom regarding the exact implementation, and allows them to adapt the procedure to unforeseen difficulties.

Dividing the hepatic baffle into two branches (using either a Y-shaped Optiflo graft, or the azygous and a regular extra-cardiac graft) lead to more mitigated results. In Patient A1 for example, splitting the hepatic flow between the azygous vein and a right-sided extra-cardiac baffle yielded unsatisfactory HFD performance, whereas the same option performed well in Patients A2 and A3. The success of these options is thus less general than the centrally-connected baffles and highly depends on the design of the left and right branch.

In all three patients, routing the HepV flow into the azygous, which was one of the best performing options for the single SVC group, resulted in poor HFD performance with a unilateral hepatic flow distribution to the lung closest to the AZ. Due to the dissociation of the left and right systemic venous returns, HepV-to-AZ connections in patient with a persistent LSVC were equivalent to a left or right-sided HepV offset. This highlights the need to break down SVHD patients into smaller subgroups, as the best performing procedures for one subgroup may be sub-optimal for others.

As pointed out above, a key factor for the centrally connected options to concurrently achieve a balanced HFD and GFD, is for the sum of the left and sum of the right superior inflows to contribute almost equally to the systemic venous return. When

this was the case, as in Patients A1 and A3, a centrally connected baffle performed ideally without any further addition. However, in cases such as Patient A2 where the sum of the LSVC and AZ flow rates represented over 70% Q_S while the SVC accounted for only 20% Q_S, a centrally connected baffle alone failed to improve HFD. This patient presented the added particularity of having a very low hepatic flow (only 10% Q_S), which resulted in a total incapacity for the HepV flow to compete against the other systemic venous returns. For that particular case, combining the AZ and HepV streams into the baffle appeared as a critical step towards the re-establishment of a balanced HFD, by both reducing the difference between the left and right superior venous returns, and increasing the energy of the flow coming through the baffle.

Finally, similarly to what was observed in the single SVC group, power losses mostly depended upon the vessel cross-sectional areas and flow rates, whereas the exact geometry of the hepatic baffle only appeared a second order parameter. As such they were not a strong decision factor for the TCPC optimization. A specificity of the persistent LSVC group was that the mid-PA segment was often undersized, leading to increased energy dissipation in that section. In the surgical planning campaign this was addressed by connecting the HepV to the mid-PA and flaring the anastomosis to dilate the stenosed segment. Alternatively, narrow mid-PA segments could be dilated by balloon angioplasty.

9.4 Conclusion

This chapter reviewed the experience gained over six patient-specific surgical planning studies. For each patient, the investigated options included 1) variations in the HepV offset, 2) variations in the surgical technique (intra-atrial vs. extra-cardia), 3) splitting the HepV conduit into two branches, and 4) combining the HepV and AZ flows. The optimization objectives were to both ensure a proper lung development via a balanced HFD and GFD, and minimize the workload imposed on the heart by minimizing the TCPC pressure drops and power losses.

This study first points to the need to break down SVHD patients into targeted subgroups as recommendations for patients with a single SVC, for example, were not applicable to patients with a persistent LSVC. In addition to anatomical considerations, the flow rates across each one of the systemic vessels (namely, the HepV, SVC, AZ and IV or LSVC) were a key determinant of the optimal option retained. Patients should thus not only be classified based on their vascular configuration but also, based on the relative contribution of the each individual vessel to the total systemic venous return. Evaluation of the pre-operative flow rates (via PC MRI or catheterization) and careful examination of the relative orientation of the systemic vessels are thus two major steps towards identifying the best procedure to follow.

It should be pointed out that the results shown herein represent over 200 individual CFD simulations. This may pose a limit to the application of such patient-specific optimization to the general population. However, by reviewing these patient-specific studies and appropriately categorizing them, a few clear cut observations were drawn which may provide guidelines towards improving the TCPC design for patients

with an interrupted IVC. Prior to any application, these guidelines would need to be verified on a larger patient pool, with clinical follow-up data to assess their validity. Cases with a large number of malformations, such as Patient B2, would still be best addressed with an individualized surgical planning investigation.

CHAPTER 10

DISCUSSION

10.1 Unstructured Cartesian Immersed-Boundary Paradigm

In this study, we developed an unstructured immersed-boundary (IB) paradigm to simulate the three-dimensional, time accurate blood flow dynamics through anatomically realistic total cavopulmonary connections (TCPC). The motivation behind this work was to develop a powerful and reliable numerical methodology that could be integrated with *in vivo* imaging (such as MRI) for a fast assessment of the *in vivo* flow fields, as well as with advanced virtual-surgery environments for the pre-operative optimization and planning of the TCPC surgery, on a patient-specific basis.

IB methods are inherently suited to tackle the geometrical complexity of *in vivo* anatomies. However, with exception the pioneering work by Peskin and McQueen [134, 139] and the more recent work of Yokoi *et al.* [140], the use of immersed boundary methods in simulating complex anatomical blood flows is not as wide-spread as one would anticipate given the ease with which such methods can handle arbitrarily complex geometries. One possible explanation for the scarcity of applications of IB methods to anatomical flows lies in the manner in which such methods handle the Cartesian grid nodes that are not part of the flow domain (i.e. the nodes that reside outside of the fluid in the solid side of a fluid/solid interface). The common practice is to retain such non-fluid grid nodes in the grid structure but blank them out of the computation. Such structured IB formulation performs well for external flow problems around bodies whose size is a

small fraction of the background Cartesian grid. However, a drastically different situation can be encountered when IB methods are applied to internal flow problems even when the geometry to be simulated is a fairly simple one. This situation is only exacerbated when attempting to model *in vivo* cardiovascular flows which typically involve tortuous, multi-connected vessels where only a small fraction of the embedding Cartesian grid is located in the interior of the flow domain (typically between 5 – 10 percent). Any attempt to carry out grid refinement studies for such configurations using standard IB approaches would quickly lead to excessively high memory and computational time requirements.

A clear example of this shortcoming can be found in the recent work of Yokoi *et al.* [140] who employed an IB approach to simulate blood flow in a complex cerebral aneurism anatomy (see Figure 10-1) immersed in a Cartesian grid with 160×50×75 nodes. Yokoi *et al.* did not provide any information about the number of nodes lying in the interior of the aneurysm model but given the complexity of their geometry it is apparent that the vast majority of the Cartesian nodes resided in the exterior of the flow domain and thus unnecessarily burdened the computation. Furthermore, Yokoi *et al* reported results for only one mesh, and the feasibility of carrying out grid convergence studies for complex anatomical geometries using IB methods remained to be demonstrated.

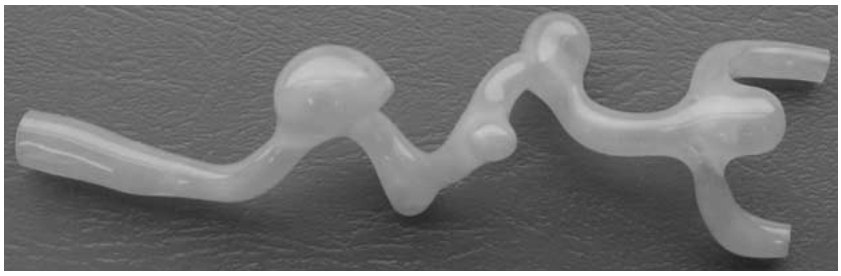

Figure 10-1: Shape model made by silicon (Image courtesy: [140])

The proposed unstructured immersed-boundary paradigm effectively alleviates the difficulties faced by structured IB methods for internal flow applications. All Cartesian grid nodes that do not belong to the fluid domain are eliminated from the data structure rather than just being blanked out of the computations, resulting in an unstructured albeit Cartesian computational mesh. The connectivity information is provided by introducing two arrays mapping the structured and unstructured Cartesian indexing systems onto one another. Such unstructured Cartesian paradigms are gaining in popularity, and have already been applied in level-set approaches to track intricate dynamic surfaces with high spatial resolution [148]. The proposed unstructured Cartesian implementation strikes a balance between computational efficiency and memory requirements and leads to a readable and easy to maintain code implementation while drastically reducing storage requirements and computational costs.

The accuracy of our flow solver is demonstrated in Chapter 7 with an in depth validation against controlled *in vitro* experiments in test-cases ranging in complexity from a 90 degree curved pipe to a patient-specific intra-atrial anatomy with high levels of flow instabilities, regions of transition to turbulence and re-laminarization. The potential of the unstructured Caretsian approach is further demonstrated in that chapter by carrying out for the first time a comprehensive grid sensitivity study for internal flow configurations as complex as that in a real-life TCPC anatomy.

Blood flows through the venae cavae and center of the TCPC connection are characterized by relatively low Reynolds numbers. The characteristic IVC Reynolds number for the cases presented in this thesis ranged from around 1000 in the two idealized TCPCs presented in Chapter 7 and Chapter 8, and between 100 and 600 for the patient-specific TCPC anatomies. The characteristic IVC Reynolds number for the intra-atrial validation test-case presented in Chapter 7 in particular is only Re = 294. As a result, the entrance flows into the TCPC are mostly dominated by the boundary layers forming along the vessel walls and their dynamic interaction at the center of the connection. The mesh refinement studies conducted in Chapter 7 demonstrated that these boundary layers and associated dominant flow structures were properly captured with a spatial discretization of h=0.03D_{IVC} in the case of the idealized TCPC and h=0.02D_{IVC} in the case of the anatomical intra-atrial TCPC. Achieving such spatial resolution with a structured Cartesian approach would have already required 8 and 10 million Cartesian grid cells, respectively, while only 650 and 740 thousand unstructured Cartesian grid elements were required here to achieve the same results. The results presented in this work thus demonstrate the potential of the unstructured Cartesian paradigm as a tool for carrying out fine mesh simulations of complex anatomical flows. It is important to point out that for all reported test-cases, even the simplest ones, the fluid cells only represented 6 – 18 percent of the total Cartesian grid cells and that this ratio could drop even further in highly tortuous geometries such as the aneurysm studied by Yokoi *et al.* [140].

The results presented throughout this thesis also underscore that despite relatively low Reynolds numbers, the interaction of the caval flows can lead to highly unstable chaotic mixing at the center of the connection, as may be visualized in the instantaneous

time-series shown for the intra-atrial validation test-case in Chapter 7. Flow in the pulmonary arteries can also host very complex dynamics including regions of transition to turbulence and re-laminarization, such as what was seen for Patient A1 in Chapter 9. These complex flow phenomena are induced by the complexity of the anatomical geometries, including regions of strong curvature and rapid changes in cross-sectional areas, and by the increased levels of 3D unsteady perturbations such geometrical features impart on the flow. These observations further reinforce the need for fine temporal and spatial discretization in order to properly characterize the *in vivo* TCPC flow structures.

Finally, beyond the validation of the numerical scheme, which was clearly demonstrated in Chapter 7, reproducing the in vivo TCPC flows requires matching the in vivo boundary conditions, including the wall motion and inlet/outlet flow conditions. While the TCPC wall motion was negelected in this thesis, efforts were made to match the in vivo flow conditions. Inlet/outlet flow rates were prescribed based on the *in vivo* PC MRI flow measurements. In the pulsatile investigation, the inlet velocity profiles were prescribed to best match the global in vivo flow directions at the inlets. As demonstrated for the intra-atrial anatomy in Chapter 7, where we compared the flow structures obtained using three different types of inflow conditions, the choice of inlet velocity profiles can have a significant impact upon the flow structures at the center of the TCPC connection. Future work may thus seek to further refine the in vivo modeling approach, by either interpolating the in vivo PC MRI measurements onto the inlets of the computational domain, or extending the domain further upstream to reduce the impact of the inlet boundary conditions on the flow structures at the center of the TCPC.

In summary, the results presented in Chapter 7 underscore the need for careful numerical validation and simulations on fine computational meshes in order to properly capture all dynamic features of the *in vivo* flow structures. This is of critical importance and should be re-emphasized as we enter an era when computational simulations for clinical applications are becoming increasingly widespread.

10.2 Investigation of the Pulsatile TCPC Hemodynamics

The first aspect of our study investigates the impact of pulsatility on the hemodynamics of different TCPC connection types. The objective of this study is two-folds: first, assess the impact of flow pulsatility on chosen clinical end-points and determine whether some procedures are more sensitive to pulsatility than others; and then assess the range of validity of our simulations by comparing the pulsatile CFD flow fields to the *in vivo* flow structures measured by PC MRI. To this end, in Chapter 8, we compare the hemodynamics and efficiency metrics obtained using the pulsatile *in vivo* flow curves to the ones obtained using the mean *in vivo* flow rates in three patients having each undergone a different TCPC procedure, as well as in an idealized representation of the TCPC. To ease our subsequent discussion, the main observations and results of Chapter 8 are summarized in Table 10-1 for each one of the four test-cases. The clinical endpoints retained are (i) the TCPC power losses taken as a surrogate metrics for the workload imposed on the single ventricle; (ii) the hepatic or IVC flow distribution taken as a surrogate measure for the risk of pulmonary artero-venous malformations; and (iii) the hepatic or IVC particle residence times taken as a measure of the differences in particle pathways and an indicator for the risk of thrombus formation in the TCPC baffle.

Table 10-1: Summary of the pulsatile investigations and of the comparison of the performance metrics under pulsatile and non-pulsatile (NP) conditions

		Idealized TCPC	Patient 1	Patient 2	Patient 3
Geometry	Connection type	4 straight pipes of equal diameter	Extra-cardiac Normal systemic venous return	Intra-atrial Normal systemic venous return	Extra-cardiac Interrupted IVC Persistent LSVC
	offset	1.5D towards the RPA	0.5D or less towards the RPA	0.5D or less towards the LPA	0D offset with SVC
	A_{IVC} (cm^2)	1.96	2.91	3.37	1.40
	min of A_{LPA}, A_{RPA} (cm^2)	1.96	0.57 (LPA)	0.75 (LPA)	0.81 (RPA)
Cardiac output (L/min)		4	2.7	1.08	2.82
Q_{IVC} (L/min)		2.66	1.79	0.74	0.16
V_{IVC} (cm/s)		22.6	10.3	3.7	1.9
GFD_{IVC} (%)	mean	67	62	68	6
	[min;max]	[64;70]	[60;73]	[51;84]	[-14;23]
GFD_{RPA} (%)	mean	53	43	58	41.1
	[min; max]	[43; 61]	[37;50]	[56;60]	[29;45]
PI (%)	IVC	28.3	48.5	61	361
	Max (other than IVC)	76.3 (LPA)	64.6 (LPA)	58.3 (SVC)	31 (AZ)
Cardiac cycle	beats/min	70	91	68	101
	ms	860	659	883	593
Comparison between pulsatile and NP Flow Fields		NP slightly underestimates the instabilities at the center of the TCPC	Very similar	NP underestimates instabilities and mixing at the center of the TCPC	NP does not capture the instabilities and mixing of the HepV baffle
Resi-dence times (ms)		comparable	Almost identical	Almost identical	Different
	Puls Mode	272	497	836	1204
	[Min; Max]	[218; 913]	[433; 1376]	[750; 3958]	[881; 3107]
	NP Mode	360	459	788	1476
	[Min; Max]	[290; 841]	[437; 1360]	[741; 3906]	[1384; 4850]
PL (mW)	Puls Mean	7.90	48.51	1.29	18.33
	Max	28.19	70.65	7.89	45.57
	NP	6.58	46.50	1.29	8.54
HFD_{RPA} (%)	Puls Mean	75.7	69	42	100
	NP	74.9	70	35	100

Imposing pulsatile flow boundary conditions will obviously lead to different instantaneous velocity and pressure fields, and in turn different instantaneous power losses and flow distributions, than non-pulsatile mean flow conditions. The first question that arises is thus to determine whether the body is most sensitive to the transient fluctuations in power losses or flow distributions, or whether it is the long-term time-averaged effect that has the largest impact. Power losses are taken as a surrogate measure of the workload imposed on the single ventricle, which is separated from the TCPC by a network of arteries, veins and capillaries. It might thus be inferred that the transient power loss fluctuations will be damped out, and that the time-averaged power loss value offers a good representation of the ventricular power requirements. Similarly, the mean HFD appears as a good representation of the overall hepatic delivery to the two lungs. Accordingly, the focus of our discussion will be on the comparison of the non-pulsatile efficiency metrics against the mean pulsatile values, averaged over the cardiac cycle.

10.2.1 Power Loss Comparisons

10.2.1.1 Power Loss Normalization

The non-pulsatile and mean pulsatile power losses reported in Table 10-1 span a wide range of values, going from losses as low as 1.29 mW in Patient 2 to losses as high as 46.50 mW in Patient 1. Such a large span is not surprising and falls well with the range of power losses reported in previous experimental and computational investigations. de Zélicourt et al. [95] reported losses between 1 and 50 mW in idealized TCPCs of varying vessel dimensions, while Whitehead et al. [92] reported losses up to 2,000 mW in patient-specific anatomies under elevated cardiac outputs (CO), simulating exercise conditions.

While increased power losses due to geometrical constraints reflect a detrimental impact of the TCPC design on the cardiovascular resistance, high power losses due to a high cardiac output reflect a good overall ventricular performance and as such should not be mistaken for a faulty TCPC design. A critical step towards understanding the contribution of different geometric factors to the overall TCPC power losses is thus to first devise a proper normalization framework. Dasi et al. [97] suggested using $\rho CO^3 / BSA^2$, where ρ is the density of blood ($\rho = 1060\, kg \cdot m^{-3}$) and *BSA* is the body surface area, as a normalization factor for all power-derived clinical metrics. Since our focus is on the TCPC itself, we modify the above expression to represent the total power entering the TCPC as:

$$\varepsilon_0 = \rho CO^3 / A_{IN}{}^2 \tag{10-1}$$

where A_{IN} is the sum of the inlet cross-sections. For normal subjects, the vessel cross-sectional areas should scale with the BSA and both metrics should be equivalent, but this might not be the case in Fontan patients who accumulate a large number of cardiovascular malformations.

10.2.1.2 Power Losses Comparison across Templates

For a fairer comparison of the power losses across templates, Table 10-2 provides the mean pulsatile power losses and their non-pulsatile counterpart normalized by the dynamic power scale of each model, $\varepsilon_0 = \rho CO^3 / A_{IN}{}^2$. After normalization, Patient 2's no longer is the best performer, but rather figures among the two least efficient connections together with Patient 1. Plotting these normalized power losses against the

minimum PA cross-sectional area (see Figure 10-2), it is apparent the normalized minimum vessel dimension is a dominant factor in the TCPC dissipation rate, while the type of connection does not appear to play a significant role.

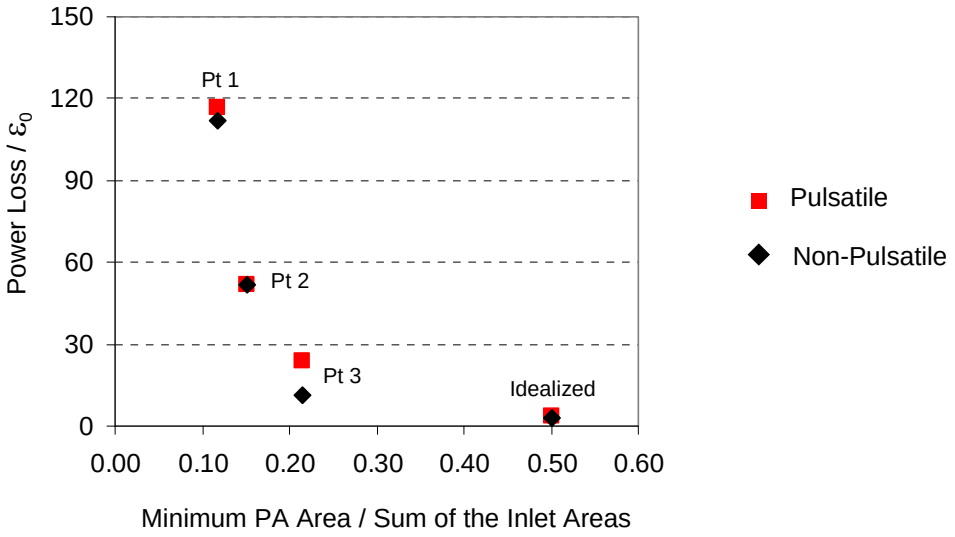

Figure 10-2: Normalized pulsatile and non-pulsatile power losses as a function of the minimum PA cross-sectional area indexed by A_{IN}.

Table 10-2: Pulsatile and non-pulsatile power losses normalized by their dynamic power scale, PL/ε_0 .

	Idealized	Patient 1	Patient 2	Patient 3
Pulsatile	3.9	116.7	51.8	23.8
Non-Pulsatile	3.2	111.8	51.8	11.1

10.2.1.3 Non-Pulsatile Power Loss Analysis

Going back to the experimental study of de Zélicourt et al. [95], the authors demonstrated that, all flow splits and geometrical factors held constant, the power losses (PL) measured under non-pulsatile conditions followed a power law dependence on the

cardiac output, as $PL = \alpha CO^{\beta}$. Depending on the model under consideration, β ranged between 2.5 to 2.8 and α between 0.17 and 3.8. The authors pointed to the vessel dimensions as the major determinant for the scaling factor α.

Dasi et al. [97] conducted a similar regression analysis using non-pulsatile experimental power loss measurements obtained in six patient-specific anatomies, and suggested the following expression for the TCPC power losses:

$$PL = \rho \frac{CO^3}{BSA^2} \mathrm{Re}^{-0.25} \left[C_{LPA} \left(\frac{A_{LPA}}{BSA} \right)^{-1.25} \left(\frac{Q_{LPA}}{CO} \right)^3 + C_{RPA} \left(\frac{A_{RPA}}{BSA} \right)^{-1.25} \left(\frac{Q_{RPA}}{CO} \right)^3 \right] \quad (10\text{-}2)$$

where A_{LPA} and A_{RPA} are the LPA and RPA cross-sectional areas, Q_{LPA} and Q_{RPA} are the LPA and RPA flow rates, and C_{LPA} and C_{RPA} are two resistance coefficients, which were determined by fitting the theoretical power loss curve to the experimental measurements. Both of the above studies established a net dependence of the non-pulsatile power losses on the flow rate to the power 2.75. The dependence on $\mathrm{Re}^{-0.25}$, which was empirically determined by Dasi et al. [97], compares well with the behavior of internal friction factor (Blasius, 1911), which is known to reduce with increasing Reynolds number as $\mathrm{Re}^{-0.25}$, for moderate Reynolds numbers but not fully developed turbulent conditions. This behavior also corroborates well with the decreasing non-dimensional energy dissipation observed by Whitehead et al. [92] in their comparison of extra-cardiacs and intra-atrial TCPCs.

A potential limitation of Equation 9-2 is that it does not isolate the contribution of the viscous dissipation occurring in each one of TCPC vessel to the overall dissipation. These terms are included in the C_{LPA} and C_{RPA} coefficients, thus requiring experimental

or CFD measurements across a range of different flow splits to be able to bets fit them. We thus formulate the viscous dissipation along the walls of each vessels, ε_V , as

$$\varepsilon_V = \sum \left(\frac{\left(Q_i / CO\right)^3}{\left(A_i / A_{IN}\right)^2} \mathrm{Re}_i^{-0.25} \cdot \frac{L_i}{\sqrt{A_{IN}}} \right) \tag{10-3}$$

where the subscript *i* spans each one of the inlet and outlet vessels; A_i, and L_i are the cross-sectional area and length of vessel *I*; Q_i, is the mean flow rate going through vessel *i*; and Re_i is the mean Reynolds number of vessel i based on Q_i and A_i.

Following the same procedure as Dasi et al. [97], we normalize the non-pulsatile power losses computed for each model by $\varepsilon_0 \cdot \varepsilon_V$, and plot them against the minimum PA diameter normalized by A_{IN}, to check for any additional dependence on the vessel diameters. The results are displayed in Figure 10-3. Similarly, to what was observed in [97], the normalized power losses show a strong dependence on the normalized minimum PA area, closely following a power law (R^2=0.98) with an exponent of -1.25.

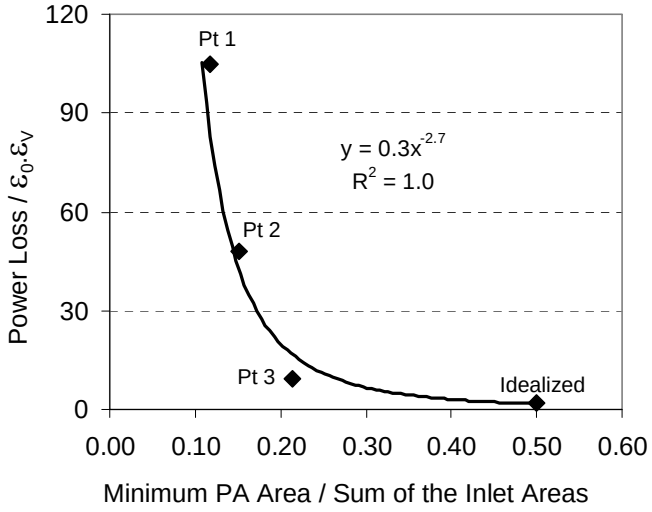

Figure 10-3: Normalized power losses plotted as a function of the normalized minimum PA area. Note the power law dependence.

The normalized PA area represents a measure of the sudden vessel constriction encountered by flow as it goes from the combined inlet vessels into the smaller pulmonary arteries.

Performing a bilinear fitting of the computed power losses to $\left(A_{LPA}/A_{IN}\right)^{-1.25}$ and $\left(A_{RPA}/A_{IN}\right)^{-1.25}$, we find an analytical power loss expression of the form:

$$\varepsilon = \varepsilon_0 \cdot \varepsilon_V \left[\alpha_{LPA} \left(\frac{A_{LPA}}{A_{IN}} \right)^{-1.25} + \alpha_{RPA} \left(\frac{A_{RPA}}{A_{IN}} \right)^{-1.25} + \gamma \right] \tag{10-4}$$

where the empirical values for the coefficients α_{LPA}, α_{RPA} and γ are 0.51, 0.62 and 1.3, respectively. γ may be seen as the contribution of the viscous energy dissipation rate along the TCPC vessel walls, assuming undisturbed vessel flows. α_{LPA} and α_{RPA} account for the deviations from this ideal behavior due to 1) the sudden constrictions and expansions encountered when going from the inlets into the LPA and RPA, and 2) to the helical flow patterns observed in the PAs, which inherently increase the amount of energy dissipated by wall friction in these vessels.

Figure 10-4 shows the comparison between the analytical power losses, ε, computed according to Equation 9-4 and the actual values obtained from the non-pulsatile CFD results. As may be noted in the figure, the CFD power losses for Patient 3 are slightly higher than the analytical prediction, while they are slightly lower than the analytical value for the idealized TCPC. These deviations find their root in the fact that α_{LPA}, α_{RPA} and γ should not be held constant across models, but rather should depend on local geometric characteristics of the connection, such as the curvature and orientation of the different vessels, as well as on the LPA/RPA flow ratio. However, the small sample size used herein did not allow for the detection of such fine dependences.

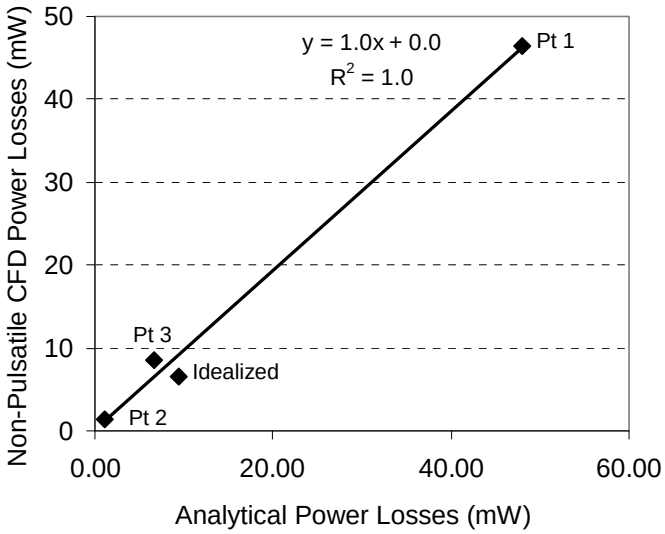

Figure 10-4: Comparison of the non-pulsatile CFD power losses and the values obtained with the analytical expression given in Equation 9-3.

Provided with a larger sample size, each one of the terms in Equation 9-3 could also be further refined to capture the impact of the local vessel characteristics. For example, in Equation 9-4, A_{LPA}/A_{IN} and A_{RPA}/A_{IN} were considered to be a good representation of the energy expense of forcing the combined inflows into the LPA and RPA. In practice, this term could be broken down into the contribution of the dimensional mismatch between the inlet vessels and the central connection area, and between the central connection area and the outlet vessels. Furthermore, using the vessel cross-sectional areas measured at the inlets and outlets of the TCPC domain might not to be the best representation of the sudden expansions or constrictions experienced by the flow. Possible alternatives include using the vessel cross-sectional areas at the anastomosis site, or the smallest cross-sectional areas measured within a certain distance of the anastomosis site, which might better capture the effect of a PA stenosis.

Finally, given the differences observed between the non-pulsatile and pulsatile losses, especially for Patient 3, it is obvious that the generalization of such an approach to

a pulsatile framework will have to account for the measured levels of pulsatility, and the associated increase in energy dissipation.

10.2.2 Hepatic Flow Distribution

For all cases, the distribution of the hepatic (or IVC) particles is preferentially oriented towards the closest pulmonary artery, namely the RPA for the idealized TCPC, Patient 1 and Patient 2, and the LPA for Patient 3. In the idealized TCPC and Patient 1, the measured HFD_{RPA} closely follows Q_{RPA}/Q_{IVC} implying that almost all of the RPA flow comes from the IVC, and that only the exceeding IVC flow is directed to the LPA. The hepatic flow distribution for Patient 2 slightly departs from that behavior, reflecting a higher IVC-SVC mixing at the center of the intra-atrial connection. For Patient 3, the connection almost behaved as two independent left- and right-sided connections, with the SVC and hepatic flows being exclusively directed to the RPA and the azygous and LSVC flows going only to the LPA. Such behavior might be attributed first to the abnormal configuration of the venous returns; then to the surgical construct, which sets the SVC and HepV far apart from the left superior venous returns; and finally to the presence of a severe mid-PA stenosis, which further limits the communication between the left and right sides of the connection.

No significant difference is seen between the pulsatile and non-pulsatile HFD predictions for the idealized TCPC, Patient 1 and Patient 3. A larger deviation is seen in the intra-atrial anatomy (Patient 2), where the addition of pulsatility increased the level of IVC-SVC mixing already noted under non-pulsatile conditions. An even more drastic increase in HepV-SVC mixing was noted for Patient 3, due to the extremely high levels

of HepV pulsatility, which could be expected to lead to large differences between the pulsatile and non-pulsatile HFD predictions had the combined HepV and SVC not all been distributed to the same lung.

10.2.3 Particle Residence Times

10.2.3.1 Residence Time Normalization

Similarly to the power losses, the particle residence will depend on the vessel flow rates, at the risk of masking differences across TCPC designs. Prior to any comparisons, the first step is thus, here again, to devise an adequate normalization factor. The time needed by an IVC or HepV particle to travel across the TCPC will depend on the characteristic velocities through the baffle and PAs, and on the vessel lengths. Since it is difficult to appropriately model the slowest velocities through the different vessels, we focus our attention on the particles flowing through the center of the vessels. Assuming that the vessel velocities adopt a fully developed parabolic profile, the characteristic velocity, V_i^*, at the center of a vessel *i* is given by:

$$V_i^* = 2 \cdot \frac{Q_i}{A_i} \tag{10-5}$$

where Q_i is the mean vessel flow rate and A_i is the vessel cross-sectional area measured at the inlet or outlet of the TCPC domain. Using the characteristic vessel velocities given by Equation 9-5, we define the characteristic particle residence time, T^*, as:

$$T^* = \frac{L_{IVC}}{V_{IVC}^*} + \frac{L_{XPA}}{V_{XPA}^*} \tag{10-6}$$

where XPA designates the PA receiving the highest portion of the hepatic flow (i.e. the RPA for the idealized TCPC, Patient 1 and Patient 3, and the LPA for Patient 2), and L_{IVC} and L_{XPA} are the lengths of the IVC (or HepV) baffle and of the chosen PA.

T^* represents the shortest residence time expected for a given set of vessel lengths and flow rates. The remaining variables include local geometric factors (such as the presence of vessel extensions or constrictions, curvature or connection angle) and local flow characteristics (such as the presence of flow recirculation or detachment regions, or mixing between different inflows), which are both tightly inter-related.

10.2.3.2 Comparison of the Characteristic and Minimum Non-Pulsatile Residence Times

Using the characteristic residence times, T*, computed using Equation 9-6, we first compare the normalized minimum residence times across cases and under pulsatile and non-pulsatile conditions. These shortest residence times are taken to be the 5% bound of the cumulative probability functions, accounting for the 5% fastest particles in the domain. The computed $T^*$and normalized shortest residence times are provided in Table 10-3 for the four models studied.

Table 10-3: Particle residence times corresponding normalized by the characteristic particle residence time, T^*.

		Idealized TCPC	Patient 1	Patient 2	Patient 3
T* (ms)		279	434	703	1337
Resd. Time Pulsatile	Mode	0.98	1.15	1.19	0.90
	[Min-Max]	[0.78; 3.28]	[1.00; 3.17]	[1.07; 5.63]	[0.66; 2.32]
Resd. Time Non-Pulsatile	Mode	1.29	1.06	1.12	1.10
	[Min-Max]	[1.04; 3.02]	[1.01; 3.14]	[1.05; 5.56]	[1.04; 3.63]

The normalized shortest residence times under non-pulsatile conditions are close to 1 for all considered cases, demonstrating that TCPC design did not significantly impact the propagation of the fastest particles, most likely flowing along the vessel centerlines away from any irregularities in the vessel walls.

10.2.3.3 Comparison of the Pulsatile and Non-Pulsatile Residence Times

Table 10-3 details the ranges in normalized particle residence times observed across the four test-cases, under both pulsatile and non-pulsatile conditions. No significant difference is observed between the normalized pulsatile and non-pulsatile residence times for Patients 1 and 2, while quite a large variation is observed for the idealized TCPC and Patient 3. As will be detailed in the subsequent paragraphs, these difference stem from two very difference mechanisms: in the idealized TCPC, the wider range in particle residence times stems from the short characteristic propagation time, T*, compared to the heart cycle duration, while for Patient 3 the shorter pulsatile residence times result from the high levels of SVC-HepV mixing.

To better illustrate the role played by the relative duration of the characteristic propagation time, T*, Figure 10-5 graphically compares T* to the cardiac cycle duration for the idealized TCPC and the two patients with a normal systemic venous return, Patients 1 and 2. For the two patient-specific cases, T* is more than half of the cardiac cycle and significantly longer than either the forward or backward flow phases (defined as the times during which the instantaneous flow rate is higher or lower than the mean, respectively). As a result, all IVC particles are exposed to both forward and backward flow rates, irrespective of the time when they enter the TCPC. In the idealized TCPC on the other hand, the characteristic propagation time, T*, is about one fourth of the cardiac

cycle duration and one half of either forward or backward flow phases. Accordingly, particles entering the TCPC at the beginning of the forward flow phase benefit from flow rates higher than the mean flow for their entire traverse of the TCPC, leading to shorter minimum residence times than under the mean non-pulsatile conditions. Symmetrically, particles seeded at the beginning of the backward phase are carried by flow rates lower than the mean flow, leading to longer maximum residence times than under the mean non-pulsatile conditions.

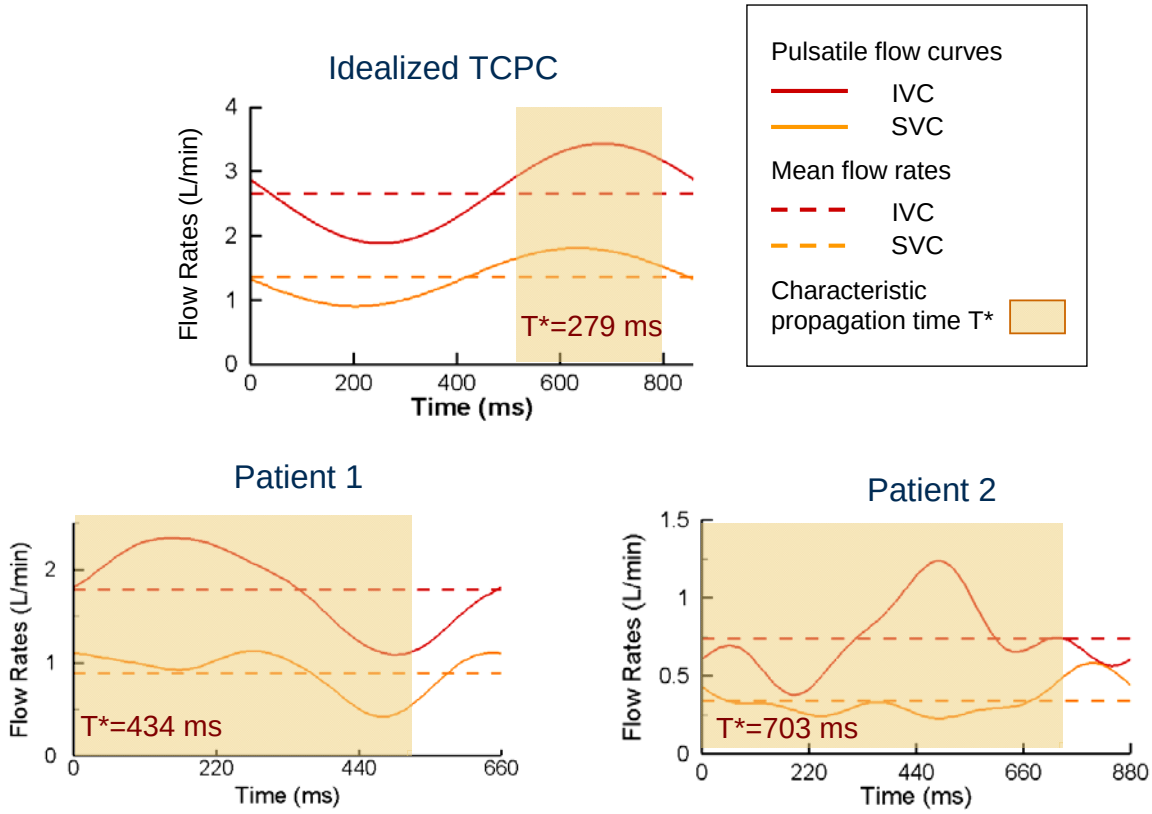

Figure 10-5: Graphical representation of the characteristic propagation time, T*, relative to the cardiac cycle and forward flow phase duration in the idealized TCPC and the two patients with a normal systemic venous return, Patients 1 and 2.

For Patient 3, the shorter pulsatile residence times do not find their roots in the faster forward flows, since even the fastest particles take close to 1.5 cardiac cycles to cross the TCPC domain, but rather in the drastic increase in mixing between the HepV and SVC streams under pulsatile conditions compared to the non-pulsatile predictions. As was pointed out in Chapter 8 (Section 8.5), due to the very high pulsatility levels recorded in Patient 3 (PI_{HepV} = 361%), the non-pulsatile flow conditions fail to represent the richness of the pulsatile dynamics, and in particular the levels of instabilities and HepV-SVC mixing observed throughout the hepatic baffle. As a result a portion of the hepatic particles is carried by the faster SVC flow, translating in a 36% decrease in the shortest and longest residence times. The peak pulsatile residence time is only 18% lower than the non-pulsatile one, reflecting the adverse effect of the backward flow phase, which, for Patient 3, actually translates into hepatic flow reversal.

In terms of the characteristic non-dimensional numbers of the problem, these observations imply that whether or not the non-pulsatile residence times adequately describe the pulsatile values depends on 1) the pulsatility index, high pulsatility indices implying increased mixing, which will change the residence times, and 2) the ratio of T* to the cardiac cycle duration, T*/T, a high ratio indicating a long relative propagation time, which will average out the pulsatile effects, while a smaller ratio would yield a larger impact of the forward and backward flow phases, leading to a lager spread between the minimum and maximum pulsatile residence times. It might also be worthwhile noting that T*/T scales as α^2/Re allowing for a fast assessment of the relative duration of the characteristic residence time.

10.2.3.4 Residence-Times Comparison across Templates

Finally, comparing the residence time ranges across the different cases, no significant difference is observed in terms of the minimum residence times (5%) or the mode (residence time associated with the highest probability) across the four different geometries, nor is there any significant difference in maximum residence times (corresponding to the 95% cumulative probability) across the three extra-cardiac TCPCs (idealized TCPC, Patient 1 and Patient 3). On the other hand, there is a notable increase in the maximum normalized residence time when going from the extra-cardiac geometries, for which it is typically on the order of 3, to the intra-atrial anatomy of Patient, for which it reaches up to 5.63 under pulsatile conditions. These extended residence times are associated with particles that get entrapped in small flow separation and recirculation regions, due to irregularities in the intra-atrial IVC baffle. Such flow features and extended residence times could be very detrimental in terms of thrombo-embolic risks, favoring platelet aggregation and thrombus formation.

10.2.4 Summary of the Pulsatile Investigation

10.2.4.1 Relevance of the Current Findings to the Broader Patient Population

In an effort to generalize our observations to a larger patient pool, Figure 10-6 and Figure 10-7 show the *in vivo* flow structures associated with three intra-atrial and three extra-cardiac anatomies as reported by Sundareswaran et al. [80]. Similarly to the intra-atrial anatomy examined in this thesis, the three intra-atrial anatomies are characterized by irregular baffle geometries, important flow recirculation at the center of the connection, and small recirculation regions localized along the irregularities in the intra-

atrial wall geometry. The extra-cardiac options, on the other hand, are associated with cylindrical geometries, and undisturbed IVC flow structures aligned with the vessel axis. The flow structures at the center of the extra-cardiac connections do not feature the large flow recirculation region seen in the intra-atrial TCPCs. The IVC and SVC streamtraces collide head-on, forming a stagnation point at the center of the connection around which they divide between the LPA and RPA.

These *in vivo* flow structures are in good qualitative agreement with the ones that were observed during our pulsatile investigation in the intra-atrial and extra-cardiac anatomies. This resemblance supports the fact that although based on a very small sample size, our findings are representative of the differences between intra-atrial and extra-cardiac TCPCs.

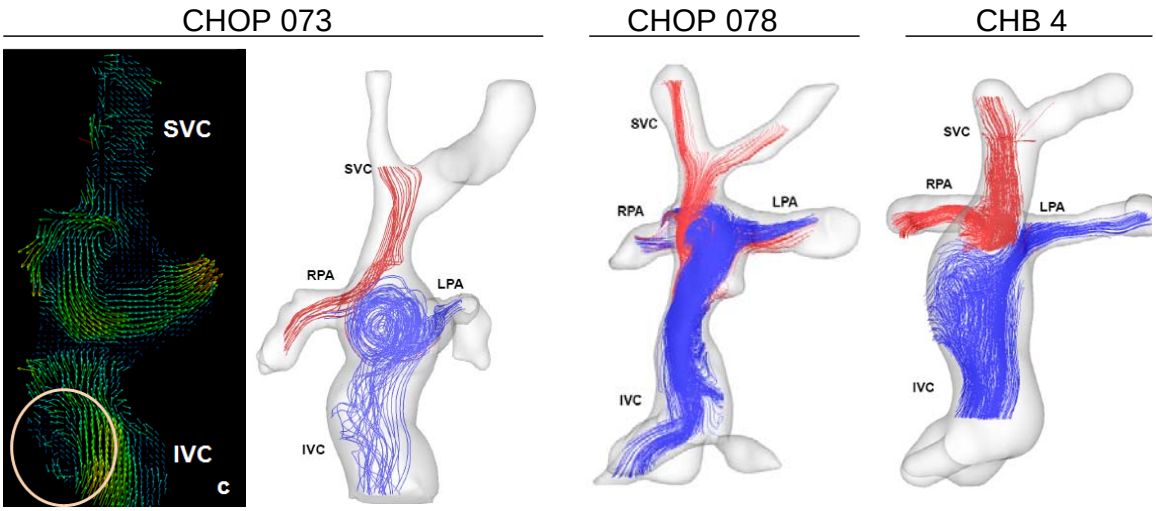

Figure 10-6: Intra-atrial flow structures as reconstructed from 3D PC MRI for three patients in the Georgia Tech Fontan database. (Image courtesy [80])

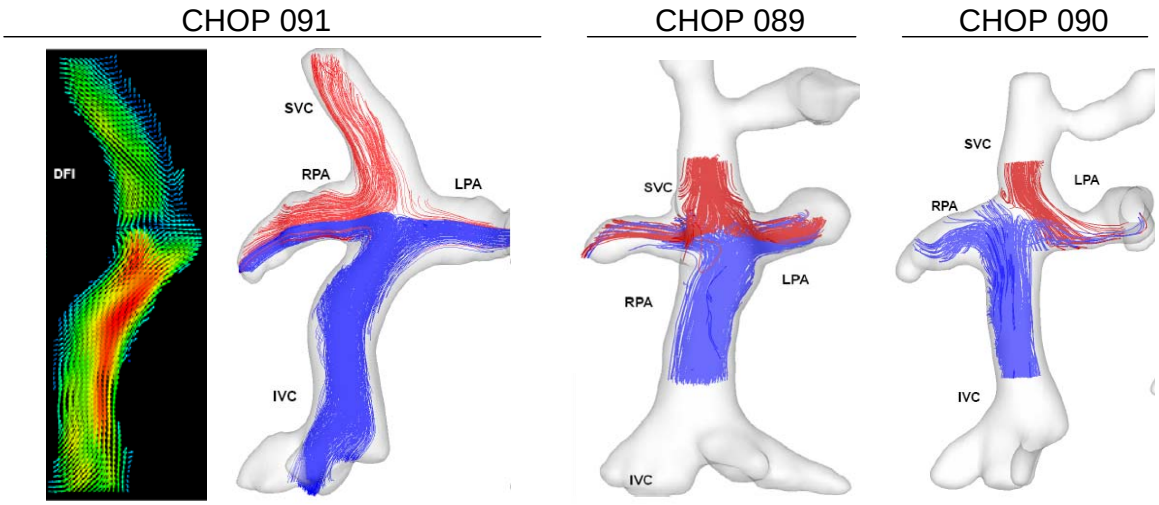

Figure 10-7: Extra-cardiac flow structures reconstructed from 3D PC MRI for three patients in the Georgia Tech Fontan database. (Image courtesy [80])

10.2.4.2 Lessons Learnt from the Intra-Atrial vs. Extra-Cardiac Comparison

Comparing the results across patients, the connection type had little impact on the reported power losses, which mostly depended upon the vessel cross-sectional areas, the strongest determinant being the minimum PA cross-sectional areas. For the Langangian metrics, on the other hand, the intra-atrial anatomy was found to favor both 1) IVC-SVC mixing at the center of the connection, due to the bulgier shape of the intra-atrial baffle compared to extra-cardiac grafts, and 2) long particle residence times, due to local irregularities in the baffle geometry. While the former point might be desirable as a mean to ensure a more balanced HFD, the latter might on the opposite be detrimental as longer particle residence times will in turn favor cell-to-cell contacts, which might yield higher thromboembolic risks.

Comparing the results across patients, the reported power losses mostly depended upon the vessel cross-sectional areas, the strongest determinant being the minimum PA

cross-sectional areas. In comparison, other geometrical parameters (intra-atrial vs. extra-cardiac, caval offset, vessel flaring or vessel curvature) only had a second order effect on the reported power loses, but had a stronger impact on the hepatic flow distribution. The primary course of action to minimize the workload imposed on the single ventricle is thus to prevent any local vessel constriction and dilate any existing pulmonary stenosis, while the other geometrical parameters might be better optimized with respect to hepatic flow distribution.

In Figure 10-7, CHOP 090 favors the IVC flow distribution to the RPA due to a right-sided caval offset, while in absence of caval offset CHOP 091 favors the IVC flow distribution towards the LPA due to the baffle curvature. Similarly, in the idealized and *in vivo* extra-cardiac connection, the IVC flow went in priority to the closest PA and only the remaining flow went to the contra-lateral lung. While this situation might be acceptable when the IVC accounts for the majority of the systemic venous return, it will become problematic if the IVC or hepatic flow rate is significantly lower than that of the SVC, such as in patients with an interrupted IVC, for example.

The intra-atrial anatomy was found to provide an advantage in that regard, as the bulgy intra-atrial baffle favored IVC-SVC mixing at the center of the connection, providing a mean to more evenly distribute hepatic flow to the two lungs. In counterpart the local irregularities and sudden changes in the baffle cross-sectional area yielded small recirculation regions where particles got entrapped, resulting in extended particle residence times in the intra-atrial anatomy compared to the extra-cardiac ones. Accordingly, while a bulgy connection area might be desirable as a mean to ensure a more balanced hepatic flow distribution, sudden geometrical changes might on the

opposite be detrimental as longer particle residence times will in turn favor cell-to-cell contacts, which might yield higher thromboembolic risks.

An interesting direction to explore might thus be to try and optimize the shape of the central connection area, in such a way that the IVC and SVC flows would thoroughly mix at the center of the connection, but that all regions of the connection would be properly washed out. Intra-atrial TCPCs building upon a hemi-Fontan procedure in the second stage, as in all the intra-atrial geometries shown in Chapter 7 and in Figure 10-6, could achieve that purpose provided intra-atrial tunnels offered sufficient control over the wall geometry to avoid local irregularities. The solution could thus potentially reside in designing an artificial graft that would reproduce the features of these hemi-Fontan plus intra-atrial connections, including the bulgy connection area, little to no IVC curvature nor left-right caval offset, and the anterior posterior offset between the vanae cavae and pulmonary arteries.

10.2.4.3 Impact of Flow Pulsatility

Across the different cases considered, flow pulsatility was found to enhance the levels of flow unsteadiness observed under non-pulsatile conditions; yield higher mean power losses than the predicted non-pulsatile value; and, in cases where IVC-SVC mixing was already observed under non-pulsatile conditions, improve the hepatic flow distribution by further enhancing the natural flow unsteadiness and mixing. The impact of pulsatility on the particle residence times mostly depended 1) the level of pulsatility, reflected by the pulsatility index, and 2) on the characteristic propagation time, T*, relative to the cardiac cycle duration, T, which might be expressed as a function of α^2/Re.

T*/T ratios below ½, as in the idealized TCPC, led to a larger spread in the recorded residence times, with faster particle propagations during the forward flow phase and longer ones during the backward flow phase.

This being said, the differences between the non-pulsatile performances and the mean pulsatile values remained very slight for the idealized TCPC, Patient 1 and Patient 2, all of which had a maximum pulsatility index lower than 80%. A drastically different situation was encountered for Patient 3, who featured a hepatic pulsatility index of 361%, and hepatic flow reversal for about half of the cardiac cycle. Pulsatile losses for that patient were more than twice the predicted non-pulsatile value; the amount of flow unsteadiness and mixing in the hepatic baffle under pulsatile conditions had no common measure with their non pulsatile counterpart; and, due to the increased HepV-SVC mixing, the pulsatile residence times were significantly shorter than under non-pulsatile conditions.

Implications for Patient-Specific Modeling: Based on the data presented in this thesis, the non-pulsatile assumption appears to predict the actual pulsatile efficiency metrics with a reasonable accuracy for lower pulsatility levels (below 80%), but there clearly is a threshold above which the non-pulsatile predictions no longer correlate to the actual *in vivo* measures. The definition of the exact threshold above which the non-pulsatile assumption fails would require a larger number of cases, progressively varying 1) the pulsatility index in each one of the vessels, 2) the phase shift between the superior and inferior waveforms, and 3) the TCPC geometry (mostly the IVC and SVC offsets, and the connection type) to assess the impact of flow pulsatility for varying degrees of IVC-SVC

interactions. Of particular interest might be the quantification of the impact of pulsatility indices around 100%, threshold over which the flow is reversed for part of the cardiac cycle, and which might thus be expected to yield significant differences.

It should also be noted that the high pulsatility levels in the hepatic baffle for Patient 3 might be a consequence of the adverse pressures and kinetic energy of the SVC flow. In such case, it might interesting to couple the CFD results with a lumped parameter model, to try and determine the configuration that would minimize the SVC and HepV interactions and potentially avoid hepatic flow reversal.

Finally, it should be re-emphasized that the efficiency metrics considered herein focused on time-averaged quantities, which are, by definition, more easily captured under mean non-pulsatile conditions than the dynamic ranges that pulsatile pressures, shear stresses or power losses may cover over a cardiac cycle. If capturing the maximum pulsatile power losses, for example, was of primary interest, this would obviously drastically lower the range of pulsatility indices for which the non-pulsatile assumption appears acceptable.

Clinical Implications: One argument that has been put forth in the long-standing debate over intra-atrial and extra-cardiac connections, is that intra-atrial TCPCs might yield higher pulsatility levels due to the contraction of the atrial wall. However, one question that arises from the results presented above is “Should pulsatility be favored, or is it actually detrimental to the TCPC efficiency?” This question is multi-faceted. On the one hand, pulsatility was observed to generally increase the mean power losses. Furthermore, pulsatile levels over 100% imply flow reversal in one of the vessels, and thus an

inefficient systemic venous return. On the other hand, pulsatility was also shown to increase mixing, especially in intra-atrial anatomies, which might help better distribute the hepatic flow to the two lungs; and the pulsatile energy bill was shown to be small compared to the baseline energy dissipation rate when the maximum pulsatility index was below 70-80%. In addition, some studies have suspected flow pulsatility in the PAs as a positive factor for PA development [184]. Accordingly, ensuring a certain level of pulsatility might indeed be beneficial, as long as it remains within reasonable bounds.

10.3 Patient Specific Surgical Planning

In the second arm of our study, we combined the accurate and versatile CFD solver developed as part of our first specific aim with the virtual-surgery interface developed by Rossignac et al. [101], thereby allowing surgeons to first interactively visualize the patient's anatomy prior the surgery, virtually perform multiple different surgical options within the virtual-surgery environment, and finally compare their hemodynamic efficiency so as to identify the best suited surgical approach on a patients-specific basis. Application and benefits of such an integrated surgical planning are demonstrated in Chapter 9, focusing on single-ventricle patients featuring an interrupted IVC with azygous continuation, who represent a particularly challenging clinical scenario. The two main optimization metrics were to minimize power losses, and evenly distribute blood flow and hepatic nutrients to the left and right lung. As this subgroup of patients is especially prone to PAVMs, emphasis was set on identifying the surgical option that best distributed the cardiac output and the hepatic nutrients.

Over the course over this study, six patients were referred for the prospective surgical planning of a completion or redo of the final stage of the TCPC, i.e. to connect the hepatic veins to the pulmonary arteries. While such individualized investigation provides a direct benefit to the patient under consideration, its impact for the global patient community is more limited, as most clinical centers to date do not have access to patient-specific surgical planning interfaces. Accordingly in this discussion section, we concentrate our attention on reviewing the results obtained across all six patients, to draw general guidelines and identify cases for which individualized surgical planning remains the only recommendable approach.

As will be discussed in the subsequent paragraphs, the hepatic flow distribution (HFD) in patients with an interrupted IVC is highly sensitive to the configuration of the superior venous returns. Accordingly, the six patients enrolled in this study were separated into two groups: (i) single SVC patients who had a normal systemic venous return, and for whom SVC, inominate and azygous flows merged together in the Kawashima connection; and (ii) patients with a persistent left superior vena cava (LSVC), which resulted in two separated superior connections, one on the right with the SVC and one on the left with the LSVC, the azygous vein connecting to either one of the SVC or LSVC.

10.3.1 Optimizing Flow Distribution and HFD for Patients with a Single SVC

Comparing the options recommended for each one of the three single SVC patients leads to controversial conclusions. Using a Y-shaped Optiflo graft, for example,

was the best performing option for patient A2 both in terms of hepatic flow distribution and energy dissipation, but was also the worst performer for Patient A1, and could not even be attempted in Patient A3 due to spatial constraints imposed by the surrounding organs. Similarly, the best option for Patient A3, namely an intra-atrial connection with no-offset compared to the SVC axis, was actually not recommended for the other two patients because the HFD in Patients A1 and A2 showed too sensitive to even slight variations in connection angle and offset.

10.3.1.1 Idealized Analysis

The common denominator behind all of these observations is the fact that due to the low hepatic flow rate compared to the sum of the superior venous returns, the optimal solution for a given patient is in large part dictated by the orientation and flow rates of the combined SVC, IV and AZ vessels. This can be better understood by looking at Figure 10-8, where we compare, in highly idealized TCPCs, the impact of a large right-sided offset on the IVC of a patient with a normal systemic venous return and the hepatic distribution of a patient with an interrupted IVC. For both cases, the cardiac output (CO) is assumed to be 4 L/min with a 50/50 RPA/LPA global flow distribution. The IVC flow rate is set to 60% CO, which is representative of the *in vivo* caval flow distributions for patients older than 6 or 7 years of age, and the HepV flow rate to 20% CO as a representative example of what was observed in our surgical planning studies.

Even with an offset such that the IVC and SVC do not have any direct interaction, the IVC flow would still split between the LPA and RPA would it only be to ensure global mass conservation. Under the conditions described, the IVC is expected to contribute 0.4 L/min to the RPA flow rate, leading to an HFD of 17%, which would

increase linearly with any increase in RPA mass flow split. In the interrupted IVC case, on the other hand, the HepV only contributes 0.8 L/min, such that all hepatic flow will go to the RPA unless the RPA flow rate falls below 0.8 L/min. A balanced 50/50 HFD would correspond to the scenario where the RPA flow rate is only 0.4 L/min, which would be an unacceptably unbalanced global flow distribution and would most likely be associated with severe left-sided PAVMs. This analysis explains the failure of all options with even a slight offset towards the RPA or LPA.

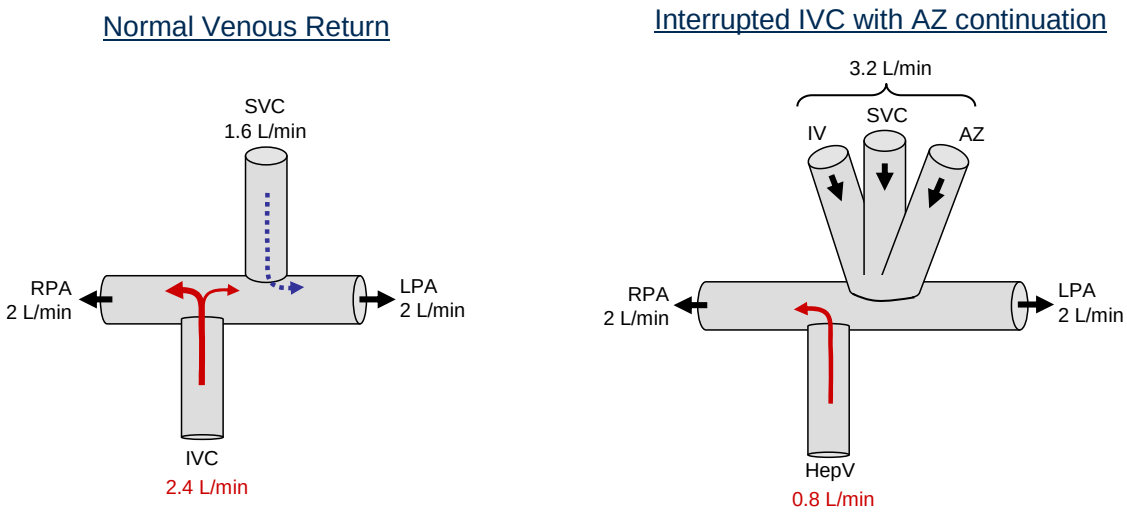

Figure 10-8: Idealized representation of the impact of a right-sided offset on the IVC flow distribution of a patient with a normal venous return and the hepatic flow distribution of a patient with an interrupted IVC. In both cases, the cardiac output is assumed to be 4 L/min with a 50/50 RPA/LPA global flow distribution. The IVC and hepatic flow rates were set at 60% CO and 20% CO, respectively, as representative examples of what is seen *in vivo*.

A potential alternative could be to avoid any caval offset. As illustrated in Figure 10-9 with similar idealized representations as in Figure 10-8, such approach might work for normal systemic venous returns leading to a head on collision between the IVC and

SVC flows and forcing both inflows to split towards the LPA and RPA. However, as was highlighted in the pulsatile investigation, a small deviation from the zero-offset configuration may lead to a preferential IVC distribution to one of the lungs, even with a normal venous return. This sensitivity is amplified in patients with an interrupted IVC due to the low HepV flow rate, which leads to a low kinetic energy and effectively prevents the HepV to compete with the superior inflows. As a result, if the superior inflows have a preferential direction towards one lung, then the path of least resistance for the HepV flow will be to flow to the other lung. Furthermore, any flaring or enlargement of the hepatic baffle towards the connection site will allow the high energy superior inflows to engulf into the hepatic baffle, further constraining the hepatic flow towards one side.

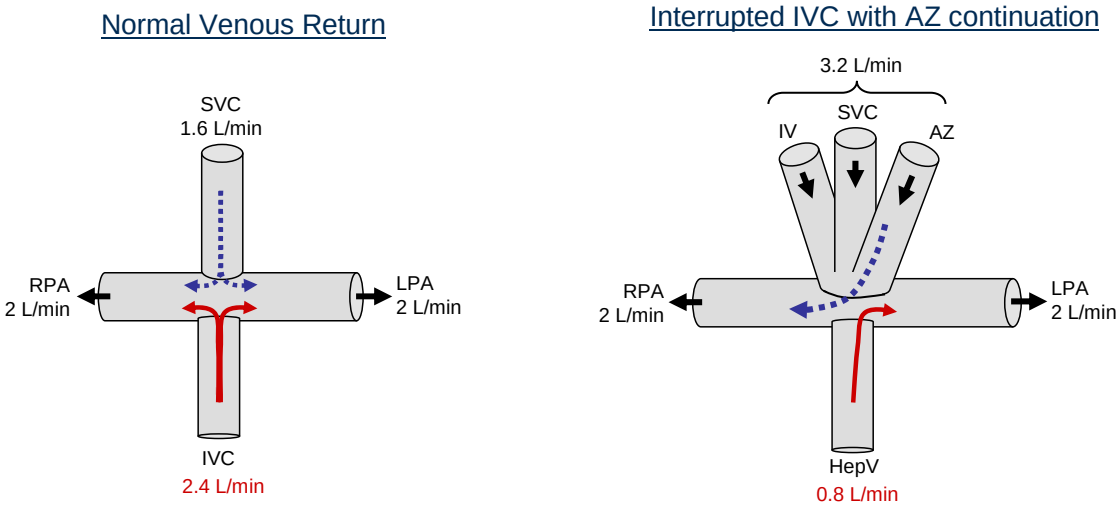

Figure 10-9: Idealized representation of the absence of any caval offset on the IVC or hepatic flow distribution for a patient with a normal venous return and a patient with an interrupted IVC. In both cases, the cardiac output is assumed to be 4 L/min with a 50/50 RPA/LPA global flow distribution. The IVC and hepatic flow rates were set to 60% CO and 20% CO, respectively, as representative examples of what is seen *in vivo*.

10.3.1.2 Application to the Understanding of HFD Behavior In Vivo

The simplified analysis conducted above sheds light onto the different performances observed for the same option in different patients. To better illustrate our point, Figure 10-10 and Figure 10-11 review the hepatic flow distribution in view of the superior inflow directions and resultant splitting point across selected options for Patients A1 and A2. As can be observed by comparing the pre-operative anatomy to Option 1 for Patient A1 (Figure 10-10) or the pre-operative anatomy and Options 1 through3 for Patient A2 (Figure 10-11), it is not so much the location of the hepatic baffle with respect to the geometrical center of the Kawashima connection that matters, than its position with respect to the splitting point imposed by the superior inflow directions.

This observation did not only apply to the classic intra-atrial or extra-cardiac approaches, but also to the Y-shaped Optiflo grafts. Failure of the Optiflo option (option 2) for Patient A1 stemmed from the fact that the left branch did not reach far enough to the LPA and offered a large opening area to the SVC. As a result, similarly to what was seen in the pre-operative anatomy, the SVC penetrated into the left hepatic branch constraining the flow to the RPA. For Patient A2 on the other hand the left and right branch of the Y-graft fell on either side of the splitting point, allowing the hepatic flow to flow freely through either one of the branches. The success of the intra-atrial option with no caval offset for Patient A3 stemmed from the fact that the hepatic flow accounted for 30% CO, which was significantly larger than in Patients A1 and A2, and allowed the HepV flow to sustain the collision with the superior inflows. In addition, the superior inflows entered the connection with no strong preferential direction, thus allowing the combined superior and hepatic flows to split in equal amounts towards the two lungs.

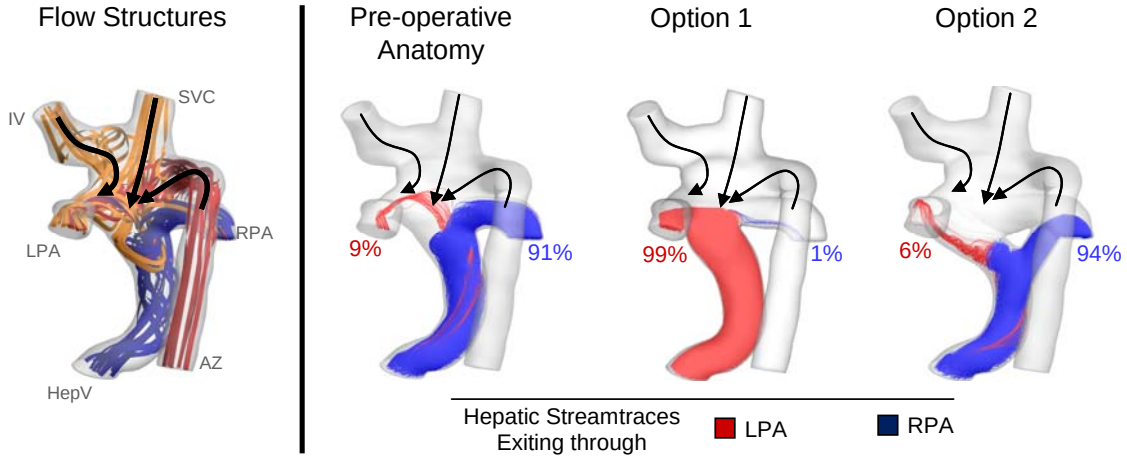

Figure 10-10: Comparison of the hepatic flow distribution to the flow splitting point imposed by the superior inflows for Patient A1 under the pre-operative flow conditions. The superior inflow directions are schematized based on the global flow structures displayed in the left panel for the pre-operative anatomy and reported onto the options shown in the right panel.

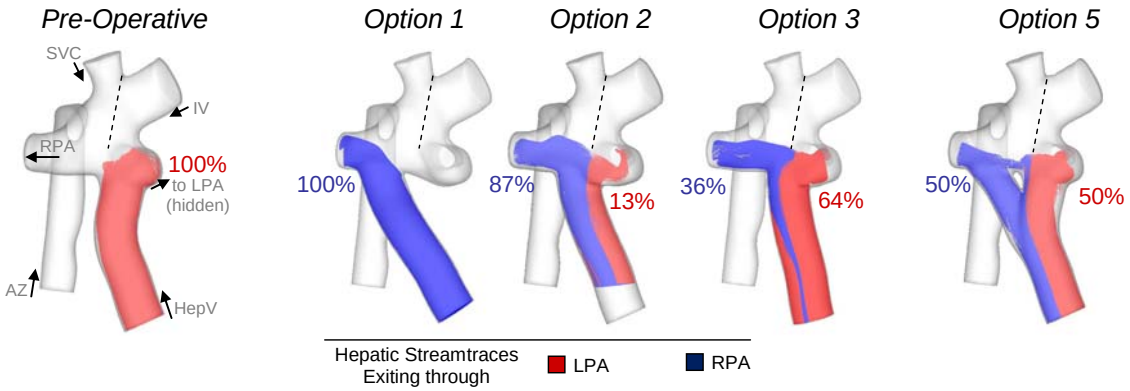

Figure 10-11: Comparison of the hepatic flow distribution to the flow splitting point imposed by the superior inflows for Patient A2 under a 50/50 RPA/LPA global flow distribution. The dotted line represents the location of the flow splitting point in Option 2, which is reported in the other options for comparison.

Finally, for all three patients, re-routing the hepatic flow into the azygous vein resulted in hepatic flow distribution that closely followed the global flow distribution due to a thorough mixing of all inflows at the center of Kawashima connection (Figure 10-12). On the other hand, this option was also consistently associated with the highest power losses of all tested options, approximately doubling the TCPC energy expenditure for the three patients considered.

	Patient A1	**Patient A2**	**Patient A3**
GFD_{RPA}	**28%**	**50%**	**51%**
HFD_{RPA}	32%	47%	64%

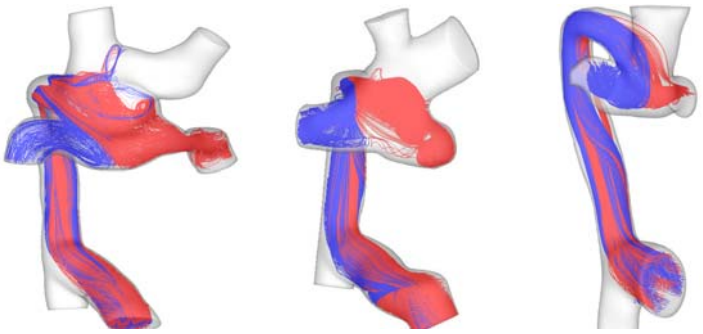

Figure 10-12: HepV-to-AZ connection for the three single SVC patients and the associated global and hepatic flow distributions to the RPA (GFD_{RPA} and HFD_{RPA}, respectively)

10.3.1.3 Summary

In summary, for patients with an interrupted IVC and a single SVC, the optimal TCPC configuration not only depends on the geometrical considerations (such as offset, flaring or curvature), but also on the superior/inferior flow ratios and flow directions, making it especially challenging for surgeons to identify the best suited approach based on anatomical considerations alone. This is a typical scenario where virtual surgical

planning may help, allowing for the optimal TCPC to be designed on a patient-by-patient basis. In lieu of a better option or individualized surgical planning, re-routing the hepatic flow into the azygous vein may be the recommended approach, as it ensures proper hepatic flow distribution for all three patient considered via a thorough blood mixing. However, this option also comes at high energy expenses, such that more efficient alternatives should be pursued whenever possible.

10.3.2 HFD Optimization for Patients with a Persistent LSVC

Similarly, to what was seen with single SVC patients, patients with a persistent LSVC demonstrated a high sensitivity to the caval offset, due to the inability of the low energy hepatic flow rate to compete against the superior venous return. However, thanks to the separation of the left and right superior inflows, this second group of patients presented a somewhat simpler scenario to handle than single SVC patients, and more systematic guidelines can be extracted from the results displayed.

10.3.2.1 Idealized Analysis

To better understand the HFD behaviors observed across our patient pool, let us first frame an idealized scenario, based upon the geometrical configuration depicted in Figure 10-13. In absence of flow collision and mixing, the venous returns will tend flow towards the path of least resistance, which can be accounted for by modeling the hydrodynamic resistance of each vascular segment, but can also be well understood based on global flow conservation considerations.

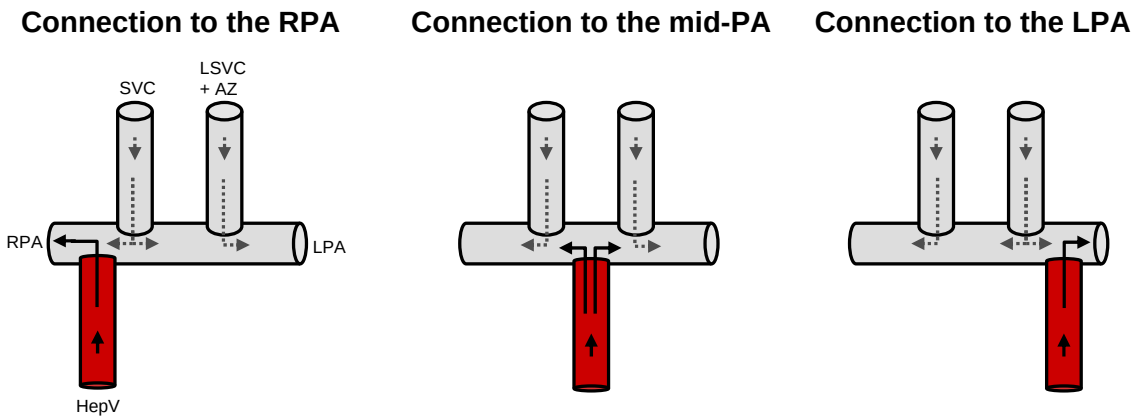

Figure 10-13: Idealized representation of the impact of various HepV offset locations on HFD distribution for a patient with an interrupted IVC and persistent LSVC.

In the case of a hepatic baffle connected to the RPA for example (left panel in Figure 10-13), all hepatic blood flow will be directed to the RPA unless the RPA flow rate drops below the hepatic one. In the later scenario, the hepatic flow would split between the right and left branches, supplying all blood flow to the RPA while the rest would flow to the LPA. HFD_{RPA} for such an option would thus be governed by the following equation:

$$HFD_{RPA} = \begin{cases} \dfrac{Q_{RPA}}{Q_{HepV}} & if\ Q_{RPA} < Q_{HepV} \\ 100\% & otherwise \end{cases} \tag{10-7}$$

where Q_{HepV} and Q_{RPA}, are the hepatic and RPA flow rates, respectively. Symmetrically, in the case of a left-sided offset, HFD_{RPA} would be governed by:

$$HFD_{RPA} = \begin{cases} 0\% & if\ Q_{RPA} < \left(Q_{SVC} + Q_{LSVC} + Q_{AZ}\right) \\ 100\% - \dfrac{Q_{LPA}}{Q_{HepV}} & otherwise \end{cases} \tag{10-8}$$

While in patients with a single SVC, the determination of the zero-offset position revealed very challenging, the separation of the left and right systemic venous returns

offers a potential solution allowing the hepatic baffle to be placed on the mid-PA, in between the SVC and LSVC. For the idealized configuration depicted in Figure 10-13 (b), we may assume that, as long as the SVC suffices to provide the desired RPA flow rate (i.e. $Q_{RPA} < Q_{SVC}$), all hepatic flow goes to the LPA. If the RPA demand exceeds what can be provided by the SVC alone, the hepatic flow splits between the right and left branch, until the point where Q_{RPA} exceeds the contribution of the hepatic and SVC flows combined and all hepatic flow goes to the RPA. The idealized HFD_{RPA} for a connection to the mid-PA reads as:

$$HFD_{RPA} = \begin{cases} 0\% & if\ Q_{RPA} \le Q_{SVC} \\ \dfrac{Q_{RPA} - Q_{SVC}}{Q_{HepV}} & if\ Q_{SVC} \le Q_{RPA} \le \left(Q_{SVC} + Q_{HepV}\right) \\ 100\% & if\ \left(Q_{SVC} + Q_{HepV}\right) \le Q_{RPA} \end{cases} \tag{10-9}$$

Although based on very simple mass conservation principles, the idealized framework derived above provides an excellent description of what was seen for the patients enrolled in our surgical planning study. This is illustrated in Figure 10-14 where we compare the HFD_{RPA} patterns predicted using Equations 9-7 to 9-9 to the ones obtained from the CFD simulations for Patient B3, observing a remarkable agreement between the two approaches for the ½ diameter offset to the RPA case and the central connection to the mid-PA.

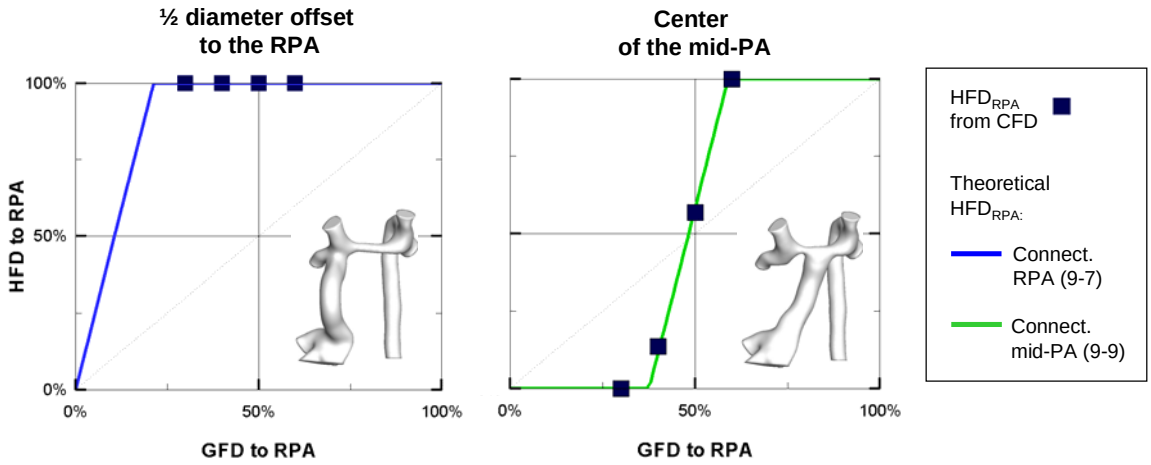

Figure 10-14: Comparison of the hepatic flow distributions predicted from the idealized Equations 9-7 to 9-9 to the values computed from CFD a right-sided and mid-PA options for Patient B3 (Options 2 and 7 in Chapter 9, Section 9.3.3)

10.3.2.2 Extraction of the General HFD Behaviors in Patients with Persistent LSVC

The strengths of our idealized framework are that it very well captures the general trends observed across our patient cohort, without the underlying patient-to-patient variations, thereby allowing for a fast understanding of the driving mechanisms behind the hepatic flow distribution in patients with a persistent LSVC.

RPA/LPA Offset and HepV-to-AZ shunts: From the Equations 9-7 and 9-8, it may be seen that offsetting the hepatic baffle towards the RPA will yield a balanced HFD_{RPA}=50% when $Q_{RPA} = 0.5Q_{HepV}$, and symmetrically that an offset towards the LPA would yield a balanced HFD for $Q_{LPA} = 0.5Q_{HepV}$. Given the fact that, in patients with an interrupted IVC, only 20% CO enters the connection through the hepatic baffle, these equations imply that an offset towards either one of the PAs will result in PAVMs in the contra-lateral lung. While apparently trivial, this result is of importance since extra-

cardiac hepatic conduits typically reach the SVC with a slight offset towards the RPA, which results in a complete unilateral distribution of the hepatic flow to the RPA, as shown in Figure 10-14. HepV-to-AZ connections are also highly not recommended for patients with a persistent LSVC, as they result in a unilateral HFD to the PA closest to the azygous vein connection very much similar in their effect to an LPA or RPA offset (see Figure 10-15).

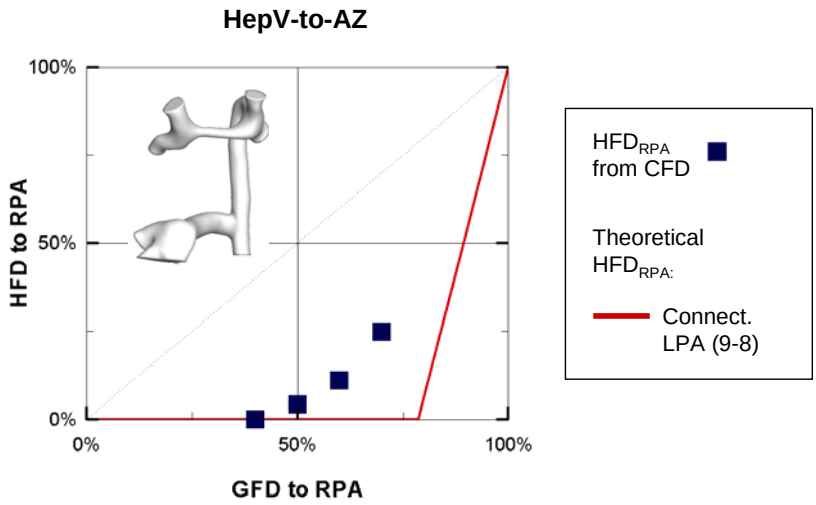

Figure 10-15: HFD performance of an HepV-to-AZ connection for Patient B1 (symbols), compared to the effect of a left sided offset as predicted by Equation 9-8.

Mid-PA Connections: The best options for Patients B1 and B3 were to connect the hepatic baffle to the mid-PA segment. The associated HFD behavior is displayed in the right panel of Figure 10-14 for Patient B3. As described for the idealized mid-PA connection, this configuration resulted in the all of the hepatic flow going to the RPA, if the LSVC+AZ flows sufficed to meet the demand of the LPA, and all to the LPA if the

RPA flow rate was below that of the SVC. For RPA/LPA flow splits falling in between those two extremes, it was the hepatic flow that adjusted its distribution to meet the LPA and RPA demands. However, this approach failed to provide satisfactory results for Patient B2. This can readily be understood by looking at the distribution of the superior venous returns for Patients B1 and B3 and contrasting them to the ones observed in Patient B2.

For Patient B1, the SVC contributed 33% CO while the LSVC and AZ flows combined accounted for 43%. As a result, the mid-PA options reached a balanced HFD of 50/50 for a global flow distribution of 45/55 RPA/LPA, which was an almost ideal configuration. Results were even better for Patient B3 (Figure 10-14), for whom the SVC and LSVC+AZ flows contributed almost equally to the systemic venous return (accounting for 38% and 41% CO, respectively), which yielded a balanced HFD for a close to perfectly balanced global flow distribution of 48.5/51.5 RPA/LPA. For patient B2 on the other hand, the LSVC flow only accounted for 19% CO while the right-sided superior venous returns (here the AZ and SVC) carried 71% of the total venous return. The resultant 50/50 HFD as predicted by Equation 9-9 would be associated with a global flow distribution of 76/24 RPA/LPA. In effect, all attempts to concurrently balance HFD and global flow distribution with a centrally connected baffle failed for that patient.

Accordingly, while mid-PA connections appear as a simple and efficient approach for patients with persistent LSVC, the in vivo flow rates should be taken into considerations prior to any implementation. In cases with highly unbalanced left and right superior venous returns, such as Patient B2, the mid-PA options should be avoided and other options should be pursued.

Sensitivity of the mid-PA connections to the hepatic baffle design and exact anastomosis location: Similarly to what was seen for single SVC patients, even a small offset variation in the surroundings of the SVC lead to a drastic shift in the HFD behavior due to the low momentum of the hepatic flow, leading from a highly preferential flow distribution to the RPA when the hepatic baffle was even slightly offset towards the right (Figure 10-14_left), to a centered HFD_{RPA} when the baffle was connected with a slight offset to the mid-PA (Figure 10-16_top left). On the other hand, provided that the hepatic baffle was placed between the SVC and LSVC (Figure 10-16), its exact position along the mid-PA segment has little impact on the overall HFD performance. Nor do the type of baffle used, angle at the connection site, vessel flaring or baffle curvature. When the hepatic baffle is connected less than ½ diameter away from the SVC (top left panel in Figure 10-16), the computed HFD_{RPA} slightly departs from the theoretical line for lower GFD_{RPA} values, reflecting some amount of mixing and interaction between the hepatic and SVC flows. Symmetrically, when the baffle is connected less than ½ diameter away from the LSVC (top right panel in Figure 10-16), the computed HFD_{RPA} values depart from the theoretical line for higher GFD_{RPA} values, due to HepV-LSVC flow interactions. However, these variations remain small overall, and all mid-PA options could be used to the same effect.

This observation is invaluable from a surgical standpoint as it implies that even small offsets may suffice to achieve the desired performance, thus rendering these options feasible even in patients where the overriding aorta significantly restricts the access to the mid-PA segment.

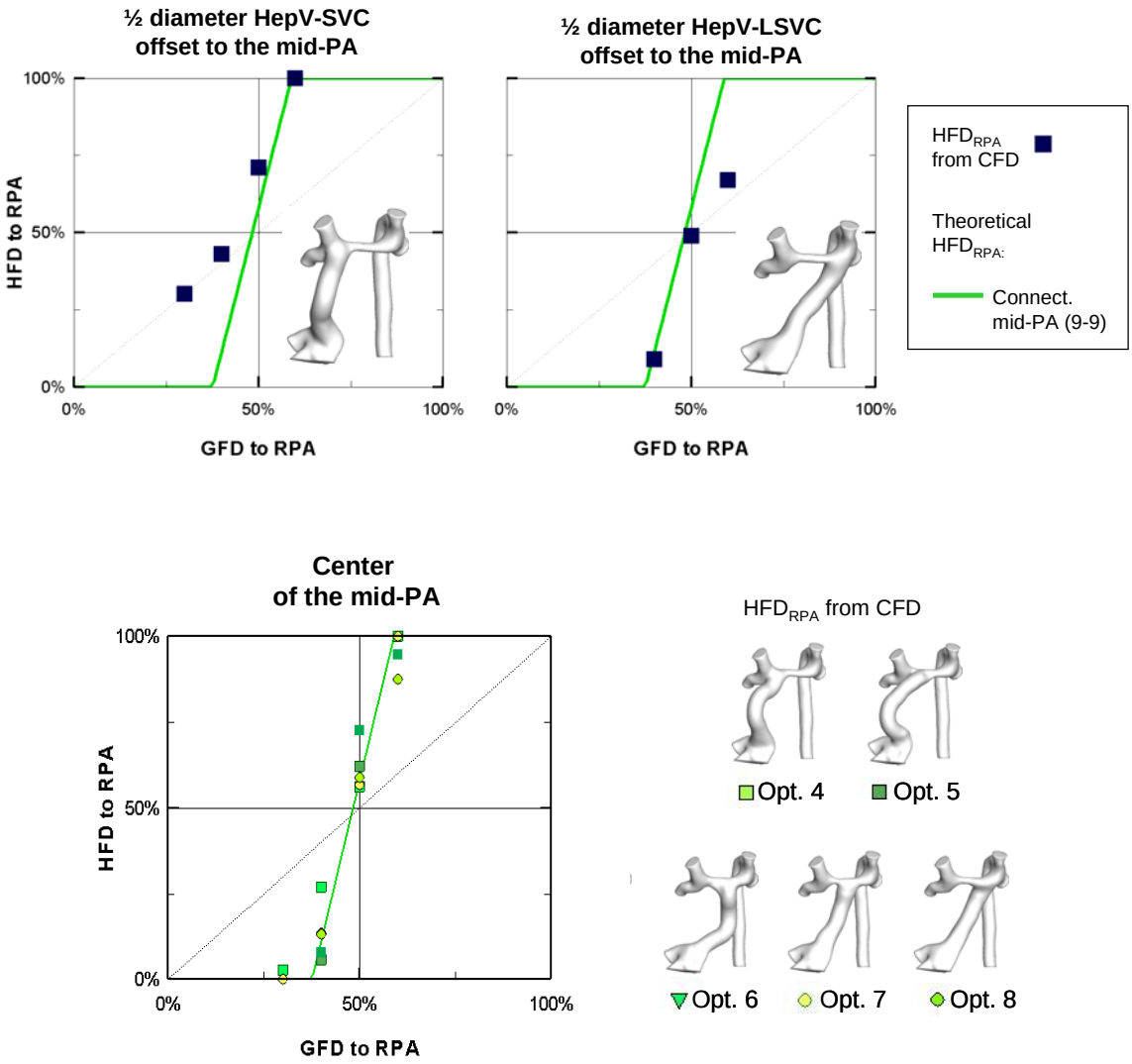

Figure 10-16: Sensitivity of the mid-PA connections to the hepatic baffle design and exact anastomosis location along the mid-PA segment (illustrated with for Patient B3)

Sensitivity of the mid-PA connections to the LPA/RPA flow distribution: The range of RPA/LPA flow ratios over which both lungs receive at least part of the hepatic flow (i.e. 0%<HFD_{RPA}<100%) is directly related to the contribution of the hepatic flow rate to the systemic venous return. For Patient B3 (Figure 10-16), for example, this transition range spanned from GFD_{RPA} = 33% to GFD_{RPA} = 57%, and ensured that both lungs received at least 20% of the hepatic flow rate for global flow distributions ranging between 38/62 and 52/48 RPA/LPA. This transition range will be drastically reduced for patients with a low hepatic flow rate, such as Patient B3 for whom Q_{HepV} only accounted for 10% CO. Such low relative hepatic flow rate will result in the hepatic flow transitioning from the LPA to the RPA over a very narrow range of RPA/LPA flow ratios, providing a very low tolerance to transient or permanent changes in pulmonary vascular resistances.

Decreasing the sensitivity to the RPA/LPA ratio, AZ-to-HepV shunts: While a low hepatic flow rate cannot be increased, combining the azygous and hepatic flows, for example, could achieve the same purpose. Assuming complete mixing of the AZ and HepV streams and a mid-PA connection, the corresponding idealized HFD distribution would read as:

$$HFD_{RPA} = \begin{cases} 0\% & if\ Q_{RPA} \le Q_{SVC} \\ \dfrac{Q_{RPA} - Q_{SVC}}{Q_{HepV} + Q_{AZ}} & if\ Q_{SVC} \le Q_{RPA} \le \left(Q_{SVC} + Q_{HepV} + Q_{AZ}\right) \\ 100\% & if\ \left(Q_{SVC} + Q_{HepV} + Q_{AZ}\right) \le Q_{RPA} \end{cases} \qquad (10\text{-}10)$$

Equation 9-10 is equivalent of Equation 9-9, with the only difference that the hepatic flow distribution is proportional to the distribution of the combined $Q_{HepV} + Q_{AZ}$ instead of Q_{HepV} alone.

The impact of redirecting the azygous flow into a centrally connected hepatic baffle is illustrated in Figure 10-17 for Patient B1. First, it might be noted that the theoretical HFD_{RPA} behavior given by Equation 9-10 falls in close agreement with the actual CFD measurement for that option. Similarly to the earlier mid-PA cases, this agreement is due to the low level of interaction between the different inflows, which to a scenario very similar to the idealized framework. The impact of combining azygous and hepatic flows can be visualized by comparing the orange and green lines in the figure. As the SVC is left untouched, both curves start to rise above 0% for the same GFD_{RPA} value of 33%. However, the addition of the azygous blood flow reduces rate of increase, since for every increase in RPA blood flow, both AZ and HepV flows adjust their distribution in favor of the RPA. As a result the range of GFDRPA values over which the hepatic flow switches from the left to the right increases from 33-54% with the hepatic flow alone to 33-78% with the combined azygous and hepatic flows.

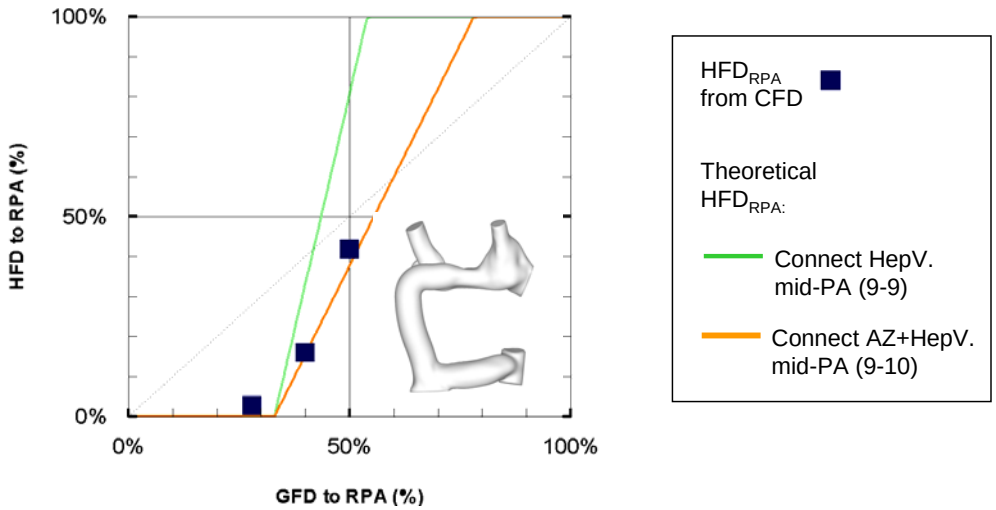

Figure 10-17: Impact of combining azygous and hepatic flows into a centrally connected baffle for Patient B1. The orange line depicts the HFD_{RPA} behavior prediceted under idealized conditions (Equation 9-10), while the green line shows the prediction for the same hepatic baffle design but without the addition of the azygous flow (Equation 9-9).

While the addition of an AZ-to-HepV shunt may not be necessary for patients such as Patients B1 or B3 for whom the hepatic blood flow contributed more than 20% to the systemic venous return, it may be a well suited or even necessary approach for patients with low hepatic flow rates. Indeed, a significant problem for Patient B2 stemmed from the fact that the hepatic flow rate was so low that the superior venous returns engulfed deep down into the baffle, creating large regions of flow disturbances and blocking the hepatic flow path. The addition of the azygous flow resolved that part of the problem, providing sufficient kinetic energy to the combined azygous and hepatic streams to avoid penetration of the SVC or LSVC into the baffle. Furthermore in cases such as patient B2, where the SVC+AZ flows accounted for a significantly larger amount of the systemic venous return compared to the lone LSVC, redirecting the azygous flow to the hepatic baffle might also be a way to re-establish a better balance between the left and right superior venous returns.

Alternate Options, Splitting the hepatic conduit in two branches: The last set of options that was attempted was to split the hepatic flow into a right and left branch using either a Y-shaped graft or an H-connection, with an HepV-to-AZ shunt on one side and a hepatic baffle on the other, which was designed with a voluntary offset away towards the closest PA. For Patients B1 and B3, these options were very similar in their HFD behavior to a centrally connected hepatic baffle, without marked advantage over the former options. The scenarios were these options might be the best suited is when the SVC and LSVC fall too close to one another for a mid-PA segment to clearly defined. In those cases, a Y-shaped graft or H-connection circumvents the problem of identifying

where the LSVC anastomosis ends and where SVC begins. Patient B2 was a good example of such situation and the best suited option for that patient was to either use an H-connection or an AZ-to-HepV shunt merging into a Y-shaped hepatic graft.

10.3.2.3 Summary

In summary, for patients with almost equal right and left superior venous returns, and a well defined mid-PA segment, the simplest and most efficient approach was to connect the hepatic baffle to the mid-PA segment. This option provides the added advantages of a low sensitivity as to the exact surgical implementation, allowing room for error and adaptation to unexpected constraints. For patients, with an identifiable mid-PA but either low hepatic flow rate or highly unbalanced right and left superior venous returns, combination of the hepatic and azygous flows might be an adequate solution. The simple set of equations presented herein provides a rough, yet efficient mean to assess whether a mid-PA connection would perform well or if the addition of an AZ-toHepV shunt might be beneficial. Finally, for patients such patient B2, with an undefined mid-PA, unbalanced right and left superior inflows and low hepatic flow rate, individualized surgical planning remains the most recommendable approach.

10.3.3 Minimizing Power Losses

Across all six patients, power losses showed little dependency on parameters such as curvature, offset or the angle of connection. The strongest power loss determinants were the vessel dimensions and vessel flow rates. This is consistent with the observations of the pulsatile study, where the baseline TCPC power losses were found to scale as:

$$\varepsilon_0 \varepsilon_V = \rho \frac{CO^3}{A_{IN}{}^2} \cdot \sum \left(\frac{(Q_i/CO)^3}{(A_i/A_{IN})^2} \mathrm{Re}_i{}^{-0.25} \cdot \frac{L_i}{\sqrt{A_{IN}}} \right) \tag{10-11}$$

The clinical implication of this observation is that, first, power losses are a low discriminator in between different surgical options. With the exception of HepV-to-AZ shunts, emphasis may be thus set on hepatic flow distribution without having to compromise the energy efficiency. Next, forcing the hepatic flow into the azygous vein was associated with high power losses across all patients. This stems from the fact that the azygous is typically one of the smaller vessels, although carrying an important portion of the inferior venous return. Further increasing the flow rate through that vessel will increase the associated losses as follows:

$$\Delta PL \quad \propto \frac{(Q_{AZ} + Q_{HepV})^3}{A_{AZ}{}^2} - \left(\frac{Q_{AZ}{}^3}{A_{AZ}{}^2} + \frac{Q_{HepV}{}^3}{A_{HepV}{}^2} \right) \tag{10-12}$$

Even if we assumed the azygous vein to have the same cross-sectional area as the hepatic baffle, the increase in power losses, ΔPL, would scale as:

$$\Delta PL \quad \propto \frac{3Q_{AZ} \cdot Q_{HepV}(Q_{AZ} + Q_{HepV})}{A_{AZ}{}^2} \tag{10-13}$$

and an even larger increase might be expected for cases where the azygous vein is smaller than the hepatic baffle. Accordingly, this option should be avoided when other alternatives are feasible. Finally, local vessel constrictions or stenoses were a major factor for high power losses and pressure drops. A typical example of high pressure drops due to an LPA stenosis is provided by Patient A1, while Patient B3 provides a typical example of a narrow mid-PA segment. These local stenoses should be dilated at the time of surgery, allowing blood to flow freely to the two lungs. For the bilateral SVC patients,

mid-PA connections might offer the advantage of combining the TCPC completion and mid-PA stenosis dilation into one single intervention.

10.3.4 Conclusion of the Surgical Planning Investigation

In this section we presented the feasibility and potential benefits of an integrated surgical planning framework for the optimization of the TCPC design for patients with an interrupted IVC. These patients are especially at need for such virtual surgery environments as they present a large number of anatomical and venous return abnormalities that make the identification of the best-suited approach based on anatomical considerations alone difficult if not impossible. As a result, patients with interrupted IVC present an especially high incidence of PAVMs due to an inadequate design of the hepatic baffle. Our patient-specific investigations provided the operating surgeon with additional information as to what may be the better suited option. Taking this framework to the next stage would now require the acquisition of patient follow-up data to asses the accuracy of our post-operative projections/predictions, as well as to gain further insights into the relative importance of different optimization metrics. For single SVC patients in particular, HepV-to-AZ shunts were systematically among the best performers in terms of HFD but the worst in terms of energy efficiency. Weighing the importance of one parameter against the other would require long-term follow-up on a large patient pool to compare the parallel evolution of pulmonary and ventricular function, and the HFD and power loss metrics.

Finally, by reviewing the experience gained over the six patients enrolled in this study, some general recommendations may be extracted for patients with bilateral SVCs.

However, these recommendations are first based on a very small patient pool, and then only apply to a subset of patients, who feature a well defined mid-PA and relatively balanced left and right superior venous returns. For patients falling outside of this template, and for all single SVC patients, individualized surgical planning remains the best suited strategy.

CHAPTER 11

CONCLUSIONS

At the beginning of this research endeavor, it was hypothesized that a robust and thoroughly validated image-based numerical modeling framework would constitute a critical asset for the surgical treatment of patients with complex single-ventricle heart defects (SVHD), and in particular for the optimization of the total cavopulmonary connection (TCPC) procedure for the most complex and rare forms of SVHDs. Towards this end, the primary contributions of this thesis are three fold: a) the development of a novel unstructured immersed boundary approach for accurate and efficient numerical simulations in arbitrarily complex *in vivo* anatomies; b) the application of this numerical framework to probe the pulsatile *in vivo* TCPC hemodynamics and understand the impact of pulsatility on the predicted efficiency metrics; and c) the establishment of a novel surgical planning approach based on hemodynamic performance and the demonstration of its potential benefits to treat patients with complex SVHDs.

11.1 Numerical Approach

The current study presents a computational fluid dynamic (CFD) solver tailored to capture the geometric intricacies of *in vivo* cardiovascular structures and the inherent instabilities of the TCPC flows. The formulation retained uses a sharp interface immersed boundary approach [123, 164], which is recast into an unstructured Cartesian grid layout. This simple, yet powerful, approach combines the following advantages: 1) an easy

handling of arbitrarily complex *in vivo* anatomies; 2) the accuracy of Cartesian methods; and 3) a significant increase in computational efficiency and reduction in memory footprint, compared to classic structured Cartesian grid solvers for internal flow applications. The efficacy and accuracy of our method is demonstrated by applying it to conduct systematic mesh refinement studies for internal flow problems ranging in complexity from steady flow in a 90 degree curved pipe to highly unsteady flows in an actual, patient-specific anatomy reconstructed from magnetic resonance images (MRI), and comparing our results against experimental measurements obtained in a controlled *in vitro* environment.

Results from these validation simulations demonstrate the robustness and accuracy of our flow solver implementation, even for cases as complex as the reported *in vivo* intra-atrial anatomy, which featured complex dynamics and chaotic mixing. The complexity of the flow dynamics observed in the *in vivo* TCPC anatomies would it be in the validation section or later during the pulsatile or patient-specific surgical planning investigations re-emphasizes the need for high resolution simulations prior to drawing any clinical recommendations. This is of prime importance, especially in an era when image-guided computational modeling is attracting increasing attention as a tool for refining *in vivo* flow measurements or predicting the outcome of different surgical scenarios.

11.2 Investigation of the Pulsatile TCPC Hemodynamics

After validation, the unstructured immersed-boundary CFD solver was applied to probe the pulsatile TCPC hemodynamics. The objective of this study was two folds: 1)

compare the TCPC hemodynamics across different templates, including one intra-atrial TCPC, one extra-cardiac TCPC, and one patient with an abnormal systemic venous return and highly pulsatile hepatic flow; and 2) assess the error introduced when neglecting the pulsatility of the *in vivo* TCPC flows, depending on the level of pulsatility.

The motivation for the first aspect of this study was to further the understanding of the pros and cons of extra-cardiac and intra-atrial TCPC implementations. Comparing the results across patients, the connection type had little impact on the reported power losses, which mostly depended upon the vessel cross-sectional areas. On the other hand, the intra-atrial anatomy was found to favor both: (i) IVC-SVC mixing at the center of the connection, due to the bulgier geometry of an intra-atrial tunnel compared to an extra-cardiac graft; and (ii) long particle residence times due to local irregularities in the baffle geometry. While the former point might be beneficial as a means to ensure a more balanced hepatic flow distribution, the latter might on the opposite be detrimental as longer particle residence times will in turn favor cell-to-cell contacts, and increase the risk of thromboembolic events. A larger connection area as is seen in intra-atrial connections could thus be a desirable feature, but such designs should be carefully reviewed to avoid sudden variations in the baffle cross-sectional area, minimize regions of flow separation, and ultimately minimize the risks of thrombus formation.

With the constant refinement and increasing complexity of numerical tools available today, one pragmatic question that arises is where to set the trade-off between the added accuracy and the added computational cost. This question is of critical importance for surgical planning applications which typically require the investigation of a large number of options for a given patient, and are subjected to stringent time-

constraints in order to provide the results between the time of diagnosis and the time of surgery. Accordingly the second aspect of the pulsatile study sought to determine when pulsatility might be neglected in favor of faster simulations, while still predicting the TCPC efficiency with reasonable accuracy.

Across the different cases considered, flow pulsatility was found to yield higher mean power losses than the predicted non-pulsatile value; and, in cases where IVC-SVC mixing was already observed under non-pulsatile conditions, improve the hepatic flow distribution by further enhancing the natural flow unsteadiness and mixing. This being said, the differences between the non-pulsatile performances and the mean pulsatile values remained very slight for the three cases with moderate pulsatility levels (falling below 80%). On the other hand, the non-pulsatile assumption failed to capture even the mean flow characteristics and efficiency metrics for the patient with the highest pulsatility levels, which reached up to 361% in the hepatic veins. Pulsatile losses for that patient were more than twice the predicted non-pulsatile value; the amount of flow unsteadiness and mixing in the hepatic baffle under pulsatile conditions had no common measure with their non pulsatile counterpart; and, due to the increased HepV-SVC mixing, the pulsatile residence times were significantly shorter than under non-pulsatile conditions.

Although limited to a very small sample size, these results indicate that there is a threshold below which non-pulsatile simulations might provide satisfactory results, but above which pulsatility ought to be included in the numerical model for accurate clinical recommendations. The precise definition of this threshold, however, would require a

larger sample size, with a better characterization of pulsatility levels falling between our lower and higher values, namely between 80% and 360%.

11.3 Patient Specific Surgical Planning

Finally, in the last arm of our study, we combined our numerical framework with the virtual surgery interface developed by Pekkan and Rossignac [101] to conduct prospective surgical planning investigations for six failing Fontan patients with severe pulmonary artero-venous malformations (PAVMs). The palliative strategy for correction of PAVMs typically involves a Fontan revision where attempts are made to redirect the hepatic effluent to the affected lung. However, as the complexity of the underlying anatomy increases, the amount of control that can be exercised decreases. This difficulty is clearly illustrated in patients having an interrupted inferior vena cava with azygous continuation (such as the six patients enrolled in our study) who represent one of the most complex forms of single ventricle heart defects, and in whom the incidence of PAVMs can be as high as 21%[69].

Clearly, the wide variety of patient anatomies makes it difficult to design a general procedure that fits all patients, while the complexity of *in vivo* anatomies poses significant challenges to identify the surgical option that best distributes hepatic flow for a given patient. This thesis introduces a whole new paradigm for addressing this problem using an image-based surgical planning approach that can be used to optimize Fontan procedures on a patient-specific basis. Different virtual operation scenarios can be investigated for each patient, allowing clinicians to conduct a multi-factorial risk/benefit analysis (balancing power losses against hepatic flow distribution and ease of completion,

for example), and thereby empowering them with the option to select the best treatment for an individual patient, which may prove beneficial and cost effective to both the hospital and the patient in the long-term.

While such individualized investigation provides a direct benefit to the patient under consideration, its impact for the global patient community is more limited, as most clinical centers to date do not have access to patient-specific surgical planning interfaces. Taking advantage of the experience gained from the six patient-specific surgical planning studies, the final arm of this study provides general surgical guidelines for Fontan patients with an interrupted IVC, and identifies cases for which individualized surgical planning remains the only viable approach. A characteristic of patients with an interrupted IVC is that most of the lower systemic venous return reaches the SVC through the azygous vein, while the TCPC baffle only carries the hepatic blood flow, resulting in a low energy blood stream that cannot compete against the superior venous returns. Consequently, all six patients demonstrated a very high sensitivity to the location of the baffle anastomosis with respect to the superior venous returns.

The recommended approach depends on whether the patient has: 1) a normal superior venous return with a single superior vena cava (SVC); or 2) a persistent left superior vena (LSVC). For patients with an interrupted IVC and a single SVC, “classic” intra-atrial or extra-cardiac options are for the most part not recommended, as even a small offset with respect to the superior inflow directions leads to a complete shift in the observed hepatic flow distribution. Hepatic-to-azygous shunts, on the other hand, are systematically among the best performers in terms of hepatic flow distribution, leading to a vigorous mixing of all systemic venous returns in the Kawashima connection, and

thereby ensuring that the hepatic flow distributions closely followed the global flow distribution to the two lungs, as would be the case in a normal circulation. However, this design also systematically comes at higher energy expenses than any other option. Accordingly, while hepatic-to-azygous shunts might be considered as a good fall-back option for patients with a single SVC, other TCPC implementations should be pursued, whenever possible, to achieve similar hepatic flow distribution but at lower energy expenses.

For patients with a persistent LSVC, the separation of the left and right superior inflows provides a natural solution to the difficulty of identifying the optimal baffle anastomosis location. Connecting the hepatic baffle anywhere along the mid-PA segment is a simple yet extremely efficient approach, provided that the following conditions are met: (i) almost equal contribution of the left and right superior inflows to the total systemic venous return; (ii) high enough hepatic flow rate; and (iii) a well-defined mid-PA segment (i.e. clear separation between the SVC and LSVC anastomosis sites). Under those circumstances, the exact baffle design and anastomosis location along the mid-PA segment have little impact on the hepatic performance, allowing surgeons to freely adjust the TCPC design to the surrounding anatomical constraints. When the superior venous returns are highly biased towards the azygous side, or when the hepatic flow is too low, an alternate solution is to first re-route the azygous blood flow into the hepatic baffle, and then connect the baffle to the mid-PA segment. Patients for whom the two SVCs are connected close to one another present a more challenging configuration, lying in between the single and bilateral SVC scenarios, and are thus better addressed using an individualized surgical planning approach.

In conclusion, all these studies clearly demonstrate that hemodynamics play a significant role in the Fontan physiology. While optimizing hemodynamics based on anatomical considerations alone used to represent a challenge, the framework developed as part of this thesis now allows bioengineers and clinicians to envision multiple different surgical scenarios, quantify their hemodynamic performance and identify the better performing one. This presents a novel approach to better understand and treat rare forms of SVHDs, providing a framework to isolate the impact of different flow or geometric variations, which would otherwise not be possible due to too small a patient population. However, while this framework allows for the optimization of the TCPC design for better hemodynamics, the link between hemodynamics and long-term patient outcome still remains vague. The next critical step would thus be to conduct a large clinical study, correlating the hemodynamic patterns with parameters of clinical outcome, to better optimize the care and management of single ventricle patients.

CHAPTER 12

LIMITATIONS AND FUTURE DIRECTIONS

In this thesis, a novel unstructured immersed-boundary method was developed for the characterization of the *in vivo* TCPC hemodynamics. This flow solver was designed with the specific goal of capturing the complexity of patient-specific anatomies and pulsatile flows, and allowing for the easy performance of patient-specific surgical planning studies. There are several opportunities for taking these technologies one step further, and more importantly re-enforcing the link between the proposed hemodynamic optimization framework and the ultimate patient outcome. These avenues are outlined in the forthcoming sections.

12.1 Larger Sample Size Studies

While the current thesis work allowed for the identification of apparent trends across the different patient groups, would it be in the pulsatile investigation or in the surgical planning studies, these analyses were conducted on very small patient populations and need to be further confirmed on a larger patient pool. The pulsatile investigation in particular, demonstrated that there is a threshold below which the impact of pulsatility might be neglected in favor of shorter computational times, but above which the inflow pulsatility should be included in order to appropriately capture the efficiency of different TCPC options. This finding could have significant implications for surgical planning applications, and as such it might be critical to: 1) conduct a larger sample size

study to better define the range of validity of the non-pulsatile assumption, and 2) to assess whether there is a threshold above which including or neglecting flow pulsatility alters the efficiency ranking of virtual surgery options.

Along the same lines, from the surgical planning study, it is apparent that the formulation of any surgical guideline will require a very detailed classification of the Fontan patients based on both anatomical and flow considerations. While the current study allowed for the establishment of detailed guidelines for patients with an interrupted IVC and bilateral SVCs, the procedure to follow for patients with a single SVC remains less clear. While the most complex cases will always be best addressed with an individualized surgical planning approach, it is believed that increasing the number of patients enrolled in the surgical planning study will ultimately allow for the definition of detailed “pathology templates”, and associated better performing surgical approaches.

12.2 Characterizing the Uncertainty in the Surgical Planning Predictions

From the results described in the surgical planning investigations, it is apparent that the hemodynamic performance (i.e. the hepatic flow distribution and power losses) is not only a function of the TCPC geometry, but also of the inflow and outflow rates. Accordingly, the relevance and accuracy of the surgical planning recommendations will be greatly impacted by our ability to predict the post-operative flow conditions.

The global flow distribution to the LPA and RPA will be dictated by the evolution of the left and right pulmonary vascular resistances, which will in turn depend on the amount of hepatic effluents distributed to these two lungs and the presence or absence of

pulmonary artero-venous malformations. In this thesis, we tried to best predict the temporal evolution of the global flow distribution to the RPA and LPA, by characterizing the hemodynamic performance of each TCPC design over a broad range of LPA/RPA flow splits, thus providing a potential evolution curve for each option.

The inflow conditions on the other hand were imposed based on the pre-operative flow rate measurements. However, the caval flow rates are expected to change after the 3rd stage of the TCPC surgery or as the patient grows, and could potentially evolve depending on the resistance of the TCPC connection and remodeling of the systemic vasculature. There is thus a need to: 1) better understand the temporal evolution of the caval flow rates before and after surgery, in healthy and failing Fontan patients; and 2) characterize how the uncertainty in the inflow boundary conditions propagates to the ranking of different surgical planning options and the final recommendation for the TCPC surgery.

12.3 Linking TCPC Hemodynamics to Patient Outcome

The current thesis proposes a novel framework for the optimization of the TCPC design based on a finite set of hemodynamic efficiency metrics, namely power losses and hepatic flow distribution. While both metrics have been clinically or theoretically shown to impact patient outcome, these links remain weak and very imprecise. There is a critical need for more clinical information in order to help prioritize between different hemodynamic metrics. Questions to be answered include, among others:

1) What is the sensitivity of the pulmonary vasculature to the hepatic effluent concentration? Is there a range of clinically acceptable hepatic flow distributions for

which both lungs will be healthy, even these distributions slightly depart from a 50/50 LPA/RPA balance?

2) What is the exact impact of the TCPC hemodynamic resistance on ventricular function? Are some patients more sensitive to the TCPC efficiency than others?

3) What is the exact role of the TCPC pressure drops or flow reversal in the development of gastro-intestinal track disorders such as protein losing enteropathy (PLE)?

Answers to the above questions would require both clinical and bioengineering analyses, as well as both cross-sectional and longitudinal studies, quantifying the changes in TCPC hemodynamics and patient outcomes and assessing whether any correlation can be made between them.

12.4 Realism of the Virtual Surgery Interface

In the course of the pulsatile investigation, the bulgy aspect of the intra-atrial TCPC was observed to favor the mixing of the systemic venous returns, which may help achieve a more balanced hepatic flow distribution. However, this geometric characteristic was not modeled in the virtual intra-atrial options considered for the surgical planning studies. There is thus a need to further refine the realism of the virtual surgery interface. A first step to determine the critical geometrical parameters to model might be to acquire post-operative MRI data and confront the TCPC performed to the corresponding virtual option, seeking to understand the causes of the differences and their impact on the predicted performances.

12.5 Combining the Unstructured Cartesian Paradigm with Local Mesh Refinement Strategies

A major characteristic of real-life anatomical flows is the fact that due to their relatively low Reynolds number the emergence of dynamically rich flow patterns can be localized only in a certain region of the overall flow domain, which makes their numerical resolution particularly challenging. Typical examples of such configurations are provided by Patient 3 in Chapter 8 and Patient A1 in Chapter 9. In the case of Patient 3, a fine computational mesh was required to properly characterize the flow through the severely stenosed mid-PA segment. Similarly, in Patient A1, the presence of a severe LPA stenosis led to important flow instabilities downstream of the stenosis characterized by chaotic mixing and small random vortical structures, which are the hallmark of transitional flow regimes and early signs of turbulence, and required a fine spatial discretization. A mesh refinement study for Patient A1 demonstrated that the grid employed in this thesis ($h = 0.022D_{IVC}$, yielding 1.82 million *active* nodes) is adequate for obtaining grid insensitive results in most of the anatomy, but it is clearly not fine enough to fully resolve the length scales that emerge in the flow downstream of the LPA constriction.

Future work should thus focus on combining the unstructured Cartesian paradigm with local grid embedding strategies in order to be able to carry out fully resolved simulations at a reasonable computational cost. The unstructured immersed-boundary approach developed as part of this thesis provides the basis for developing such methods and for implementing them efficiently for complex anatomical simulations.

12.6 Further Refinements of the Computational Model

Inlet Velocity Profiles: As was discussed when comparing the numerical results to either controlled in vitro experiments in Chapter 7 or against the in vivo PC MRI measurements in Chapter 8, the flow structures at the center of the TCPC can be very dependent upon the choice of inlet velocity profiles. Potential avenues to further refine the realism of the CFD simulations include: 1) interpolating the in vivo PC MRI measurements onto the inlet cross-sections of the numerical model; or 2) expanding the computational domain further upstream, to model the merging of the hepatic and IVC flows on the inferior side, and of the innominate and SVC flows on the superior side. A potential difficulty associated with the latter approach might be an increasing PC MRI measurement error as the dimensions of the vessels of interest decrease from the IVC and SVC to the upstream branches.

Outlet Boundary Conditions: All simulations reported in this thesis were conducted using prescribed mass flow splits at the outlets. While this approach is reasonable for non-pulsatile simulations, or for pulsatile simulations for which the dynamic flow split variations can be obtained from PC MRI, it may be more questionable if surgical planning studies were to be conducted under pulsatile conditions or using moving walls. For either of these cases, it might be better suited to change the outflow boundary conditions to resistance or impedance boundary conditions, allowing for the LPA/RPA flow splits to dynamically adapt to the inlet flow curves.

Rigid Walls: All simulations and *in vitro* experiments reported in this thesis were conducted neglecting wall motion, and focusing on the impact of the TCPC flow pulsatility. This simplification was deemed reasonable in view of the *in vivo* MR images, where the *in vivo* motion of the TCPC wall appeared to be of small magnitude, even in intra-atrial cases. However, under pulsatile conditions, wall compliance might play an important role in the transmission and absorption of the pulsatile pressure waves.

It should be kept in mind that both of the above numerical refinements might significantly increase the computational complexity and costs. There might thus be a need to quantify the gain achieved by including wall motion and weigh it against the added computational cost, following a similar process as the pulsatile sensitivity analysis performed in this thesis.

APPENDIX A. STEP-BY-STEP GENERATION OF PATIENT-SPECIFIC COMPUTATIONAL MESHES

This section describes the steps leading from the point clouds description of an *in vivo* anatomy obtained from the reconstruction of the magnetic resonance images (MRI) to the unstructured Cartesian mesh that will be used in the computational fluid dynamic simulations. An overview of the entire process is provided in Figure A-1.

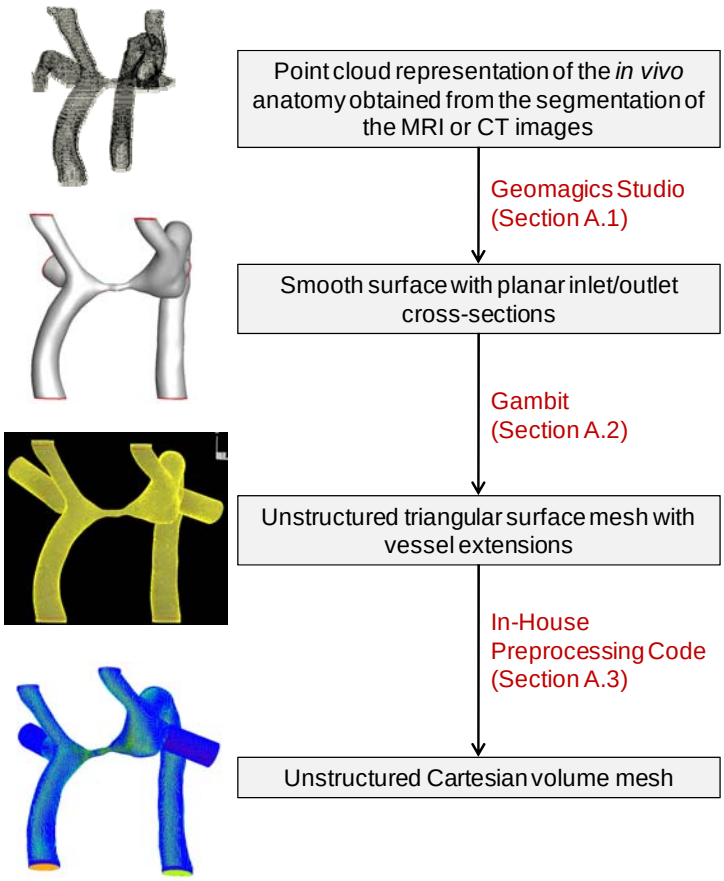

Figure A-1: Mesh generation overview

A.1 Surface Preparation, Geomagic Studio 11 (Geomagic Inc., NC, USA)

1. Import the point cloud data obtained from the MRI segmentation and 3D reconstruction (Go to File/Import)

2. Fit surface:
   a. Surface Wrap: Go to Points/Wrap, the default settings should work.
   b. Fill the holes left after the surface wrapping (Go to Polygons/Fill holes or select ). Use the default settings first.
      i) If filling some of the holes yield to the formation of artificial bumps, change the "Fill type" from "Curvature" to "Flat"
      ii) Another option might be to create a bridge () across the center of the hole and then fill the smaller holes independently

3. Remove the local surface irregularities:
   a. If the geometry is very irregular the first step might be to apply smoothing the the entire geometry (Polygons/Smooth/Relax or Polygons/Smooth/ Reduce Noise)
   b. If the irregularities are more limited in space, then the two best performing options are either:
      i) To apply a local smoothing with Polygons/Smooth/Sandpaper
      ii) To delete the local irregularity and fill back the hole using the curvature-based filling
   c. Attention should be paid to delete all inverted surface elements and fill back the corresponding holes (Figure A-2)
      i) The inverted surface elements can easily be visualized as they will appear in yellow, whereas the rest of the surface should appear in blue.
      ii) Rotating the anatomy helps detect the inverted elements as the surface rendering used by Geomagic Studio will lead these yellow triangles to "shine"

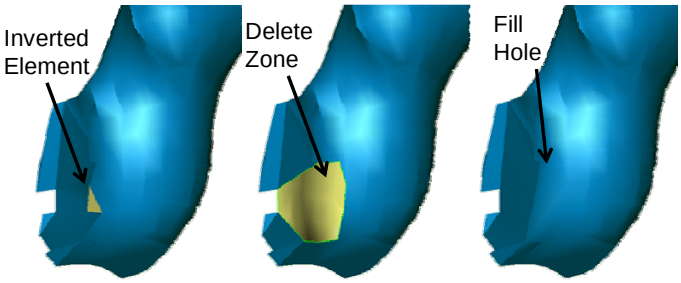

Figure A-2: Detection and removal of an inverted surface element in Geomagic Studio.

4. Create the inlet/outlet cross-sections (Figure A-3)
    a. Select the vessel to be cut
        i) Right click on the mouse and choose "Select Through". In the same menu, go to "Selection Tools" and pick the method of choice. "Lasso" typically is the easiest to use
    b. Cut the vessel
        i) Go to Polygons/Trim/Trim with Plane or select the icon
        ii) Change the plane orientation method from "System Plane" to "Three Points" and select three points on the vessel surface such that the plane is visually perpendicular to the vessel axis. Click "Align" to align the plane with the selected points.
        iii) "Intersect Plane"

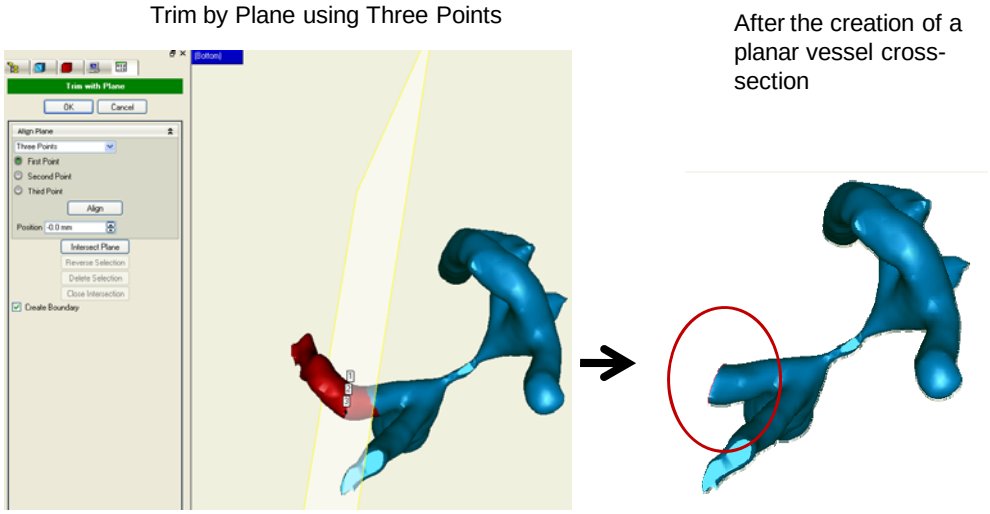

Figure A-3: Creation of a planar outlet cross-section.

iv) "Delete Selection". The section that will be deleted is the section highlighted in red after the plane intersection. If this section is not that has to be removed first select "Reverse Selection" and then "Delete Selection"

v) "Close Intersection" to create a water-tight geometry

vi) "OK" to accept the thus created vessel cross-section

c. Repeat the operation for each inlet and outlet

5. Convert the surface from its triangular structure to a format that can easily be imported into other computer aided design (CAD) or meshing software by creating a limited number of B-spline patches rather than the large number of surface triangles.
   a. Switch from the polygon to the shape phase: Go to Edit/Phase/Shape Phase
   b. Create Patches: Go to Patches/Construct Patches. Use "Auto-estimate" for the number of patches required. The default options work for most geometries
   c. If the defaults fail to adequately describe the geometry
      i) Go to Contours/Detect Curvature
      ii) Go to Contours/Shuffle Curvature Lines. Modify the main curvature lines (in orange) so as to provide proper guidelines for the patch generation. As a general rule, two curvature lines should run along the sides of each vessel, diametrically opposite to one another. Another curvature line should run all along the base of each vessel when two vessels merge together.
      iii) Go to Contours/Construct Patches. The patches will be defined using the curvature lines defined above.
   d. Go to Patches/Repair Patches and check the quality of the patch layout. The most important point is to avoid patch overlap. The easiest option to use is to edit patches () and move the patch corners until no patches overlap any longer.
6. Construct the grid (Grids/Construct Grids). The defaults should work.
   a. If they fail, the faulty patches will be highlighted in red and the user should cancel the operation and correct these patches accordingly
7. Fit surface
   a. Go to Grids/Specify Planar Region. Select all the patches on a given inlet or outlet and click "Next". Repeat until the operation is completed.

b. Go to NURBS/Fit Surface. A baseline tension of 0.7 should provide a smooth geometry. The user may adjust that value until a satisfying rendering is achieved

8. Export as an .igs file format

A.2 Surface Mesh Generation, Gambit 2.4 (ANSYS Inc., PA, USA)

1. Import the .igs file exported from Geomagic Studio (File/Import/IGES)
   a. The default import settings should be fine
   b. If the import operation takes longer than normal, the most likely cause is a faulty surface generation in Geomagic Studio and the user should go back to the previous step
2. Merge patches: after the surface preparation in Geomagic Studio 11.0, the TCPC surface is typically discretized with hundreds of patches, which is inadequate for the prescription of the inlet/outlet boundary conditions. The patches should thus be merged into larger surfaces by boundary type (Figure A-4).
   a. Under "Operation", select the Geometry mode ( )
   b. Under "Geometry", select the faces ( )
   c. Under the "Face" options, select "Merge Surfaces" ( )
   d. Select all the patches that belong to the same boundary (e.g. all IVC surfaces), and apply

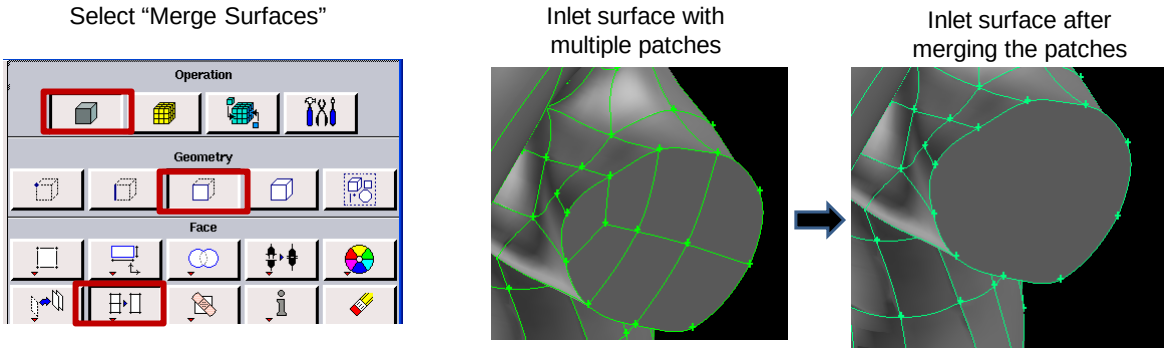

Figure A-4: Merge the patches belonging to the same boundary type

3. Extend the inlet/outlet entrance lengths

   a. In the geometry/vertex menu, select "create vertex on edge" and create N number of points such that each edge has at least 3 distinct points (Figure A-5).

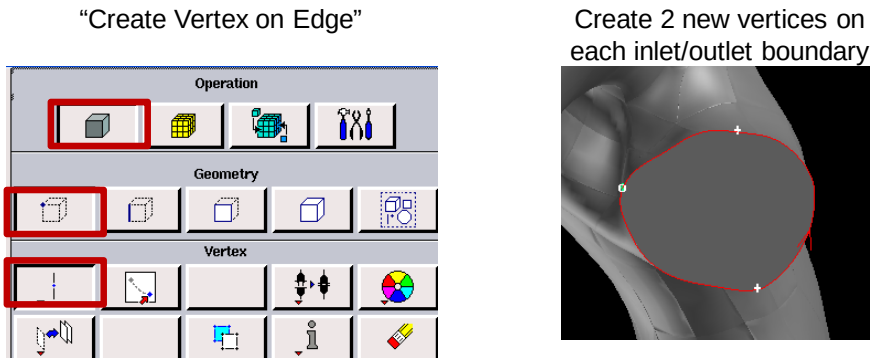

Figure A-5: Create N independent points on each inlet/outlet boundary to ensure that each one of them has at least three distinct, unaligned points.

   b. Under Operation, choose the "Toolbox" menu ( ), select "Axis" ( ) and then "Create Coordinate System" ( ). Check the box "Vertices" to define the coordinate system using the vertices created in the previous step. Select three distinct vertices on a given edge, and accept (Figure A-6).

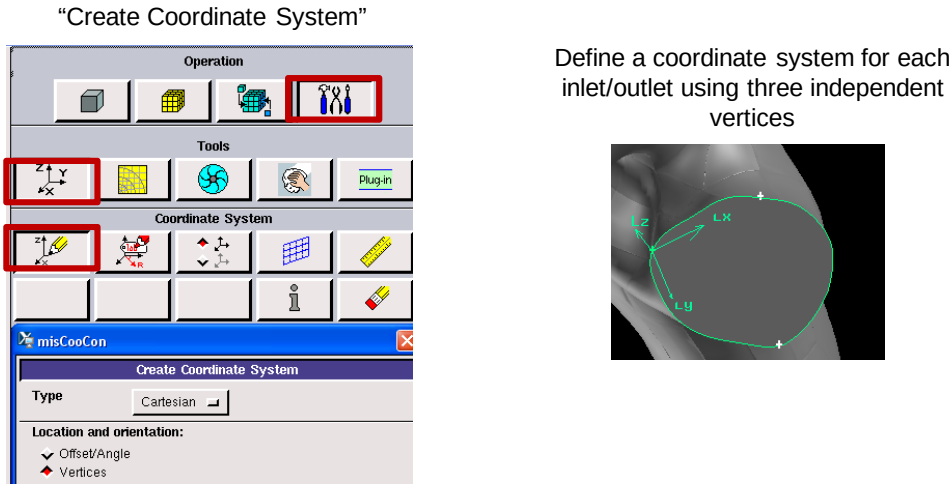

Figure A-6: Create a new coordinate system for each inlet/outlet

c. Extend the inlet and outlet vessel lengths in the direction normal to the cross-sectional plane (Figure A-7).

i) Go to the "Geometry/Volume" menu and select "Sweep surface"

ii) Select the cross-section of the inlet/outlet to be extended

iii) For the "Path" option, check the "Vector" box and then click "Define" to define the extension direction

iv) Select the coordinates axis defined on the inlet/outlet to be extended. The z-axis will be oriented normally to the surface. If the z-axis is pointing towards the inside of the TCPC choose the "negative" direction, otherwise "positive".

v) Set the extension length and accept

For the cases studied in this thesis, the inlet vessels were typically extended by 10mm, while the outlets were typically extended by 50mm.

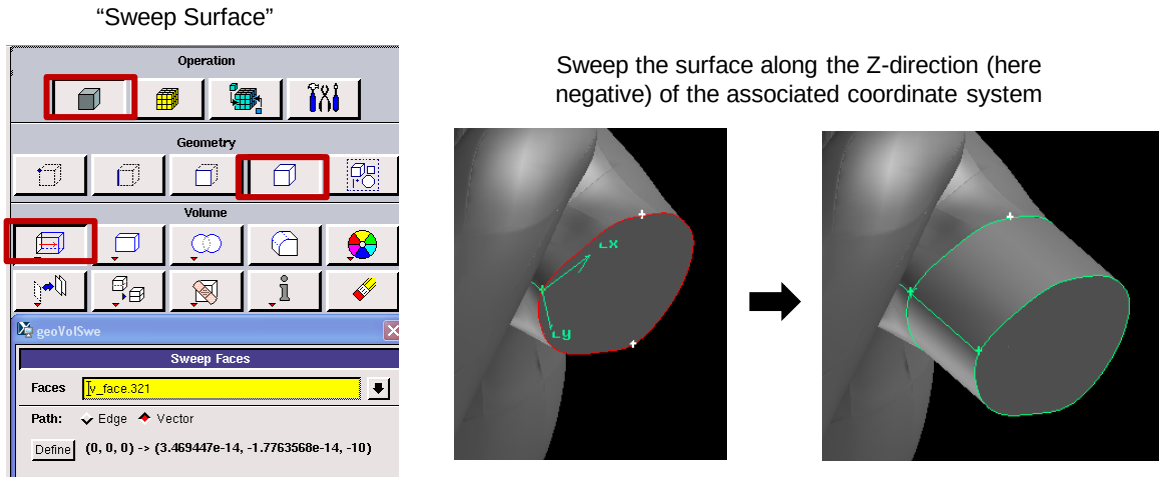

Figure A-7: Inlet/outlet extension

4. Unstructured Surface Mesh Generation

a. Mesh all edges (Figure A-8). Using the edges to define the mesh resolution allows for an easy control over the surface mesh spacing. If a finer resolution is needed along one the pulmonary arteries for example, then this can be ensured by simply defining a finer mesh spacing along the corresponding edges.

i) Go to the mesh/edges menu

ii) Select all edges and set your mesh spacing (typically 1 or 1.5mm).

iii) In cases where one vessel is significantly smaller than the others, the corresponding edge may be meshed independently with a finer setting.

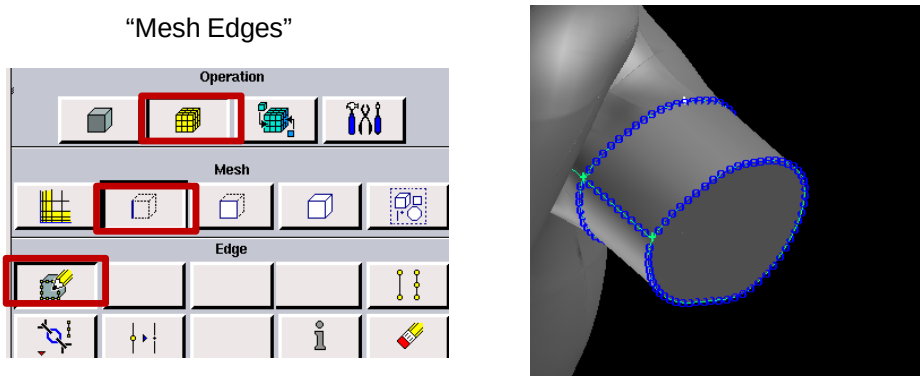

Figure A-8: Edge mesh generation. Meshing the edges first allows for a detailed control over the surface mesh resolution, allowing for finer resolutions in regions where it is needed.

b. Mesh surfaces (Figure A-9)

i) Select the TCPC wall, the extension walls and the outer inlet/outlet cross-sections (do not select the cross-section lying at the interface between the TCPC and the extensions)

ii) Change the mesh type to "Tri", uncheck "Spacing" and "Apply"

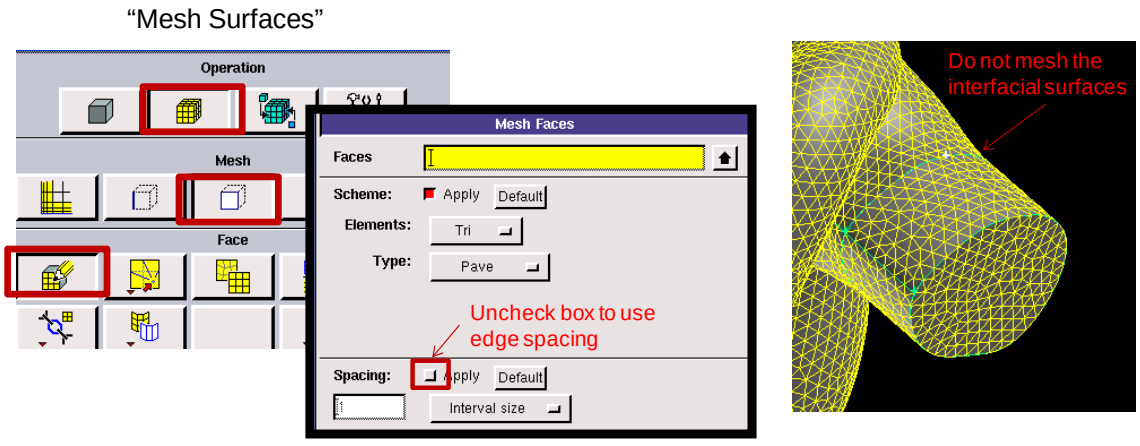

Figure A-9: Surface mesh generation

5. Label the inlet/outlet cross-sections (Figure A-10)

   This operation will ease the prescription of the inlet and outlet boundary conditions with the in-house code.

   a. Change solver type to FIDAP

   b. In operation select "Zones" ( ), and then select "Specify Continuum Type" ( )

   c. The default setting for the continuum types to be select is "Volume", change to "Faces"

   d. Select one inlet or outlet, name it (e.g. IVC or LPA) and apply

   e. Repeat the operation for all inlets and outlets

   The advantage of labeling the inlets and outlets is that Gambit will export the mesh surfaces in the order in which they are labeled. Controlling the order in which the surfaces are labeled allows for an easier prescription of the boundary conditions.

6. Export the mesh (File/Export/Mesh) "mesh_name.FDNEUT"

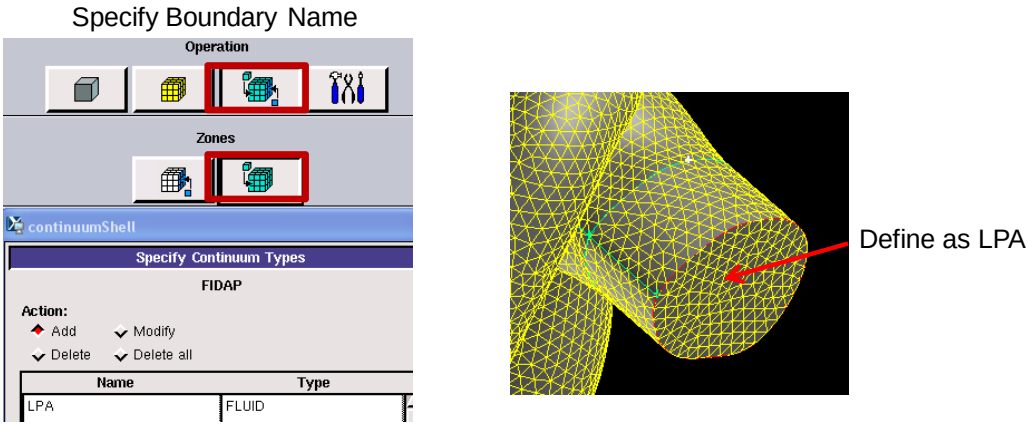

Figure A-10: Label each inlet and outlet, in the same order as the one that will be used for the boundary condition prescription in the in-house code.

A.3 Volume Mesh Generation, In-House Code

All settings for the volume mesh generation are controlled from the text file input_MPI.txt. This file includes parameters that pertain both to the flow solver and to the pre-processor. We will only present the parameters associated with the mesh generation. The input_MPI.txt file is divided into sections with specific instructions, which are here listed, with examples of parameter settings.

1. General information
    a. NAME_PROBLEM: This can be any word or short sentence helping the user remember characteristics of the simulation. NAME_PROBLEM will appear on the top of the screen output.
    b. REST_Q_UH and REST_GEOM: these are the numbers associated with the geometric and flow restart files.
        i. For the pre-processor REST_Q_UH does not come into play.
        ii. Setting REST_GEOM = 0 means that the pre-processing should be started from scratch
        iii. Setting REST_GEOM > 0 means that the pre-processing has already been done, but that the user wants to associate the volume mesh with a finer surface mesh for example.

2. Parameters to read the immersed boundary
    a. F_FDNEUT: The name of the .FDNEUT file with the unstructured triangular surface mesh

b. (N)PT_TO_REMOVE, (N)NC_TO_REMOVE, (N)NC_TO_ADD, NC_TO_ADD, and are options allowing the user to correct selected surface elements if there are a few defects after the Gambit mesh generation steps. If there are too many holes or inverted elements, then it is simpler to go back to Gambit or Geomagics.

   i. If there are no defects in the surface mesh, all these parameters should be set to 0

c. NINVERT_NORMAL allows the user to invert the normal directions over an entire boundary so to ensure that all normals are pointing towards the fluid.

   i. For most cases Gambit exports the mesh with all normals not pointing towards the fluid domain. For these cases. Set NINVERT_NORMAL to any value larger than the number of boundaries in your surface mesh.

   ii. If only some boundaries but not all, say two, have inverted normals, then set NINVERT_NORMAL=2, and then list the corresponding zone numbers as GROUPS_TO_INVERT(1:2)=7,11 if the two zones with inverted normals were zones number 7 and 11 in your surface mesh.

3. Scaling of the physical dimensions

The in-house code is written using the non-dimensional form of the Navier-Stokes equations. A first step is thus to normalize the geometry by a characteristic length.

a. IJK_BODY_LENGTH offers a number of pre-set options, including the maximum x, y, or z dimensions (IJK_BODY_LENGTH = 1 to 3) or using the equivalent hydraulic diameter of a given inlet or outlet (IJK_BODY_LENGTH > 100)

b. For all other characteristic lengths set IJK_BODY_LENGTH = 0 and type in the normalization parameter to use as L_REF.

4. Spatial resolution of the Cartesian volume mesh

   Two options are offered to define the spatial resolution:

   a. If GRID_OPTION = 1, then the user fixes the number of grid cells in each direction (IMG, JMG, KMG) and the code adjusts the mesh resolution to cover the entire geometry
   b. If GRID_OPTION = 2, then the user fixes the mesh spacing (GRID_DX) after non-dimensionalization and the code adjusts the number of grid cells in each directions to cover the entire geometry.

   In this thesis the geometries were discretized using option 2, and the mesh spacing was typically set to be isotropic and equal to 0.02 non-dimensional units (i.e. $h = 0.02\ D_{IVC}$)

5. IB-node detection parameter

   a. In order to sort the Cartesian grid nodes between those that fall inside or outside of the fluid domain, a preliminary search is performed that only takes into consideration the Cartesian cell centers that fall within a certain search radius of the immersed boundary nodes (see Figure A-11). This search radius is defined as $R = COEFF\_DSMAX \cdot \Delta x$
   b. COEFF_DSMAX should be set to a large enough value for none of the IB cell centers to be overlooked, but kept small enough to minimize computational time. The typical steting used in this thesis was COEFF_DSMAX = 9.0.
   c. EPS_VEC is the tolerance for points to be considered as being within the fluid domain or outside of it. This parameter was typically set to EPS_VEC=0.001.

With all these parameters in place, the preprocessing code will automatically generate the desired unstructured Cartesian grid. All geometric information will be written in the geometric restart file Rest_Geom0000. It is advised to change the restart file name to any number other than the default value of 0000.

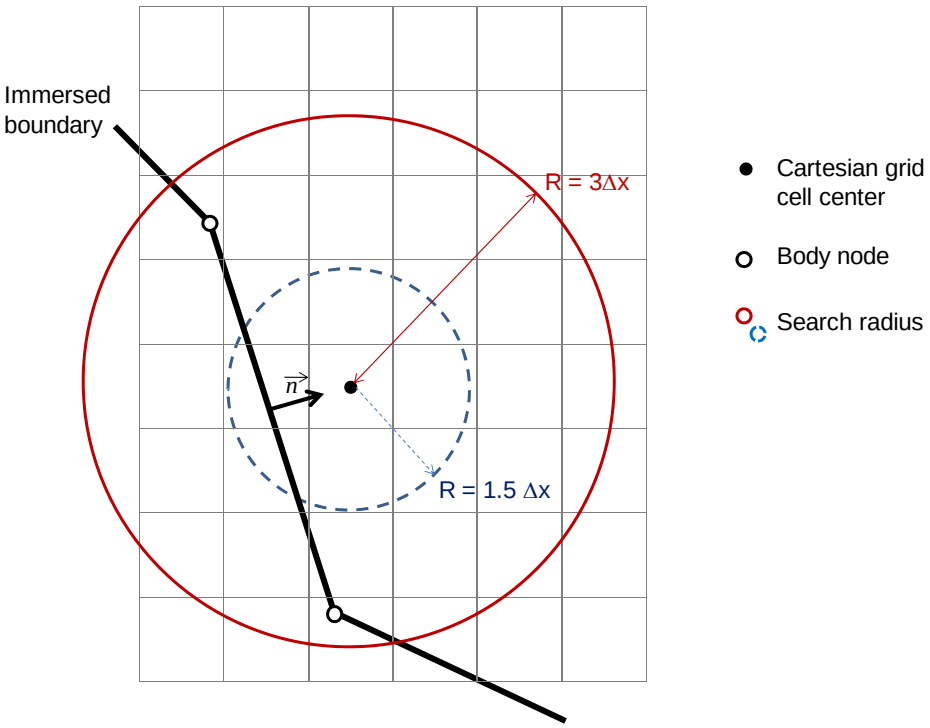

Figure A-11: IB-detection. In the preliminary search, only the Cartesian grid cell centers that fall within a certain distance R of the immersed boundary node are differentiated between those that fall inside or outside of the fluid domain. If R is too small (e.g. R= 1.5Δx), then some IB cell centers may be overlooked.

APPENDIX B.

SIMULATION SET-UP

In order to help in the data organization and clean-up, all code inputs are provided as *.txt files, while the code outputs are either in binary format (for the flow restart files, Rest_Q_Uh_XXXX) or in Tecplot readable *.dat format. The three following files are required to start any simulation:

1. The binary restart file with all geometric information obtained from the pre-processor (Rest_GeomXXXX)
2. The general input file: input_MPI.txt
3. The settings to use for the Poisson solver: control.txt

Additional files (optional) may be provided to further specify the inlet and outlet boundary conditions:

4. For pulsatile simulations, list the time-varying cardiac output and inlet/outlet flow splits in BC.txt
5. Specific inlet velocity profiles

The different input parameters are described in details in the following sections.

B.1 General information (in input_MPI.txt)

- NAME_PROBLEM: This can be any word or short sentence helping the user remember characteristics of the simulation. NAME_PROBLEM will appear on the top of the screen output.

- REST_GEOM: index for the geometric restart file, ought to be > 0
- REST_Q_UH: index for the flow restart file.
  - REST_Q_UH = 0: the flow simulations will be started from scratch
  - REST_Q_UH > 0: the flow simulations will be initialized with the flow information contained in the associated Rest_Q_Uh_XXXX file (where XXXX is equal to REST_Q_UH).
    - If Rest_Q_Uh_XXXX cannot be found, the simulations will be initialized with zero velocities and pressures and started from scratch.
    - If MONITOR_RESET < 0, the running average will keep building upon the values stored in the restart file, otherwise it will be reset.
- DELTI: physical time-step (in non-dimensional time units)
- NT2: maximum number of physical time-steps to be done
- ITMAX_PPROJ: number of inner iterations to be done in the momentum step (typically set to 10)
- ERR_TOL: tolerance threshold below which a value should be considered as a machine 0 (typically set to 1E-15)

B.2 Code outputs (in input_MPI.txt)

- Frequency at which the flow fields should be outputted
  - NWOUT: instantaneous pressure and velocity fields in Tecplot format
  - NWAVE: running-average (velocity and pressure) in Tecplot format
  - NWDUMP: flow restart file in binary format

- DUMP_OVERWRITE: if this is set to F (false) then each output will be written to a new file, indexed by the time-step number. If it is set to T (true) the restart files will be overwritten, in order to save space. For pulsatile simulations this value is automatically switched to F within the code itself.

- Monitoring the simulations and convergence: The user can specify a series of points for which he wants the time-history of the pressure and velocity components. For each one of these points the code will output a Tecplot-compatible file containing the time-series of the instantaneous pressure and velocity components (P,U,V,W) and the corresponding running averages (PM,UM,VM,WM)
  - MONITOR_FILE: file header
  - MONITOR_NUM_POINTS: number of points to track
  - MONITOR_XYZ(N,1:3) = X,Y,Z: coordinates of the N^{th} point monitor
- Checks for debugging: Unless the user wants to debug a specific problem, these checks should be set to F (false) as they will result in a large number of screen and file outputs that will drastically slow down the simulations. Check information will be outputted to the files MPIYYY_output_ZZZ.dat where YYY is the number of processors and ZZZ is the processor identification number.
  - CHECK and CHECK_P = T or F: general information for the momentum and pressure projection step, respectively
  - CHECK2_INPUT = F or T: track the computation at a specific grid cell of index L_TO_PRN_INPUT. This cell index is the global cell index, the code will then identify which processor it is associated with and its local index.

B.3 Boundary conditions (in input_MPI.txt)

- REN: Reynolds Number
- BC_STEADY = T or F: If this value is set to T (true) then the code will use the constant boundary conditions and boundary types prescribed below, otherwise it will look for a time-varying input prescribed in BC.txt

B.3.1.1 Non-Pulsatile boundary conditions

- BC_NUM: number of boundaries for which the boundary conditions will be specified. This number should be at least equal to the number of inlets and outlets.
- BC_NGROUP: index of the BC_NUM boundaries for which the boundary conditions will be specified
- BC_TYPE(1:BC_NUM): type of boundary condition to use
  - BC_TYPE(N) > 0: inlet. 1=flat velocity profile, 2=parabolic velocity profile based on the inlet equivalent diameter, 3=prescribed velocity profile to be specified in text files stored in a folder named BC_N_profiles
  - BC_TYPE(N) = -3: outlet
  - BC_TYPE(N) ≤ -100: wall. -100: IB velocity set to 0, -101: no slip wall with the IB velocity reconstructed using a bi-quadratic interpolation, -102: slip wall
- BC_SPLIT: portion of the flow coming or exiting through a given boundary. This value should be 0 for walls, >0 for an inlet and <0 for an outlet. The sum of the inlet ratios should be 1 and the sum of the outlet ratios should be -1

Note: If nothing is specified for a given boundary, the default setting will be BC_SPLIT = 0 (i.e. no flow) and BC_TYPE = -101 (i.e. no slip wall).

- The total flow rate or cardiac output coming in and out of the geometry may be set in one of two ways:
  - If the Reynolds number was computed using the mean velocity through inlet N as a characteristic velocity then, set NORM_VEL = N. The total flow rate, DVOL_0, will be computed as the ratio of the cross-sectional are of inlet N and BC_SPLIT(N). This will ensure a mean non-dimensional velocity of 1 through the inlet taken as a reference.
  - Otherwise, set NORM_VEL =0 and DVOL_0 to the desired value. Ensure that DVOL_0 is consistent with the characteristic distances and velocities chosen to compute the Reynolds number REN.

B.3.1.2 Pulsatile boundary conditions (in BC.txt)

For pulsatile simulations, the two following parameters should be set in input_MPI.txt: REN and BC_STEADY=F. The time-dependent cardiac output, flow splits and boundary types should be specified in BC.txt according to the format exemplified in Figure B-1 and detailed below:

- NT_UNSTBC_MAX: number of time-points for which the boundary conditions are specified
- List of the non-dimensional time-points
- List of the total non-dimension flow rate for each time point
- For each boundary (indexed by NBC= N), the lists of
  - BC_TYPE for each time-point
  - BC_SPLIT for each time point

```
NT_UNSTBC_MAX= 4
Non-dimensional time
0.00  0.25  0.50 0.75

Total Non-Dimensional Flow Rate
1.23  1.45  1.01  0.60

NBC= 1
 1  1  -3  -3
0.01  0.1 -0.01 -0.1

NBC= 2
1 1 1 1
0.99 0.9 1.0 1.0

NBC= 3
-3 -3 -3 -3
-1.00 -1.00 -0.99 -0.90
```

Figure B-1: Example of a BC.txt file with 4 time-steps and three different types of inlet/outlet boundary conditions.

Any boundary not listed in BC.txt will be considered as a no-slip wall for all time-steps (i.e. BC_TYPE = -101 and BC_SPLIT = 0). Similarly to the non-pulsatile settings the sum of the inflow splits should be equal to 1 at every time-step, while the sum of the outflow splits should be equal to -1. If the temporal resolution used in the simulations is finer than that used in BC.txt, the intermediate velocity and flow split values are reconstructed by quadratic interpolation.

Attention should be paid to ensure that the time-varying non-dimensional total flow rate is consistent with the characteristic distance and velocity retained to compute the Reynolds number. For the simulations conducted in this thesis, the characteristic distance was chosen to be the equivalent hydraulic diameter of the IVC inlet cross-section, D_{IVC}, and the characteristic velocity to be the mean IVC velocity averaged both over the cardiac cycle and the inlet cross-section, $\overline{U}_{IVC}$. With these notations the time-

varying non-dimensional flow rate, CO^*, is given by:

$$CO^*(t^*) = \frac{CO(t)}{\overline{U}_{IVC} \cdot D_{IVC}{}^2} \tag{B-1}$$

where CO is the measured time varying flow rate, t is the physical time, and t^* is the corresponding non-dimensional time-instant given by $t^* = t \cdot \overline{U}_{IVC} / D_{IVC}$.

B.4 Flow Solver Parameters

These parameters should for the most part be left to their default values. Their significance is given below. The parameters pertaining to the momentum step are listed in input_MPI.txt, while the parameters pertaining to the pressure projection step are listed in control.txt in a format readable by the PetSc libraries.

B.4.1.1 Momentum step (in input_MPI.txt)

- IRK and ALPHA: order of accuracy for the Runge-Kutta iterations in the momentum step, and associated ALPHA coefficients. Unless debugging, these values should be set to IRK = 4 and ALPHA(1:4) = 0.25, 0.33, 0.5, 1.0
- On and off switches for the different subroutines. Unless debugging these values should be set to 1 (0 will turn off the subroutines)
  - IUNST: unsteady term ($\partial\vec{\mathbf{u}}/\partial t$)
  - IVISC: viscous terms ($\mathrm{Re}^{-1}\nabla^2\vec{\mathbf{u}}$)
  - ICONV: convective term ($\vec{\mathbf{u}}\cdot\nabla\vec{\mathbf{u}}$)
  - APPLY_BCOND: apply boundary conditions for all boundary types, including inlets, outlets and walls

- APPLY_IBM_INTERPOL: velocity interpolation for the wall boundary conditions

- CONVEC_ORDER = 1 or 2: Order of accuracy for computation of the spatial derivatives in the convective term. Unless debugging this value should be set to 2.

B.4.1.2 Pressure Projection Step (in Control.txt)

- Main solver
  - ps_ksp_type: type of solver to use, this was always set to fgmres.
    - For the FGMRES approach an additional parameter to set is ps_ksp_gmres_restart. The FGMRES method iteratively builds a Krylov subspace refining the solution towards its exact value. This, however, may pose memory limitations. The solver can thus be restarted at regular intervals to reset the memory. For most cases ps_ksp_gmres_restart was set to 20 or 30. In cases where the simulations ran out of memory, the value was decreased further.
  - Convergence criteria: the Poisson solver exits when either one of the following conditions is met:
    - When the absolute error is less than ps_ksp_atol (typically set to 1.e-8)
    - When the relative error is less than ps_ksp_rtol (typically set to 1.e-5)
    - When the number of FGMRES iterations exceeds ps_ksp_max_it (set to 200, although the other criteria were typically met in less than 50 iterations)
- Preconditioner
  - mypc_type: type of preconditioner to use, typically set to either mg or bjacobi, for the multi-grid or biJacobi approaches, respectively.

- For the multi-grid approach a few additional parameters need to be set
  - ps_mg_level: number of multigrid levels to use (1 is the equivalent of no multi-grid approach). This parameter was typically set to 2 or 3.
  - ps_mg_refine: directions in which the grid should be coarsened for the multi-grid approach. 111 means in all directions, 100 means in the X direction only, 010 in the Y direction only, 110 in the X and Y directions only, etc.
  - after_mg: whether to perform a post-smoothing step after the multi-grid. Typically set to no.

APPENDIX C.

IMPLEMENTATION DETAILS

C.1 Flow Solver Implementation Overview

The mathematical formulation of the fractional step method used in this thesis is presented in Chapter 5. Its practical implementation is described in Figure C-1, as a pseudo-code. This pseudo-code breaks down the solver into its individual steps, lists the subroutine performing each step as well as the files where these subroutines may be found.

All initialization and time-integration steps are orchestrated from the main program file in main.F90. Subroutines specific to the momentum step can be found in rk4_solver.F90, while the subroutines pertaining to the pressure projection step are given in poisson_solver.F90.All boundary condition types are provided in bcond.F90 and ibm_interpol.F90 for the velocity interpolation along the wall boundaries. Finally, the different options for the flow field outputs are provided in plot_picture.F90 for the outputs in tecplot format and in rest_dmp.F90 for the binary restart files.

Initialize the simulation

- read the input text files: input_MPI.txt, control.txt and BC.txt
- allocate the structures associated with all grid levels
  ALLOCATE(XMG(MG_LMIN:MG_LMAX))
- split the computational domain among the different processors for parallel simulations with MPI (in split_domain.F90). This operation is done by one processor only (IAM=0)
  CALL SPLIT_DOMAIN(REST_GEOM)
- read the flow and geometry restart files for the finest grid level, MG_LMAX (in rest_dmp.F90):
  - CALL REST_DMP(REST_GEOM,0): read the array sizes and allocate all arrays
  - CALL REST_DMP(REST_GEOM,-1): read the geometry (Rest_GeomXXXX where XXXX= REST_GEOM)
  - CALL REST_DMP(REST_Q_UH,-2): read the flow restart file (Rest_Q_Uh_XXXX where XXXX=REST_Q_UH)

Iterate in time for NTIME = NT1 to NT2

- Store previous time steps (U_HNM1=U_HN and U_HN =U_H)
- Apply boundary conditions for the new time step (in bcond.F90)
  CALL BCOND
- If NTIME = NT1 compute the discrete 3D Laplacian operator (LHS) for all grid levels, and store it for all subsequent time iteration
- Advance in time using the fractional step method (in mg_fs_implicit_RK4.f90)
  - Momentum step: compute the intermediate velocity field with an explicit Runge-Kutta formulation (in rk4_solver.F90)
    DO IT = 1, ITMAX_PPROJ
      CALL SOLVER_RK
    END DO
  - Pressure projection step: solve the Poisson equation for the incremental pressure (in poisson_solver.F90)
    CALL POISSON_SOLVER
    - Compute the divergence of the intermediate velocity field on the finest grid level
      CALL POISSON_RHS(MG_LMAX)
    - Initialize the Krylov-Subspace solver using the PetSc libraries
      - use GMRES on the finest level MG_LMAX
      - set-up the preconditioner (which is set in control.txt, and was typically chosen to be either a multi-grid or a BiJacobi preconditioner)
    - solve the system to establish the incremental pressure PHI, such that LHS*PHI=RHS
    - destroy the PetSc environment
  - Pressure and velocity corrections on the finest level (in mg_fs_implicit.F90)
    CALL UPDATE_PRES_VEL
    - U_H = U_H + grad(PHI)
    - P = P+PHI
    - Apply boundary conditions (in bcond.F90)
- Outputs
  - Tecplot files at the following frequencies (in plot_picture.F90)
    - NWOUT for the instantaneous velocity and pressure fields
    - NWAVE for the running average of the velocity and pressure fields
  - Flow restart file at the frequency NWDUMP (in rest_dmp.F90)
    - If DUMP_OVERWRITE = TRUE then every even output will be written to Rest_Q_Uh_1000 and every odd output to Rest_Q_Uh_1001

Figure C-1: Pseudo-code depicting the general organization of the in-house flow solver. Calls to the specific subroutines are provided in blue to guide the reader through the solver. The files were these subroutines may be found are given in parenthesis.

C.2 Multi-Linear Interpolation Operators for the Multi-Grid Poisson Solver

The multi-grid implementation retained for the pressure correction step makes use of two multi-linear interpolation operators to communicate the computed residuals and solutions between a fine level $\ell+1$ and a coarse level ℓ. These operators are constructed by performing a linear interpolation along each grid direction. This might be better visualized in two dimensions as shown in Figure C-2. Let us consider a variable $\theta_{\ell+1}$, available at level $\ell+1$. The restriction of $\theta_{\ell+1}$ onto a cell center, C, of level ℓ will be obtained by interpolating between the four closest fine grid cells (F_1, F_2, F_3 and F_4 in Figure C-2) in the following manner:

$$\theta_C^{\ell} = \beta\left\{\alpha_{12}\cdot\theta_{F_1}^{\ell+1} + (1-\alpha_{12})\cdot\theta_{F_2}^{\ell+1}\right\} + (1-\beta)\left\{\alpha_{34}\cdot\theta_{F_3}^{\ell+1} + (1-\alpha_{34})\cdot\theta_{F_4}^{\ell+1}\right\} \tag{C-1}$$

where $\alpha_{12} = d_{\delta_{12}F_2}/d_{F_1F_2}$, $\alpha_{34} = d_{\delta_{34}F_4}/d_{F_3F_4}$, $\beta = d_{C\delta_{34}}/d_{\delta_{12}\delta_{34}}$ and d_{XZ} is the distance between the corresponding points. Since the Cartesian grid is uniform, each of these coefficients is in practice constant throughout the domain and equal to $1/2$. The 2D multi-linear interpolation operator would thus simplify into:

$$\theta_C^{\ell} = \frac{\theta_{F_1}^{\ell+1} + \theta_{F_2}^{\ell+1} + \theta_{F_3}^{\ell+1} + \theta_{F_4}^{\ell+1}}{4} \tag{C-2}$$

Applying the same reasoning for the restriction procedure, the 2D formulation of the multi-linear operator $R_{\ell\to\ell+1}$ would read as:

$$\theta_F^{\ell+1} = \frac{9\cdot\theta_{C_1}^{\ell} + 3\cdot\theta_{C_2}^{\ell} + 3\cdot\theta_{C_3}^{\ell} + 1\cdot\theta_{C_4}^{\ell}}{16} \tag{C-3}$$

where the fine grid nodes are numbered in order of proximity to node F as in Figure C-2.

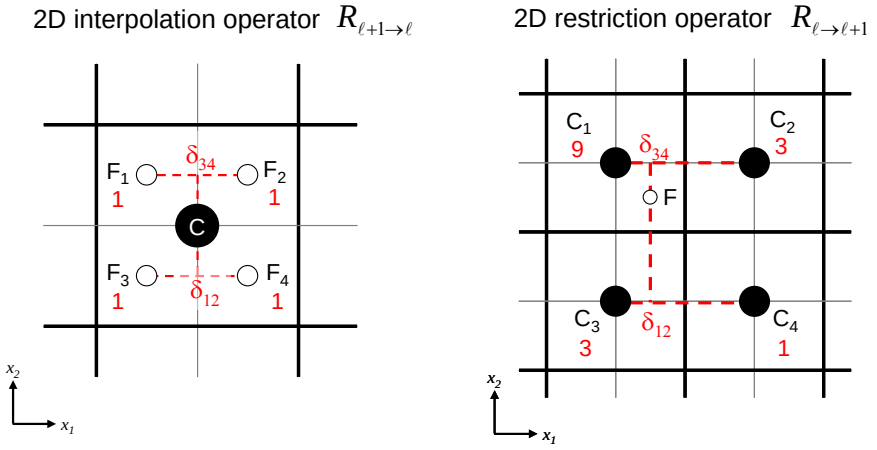

Figure C-2: Multi-linear interpolation and restriction operators exemplified on a 2D grid. δ_{12} and δ_{34} depict the intermediate interpolation points. The coefficients indicated in red indicate the weight attributed to each point on the interpolation/restriction stencil.

The generalization of these operators in three dimensions is illustrated in Figure C-3 and reads as:

$$R_{\ell+1\to\ell}(\theta): \quad \theta_C^{\ell} = \frac{1}{8}\sum_{j=1}^{8}\theta_{F_j}^{\ell+1} \tag{C-4}$$

$$R_{\ell\to\ell+1}(\theta): \quad \theta_F^{\ell+1} = \frac{27\cdot\theta_{C_1}^{\ell} + 9\cdot\theta_{C_2}^{\ell} + 9\cdot\theta_{C_3}^{\ell} + 9\cdot\theta_{C_4}^{\ell} + 3\cdot\theta_{C_5}^{\ell} + 3\cdot\theta_{C_6}^{\ell} + 3\cdot\theta_{C_7}^{\ell} + 1\cdot\theta_{C_8}^{\ell}}{64} \tag{C-5}$$

where F_j with $j \in \{1,8\}$ denote the eight fine grid cell centers closest to the coarse cell center C, and C_j with $j \in \{1,8\}$ denote the eight coarse grid cell centers closest to the fine cell center F ordered by proximity.

3D interpolation operator $R_{\ell+1\to\ell}$ 3D restriction operator $R_{\ell\to\ell+1}$

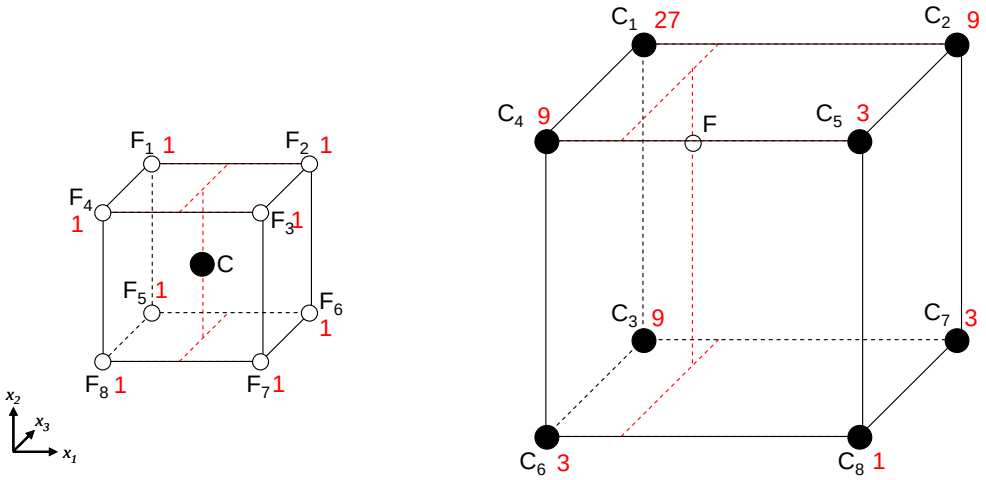

Figure C-3: Trilinear interpolation operator exemplified for 3D grid. It should be noted that in order to simplify the display, the black lines do not represent the edges of the grid cells, but rather the connections between adjacent cell centers. The coefficients indicated in red indicate the weight attributed to each point on the interpolation/restriction stencil.

APPENDIX D.

SURGICAL PLANNING DATA

This appendix provides all the data used to create the plots shown in the patient-specific surgical planning study (Chapter 9). For each Patient, we provide the cardiac output and inflow distribution. The outflow distributions tested for each one of the different options are listed in the associated tables in terms of global flow distribution to the RPA (GFD_{RPA}). The tables also provide the associated efficiency metrics in terms of

- The hepatic flow distribution to the RPA (HFD_{RPA})
- The pressures at each inlet and outlet cross-sections, which is to say in the hepatic veins (HepV), azygous vein (AZ), superior vena cava (SVC), and innominate vein (IV) or left superior vena cava (LSVC) for the inlets, and at the outlet cross-sections of the left and right pulmonary arteries (LPA and RPA, respectively). The pressure at the HepV inlet cross-section is taken as a reference to express all the other pressures.
- The control volume power losses.

D.1 Patient A1 (CHOP M1)

Patient A1 was a 4 year-old female, with a completed extra-cardiac TCPC (denoted as Pre-Op.) and left lung pulmonary arterovenous malformations (PAVMs). The cardiac output was 3.43 L/min, 21%, 22%, 24% and 33% of which came in through the

HepV, IV, AZ and SVC, respectively. The pre-operative outflow distribution was GFD_{RPA} = 30%. The results are discussed in Section 9.2.1.

Table D-1: Efficiency metrics associated with Patient A1's pre-operative TCPC anatomy and the four surgical planning options, for varying outflow conditions.

Option Number	GFD_{RPA} (%)	HFD_{RPA} (%)	Pressure (mmHg)						Power Loss (mW)
			HepV	AZ	IV	SVC	LPA	RPA	
Pre-Op	30	90.7	0.000	-0.048	-0.103	-0.100	-8.543	-0.317	44.78
Option 1	30	0.5	0.000	0.029	-0.046	-0.064	-5.829	-0.347	30.35
	50	4.4	0.000	-0.074	-0.128	-0.150	-3.318	-1.001	14.35
Option 2	30	93.9	0.000	-0.025	-0.069	-0.063	-7.400	-0.395	38.63
Option 3	20	41.8	0.000	0.159	-0.124	-0.121	-8.217	-0.179	48.57
	30	62.7	0.000	0.158	-0.122	-0.134	-6.402	-0.264	33.40
	50	79.2	0.000	0.168	-0.117	-0.130	-3.387	-0.644	13.84
Option 4	30	31.8	0.000	-0.030	-0.463	-0.448	-6.624	-0.723	33.97
	50	56.7	0.000	-0.040	-0.521	-0.534	-3.621	-1.232	14.95

D.2 Patient A2 (CHOA M1)

Patient A2 was a 6 year old male, with a completed intra-atrial TCPC (denoted as Pre-Op.) and right lung PAVMs. The inflow and outflow conditions were not available for that patient and were determined based on the data available for previous patients. The cardiac output was set to 3.43 L/min distributed as follows: 21%, 22%, 24% and 33% coming through the HepV, IV, AZ and SVC, respectively. The pre-operative outflow distribution was unavailable as well, but based on the presence of right PAVMs it might be assumed that it corresponded to a GFD_{RPA} greater than 50%. The results are discussed in Section 9.2.2.

Table D-2: Efficiency metrics associated with Patient A2's pre-operative TCPC anatomy and the eight surgical planning options, for varying outflow conditions.

Option Number	GFD_{RPA} (%)	HFD_{RPA} (%)	Pressure (mmHg)						Power Loss (mW)
			HepV	AZ	IV	SVC	LPA	RPA	
Pre-Op	80	13.3	0.000	0.090	0.004	0.017	-0.196	-0.314	1.78
	70	1.8	0.000	0.083	-0.007	0.006	-0.369	-0.269	1.79
	60	0.0	0.000	0.088	-0.008	0.007	-0.644	-0.184	1.99
	50	0.0	0.000	0.089	-0.009	0.011	-0.884	-0.148	2.36
Option 1	60	100.0	0.000	0.062	-0.024	-0.002	-0.576	-0.222	1.85
	50	100.0	0.000	0.066	-0.017	0.006	-0.837	-0.168	2.19
	30	93.7	0.000	0.079	-0.007	0.017	-1.530	-0.090	3.67
	20	75.2	0.000	0.101	0.015	0.040	-1.959	-0.050	4.93
Option 2	30	53.3	0.000	0.087	-0.003	0.021	-1.524	-0.094	3.77
	40	63.5	0.000	0.078	-0.012	0.013	-1.143	-0.134	2.82
	50	81.3	0.000	0.078	-0.015	0.000	-0.659	-0.145	1.46
Option 3	50	31.3	0.000	0.087	-0.009	0.012	-0.846	-0.160	2.31
	40	19.1	0.000	0.089	-0.002	0.019	-1.179	-0.112	3.00
	30	9.7	0.000	0.088	-0.003	0.019	-1.546	-0.080	3.90
Option 4	50	77.5	0.000	0.087	-0.005	0.017	-0.815	-0.154	2.12
	40	64.1	0.000	0.091	-0.001	0.022	-1.151	-0.117	2.79
	30	29.8	0.000	0.089	-0.006	0.017	-1.539	-0.090	3.68
Option 5	50	49.7	0.000	0.095	-0.001	0.015	-0.615	-0.124	1.28
Option 6	50	45.9	0.000	0.067	0.000	0.015	-0.634	-0.116	1.28
Option 7	70	28.8	0.000	0.005	-0.026	-0.019	-0.357	-0.256	1.45
	60	23.7	0.000	0.005	-0.031	-0.024	-0.511	-0.190	1.33
	50	12.4	0.000	0.009	-0.067	-0.061	-0.791	-0.206	1.80
Option 8	50	33.2	0.000	-0.016	-0.407	-0.397	-1.294	-0.593	3.74
	40	35.1	0.000	-0.017	-0.408	-0.398	-1.652	-0.554	4.52
	30	34.4	0.000	-0.018	-0.408	-0.399	-2.016	-0.522	5.37

D.3 Patient A3 (CHOP M4)

Patient A3 was a 3 year old female who had not yet undergone the final stage of the TCPC surgery, and was diagnosed with bilateral PAVMs. The cardiac output was 3.86 L/min, 32%, 17%, and 51% of which came through the HepV, AZ and SVC, respectively. The pre-operative GFD_{RPA} was 51%. The results are discussed in Section 9.2.3.

Table D-3: Efficiency metrics associated with the eight surgical planning options implemented for Patient A3, under varying outflow conditions.

Option Number	GFD_{RPA} (%)	HFD_{RPA} (%)	Pressure (mmHg)					Power Loss (mW)
			HepV	AZ	SVC	LPA	RPA	
Option 1	30	70.6	0.000	0.008	-0.060	-4.216	-0.613	19.59
	40	75.8	0.000	-0.025	-0.133	-2.981	-0.799	12.99
	51	84.3	0.000	0.038	-0.072	-2.139	-1.053	10.39
Option 2	40	49.5	0.000	0.095	-0.036	-3.854	-0.670	18.20
	51	66.9	0.000	0.081	-0.056	-2.591	-0.909	12.62
	60	83.5	0.000	0.069	-0.079	-1.728	-1.154	10.21
Option 3	20	29.9	0.000	0.108	-0.145	-5.141	-0.384	24.84
	30	48.6	0.000	0.111	-0.117	-3.998	-0.704	18.66
	40	40.9	0.000	0.234	-0.047	-2.913	-0.560	12.96
	51	59.9	0.000	0.027	-0.068	-2.336	-0.890	11.21
	60	73.4	0.000	0.016	-0.083	-1.574	-1.123	9.31
Option 4	0	0.0	0.000	0.000	0.000	0.000	0.000	0.00
	40	29.7	0.000	0.029	-0.107	-3.349	-0.841	15.60
	51	40.4	0.000	0.008	-0.105	-2.227	-1.119	9.72
	60	50.6	0.000	0.003	-0.106	-1.551	-1.412	6.90
Option 5	40	6.3	0.000	0.041	-0.091	-2.433	-0.864	11.07
	51	9.8	0.000	0.028	-0.094	-1.690	-1.162	7.73
	60	14.2	0.000	0.011	-0.075	-1.088	-1.460	5.70
	70	21.5	0.000	0.027	-0.085	-0.631	-1.887	4.87
Option 6	40	0.0	0.000	-0.173	-0.306	-3.215	-1.167	14.87
	51	7.7	0.000	-0.069	-0.202	-2.387	-1.387	11.03
	60	10.1	0.000	0.002	-0.146	-1.680	-1.617	8.22
	70	12.1	0.000	0.097	-0.043	-0.975	-1.910	6.20
	80	48.4	0.000	0.146	0.003	-0.440	-3.961	16.54
	90	69.6	0.000	0.286	0.141	-0.122	-5.021	23.01
Option 7	40	65.0	0.000	0.098	-0.176	-2.876	-0.581	12.11
	51	82.6	0.000	0.098	-0.156	-1.973	-0.839	7.36
Option 8	30	24.6	0.000	0.023	-2.515	-7.748	-4.581	40.03
	40	30.2	0.000	0.019	-2.444	-6.209	-4.479	32.21
	51	59.3	0.000	0.013	-2.341	-4.616	-4.039	24.38
	60	65.5	0.000	0.017	-2.408	-4.056	-4.552	25.13

D.4 Patient B1 (CHOP M3)

Patient B1 was a 12 year old female, with a completed extra-cardiac TCPC and left-sided PAVMs. The cardiac output was 3.25 L/min. Inflow distributions were not available and determined based on the data available for the earlier surgical planning

cases, resulting in 21%, 22%, 24% and 33% of the cardiac output coming in through the HepV, LSVC, AZ and SVC, respectively. The pre-operative GFD_{RPA} was 28%. The associated results are discussed in Section 9.3.1.

Table D-4: Efficiency metrics associated with Patient B1's pre-operative anatomy and the nine surgical planning options, under varying outflow conditions.

Option Number	GFD_{RPA} (%)	HFD_{RPA} (%)	Pressure (mmHg)						Power Loss (mW)
			HepV	AZ	LSVC	SVC	LPA	RPA	
Pre-Op	28	85.3	0.000	-0.224	-0.256	0.040	-0.393	-0.047	1.25
Option 1	28	9.0	0.000	-0.068	-0.097	-0.008	-0.248	-0.103	1.02
	40	33.7	0.000	-0.036	-0.021	-0.009	-0.127	-0.119	0.76
	50	90.0	0.000	0.000	-0.029	-0.048	-0.102	-0.156	0.82
Option 2	28	7.0	0.000	-0.077	-0.103	0.055	-0.265	-0.061	1.13
	40	36.5	0.000	-0.028	-0.052	0.000	-0.176	-0.130	0.98
	45	65.9	0.000	-0.026	-0.012	-0.013	-0.105	-0.131	0.76
	50	82.5	0.000	-0.007	-0.034	-0.018	-0.126	-0.150	0.93
Option 3	28	7.4	0.000	-0.083	-0.113	0.020	-0.289	-0.081	1.22
	40	52.0	0.000	-0.037	-0.021	0.001	-0.132	-0.121	0.82
	50	92.7	0.000	-0.003	-0.035	0.020	-0.112	-0.164	1.04
Option 4	28	1.2	0.000	-0.073	-0.089	0.013	-0.266	-0.084	1.13
	40	39.2	0.000	-0.029	-0.015	-0.001	-0.132	-0.121	0.82
	50	100.0	0.000	-0.001	-0.031	0.019	-0.110	-0.199	1.16
Option 5	28	0.0	0.000	-0.008	-0.034	0.021	-0.214	-0.072	1.06
	50	25.8	0.000	-0.004	-0.041	-0.168	-0.139	-0.314	1.21
	60	35.2	0.000	0.002	-0.038	-0.398	-0.120	-0.532	1.71
Option 6	28	0.0	0.000	-0.046	-0.199	-0.162	-0.450	-0.261	1.89
	50	2.4	0.000	-0.048	-0.209	-0.343	-0.448	-0.503	2.25
	60	18.7	0.000	-0.042	-0.204	-0.575	-0.462	-0.777	2.99
Option 7	28	25.0	0.000	0.089	-0.714	0.004	-0.845	-0.085	3.42
	40	53.7	0.000	0.065	-0.365	-0.065	-0.465	-0.140	1.78
	50	65.3	0.000	0.084	-0.329	-0.003	-0.377	-0.147	1.56
	60	75.2	0.000	0.084	-0.192	-0.006	-0.213	-0.168	1.23
Option 8	28	2.6	0.000	0.054	-0.304	-0.149	-0.395	-0.227	1.60
	40	15.9	0.000	0.053	-0.198	-0.133	-0.257	-0.262	1.32
	50	41.9	0.000	0.054	-0.139	-0.170	-0.181	-0.304	1.27
Option 9	20	20.9	0.000	-0.031	-0.077	0.001	-0.319	-0.056	1.38
	28	58.7	0.000	-0.018	-0.097	0.045	-0.264	-0.041	1.18
	50	93.4	0.000	0.001	-0.041	0.028	-0.140	-0.109	0.94
	60	100.0	0.000	0.006	-0.019	0.025	-0.068	-0.150	0.94

D.5 Patient B2 (CHOP M7)

Patient B2 was an 11 year old male, with a completed extra-cardiac TCPC and right-sided PAVMs. The cardiac output was 4.01 L/min, distributed as follows: 10%, 19%, 31%, 40% coming in through the HepV, LSVC, AZ and SVC, respectively. The pre-operative GFD_{RPA} was 35%. The corresponding results are discussed in Section 9.3.2.

Table D-5: Efficiency metrics associated with Patient B2's pre-operative anatomy and the seven surgical planning options, under varying outflow conditions.

	GFD_{RPA} (%)	HFD_{RPA} (%)	Pressure (mmHg)						Power Loss (mW)
			HepV	AZ	LSVC	SVC	LPA	RPA	
Pre-Op	40	0.0	0.000	0.066	0.268	0.079	-0.606	-0.681	5.64
	50	0.0	0.000	-0.011	0.289	0.006	-0.454	-1.028	5.61
	60	0.0	0.000	-0.101	0.339	-0.086	-0.360	-1.337	5.80
	70	0.0	0.000	-0.206	0.294	-0.173	-0.318	-1.823	7.06
Option 1	40	10.3	0.000	-0.080	0.024	-0.068	-0.841	-0.849	6.15
	50	0.4	0.000	-0.118	0.122	-0.109	-0.705	-1.111	6.04
	60	0.6	0.000	-0.077	0.311	-0.066	-0.411	-1.385	6.14
	70	0.3	0.000	-0.104	0.357	-0.073	-0.247	-1.791	7.07
Option 2	40	0.0	0.000	-0.047	0.188	-0.030	-0.605	-0.793	5.12
	50	0.7	0.000	-0.095	0.218	-0.073	-0.498	-1.068	5.19
	60	3.6	0.000	-0.105	0.305	-0.079	-0.339	-1.353	5.46
	70	12.6	0.000	-0.144	0.306	-0.096	-0.239	-1.753	6.36
Option 3	40	33.6	0.000	0.024	0.278	0.037	-0.511	-0.711	4.95
	50	45.7	0.000	-0.009	0.273	0.002	-0.424	-1.047	5.41
	55	37.4	0.000	-0.122	0.242	-0.098	-0.400	-1.266	5.39
	60	24.9	0.000	-0.082	0.304	-0.071	-0.374	-1.388	5.92
	70	22.7	0.000	-0.127	0.294	-0.103	-0.256	-1.789	6.72
Option 4	40	99.5	0.000	-0.003	-0.031	-0.110	-0.785	-0.945	6.10
	50	100.0	0.000	-0.001	0.152	-0.091	-0.566	-1.220	6.28
	60	100.0	0.000	-0.001	0.274	-0.086	-0.402	-1.573	7.10
	70	100.0	0.000	-0.005	0.344	-0.068	-0.220	-1.864	7.60
Option 5	30	0.4	0.000	0.040	-0.048	-0.172	-0.923	-0.499	5.47
	40	2.2	0.000	0.058	0.066	-0.149	-0.743	-0.750	5.32
	50	5.5	0.000	0.057	0.117	-0.165	-0.596	-1.017	5.21
	60	16.1	0.000	0.057	0.150	-0.234	-0.502	-1.464	6.11
Option 6	40	0.0	0.000	0.021	0.314	0.061	-0.641	-0.801	6.13
	50	71.0	0.000	0.000	0.270	-0.039	-0.469	-1.235	6.37
	60	100.0	0.000	-0.007	0.263	-0.091	-0.356	-1.738	7.85
Option 7	40	22.5	0.000	0.042	0.210	-0.112	-0.650	-0.739	5.14
	50	34.6	0.000	0.029	0.208	-0.142	-0.534	-1.079	5.43
	60	61.4	0.000	0.047	0.258	-0.088	-0.452	-1.400	6.34

D.6 Patient B3 (CHOP M2)

Patient B3 was 4 year old female whose hepatic baffle had been taken down, such the connection was equivalent to a second-stage Kawashima connection. She was diagnosed with bilateral PAVMs. The cardiac output was 2.93 L/min, 21%, 26%, 15%, 38% of which came through the HepV, LSVC, AZ and SVC. The pre-operative GFD_{RPA} was 39%. The corresponding results are discussed in Section 9.3.3.

Table D-6: Efficiency metrics associated with the fourteen surgical planning options implemented for Patient B3, under varying outflow conditions.

Option Number	GFD_{RPA} (%)	HFD_{RPA} (%)	Pressure (mmHg)						Power Loss (mW)
			HepV	AZ	LSVC	SVC	LPA	RPA	
Option 1	30	93.6	0.006	-1.658	-1.565	-0.064	-2.334	-0.372	5.69
	40	100.0	0.006	-0.754	-0.645	-0.075	-1.249	-0.602	3.38
	50	100.0	0.007	-0.206	-0.114	-0.052	-0.554	-0.855	2.88
	61	100.0	0.007	-0.025	0.062	-0.013	-0.264	-1.214	3.78
Option 2	30	100.0	0.007	-1.604	-1.521	-0.071	-2.329	-0.414	5.88
	40	100.0	0.007	-0.725	-0.618	-0.083	-1.213	-0.695	3.58
	50	100.0	0.007	-0.233	-0.141	-0.077	-0.579	-0.991	3.33
	61	100.0	0.007	-0.051	0.035	-0.045	-0.292	-1.350	4.35
Option 3	30	36.3	0.007	-1.624	-1.673	-0.060	-2.494	-0.363	6.30
	40	49.3	0.007	-0.801	-0.693	-0.055	-1.313	-0.596	3.59
	50	72.5	0.007	-0.185	-0.090	-0.047	-0.536	-0.910	3.14
	61	100.0	0.007	-0.033	0.056	-0.024	-0.275	-1.304	4.24
Option 4	30	2.2	0.007	-1.388	-1.284	-0.069	-2.028	-0.391	5.08
	40	24.6	0.005	-0.655	-0.543	-0.062	-1.103	-0.630	3.22
	50	52.6	0.007	-0.185	-0.092	-0.029	-0.531	-0.908	3.15
	61	100.0	0.007	-0.057	0.032	-0.029	-0.293	-1.318	4.25
Option 5	40	5.8	0.009	-0.310	-0.476	-0.064	-1.014	-0.617	3.22
	50	62.1	0.009	-0.097	-0.005	-0.158	-0.517	-1.264	4.04
Option 6	40	8.0	0.009	-0.135	-0.047	-0.052	-0.614	-0.631	2.61
	50	72.7	0.009	-0.097	-0.005	-0.158	-0.435	-1.145	3.42
	61	94.7	0.009	-0.095	-0.007	-0.379	-0.325	-1.779	5.05
Option 7	30	0.0	0.007	-0.303	-0.184	0.070	-0.898	-0.247	2.96
	40	21.5	0.007	-0.158	-0.059	-0.026	-0.607	-0.583	2.59
	50	64.1	0.007	-0.051	0.041	-0.344	-0.415	-1.233	3.46
	61	100.0	0.007	-0.031	0.058	-1.127	-0.275	-2.449	6.15
Option 8	40	20.4	0.007	-0.035	0.057	-0.061	-0.585	-0.614	2.80
	50	67.3	0.007	-0.046	0.048	-0.419	-0.425	-1.293	3.49
	61	90.4	0.007	-0.095	-0.004	-1.223	-0.352	-2.443	5.87

Table D-6 continued: Efficiency metrics associated with the fourteen surgical planning options implemented for Patient B3, under varying outflow conditions.

Option 9	40	10.0	0.007	-0.029	0.054	-0.086	-0.566	-0.638	2.72
	50	50.2	0.007	-0.076	0.009	-0.510	-0.475	-1.396	3.67
	61	64.3	0.007	-0.084	0.000	-1.436	-0.383	-2.649	6.26
Option 10	40	0.0	0.007	-0.083	-0.227	-0.345	-1.001	-0.890	4.94
	50	3.4	0.007	-0.080	-0.238	-0.756	-0.889	-1.607	5.82
	61	10.4	0.007	-0.083	-0.266	-1.878	-0.864	-3.090	7.70
	70	23.5	0.007	-0.077	-0.244	-2.702	-0.760	-4.097	13.10
Option 11	40	9.8	0.008	0.016	-1.366	-0.180	-1.851	-0.742	5.35
	50	48.0	0.011	0.012	-1.940	-0.522	-2.521	-1.378	6.93
	60	56.2	0.008	0.018	-0.356	-0.667	-0.566	-2.057	5.56
Option 12	50	20.4	0.009	-0.030	-0.170	-0.199	-0.603	-1.008	3.17
	61	43.8	0.009	-0.029	-0.108	-0.330	-0.411	-1.493	4.13
	70	62.9	0.008	1.041	-0.097	-0.508	-0.306	-1.959	6.45
Option 13	30	0.2	0.009	-0.032	-0.077	-0.058	-0.959	-0.449	3.65
	40	26.2	0.009	-0.015	-0.026	-0.055	-0.699	-0.748	3.41
	50	61.2	0.009	-0.005	0.028	-0.056	-0.454	-1.066	3.59
	61	100.0	0.009	0.003	0.088	-0.059	-0.209	-1.558	4.91
Option 14	30	7.0	0.010	-0.168	-0.072	-0.079	-0.774	-0.463	2.65
	40	26.5	0.010	-0.105	-0.010	-0.060	-0.583	-0.719	2.80
	50	62.1	0.010	-0.069	0.027	-0.050	-0.406	-1.055	3.34
	61	95.2	0.010	-0.042	0.049	-0.060	-0.273	-1.551	4.94

REFERENCES

1. Polar Electro. *The Heart's Function*. http://www.pursuit-performance.com.au/polar/html/polar/about_hrm.html 2005 [cited 2009 Sept].
2. Schneider Children's Hospital, N.Y. *Cardiovascular Disorders, Hypoplastic Left Heart Syndrome*. http://www.schneiderchildrenshospital.org/peds_html_fixed/peds/cardiac/hlhs.htm 2004 [cited 2009 Sept].
3. The Children's Heart Foundation. *Fact Sheets*. http://www.childrensheartfoundation.org/about-chf/fact-sheets 2009 [cited 2009 Sept].
4. National Heart and Lung Institute, N.I.H. *What Are Congenital Heart Defects?* http://www.nhlbi.nih.gov/health/dci/Diseases/chd/chd_what.html August 2009 [cited 2009 September].
5. Moller, J.H. and R.C. Anderson, *1,000 consecutive children with a cardiac malformation with 26- to 37-year follow-up*. Am J Cardiol, 1992. 70(6): p. 661-7.
6. Schneider Children's Hospital, N.Y. *Cardiovascular Disorders, Tricuspid Atresia*. http://www.schneiderchildrenshospital.org/peds_html_fixed/peds/cardiac/ta.htm 2004 [cited 2009 Sept].
7. Norwood, W.I., J.K. Kirklin, and S.P. Sanders, *Hypoplastic left heart syndrome: experience with palliative surgery.* Am J Cardiol, 1980. 45(1): p. 87-91.
8. Gilljam, T., B.W. McCrindle, J.F. Smallhorn, W.G. Williams, and R.M. Freedom, *Outcomes of left atrial isomerism over a 28-year period at a single institution.* J Am Coll Cardiol, 2000. 36(3): p. 908-16.
9. Cohen, M.S., *Clarifying anatomical complexity: Diagnosing heterotaxy syndrome in the fetus.* Progress in Pediatric Cardiology, 2006. 22(1): p. 61-70.
10. Blalock, A. and H.B. Taussig, *The surgical treatment of malformations of the heart in which there is pulmonary stenosis or pulmonary atresia.* J. Amer. Med. Assoc., 1945. 128: p. 189-202.
11. Fontan, F. and E. Baudet, *Surgical repair of tricuspid atresia.* Thorax, 1971. 26: p. 240-248.
12. Shemin, R.J., W.H. Merrill, J.S. Pfeifer, D.M. Conkle, and A.G. Morrow, *Evaluation of right atrial-pulmonary artery conduits for tricuspid atresia. Experimental study.* J Thorac Cardiovasc Surg, 1979. 77(5): p. 685-90.
13. Justino, H., L.N. Benson, and R.M. Freedom, *Development of unilateral pulmonary arteriovenous malformations due to unequal distribution of hepatic venous flow.* Circulation, 2001. 103(8): p. E39-40.
14. Pike, N.A., L.A. Vricella, J.A. Feinstein, M.D. Black, and B.A. Reitz, *Regression of severe pulmonary arteriovenous malformations after Fontan revision and "hepatic factor" rerouting.* Ann Thorac Surg, 2004. 78(2): p. 697-9.
15. Srivastava, D., T. Preminger, J.E. Lock, V. Mandell, J.F. Keane, J.E. Mayer, Jr., H. Kozakewich, and P.J. Spevak, *Hepatic venous blood and the development of*

pulmonary arteriovenous malformations in congenital heart disease. Circulation, 1995. 92(5): p. 1217-22.
16. Kreutzer, G., E. Galindez, H. Bono, C. De Palma, and J.P. Laura, *An operation for the correction of tricuspid atresia.* J Thorac Cardiovasc Surg, 1973. 66(4): p. 613-21.
17. Dobell, A.R., G.A. Trusler, J.F. Smallhorn, and W.G. Williams, *Atrial thrombi after the Fontan operation.* Ann Thorac Surg, 1986. 42(6): p. 664-7.
18. Driscoll, D.J., K.P. Offord, R.H. Feldt, H.V. Schaff, F.J. Puga, and G.K. Danielson, *Five- to fifteen-year follow-up after Fontan operation.* Circulation, 1992. 85(2): p. 469-96.
19. Fontan, F., J.W. Kirklin, G. Fernandez, F. Costa, D.C. Naftel, F. Tritto, and E.H. Blackstone, *Outcome after a "perfect" Fontan operation.* Circulation, 1990. 81(5): p. 1520-36.
20. Mair, D.D., F.J. Puga, and G.K. Danielson, *Late functional status of survivors of the Fontan procedure performed during the 1970s.* Circulation, 1992. 86(5 Suppl): p. II106-9.
21. Lardo, A.C., P.J. del Nido, S.A. Webber, I. Friehs, and E.G. Cape, *Hemodynamic effect of progressive right atrial dilatation in atriopulmonary connections.* J Thorac Cardiovasc Surg, 1997. 114(1): p. 2-8.
22. de Leval, M.R., P. Kilner, M. Gewillig, and C. Bull, *Total cavopulmonary connection: a logical alternative to atriopulmonary connection for complex Fontan operations. Experimental studies and early clinical experience.* J Thorac Cardiovasc Surg, 1988. 96(5): p. 682-95.
23. Marcelletti, C.F., F.L. Hanley, C. Mavroudis, D.B. McElhinney, R.F. Abella, S.M. Marianeschi, F. Seddio, V.M. Reddy, E. Petrossian, T. de la Torre, L. Colagrande, C.L. Backer, A. Cipriani, F.S. Iorio, and F. Fontan, *Revision of previous Fontan connections to total extracardiac cavopulmonary anastomosis: A multicenter experience.* J Thorac Cardiovasc Surg, 2000. 119(2): p. 340-6.
24. Pearl, J.M., H. Laks, D.G. Stein, D.C. Drinkwater, B.L. George, and R.G. Williams, *Total cavopulmonary anastomosis versus conventional modified Fontan procedure.* Ann Thorac Surg, 1991. 52(2): p. 189-96.
25. Podzolkov, V.P., S.B. Zaets, M.R. Chiaureli, B.G. Alekyan, L.M. Zotova, and I.G. Chernikh, *Comparative assessment of Fontan operation in modifications of atriopulmonary and total cavopulmonary anastomoses.* Eur J Cardiothorac Surg, 1997. 11(3): p. 458-65.
26. McGuirk, S.P., D.S. Winlaw, S.M. Langley, O.F. Stumper, J.V. de Giovanni, J.G. Wright, W.J. Brawn, and D.J. Barron, *The impact of ventricular morphology on midterm outcome following completion total cavopulmonary connection.* Eur J Cardiothorac Surg, 2003. 24(1): p. 37-46.
27. Norwood, W.I. and M.L. Jacobs, *Fontan's procedure in two stages.* Am J Surg, 1993. 166(5): p. 548-51.
28. Bridges, N.D., R.A. Jonas, J.E. Mayer, M.F. Flanagan, J.F. Keane, and A.R. Castaneda, *Bidirectional cavopulmonary anastomosis as interim palliation for high-risk Fontan candidates. Early results.* Circulation, 1990. 82(5 Suppl): p. IV170-6.

29. Tanoue, Y., A. Sese, Y. Imoto, and K. Joh, *Ventricular mechanics in the bidirectional glenn procedure and total cavopulmonary connection.* Ann Thorac Surg, 2003. 76(2): p. 562-6.
30. Children's Memorial Hospital. *Hypoplastic Left Heart Syndrome*. http://www.childrensmemorial.org/depts/cardio/thoracic/hlhs.aspx [cited 2009 Sept].
31. Children's Hospital Boston. *Hypoplastic Left Heart Syndrome - Heart Diagram.* http://www.childrenshospital.org/cfapps/mml/index.cfm?CAT=subtopic&SUBTOPIC_ID=1113 2009 [cited Sept 2009].
32. de Leval, M.R., G. Dubini, F. Migliavacca, H. Jalali, G. Camporini, A. Redington, and R. Pietrabissa, *Use of computational fluid dynamics in the design of surgical procedures: application to the study of competitive flows in cavo-pulmonary connections.* J Thorac Cardiovasc Surg, 1996. 111(3): p. 502-13.
33. de Zelicourt, D.A., K. Pekkan, L. Wills, K. Kanter, J. Forbess, S. Sharma, M. Fogel, and A.P. Yoganathan, *In vitro flow analysis of a patient-specific intraatrial total cavopulmonary connection.* Ann Thorac Surg, 2005. 79(6): p. 2094-102.
34. Petrossian, E., V.M. Reddy, D.B. McElhinney, G.P. Akkersdijk, P. Moore, A.J. Parry, L.D. Thompson, and F.L. Hanley, *Early results of the extracardiac conduit Fontan operation.* J Thorac Cardiovasc Surg, 1999. 117(4): p. 688-96.
35. Amodeo, A., L. Galletti, S. Marianeschi, S. Picardo, S. Giannico, P. Di Renzi, and C. Marcelletti, *Extracardiac Fontan operation for complex cardiac anomalies: seven years' experience.* J Thorac Cardiovasc Surg, 1997. 114(6): p. 1020-30; discussion 1030-1.
36. Haas, G.S., H. Hess, M. Black, J. Onnasch, F.W. Mohr, and J.A. van Son, *Extracardiac conduit fontan procedure: early and intermediate results.* Eur J Cardiothorac Surg, 2000. 17(6): p. 648-54.
37. Tam, V.K., B.E. Miller, and K. Murphy, *Modified Fontan without use of cardiopulmonary bypass.* Ann Thorac Surg, 1999. 68(5): p. 1698-703; discussion 1703-4.
38. Yalcinbas, Y.K., E. Erek, E. Salihoglu, A. Sarioglu, and T. Sarioglu, *Early results of extracardiac Fontan procedure with autologous pericardial tube conduit.* Thorac Cardiovasc Surg, 2005. 53(1): p. 37-40.
39. Mavroudis, C., V.R. Zales, C.L. Backer, A.J. Muster, and L.A. Latson, *Fenestrated Fontan with delayed catheter closure. Effects of volume loading and baffle fenestration on cardiac index and oxygen delivery.* Circulation, 1992. 86(5 Suppl): p. II85-92.
40. Thompson, L.D., E. Petrossian, D.B. McElhinney, N.A. Abrikosova, P. Moore, V.M. Reddy, and F.L. Hanley, *Is it necessary to routinely fenestrate an extracardiac fontan?* J Am Coll Cardiol, 1999. 34(2): p. 539-44.
41. Lemler, M.S., W.A. Scott, S.R. Leonard, D. Stromberg, and C. Ramaciotti, *Fenestration improves clinical outcome of the fontan procedure: a prospective, randomized study.* Circulation, 2002. 105(2): p. 207-12.
42. Francois, K., M. Tamim, T. Bove, K.D. Groote, D. De Wolf, D. Matthys, B. Suys, H. Verhaaren, and G. Van Nooten, *Is Morbidity Influenced by Staging in the Fontan Palliation? A Single Center Review.* Pediatr Cardiol, 2004.

43. DeGroff, C.G., J.D. Carlton, C.E. Weinberg, M.C. Ellison, R. Shandas, and L. Valdes-Cruz, *Effect of vessel size on the flow efficiency of the total cavopulmonary connection: in vitro studies.* Pediatr Cardiol, 2002. 23(2): p. 171-7.
44. Gaynor, J.W., N.D. Bridges, M.I. Cohen, W.T. Mahle, W.M. Decampli, J.M. Steven, S.C. Nicolson, and T.L. Spray, *Predictors of outcome after the Fontan operation: is hypoplastic left heart syndrome still a risk factor?* J Thorac Cardiovasc Surg, 2002. 123(2): p. 237-45.
45. Mair, D.D., F.J. Puga, and G.K. Danielson, *The Fontan procedure for tricuspid atresia: early and late results of a 25-year experience with 216 patients.* J Am Coll Cardiol, 2001. 37(3): p. 933-9.
46. Mott, A.R., T.L. Spray, J.W. Gaynor, R.I. Godinez, S.C. Nicolson, J.M. Steven, W.M. DeCampli, G.J. Schears, and G. Wernovsky, *Improved early results with cavopulmonary connections.* Cardiol Young, 2001. 11(1): p. 3-11.
47. Jayakumar, K.A., L.J. Addonizio, M.R. Kichuk-Chrisant, M.E. Galantowicz, J.M. Lamour, J.M. Quaegebeur, and D.T. Hsu, *Cardiac transplantation after the Fontan or Glenn procedure.* J Am Coll Cardiol, 2004. 44(10): p. 2065-72.
48. Sittiwangkul, R., A. Azakie, G.S. Van Arsdell, W.G. Williams, and B.W. McCrindle, *Outcomes of tricuspid atresia in the Fontan era.* Ann Thorac Surg, 2004. 77(3): p. 889-94.
49. Lee, J.R., J.S. Choi, C.H. Kang, E.J. Bae, Y.J. Kim, and J.R. Rho, *Surgical results of patients with a functional single ventricle.* Eur J Cardiothorac Surg, 2003. 24(5): p. 716-22.
50. Rychik, J. and M.I. Cohen, *Long-term outcome and complications of patients with single ventricle.* Progress in Pediatric Cardiology, 2002. 16(1): p. 89-103.
51. Huddleston, C.B., *The failing Fontan: options for surgical therapy.* Pediatr Cardiol, 2007. 28(6): p. 472-6.
52. Kiaffas, M.G., R. Van Praagh, C. Hanioti, and D.W. Green, *The modified Fontan procedure: morphometry and surgical implications.* Ann Thorac Surg, 1999. 67(6): p. 1746-53.
53. Mertens, L., D.J. Hagler, U. Sauer, J. Somerville, and M. Gewillig, *Protein-losing enteropathy after the Fontan operation: an international multicenter study. PLE study group.* J Thorac Cardiovasc Surg, 1998. 115(5): p. 1063-73.
54. Coon, P.D., J. Rychik, R.T. Novello, P.S. Ro, J.W. Gaynor, and T.L. Spray, *Thrombus formation after the Fontan operation.* Ann Thorac Surg, 2001. 71(6): p. 1990-4.
55. Kirklin, J.K., E.H. Blackstone, J.W. Kirklin, A.D. Pacifico, and L.M. Bargeron, Jr., *The Fontan operation. Ventricular hypertrophy, age, and date of operation as risk factors.* J Thorac Cardiovasc Surg, 1986. 92(6): p. 1049-64.
56. Senzaki, H., S. Masutani, H. Ishido, M. Taketazu, T. Kobayashi, N. Sasaki, H. Asano, T. Katogi, S. Kyo, and Y. Yokote, *Cardiac rest and reserve function in patients with Fontan circulation.* J Am Coll Cardiol, 2006. 47(12): p. 2528-35.
57. Altmann, K., B.F. Printz, D.E. Solowiejczky, W.M. Gersony, J. Quaegebeur, and H.D. Apfel, *Two-dimensional echocardiographic assessment of right ventricular function as a predictor of outcome in hypoplastic left heart syndrome.* Am J Cardiol, 2000. 86(9): p. 964-8.

58. Sundareswaran, K.S., K.R. Kanter, H.D. Kitajima, R. Krishnankutty, J.F. Sabatier, W.J. Parks, S. Sharma, A.P. Yoganathan, and M. Fogel, *Impaired power output and cardiac index with hypoplastic left heart syndrome: a magnetic resonance imaging study.* Ann Thorac Surg, 2006. 82(4): p. 1267-75; discussion 1275-7.
59. Senzaki, H., S. Masutani, J. Kobayashi, T. Kobayashi, N. Sasaki, H. Asano, S. Kyo, Y. Yokote, and A. Ishizawa, *Ventricular afterload and ventricular work in fontan circulation: comparison with normal two-ventricle circulation and single-ventricle circulation with blalock-taussig shunts.* Circulation, 2002. 105(24): p. 2885-92.
60. Kiesewetter, C.H., N. Sheron, J.J. Vettukattill, N. Hacking, B. Stedman, H. Millward-Sadler, M. Haw, R. Cope, A.P. Salmon, M.C. Sivaprakasam, T. Kendall, B.R. Keeton, J.P. Iredale, and G.R. Veldtman, *Hepatic changes in the failing Fontan circulation.* Heart, 2007. 93(5): p. 579-84.
61. Procelewska, M., J. Kolcz, K. Januszewska, T. Mroczek, and E. Malec, *Coagulation abnormalities and liver function after hemi-Fontan and Fontan procedures - the importance of hemodynamics in the early postoperative period.* Eur J Cardiothorac Surg, 2007. 31(5): p. 866-72.
62. Guyton, A.C., *Cardiac Output, Venous Return, and Their Regulation.* 1961: Saundersm Philadelphia, PA.
63. Guyton, A.C., B. Abernathy, J.B. Langston, B.N. Kaufmann, and H.M. Fairchild, *Relative importance of venous and arterial resistances in controlling venous return and cardiac output.* Am J Physiol, 1959. 196(5): p. 1008-14.
64. Torres Pharm, M.D. and J.A. Nieves, *Progress in Congenital Cardiac Care for Newborns and Infants: The Emerging Role of "Off-label" Medications* Neonatal Pharmacology, 2009. 9(1): p. 18-30.
65. Sundareswaran, K.S., K. Pekkan, L.P. Dasi, K. Whitehead, S. Sharma, K.R. Kanter, M.A. Fogel, and A.P. Yoganathan, *The total cavopulmonary connection resistance: a significant impact on single ventricle hemodynamics at rest and exercise.* Am J Physiol Heart Circ Physiol, 2008. 295(6): p. H2427-35.
66. Brown, J.W., M. Ruzmetov, P. Vijay, M.D. Rodefeld, and M.W. Turrentine, *Pulmonary arteriovenous malformations in children after the Kawashima operation.* Ann Thorac Surg, 2005. 80(5): p. 1592-6.
67. Duncan, B.W. and S. Desai, *Pulmonary arteriovenous malformations after cavopulmonary anastomosis.* Ann Thorac Surg, 2003. 76(5): p. 1759-66.
68. Moore, J.W., W.C. Kirby, W.A. Madden, and N.S. Gaither, *Development of pulmonary arteriovenous malformations after modified Fontan operations.* J Thorac Cardiovasc Surg, 1989. 98(6): p. 1045-50.
69. Pandurangi, U.M., M.J. Shah, R. Murali, and K.M. Cherian, *Rapid onset of pulmonary arteriovenous malformations after cavopulmonary anastomosis.* Ann Thorac Surg, 1999. 68(1): p. 237-9.
70. Shinohara, T. and T. Yokoyama, *Pulmonary arteriovenous malformation in patients with total cavopulmonary shunt: what role does lack of hepatic venous blood flow to the lungs play?* Pediatr Cardiol, 2001. 22(4): p. 343-6.
71. AboulHosn, J., S. Danon, D. Levi, Y. Castellon, J. Child, and J. Moore, *Regression of pulmonary arteriovenous malformations after transcatheter*

reconnection of the pulmonary arteries in patients with unidirectional Fontan. Congenit Heart Dis, 2007. 2(3): p. 179-84.
72. Steinberg, J., G.M. Alfieris, B. Brandt, 3rd, F. Smith, C.J. Byrum, G.W. Fink, and J. Halter, *New approach to the surgical management of pulmonary arteriovenous malformations after cavopulmonary anastomosis.* Ann Thorac Surg, 2003. 75(5): p. 1640-2.
73. Uemura, H., T. Yagihara, R. Hattori, Y. Kawahira, S. Tsukano, and K. Watanabe, *Redirection of hepatic venous drainage after total cavopulmonary shunt in left isomerism.* Ann Thorac Surg, 1999. 68(5): p. 1731-5.
74. Wu, I.H. and K.H. Nguyen, *Redirection of hepatic drainage for treatment of pulmonary arteriovenous malformations following the Fontan procedure.* Pediatr Cardiol, 2006. 27(4): p. 519-22.
75. KrishnankuttyRema, R., L.P. Dasi, K. Pekkan, K. Sundareswaran, M. Fogel, S. Sharma, K. Kanter, T. Spray, and A.P. Yoganathan, *Quantitative analysis of extracardiac versus intraatrial Fontan anatomic geometries.* Ann Thorac Surg, 2008. 85(3): p. 810-7.
76. Fogel, M.A., P.M. Weinberg, J. Rychik, A. Hubbard, M. Jacobs, T.L. Spray, and J. Haselgrove, *Caval contribution to flow in the branch pulmonary arteries of Fontan patients with a novel application of magnetic resonance presaturation pulse.* Circulation, 1999. 99(9): p. 1215-21.
77. Hjortdal, V.E., K. Emmertsen, E. Stenbog, T. Frund, M.R. Schmidt, O. Kromann, K. Sorensen, and E.M. Pedersen, *Effects of exercise and respiration on blood flow in total cavopulmonary connection: a real-time magnetic resonance flow study.* Circulation, 2003. 108(10): p. 1227-31.
78. Be'eri, E., S.E. Maier, M.J. Landzberg, T. Chung, and T. Geva, *In vivo evaluation of Fontan pathway flow dynamics by multidimensional phase-velocity magnetic resonance imaging.* Circulation, 1998. 98(25): p. 2873-82.
79. Frakes, D.H., M.J. Smith, D.A. de Zélicourt, K. Pekkan, and A.P. Yoganathan, *Three-dimensional velocity reconstruction.* J Biomech Eng, 2004. 126(6): p. 727-35.
80. Sundareswaran, K., *Characterizing Single Ventricle Hemodynamics Using Phase Contrast Magnetic Resonance Imaging*, in *Biomedical Engineering*. 2008, Georgia Institute of Technology.
81. Sundareswaran, K.S., D. de Zelicourt, S. Sharma, K.R. Kanter, T.L. Spray, J. Rossignac, F. Sotiropoulos, M.A. Fogel, and A.P. Yoganathan, *Correction of pulmonary arteriovenous malformation using image-based surgical planning.* JACC Cardiovasc Imaging, 2009. 2(8): p. 1024-30.
82. Sharma, S., S. Goudy, P. Walker, S. Panchal, A. Ensley, K. Kanter, V. Tam, D. Fyfe, and A. Yoganathan, *In vitro flow experiments for determination of optimal geometry of total cavopulmonary connection for surgical repair of children with functional single ventricle.* J Am Coll Cardiol, 1996. 27(5): p. 1264-9.
83. Gerdes, A., J. Kunze, G. Pfister, and H.H. Sievers, *Addition of a small curvature reduces power losses across total cavopulmonary connections.* Ann Thorac Surg, 1999. 67(6): p. 1760-4.
84. Ryu, K., T.M. Healy, A.E. Ensley, S. Sharma, C. Lucas, and A.P. Yoganathan, *Importance of accurate geometry in the study of the total cavopulmonary*

connection: computational simulations and in vitro experiments. Ann Biomed Eng, 2001. 29(10): p. 844-53.
85. Khunatorn, Y., R. Shandas, C. DeGroff, and S. Mahalingam, *Comparison of in vitro velocity measurements in a scaled total cavopulmonary connection with computational predictions.* Ann Biomed Eng, 2003. 31(7): p. 810-22.
86. Hsia, T.Y., F. Migliavacca, S. Pittaccio, A. Radaelli, G. Dubini, G. Pennati, and M. de Leval, *Computational fluid dynamic study of flow optimization in realistic models of the total cavopulmonary connections.* J Surg Res, 2004. 116(2): p. 305-13.
87. Pekkan, K., D. de Zelicourt, L. Ge, F. Sotiropoulos, D. Frakes, M.A. Fogel, and A.P. Yoganathan, *Physics-driven CFD modeling of complex anatomical cardiovascular flows-a TCPC case study.* Ann Biomed Eng, 2005. 33(3): p. 284-300.
88. Pekkan, K., H.D. Kitajima, D. de Zelicourt, J.M. Forbess, W.J. Parks, M.A. Fogel, S. Sharma, K.R. Kanter, D. Frakes, and A.P. Yoganathan, *Total cavopulmonary connection flow with functional left pulmonary artery stenosis: angioplasty and fenestration in vitro.* Circulation, 2005. 112(21): p. 3264-71.
89. de Zelicourt, D.A., K. Pekkan, J. Parks, K. Kanter, M. Fogel, and A.P. Yoganathan, *Flow study of an extracardiac connection with persistent left superior vena cava.* J Thorac Cardiovasc Surg, 2006. 131(4): p. 785-91.
90. Marsden, A.L., I.E. Vignon-Clementel, F.P. Chan, J.A. Feinstein, and C.A. Taylor, *Effects of exercise and respiration on hemodynamic efficiency in CFD simulations of the total cavopulmonary connection.* Ann Biomed Eng, 2007. 35(2): p. 250-63.
91. Wang, C., K. Pekkan, D. de Zelicourt, M. Horner, A. Parihar, A. Kulkarni, and A.P. Yoganathan, *Progress in the CFD modeling of flow instabilities in anatomical total cavopulmonary connections.* Ann Biomed Eng, 2007. 35(11): p. 1840-56.
92. Whitehead, K.K., K. Pekkan, H.D. Kitajima, S.M. Paridon, A.P. Yoganathan, and M.A. Fogel, *Nonlinear power loss during exercise in single-ventricle patients after the Fontan: insights from computational fluid dynamics.* Circulation, 2007. 116(11 Suppl): p. I165-71.
93. Kitajima, H.D., K.S. Sundareswaran, T.Z. Teisseyre, G.W. Astary, W.J. Parks, O. Skrinjar, J.N. Oshinski, and A.P. Yoganathan, *Comparison of particle image velocimetry and phase contrast MRI in a patient-specific extracardiac total cavopulmonary connection.* J Biomech Eng, 2008. 130(4): p. 041004.
94. Migliavacca, F., G. Dubini, E.L. Bove, and M.R. de Leval, *Computational fluid dynamics simulations in realistic 3-D geometries of the total cavopulmonary anastomosis: the influence of the inferior caval anastomosis.* J Biomech Eng, 2003. 125(6): p. 805-13.
95. de Zélicourt, D., *A Mechanical Fluid Assessment of Anatomical Models of the Total Cavopulmonary Connection (TCPC)*, in *Biomedical Engineering*. 2004.
96. Dasi, L.P., R. Krishnankuttyrema, H.D. Kitajima, K. Pekkan, K.S. Sundareswaran, M. Fogel, S. Sharma, K. Whitehead, K. Kanter, and A.P. Yoganathan, *Fontan hemodynamics: importance of pulmonary artery diameter.* J Thorac Cardiovasc Surg, 2009. 137(3): p. 560-4.

97. Dasi, L.P., K. Pekkan, H.D. Katajima, and A.P. Yoganathan, *Functional analysis of Fontan energy dissipation.* J Biomech, 2008. 41(10): p. 2246-52.
98. Soerensen, D.D., K. Pekkan, D. de Zelicourt, S. Sharma, K. Kanter, M. Fogel, and A.P. Yoganathan, *Introduction of a new optimized total cavopulmonary connection.* Ann Thorac Surg, 2007. 83(6): p. 2182-90.
99. Marsden, A.L., A.J. Bernstein, V.M. Reddy, S.C. Shadden, R.L. Spilker, F.P. Chan, C.A. Taylor, and J.A. Feinstein, *Evaluation of a novel Y-shaped extracardiac Fontan baffle using computational fluid dynamics.* J Thorac Cardiovasc Surg, 2009. 137(2): p. 394-403 e2.
100. Marsden, A.L., J.A. Feinstein, and C.A. Taylor, *A computational framework for derivative-free optimization of cardiovascular geometries.* Computer Methods in Applied Mechanics and Engineering, 2008. 197(21-24): p. 1890-1905.
101. Pekkan, K., B. Whited, K. Kanter, S. Sharma, D. de Zelicourt, K. Sundareswaran, D. Frakes, J. Rossignac, and A.P. Yoganathan, *Patient-specific surgical planning and hemodynamic computational fluid dynamics optimization through free-form haptic anatomy editing tool (SURGEM).* Med Biol Eng Comput, 2008. 46(11): p. 1139-52.
102. O'Leary, S.J., M.A. Hutchins, D.R. Stevenson, C. Gunn, A. Krumpholz, G. Kennedy, M. Tykocinski, M. Dahm, and B. Pyman. *Validation of a Networked Virtual Reality Simulation of Temporal Bone Surgery*. 2008: Lippincott Williams & Wilkins.
103. Rosen, J.M., S.A. Long, D.M. McGrath, and S.E. Greer, *Simulation in plastic surgery training and education: the path forward.* Plast Reconstr Surg, 2009. 123(2): p. 729-38; discussion 739-40.
104. Hart, R. and K. Karthigasu, *The benefits of virtual reality simulator training for laparoscopic surgery.* Curr Opin Obstet Gynecol, 2007. 19(4): p. 297-302.
105. Orlando, W., J. Hertzberg, R. Shandas, and C. DeGroff, *Reverse flow in compliant vessels and its implications for the Fontan procedure: numerical studies.* Biomed Sci Instrum, 2002. 38: p. 321-6.
106. Minich, L.L., L.Y. Tani, A.L. Olson, G.S. Orsmond, and R.E. Shaddy, *Reversal of flow in the left pulmonary artery after cavopulmonary connection.* J Am Soc Echocardiogr, 1996. 9(2): p. 202-5.
107. Penny, D.J. and A.N. Redington, *Doppler echocardiographic evaluation of pulmonary blood flow after the Fontan operation: the role of the lungs.* Br Heart J, 1991. 66(5): p. 372-4.
108. DeGroff, C.G. and R. Shandas, *Designing the optimal Total Cavopulmonary Connection: pulsatile versus steady flow experiments.* Med Sci Monit, 2002. 8(3): p. MT41-5.
109. Clipp, R.B. and B.N. Steele. *A Dynamic Boundary Condition For The Pulmonary Vasculature*. in *ASME Summer Bioengineering Conference*. 2008.
110. Clipp, R.B. and B.N. Steele, *Impedance Boundary Conditions for the Pulmonary Vasculature including the Effects of Geometry, Compliance and Respiration.* IEEE Transactions on Biomedical Engineering, 2009. accepted.
111. Pekkan, K., D. Frakes, D. De Zelicourt, C.W. Lucas, W.J. Parks, and A.P. Yoganathan, *Coupling pediatric ventricle assist devices to the Fontan circulation: simulations with a lumped-parameter model.* ASAIO J, 2005. 51(5): p. 618-28.

112. Khunatorn, Y., S. Mahalingam, C.G. DeGroff, and R. Shandas, *Influence of connection geometry and SVC-IVC flow rate ratio on flow structures within the total cavopulmonary connection: a numerical study.* J Biomech Eng, 2002. 124(4): p. 364-77.
113. Freitas, C.J., *Perspective: Selected benchmarks from commercial CFD codes.* J. Fluids Eng. , 1995. 117.
114. Laccarino, G., *Predictions of a turbulent separated flow using commercial CFD codes.* J. Fluids Eng. , 2001. 123(1): p. 819-28.
115. Freitas, C.J., *Journal of fluids engineering editorial policy statement on the control of numerical accuracy.* J. Fluids Eng. , 1993. 115(1): p. 339-40.
116. Chorin, A.J., *A numerical method for solving incompressible viscous flow problems.* Journal of Computational Physics, 1967. 2(1): p. 12.
117. Harlow, F.H. and J.E. Welch, *Numerical Calculation of Time-Dependent Viscous Incompressible Flow of Fluid with Free Surface* Physics of Fluids, 1965. 8(5): p. 2182.
118. Armfield, S. and R. Street, *An analysis and comparison of the time accuracy of fractional-step methods for the Navier-Stokes equations on staggered grids.* International Journal for Numerical Methods in Fluids, 2002. 38(3): p. 255-282.
119. Armfield, S. and R. Street, *An analysis and comparison of the time accuracy of fractional-step methods for the Navier-Stokes equations on staggered grids.* International Journal for Numerical Methods in Fluids, 2002. 38(3): p. 255-282.
120. Kim, J. and P. Moin, *Application of a fractional-step method to incompressible Navier-Stokes equations.* Journal of Computational Physics, 1985. 59(2): p. 308-323.
121. Ge, L. and F. Sotiropoulos, *A numerical method for solving the 3D unsteady incompressible Navier-Stokes equations in curvilinear domains with complex immersed boundaries.* Journal of Computational Physics, 2007. In Press, Corrected Proof: p. 986.
122. Gilmanov, A. and F. Sotiropoulos, *A hybrid Cartesian/immersed boundary method for simulating flows with 3D, geometrically complex, moving bodies.* Journal of Computational Physics, 2005. 207(2): p. 457-492.
123. Ge, L. and F. Sotiropoulos, *A Numerical Method for Solving the 3D Unsteady Incompressible Navier-Stokes Equations in Curvilinear Domains with Complex Immersed Boundaries.* J Comput Phys, 2007. 225(2): p. 1782-1809.
124. Figueroa, C.A., I.E. Vignon-Clementel, K.E. Jansen, T.J.R. Hughes, and C.A. Taylor, *A coupled momentum method for modeling blood flow in three-dimensional deformable arteries.* Computer Methods in Applied Mechanics and Engineering, 2006. 195(41-43): p. 5685.
125. Taylor, C.A., T.J.R. Hughes, and C.K. Zarins, *Effect of exercise on hemodynamic conditions in the abdominal aorta.* Journal of Vascular Surgery, 1999. 29(6): p. 1077.
126. Zhang, Y., Y. Bazilevs, S. Goswami, C.L. Bajaj, and T.J.R. Hughes, *Patient-specific vascular NURBS modeling for isogeometric analysis of blood flow.* Computer Methods in Applied Mechanics and Engineering, 2007. 196(29-30): p. 2943.

127. Le, D.V., B.C. Khoo, and J. Peraire, *An immersed interface method for viscous incompressible flows involving rigid and flexible boundaries.* Journal of Computational Physics, 2006. 220(1): p. 109-138.
128. Fauci, L.J. and C.S. Peskin, *A computational model of aquatic animal locomotion.* Journal of Computational Physics, 1988. 77(1): p. 85-108.
129. Mittal, R. and G. Iaccarino, *IMMERSED BOUNDARY METHODS.* 2005. p. 239-261.
130. Udaykumar, H.S., R. Mittal, P. Rampunggoon, and A. Khanna, *A Sharp Interface Cartesian Grid Method for Simulating Flows with Complex Moving Boundaries.* Journal of Computational Physics, 2001. 174(1): p. 345.
131. Ye, T., R. Mittal, H.S. Udaykumar, and W. Shyy, *An Accurate Cartesian Grid Method for Viscous Incompressible Flows with Complex Immersed Boundaries.* Journal of Computational Physics, 1999. 156(2): p. 209.
132. Bayyuk, S.A., K.G. Powell, and B. van Leer, *An Algorithm for the Simulation of 2-D Unsteady Inviscid Flows around Moving and Deforming Bodies of Aribitrary Geometry*. 1993, AIAA Paper-93-3391.
133. Peskin, C.S., *Numerical analysis of blood flow in the heart.* Journal of Computational Physics, 1977. 25(3): p. 220.
134. Peskin, C.S. and D.M. McQueen, *A three-dimensional computational method for blood flow in the heart. 1. Immersed elastic fibers in a viscous incompressible fluid.* Journal of Computational Physics, 1989. 81(2): p. 372-405.
135. Griffith, B.E., R.D. Hornung, D.M. McQueen, and C.S. Peskin, *An adaptive, formally second order accurate version of the immersed boundary method.* Journal of Computational Physics, 2007. 223(1): p. 10.
136. Fadlun, E.A., R. Verzicco, P. Orlandi, and J. Mohd-Yusof, *Combined immersed-boundary finite-difference methods for threedimensional complex flow simulations.* J. Comput. Phys., 2000. 161: p. 35-60.
137. Mohd-Yusof, J., *Combined immersed boundaries/b-splines methods for simulations of flows in complex geometries.* Ctr annual research briefs, Stanford University, NASA Ames, 1997.
138. Choi, J.-I., R.C. Oberoi, J.R. Edwards, and J.A. Rosati, *An immersed boundary method for complex incompressible flows.* Journal of Computational Physics, 2007. 224(2): p. 757-784.
139. McQueen, D.M. and C.S. Peskin, *A three-dimensional computer model of the human heart for studying cardiac fluid dynamics.* ACM SIGGRAPH Computer Graphics, 2000. 34(1): p. 56-60.
140. Yokoi, K., F. Xiao, H. Liu, and K. Fukasaku, *Three-dimensional numerical simulation of flows with complex geometries in a regular Cartesian grid and its application to blood flow in cerebral artery with multiple aneurysms.* Journal of Computational Physics, 2005. 202(1): p. 1-19.
141. Rantakokko, J., *Partitioning strategies for structured multiblock grids.* Parallel Computing, 2000. 26(12): p. 1661-1680.
142. McCorquodale, P., P. Colella, D.P. Grote, and J.-L. Vay, *A node-centered local refinement algorithm for Poisson's equation in complex geometries.* Journal of Computational Physics, 2004. 201(1): p. 34.

143. Schwartz, P., M. Barad, P. Colella, and T. Ligocki, *A Cartesian grid embedded boundary method for the heat equation and Poisson's equation in three dimensions.* Journal of Computational Physics, 2006. 211(2): p. 531.
144. McCorquodale, P., P. Colella, and H. Johansen, *A Cartesian Grid Embedded Boundary Method for the Heat Equation on Irregular Domains.* Journal of Computational Physics, 2001. 173(2): p. 620.
145. Roma, A.M., C.S. Peskin, and M.J. Berger, *An Adaptive Version of the Immersed Boundary Method.* Journal of Computational Physics, 1999. 153(2): p. 509.
146. Khokhlov, A.M., *Fully Threaded Tree Algorithms for Adaptive Refinement Fluid Dynamics Simulations.* Journal of Computational Physics, 1998. 143(2): p. 519.
147. Losasso, F., R. Fedkiw, and S. Osher, *Spatially adaptive techniques for level set methods and incompressible flow.* Computers & Fluids, 2006. 35(10): p. 995-1010.
148. Nielsen, M. and K. Museth, *Dynamic Tubular Grid: An Efficient Data Structure and Algorithms for High Resolution Level Sets.* Journal of Scientific Computing, 2006. 26(3): p. 261-299.
149. Marino, B.S., *Outcomes after the Fontan procedure.* Curr Opin Pediatr, 2002. 14(5): p. 620-6.
150. Gersony, D.R. and W.M. Gersony, *Management of the Postoperative Fontan patient.* Progress in Pediatric Cardiology, 2003. 17(1): p. 73-79.
151. Ensley, A.E., A. Ramuzat, T.M. Healy, G.P. Chatzimavroudis, C. Lucas, S. Sharma, R. Pettigrew, and A.P. Yoganathan, *Fluid mechanic assessment of the total cavopulmonary connection using magnetic resonance phase velocity mapping and digital particle image velocimetry.* Ann Biomed Eng, 2000. 28(10): p. 1172-83.
152. Soerensen, D.D., K. Pekkan, K.S. Sundareswaran, and A.P. Yoganathan. *New power loss optimized Fontan connection evaluated by calculation of power loss using high resolution PC-MRI and CFD.* in *Conf Proc IEEE Eng Med Biol Soc*. 2004.
153. Ge, L., L.P. Dasi, F. Sotiropoulos, and A.P. Yoganathan, *Characterization of hemodynamic forces induced by mechanical heart valves: Reynolds vs. viscous stresses.* Ann Biomed Eng, 2008. 36(2): p. 276-97.
154. Ge, L., S.C. Jones, F. Sotiropoulos, T.M. Healy, and A.P. Yoganathan, *Numerical simulation of flow in mechanical heart valves: grid resolution and the assumption of flow symmetry.* J Biomech Eng, 2003. 125(5): p. 709-18.
155. Ge, L., H.L. Leo, F. Sotiropoulos, and A.P. Yoganathan, *Flow in a mechanical bileaflet heart valve at laminar and near-peak systole flow rates: CFD simulations and experiments.* J Biomech Eng, 2005. 127(5): p. 782-97.
156. Borazjani, I., L. Ge, and F. Sotiropoulos, *High-Resolution Fluid-Structure Interaction Simulations of Flow Through a Bi-Leaflet Mechanical Heart Valve in an Anatomic Aorta.* Ann Biomed Eng, 2009.
157. Frakes, D.H., C.P. Conrad, T.M. Healy, J.W. Monaco, M. Fogel, S. Sharma, M.J. Smith, and A.P. Yoganathan, *Application of an adaptive control grid interpolation technique to morphological vascular reconstruction.* IEEE Trans Biomed Eng, 2003. 50(2): p. 197-206.

158. Frakes, D.H., M.J. Smith, J. Parks, S. Sharma, S.M. Fogel, and A.P. Yoganathan, *New techniques for the reconstruction of complex vascular anatomies from MRI images.* J Cardiovasc Magn Reson, 2005. 7(2): p. 425-32.
159. LLamas, A., Powell, A, Rossignac,J, Shaw,C, *Twister: A space-warp operator for the two-handed editing of 3D shapes.* Proceedings of ACM SIGGRAPH, 2003. 22(3): p. 663-668.
160. Gargus, J., B. Kim, I. Llmas, and J. Rossignac, *Finger sculpturing with digital clay*. 2002, GVU Tech.
161. Rossignac, J., K. Pekkan, B. Whited, K. Kanter, and A.P. Yoganathan. *SURGEM: Next generation CAD tools targeting anatomical complexity for patient-specific surgical planning*. in *2006 Summer Bioengineering Conference*. 2006. Florida.
162. Llamas, I., A. Powell, J. Rossignac, and C. Shaw. *Bender: Deforming and animating 3D shapes by bending and twisting a virtual ribbon with both hands*. in *ACM Symposium on Solid and Physical Modeling*. 2005. MIT, Boston, MA.
163. Sundareswaran, K.S., D.H. Frakes, and A.P. Yoganathan. *Rule-based fuzzy vector median filters for 3D phase contrast MRI segmentation*. 2008: SPIE.
164. Gilmanov, A. and F. Sotiropoulos, *A hybrid Cartesian/immersed boundary method for simulating flows with 3D, geometrically complex, moving bodies.* Journal of Computational Physics, 2005. 207(2): p. 457.
165. Harlow, F.H. and J.E. Welch, *Numerical calculation of time-dependent viscous incompressible flows with free surface.* Physics of Fluids, 1965. 8: p. 2182–9.
166. Gilmanov, A., F. Sotiropoulos, and E. Balaras, *A general reconstruction algorithm for simulating flows with complex 3D immersed boundaries on Cartesian grids.* Journal of Computational Physics, 2003. 191(2): p. 660-669.
167. Borazjani, I., L. Ge, and F. Sotiropoulos, *Curvilinear immersed boundary method for simulating fluid structure interaction with complex 3d rigid bodies.* Journal of Computational Physics, 2008. 227(16): p. 7587-7620.
168. Buzbee, B.L., G.H. Golub, and C.W. Nielson, *Direct methods for solving poissons equations.* SIAM Journal of Numerical Analysis, 1970. 7(4): p. 627–56.
169. Swarztrauber, P.N., *A direct method for the discrete solution of separable elliptic equations.* SIAM Journal on Numerical Analysis, 1974. 11(6): p. 1136–50.
170. Kelley, C.T., *Iterative methods for linear and nonlinear equations*. 1995: Society for Industrial Mathematics.
171. Saad, Y., *A flexible inner–outer preconditioned GMRES.* SIAM Journal on Scientific Computing, 1993. 14: p. 461–9.
172. der Vorst, H., *BiCGSTAB: A fast and smoothly converging variant of BiCG for the solution of non-symmetric linear systems.* SIAM Journal of Scientific and Statistical Computing, 1992. 13: p. 631–44.
173. Balay, S., K. Buschelman, V. Eijkhout, W.D. Gropp, D. Kaushik, M.G. Knepley, L.C. McInnes, B.F. Smith, and H. Zhang, *PETSC Users Manual*. 2004, Argonne National Laboratory.
174. Balay, S., K. Buschelman, W.D. Gropp, D. Kaushik, M.G. Knepley, L.C. McInnes, B.F. Smith, and H. Zhang. *PETSc Web page <http:// www.mcs.anl.gov/petsc>*. 2001 [cited 2010].
175. Bovendeerd, P.H.M., A.A. van Steenhoven, F.N. van de Vosse, and G. Vossers, *Steady Entry Flow in a Curved Pipe.* J. Fluid. Mech, 1987. 177: p. 233-246.

176. Ensley, A.E., P. Lynch, G.P. Chatzimavroudis, C. Lucas, S. Sharma, and A.P. Yoganathan, *Toward designing the optimal total cavopulmonary connection: an in vitro study.* The Annals of Thoracic Surgery, 1999. 68(4): p. 1384-1390.
177. de Zelicourt, D., K. Pekkan, H. Kitajima, D. Frakes, and A.P. Yoganathan, *Single-step stereolithography of complex anatomical models for optical flow measurements.* J Biomech Eng, 2005. 127(1): p. 204-7.
178. Hunt, J.C.R., A. Wray, and P. Moin, *Eddies, stream, and convergence zones in turbulent flows.* Technical Report, Center for Turbulence Research Report CTR-S88, 1988.
179. Kanter, J., C. Haggerty, K. Desai, L. Bracaglia, and A.P. Yoganathan. *Effect of Pulsatile Flow in an in vitro model of the Total Cavopulmonary Connection.* in *Biomedical Engineering Society annual meeting*. 2009. Pittsburgh, PA.
180. Womersley, J.R., *Method for the calculation of velocity, rate of flow and viscous drag in arteries when the pressure gradient is known.* J Physiol, 1955. 127(3): p. 553-63.
181. Whitehead, K.K., K.S. Sundareswaran, W.J. Parks, M.A. Harris, A.P. Yoganathan, and M.A. Fogel, *Blood flow distribution in a large series of patients having the Fontan operation: a cardiac magnetic resonance velocity mapping study.* J Thorac Cardiovasc Surg, 2009. 138(1): p. 96-102.
182. Atz, A.M., M.S. Cohen, L.A. Sleeper, B.W. McCrindle, M. Lu, A. Prakash, R.E. Breitbart, R.V. Williams, C.J. Sang, and G. Wernovsky, *Functional state of patients with heterotaxy syndrome following the Fontan operation.* Cardiol Young, 2007. 17 Suppl 2: p. 44-53.
183. de Zelicourt, D.A., K. Pekkan, L. Wills, K. Kanter, J. Forbess, S. Sharma, M. Fogel, and A.P. Yoganathan, *In Vitro Flow Analysis of a Patient-Specific Intraatrial Total Cavopulmonary Connection.* The Annals of Thoracic Surgery, 2005. 79(6): p. 2094.
184. Ovroutski, S., P. Ewert, V. Alexi-Meskishvili, K. Holscher, O. Miera, B. Peters, R. Hetzer, and F. Berger, *Absence of pulmonary artery growth after fontan operation and its possible impact on late outcome.* Ann Thorac Surg, 2009. 87(3): p. 826-31.